



PHD

## The Synthesis and Application of Metal–Based Complexes for Sustainable Catalysis

Driscoll, Oliver

*Award date:*  
2022

*Awarding institution:*  
University of Bath

[Link to publication](#)

### Alternative formats

If you require this document in an alternative format, please contact:  
[openaccess@bath.ac.uk](mailto:openaccess@bath.ac.uk)

Copyright of this thesis rests with the author. Access is subject to the above licence, if given. If no licence is specified above, original content in this thesis is licensed under the terms of the Creative Commons Attribution-NonCommercial 4.0 International (CC BY-NC-ND 4.0) Licence (<https://creativecommons.org/licenses/by-nc-nd/4.0/>). Any third-party copyright material present remains the property of its respective owner(s) and is licensed under its existing terms.

#### Take down policy

If you consider content within Bath's Research Portal to be in breach of UK law, please contact: [openaccess@bath.ac.uk](mailto:openaccess@bath.ac.uk) with the details. Your claim will be investigated and, where appropriate, the item will be removed from public view as soon as possible.



# **The Synthesis and Application of Metal–Based Complexes for Sustainable Catalysis**

Oliver J. Driscoll

A thesis submitted for the degree of Doctor of Philosophy

Department of Chemistry

University of Bath

September 2021

## **COPYRIGHT**

Attention is drawn to the fact that copyright of this thesis rests with the author. A copy of this thesis has been supplied on condition that anyone who consults it is understood to recognise that its copyright rests with the author and that they must not copy it or use material from it except as permitted by law or with the consent of the author.



## A. Contents

<b>A. Contents</b> .....	i
<b>B. Acknowledgements</b> .....	vi
<b>C. Abstract</b> .....	viii
<b>D. Abbreviations</b> .....	ix
<b>E. Publications</b> .....	xii
<b>1. Introduction and outlook</b> .....	1
1.1 The current situation and transitioning to a sustainable world .....	2
1.2 Contemporary, sustainable, green chemistry .....	4
1.3 Earth-abundant metal catalysis .....	5
1.4 CO <sub>2</sub> utilisation and chemical transformation .....	6
1.5 The development and need for alternative biopolymers .....	7
1.6 Research aims .....	8
1.7 References .....	9
<b>2. The synthesis and characterisation of Fe(III) complexes</b> .....	15
2.1 Fe(III)–salalen, –salen and –salen–chloride complexes and project aims .....	15
2.2 Preparation of salalen, salen and salan ligands .....	17
2.3 Complexation and synthesis of Fe(III)–salalen–chloride complexes .....	20
2.4 Complexation and synthesis of Fe(III)–salan complexes .....	28
2.5 Complexation and synthesis of Fe(III)–acetate complexes .....	32
2.6 Discussion of the Fe(III)–to–acetate bond lengths .....	44
2.7 Discussion of the synthesis for the Fe(III)–salen–acetate vs. $\mu$ -oxo-bridged Fe(III)–salen complex .....	47
2.8 Exploring the chirality of the ligand backbone using 2,2'–bipyrrrolidine salan scaffolds .....	49
2.9 Synthesis and attempted synthesis of Fe(III)–alkoxide and Fe(III)–bis(phenoxy–imine) complexes .....	50
2.10 Synthesis and attempted synthesis of dinuclear Fe(III) complexes and other Fe(III) complexes .....	57
2.11 Conclusion and future work .....	61
2.12 References .....	65



<b>3. Ring opening polymerisation of <i>rac</i>-lactide using Fe(III) complexes.....</b>	<b>71</b>
3.1 Introduction to poly(lactic acid) and its preparation .....	71
3.2 The ring opening polymerisation of lactide to PLA: mechanistic and stereochemical considerations .....	74
3.3 Fe-mediated ring opening polymerisation and project aims .....	81
3.4 Ring opening polymerisation of <i>rac</i> -lactide using Fe(3)Cl.....	98
3.5 Batch kinetic investigation using Fe(3)Cl .....	104
3.6 Ring opening polymerisation of <i>rac</i> -lactide using other Fe(III)-chloride complexes.....	106
3.7 End group analysis and bimodality discussion .....	109
3.8 Investigation of initiators and conditions for the ring opening polymerisation of <i>rac</i> -lactide using an Fe(III)-acetate complex .....	114
3.9 Ring opening polymerisation of <i>rac</i> -lactide using Fe(III)-acetate complexes.....	117
3.10 Conclusion and future work .....	122
3.11 References.....	123
<b>4. Catalytic CO<sub>2</sub> / epoxide coupling and cyclic carbonate formation .....</b>	<b>129</b>
4.1 Introduction to catalytic CO <sub>2</sub> / epoxide coupling.....	129
4.2 Fe-mediated CO <sub>2</sub> / epoxide coupling: phenoxy-amine and phenoxy-imine frameworks .....	137
4.3 Fe-mediated CO <sub>2</sub> / epoxide coupling: thioether-phenolate frameworks ....	160
4.4 Project aims.....	166
4.5 CO <sub>2</sub> / cyclohexene oxide coupling using Fe(III)-acetate complexes and tetrabutylammonium chloride co-catalyst.....	167
4.6 Exploring CO <sub>2</sub> / cyclohexene oxide coupling with chiral complexes.....	175
4.7 Applying various co-catalysts and conducting an epoxide scope using the Fe(III)-acetate complex, Fe(13)OAc .....	176
4.8 Examining colour change using ultraviolet-visible spectroscopy.....	179
4.9 CO <sub>2</sub> / cyclohexene oxide coupling using Fe(III)-salalen and -thiolen complexes and tetrabutylammonium chloride co-catalyst.....	182
4.10 Investigating variant equivalents of co-catalyst and conducting an epoxide scope using the Fe(III)-thiolen-chloride complex, Fe(65)Cl.....	187
4.11 Conclusion and future work .....	190
4.12 References.....	193

<b>5. The further application of Fe(III) complexes: ring opening copolymerisation, terpolymerisation and degradation.....</b>	<b>197</b>
5.1 Introduction, Fe-mediated ring opening copolymerisation and project aims .....	197
5.2 Initial investigations using Fe( <b>13</b> )OAc for ring opening copolymerisation in solution and hypothesis .....	209
5.3 Ring opening copolymerisation of phthalic anhydride and cyclohexene oxide using Fe(III) complexes in solution conditions .....	212
5.4 Ring opening copolymerisation of phthalic anhydride and cyclohexene oxide using Fe(III) complexes in neat conditions .....	222
5.5 Thermal analysis .....	226
5.6 Attempted terpolymerisation using Fe(III) complexes.....	228
5.7 Poly(lactic acid) degradation using Fe(III) complexes .....	234
5.8 Conclusion and future work .....	240
5.9 References .....	243
<b>6. Experimental section.....</b>	<b>250</b>
6.1 General considerations .....	250
6.2 General procedure for salalen ligand preparation.....	255
6.3 General procedure for 3,5-di- <i>tert</i> -butyl-2-hydroxybenzyl bromide precursor (R <sup>3</sup> = <i>t</i> Bu) preparation .....	255
6.4 General procedure for the synthesis of bipyrrolidine salan ligands .....	256
6.5 General procedure for the synthesis of salan ligands <i>via</i> reduction .....	256
6.6 General procedure for the synthesis of salen ligands.....	257
6.7 General complexation procedure carried out under air for Fe(III)-salalen-chloride complexes {Fe( <b>1/3/5</b> )Cl}.....	257
6.8 General complexation procedure carried out under argon for Fe(III)-salalen-chloride complexes {Fe( <b>2/4/6/7</b> )Cl} .....	257
6.9 General complexation procedure carried out under air for Fe(III)-acetate complexes.....	257
6.10 Synthesis and characterisation of Fe(III) complexes .....	258
6.11 MALDI-ToF analysis of the Fe( <b>3</b> )Cl complex .....	273
6.12 Measured pXRD pattern of Fe( <b>14</b> )OAc complex .....	273
6.13 General solution ROP procedure using Fe(III)-salalen-chloride complexes in propylene oxide solvent .....	274

6.14	General solution ROP procedure using Fe(III)–acetate complexes in toluene solvent and catalytic amounts of triethylamine and benzyl alcohol .....	275
6.15	Solution ROP procedure using Fe(3)Cl in toluene solvent and catalytic amounts of triethylamine and benzyl alcohol .....	275
6.16	General CO <sub>2</sub> / epoxide coupling reaction procedure .....	275
6.17	Crude <sup>1</sup> H NMR spectra of CO <sub>2</sub> / epoxide coupling reaction mixtures.....	276
6.18	General procedure for the solution ROCOP of PA / CHO using Fe(III)–complexes or organic ligands in toluene solvent.....	284
6.19	General procedure for the neat ROCOP of PA / CHO using Fe(III)–complexes or organic ligands in toluene solvent .....	285
6.20	<sup>1</sup> H NMR and DOSY spectroscopic analysis on the polymers obtained from ROCOP .....	286
6.21	IR spectra of isolated polymer obtained from PA / CHO ROCOP.....	288
6.22	General procedure for the attempted solution terpolymerisation of PA / CHO / <i>rac</i> –LA using Fe(III)–complexes or organic ligands in toluene solvent.....	289
6.23	<sup>1</sup> H NMR spectra of crude reaction mixture and isolated polyester obtained from the attempted terpolymerisation of PA / CHO / <i>rac</i> –LA.....	290
6.24	General PLA degradation procedure using Fe(III)–salalen–chloride complexes and FeCl <sub>3</sub> .....	291
6.25	References.....	292
<b>7.</b>	<b>Appendix.....</b>	<b>295</b>
7.1	Iron(III) complex single–crystal X–ray diffraction data .....	295
7.2	Homonuclear decoupled spectra of the PLA derived from Fe(3)Cl .....	314
7.3	GPC chromatograms of PLA derived from the Fe(III)–salalen–chloride complexes.....	315
7.4	MALDI–ToF analysis of the PLA derived from the Fe–salalen–chloride complexes.....	318
7.5	Homonuclear decoupled spectra of the PLA derived from the Fe(III)–acetate complexes.....	322
7.6	GPC chromatograms of PLA derived from the Fe(III)–acetate complexes ....	324
7.7	MALDI–ToF analysis of the PLA derived from the Fe(III)–acetate complexes.....	330
7.8	GPC chromatograms of the polymer derived from the ROCOP of PA and CHO.....	333
7.9	DSC curves of the polymer derived from the ROCOP of PA and CHO .....	341

7.10 MALDI–ToF analysis of the polymer derived from the ROCOP of PA and CHO.....347

## B. Acknowledgements

Firstly, I would like to thank Prof. Matthew Jones, I am extremely grateful for his enthusiasm, supervision, guidance, advice and support the last four years. If there was a 'Mary Tasker Award for PhD supervision' he should win it in my eyes. Without his help, the work presented herein would not have got anywhere; particularly considering how the PhD project completely changed after my first year (the original 'Earth-Abundant Metals for Small Coupling Reactions' title being more accurately described then by 'Metals for Reactions' and was nearly just 'Reactions'). I would also, crucially, like to thank Dr. Paul McKeown (HI PDP). Despite the shrugging of his head in pretend (?) disappointment, the muttering of 'Olliiii', and the overplaying of Billy Joel in the lab, I could not have asked for a better post doc and friend in the lab, and indeed role model for research. I have learnt so much from him. I still have no idea how he managed to do so much research when he seemed to help every chemist in 5W. I was also very lucky to have both Matthew's and Paul's assistance with crystallography; their motivation unperturbed despite some of the challenging crystals and muck I handed to them.

I have also been incredibly lucky to be a part of such a proactive and supportive research group. Fellow colleagues and friends who made the work place an enjoyable environment too; so, thank you Jack Stewart ('the dad'), Sandeep Kaler ('the secretary') and Jack Payne ('the overlord') for putting up with me! Sandeep you can now adopt my fume hood. It was a pleasure also to work with Daniel Ditz when he visited for a summer from Aachen. I was also very lucky to have had such hard working and diligent MChem final year project students to supervise. A particular mention to Claudia Hafford-Tear and Christopher Leung for their help with this work.

I am grateful to have met so many good friends through the PhD (too many to mention), been surrounded by so many super office mates (Office 3.11 and 3.3) and lab colleagues ('5W suschem group') who have made the last four years so enjoyable. Particular mention to: Ioli Howard, Natalie Sims, Jamie Boden, Daniel Berry, Rachel Johnston, Stefanie Federle, Izzy Thomlinson, Muhammad Kamran, Craig Hardy.

I have been incredibly fortunate to be a part of the approachable, friendly and helpful community in the Department of Chemistry. I will certainly miss the countless people I've met, the touch rugby sessions, the Departmental socials (Christmas meal and the Cork!), the Friday football matches and the gossip / random chat from when I was in the PG Exec committee. I would like to thank the staff and specialists that have provided support to my research such as Dr. Tim Woodman, Dr. Rémi Castaing, Dr. John Lowe, Dr. Martin Levere, Dr. Mary Mahon, Dr. Gabriele Kociok-Kohn and Mr. Jonathan Rowney.

I would like to give a special thanks to Kerry Flanagan (Ferry) and Richard Lunn (Roberto) who have lived with me the last four years and kept me sane during the COVID lockdowns; the film nights, tv binging, cheeky banter, takeaway nights and putting up with me (especially when I started attempting to learn the piano). In addition to them, thank you so much Ben Emery, Anna Kinsella, Ioli and Natalie who have made living in Bath so enjoyable.

The last six years have been challenging, tough and stressful outside university and there are individuals that have helped me through some tough personal times. Without which I most probably would have dropped out. These challenges and battles have certainly put life into perspective for me. This includes people who did not know it and still displayed random acts of kindness and humour: 'Everyone you meet is fighting a battle you know nothing about. Be kind. Always.' I can't thank Lisa Price enough for being such a close, great friend the last few years, being there for me and the fun times / adventures.

I certainly wouldn't have completed this PhD without the support of my family: Kim, Jon and Joe. They have been my rocks and are my role models. Thank you, King's College London Hospital, for allowing us the opportunity to remain together.

## C. Abstract

Society is currently reliant on non-renewable fossil fuels and petrochemical derivatives. With global population increasing, resulting in escalating demands on both energy and materials, these resources are rapidly diminishing and a drastic, responsive transition to a more sustainable world is required. Chemistry is at the forefront of these global challenges and recently, a number of contemporary areas of chemistry research have seen a resurgence such as: the use of Fe for catalysis, CO<sub>2</sub> chemical transformations and the development of alternative biopolymers. **Chapter 1** attempts to give a brief introduction into these concepts and the research aims.

In **Chapter 2**, a range of Fe(III) complexes were synthesised and characterised using a range of techniques. This included both a range of Fe(III)–salalen–chloride complexes and air–stable Fe(III)–acetate complexes, comprising of salalen, salan and salen frameworks.

In **Chapter 3**, these Fe(III) complexes were assessed as active initiators for the controlled ring opening polymerisation (ROP) of *rac*-lactide (*rac*-LA) to form the alternative, biopolymer poly(lactic acid) (PLA). Fe(**3**)Cl was an effective initiator and observed a moderate isotactic bias ( $P_m = 0.75\text{--}0.80$ ). Batch kinetics were conducted and the observed bimodality on the GPC chromatograms was scrutinised. In **Chapter 4**, the Fe(III) complexes were applied as catalysts to the coupling of CO<sub>2</sub> with cyclohexene oxide (CHO) to form the *cis*-cyclohexene carbonate (*cis*-CHC) product exclusively. Fe(**13**)OAc was observed to be the most active catalyst and was applied to further terminal epoxides. UV–Vis spectroscopy was used to investigate the observed colour change in the reaction mixtures.

In **Chapter 5**, the application of these Fe(III) complexes was extended to the ring opening copolymerisation of phthalic anhydride (PA) and CHO with no need for co-catalyst. It was discovered from control reactions that the ligands were active as organocatalysts with salophen **17** observing the highest molecular weight polyester with 29100 gmol<sup>-1</sup>. The addition of a third monomer, *rac*-LA, was attempted for terpolymerisation, but two separate polymer species were formed. Lastly, the degradation of PLA to methyl lactate (Me-LA) was investigated.

## D. Abbreviations

AGE	Allylglycidyl ether
AIBN	2,2'-azobis(2-methylpropionitrile)
APC	Aliphatic polycarbonate
asme	Anthranilic acid methyl ester
ATRP	Atom transfer radical polymerisation
BED	$\beta$ -Elemene dioxide
BEM	$\beta$ -Elemene monoxide
BET	$\beta$ -Elemene trioxide
CCS	Carbon capture and storage
CDA	Carbenodiamidine
CDU	Carbon dioxide utilisation
CEM	Chain-end-control mechanism
CHC	Cyclohexene carbonate
CHO	Cyclohexene oxide
COC	Cyclic organic carbonate
CTA	Chain transfer agent
D	Diffusion coefficient
$\bar{D}$	Dispersity (molecular weight distribution)
DFT	Density functional theory
Dipp	2,6-diisopropylphenyl
DMAP	4-(dimethylamino)pyridine
DOSY	Diffusion ordered spectroscopy
DSC	Differential scanning calorimetry
ECH	Epichlorohydrin
EDG	Electron-donating groups
EOL	End-of-life
ESI	Electron spray ionisation
EWG	Electron-withdrawing groups
FDA	Food and Drug Administration

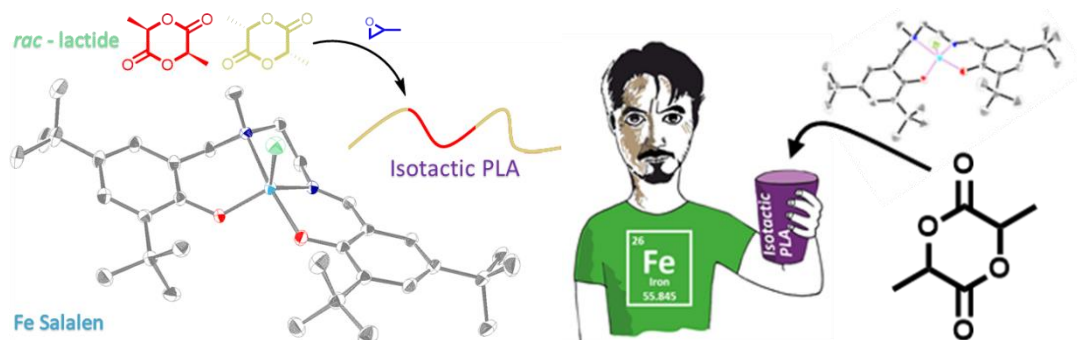


GLY	Glycidol
GPC	Gel permeation chromatography
HR–MS	High resolution mass–spectrometry
ILs	Ionic liquids
$k_{app}$	Apparent rate constant
$K_c$	Equilibrium constant
L	Ancillary ligand
LA	Lactide
LCA	Life cycle assessment
MALDI	Matrix–assisted laser desorption / ionisation
MEK	Methyl ethyl ketone
$M_n$	Number average molecular weight
NHC	N–heterocyclic carbene
NMR	Nuclear magnetic resonance
NPCA	Non–polymerisable catalytic adjunct
Oct	Octanoate
PA	Phthalic anhydride
PCHC	Poly(cyclohexene carbonate)
PD	Propane–1,2–diol
PE	Polyester
PGE	Phenylglycidyl ether
$pK_a$	Acid dissociation constant
PLA	Poly(lactic acid)
$P_m$	Probability of isotactic enchainment
PO	Propylene oxide
ppm	Parts per million
PPNCl	<i>bis</i> (triphenylphosphoranylidene) ammonium chloride
PS	Poly(styrene)
<i>rac</i>	Racemic
RDS	Rate determining step
RI	Refractive index

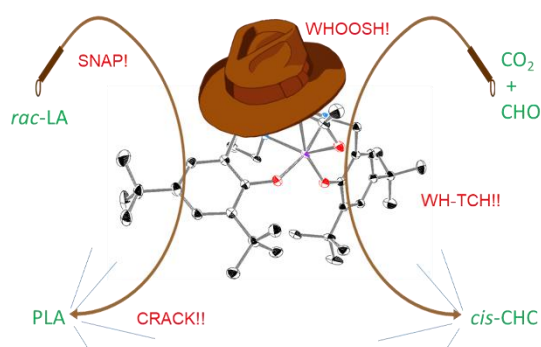
ROCOP	Ring opening copolymerisation
ROP	Ring opening polymerisation
SARs	Structure–activity–relationships
SCM	Enantiomeric–site–control mechanism
SO	Styrene oxide
TBAC	tetrabutylammonium chloride
$T_c$	Crystallisation temperature
$T_d$	Decomposition temperature
TEMPO	2,2,6,6–tetramethyl–1–piperidinyloxy
$T_g$	Glass transition temperature
TGA	Thermal gravimetric analysis
$T_m$	Melting temperature
ToF	Time of flight
TOF	Turnover frequency
X	Auxiliary ligand
XRD	X–ray diffraction
$\tau_5$	Structural index parameter / geometric preference value

## E. Publications

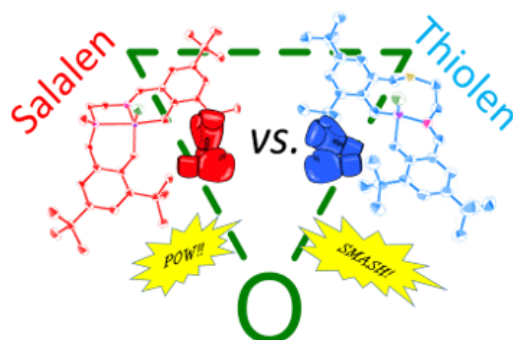
1) O. J. Driscoll, C. K. C. Leung, M. F. Mahon, P. McKeown, M. D. Jones, Iron(III) Salalen Complexes for the Polymerisation of Lactide, *Eur. J. Inorg. Chem.* **2018**, 5129–5135, DOI: 10.1002/ejic.201801239.



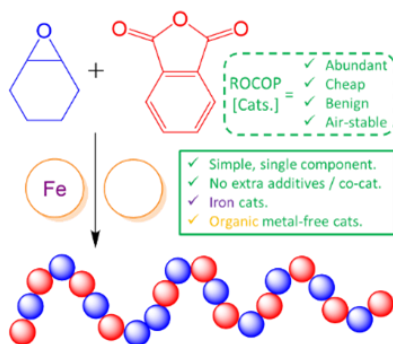
2) O. J. Driscoll, C. H. Hafford–Tear, P. McKeown, J. A. Stewart, G. Kociok-Köhn, M. F. Mahon, M. D. Jones, The synthesis, characterisation and application of iron(III)–acetate complexes for cyclic carbonate formation and the polymerisation of lactide, *Dalton Trans.* **2019**, 48, 15049–15058, DOI: 10.1039/c9dt03327k.



3) O. J. Driscoll, J. A. Stewart, P. McKeown, M. D. Jones, Salalen vs. thiolen: in the ring(–opening of epoxide and cyclic carbonate formation), *New J. Chem.* **2020**, 44, 6063–6067, DOI: 10.1039/d0nj00725k.



4) O. J. Driscoll, J. A. Stewart, P. McKeown, M. D. Jones, Ring opening copolymerization using simple Fe(III) complexes and metal- and halide-free organic catalysts, *Macromolecules* **2021**, *54*, 8443–8452, DOI: 10.1021/acs.macromol.1c01211.



## **Chapter 1.**

### **Introduction and outlook**

# 1. Introduction and outlook

## 1.1 The current situation and transitioning to a sustainable world

Society is currently at a crucial turning point in history; a pivotal moment where mankind has become reliant on non-renewable fossil fuels and petrochemical derivatives with the environment significantly damaged because of their use.<sup>[1-3]</sup> For instance, this has contributed considerably to Global Warming, climate change and rising CO<sub>2</sub> levels which, for the first time in human history, has recently risen above 400 ppm in the atmosphere.<sup>[1,4-9]</sup> Global population and quality of life is rapidly increasing, resulting in escalating demands on both energy and materials (*Figure 1*).<sup>[10-12]</sup> With these resources rapidly diminishing, a drastic, responsive transition to more sustainable, alternative approaches and a sustainable world is required.<sup>[1,2,11]</sup> While this opening is blunt, it is not an overstatement, and despite the current situation, there has been early and promising developments.

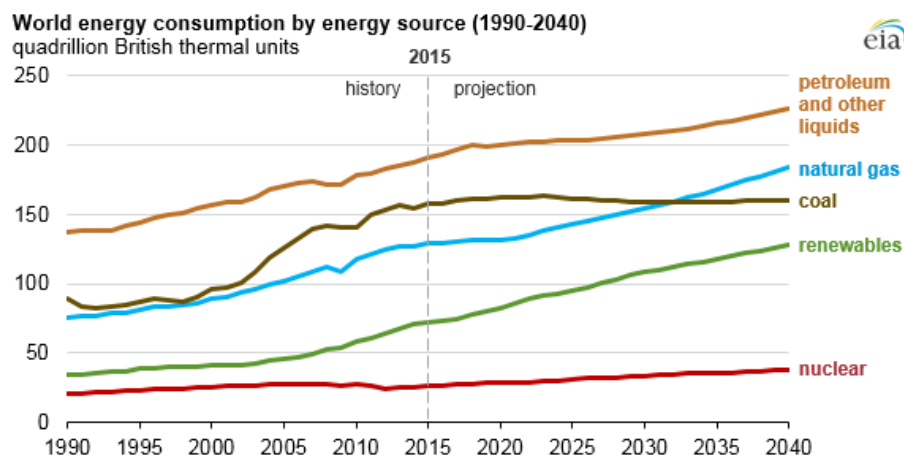


Figure 1. Increasing global demands and consumption of energy. (Taken from reference).<sup>[10]</sup>

Multiple international approaches have been implemented in our endeavours to transition to a more sustainable, renewable world.<sup>[13,14]</sup> In 2015, the United Nations (UN) introduced a framework containing 17 Sustainable Development Goals (SDGs) to target by 2030 (*Figure 2*).<sup>[15,16]</sup> This initiative has been critical as it has resulted in their adoption by governments, industries and organisations. Indeed, for this to be successful, it is crucial governments implement these practises into policy and

legislation, incentivise their industrial sectors to embrace these standards and also educate and promote its use in everyday life by its citizens.<sup>[14,17–19]</sup>

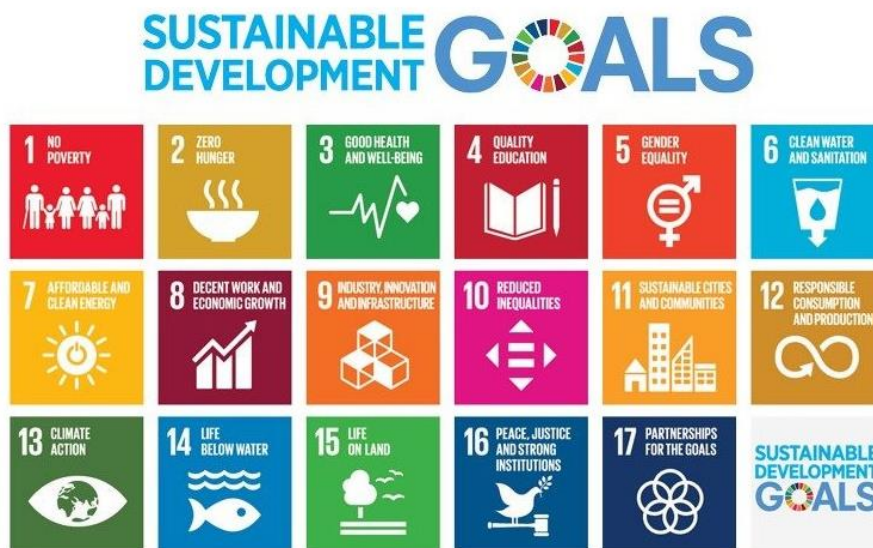
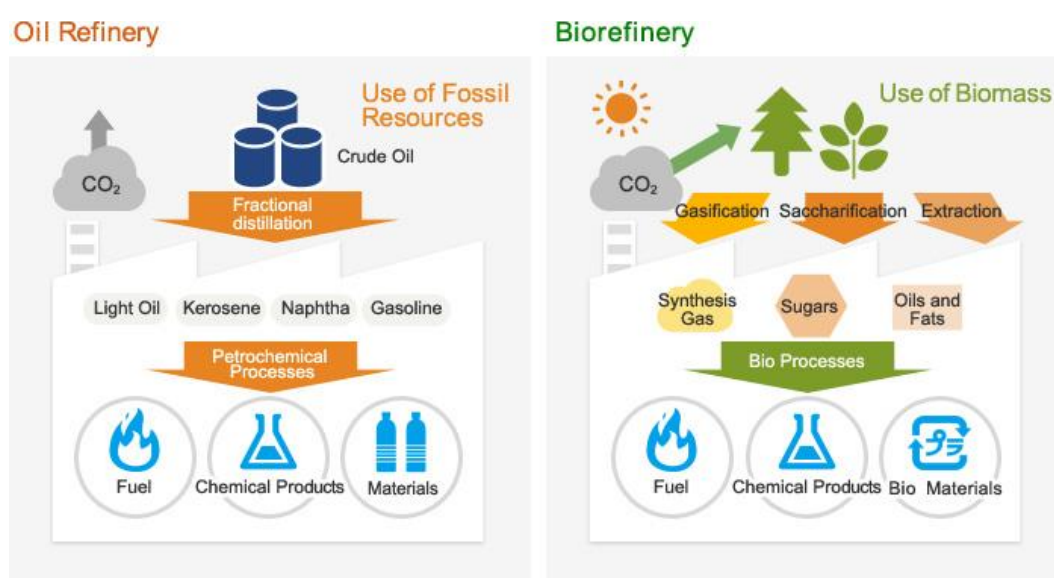


Figure 2. The 'Sustainable Development Goals' developed by the United Nations. (Taken from reference).<sup>[16]</sup>

Another systemic, restorative and regenerative approach is moving economies away from a linear model, based on the take–make–waste of resources, to that of a circular one based on decoupling growth from the consumption of limited resources. The Ellen MacArthur Foundation is at the forefront of promoting this model. It encompasses the 'R's' of sustainability: refuse, rethink, reduce, reuse, repair, refurbish, remanufacture, repurpose, recycle and recover. A concept where waste and pollution is reduced, recycled and designed out. Materials and products are kept in use and value recaptured in the cycle, with nature crucially regenerated.<sup>[20,21]</sup>

Therefore, in addition to this circular economy, there needs to be a shift away from the extraction and use of fossil fuels to obtain the useful petrochemical derived products and energy; the crude oil refinery process at the start of the lifecycle.<sup>[11]</sup> In terms of obtaining renewable energy, significant research, capital and infrastructure has been invested globally into methods such as solar, wind, hydrothermal, geothermal, tidal and biomass sources. For products, attention has been increasing into renewably sourced resources.<sup>[11,22]</sup> A major, potential solution that will be crucial to solving this in the future, is biomass. Natural or waste, plant–, wood– and sugar–

derived resources, preferably from non-edible sources, such as lignocellulosic biomass.<sup>[11,13,22–30]</sup> This forms an alternate biorefinery process (*Figure 3*) and incorporates a bio-based, circular (bio-circular) economy.<sup>[11,23,27,28,31–34]</sup> However, for the time being, biomass conversion is significantly more costly and inefficient compared to crude oil but at the early stages of development. With further research in this area, the valorisation of possible products that can be obtained: such as lignin, cellulose and hemi-cellulose, and because of the rising, volatile prices of oil, the biorefinery process will become more competitive and established globally.<sup>[1,11,23,33,34]</sup>



*Figure 3.* An illustration of the biorefinery process in comparison to the oil refinery process. (Taken from reference).<sup>[32]</sup>

## 1.2 Contemporary, sustainable, green chemistry

From these concepts briefly introduced in **Section 1.1**, chemistry is at the forefront of these global challenges as we attempt to transition to a more sustainable world. The discipline spans a range of industrial sectors such as: health, pharmaceuticals, manufacturing, food, water, agriculture, energy and construction to name just a few, and contributes to many of the SDGs listed by the UN (*Figure 2*).<sup>[13]</sup> Consequently, to try and address these critical issues being faced, contemporary chemistry research is and needs to be focussed on sustainable principles, attempt to follow the ‘12 principles of green chemistry’ and if possible, relate to areas of chemistry and



industrial processes that are in need for further improvement.<sup>[13,35]</sup> This has resulted in the rapid expansion of the emerging field of green chemistry, that only started in the late 1990s, with the '12 Principles of Green Chemistry' published in 1998 and the first journal specialising in this area, *Green Chemistry*, being founded in 1999.<sup>[35]</sup> Recently, in response to this, a number of contemporary areas of chemistry have seen a resurgence such as: the use of Earth-abundant metals for catalysis, CO<sub>2</sub> utilisation / chemical transformation and the development of alternative biopolymers.

### **1.3 Earth-abundant metal catalysis**

Catalysts are essential to industry, being used in over 80% of manufactured products and 85% of all industrial chemicals.<sup>[36–38]</sup> Their use allows processes to be completed faster, with greater selectivity and atom efficiency (AE), at milder reaction conditions, lower costs and energy requirements.<sup>[12,36]</sup> To reflect their importance to sustainability, catalysis is itself a principle of green chemistry.<sup>[13,35]</sup> Traditionally, catalysis has relied extensively on unsustainable elements such as the Platinum Group Metals (PGMs) including ruthenium, rhodium, palladium, osmium, iridium and platinum.<sup>[12,23,39–45]</sup> Their current use creates growing challenges due to their high, fluctuating prices and toxicity. This coupled with their low abundance and being listed as endangered elements.<sup>[46]</sup> In reaction to this, with the expected issues escalating by their use in the near future, there has been impetus to synthesise and develop more sustainable catalytic alternatives. In the field of homogeneous catalysis, Earth-abundant, base metals have traditionally been overlooked in their application, but there has been renewed attention in exploring these elements because of the numerous benefits they hold: they are less expensive (both at industrial and commercial scales), benign with less toxicity issues associated with their use and more widely available globally and abundant.<sup>[12,23,36,39–45]</sup> Indeed, elements such as aluminium, iron, titanium and manganese are the 3<sup>rd</sup>, 4<sup>th</sup>, 9<sup>th</sup> and 12<sup>th</sup> most abundant elements in the Earth's crust respectively.<sup>[39]</sup>

## 1.4 CO<sub>2</sub> utilisation and chemical transformation

Over the last two decades, there has been growing attention in the carbon capture and storage (CCS) and utilisation of CO<sub>2</sub> (CDU) as result of climate change.<sup>[1,2,47-49]</sup> It is a conceptual approach to reduce the net costs, increase profits of reducing CO<sub>2</sub> emissions; particularly in industrial waste streams, and subsequently removing CO<sub>2</sub> from the atmosphere. This is accomplished by using CO<sub>2</sub> as a sustainable feedstock to produce valuable products cheaper and more cleanly compared to conventional hydrocarbons derived from fossil fuels.<sup>[2,47,48]</sup> It is important to note, while CDU can positively aide and complement the reduction of CO<sub>2</sub> emissions and CO<sub>2</sub> mitigation; decreasing the carbon footprint in industrial processes and subsequently the removal of CO<sub>2</sub> from the atmosphere, these are not its direct aims and objectives. Hence the phrases 'CDU' and 'CO<sub>2</sub> mitigation' cannot be used interchangeably.<sup>[50]</sup>

This desire to use CO<sub>2</sub> as a sustainable, 'waste', alternative feedstock has led to rapid developments in the chemical conversion or transformation of CO<sub>2</sub> to a range of value added products such as fuels, materials and, both fine and bulk, chemicals.<sup>[1,2,6-8,47-51]</sup> As a reagent, CO<sub>2</sub> is a non-toxic, cheap, abundant and C1-synthon building block that can form a range of possible products.<sup>[2,4,47,51,52]</sup> To achieve this, the high thermodynamic stability and kinetic inertness of the CO<sub>2</sub> molecule needs to be overcome.<sup>[1,47,50]</sup> The two major strategies for this involve: the coupling of CO<sub>2</sub> with reactive, thermodynamically unstable nucleophiles to form carbonate, carbamate or carboxylic acid products or the electrochemical reduction of CO<sub>2</sub> to C1 product species such as methanol or formate.<sup>[47,49,52,53]</sup> One of the most widely studied and promising reactions for CO<sub>2</sub> catalysis is their coupling with epoxides in the formation of cyclic organic products (COCs) or aliphatic polycarbonate products (APCs) with the use of a catalytic system.<sup>[2,4,6,51,54,55]</sup> Both products are useful, in high demand, produced on an industrial scale and hold a range of applications across multiple industries.<sup>[4,6,51,54-56]</sup> Therefore, the drive in this area for research is to synthesise new, useful COC / APC products from CO<sub>2</sub> for further applications, develop more effective catalytic systems, access industrially attractive routes and the desire to use more Earth-abundant metals or organic compounds for the catalysts.<sup>[1,2,5,51,57]</sup>

## 1.5 The development and need for alternative biopolymers

Plastics and the field of polymer science has progressed exponentially since the last century.<sup>[30,58–60]</sup> Indeed, they have been instrumental in the development of modern society and enhancing quality of life by the immense range of applications and industrial sectors plastics are used for.<sup>[22,30,60,61]</sup> This has stemmed from their superior properties and versatility compared to traditional alternatives, such as paper, glass and metal: inherent durability, strength, lightweight, chemical resistance, low cost coupled with their thermoelectrical insulating properties and processability.<sup>[58–60,62–65]</sup> However, this advancement, relying on a linear economic model, has resulted in significant ecological harm at both ends of the polymer lifecycle.<sup>[30]</sup> In 2015, 99% of global polymer production was sourced from non-renewable crude oil, with less than 1% derived from renewable, bio-based sources. Annually this production exceeds 300 million tonnes which is anticipated to rise to 20% by 2050 or potentially even double within the next 20 years.<sup>[22,30,58–60,62–68]</sup> The polymer industry accounts for about 6% of global crude oil consumption and is considered a major contributor to greenhouse gas emissions and environmental damage.<sup>[22,30,63,68]</sup> Shifting to the end of the polymer lifecycle, between 1950 to 2015, it was estimated that of the 8.3 billion tonnes of plastic produced, only 9% of all the 6.3 billion tonnes of plastic waste generated had been recycled.<sup>[30,58,66]</sup> With a further 12% incinerated and the remaining 79% discarded into landfill and much of it reaching the natural environment and oceans.<sup>[30,58]</sup> The waste problem is well exemplified by the ‘The Great Pacific Garbage Patch’ that is estimated to be 79000 tonnes and continues to grow annually.<sup>[58,69]</sup> Another startling statistic is, if current trends continue, it is predicted that by 2050, the mass of plastic waste in the ocean will exceed that of the mass of fish.<sup>[60,63]</sup>

Therefore, change is vital in the future, and the plastics economy is at the forefront of the themes introduced in **Section 1.1**.<sup>[13,58,61]</sup> Industry and governments need to proactively transition to a circular, bio-based economy.<sup>[13,63,65]</sup> Alternative biopolymers and biomaterials need to be developed from renewably sourced, natural or waste, plant-derived resources to replace unsustainable fossil fuel derived products.<sup>[11,13,22–30]</sup> Foremost, the properties of these bioderived polymers need to

be competitive or superior to that of the non-renewable traditional plastics, as to allow replacement for any plastic application. End-of-life (EOL) consideration is crucial and needs to be designed so material value can be recaptured and recycled, such as for polymers *via* chemical recycling (degradation or depolymerisation).<sup>[11,22,60]</sup> If this is not possible, the biopolymers need to be biodegradable as to not contribute to the plastic waste problem.<sup>[60]</sup> There are certainly new, exciting opportunities to exploit when shifting to renewable feedstocks; after extracting the useful bioderived chemicals, these possess inherent chemical functionality and polarity which can be utilised to synthesise new platform chemicals and materials for further applications.<sup>[30]</sup> These ‘top-down’ approaches employ the inherent heteroatoms present in the biomass and contrasts to that of traditional petrochemical derivatives sourced from the oil refinery process, where basic hydrocarbon molecules are built ‘bottom-up’ by adding any required functionality.<sup>[30]</sup> Therefore, further research in biopolymer chemistry will be vital to our endeavours for a more sustainable, bio-circular economic future and meet the growing demands on the plastics economy. <sup>[22,30,60,61]</sup>

## 1.6 Research aims

As a result of the reasons outlined in **Sections 1.1–1.5**, the main focus of the research conducted the last four years and discussed herein, in the following Chapters, has been on the resurging, contemporary chemistry themes of synthesising and using Earth-abundant metals for the development of sustainable biopolymers and CO<sub>2</sub> chemical transformation; both industrially relevant areas.

Along with the numerous benefits associated and the recent resurgence in catalysis with its use; as outlined in in *Figure 4*, iron was selected as the precursor to attempt to synthesise a range of Fe(III) complexes using structural frameworks such as salalen, salen and salan ligands (**Chapter 2**). The attempted application of these complexes would be tried, as initiators for the ring opening polymerisation of *rac*-lactide to form the alternative, biopolymer poly(lactic acid) (PLA) and as catalysts for the coupling of CO<sub>2</sub> with epoxides to form useful products (**Chapters 3 and 4**). The complexes would then be applied further to probe their efficacy to produce

copolymers *via* the ring opening copolymerisation of anhydrides and epoxides and terpolymerisation by the addition of a third monomer (**Chapter 5**). As a proof of concept and because of the circular economic potential for PLA, the Fe(III) complexes would be tested for PLA chemical degradation (**Chapter 5**) to see if it were possible.

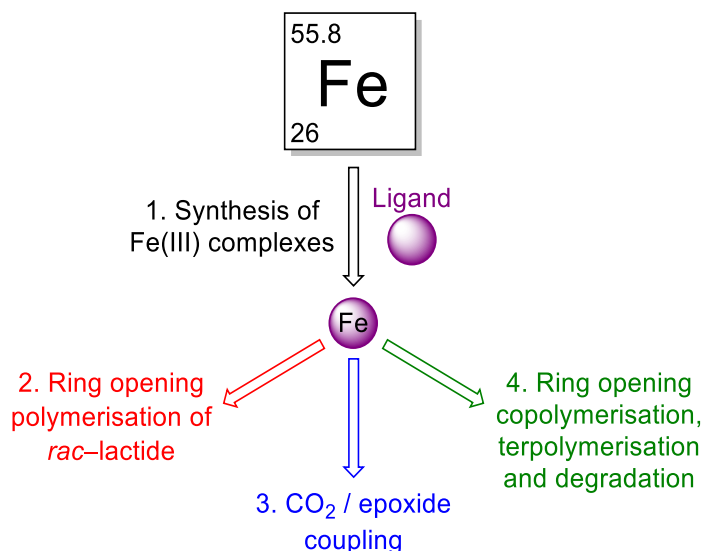


Figure 4. Overall outline of the core aims for the research.

## 1.7 References

- [1] M. North, P. Styring, *Faraday Discuss.* **2015**, *183*, 489–502.
- [2] M. North, R. Pasquale, C. Young, *Green Chem.* **2010**, *12*, 1514–1539.
- [3] M. McGrath, *Climate change: IPCC report is 'code red for humanity'*, <https://www.bbc.co.uk/news/science-environment-58130705>, **2021** (Accessed 12<sup>th</sup> August 2021).
- [4] K. A. Andrea, F. M. Kerton, *Polym. J.* **2021**, *53*, 29–46.
- [5] F. Della Monica, M. Leone, A. Buonerba, A. Grassi, S. Milione, C. Capacchione, *Mol. Catal.* **2018**, *460*, 46–52.
- [6] H. Büttner, L. Longwitz, J. Steinbauer, C. Wulf, T. Werner, *Top. Curr. Chem.* **2017**, *375*, 1–56.
- [7] Q. Liu, L. Wu, R. Jackstell, M. Beller, *Nat. Commun.* **2015**, *6*, 1–15.
- [8] M. Cokoja, C. Bruckmeier, B. Rieger, W. A. Herrmann, F. E. Kühn, *Angew. Chem. Int. Ed.* **2011**, *50*, 8510–8537.
- [9] IPCC, *Global Warming of 1.5 °C*, <https://www.ipcc.ch/sr15/>, **2018** (Accessed 12<sup>th</sup> August 2021)
- [10] L. Doman, *EIA projects 28% increase in world energy use by 2040*, <https://www.eia.gov/todayinenergy/detail.php?id=32912>, **2017** (Accessed

26<sup>th</sup> July 2021).

- [11] A. J. Ragauskas, C. K. Williams, B. H. Davison, G. Britovsek, J. Cairney, C. A. Eckert, W. J. Frederick Jr, J. P. Hallett, D. J. Leak, C. L. Liotta, J. R. Mielenz, R. Murphy, R. Templer, T. Tschaplinski, *Science* **2006**, *311*, 484–489.
- [12] B. Plietker, Ed., *Iron Catalysis: Fundamentals and Applications*, Springer-Verlag, Berlin, Heidelberg, **2011**.
- [13] T. Tabanelli, D. Cespi, R. Cucciniello, *Catalysts* **2021**, *11*, 1–5.
- [14] UK Circular Plastics Network (UKCPN), *Plastics Roadmap: Future Opportunities and Needs in the UK Plastics Supply Chain*, <https://www.ukcpn.co.uk/prif-roadmap/> **2021** (Accessed 30<sup>th</sup> July 2021).
- [15] United Nations (UN), *Sustainable Development Goals*, <https://www.un.org/sustainabledevelopment/>, (Accessed 26<sup>th</sup> July 2021).
- [16] American Chemical Society (ACS), *Chemistry & Sustainable Development Goals*, <https://www.acs.org/content/acs/en/sustainability/chemistry-sustainable-development-goals.html>, (Accessed 26<sup>th</sup> July 2021).
- [17] European Commission, *Circular Economy Action Plan: The European Green Deal*, [https://ec.europa.eu/environment/strategy/circular-economy-action-plan\\_en#ecl-inpage-878](https://ec.europa.eu/environment/strategy/circular-economy-action-plan_en#ecl-inpage-878), **2020** (Accessed 30<sup>th</sup> July 2021).
- [18] The UK Plastics Pact (WRAP), *A Roadmap to 2025: The UK Plastics Pact*, <https://wrap.org.uk/resources/guide/roadmap-2025-uk-plastics-pact#>, **2016** (Accessed 30<sup>th</sup> July 2021).
- [19] Department for Environment, Food and Rural Affairs (Defra), *UK Circular Economy Package policy statement*, <https://www.gov.uk/government/publications/circular-economy-package-policy-statement/circular-economy-package-policy-statement>, **2020** (Accessed 30<sup>th</sup> July 2021).
- [20] Ellen MacArthur Foundation, *The circular economy in detail*, <https://www.ellenmacarthurfoundation.org/explore/the-circular-economy-in-detail>, (Accessed 29<sup>th</sup> July 2021).
- [21] Ellen MacArthur Foundation, *Circularity and the nine 'Rs'*, [https://www.ellenmacarthurfoundation.org/assets/galleries/CEinaction-Activity06-nine-Rs-6R3\\_from-graham-081217.pdf](https://www.ellenmacarthurfoundation.org/assets/galleries/CEinaction-Activity06-nine-Rs-6R3_from-graham-081217.pdf), (Accessed 29<sup>th</sup> July 2021).
- [22] Y. Zhu, C. Romain, C. K. Williams, *Nature* **2016**, *540*, 354–362.
- [23] Y. Feng, S. Long, X. Tang, Y. Sun, R. Luque, X. Zeng, L. Lin, *Chem. Soc. Rev.* **2021**, *50*, 6042–6093.
- [24] V. Balan, *ISRN Biotechnol.* **2014**, *2014*, DOI: 10.1155/2014/463074.
- [25] C. Chio, M. Sain, W. Qin, *Renew. Sustain. Energy Rev.* **2019**, *107*, 232–249.
- [26] C. Li, X. Zhao, A. Wang, G. W. Huber, T. Zhang, *Chem. Rev.* **2015**, *115*, 11559–

- 11624.
- [27] Z. Sun, B. Fridrich, A. de Santi, S. Elangovan, K. Barta, *Chem. Rev.* **2018**, *118*, 614–678.
- [28] M. V. Galkin, J. S. M. Samec, *ChemSusChem* **2016**, *9*, 1544–1558.
- [29] F. Della Monica, A. W. Kleij, *Polym. Chem.* **2020**, *11*, 5109–5127.
- [30] R. M. O’Dea, J. A. Willie, T. H. Epps, *ACS Macro Lett.* **2020**, *9*, 476–493.
- [31] J. Amoah, P. Kahar, C. Ogino, A. Kondo, *Biotechnol. J.* **2019**, *14*, DOI: 10.1002/biot.201800494.
- [32] VIASPACE, *Biorefinery: Biofuels, Biochemicals and Bioplastics*, [https://www.viaspace.com/biochemicals\\_bio\\_plastics.php](https://www.viaspace.com/biochemicals_bio_plastics.php), (Accessed 29<sup>th</sup> July 2021).
- [33] J. Zakzeski, P. C. A. Bruijninx, A. L. Jongerius, B. M. Weckhuysen, *Chem. Rev.* **2010**, *110*, 3552–3599.
- [34] W. Schutyser, T. Renders, S. Van Den Bosch, S. F. Koelewijn, G. T. Beckham, B. F. Sels, *Chem. Soc. Rev.* **2018**, *47*, 852–908.
- [35] P. Anastas, N. Eghbali, *Chem. Soc. Rev.* **2010**, *39*, 301–312.
- [36] E. Bauer, Ed., *Iron Catalysis II*, Springer International Publishing, Switserzerland, **2015**.
- [37] L. Lerner, *7 things you may not know about catalysis*, <https://www.anl.gov/article/7-things-you-may-not-know-about-catalysis>, **2011** (Accessed 30<sup>th</sup> July 2021).
- [38] D. C. Millholland, *Industrial Uses Of Catalysts*, <https://www.thermofisher.com/blog/materials/characterizing-the-effectiveness-of-industrial-catalysts/>, **2021** (Accessed 30<sup>th</sup> July 2021).
- [39] P. Chirik, R. Morris, *Acc. Chem. Res.* **2015**, *48*, 2495.
- [40] M. Albrecht, R. Bedford, B. Plietker, *Organometallics* **2014**, *33*, 5619–5621.
- [41] C. Darcel, J.-B. Sortais, *Isr. J. Chem.* **2017**, *57*, 1069.
- [42] L. L. Schafer, P. Mountford, W. E. Piers, *Dalton Trans.* **2015**, *44*, 12027–12028.
- [43] J. H. Docherty, S. P. Thomas, *Sustainable Catalysis: With Non-Endangered Metals, Part 1*, Royal Society of Chemistry (RSC), **2015**, pp. 344–372.
- [44] A. Fürstner, *ACS Cent. Sci.* **2016**, *2*, 778–789.
- [45] H.-J. Knölker, Ed., *Recent Advances in Iron Catalysis*, MDPI, Basel, **2020**.
- [46] ACS Green Chemistry Institute, *The periodic table’s endangered elements*, <https://www.acs.org/content/acs/en/greenchemistry/research-innovation/endangered-elements.html> (Accessed 16<sup>th</sup> July 2021).
- [47] F. Della Monica, B. Maity, T. Pehl, A. Buonerba, A. De Nisi, M. Monari, A. Grassi,

- B. Rieger, L. Cavallo, C. Capacchione, *ACS Catal.* **2018**, *8*, 6882–6893.
- [48] C. Hepburn, E. Adlen, J. Beddington, E. A. Carter, S. Fuss, N. Mac Dowell, J. C. Minx, P. Smith, C. K. Williams, *Nature* **2019**, *575*, 87–97.
- [49] N. Hazari, N. Iwasawa, K. H. Hopmann, *Organometallics* **2020**, *39*, 1457–1460.
- [50] J. Artz, T. E. Müller, K. Thenert, J. Kleinekorte, R. Meys, A. Sternberg, A. Bardow, W. Leitner, *Chem. Rev.* **2018**, *118*, 434–504.
- [51] J. W. Comerford, I. D. V Ingram, M. North, X. Wu, *Green Chem.* **2015**, *17*, 1966–1987.
- [52] A.-A. G. Shaikh, S. Sivaram, *Chem. Rev.* **1996**, *96*, 951–976.
- [53] R. G. Grim, Z. Huang, M. T. Guarnieri, J. R. Ferrell, L. Tao, J. A. Schaidle, *Energy Environ. Sci.* **2020**, *13*, 472–494.
- [54] F. Della Monica, A. W. Kleij, *Catal. Sci. Technol.* **2020**, *10*, 3483–3501.
- [55] F. Della Monica, A. Buonerba, C. Capacchione, *Adv. Synth. Catal.* **2019**, *361*, 265–282.
- [56] H. Zhang, H. Liu, J. Yue, *Chem. Rev.* **2014**, *114*, 883–898.
- [57] F. Della Monica, S. V. C. Vummaleti, A. Buonerba, A. De Nisi, M. Monari, S. Milione, A. Grassi, L. Cavallo, C. Capacchione, *Adv. Synth. Catal.* **2016**, *358*, 3231–3243.
- [58] M. D. Jones, J. Payne, *ChemSusChem* **2021**, *14*, 4041–4070.
- [59] J. Payne, P. McKeown, M. D. Jones, *Polym. Degrad. Stab.* **2019**, *165*, 170–181.
- [60] D. K. Schneiderman, M. A. Hillmyer, *Macromolecules* **2017**, *50*, 3733–3749.
- [61] C. K. Ober, S. Z. D. Cheng, P. T. Hammond, M. Muthukumar, E. Reichmanis, K. L. Wooley, T. P. Lodge, *Macromolecules* **2009**, *42*, 465–471.
- [62] P. McKeown, M. D. Jones, *Sustain. Chem.* **2020**, *1*, 1–22.
- [63] Ellen MacArthur Foundation, *The New Plastics Economy: Rethinking the future of plastics*, <https://www.ellenmacarthurfoundation.org/our-work/activities/new-plastics-economy/publications/reports>, (Accessed 30<sup>th</sup> July 2021).
- [64] G. W. Coates, Y. D. Y. L. Getzler, *Nat. Rev. Mater.* **2020**, *5*, 501–516.
- [65] Ellen MacArthur Foundation, *The New Plastics Economy: Rethinking the Future of Plastics & Catalysing Action*, <https://www.ellenmacarthurfoundation.org/publications/the-new-plastics-economy-rethinking-the-future-of-plastics-catalysing-action>, **2017** (Accessed 30<sup>th</sup> July 2021).
- [66] R. Geyer, J. R. Jambeck, K. L. Law, *Sci. Adv.* **2017**, *3*, e1700782.
- [67] L. Lebreton, A. Andrady, *Palgrave Commun.* **2019**, *5*, DOI: 10.1057/s41599-



018-0212-7.

- [68] M. Rabnawaz, I. Wyman, R. Auras, S. Cheng, *Green Chem.* **2017**, *19*, 4737–4753.
- [69] L. Lebreton, B. Slat, F. Ferrari, B. Sainte-Rose, J. Aitken, R. Marthouse, S. Hajbane, S. Cunsolo, A. Schwarz, A. Levivier, K. Noble, P. Debeljak, H. Maral, R. Schoeneich-Argent, R. Brambini, J. Reisser, *Sci. Rep.* **2018**, *8*, DOI: 10.1038/s41598-018-22939-w.

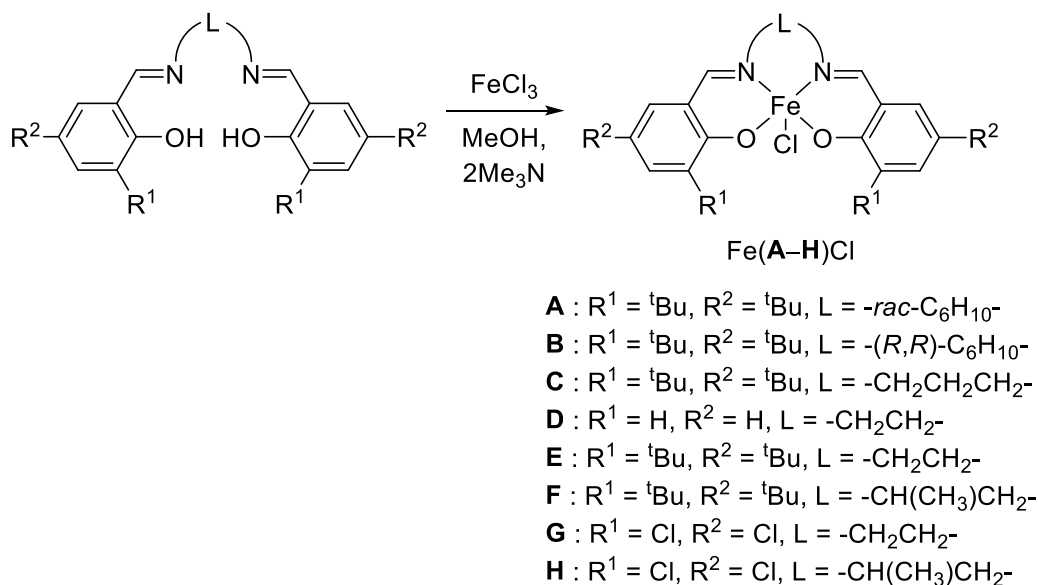
## **Chapter 2.**

### **The synthesis and characterisation of Fe(III) complexes**

## 2. The synthesis and characterisation of Fe(III) complexes

### 2.1 Fe(III)–salalen, –salen and –salen–chloride complexes and project aims

Despite the numerous benefits associated with iron (Fe), examples of the synthesis and application of Fe complexes in many areas of catalysis remain less prevalent and understudied.<sup>[1–12]</sup> These areas include CO<sub>2</sub> / epoxide coupling and, more specifically for this discussion, the ring opening polymerisation (ROP) of cyclic esters and lactide (LA) (**Chapter 3**). Reports of Fe–chloride and Fe–Schiff base / –salen complexes for the ROP of LA were scarce in literature despite other metal–salen complexes being widely used for a range catalytic transformations.<sup>[13–16]</sup> Duan *et al.* prepared a range of air–stable Fe(III)–salen–chloride complexes, with controlled isotactic stereoselectivity observed, for the ROP of *rac*–LA (*Scheme 1*).<sup>[10]</sup> Both the ligand backbone and aromatic substituents were varied. Complexation was achieved under mild conditions using anhydrous ferric chloride, salen–ligand and trimethylamine in a 1:1:2 molar ratio with methanol solvent. Generally, recrystallisation was performed using a mixture of methanol / dichloromethane. However, in cases, separate recrystallisations were attempted, using different solvents and slow evaporation, to achieve crystals suitable for single–crystal X–ray diffraction studies.



*Scheme 1.* Duan's reaction sequence for the range of Fe(III)-salen-chloride complexes synthesised.<sup>[10]</sup>

At that time, an Fe(III)-salalen complex had not been synthesised and reported. Therefore, our intention and aim was to synthesise a range of novel Fe(III)-salalen-chloride complexes, building on the work conducted by Duan, and apply them to the ROP of *rac*-LA and catalytic CO<sub>2</sub> / epoxide coupling.<sup>[10]</sup> It was of interest to see if the isotactic stereoselectivity was maintained and remained competitive, while varying the aromatic and ligand backbone modularities for structure-activity-relationships (SARs) to be studied.

However, soon after synthesising the Fe(III)-salalen-chloride complexes and applying them for the ROP of *rac*-LA, Lamberti and co-workers reported the preparation of the first Fe(III)-salalen complex {Fe(I)Cl}, together with Fe(III)-salan {Fe(J)Cl} and -salen {Fe(K/L)} complexes (*Figure 5*), and their application to the ROP of *L*-LA and  $\epsilon$ -caprolactone and the coupling of CO<sub>2</sub> with propylene oxide (PO), styrene oxide (SO) and cyclohexene oxide (CHO).<sup>[11]</sup> The complexes were not trialled with *rac*-LA and the attempt of the ROP of *L*-LA was unsuccessful under the reaction conditions employed; as it was discovered in this work this was most likely due to the reaction time being too short due to an induction period for initiation.<sup>[11]</sup> Therefore, the application and further exploration of these Fe(III)-salalen-chloride complexes was resumed.

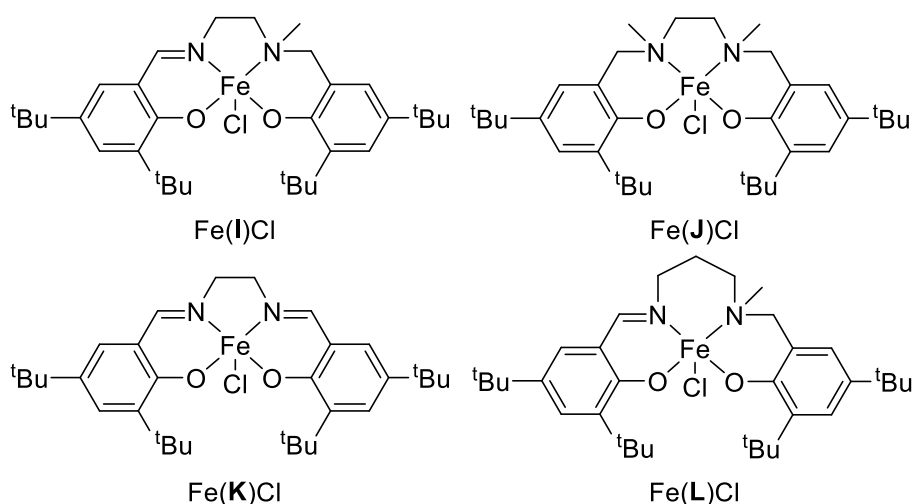


Figure 5. Lamberti's reported Fe(III)–salalen, –salan and –salen complexes.<sup>[11]</sup>

## 2.2 Preparation of salalen, salen and salan ligands

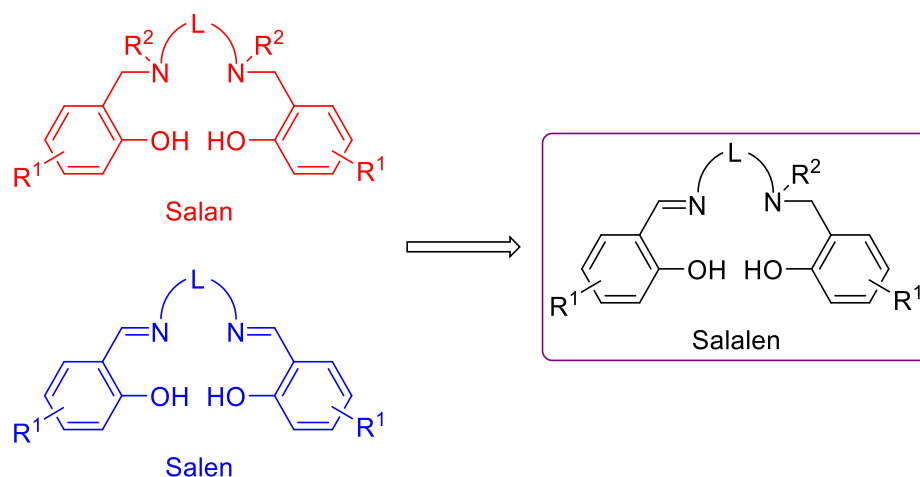
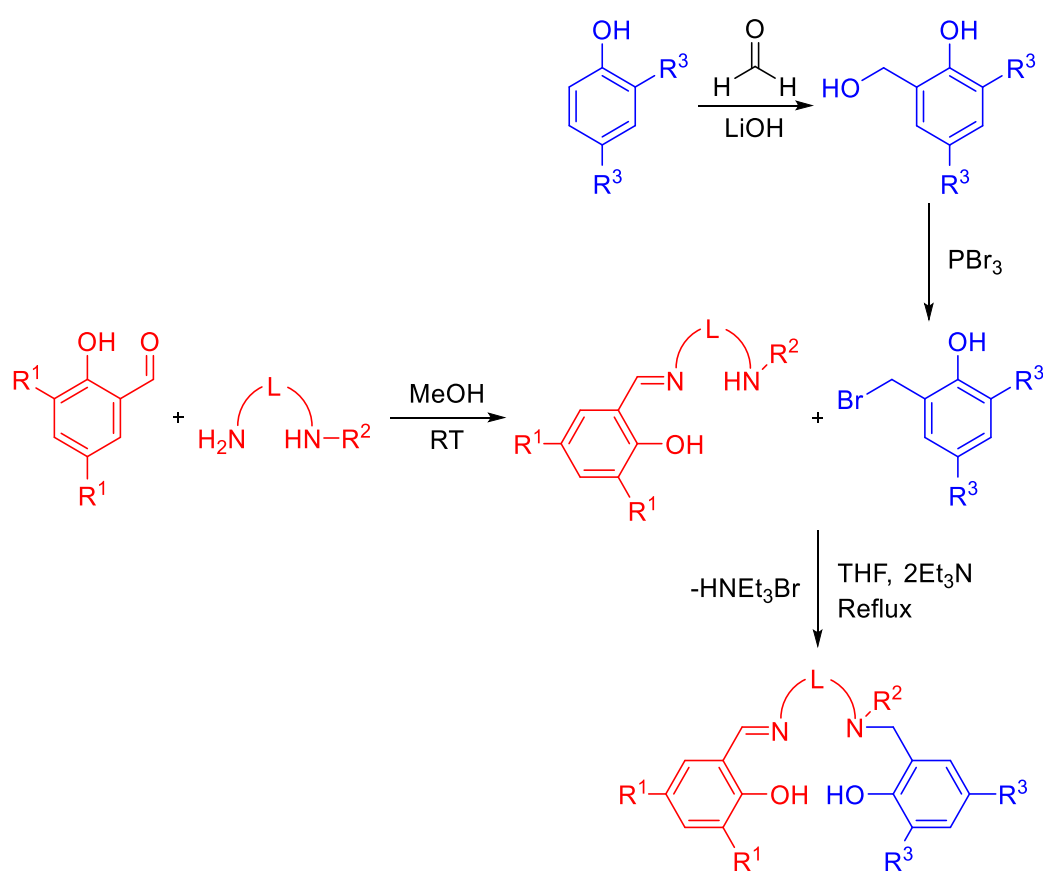


Figure 6. The general 'hybrid' structure of the salalen ligand.<sup>[13,17]</sup>

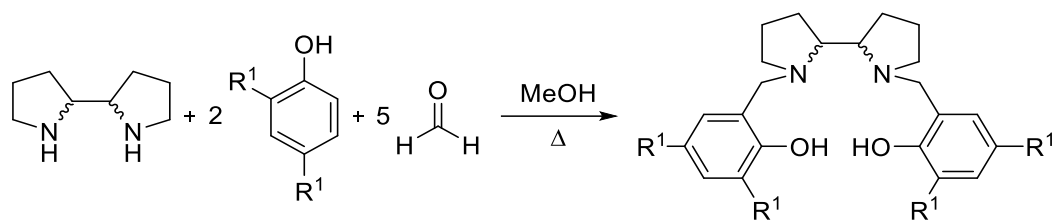
The synthesis of the first salalen ligand was reported by Kol and co-workers *via* the use of condensation reactions.<sup>[17]</sup> Single-crystal X-ray crystallography on the titanium and zirconium–salalen complexes revealed the unsymmetrical nature of the ligand and behaviour resembling a 'hybrid' of the symmetrical salen and salan structures, as illustrated by Figure 6.<sup>[13,17]</sup> Salalen ligands have since been extensively studied, in literature and the Jones group, and reported for a range of applications.<sup>[13,18–24]</sup> Of particular mention, Katsuki and co-workers have made significant development in the application of metal–salalen complexes to asymmetric catalysis.<sup>[13,25–27]</sup> This is owed to their ease of synthesis and the range of modularities

available for their steric and electronic fine tuning of the ligand structure.<sup>[18–24]</sup> As shown in *Scheme 2*, these include the aromatic substituents ( $R^1$  and  $R^3$ ), nitrogen donor aromatic substituent ( $R^2$ ) and the ligand backbone (L). These modularities enable the formation of potentially selective catalysts when complexed to metal precursors. A general sequence for their synthesis (*Scheme 2*), consists of an imine condensation of salicylaldehyde (red reaction path) followed by a sequential  $S_N2$  attack of a benzyl bromide precursor (prepared from the blue reaction path) at the benzyl position to afford the product and ammonium salt by-product. The salalen product can be isolated after filtration and a hot methanol recrystallisation.



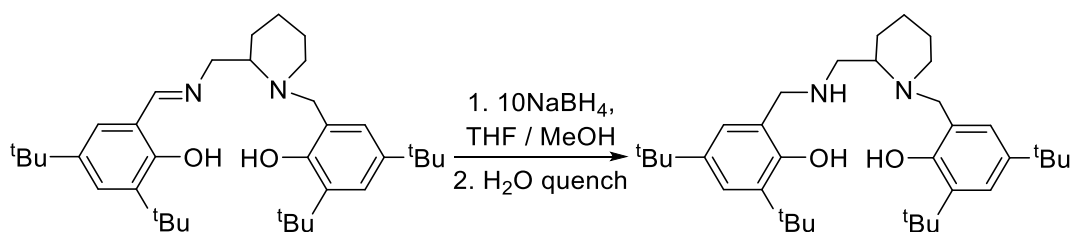
*Scheme 2.* General reaction sequence for the synthesis of a salalen ligand.

Salen ligands can be prepared from the single-step imine condensation step of *Scheme 2* using two equivalents of the salicylaldehyde. Salan ligands are synthesised *via* two experimental procedures. To prepare 2,2'-bipyrrolidine salan derived ligands, a Mannich reaction was employed (*Scheme 3*).<sup>[28–32]</sup>



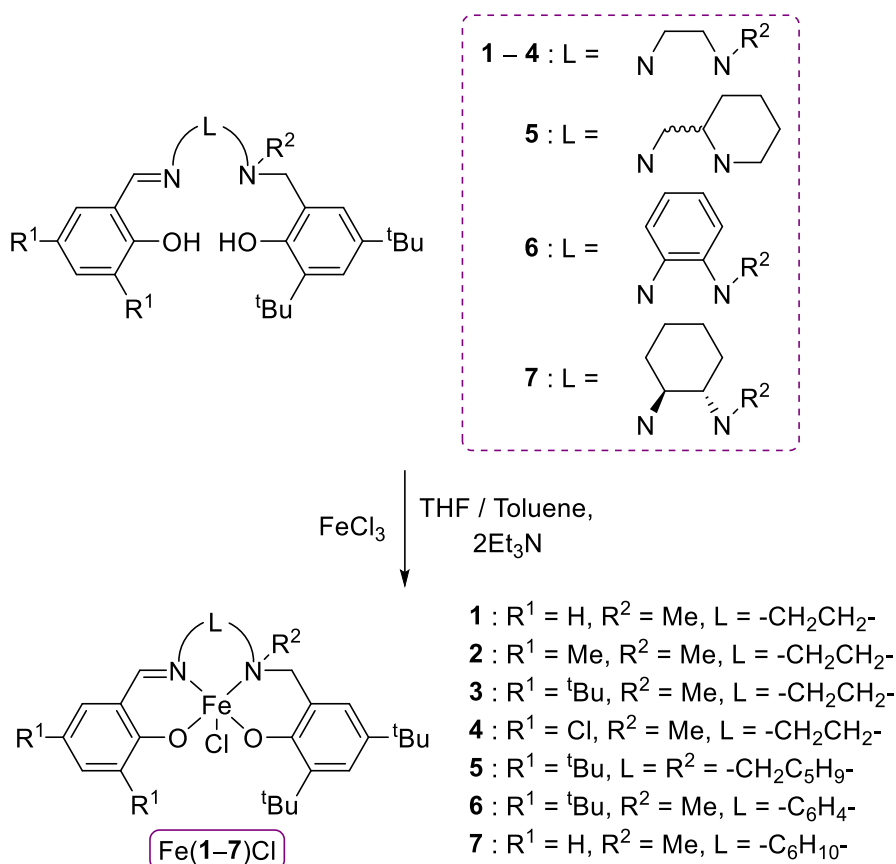
*Scheme 3.* Reaction sequence for the synthesis of 2,2'-bipyrrolidine salan ligands.

Another procedure employed to synthesise salan ligands, with a secondary amine NH functionality, is a sodium borohydride reduction of a salalen ligand (*Scheme 4*). Excess sodium borohydride is added in portions to the salalen ligand in tetrahydrofuran / methanol solution. The mixture is stirred at room temperature overnight, quenched with water and the white solid product isolated.



*Scheme 4.* Reaction sequence for the synthesis of a NH salan ligand *via* sodium borohydride reduction.

## 2.3 Complexation and synthesis of Fe(III)–salalen–chloride complexes



Scheme 5. Synthesis of the Fe(III)–salalen–chloride complexes.

Adapting the experimental procedure used by Duan<sup>[10]</sup> for the Fe(III)–salen–chloride complexes, anhydrous ferric chloride was used for the complexation of the salalen ligands to an Fe(III) centre, in the presence of triethylamine; to remove generated hydrochloric acid and maintain basicity, and yield Fe(1–7)Cl (Scheme 5). Initially, for complexes Fe(1/3/5)Cl, this was achieved in air using refluxing tetrahydrofuran. High resolution mass–spectrometry (HR–MS) and elemental analysis confirmed the purified dark purple product was obtained after filtration and rinsing with hexane. The HR–MS confirmed the coordination of the salalen ligand to the Fe(III) metal centre; the observation of the Fe(L)<sup>+</sup> ion was formed *via* the loss of the Cl<sup>–</sup> ion. Acetonitrile was used as the solvent for HR–MS, resulting in purple solutions similar to that observed during the synthesis; methanol was avoided because the solutions were blue in colour implying possible coordination of the methanol to the Fe(III) centre. Elemental analysis confirmed the monomeric Fe(III)–salalen–chloride



complex was present in the bulk of the rinsed samples. MALDI–ToF mass spectrometry and Evans’ NMR spectroscopic method was also applied to Fe(**3**)Cl for further characterisation. The MALDI–ToF analysis displayed a good match of the experimental isotopic distribution pattern with the theoretical (**Section 6.11**, *Figure 79*). Evans’ NMR spectroscopic method observed the effective magnetic moment to be  $5.71 \mu_B$  at 298 K in deuterated chloroform. This was closer to the  $5.92 \mu_B$  spin-only value for high-spin  $d^5$  Fe(III) complexes ( $S = 5/2$ ) than the  $1.73 \mu_B$  spin-only value for low-spin  $d^5$  Fe(III) complexes ( $S = 1/2$ ). This further confirmed, and agreed with the elemental analysis, that the monomeric Fe(III)–salalen–chloride complex was present in the bulk. As opposed to dinuclear  $\mu$ -oxo–bridged Fe(III) species that are reported to display lower effective magnetic moments at room temperature in literature due to antiferromagnetic coupling.<sup>[33,34]</sup> These dinuclear  $\mu$ -oxo–bridged Fe(III) species may form due to water contamination in the solution, *via* the sequence  $\text{Fe(L)Cl} \rightarrow \text{Fe(L)OH} \rightarrow [\text{Fe(L)}]_2\text{O}$ , or due to  $\text{O}_2$  activation from air.<sup>[33,35–38]</sup>

Recrystallisation was attempted separately by taking a fraction of the sample, as was done in cases by Duan,<sup>[10]</sup> with different solvents in air (**Section 6.10**) to achieve suitable crystals for single–crystal X–ray diffraction. The solid–state structures were confirmed as Fe(**3**)Cl and Fe(**5**)Cl (*Figure 7*); these complexes were dark purple whereas  $\mu$ -oxo–bridged Fe(III) species tend to afford red complexes.<sup>[36,38]</sup>

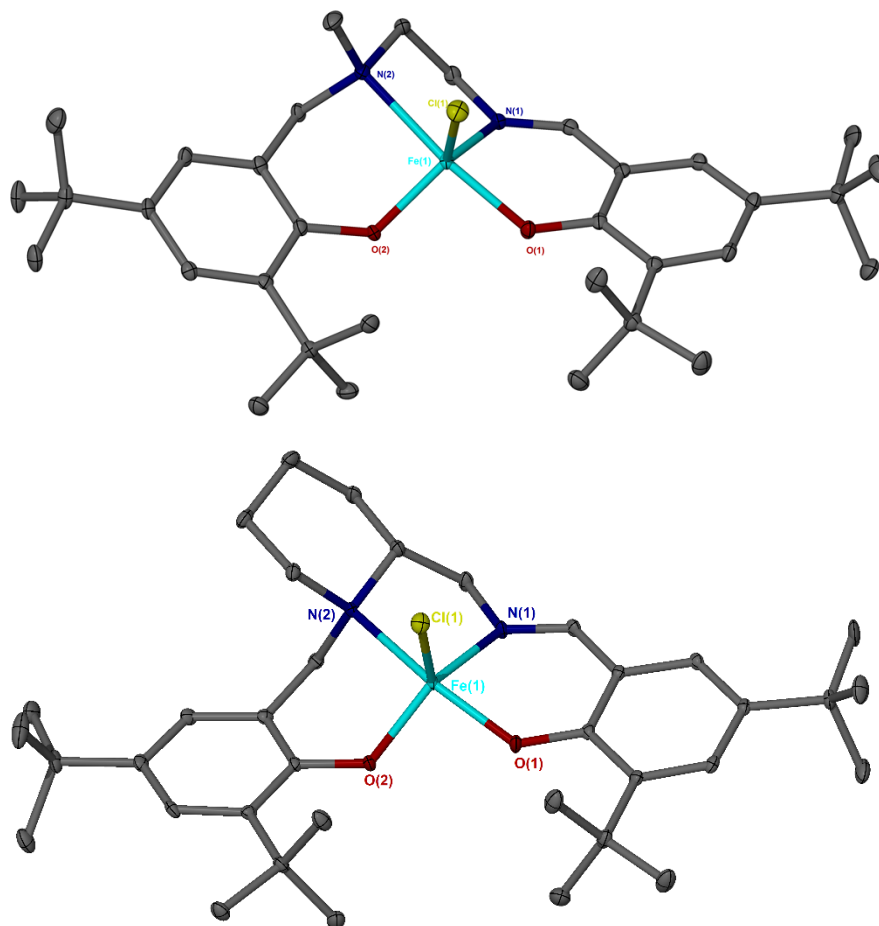


Figure 7. Solid-state structures of Fe(3)Cl (top) and Fe(5)Cl (bottom). Ellipsoids are shown at the 30% probability level and all hydrogen atoms have been removed for clarity. For Fe(3)Cl, the ligand and the chloro group were disordered over two positions in a 92:8 ratio. Constraints were necessary to aid convergence. The minor component has been left isotropic. For Fe(5)Cl, the model is a two component twin with twinning (44%) by virtue of a 180° rotation about the (0.71, 0, -0.71) reciprocal axis.

Both complexes adopted a five-coordinate geometry. The structure for Fe(3)Cl was recently reported with data recorded at room temperature; whereas the structure reported here was produced from data recorded at 150 K.<sup>[11]</sup> The structural index parameter or geometric preference ( $\tau_5$ ), calculated using the two largest valence coordination angles (Equation 1), revealed a slight preference {Fe(3)Cl, L = -CH<sub>2</sub>CH<sub>2</sub>-,  $\tau_5 = 0.66$ } for a trigonal bipyramidal (tbp) geometry ( $\tau_5 = 1$ ) over a square based pyramidal (sbp) geometry ( $\tau_5 = 0$ ); therefore a distorted trigonal bipyramidal geometry in the solid-state.<sup>[39]</sup> Installing the rigid six-membered aminopiperidine ring and reducing the flexibility of the ligand backbone decreased this tbp geometric preference {Fe(5)Cl, L = -CH<sub>2</sub>C<sub>5</sub>H<sub>9</sub>-,  $\tau_5 = 0.56$ }.

$$\tau_5 = \frac{\beta - \alpha}{60^\circ}$$

Equation 1. Geometric preference ( $\tau_5$ ) calculation for a five-coordinate complex whereby  $\beta$  and  $\alpha$  are the two largest valence coordination angles to the metal centre ( $\beta > \alpha$ ).<sup>[39]</sup>

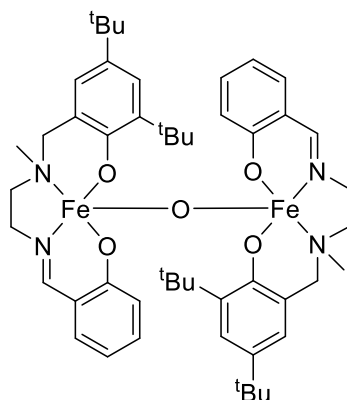
For both distorted t<sub>bp</sub> complexes, the axial positions were occupied by phenoxy donor O(1) and the secondary amine donor N(2). The distortion in the molecular geometry was evident in the deviation of the ideal axial angle {Table 1: O(1)–Fe–N(2); Fe(3)Cl = 164.77(8)° and Fe(5)Cl = 161.92(7)°} and this was the largest metal coordination angle ( $\beta$ ) observed. The largest equatorial angle ( $\alpha$ ) was either between the imine donor and chloride auxiliary ligand {Fe(3)Cl, N(1)–Fe–Cl(1) = 124.94°} or the imine donor and phenoxy donor {Fe(5)Cl, O(2)–Fe–N(1) = 128.35(7)°}. Due to the ligand backbones, the imine–Fe–amine bite angles were forced closer together {N(1)–Fe–N(2); Fe(3)Cl = 78.99(8)° and Fe(5)Cl = 78.73(6)°} compared to the phenoxy–Fe–phenoxy bite angles which were allowed more space {O(1)–Fe–O(2); Fe(3)Cl = 95.77(8)° and Fe(5)Cl = 93.65(6)°} and both deviated from the ideal 90° angle.

Table 1. Selected bond lengths [Å] and angles [°] for Fe(3/5)Cl.

	Fe(3)Cl	Fe(5)Cl
$\tau_5$	0.66	0.56
Fe–Cl(1)	2.2432(7)	2.2492(7)
Fe–O(1)	1.9081(18)	1.8977(15)
Fe–O(2)	1.8445(16)	1.8532(14)
Fe–N(1)	2.047(2)	2.0634(17)
Fe–N(2)	2.300(2)	2.2486(18)
O(1)–Fe–N(2)	164.77(8)	161.92(7)
O(1)–Fe–O(2)	95.77(8)	93.65(6)
O(2)–Fe–N(1)	117.14(8)	128.35(7)
O(2)–Fe–Cl(1)	117.14(6)	116.33(5)
N(1)–Fe–Cl(1)	124.94(6)	119.03(18)
N(1)–Fe–N(2)	78.99(8)	78.73(6)

Furthermore, the axial donor–Fe bonds were longer than the equatorial donor–Fe bonds {*Table 1*: Fe(**3**)Cl; Fe–N(2) = 2.300(2) Å vs. Fe–N(1) = 2.047(2) Å and Fe–O(1) = 1.9081(18) Å vs. Fe–O(2) = 1.8445(16) Å}. This difference in bond length for the nitrogen donor atoms was further accounted for by the difference in functionality; Fe–imine ( $sp^2$ ) vs. Fe–amine ( $sp^3$ ).

For the synthesis of Fe(**1**)Cl, elemental analysis supported that the Fe(III)–salalen–chloride had indeed been formed in the bulk of the hexane rinsed sample. However, single–crystal X–ray diffraction revealed the  $\mu$ –oxo–bridged Fe(III) dimer, [Fe(**1**)]<sub>2</sub>O, (*Figure 8*) when a fraction of the sample was recrystallised in air to afford dark red / orange crystals. The data collected gave a partial solution but was unambiguous. In addition to the elemental analysis, there was also no observed reduction in the catalytic control for ROP (**Sections 3.4–3.6**) of the isolated hexane rinsed, non–recrystallised samples for Fe(**1/3/5**)Cl from decomposition and being stored in air. This indicated that the  $\mu$ –oxo–bridged Fe(III) dimer did not represent the bulk of the hexane rinsed, non–recrystallised sample. Forming instead, during the separate recrystallisation process conducted in air, due to a prolonged time and exposure to oxygen and moisture in solution.



*Figure 8.* The [Fe(**1**)]<sub>2</sub>O  $\mu$ –oxo–bridged Fe(III) dimer observed.

To ensure the formation of the  $\mu$ –oxo–bridged Fe(III) dimer was not due to carrying out the synthesis in air, the following Fe(**2/4/6/7**)Cl complexes were prepared under anhydrous conditions using dry toluene (*Scheme 5*), filtered to remove the triethylammonium chloride salt, and rinsed with dry hexane. HR–MS and elemental analysis were again used to confirm the intended products had indeed been formed.

Single-crystal X-ray diffraction confirmed the solid-structures for Fe(2/6)Cl after recrystallisation (Figure 9).

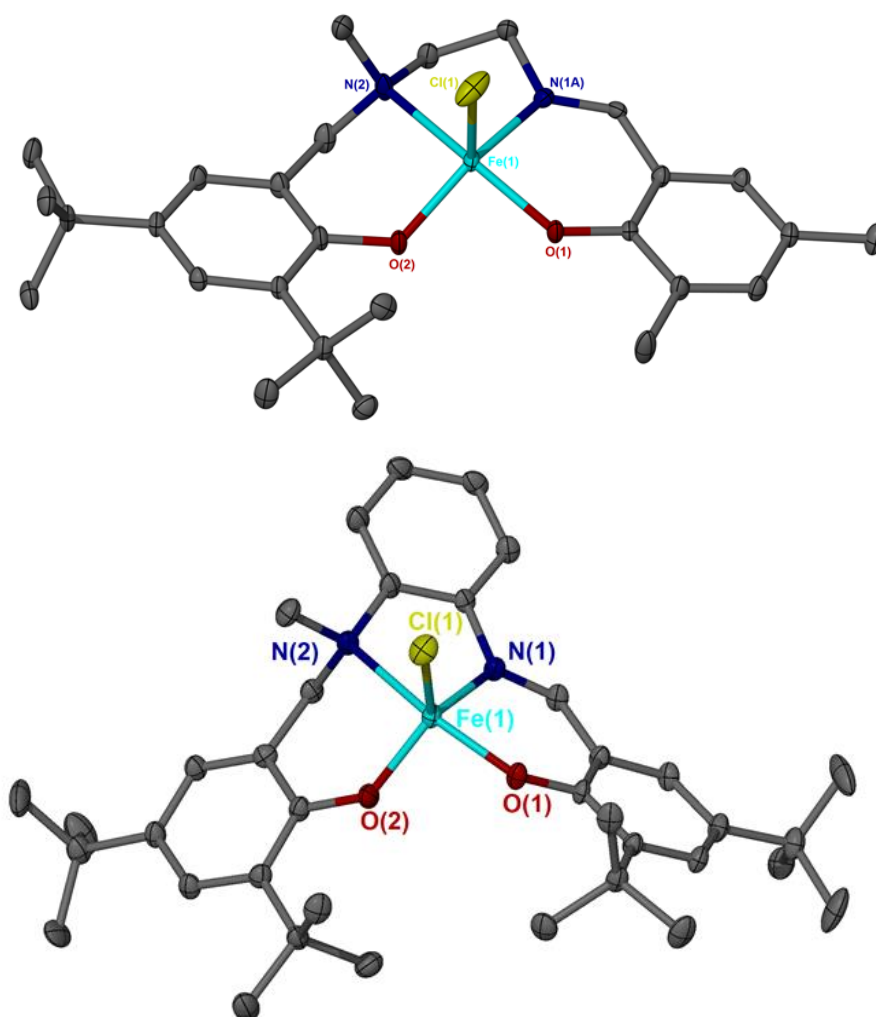


Figure 9. Solid-state structures of Fe(2)Cl (top) and Fe(6)Cl (bottom). Ellipsoids are shown at the 30% probability level and all hydrogen atoms have been removed for clarity. For Fe(2), the ligand backbone was disordered over two positions in a 60:40 ratio. For Fe(6)Cl, disordered *tert*-butyl groups have been removed for clarity.

As was the case for Fe(3/5)Cl, complexes, Fe(2)Cl and Fe(6)Cl both adopted five-coordinate, distorted *tbp* geometries in the solid-state with the axial positions occupied by O(1) and N(2) (Figure 9). The largest metal coordination angle ( $\beta$ ) observed was the distorted axial angle {Table 2: O(1)–Fe–N(2); Fe(2)Cl = 157.48(9) $^\circ$  and Fe(6)Cl = 162.18(17) $^\circ$ } and the largest equatorial angle ( $\alpha$ ) between the imine donor and phenoxy donor {O(2)–Fe–N(1); Fe(2)Cl = 123.48(19) $^\circ$  and Fe(6)Cl = 121.2(2) $^\circ$ }. Compared to Fe(3)Cl, a reduction in the steric bulk of the aromatic

substituents decreased the preference towards the tdp geometry {Fe(2)Cl, R<sup>1</sup> = Me,  $\tau_5$  = 0.57 vs. Fe(3)Cl, R<sup>1</sup> = <sup>t</sup>Bu,  $\tau_5$  = 0.66}. Introducing planarity and a phenyl ring into the ethylene backbone made minimal difference on this preference {Fe(3)Cl, L = -CH<sub>2</sub>CH<sub>2</sub>-,  $\tau_5$  = 0.66 vs. Fe(6)Cl, L = -C<sub>6</sub>H<sub>4</sub>-,  $\tau_5$  = 0.68}. The discussed trends for Fe(3/5)Cl were again observed for Fe(2)Cl and Fe(6)Cl; the imine–Fe–amine bite angles were forced closer together due to the ligand backbones {Table 2: N(1)–Fe–N(2); Fe(2)Cl = 76.8(2)° and Fe(6)Cl = 78.32(18)°} and the phenoxy–Fe–phenoxy bite angles were less restrained {O(1)–Fe–O(2); Fe(2)Cl = 91.91(7)° and Fe(6)Cl = 94.97(18)°}. The axial donor–Fe bonds were once again longer than the equatorial donor–Fe bonds, with the difference in bond length for the nitrogen donor atoms further accounted for by the difference in functionality; Fe–imine (*sp*<sup>2</sup>) vs. Fe–amine (*sp*<sup>3</sup>) {Table 2: Fe(2)Cl; Fe–N(2) = 2.269(2) Å vs. Fe–N(1) = 2.044(7) Å and Fe–O(1) = 1.8941(15) Å vs. Fe–O(2) = 1.8734(16) Å and Fe(6)Cl; Fe–N(2) = 2.260(5) Å vs. Fe–N(1) = 2.064(4) Å and Fe–O(1) = 1.892(4) Å vs. Fe–O(2) = 1.835(4) Å}.

Table 2. Selected bond lengths [Å] and angles [°] for Fe(2/6)Cl.

	Fe(2)Cl	Fe(6)Cl
$\tau_5$	0.57	0.68
Fe–Cl(1)	2.2264(8)	2.236(2)
Fe–O(1)	1.8941(15)	1.892(4)
Fe–O(2)	1.8734(16)	1.835(4)
Fe–N(1)	2.044(7)	2.064(4)
Fe–N(2)	2.269(2)	2.260(5)
O(1)–Fe–N(2)	157.48(9)	162.18(17)
O(1)–Fe–O(2)	91.91(7)	94.97(18)
O(2)–Fe–N(1)	123.48(19)	121.2(2)
O(2)–Fe–Cl(1)	116.56(56)	120.79(15)
N(1)–Fe–Cl(1)	119.03(18)	116.58(16)
N(1)–Fe–N(2)	76.8(2)	76.32(18)

X–ray diffraction was also applied to crystals formed in the recrystallisation of Fe(4)Cl and the solid–structure was confirmed to be the  $\mu$ –oxo–bridged Fe(III) dimer,

[Fe(4)]<sub>2</sub>O (Figure 10). The synthesis was conducted under anhydrous conditions and the elemental analysis of the hexane rinsed, non-recrystallised sample agreed that the expected product had been formed in the bulk. This provided further evidence that the  $\mu$ -oxo-bridged species was indeed forming in the separate recrystallisation process in air, due to prolonged time in solution, as was proposed for [Fe(1)]<sub>2</sub>O observed earlier.

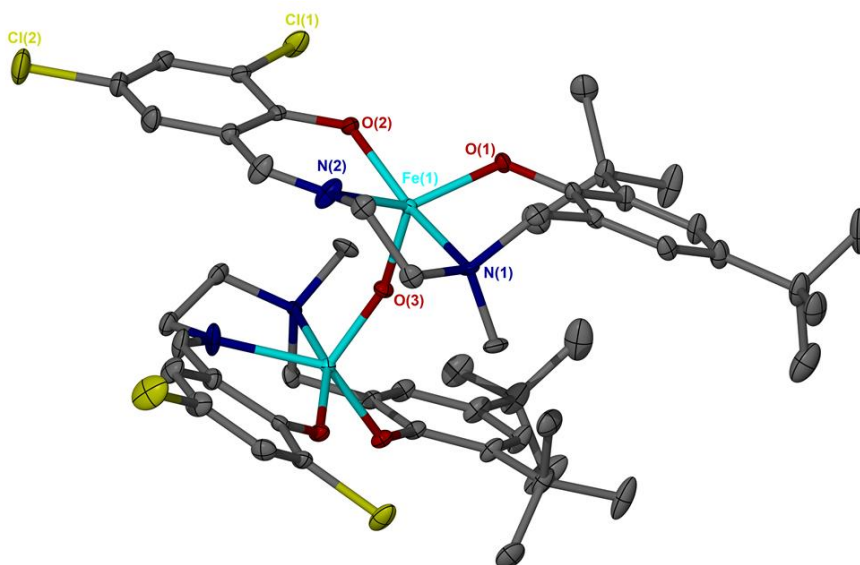
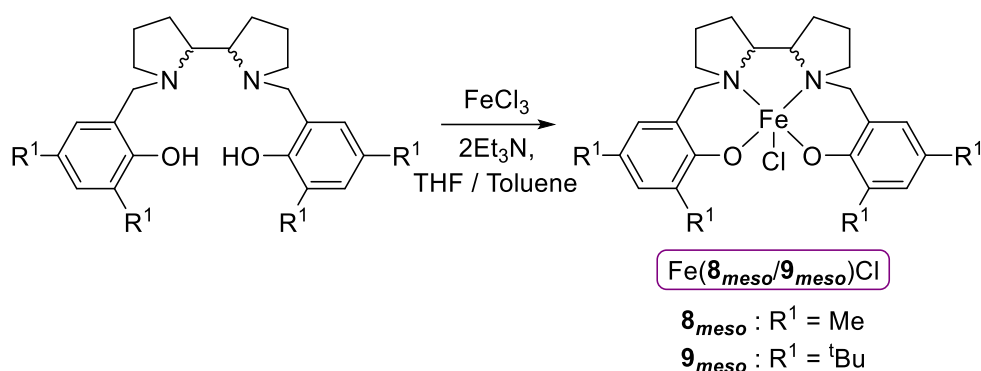


Figure 10. Solid-state structure of [Fe(4)]<sub>2</sub>O. Ellipsoids are shown at the 30% probability level and all hydrogen atoms have been removed for clarity. Half a molecule of diethylether present in unit cell has also been omitted. Disorder was present in the ligand backbone at a ratio of 55:45.

In the solid-state, each Fe(III) centre for [Fe(4)]<sub>2</sub>O was five-coordinate and, unlike for complexes Fe(2/3/5/6)Cl, moderately resembled a more planar distorted sbp geometry ( $\tau_5 = 0.35$ ) with the bridging oxygen atom in the apical position. The two salalen ligands are arranged staggered; rotated by 90° with the  $\mu$ -oxo-bridge bent {Section 2.4, Table 3: Fe(1)–O(3)–Fe(1)#1 = 159.63(12)}. This distortion in the molecular geometry was evident in the deviation of the ideal axial angle, and compared with Fe(3)Cl deviated further away from 180° as expected with a lower geometric preference {Section 2.4, Table 3: [Fe(4)]<sub>2</sub>O, O(2)–Fe(1)–N(1) = 158.27(15)°,  $\tau_5 = 0.35$  vs. Table 1: Fe(3)Cl, O(1)–Fe–N(2) = 164.77(8)°,  $\tau_5 = 0.66$ } and was the largest metal coordination angle ( $\beta$ ) observed. The largest equatorial angle ( $\alpha$ ) was between the imine donor and phenoxy donor {O(1)–Fe–N(2) = 137.37(8)°}. Additionally, the axial donor ( $sp^3$ )–Fe bonds were longer than the equatorial donor ( $sp^2$ )–Fe bonds

{Section 2.4, Table 3: Fe–N(1) = 2.259(11) Å vs. Fe–N(2) = 2.1125(17) Å and Fe–O(2) = 1.9629(13) Å vs. Fe–O(1) = 1.8846(12) Å}. The auxiliary oxygen atom–Fe bond was shorter than observed Fe–Cl bonds {[Fe(4)]<sub>2</sub>O, Fe–O(1) = 1.7717(4) Å vs. Fe(3)Cl, Fe–Cl(1) = 2.2432(7) Å} and similar to that reported for  $\mu$ -oxo-bridged Fe(III)–salen complexes; however there were observed differences in the deviation from linearity of the Fe(1)–O(3)–Fe(1)#1 bridge.<sup>[40]</sup>

## 2.4 Complexation and synthesis of Fe(III)–salan complexes



Scheme 6. Complexation of *meso*-2,2'-bipyrrrolidine salan ligands to FeCl<sub>3</sub>.

Another postulation for the observation of the  $\mu$ -oxo-bridged species, in the synthesis of Fe(1)Cl and Fe(4)Cl, was that they formed due to a reduction in steric bulk or increased Lewis acidity {R<sup>1</sup> = H and = Cl}. This can be reinforced in the solid-state structures obtained, using single-crystal X-ray diffraction, in the attempted synthesis of Fe(III)–salan–chloride complexes 'Fe(8<sub>meso</sub>)Cl' and Fe(9<sub>meso</sub>)Cl using *meso*-2,2'-bipyrrrolidine salan ligands (Scheme 6); the bipyrrrolidine ligand prepared following Scheme 3 (Section 2.1). With the two stereocentres present in the 2,2'-bipyrrrolidine moiety, this results in three possible stereoisomers for this ligand framework: as the enantiomers (*R,R*-) and (*S,S*-) or the *meso*-2,2'-bipyrrrolidine ligand framework employed here.<sup>[29,41]</sup> The stereochemistry and chirality of this ligand backbone will be further explored and focused on in Section 2.8. Recrystallisation was carried out using a mixed acetonitrile / methanol solution for 'Fe(8<sub>meso</sub>)Cl' or diethylether / dichloromethane solution for Fe(9<sub>meso</sub>)Cl and slow evaporation. For which, the  $\mu$ -oxo-bridged Fe(III) dimer; [Fe(8<sub>meso</sub>)<sub>2</sub>O] was observed for Fe(8<sub>meso</sub>)Cl and the Fe(III)–salan–chloride for Fe(9<sub>meso</sub>)Cl with increased steric bulk on the aromatic ring {[Fe(8<sub>meso</sub>)<sub>2</sub>O], R<sup>1</sup> = Me vs. Fe(9<sub>meso</sub>)Cl, R<sup>1</sup> = <sup>t</sup>Bu} (Figure 11).



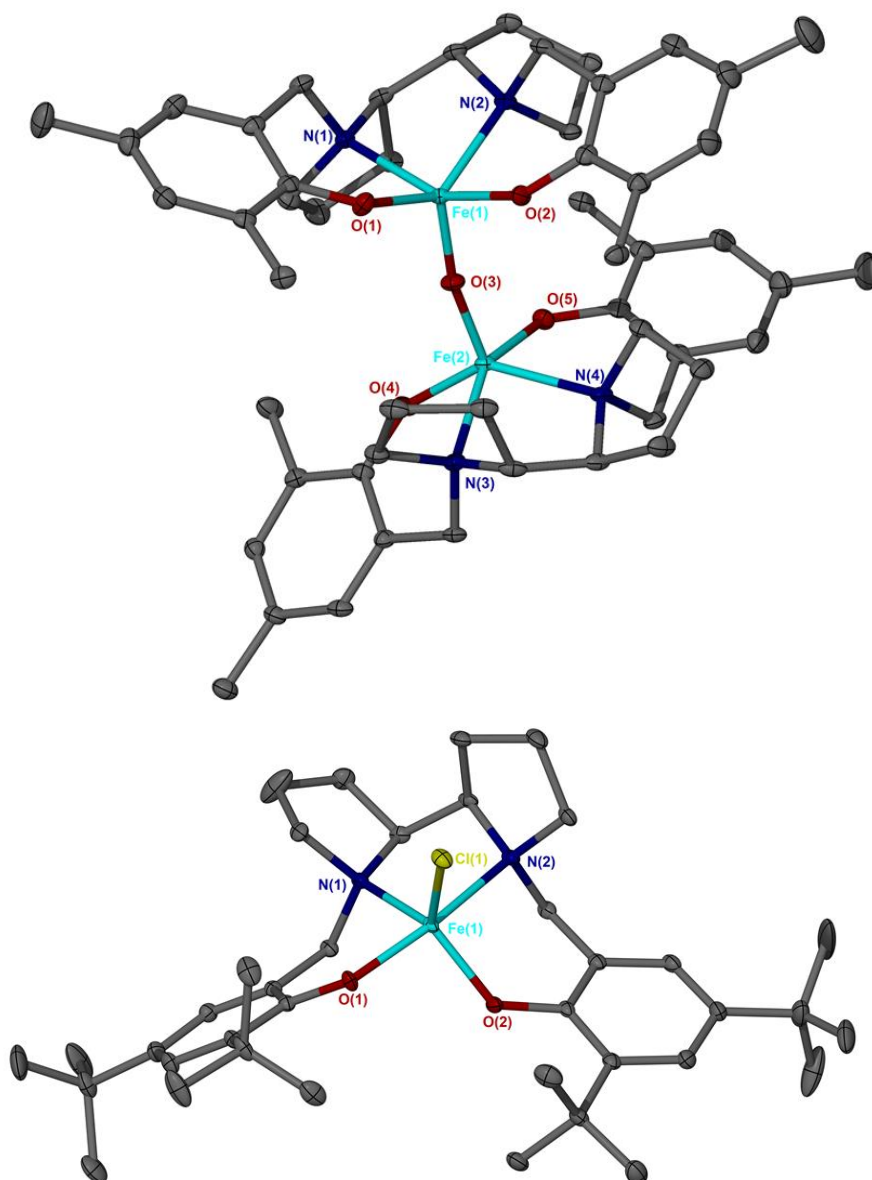


Figure 11. Solid-state structures of  $[\text{Fe}(\mathbf{8}_{\text{meso}})]_2\text{O}$  (top) and  $\text{Fe}(\mathbf{9}_{\text{meso}})\text{Cl}$  (bottom). Ellipsoids are shown at the 30% probability level and all hydrogen atoms have been removed for clarity. For  $[\text{Fe}(\mathbf{8}_{\text{meso}})]_2\text{O}$ , two molecules of acetonitrile are also present in the asymmetric unit but have been removed for clarity.

For  $[\text{Fe}(\mathbf{8}_{\text{meso}})]_2\text{O}$ , each Fe(III) centre was five-coordinate with the auxiliary oxygen atom in the apical position. The two *meso*-2,2'-bipyrrrolidine ligands are arranged eclipsed with the  $\mu$ -oxo-bridge bent. However, this bridge is more linear and closer to the ideal axial angle compared to  $[\text{Fe}(\mathbf{4})]_2\text{O}$  {Table 3:  $[\text{Fe}(\mathbf{8}_{\text{meso}})]_2\text{O}$ ,  $\text{Fe}(1)\text{--O}(3)\text{--Fe}(2) = 159.63(12)^\circ$  vs.  $[\text{Fe}(\mathbf{4})]_2\text{O}$ ,  $\text{Fe}(1)\text{--O}(3)\text{--Fe}(1)\#1 = 169.2(3)^\circ$ } potentially due to maximising  $\pi\text{--}\pi$  stacking interactions. As was observed for  $[\text{Fe}(\mathbf{4})]_2\text{O}$ , there was a considerable geometric preference to the distorted sbp. Interestingly,  $[\text{Fe}(\mathbf{8}_{\text{meso}})]_2\text{O}$

was not symmetrical and two geometric preference values were obtained {Fe(1) centre,  $\tau_5 = 0.27$  and Fe(2) centre,  $\tau_5 = 0.17$ }.

Table 3. Selected bond lengths [Å] and angles [°] for Fe(4/8<sub>meso</sub>)]<sub>2</sub>O.

	[Fe(4)] <sub>2</sub> O	[Fe(8 <sub>meso</sub> )] <sub>2</sub> O
$\tau_5$	0.35	0.27 / 0.17
Fe(1)–O(3)	1.7717(4)	1.788(4)
Fe(1)–O(1)	1.8846(12)	1.917(4)
Fe(1)–O(2)	1.9629(13)	1.927(4)
Fe(1)–N(1)	2.259(11)	2.211(4)
Fe(1)–N(2)	2.1125	2.179(4)
Fe(1)–O(3)–Fe(1)#1	159.63(12)	–
Fe(1)–O(3)–Fe(2)	–	169.2(3)
O(1)–Fe(1)–N(2)	137.37(8)	136.74(18)
O(2)–Fe(1)–N(1)	158.27(15)	152.98(16)
O(2)–Fe(1)–O(3)	103.17(5)	108.30(18)
N(1)–Fe(1)–O(3)	95.57(15)	97.85(17)
O(4)–Fe(2)–N(4)	–	140.89(17)
O(5)–Fe(2)–N(3)	–	151.24(17)

The solid-state structure for Fe(9<sub>meso</sub>)Cl followed similar trends observed for complexes Fe(2/3/5/6)Cl. The five-coordinate geometry, adopted in the solid-state, resembling a distorted t<sub>bp</sub> compared with the more distorted s<sub>bp</sub> for [Fe(8<sub>meso</sub>)]<sub>2</sub>O; the ligand backbones differing only by the alkyl group at position R<sup>1</sup> {Fe(9<sub>meso</sub>)Cl, R<sup>1</sup> = <sup>t</sup>Bu,  $\tau_5 = 0.63$  vs. [Fe(8<sub>meso</sub>)]<sub>2</sub>O, R<sup>1</sup> = Me,  $\tau_5 = 0.27 / 0.17$ }. The axial angle; the largest metal coordination angle ( $\beta$ ), deviated from the ideal value {Table 4: O(1)–Fe–N(2) = 162.25(7)°} and the largest equatorial angle ( $\alpha$ ) was between the other amine and phenoxy donor atoms {O(2)–Fe–N(1) = 124.54(7)°}. The trend was different, however, observing the bond lengths. The axial donor–Fe bonds were similar to the equatorial donor–Fe bonds, unlike for the Fe(III)–salalen complexes, with the Fe–phenoxy bonds the same length and the Fe–amine bonds differing only slightly {Table

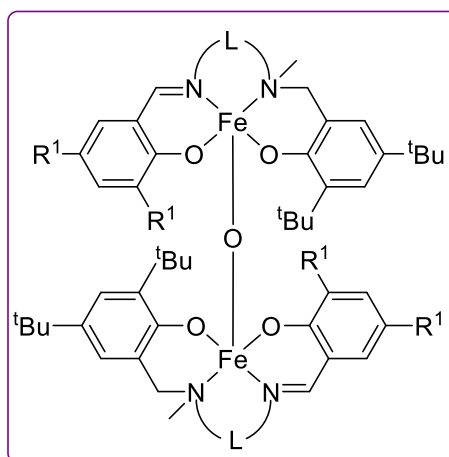
4: Fe–O(1) = 1.8648(16) Å vs. Fe–O(2) = 1.8692(16) Å and Fe–N(2) = 2.264(2) Å vs. Fe–N(1) = 2.153(2) Å}. This was also observed for [Fe(**8***meso*)]<sub>2</sub>O and is not unexpected considering both donor nitrogen atoms are the same amine functionality (*sp*<sup>3</sup>) for the *meso*–2,2'–bipyrrolidine salen framework, unlike for the salalen class, and the symmetrical nature of the ligand.

Table 4. Selected bond lengths [Å] and angles [°] for Fe(**9***meso*)Cl.

Fe( <b>9</b> <i>meso</i> )Cl	
$\tau_5$	0.63
Fe–Cl(1)	2.2438(7)
Fe–O(1)	1.8648(16)
Fe–O(2)	1.8692(16)
Fe–N(1)	2.153(2)
Fe–N(2)	2.264(2)
O(1)–Fe–N(2)	162.25(7)
O(1)–Fe–O(2)	95.87(7)
O(2)–Fe–N(1)	124.54(7)
O(2)–Fe–Cl(1)	117.83(6)
N(1)–Fe–Cl(1)	116.86(5)
N(1)–Fe–N(2)	78.49(7)

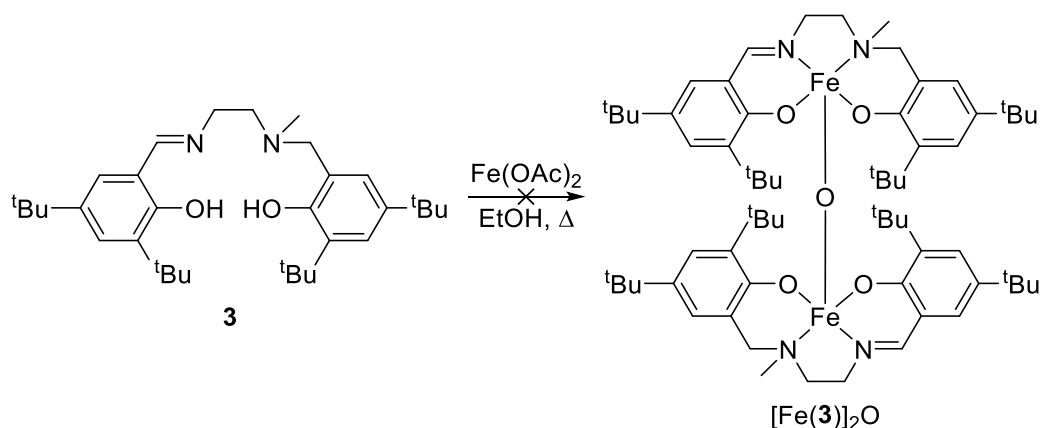
## 2.5 Complexation and synthesis of Fe(III)–acetate complexes

After synthesising and studying the distorted *tbp* Fe(III)–salalan–chloride complexes, and observing the Fe(III)  $\mu$ -oxo-bridged species in some cases in the solid-state. It was decided to draw attention to these more planar and *sbp* complexes; aiming to synthesise a range of novel  $\mu$ -oxo-bridged Fe(III)–salalen complexes (*Figure 12*).



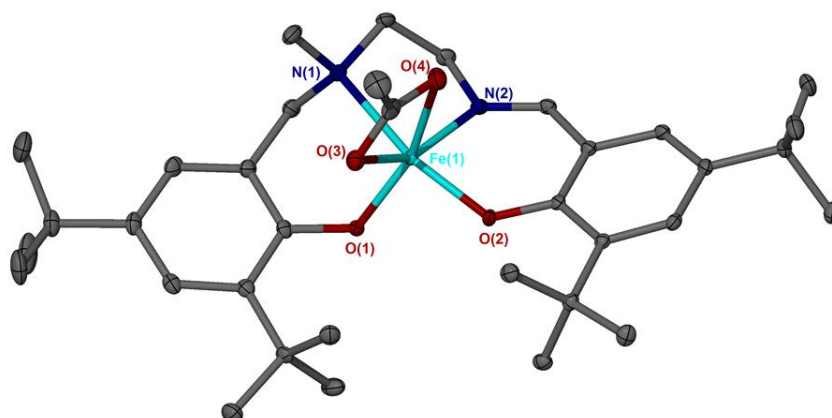
*Figure 12.* The desired  $\mu$ -oxo-bridged Fe(III)–salalen complexes.

There are numerous examples of  $\mu$ -oxo-bridged Fe complexes in literature and more specifically complexes similar to the desired salalen above (*Figure 12*); such as  $\mu$ -oxo-bridged Fe(III)–salen complexes.<sup>[36,37,38,42–52]</sup> Fe(III)–salen complexes and  $\mu$ -oxo-bridged Fe complexes have been applied to a range of catalytic processes such as olefin hydrophosphination, olefin cyclopropanation, epoxyalkene ring expansion, asymmetric hydrophosphorylation or hydrophosphonylation of aldehydes, CO<sub>2</sub> / epoxide copolymerisation and in the catalytic synthesis of benzoxazoles.<sup>[36,37,42–45,53–59]</sup> Therefore, if the  $\mu$ -oxo-bridged Fe(III)–salalen complexes were made, the aim was to then apply them to catalytic processes such as the ring opening polymerisation of lactide, olefin hydrophosphination and CO<sub>2</sub> / epoxide coupling (**Chapters 3 and 4**).



*Scheme 7.* Attempted reaction sequence to synthesise the  $\mu$ -oxo-bridged Fe(III)-salalen  $\{[\text{Fe(3)}]_2\text{O}\}$  complex.

Following the experimental procedure previously reported in literature and used to synthesise a  $\mu$ -oxo-bridged Fe(III)-salen complex,<sup>[36]</sup> the salalen ligand was added as a yellow solid to the 'sandy' brown mixture of the  $\text{Fe(OAc)}_2$  metal precursor in ethanol under air (*Scheme 7*). This addition was accompanied by a colour change to an intense dark purple. The mixture was then refluxed for two hours and left to cool with no stopper for slow evaporation. Dark purples crystals formed in the ethanol solution and these were analysed using single-crystal X-ray diffraction. However, instead of the expected  $\mu$ -oxo-bridged species  $\{[\text{Fe(3)}]_2\text{O}\}$ , the Fe(III)-salalen-acetate complex  $\{\text{Fe(3)OAc}\}$  was observed, with the solid-state structure confirming the acetate auxiliary group was present on the Fe(III) centre (*Figure 13*).



*Figure 13.* Solid-state structure of  $\text{Fe(3)OAc}$ . Ellipsoids are shown at the 30% probability level. All hydrogen atoms and a molecule of ethanol have been removed for clarity.

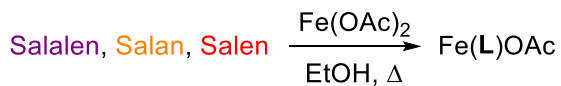
The isolated recrystallised product was analysed using HR-MS, elemental analysis and Infra-Red spectroscopy (FT-IR). As was the case for Fe(1-7)Cl, HR-MS confirmed the coordination of the salalen ligand to the Fe(III) metal centre and the observation of the Fe(L)<sup>+</sup> ion, with ionisation achieved *via* the loss of the acetate anion. The elemental analysis, including the molecule of ethanol incorporated in the crystal lattice, was closer to and confirmed that the Fe(III)-acetate was present in the bulk of the sample and not the expected  $\mu$ -oxo-bridged species. Stretches were observed in the region of 1400–1550 cm<sup>-1</sup> for FT-IR and assigned to be aromatic C=C and acetate bond stretches.

As this represented the first synthesis of an air-stable Fe(III)-salalen-acetate complex and owing to the simple synthetic procedure employed, our aims deviated away from the  $\mu$ -oxo-bridged Fe(III) species and towards studying these Fe(III)-acetate complexes. To our surprise there are scarce examples of Fe(III)-acetate complexes bearing {ONNO} ligands, characterised in the solid-state, in literature and to our knowledge there were no examples for their use in polymerisation and CO<sub>2</sub> / epoxide coupling. In addition to this, while synthesising these complexes, Kerton and co-workers reported the synthesis and application of dinuclear  $\mu$ -oxo-bridged Fe(III)-amino-*bis*(phenolate) complexes; these Fe(III)-salan complexes relatively similar to the initially targeted  $\mu$ -oxo-bridged Fe(III)-salalen complexes (*Figure 12*). As will be discussed in **Section 4.2**, these dinuclear complexes were less active than the mononuclear Fe(III)-Cl analogues for CO<sub>2</sub> / epoxide coupling and both sets of these sbp complexes were less active than tbp alternatives.<sup>[33,60,61]</sup>

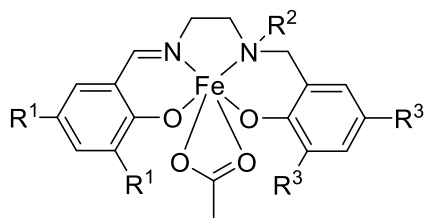
A range of ligands, such as salalen, salan and salen, were complexed in air with the Fe(OAc)<sub>2</sub> metal precursor. The Fe(L)OAc complex was consistently isolated after recrystallisation / slow evaporation and rinsing with cold ethanol to yield overall complexes Fe(1/3/5/6/8-17)OAc. These are shown in *Scheme 8* and colour coded; Fe(III)-salalen complexes were typically dark purple products, Fe(III)-salen complexes were typically dark red and Fe(III)-salan complexes were a mixture of red and purple. Characterisation for the complexes was carried out using HR-MS, elemental analysis and FT-IR. For all complexes, HR-MS confirmed the coordination of the ligand and elemental analysis was consistent with the Fe(III)-acetate being

present in the bulk of the sample; a molecule of ethanol was included in the calculation for Fe(**1/3/8<sub>meso</sub>/10**)OAc. This agreed with FT-IR where alcohol OH stretches were observed for the complexes with aromatic C=C and acetate bond stretches in all cases. Eight further solid-state structures were confirmed using single-crystal X-ray diffraction.

Evans' NMR spectroscopic method was applied to all the complexes. The effective magnetic moment ranged from 4.57–5.74  $\mu_B$  at 298 K in deuterated chloroform. This is closer to the 5.92  $\mu_B$  spin-only value for high-spin  $d^5$  Fe(III) complexes ( $S = 5/2$ ) than the 1.73  $\mu_B$  spin-only value for low-spin  $d^5$  Fe(III) complexes ( $S = 1/2$ ). This is with the exception of Fe(**17**)OAc which had a value of 2.10  $\mu_B$ . It is reported in literature<sup>[33,34]</sup> that  $\mu$ -oxo-bridged Fe(III) species display lower effective magnetic moments at room temperature; Kerton's  $\mu$ -oxo-bridged Fe(III)-salan complexes ranging from 2.41–3.20  $\mu_B$  proposed to be caused by the antiferromagnetic coupling occurring across the bridging oxygen.<sup>[33]</sup> This further confirms complexes Fe(**1/3/5/6/8–13/15/16**)OAc were isolated in the bulk of samples and Evans' method suggests potential  $\mu$ -oxo-bridged or Fe(OAc)<sub>2</sub> impurities for Fe(**17**)OAc.

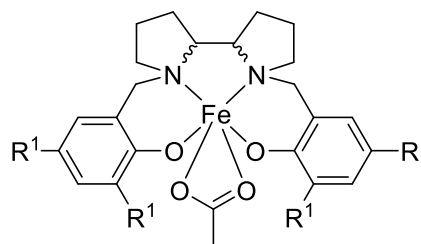


**Salalen**

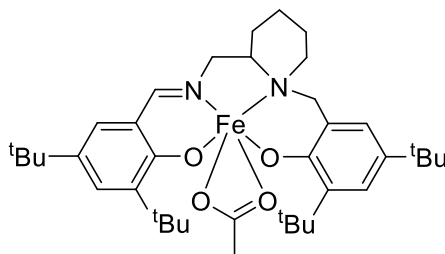


- Fe(1)OAc** R<sup>1</sup> = H, R<sup>2</sup> = Me, R<sup>3</sup> = <sup>t</sup>Bu  
**Fe(3)OAc** R<sup>1</sup> = <sup>t</sup>Bu, R<sup>2</sup> = Me, R<sup>3</sup> = <sup>t</sup>Bu  
**Fe(10)OAc** R<sup>1</sup> = <sup>t</sup>Bu, R<sup>2</sup> = Ph, R<sup>3</sup> = <sup>t</sup>Bu  
**Fe(11)OAc** R<sup>1</sup> = H, R<sup>2</sup> = Me, R<sup>3</sup> = Br

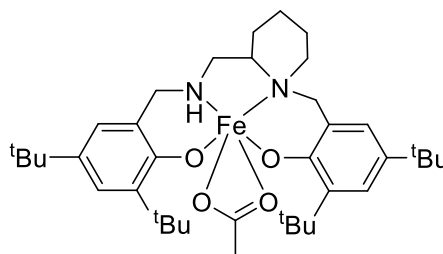
**Salan**



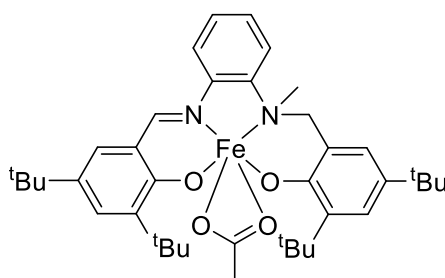
- Fe(8<sub>meso</sub>)OAc** R<sup>1</sup> = Me  
**Fe(8<sub>RR</sub>)OAc** R<sup>1</sup> = Me  
**Fe(8<sub>SS</sub>)OAc** R<sup>1</sup> = Me  
**Fe(9<sub>meso</sub>)OAc** R<sup>1</sup> = <sup>t</sup>Bu



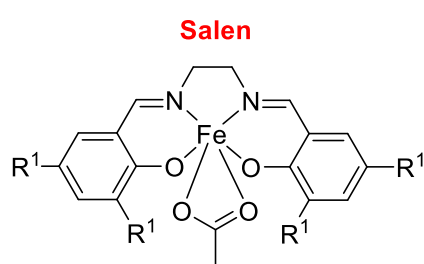
**Fe(5)OAc**



**Fe(13)OAc**

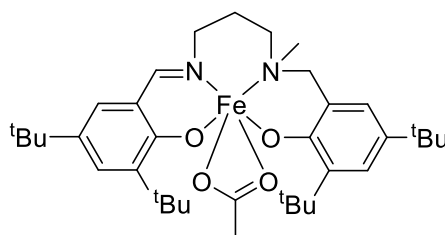


**Fe(6)OAc**

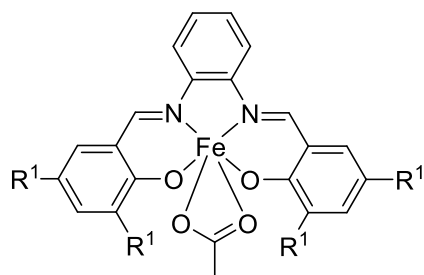


**Salen**

- Fe(14)OAc** R<sup>1</sup> = H  
**Fe(15)OAc** R<sup>1</sup> = <sup>t</sup>Bu



**Fe(12)OAc**



- Fe(16)OAc** R<sup>1</sup> = H  
**Fe(17)OAc** R<sup>1</sup> = <sup>t</sup>Bu

Scheme 8. The overall range of Fe(III)–salalen, –salan and –salen {Fe(L)OAc} complexes synthesised.



In addition to Fe(3)OAc, the solid-state structures for Fe(5/6/8<sub>meso</sub>/9<sub>meso</sub>/10/11/13/15)OAc were confirmed. All complexes were six-coordinate with distorted *pseudo*-trigonal bipyramidal geometries (*pseudo*-tbp) and not the expected octahedral geometry. The acetate auxiliary group occupied an equatorial site and behaved as a monodentate ligand due to the tight bite angle {Table 5: Fe(3)OAc, O(3)–Fe–O(4) = 60.82(6)}.

This distorted *pseudo*-trigonal bipyramidal geometry, adopted by all complexes, was analogous to the Fe(III)–salalen–chloride complexes (Section 2.3). This can be particularly evident when overlaying the solid-state structures for Fe(3)OAc and the analogous Fe(3)Cl (Figure 14). The central acetate carbon atom {C(acetate)} occupies the same equatorial site as the chloride. The geometric preference was similar for both complexes {Fe(3)OAc,  $\tau_5 = 0.65$  vs. Fe(3)Cl,  $\tau_5 = 0.66$ } towards the distorted tbp geometry. The geometric preference was calculated for Fe(3)OAc by focussing on the C(acetate) atom and disregarding the two acetate oxygen atoms; as the ligand behaves in a monodentate manner.

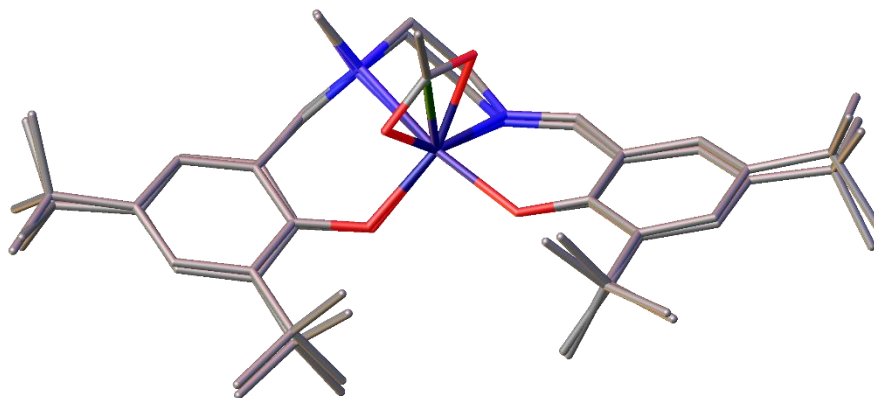
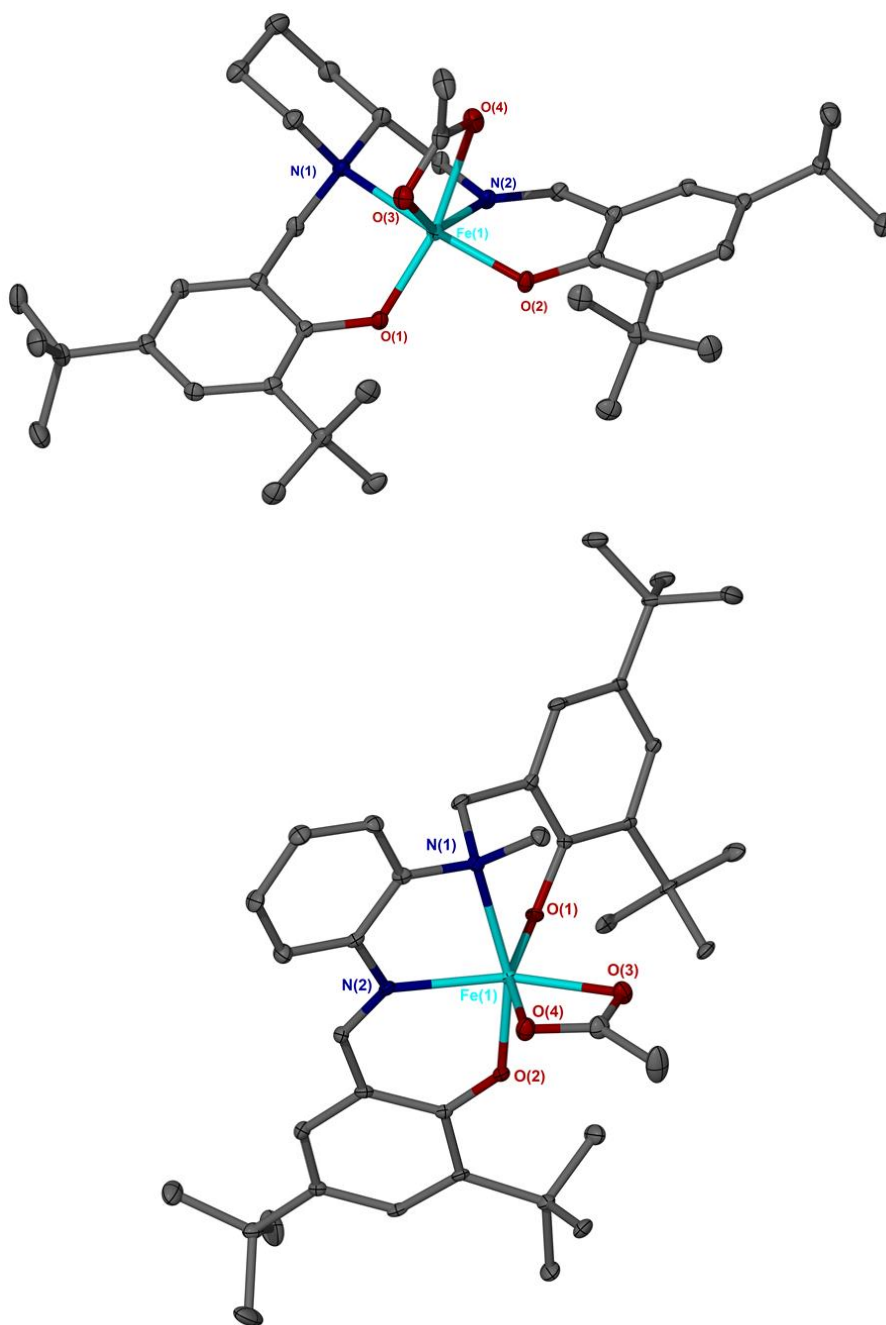


Figure 14. Solid-state structures for Fe(3)OAc and the analogous Fe(3)Cl with the acetate and chloride auxiliary groups occupying the same equatorial site.

Similar trends discussed for the distorted tbp solid-state structures of Fe(2/3/5/6)Cl were observed for the Fe(III)–salalen–acetate complexes {Fe(3/5/6/10/11)OAc} (Figures 13, 15 and 16). The axial positions were occupied by phenoxy donor O(2) and the secondary amine donor N(1) with distortion in the molecular geometry evident in the deviation of the ideal axial angle; generally consistent at 165° {Table 5: O(2)–Fe–(1); Fe(3)OAc = 165.35(6)°, Fe(5)OAc = 165.13(6)°, Fe(6)OAc = 162.01(9)°,

$\text{Fe(10)OAc} = 165.42(7)^\circ$  and  $\text{Fe(11)OAc} = 166.12(15)^\circ$ . The largest equatorial angle ( $\alpha$ ) was between the central acetate carbon atom and a phenoxy donor  $\{\text{O(1)}\text{-Fe-C(acetate)}\}$ ;  $\text{Fe(3)OAc} = 126.20(7)^\circ$ ,  $\text{Fe(5)OAc} = 130.56^\circ$  and  $\text{Fe(10)OAc} = 129.2^\circ$  or the central acetate carbon atom and imine donor  $\{\text{N(2)}\text{-Fe-C(acetate)}\}$ ;  $\text{Fe(11)OAc} = 123.64(17)^\circ$ . The geometric preference was calculated using these two largest metal coordination angles ( $\beta$  and  $\alpha$ ). Comparing to  $\text{Fe(3)OAc}$  ( $R^2 = \text{Me}$ ,  $\tau_5 = 0.65$ ), the geometric preference decreased when an electron withdrawing phenyl group was installed on the amine donor  $\{\text{Fe(10)OAc}$ ,  $R^2 = \text{Ph}$ ,  $\tau_5 = 0.60$ ) and further still when installing the rigid six-membered aminopiperidine ring and reducing the flexibility of the ligand backbone  $\{\text{Fe(5)OAc}$ ,  $\tau_5 = 0.58\}$ , as was observed by  $\text{Fe(3/5)Cl}$ . Despite the introduction of planarity and a phenyl ring into the ethylene backbone, resulting in minimal difference for  $\text{Fe(6)Cl}$  compared to  $\text{Fe(3)Cl}$ , the geometric preference decreased for  $\text{Fe(6)OAc}$  compared to  $\text{Fe(3)OAc}$   $\{\text{Fe(6)OAc}$ ,  $L = \text{-C}_6\text{H}_4\text{-}$ ,  $\tau_5 = 0.58$  vs.  $\text{Fe(6)Cl}$ ,  $L = \text{-C}_6\text{H}_4\text{-}$ ,  $\tau_5 = 0.68\}$ . The *tbp* preference increased for the more Lewis acidic Fe(III) centre with a unsubstituted imine aromatic ring and bromo-substitution on the amine aromatic ring  $\{\text{Fe(11)OAc}$ ,  $R^1 = \text{H}$ ,  $R^3 = \text{Br}$ ,  $\tau_5 = 0.71\}$ . The imine-Fe-amine bite angles were forced closer together due to the ligand backbones relative to the phenoxy-Fe-phenoxy bite angles; and all deviated from the ideal  $90^\circ$  (*Table 5*). Due to the difference in nitrogen functionality for the salalen ligand and distorted *pseudo-tbp* geometry, the axial donor-Fe bonds were longer than the equatorial donor-Fe bonds (*Table 5*:  $\text{Fe(3)OAc}$ ,  $\text{Fe-N(1)} = 2.2633(17) \text{ \AA}$  vs.  $\text{Fe-N(2)} = 2.0716(17) \text{ \AA}$  and  $\text{Fe-O(2)} = 1.9011(13) \text{ \AA}$  vs.  $\text{Fe-O(1)} = 1.8719(13) \text{ \AA}$ ).



*Figure 15.* The solid-state structures for Fe(5)OAc (top) and Fe(6)OAc (bottom). Ellipsoids are shown at the 30% probability level and all hydrogen atoms have been removed for clarity.

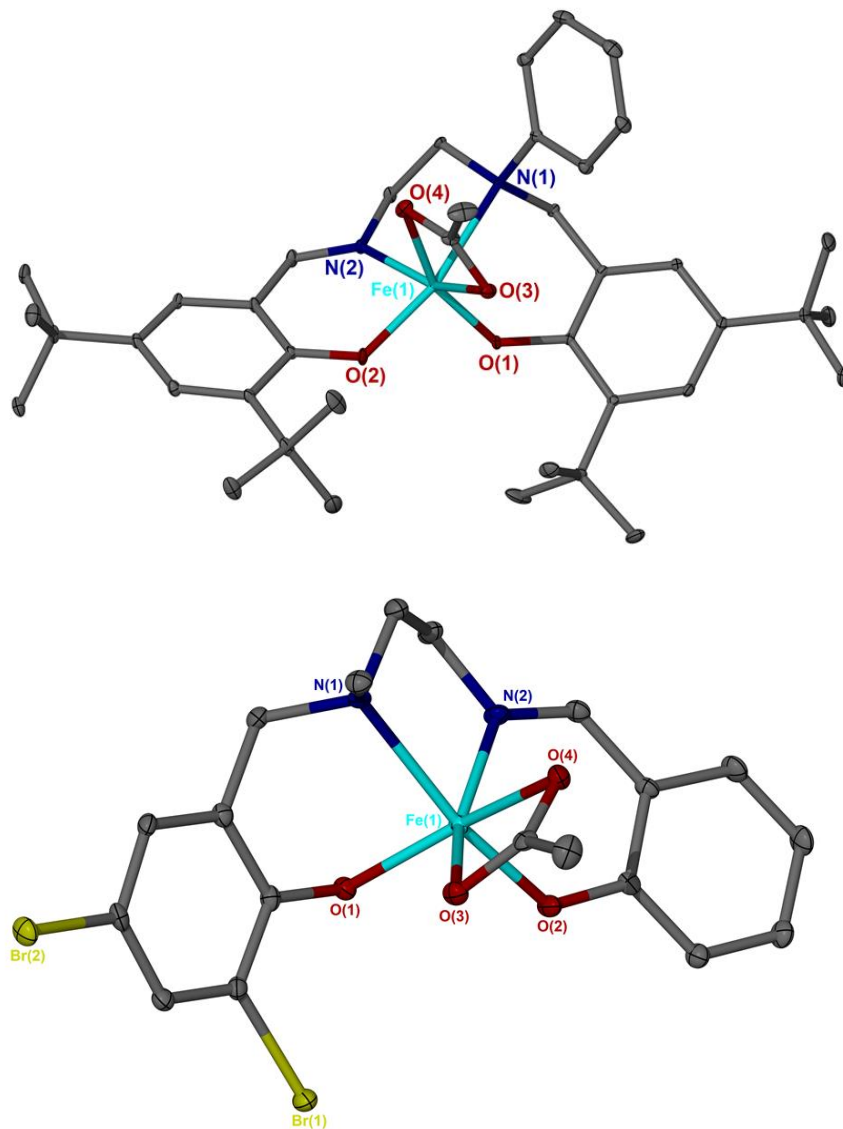


Figure 16. The solid-state structures for Fe(10)OAc (top) and Fe(11)OAc (bottom). Ellipsoids are shown at the 30% probability level and all hydrogen atoms have been removed for clarity.

Table 5. Selected bond lengths [Å] and angles [°] for Fe(**3/5/6/10/11**).

	Fe( <b>3</b> )OAc	Fe( <b>5</b> )OAc	Fe( <b>6</b> )OAc	Fe( <b>10</b> )OAc	Fe( <b>11</b> )OAc
$\tau_5$	0.65	0.58	0.58	0.60	0.71
Fe–O(1)	1.8719(13)	1.8729(13)	1.881(2)	1.8572(18)	1.893(3)
Fe–O(2)	1.9011(13)	1.9081(13)	1.914(2)	1.9046(19)	1.905(3)
Fe–N(1)	2.2633(17)	2.2690(15)	2.271(3)	2.399(2)	2.320(4)
Fe–N(2)	2.0716(17)	2.0828(15)	2.099(3)	2.058(2)	2.060(4)
Fe–O(3)	2.0872(15)	2.0826(14)	2.063(2)	2.0886(19)	2.107(3)
Fe–O(4)	2.2008(15)	2.2168(15)	2.170(3)	2.145(2)	2.125(3)
O(1)–Fe–N(1)	89.42(6)	89.73(6)	87.66(10)	85.84(7)	87.16(14)
O(1)–Fe–N(2)	111.80(6)	113.50(6)	113.86(10)	103.39(8)	110.88(16)
O(1)–Fe–O(2)	96.25(6)	93.83(6)	95.67(10)	100.40(8)	97.20(15)
O(1)–Fe– C(acetate)	126.20(7)	130.56	127.43	129.2	123.49(16)
O(2)–Fe– C(acetate)	96.78(7)	96.05	95.28	95.6	98.34(15)
O(2)–Fe–N(1)	165.35(6)	165.13(6)	162.01(9)	165.42(7)	166.12(15)
O(3)–Fe–O(4)	60.82(6)	60.72(5)	61.65(9)	62.06(8)	61.87(13)
N(1)–Fe–N(2)	78.88(7)	78.40(6)	76.47(10)	78.80(8)	78.17(15)

Moving to the Fe(III)–salan and –salen–acetate complexes, the solid–state structures for Fe(**8<sub>meso</sub>**/**9<sub>meso</sub>**/**13/15**)OAc were confirmed (*Figures 17 and 18*). Unlike the other Fe(III)–complexes, the largest equatorial angle ( $\alpha$ ) for the symmetrical Fe(**15**)OAc was not between the central acetate carbon atom and phenoxy donor but between the imine donor and phenoxy donor {*Table 6*: O(1)–Fe–N(2) = 123.48(7) $^\circ$ } as was the case for Fe(**11**)OAc and Fe(**5**)Cl. The restrictive 2,2'–bipyrrrolidine ligand backbone with methyl substituents on the phenyl rings revealed a smaller tbp geometric preference, as was observed for the methyl substituted Fe(III)–salalen–chloride complex {Fe(**8<sub>meso</sub>**)OAc,  $\tau_5 = 0.58$  vs. Fe(**2**)Cl, R<sup>1</sup> = Me,  $\tau_5 = 0.57$ ). Increasing steric bulk at R<sup>1</sup> moderately increased this tbp preference and resulted in the same value as the analogous *meso*–2,2'–bipyrrrolidine salan Fe(III)–Cl complex {Fe(**9<sub>meso</sub>**)OAc, R<sup>1</sup> = <sup>t</sup>Bu,

$\tau_5 = 0.63$  vs. Fe(**9**<sub>meso</sub>)Cl, R<sup>1</sup> = <sup>t</sup>Bu,  $\tau_5 = 0.63$ ). Compared to the Fe(**3**)OAc salalen complex, this *tbp* preference also decreased when modifying to the more symmetrical salen analogue with two imine nitrogen functionalities {Fe(**15**)OAc,  $\tau_5 = 0.59$  vs. Fe(**3**)OAc, R<sup>1</sup> = <sup>t</sup>Bu,  $\tau_5 = 0.65$ }. The lowest *tbp* preference, and therefore highest degree of *sbp* preference, observed was with Fe(**13**)OAc ( $\tau_5 = 0.54$ ). The ligand backbone consisted of an unsubstituted NH donor and a rigid six-membered aminopiperidine ring on the other nitrogen donor. This complex was structurally different compared with the aminopiperidine salalen Fe(**5**)OAc complex; Fe(**13**)OAc preferring to configure the aminopiperidine ring in an equatorial site and not axial. This observation correlates and agrees with analogous aluminium complexes.<sup>[22,23]</sup>

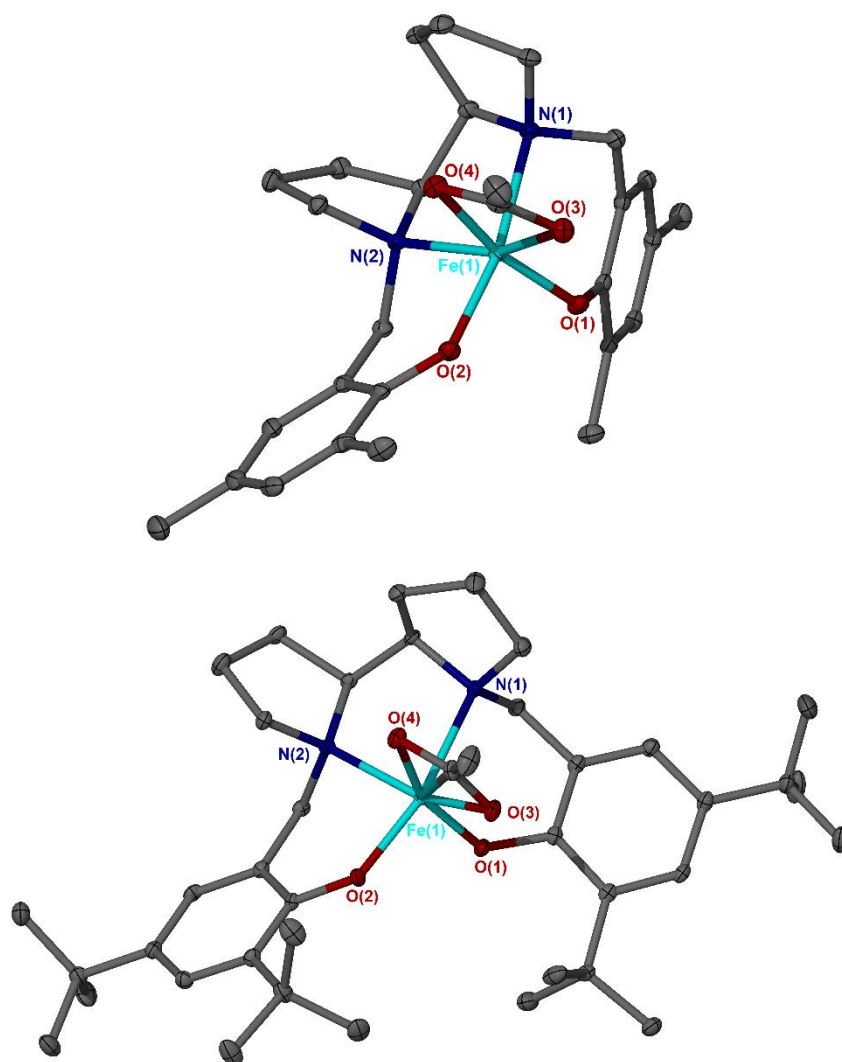
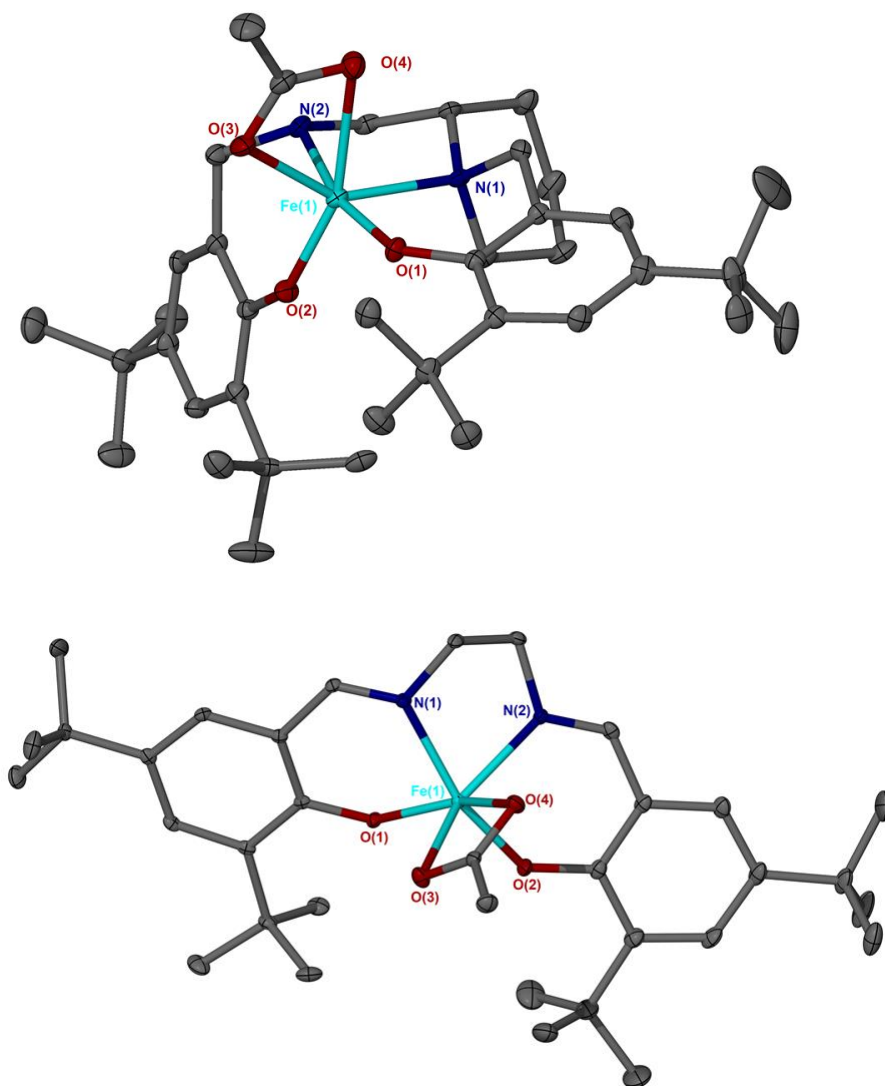


Figure 17. The solid-state structures for Fe(**8**<sub>meso</sub>)OAc (top) and Fe(**9**<sub>meso</sub>)OAc (bottom) based upon *meso*-2,2'-bipyrrolidine salen ligand backbones. Ellipsoids are shown at the 30% probability level and all hydrogen atoms have been removed for clarity.

As was the case for Fe(**9**<sub>meso</sub>)Cl, due to both donor nitrogen atoms being the same amine functionality ( $sp^3$ ) in the ligand backbone and the symmetrical nature, for Fe(**8**<sub>meso</sub>/**9**<sub>meso</sub>/**13**/**15**)OAc, the observed bond lengths are more similar compared with the Fe(III)–salalen complexes {*Table 6*: Fe(**15**)OAc, Fe–O(1) = 1.8978(15) Å vs. Fe–O(2) = 1.8894(16) Å and Fe–N(2) = 2.1224(19) Å vs. Fe–N(1) = 2.1224(19) Å}.



*Figure 18.* The solid–state structures for Fe(**13**)OAc (top) and Fe(**15**)OAc (bottom). Ellipsoids are shown at the 30% probability level and all hydrogen atoms have been removed for clarity.

Table 6. Selected bond lengths [ $\text{\AA}$ ] and angles [ $^\circ$ ] for Fe(**8**<sub>meso</sub>/**9**<sub>meso</sub>/**13**/**15**).

	Fe( <b>8</b> <sub>meso</sub> )OAc	Fe( <b>9</b> <sub>meso</sub> )OAc	Fe( <b>13</b> )OAc	Fe( <b>15</b> )OAc
$\tau_5$	0.58	0.63	0.54	0.59
Fe–O(1)	1.8955(15)	1.900(2)	1.872(2)	1.8978(15)
Fe–O(2)	1.8944(15)	1.881(2)	1.859(2)	1.8894(16)
Fe–N(1)	2.2726(18)	2.321(3)	2.201(3)	2.0885(19)
Fe–N(2)	2.1588(18)	2.177(2)	2.148(3)	2.1224(19)
Fe–O(3)	2.0652(16)	2.080(2)	2.072(2)	2.1124(17)
Fe–O(4)	2.2010(15)	2.142(2)	2.353(3)	2.2000(17)
O(1)–Fe–N(1)	88.77(6)	85.92(9)	86.84(10)	85.23(7)
O(1)–Fe–N(2)	100.53(7)	109.76(9)	165.70(11)	123.48(7)
O(1)–Fe–O(2)	96.93(7)	96.58(10)	99.74(11)	95.67(7)
O(1)–Fe–C(acetate)	133.31	126.81(10)	92.52	122.65(7)
O(2)–Fe–C(acetate)	86.41	95.72(10)	133.10	96.51(7)
O(2)–Fe–N(1)	168.18(7)	164.53(9)	108.52(11)	158.86(7)
O(3)–Fe–O(4)	61.43(6)	61.72(8)	58.66(10)	60.50(6)
N(1)–Fe–N(2)	79.38(7)	78.71(9)	79.48(10)	76.45(7)

## 2.6 Discussion of the Fe(III)–to–acetate bond lengths

Interestingly, one observation made with all the solid–state structures confirmed for the Fe(L)OAc complexes, using single–crystal X–ray diffraction, was that the Fe(III)–acetate bond lengths from each oxygen donor atom were different, non–delocalised and not identical for all complexes as illustrated in *Table 7*. For example, the bond lengths varied by 0.1136  $\text{\AA}$  in Fe(**3**)OAc {*Table 7*: Fe–O(3) = 2.0872(15)  $\text{\AA}$  and Fe–O(4) = 2.2008(15)  $\text{\AA}$ }. For this particular solid–state structure, there is an additional hydrogen bonding interaction between an ethanol moiety and O(3). This indicated asymmetry of the acetate geometry, non–bond delocalisation and a degree of distinct carboxylate and carbonyl coordination occurring to the Fe(III) centre, in agreement with the two distinct observed Fe(III)–acetate bond lengths. In addition



to this, there does not seem to be a trend when you compare the classes of structural frameworks for these Fe(III)–acetate complexes: salalen vs. salan vs. salen (*Table 7*).

*Table 7.* Variation in the Fe(III)–to–acetate oxygen bond lengths [Å] for Fe(**3/5/6/10/11/8<sub>meso</sub>/9<sub>meso</sub>/13/15**).

Class of complex	Complex	Fe–O(3)	Fe–O(4)	Difference in bond length between Fe–O(3/4)
Salalen	Fe( <b>3</b> )OAc	2.0872(15)	2.2008(15)	0.1136
	Fe( <b>5</b> )OAc	2.0826(14)	2.2168(15)	0.1342
	Fe( <b>6</b> )OAc	2.063(2)	2.170(3)	0.1070
	Fe( <b>10</b> )OAc	2.0886(19)	2.145(2)	0.0564
	Fe( <b>11</b> )OAc	2.107(3)	2.125(3)	0.0180
Salan	Fe( <b>8<sub>meso</sub></b> )OAc	2.0652(16)	2.2010(15)	0.1358
	Fe( <b>9<sub>meso</sub></b> )OAc	2.080(2)	2.142(2)	0.0620
Salen	Fe( <b>13</b> )OAc	2.072(2)	2.353(3)	0.2810
	Fe( <b>15</b> )OAc	2.1124(17)	2.2000(17)	0.0876

Indeed, this asymmetry was observable for Fe(**8<sub>meso</sub>**)OAc and Fe(**13**)OAc where it was possible to observe a slight bend or ‘kink’ (*Figure 19*) in the central acetate carbon atom and methyl carbon atom with distortion of the  $sp^2$  hybridisation. These were the only solid–state structures for the Fe(III)–acetate complexes to observe a noticeable ‘kink’, with the methyl carbon acetate atoms visibly lying in the equatorial plane for all other structures.

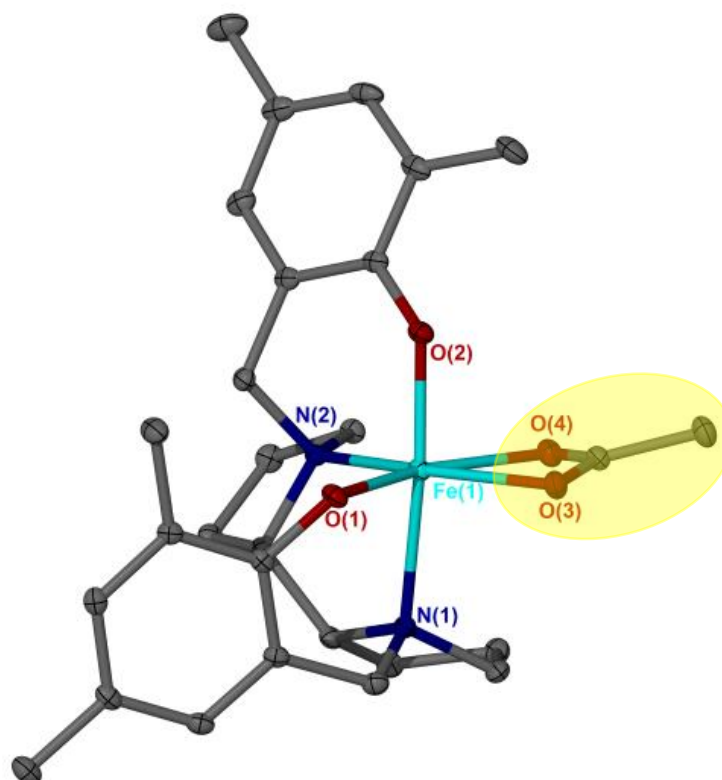
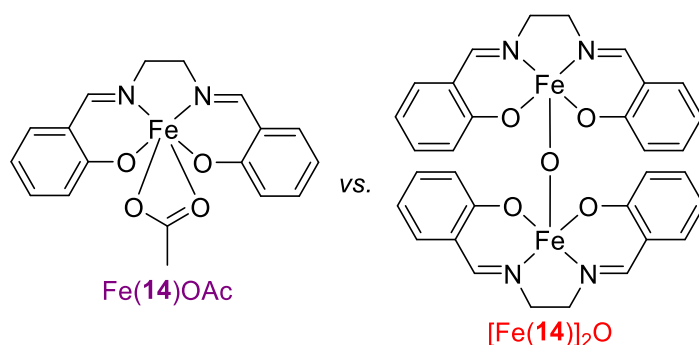


Figure 19. The solid-state structure for Fe(**8**<sub>meso</sub>)OAc rotated and the observable bend in the equatorial plane highlighted yellow.

The overall trend for the unsymmetrical Fe(III)–salalen complexes, was the Fe(III)–acetate bond length being longer for the acetate oxygen donor atom O(4) *cis* to the imine nitrogen donor atom N(2). However, the imine functionalisation does not rationalise this observation as the Fe(III)–acetate bond lengths vary still for the salan and salen complexes despite the functionalities of the nitrogen donor atoms being identical in each case. Potentially, this shortening of the Fe–O(3) bond and lengthening of the Fe–O(4) bond or distinct carboxylate and carbonyl coordination respectively could be due to minimising steric repulsion and stabilising the structure. In the case of the solid-state structure for Fe(**8**<sub>meso</sub>)OAc, the shortened Fe–O(3) bond or carboxylate coordination is relatively directed towards a methyl substituted aromatic ring unlike the lengthened Fe–O(4) or carbonyl coordination directed more towards the ligand backbone (Figure 17) and away from the electron rich aromatic ring to minimise steric or electrostatic repulsion.

## 2.7 Discussion of the synthesis for the Fe(III)–salen–acetate vs. $\mu$ -oxo-bridged Fe(III)–salen complex

Unfortunately, while the solid–state structure for the substituted Fe(**15**)OAc complex was observed, the solid–state structure for the unsubstituted Fe(**14**)OAc could not be obtained due to the insufficient quality of the crystals. This did not allow comparison between Fe(**14**)OAc and the  $\mu$ -oxo-bridged Fe(III)–salen complex [Fe(**14**)<sub>2</sub>O] confirmed in literature by Webster (*Figure 20*).<sup>[36]</sup> The elemental analysis was not ideal but still closer to the acetate species than the  $\mu$ -oxo-bridged species in the bulk {Calculated for Fe(**14**)OAc vs. [Fe(**14**)<sub>2</sub>O (found): C, 56.72 vs. 58.21 (57.43); H, 4.50 vs. 4.27 (4.51); N, 7.35 vs. 8.49 (7.62)} (**Section 6.10**).



*Figure 20.* The synthesised Fe(**14**)OAc and  $\mu$ -oxo-bridged [Fe(**14**)<sub>2</sub>O] reported in literature.<sup>[36]</sup>

Despite not obtaining a solid–state structure, a pXRD was obtained of the isolated Fe(**14**)OAc (measured pXRD pattern shown in **Section 6.12**, *Figure 80*). This diffraction pattern differed when compared to that calculated for the single–crystal X–ray crystallography data of the  $\mu$ -oxo-bridged Fe(III)–salen complex [Fe(**14**)<sub>2</sub>O] reported in literature (*Figure 21*).<sup>[36]</sup> This provided further additional evidence that the Fe(III)–acetate complexes were being produced and not the  $\mu$ -oxo-bridged; and specifically the Fe(**14**)OAc species was isolated in the bulk of this sample and not the [Fe(**14**)<sub>2</sub>O].

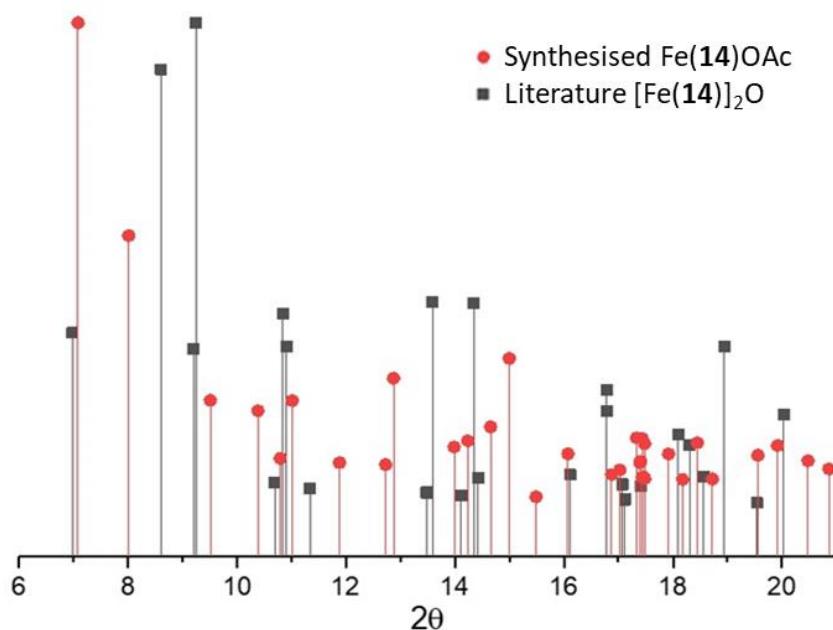


Figure 21. Measured pXRD pattern for the synthesised Fe(**14**)OAc and generated pattern for [Fe(**14**)]<sub>2</sub>O from literature.<sup>[36]</sup> Both patterns have been normalised to their most intense reflection.

It was perplexing that using the same experimental procedure (*Schemes 7 and 8*),<sup>[36]</sup> the  $\mu$ -oxo-bridged Fe(III) species was formed in literature and the Fe(III)-acetate species in this study. Eventually, it was found that carrying out the procedure and then a consecutive recrystallisation in acetonitrile promoted the formation of the  $\mu$ -oxo-bridged Fe(III) species. The synthesis used to form Fe(**14**)OAc was repeated and purple crystals were obtained once again from slow evaporation in the ethanol reaction solvent. Some of this solid was 're-recrystallised' in hot acetonitrile and further red crystals obtained. A unit cell check using single-crystal X-ray diffraction was consistent and matched with the data of the  $\mu$ -oxo-bridged Fe(III)-salen complex [Fe(**14**)]<sub>2</sub>O reported in literature.<sup>[36]</sup> The elemental results were mixed; in hydrogen and nitrogen close to the expected  $\mu$ -oxo-bridged but in carbon closer to the Fe(III)-acetate species (**Section 6.10**).

## 2.8 Exploring the chirality of the ligand backbone using 2,2'-bipyrrolidine salan scaffolds

As shown earlier by *Scheme 8* (Section 2.5), the chirality of the 2,2'-bipyrrolidine salan backbone of Fe(**8<sub>meso</sub>**)OAc was explored and the synthesis of the two other possible stereoisomers Fe(**8<sub>RR</sub>**)OAc and Fe(**8<sub>SS</sub>**)OAc was attempted. The structure and coordination around the Fe(III) centre could be altered *via* the chirality of the ligand backbone to form potentially new species with increased activity when applied to different processes, such as ring opening polymerisation and CO<sub>2</sub> / epoxide coupling (Chapters 3 and 4).<sup>[29]</sup>

For both Fe(**8<sub>RR</sub>**)OAc and Fe(**8<sub>SS</sub>**)OAc, HR-MS confirmed the coordination of the 2,2'-bipyrrolidine ligand to the Fe(III) metal centre and the observation of the Fe(**8<sub>RR</sub>/8<sub>SS</sub>**)<sup>+</sup> ion. FT-IR was in agreement that the Fe(III)-acetate complex was formed by the observation of aromatic C=C and acetate bond stretches. However, for Fe(**8<sub>RR</sub>**)OAc, using single-crystal X-ray diffraction, the solid-state structure was confirmed to be Fe(**8<sub>RR</sub>**)Y<sub>2</sub> (Y = EtO / AcO and EtOH / AcOH) (*Figure 22*). The structure was six-coordinate with a *pseudo*-octahedral geometry and two monodentate auxiliary groups instead of the expected single bidentate acetate auxiliary group. The (*R,R*)-2,2'-bipyrrolidine ligand wrapped around the Fe(III) centre in a *fac-fac* fashion observing the  $\Delta$ -*cis*- $\alpha$  isomer in the solid-state; this bears resemblance to the titanium and zirconium analogues reported previously by Kol and Jones.<sup>[14,29,41]</sup> Using Evans' NMR spectroscopic method, the effective magnetic moment was calculated to be 5.58  $\mu_B$  at 298 K in deuterated chloroform for Fe(**8<sub>RR</sub>**)Y<sub>2</sub>. The monodentate auxiliary groups (Y) in this solid-state structure were disordered and modelled as partially occupied OEt or OAc moieties. As the observed effective magnetic moment was consistent with a high-spin d<sup>5</sup> Fe(III) centre, to retain this oxidation state, one of these moieties must be protonated and a mix of EtO / AcO and EtOH / AcOH auxiliary ligands present. The elemental analysis was close to the Fe(**8<sub>RR</sub>**)Y<sub>2</sub>. Unfortunately, crystals sufficient for single-crystal X-ray diffraction were not obtained for Fe(**8<sub>SS</sub>**)OAc and therefore it is conceivable a structure similar to Fe(**8<sub>RR</sub>**)Y<sub>2</sub> could be present.

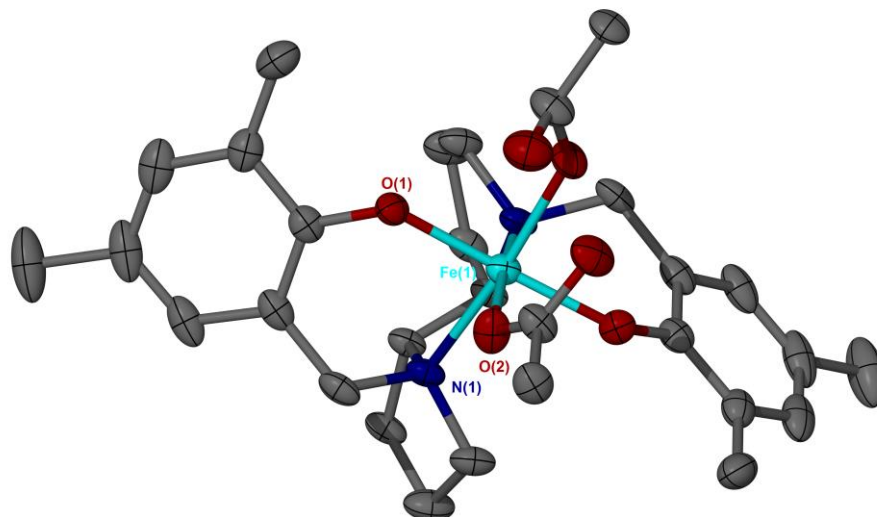
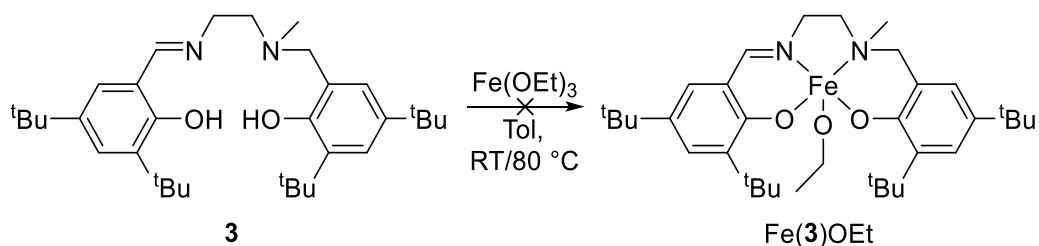


Figure 22. The solid-state structure for  $\text{Fe}(\mathbf{8}_{\text{RR}})\text{Y}_2$  ( $\text{Y} = \text{EtO} / \text{AcO}$  and  $\text{EtOH} / \text{AcOH}$ ). Ellipsoids are shown at the 30% probability level and all hydrogen atoms have been removed for clarity.

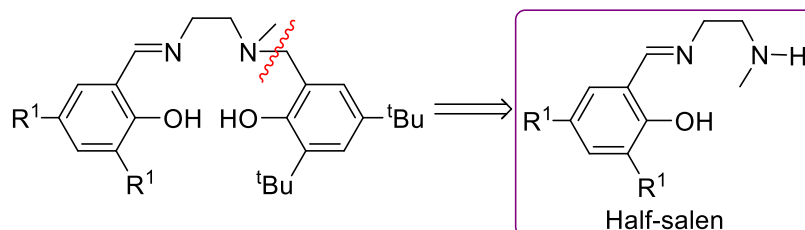
## 2.9 Synthesis and attempted synthesis of Fe(III)–alkoxide and Fe(III)–bis(phenoxy–imine) complexes

Alongside attempting to synthesise the  $\mu$ -oxo-bridged Fe(III)–salalen complexes, the synthesis of a Fe(III)–salalen–ethoxide complex was briefly attempted. Fe(III)–alkoxide complexes can be more reactive than [Fe]–Cl salt complexes in catalysis while also providing other advantages.<sup>[1,3,6]</sup> For example, in the ring opening polymerisation of lactide, the use of an Fe(III)–alkoxide complex would circumvent the need for the addition of co-initiators such as benzyl alcohol and triethylamine as was the case for the Fe(III)–salalen–chloride and –acetate complexes (**Sections 3.4, 3.8 and 3.9**). Under inert conditions, the greyish–brown  $\text{Fe}(\text{OEt})_3$  metal precursor was added as a solid to the salalen ligand in toluene solution (*Scheme 9*). The resulting brown suspension was stirred for four days at room temperature and the experiment repeated and stirred at 80 °C for 19 days. Unfortunately, HR–MS indicated no complexation had taken place for any solid isolated. This was proposed to be due to insufficient solubility of both reagents. An alternative synthetic route, that could have been attempted, would be a salt metathesis reaction of the  $\text{Fe}(\mathbf{3})\text{Cl}$  with  $\text{NaOEt}$  or  $\text{NaOMe}$ .



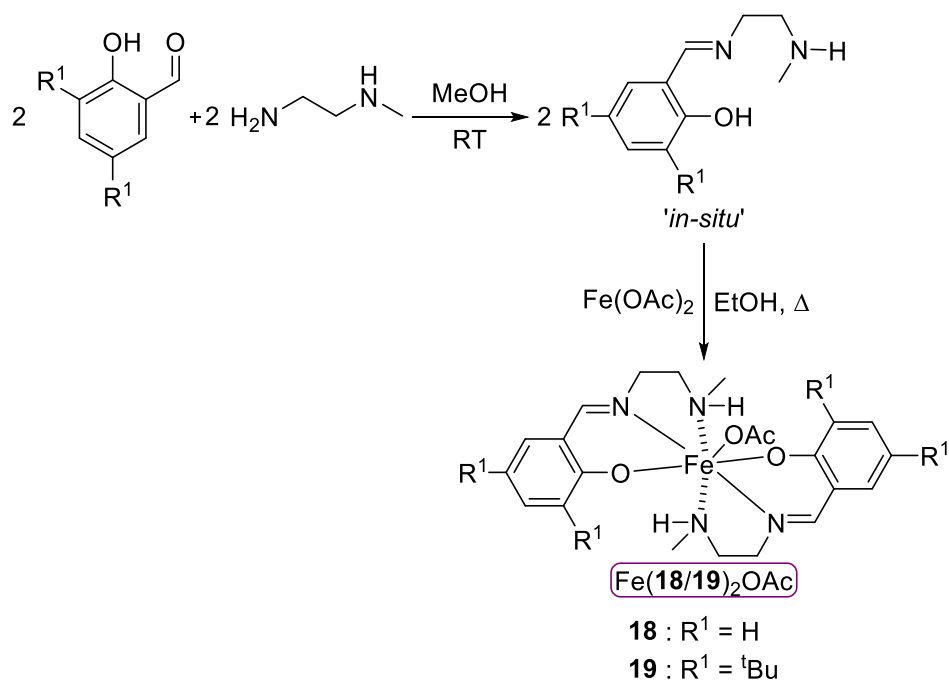
Scheme 9. Attempted reaction sequence to synthesise the Fe(3)OEt complex.

As will be discussed in **Section 4.2**, there are many examples of Fe(III)–bis(phenoxy–imine) complexes in literature. These more flexible, simple, bidentate ‘half–salen’, Schiff base frameworks can exhibit superior activities, for transformations such as CO<sub>2</sub> / epoxide coupling (**Chapter 4**), compared to more rigid salen or salalen frameworks.<sup>[11,62]</sup> For this reason, it was decided to target the related Schiff base derivatives (Scheme 10) that were formed *in-situ* as precursors to the ligands used to synthesise the corresponding Fe(III)–salalen and –salen–chloride and –acetate complexes (**Sections 2.3** and **2.5**). Furthermore, as there are already similar Fe examples bearing chloride auxiliary ligands in literature, complexation to the analogous Fe(III)–acetate complexes was prioritised.<sup>[62–65]</sup>



Scheme 10. Theoretically working backwards from the salalen ligand to simple half–salen, Schiff base derivatives.

After synthesising the phenoxy–imine ligand *in-situ* via an imine condensation, the Fe(OAc)<sub>2</sub> metal precursor was added as a ‘sandy’ brown solid to the ligand dissolved in ethanol (Scheme 11). As was the case for the other Fe(III)–acetate complexations (**Section 2.5**), this addition was accompanied by a colour change to an intense dark purple and the mixture was refluxed for three hours and left to cool. Solid failed to precipitate when leaving for slow evaporation and a dark purple oily product was isolated after the solvent was removed *in-vacuo*. Hexane was required as an anti–solvent to afford solid products that were isolated by Büchner filtration and rinsing with further hexane.



*Scheme 11.* Attempted reaction sequence for the attempted synthesis of Fe(III)–bis(phenoxy–imine)–acetate complexes.

The isolated products were analysed using HR–MS, elemental analysis and FT–IR spectroscopy. HR–MS confirmed the coordination of the two phenoxy–imine ligands to the Fe(III) metal centre; the observation of the  $\text{Fe(L)}_2^+$  ion and ionisation was achieved *via* the loss of the acetate anion. Stretches were observed in the region of  $1390\text{--}1630\text{ cm}^{-1}$  for FT–IR and assigned to be aromatic C=C, acetate and imine C=N bond stretches. The elemental analysis was reasonably close, but not optimal compared to that expected. This was attributed to the possible formation of  $\text{Fe(L)}_2\text{OAc}\cdot\text{H}_2\text{O}$ ; potentially indicative of the complex displaying a hygroscopic nature, or the incorporation of a molecule of ethanol  $\{\text{Fe(L)}_2\text{OAc}\cdot\text{EtOH}\}$  or unreacted  $\text{Fe(OAc)}_2$  present in the sample.

It was possible to obtain crystals of  $\text{Fe(19)}_2\text{OAc}$  suitable for single–crystal X–ray diffraction by taking a fraction of the product (50 mg) and recrystallising using hot hexane. The solid–state structure confirmed for  $\text{Fe(19)}_2\text{OAc}$  is shown in *Figure 23*, with the *tert*–butyl substituents ( $R^1$ ) removed for clarity. Instead of the expected coordination of the acetate auxiliary ligand to the Fe(III) centre, as was the case for the Fe(III)–acetate complexes synthesised earlier in **Section 2.5**, the metal centre was cationic and the acetate anion was participating in H–bonding interactions with a



amine nitrogen donor atom {Fe(**19**)<sub>2</sub><sup>+</sup>AcO<sup>-</sup>, Figure 24}. These H–bonding interactions seem crucial as attempts at synthesising the dimethylamido Fe(III)–bis(phenoxy–imine) analogue, bearing no hydrogen atoms on the amine donor atoms, were unsuccessful and no product could be solidified. Unfortunately, crystals sufficient for single–crystal X–ray diffraction were not obtained for Fe(**18**)<sub>2</sub>OAc but, it is conceived that the structure was also cationic and was similar to Fe(**19**)<sub>2</sub><sup>+</sup>AcO<sup>-</sup>.

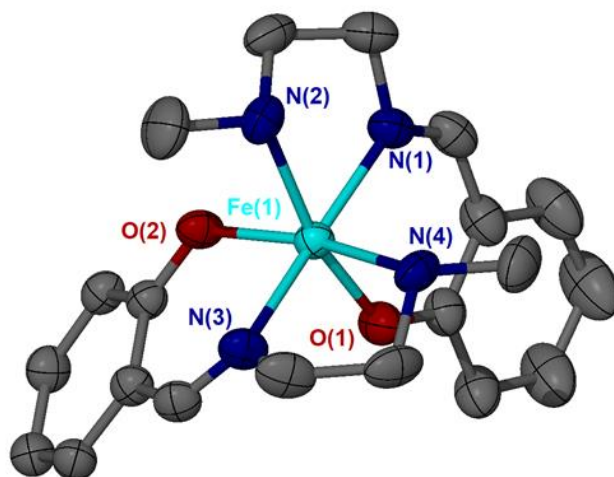


Figure 23. The solid–state structure for Fe(**19**)<sub>2</sub><sup>+</sup>AcO<sup>-</sup>. Ellipsoids are shown at the 50% probability level, all hydrogen atoms and carbon atoms of the *tert*–butyl substituents have been removed for clarity. A charge balancing acetate anion was also observed together with solvent molecules.

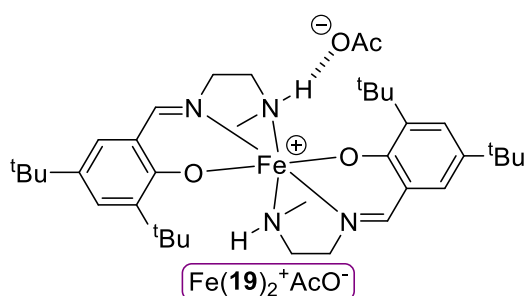


Figure 24. The observed Fe(**19**)<sub>2</sub><sup>+</sup>AcO<sup>-</sup> complex observed in the solid–state.

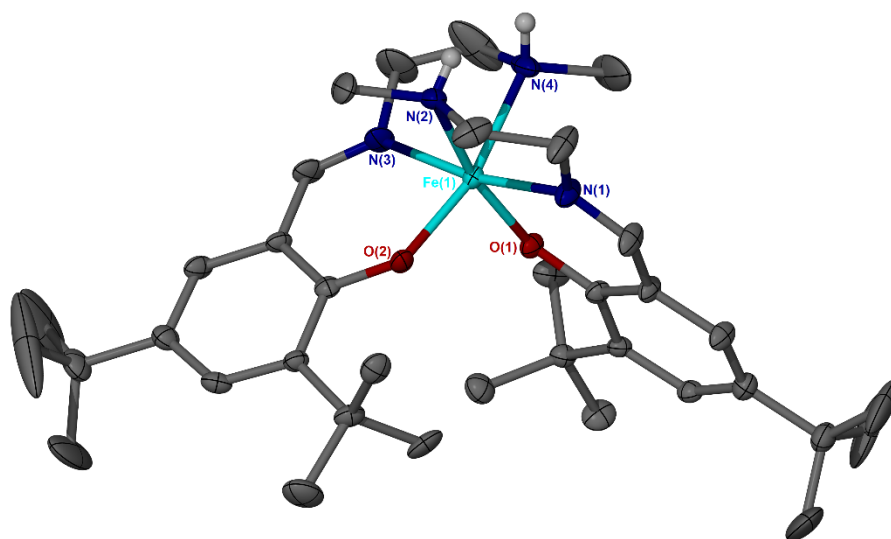
The complex adopted a six–coordinate, distorted octahedral geometry with the two phenoxy–imine ligands wrapped around the Fe(III) centre in a *mer–mer* fashion. The amine nitrogen donor atoms occupied *cis* positions in relation to each other and the imine nitrogen donor atoms occupied *trans* positions in relation to each other {Table 8: N(2)–Fe–N(4) = 88.51(9)° and N(1)–Fe–N(3) = 174.57(9)°}. The distortion in the

molecular geometry was evident in the deviation of the ideal octahedral bite angles; these were either forced closer together due to the ligand backbones {Table 8: N(1)–Fe–N(2) = 78.55(10)°, O(1)–Fe–N(1) = 87.21(9)°} or allowed more space between donor atoms on different phenoxy–imine ligand frameworks {Table 8: O(1)–Fe–O(2) = 95.73(8)°, N(1)–Fe–N(4) = 96.29(10)°, O(2)–Fe–N(1) = 98.19(9)°}. The methyl groups on the amine nitrogen donor atoms are pointing away from each other to minimise steric strain between these groups and to allow the hydrogen atoms, on the amine nitrogen, to arrange themselves *cis* with respect to each other. This arrangement maximises H–bonding interactions with the acetate anion. As was observed earlier (Sections 2.3–2.5), for the solid–state structures of Fe(III)–salalen complexes, due to the difference in nitrogen functionality, the Fe–imine bonds were shorter than the Fe–amine bonds ( $sp^2$  vs.  $sp^3$  for the respective nitrogen donor atoms) in the Fe(19)<sub>2</sub><sup>+</sup>AcO<sup>−</sup> solid–state structure {Table 8: Fe–N(1) = 2.070(2) Å vs. Fe–N(2) = 2.168(2) Å}.

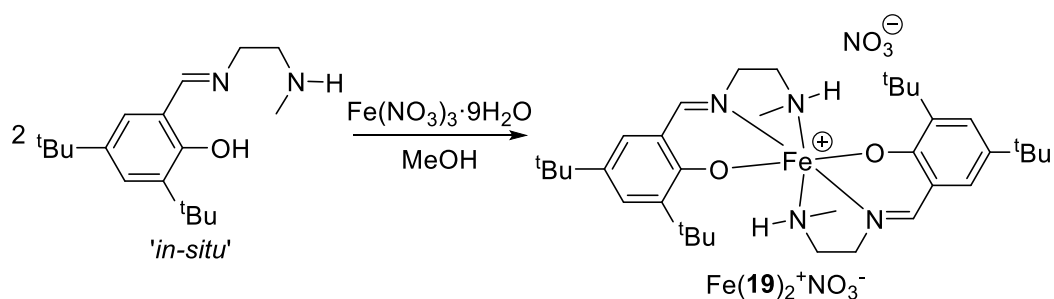
Table 8. Selected bond lengths [Å] and angles [°] for Fe(19)<sub>2</sub><sup>+</sup>AcO<sup>−</sup>.

Fe(19) <sub>2</sub> <sup>+</sup> AcO <sup>−</sup>	
Fe–O(1)	1.911(2)
Fe–O(2)	1.9141(19)
Fe–N(1)	2.070(2)
Fe–N(2)	2.168(2)
Fe–N(3)	2.066(2)
Fe–N(4)	2.182(2)
O(1)–Fe–O(2)	95.73(8)
O(1)–Fe–N(1)	87.21(9)
O(2)–Fe–N(1)	98.19(9)
N(1)–Fe–N(2)	78.55(10)
N(1)–Fe–N(3)	174.57(9)
N(1)–Fe–N(4)	96.29(10)
N(2)–Fe–N(4)	88.51(9)

Another commercially available Fe metal precursor is Fe(III) nitrate nonahydrate  $\{\text{Fe}(\text{NO}_3)_3 \cdot 9\text{H}_2\text{O}\}$ . Therefore, the synthesis of a Fe(III)–*bis*(phenoxy–imine) complex using this precursor was attempted *via* the complexation with two equivalents of the phenoxy–imine ligand **19** in methanol overnight. Crystals, suitable for single–crystal X–ray diffraction, were afforded from the mixture and the cationic solid–state structure,  $\text{Fe}(\mathbf{19})_2^+\text{NO}_3^-$ , shown in *Figure 25* was confirmed. The formation of this species is displayed by the reaction sequence shown in *Scheme 12*.



*Figure 25.* The solid–state structure for  $\text{Fe}(\mathbf{19})_2^+\text{NO}_3^-$ . Ellipsoids are shown at the 30% probability level and all hydrogen atoms, except those bonded to the amine nitrogen donor atoms, have been removed for clarity. A disordered nitrate anion, that was H–bonding with both NH groups, and a solvent molecule were also present in the unit cell.



*Scheme 12.* Reaction sequence for the synthesis of  $\text{Fe}(\mathbf{19})_2^+\text{NO}_3^-$ .

The solid–state structure for  $\text{Fe}(\mathbf{19})_2^+\text{NO}_3^-$ , followed identical trends to that observed for  $\text{Fe}(\mathbf{19})_2^+\text{AcO}^-$ . The complex,  $\text{Fe}(\mathbf{19})_2^+\text{NO}_3^-$ , adopted a six–coordinate, distorted octahedral geometry. The two phenoxy–imine ligands wrapped around the Fe(III)

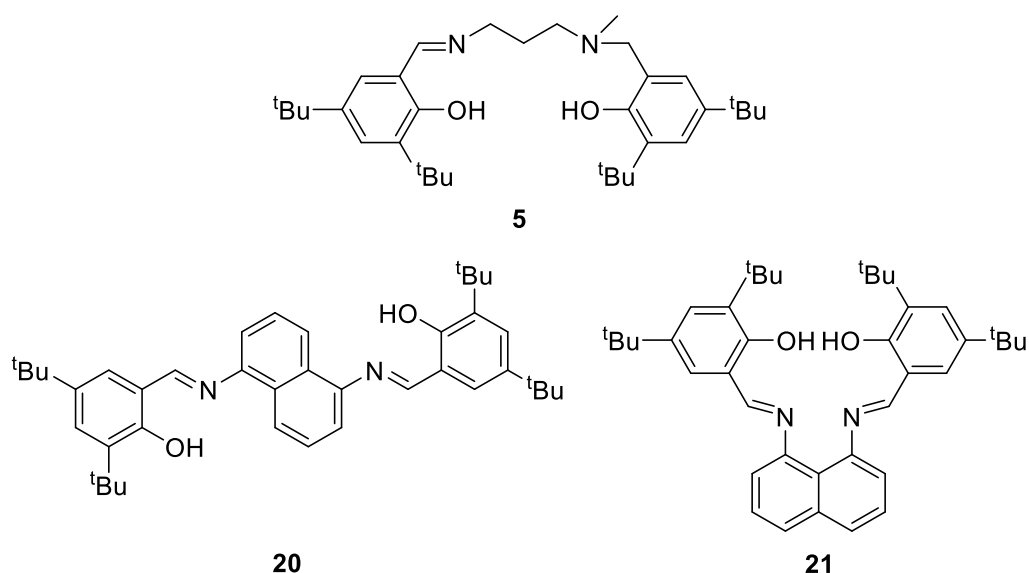
centre in a *mer-mer* fashion with the amine nitrogen donor atoms occupying *cis* positions in relation to each other and the imine nitrogen donor atoms occupying *trans* positions in relation to each other {Table 9: N(2)–Fe–N(4) = 86.9(2)° and N(1)–Fe–N(3) = 169.8(2)°}. The distortion in the molecular geometry was evident in the deviation of the ideal octahedral bite angles; these were either forced closer together due to the ligand backbones {Table 9: N(1)–Fe–N(2) = 78.8(2)°, O(1)–Fe–N(1) = 87.68(18)°} or allowed more space between donor atoms on different phenoxy–imine ligand frameworks {Table 9: O(1)–Fe–O(2) = 95.39(17)°, N(1)–Fe–N(4) = 94.5(2)°, O(2)–Fe–N(1) = 99.28(19)°}. The methyl groups on the amine nitrogen donor atoms are pointing away from each other to allow for H–bonding interactions, between the hydrogen atoms on the nitrogen donor to the weakly coordinating nitrate anion, with the hydrogen atoms arranging themselves *cis* with respect to each other. Simultaneously, this arrangement also minimises steric strain between the methyl groups. As was the case earlier (Sections 2.3–2.5), for the synthesised Fe(III)–salalen complexes, the Fe–imine bonds were shorter than the Fe–amine bonds {Table 9: Fe–N(1) = 2.047(5) Å vs. Fe–N(2) = 2.190(5) Å} for Fe(19)<sub>2</sub><sup>+</sup>NO<sub>3</sub><sup>−</sup>.

Table 9. Selected bond lengths [Å] and angles [°] for Fe(19)<sub>2</sub><sup>+</sup>NO<sub>3</sub><sup>−</sup>.

Fe(19) <sub>2</sub> <sup>+</sup> NO <sub>3</sub> <sup>−</sup>	
Fe–O(1)	1.896(4)
Fe–O(2)	1.895(4)
Fe–N(1)	2.047(5)
Fe–N(2)	2.190(5)
Fe–N(3)	2.063(5)
Fe–N(4)	2.193(5)
O(1)–Fe–O(2)	95.39(17)
O(1)–Fe–N(1)	87.68(18)
O(2)–Fe–N(1)	99.28(19)
N(1)–Fe–N(2)	78.8(2)
N(1)–Fe–N(3)	169.8(2)
N(1)–Fe–N(4)	94.5(2)
N(2)–Fe–N(4)	86.9(2)

## 2.10 Synthesis and attempted synthesis of dinuclear Fe(III) complexes and other Fe(III) complexes

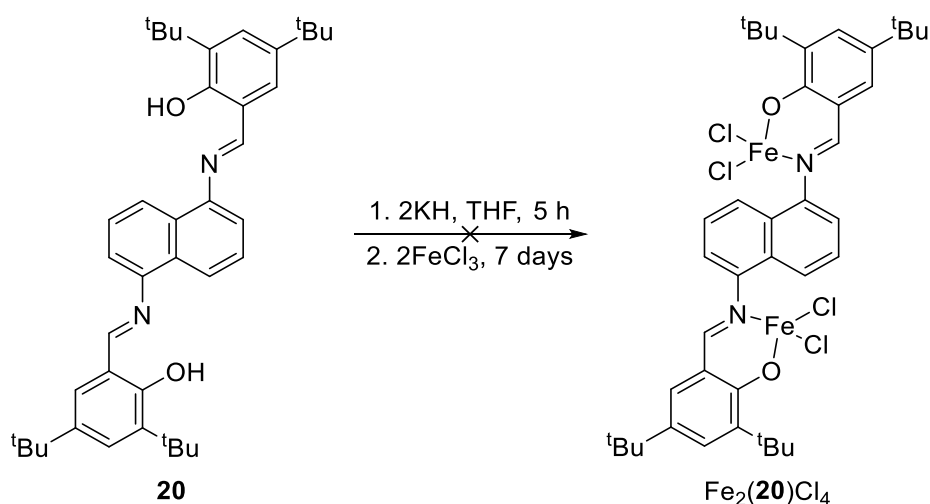
There were attempts to synthesise dinuclear variants of the mononuclear Fe(L)Cl and Fe(L)OAc complexes. Dinuclear or bimetallic complexes remain highly active in catalysis, for example in CO<sub>2</sub> / epoxide coupling (as will be discussed in **Sections 4.2** and **4.3**), Williams' dinuclear [Fe]–Cl complex is highly selective and active under 1 bar CO<sub>2</sub>.<sup>[66]</sup> Furthermore, synthesising these dinuclear complexes allows the study of metal cooperativity in catalysis and small molecule activation. The aim was to complex ligands **5**, **20** and **21** with 2Fe(OAc)<sub>2</sub> or 2FeCl<sub>3</sub> (*Figure 26*). Ligand **5** was chosen due to the extra methylene on the backbone compared to ligand **3**, with the hope that this would result in sufficient space for two Fe(III) centres to reside in the chelate ring. The naphthyl derived ligands **20** and **21** differ only by which side the imine lies on the aromatic scaffold (*cis*- vs. *trans*-) and recently, these were complexed to aluminium in the research group.<sup>[67]</sup> Complexation to iron would allow the study of how the proximity of the two Fe(III) centres effects catalysis with the potential for cooperativity and an enhancement in activity for **21** with the Fe(III) centres closer.



*Figure 26.* Ligands of interest for dinuclear synthesis.

Repeating the procedure used for the preparation of mononuclear Fe(III)–acetate complexes (**Section 2.5, Scheme 7**), applying two equivalents of Fe(OAc)<sub>2</sub> to ligands

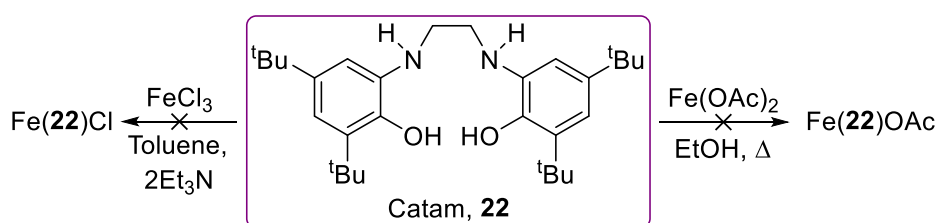
**5** and **20** was unsuccessful. While adapting the procedure, to encourage the formation of the dinuclear species and not the mononuclear species, ligand **5** was added as a solution to a more concentrated  $\text{Fe}(\text{OAc})_2$  mixture. Both ethanol and tetrahydrofuran were tried as the reaction solvent, but this afforded no success with the mononuclear species being observed in the HR-MS and single-crystal X-ray diffraction. Alternatively, using two equivalents of  $\text{FeCl}_3$  to **5** and **20**, following *Scheme 5 (Section 2.3)*, in toluene with two equivalents of triethylamine under inert conditions observed no formation of the dinuclear species using HR-MS. Harsher conditions were tried, adapting reported literature to synthesising dinuclear metal complexes (*Scheme 13*) *via* salt metathesis.<sup>[66]</sup> Both sodium and potassium hydride were attempted to synthesise  $\text{Fe}_2(\mathbf{20})\text{Cl}_4$ , however, HR-MS gave no indication for the dinuclear species. For *Scheme 13*, two equivalents of potassium hydride was added to the yellow suspension of ligand **20** in tetrahydrofuran and stirred for five hours in the glovebox.  $\text{FeCl}_3$  was added as a black solid to the potassium-ligand salt and the black mixture stirred for a week in an attempt to ensure reactivity. The mixture was filtered *via* cannula to remove the KCl salt by-product, solvent removed *in-vacuo* and the solid rinsed with hexane (2 x 5 mL).



*Scheme 13.* Attempted reaction sequence to synthesise the dinuclear  $\text{Fe}_2(\mathbf{20})\text{Cl}_4$  using potassium hydride.

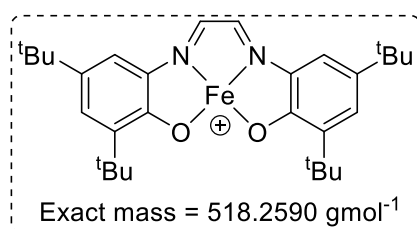
Another class of ligand framework worthy of discussion is catechol-amine or ‘catam’ ligands (*Scheme 14*). Recently, Romain and co-workers have complexed these to aluminium and found tremendous success with their use in the ROP of *rac*-LA;

demonstrating high activity at room temperature and, owing to the nitrogen donor atoms being directly connected to the phenolate moieties, were considerably more reactive than the salan ligand framework.<sup>[68–70]</sup> Their use in catalysis is scarce and, as far as we are aware, there is only one report for the synthesis of an Fe–catam complex.<sup>[68,71]</sup> For this reason, the complexation of catam **22**; prepared by the addition of ethylene diamine to 3,5–di-*tert*-butylcatechol in methanol, with FeCl<sub>3</sub> and Fe(OAc)<sub>2</sub> to synthesise the respective Fe(III)–catam–chloride and –acetate complexes was attempted (*Scheme 14*).



*Scheme 14.* Attempted synthesis of Fe(III)–catam–chloride and –acetate complexes.

Despite the isolation of dark purple solids for both attempted reactions, HR–MS did not confidently confirm coordination of the catam ligand to the Fe(III) centre *via* observation of the Fe(**22**)<sup>+</sup> cation (exact mass = 522.29 gmol<sup>-1</sup>). Instead, in both cases, an unknown intense peak at 518.26 *m/z* was observed with peaks potentially relating to isotopic distribution and / or complicated fragmentation thereafter {‘Fe(**22**)Cl’: 518.2630 (100.0%), 519.2663 (39.6%), 520.2752 (29.9%), 521.2833 (39.8%), 522.2898 (30.7%) and ‘Fe(**22**)OAc’: 518.2579 (100.0%), 519.2617 (34.6%), 520.2708 (29.9%), 521.2774 (24.3%), 522.2855 (21.4%)}. This 518.26 *m/z* peak could not be assigned with confidence, but may potentially be the cationic Fe species shown in *Figure 27*. Although it is unknown how this species would be formed. Unfortunately, a solid–state structure was not obtained due to being unable to isolate crystals of sufficient quality for single–crystal X–ray diffraction.



*Figure 27.* Potential cationic species, derived from Fe(**22**)<sup>+</sup>, with a similar *m/z* value.

From these reactions and the ligand preparation, the catam displayed an unpredictable nature and unusual observations that may result from its higher reactivity. Indeed, in the ligand preparation alone, upon addition of the reagents a white solid precipitated from a blue / green solution that redissolved upon heating under reflux. Upon further refluxing, the mixture changed to a pale brown / yellow solution and a dark green solution upon cooling back to room temperature. The product was isolated as a beige solid and, when attempting HR–MS, was a blue solution in methanol and a green solution in acetonitrile.

Although a small digression, this unpredictable reactivity and instability of the catam was further evident in its attempted complexation to copper acetate  $\{\text{Cu}(\text{OAc})_2 \cdot \text{H}_2\text{O}\}$  in methanol. Interestingly, *via* single–crystal X–ray diffraction, it seems the copper metal first catalysed the breakdown of the catam ligand by cleaving the ethylene C–C bond backbone to afford catechol and amine components. Then secondly, catalysed the formation of a benzoxazole species that acted as a new ligand resulting in a dinuclear Cu–benzoxazole complex with four bridging acetate groups  $\{\text{Cu}_2(\text{benzoxazole})_2(\text{OAc})_4\}$  (Figure 28).

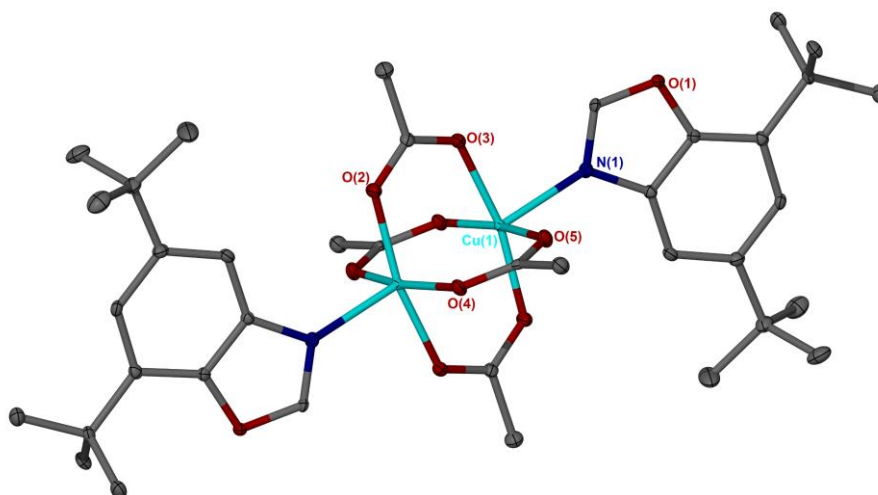


Figure 28. The solid–state structure for the  $\text{Cu}_2(\text{benzoxazole})_2(\text{OAc})_4$  species isolated. Ellipsoids are shown at the 30% probability level and all hydrogen atoms have been removed for clarity. The residual solvent was modelled as methanol but the ellipsoids remain relatively large.



This bears resemblance to work of Yin and Zhao, where [Cu] catalysts are used in oxidative C(Aryl)–OH bond functionalisation to couple amines with catechols to form benzoxazoles; this solid–state structure may be an intermediate in the catalytic cycle when Cu(OAc)<sub>2</sub> is used as the catalyst.<sup>[72,73]</sup> Despite these findings, the potential to discover more reactive Fe complexes using catam or catam derivative ligand frameworks is worth pursuing. Recently, Payne has reported in the group the use of such a derivative, the catalen ligand complexed to aluminium, magnesium and zinc for PLA formation and degradation.<sup>[74,75]</sup>

## 2.11 Conclusion and future work

A range of Fe(III)–salalen–chloride complexes, with varying ligand frameworks, were synthesised and characterised. It was confirmed these monomeric complexes were formed in the bulk of the isolated product samples and not the  $\mu$ -oxo–bridged Fe(III) dimer. Using single–crystal X–ray diffraction, solid–state structures were studied and the Fe(III)–salalen–chloride complexes were deemed to be five–coordinate with distorted trigonal bipyramidal geometries. The amount of preference these structures favoured the trigonal bipyramidal geometry compared to the square based pyramidal depended on the aromatic substituents and ligand backbone ( $\tau_5 = 0.57$ – $0.68$ ). However, Fe(III)  $\mu$ -oxo–bridged dinuclear species were observed and, while they were not predominate in the bulk of the samples, their formation was discussed. It was determined, their formation occurred during the separate recrystallisation process in air. A reduction in steric bulk or increased Lewis acidity seemed to favour the observed  $\mu$ -oxo–bridged structure and this was reinforced in the attempted synthesis of two Fe(III)–salan–chloride complexes bearing *meso*-2,2'–bipyrrolidine ligand frameworks with differing steric constraints.

In comparison with the Fe(III)–salalen–chloride complexes, these Fe(III)  $\mu$ -oxo–bridged solid–state structures were more planar and preferred square based pyramidal geometries ( $\tau_5 = 0.17$ – $0.35$ ). While attempting to further focus and synthesise these species, using Fe(OAc)<sub>2</sub> metal precursor following a literature procedure, the Fe(III)–salalen–acetate complex was unexpectedly produced instead. Aims deviated and a large range of synthetically simple, air–stable Fe(III)–acetate

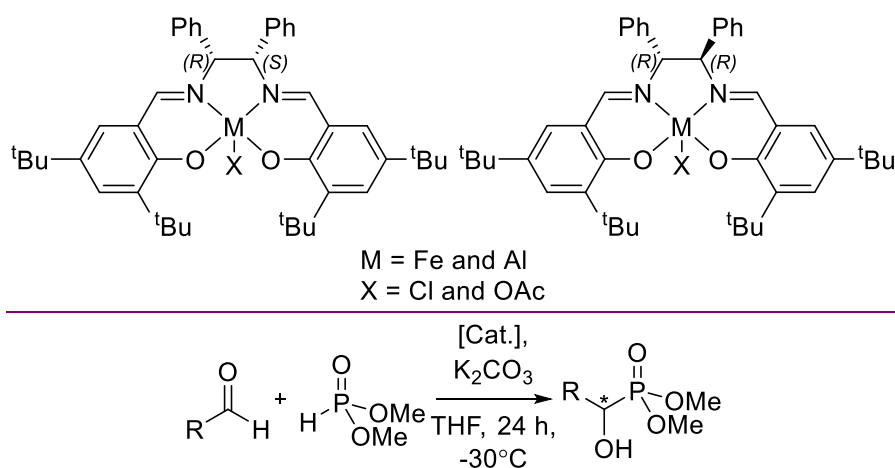
complexes, comprising of salalen, salan and salen frameworks, were consistently isolated and characterised. The solid-state structures were five-coordinate; confirmed the presence of the acetate auxiliary group present on the Fe(III) centre, with distorted trigonal pyramidal geometries and the amount of preference dependent on both the aromatic substituents and ligand backbone ( $\tau_5 = 0.54\text{--}0.71$ ).

It was perplexing as to why the Fe(III)–acetate complexes were formed here and not the  $\mu$ -oxo-bridged Fe(III) species in literature, despite following the same apparent experimental procedure. It was eventually discovered that acetonitrile solvent encouraged the formation of the  $\mu$ -oxo-bridged Fe(III) species. The chirality of the ligand backbone was also explored for the Fe(III)–acetate complexes, using 2,2'–bipyrrolidine salan frameworks, and it was discovered the coordination around the Fe centre could be altered. Using the *R,R* stereoisomer, a six-coordinate, octahedral solid-state structure was confirmed bearing two monodentate auxiliary ligands.

The synthesis of other Fe(III) complexes were attempted such as Fe(III)–alkoxide, Fe(III)–*bis*(phenoxy–imine), dinuclear and Fe(III)–catam complexes. This should be investigated further and, in particular, one such example would be the complexation of the catalen ligand to Fe.<sup>[74,75]</sup>

As stated earlier (**Section 2.5**), Fe(III)–salen complexes have been applied to such processes as olefin hydrophosphination; and indeed early investigations were made in applying the Fe(III)–acetate complexes to this process to compare their catalytic efficiency compared to that of the  $\mu$ -oxo-bridged in literature.<sup>[36,44]</sup> However, it was found the Fe(III)–acetate complexes were slower. Another intriguing and interesting catalytic reaction is that of the asymmetric hydrophosphonylation of aldehydes to form  $\alpha$ -hydroxyphosphonates (*Figure 29*) and these products are growing in importance for pharmaceutical and biological applications.<sup>[25,26,76–78]</sup> Katsuki has heavily explored this field and used catalysts such as chiral Al–salalen–chloride complexes, bearing the chiral 1,2–diaminocyclohexane backbone also present in Jacobsen's ligand.<sup>[13,27]</sup> The chiral diamines used to synthesise these catalysts are generally expensive to purchase commercially although the cheapest available is 1,2–diaminocyclohexane.

As far as we are aware, another diamine that has not been targeted and reported, for hydrophosphonylation, as of yet, is 1,2-diphenylethylenediamine (DPEN); with the chiral derivative, tosyl-DPEN (TsDPEN) well-known because of Noyori catalysis. This diamine is considerably less expensive than alternatives and both enantiomers are commercially available. On the side of the work discussed in these chapters, the corresponding salen ligands were synthesised using DPEN, attempts were made for its complexation to aluminium and iron (*Figure 29*), and initial applications to hydrophosphonylation were investigated. The HR-MS was promising for the chiral Fe-salen-acetate complex but further characterisation is needed. As was envisaged, it would be interesting to synthesise and apply these targeted chiral Al- and Fe-chloride and -acetate complexes to asymmetric hydrophosphonylation (*Figure 29*) and, additionally, these could be applied to the ROP of *rac*-LA and CO<sub>2</sub> / epoxide coupling (**Chapters 3 and 4**).



*Figure 29.* Potential Fe and Al catalysts, bearing DPEN backbones, for asymmetric hydrophosphonylation (general reaction sequence shown).<sup>[25]</sup>

Alternatively, a range of chiral monoamines (*Figure 30*) are commercially available with both enantiomers relatively inexpensive and, after a simple imine condensation, further Fe(III)-*bis*(phenoxy-imine) complexes may be targeted.

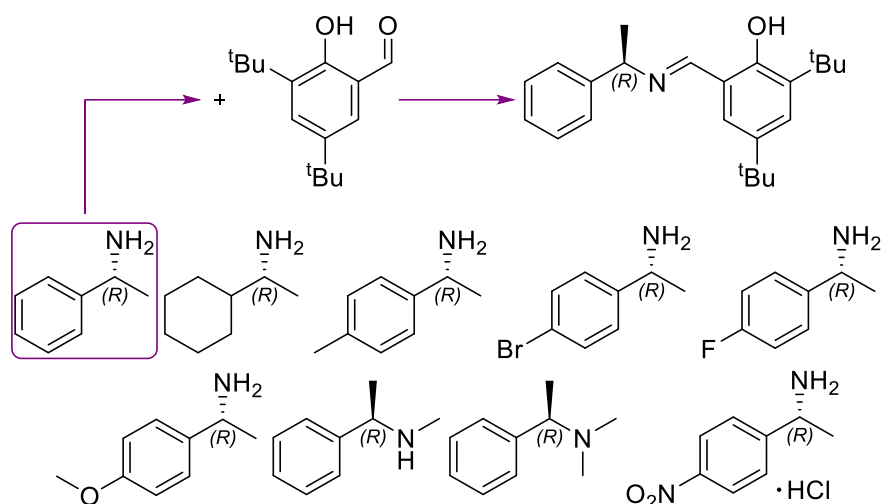


Figure 30. A range of various chiral benzylamines, with both enantiomers, commercially available from Merck and the example synthetic route to the phenoxy–imine ligand framework for metal complexation.

Despite its numerous benefits and wide use in catalysis historically, another Earth–abundant metal that will be essential to the future of chemistry is manganese.<sup>[7,9,79–82]</sup> Similar to iron, the element manganese (Mn) has been underutilised and is less prevalent in areas such as ROP and CO<sub>2</sub> / epoxide coupling.<sup>[83–89]</sup> Recently, Mn(III)–amino–*bis*(phenolate) complexes were applied to the ROP of *rac*–LA by Schaper and CO<sub>2</sub> / epoxide coupling by Kerton.<sup>[88,89]</sup> Therefore, early work was explored on synthesising the Mn(III)–salalen, –salan and –salen complexes, shown in Figure 31, using Mn(OAc)<sub>3</sub>·2H<sub>2</sub>O and MnCl<sub>2</sub> metal precursors. HR–MS was promising for all the complexes, and confirmed coordination of the ligands to the Mn(III) metal centre was taking place. Unfortunately, crystals of sufficient quality for X–ray diffraction could not be isolated and the elemental analyses were not optimal; further recrystallisation and purification protocols would need to be developed. Furthermore, as highlighted by Schaper, the synthesis of the Mn(III)–salalen–chloride complex {Mn(**3**)Cl} is more challenging as a vacant coordination on the metal centre needs to be stabilised, and this was attempted here using either tetrahydrofuran or methanol.<sup>[88]</sup> With the growing importance of metals such as manganese in contemporary catalysis, the continuation of these findings may be worthwhile.

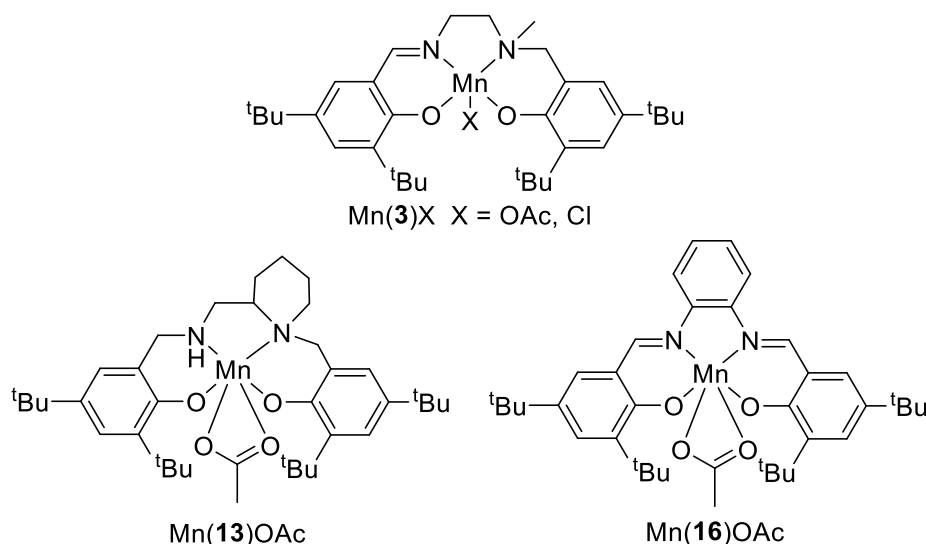


Figure 31. Attempted synthesis of Mn(III)–salalen, –salan and –salen complexes.

## 2.12 References

- [1] E. Bauer, Ed., *Iron Catalysis II*, Springer International Publishing, Switserzerland, **2015**.
- [2] A. Fürstner, *ACS Cent. Sci.* **2016**, *2*, 778–789.
- [3] B. Plietker, Ed., *Iron Catalysis: Fundamentals and Applications*, Springer-Verlag, Berlin, Heidelberg, **2011**.
- [4] F. Della Monica, A. Buonerba, C. Capacchione, *Adv. Synth. Catal.* **2019**, *361*, 265–282.
- [5] K. A. Andrea, F. M. Kerton, *Polym. J.* **2021**, *53*, 29–46.
- [6] H.-J. Knölker, Ed., *Recent Advances in Iron Catalysis*, MDPI, Basel, **2020**.
- [7] P. Chirik, R. Morris, *Acc. Chem. Res.* **2015**, *48*, 2495.
- [8] C. Darcel, J.-B. Sortais, *Isr. J. Chem.* **2017**, *57*, 1069.
- [9] M. Albrecht, R. Bedford, B. Plietker, *Organometallics* **2014**, *33*, 5619–5621.
- [10] R. Duan, C. Hu, X. Li, X. Pang, Z. Sun, X. Chen, X. Wang, *Macromolecules* **2017**, *50*, 9188–9195.
- [11] M. Cozzolino, V. Leo, C. Tedesco, M. Mazzeo, M. Lamberti, *Dalton Trans.* **2018**, *47*, 13229–13238.
- [12] E. Fazekas, G. S. Nichol, J. A. Garden, M. P. Shaver, *ACS Omega* **2018**, *3*, 16945–16953.
- [13] K. Matsumoto, B. Saito, T. Katsuki, *Chem. Commun.* **2007**, 3619–3627.
- [14] T. Katsuki, *Chem. Soc. Rev.* **2004**, *33*, 437–444.

- [15] O. Dechy-Cabaret, B. Martin-Vaca, D. Bourissou, *Chem. Rev.* **2004**, *104*, 6147–6176.
- [16] C. M. Thomas, *Chem. Soc. Rev.* **2010**, *39*, 165–173.
- [17] A. Yeori, S. Gendler, S. Groysman, I. Goldberg, M. Kol, *Inorg. Chem. Commun.* **2004**, *7*, 280–282.
- [18] E. L. Whitelaw, G. Loraine, M. F. Mahon, M. D. Jones, *Dalton Trans.* **2011**, *40*, 11469–11469.
- [19] E. L. Whitelaw, M. G. Davidson, M. D. Jones, *Chem. Commun.* **2011**, *47*, 10004–10006.
- [20] E. L. Whitelaw, M. D. Jones, M. F. Mahon, *Inorg. Chem.* **2010**, *49*, 7176–7181.
- [21] S. M. Kirk, G. Kociok-Köhn, M. D. Jones, *Organometallics* **2016**, *35*, 3837–3843.
- [22] P. McKeown, M. G. Davidson, J. P. Lowe, M. F. Mahon, L. H. Thomas, T. J. Woodman, M. D. Jones, *Dalton Trans.* **2016**, *45*, 5374–5387.
- [23] P. McKeown, M. G. Davidson, G. Kociok-Köhn, M. D. Jones, *Chem. Commun.* **2016**, *52*, 10431–10434.
- [24] S. L. Hancock, M. F. Mahon, M. D. Jones, *Dalton Trans.* **2013**, *42*, 9279–9285.
- [25] K. Suyama, Y. Sakai, K. Matsumoto, B. Saito, T. Katsuki, *Angew. Chem. Int. Ed.* **2010**, *49*, 797–799.
- [26] B. Saito, H. Egami, T. Katsuki, *J. Am. Chem. Soc.* **2007**, *129*, 1978–1986.
- [27] B. Saito, T. Katsuki, *Angew. Chem. Int. Ed.* **2005**, *117*, 4676–4678.
- [28] A. J. Chmura, M. G. Davidson, M. D. Jones, M. D. Lunn, M. F. Mahon, A. F. Johnson, P. Khunkamchoo, S. L. Roberts, S. S. F. Wong, *Macromolecules* **2006**, *39*, 7250–7257.
- [29] M. D. Jones, S. L. Hancock, P. McKeown, P. M. Schäfer, A. Buchard, L. H. Thomas, M. F. Mahon, J. P. Lowe, *Chem. Commun.* **2014**, *50*, 15967–15970.
- [30] M. D. Jones, L. Brady, P. McKeown, A. Buchard, P. M. Schäfer, L. H. Thomas, M. F. Mahon, T. J. Woodman, J. P. Lowe, *Chem. Sci.* **2015**, *6*, 5034–5039.
- [31] J. Beament, M. F. Mahon, A. Buchard, M. D. Jones, *New J. Chem.* **2017**, *41*, 2198–2203.
- [32] M. Miller, E. Y. Tshuva, *Eur. J. Inorg. Chem.* **2014**, 1485–1491.
- [33] K. A. Andrea, T. R. Brown, J. N. Murphy, D. Jagota, D. McKearney, C. M. Kozak, F. M. Kerton, *Inorg. Chem.* **2018**, *57*, 13494–13504.
- [34] J. A. Bertrand, J. L. Breece, P. G. Eller, *Inorg. Chem.* **1974**, *13*, 125–131.
- [35] J. A. Stewart, P. McKeown, O. J. Driscoll, M. F. Mahon, B. D. Ward, M. D. Jones, *Macromolecules* **2019**, *52*, 5977–5984.
- [36] K. J. Gallagher, R. L. Webster, *Chem. Commun.* **2014**, *50*, 12109–12111.

- [37] S. K. Edulji, S. B. T. Nguyen, *Organometallics* **2003**, *22*, 3374–3381.
- [38] J. E. Davies, B. M. Gatehouse, *Acta Crystallogr. Sect. B: Struct. Crystallogr. Cryst. Chem.* **1973**, *29*, 1934–1942.
- [39] A. W. Addison, T. N. Rao, J. Reedijk, J. Van Rijn, C. Verschoor, G, *J. Chem. Soc. Dalton. Trans.* **1984**, 1349–1356.
- [40] K. S. Murray, *Coord. Chem. Rev.* **1974**, *12*, 1–35.
- [41] E. Sergeeva, J. Kopilov, I. Goldberg, M. Kol, *Chem. Commun.* **2009**, 3053–3055.
- [42] K. Nakano, K. Kobayashi, T. Ohkawara, H. Imoto, K. Nozaki, *J. Am. Chem. Soc.* **2013**, *135*, 8456–8459.
- [43] C. Robert, T. Ohkawara, K. Nozaki, *Chem. Eur. J.* **2014**, *20*, 4789–4795.
- [44] K. J. Gallagher, M. Espinal-Viguri, M. F. Mahon, R. L. Webster, *Adv. Synth. Catal.* **2016**, *358*, 2460–2468.
- [45] P. Muthupandi, G. Sekar, *Org. Biomol. Chem.* **2012**, *10*, 5347–5352.
- [46] A. Jozwiuk, A. L. Ingram, D. R. Powell, B. Moubaraki, N. F. Chilton, K. S. Murray, R. P. Houser, *J. Chem. Soc. Dalton. Trans.* **2014**, *43*, 9740–9753.
- [47] D. J. Darensbourg, C. G. Ortiz, D. R. Billodeaux, *Inorganica Chim. Acta* **2004**, *357*, 2143–2149.
- [48] S. Koner, S. Iijima, M. Watanabe, M. Sato, *J. Coord. Chem.* **2003**, *56*, 103–111.
- [49] C. Floriani, G. Fachinetti, *J. Chem. Soc. Chem. Commun.* **1973**, 17–18.
- [50] P. Coggon, A. T. Mcphail, F. E. Mabbs, V. N. McLachlan, *J. Chem. Soc. A* **1971**, 1014–1019.
- [51] M. Gerloch, E. D. McKenzie, A. D. C. Towl, *J. Chem. Soc. A* **1969**, 2850–2858.
- [52] F. Calderazzo, C. Floriani, R. Henzi, F. L'Éplattenier, *J. Chem. Soc. A* **1969**, 1378–1386.
- [53] G. Hilt, C. Walter, P. Bolze, *Adv. Synth. Catal.* **2006**, *348*, 1241–1247.
- [54] S. K. Edulji, S. T. Nguyen, *Pure Appl. Chem.* **2004**, *76*, 645–649.
- [55] G. Hilt, P. Bolze, M. Heitbaum, K. Hasse, K. Harms, W. Massa, *Adv. Synth. Catal.* **2007**, *349*, 2018–2026.
- [56] F. Xu, Y. Liu, J. Tu, C. Lei, G. Li, *Tetrahedron Asymmetry* **2015**, *26*, 891–896.
- [57] R. Boobalan, C. Chen, *Adv. Synth. Catal.* **2013**, *355*, 3443–3450.
- [58] S. Bezenine-Lafollée, R. Gil, D. Prim, J. Hannedouch, *Molecules* **2017**, *22*, 1901.
- [59] E. Safaei, Z. Alaji, F. Panahi, A. Wojtczak, J. Z. Jagličić, *New J. Chem.* **2018**, *42*, 7230–7236.
- [60] D. Alhashmialameer, J. Collins, K. Hattenhauer, F. M. Kerton, *Catal. Sci. Technol.* **2016**, *6*, 5364–5373.

- [61] K. A. Andrea, E. D. Butler, T. R. Brown, T. S. Anderson, D. Jagota, C. Rose, E. M. Lee, S. D. Goulding, J. N. Murphy, F. M. Kerton, C. M. Kozak, *Inorg. Chem.* **2019**, *58*, 11231–11240.
- [62] E. Fazekas, G. S. Nichol, M. P. Shaver, J. A. Garden, *Dalton Trans.* **2018**, *47*, 13106–13112.
- [63] F. M. Al-Qaisi, M. Nieger, M. L. Kemell, T. J. Repo, *ChemistrySelect* **2016**, *1*, 545–548.
- [64] J. Peng, H.-J. Yang, Y. Geng, Z. Wei, L. Wang, C.-Y. Guo, *J. CO<sub>2</sub> Util.* **2017**, *17*, 243–255.
- [65] M. Sunjuk, A. S. Abu-Surrah, E. Al-Ramahi, A. K. Qaroush, A. Saleh, *Transit. Met. Chem.* **2013**, *38*, 253–257.
- [66] A. Buchard, M. R. Kember, K. G. Sandeman, C. K. Williams, *Chem. Commun.* **2011**, *47*, 212–214.
- [67] S. M. Kirk, H. C. Quilter, A. Buchard, L. H. Thomas, G. Kociok-Köhn, M. D. Jones, *Dalton Trans.* **2016**, *45*, 13846–13852.
- [68] S. Gesslbauer, H. Cheek, A. J. P. White, C. Romain, *Dalton Trans.* **2018**, *47*, 10410–10414.
- [69] S. Gesslbauer, R. Savela, Y. Chen, A. J. P. White, C. Romain, *ACS Catal.* **2019**, *9*, 7912–7920.
- [70] S. Gesslbauer, G. Hutchinson, A. J. P. White, J. Burés, C. Romain, *ACS Catal.* **2021**, *11*, 4084–4093.
- [71] C. J. Whiteoak, R. T. Martin De Rosales, A. J. P. White, G. J. P. Britovsek, *Inorg. Chem.* **2010**, *49*, 11106–11117.
- [72] X. Chen, F. Ji, Y. Zhao, Y. Liu, Y. Zhou, T. Chen, S.-F. Yin, *Adv. Synth. Catal.* **2015**, *357*, 2924–2930.
- [73] X. Meng, Y. Wang, Y. Wang, B. Chen, Z. Jing, G. Chen, P. Zhao, *J. Org. Chem.* **2017**, *82*, 6922–6931.
- [74] J. Payne, P. McKeown, G. Kociok-Köhn, M. D. Jones, *Chem. Commun.* **2020**, *56*, 7163–7166.
- [75] J. Payne, P. McKeown, O. Driscoll, G. Kociok-Köhn, E. A. C. Emanuelsson, M. D. Jones, *Polym. Chem.* **2021**, *12*, 1086–1096.
- [76] H. Gröger, B. Hammer, *Chem. Eur. J.* **2000**, *6*, 943–948.
- [77] J.-A. Ma, *Chem. Soc. Rev.* **2006**, *35*, 630–636.
- [78] P. Merino, E. Marqués-López, R. P. Herrera, *Adv. Synth. Catal.* **2008**, *350*, 1195–1208.
- [79] J. R. Carney, B. R. Dillon, S. P. Thomas, *Eur. J. Org. Chem.* **2016**, *2016*, 3912–3929.



- [80] D. A. Valyaev, G. Lavigne, N. Lugan, *Coord. Chem. Rev.* **2016**, *308*, 191–235.
- [81] X.-F. Wu, M. Beller, *Economic Synthesis Heterocycles: Zinc, Iron, Copper, Cobalt, Manganese and Nickel Catalysts*, Royal Society Of Chemistry, **2014**, ch. 6, pp. 386–434.
- [82] C. Freire, C. Pereira, A. F. Peixoto, D. M. Fernandes, *Sustainable Catalysis: With Non-Endangered Metals, Part 1*, Royal Society Of Chemistry, **2015**, ch. 11, pp. 278–341.
- [83] Z. Yang, C. Hu, R. Duan, Z. Sun, H. Zhang, X. Pang, L. Li, *Asian J. Org. Chem.* **2019**, *8*, 376–384.
- [84] M. Tiffner, S. Gonglach, M. Haas, W. Schöfberger, M. Waser, *Chem. Asian J.* **2017**, *12*, 1048–1051.
- [85] J. L. S. Milani, A. M. Meireles, W. A. Bezerra, D. C. S. Martins, D. Cangussu, R. P. das Chagas, *ChemCatChem* **2019**, *11*, 4393–4402.
- [86] W. N. Sit, S. M. Ng, K. Y. Kwong, C. P. Lau, *J. Org. Chem.* **2005**, *70*, 8583–8586.
- [87] Y. Yang, C.-Y. Gao, H.-R. Tian, J. Ai, X. Min, Z.-M. Sun, *Chem. Commun.* **2018**, *54*, 1758–1761.
- [88] P. Daneshmand, F. Schaper, *Dalton Trans.* **2015**, *44*, 20449–20458.
- [89] A. I. Elkurtehi, F. M. Kerton, *Can. J. Chem.* **2021**, *99*, 202–208.

## **Chapter 3.**

### **Ring opening polymerisation of *rac*-lactide using Fe(III) complexes**

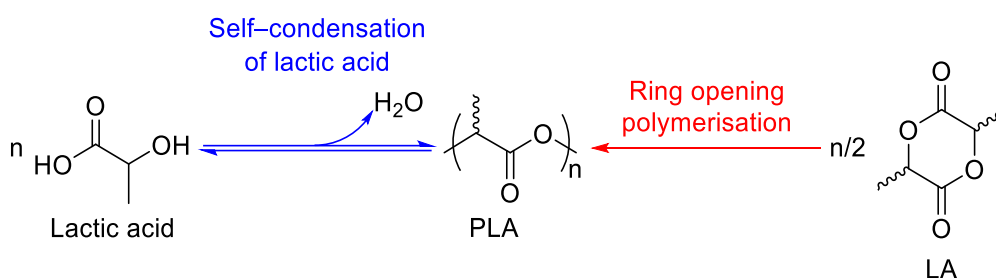
### 3. Ring opening polymerisation of *rac*-lactide using Fe(III) complexes

#### 3.1 Introduction to poly(lactic acid) and its preparation

Poly(lactic acid) (PLA) is a renewable, sustainable, biocompatible and biodegradable alternative biopolymer in comparison to plastics derived from crude oil and petroleum-based resources.<sup>[1-8]</sup> Due to these reasons and the material's physical, thermal, mechanical properties, PLA has received extensive attention and research, in both academia and industry. It has been used in many applications and as a replacement for petroleum-based plastics.<sup>[1,7,9,10]</sup> These include as packing, food and beverage, materials, and in the biomedical sector such as for drug delivery, implants and tissue engineering due to its benign nature and biocompatibility.<sup>[3,7,10-17]</sup> PLA is also a promising alternative because of the potential for a circular economic approach for its use rather than an unsustainable linear model.<sup>[2,3,5,18-20]</sup> Adopting this model would reduce environmental concerns, carbon footprints, the use of finite resources such as fossil fuels and plastic waste pollution. While retaining or adding material value and holding potential socio-economic benefits, attractive to industry and countries. Efficient end-of-life (EOL) management is crucial to this approach with landfill and incineration strategies removed and mechanical recycling not feasible due to the deterioration of the material's physical properties, potential applications and market value as the number of cycles around the circular model accumulates.<sup>[2,3,5,20,21]</sup> Chemical recycling, to recapture monomer (closed loop) or useful chemicals (open loop), will be crucial to solve this and, recently, there has been increasing interest in this area for PLA.<sup>[2,5,20,21]</sup> The two approaches for PLA being depolymerisation to recapture the lactide (LA) monomer or degradation to lactate esters that can be used as alternative green solvents; both products additionally being platform chemicals that can retain or add material value and create a beneficial incentive for industry.<sup>[2,5,20,22-25]</sup> Although a small digression here, chemical recycling and degradation will be explored and further discussed in **Section 5.7**. This potentially industrially relevant, chemical recycling benefit of biopolymers is not

always commonly or clearly stated in literature and PLA reviews but will be essential for a sustainable future globally.

Chemically, PLA is an aliphatic polyester (PE) with a repeating LA monomer unit (*Scheme 15*). The polymer can be synthesised by either the polycondensation of lactic acid, *via* step-growth polymerisation, or the ring opening polymerisation (ROP) of lactide (LA), the cyclic dimer unit of lactic acid, *via* chain-growth polymerisation.<sup>[2,5,8–10,26–29]</sup>



*Scheme 15.* The two main synthetic methods to PLA.

Self-condensation has many drawbacks including the stoichiometric liberation of water during propagation; that can react with the ester functionalities of the PLA product, and the requirement for its removal to drive the reversible condensation reaction forward.<sup>[5,8,10,15,29]</sup> This is commonly achieved by carrying out the reaction at high temperatures and neat conditions.<sup>[10]</sup> The consequence of this is that low molecular weight polymer and inferior PLA is often obtained and, because this is a step growth-polymerisation, it is not possible to control the molecular weight, molecular weight distribution and stereochemistry of the PLA, limiting the applications of the produced PLA.<sup>[1,8,10]</sup>

The alternative synthetic method, and industrially preferred route, is the ring opening polymerisation of lactide, the cyclic dimer and diester of lactic acid, with no water produced.<sup>[1,3–5,7–10,16]</sup> This is most commonly achieved using a metal complex as a mediator to promote the ROP reaction pathway. Despite the polymerisation being intrinsically unfavourable entropically, the release of enthalpic ring strain drives the reaction forward and enables access to high molecular weight PLA.<sup>[2,8,28,30]</sup> The process also allows greater control over the polymer's properties compared to self-condensation and crucially, the stereochemistry can be tuned allowing for PLA

with superior properties.<sup>[1,8,28]</sup> Traditionally, LA is formed *via* the oligomerisation and condensation of lactic acid and then depolymerisation of the pre-polymer using intramolecular, 'back-biting' transesterification reactions to form the cyclic LA.<sup>[5,7,10,29,31]</sup> Although, this method is costly and can contribute up to 30% of the total cost for the prepared PLA.<sup>[5]</sup> Therefore, this has led to attempts at making the LA directly from lactic acid, and avoiding the two-step process, *via* the potential use of zeolites.<sup>[5,10,31]</sup>

Lactic acid is obtained from the fermentation and subsequent purification of renewable feed stocks with naturally high levels of starch or cellulose, such as corn and sugar cane.<sup>[5,9,10,16,17,32,33]</sup> Food competition concerns can be alleviated by using waste material and focussing on sugars (polysaccharides) where only 1% of that produced by volume is used for human consumption.<sup>[2,10,32]</sup> The microbial fermentation of the starch and *D*-glucose is achieved using homolactic bacteria to obtain the desired lactic acid.<sup>[10,32-34]</sup> Industrially, this is carried out on a batch scale for 3-6 days under a high lactic acid concentration. The addition of calcium carbonate or calcium hydroxide assures the pH remains neutral for optimal microbial activity and crude lactic acid is obtained after purification by crystallising and acidifying the produced calcium lactate.<sup>[9,10,33,34]</sup> Fermentation is generally preferred over chemical synthesis because it is more renewable and economical.<sup>[16]</sup> This is despite the requirement for the use of the neutralising agents and energy to maintain the fermentation conditions, it remains more cost effective with fewer environmental concerns raised in comparison. Fermentation also crucially gives high product selectivity and by altering the fermentation conditions, either *D*-, *L*- or *rac*-lactic acid can be produced while only *rac*-lactic acid can be achieved *via* chemical synthesis.<sup>[9]</sup> These *D*- and *L*- enantiomers of lactic acid can therefore consequently give three stereoisomers of LA.

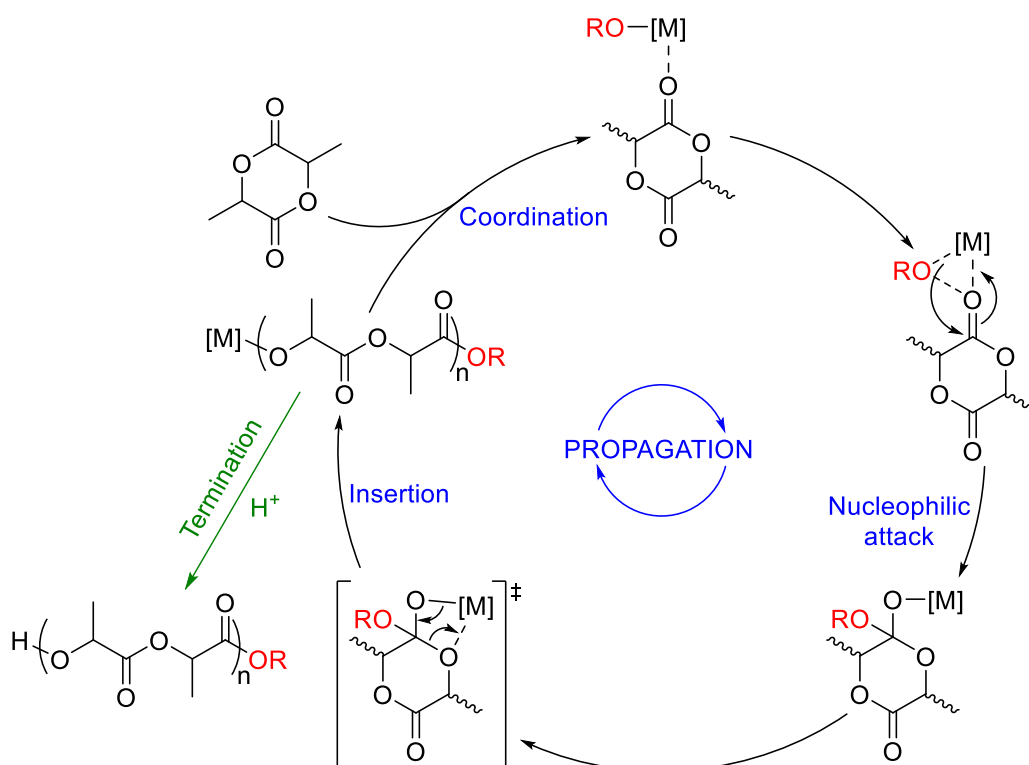
Furthermore, recently there has been increased research into chemical recycling and Piemonte *et al.* revealed that the depolymerisation of PLA to lactic acid was less energy intensive than glucose fermentation; beneficial for industry from an economic aspect, environmentally with the potential of decreasing plastic waste and socially as this alleviates potential food chain competition by sourcing the lactic acid

from used PLA rather than feedstocks.<sup>[21]</sup> With chemical recycling becoming more studied and important, to society and industry in achieving a bio-based circular economy, there is potential for this method to contribute more to lactic acid production in the future, alongside fermentation, and meet the increased demand for plastic in the future. There have been many various life cycle assessments (LCAs) into PLA production in literature; specifically NatureWorks™ have reported their LCA details for the industrial production of PLA.<sup>[7,35,36]</sup>

### **3.2 The ring opening polymerisation of lactide to PLA: mechanistic and stereochemical considerations**

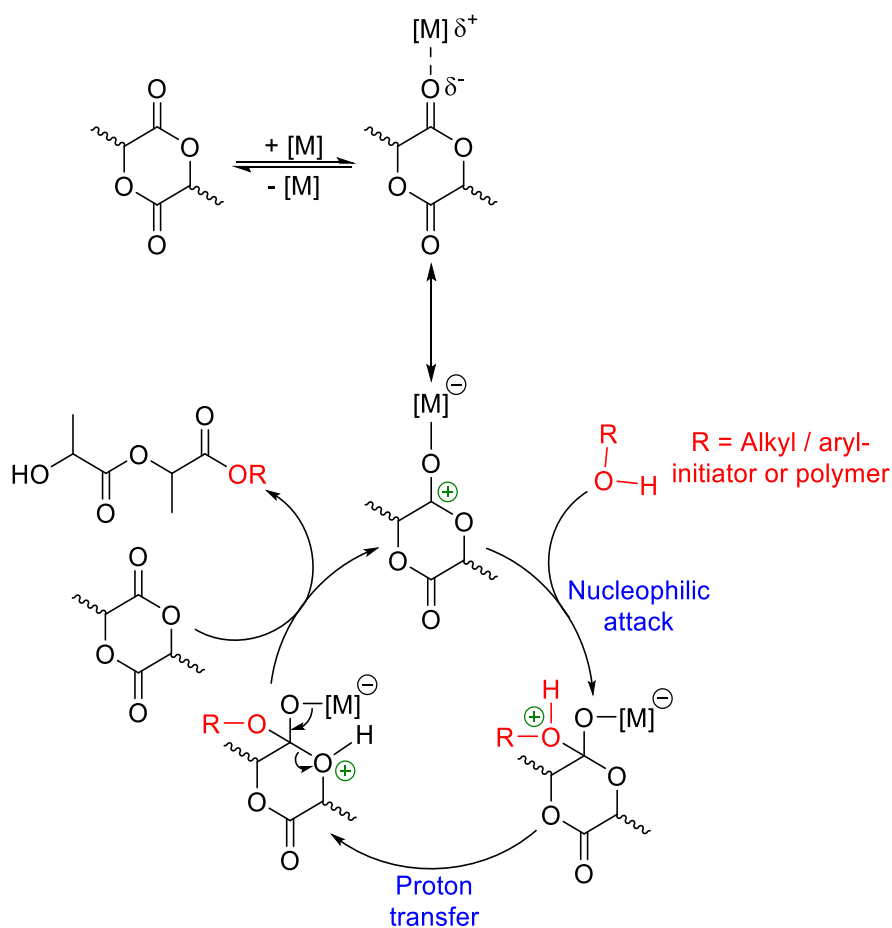
There are a number of mechanisms for the ROP of LA to form PLA, such as cationic, anionic, pseudo-anionic and nucleophilic activation, but the two most common and synthetically useful mechanisms that have received significant attention in literature, are coordination–insertion and activated monomer.<sup>[1,7,9,16,34]</sup>

The coordination–insertion mechanism, as shown by *Scheme 16*, initially entails the coordination of a lactide monomer to a Lewis acidic metal centre, most generally a complex bearing a labile alkoxide auxiliary ligand.<sup>[1,2,4,5,8,28,29]</sup> This results in the electrophilic activation, of the carbonyl functionality on the lactide, and subsequent nucleophilic attack by the alkoxide group to generate a tetrahedral intermediate. The alkoxide is inserted *via* the collapse of the intermediate, by cleavage of the original ester bond, to re-form a metal–alkoxide complex, with one lactide monomer unit incorporated and a new metal–alkoxide bond. Propagation then proceeds with successive lactide coordination and insertion of the growing alkoxide group until the metal–alkoxide bond is cleaved *via* termination, by post acid work-up of the polymer, to obtain the produced PLA with the ester end group (OR) deriving from the metal complex initiator.<sup>[1,2,4,5,8,28,29]</sup>



Scheme 16. The generally accepted coordination–insertion mechanism for the ROP of LA.<sup>[2,8,28,29]</sup>

In resemblance to coordination–insertion, the activated monomer mechanism (Scheme 17) also initially occurs *via* electrophilic activation of the carbonyl functionality on the lactide using a coordinatively saturated Lewis acidic metal complex, Brønsted acid initiator or organocatalyst capable of activation *via* hydrogen bonding interactions.<sup>[8,37,38]</sup> The charge is delocalised and represented by two resonance structures, where the oxo–carbenium cation activates the monomer and is susceptible to nucleophilic attack by either an added alcohol co–initiator; essential to the polymerisation due to the absence of a labile auxiliary group on the metal complex for insertion, or the hydroxy end group of the growing polymer chain. The alcohol attacks the cation to generate a tetrahedral intermediate. Driven by enthalpic ring strain, after proton transfer, there is ring opening and the intermediate collapses with one lactide monomer unit incorporated in the growing PLA. Propagation then proceeds with successive incoming lactide molecules activated by the Lewis acidic metal complex, attack of the oxo–carbenium cation by the growing polymer chain and subsequent ring opening with an increasing number of lactide monomer units incorporated.<sup>[8]</sup>



Scheme 17. The activated monomer mechanism for the ROP of LA.<sup>[8]</sup>

Industrially, PLA produced *via* ROP is achieved using Sn(II)-*bis*(2-ethylhexanoate), more commonly known as Sn(II)-octanoate  $\{Sn(Oct)_2\}$ , with *L*-LA under melt or solvent-free, neat conditions with alcohol co-initiator; as such this is the current industrial standard and benchmark.<sup>[1,2,4,8,9,28,39]</sup> There are a number of advantages and disadvantages to using  $Sn(Oct)_2$  as an initiator. The system is commercially available, inexpensive, robust and tolerant to environmental factors such as oxygen, easy to handle and displays excellent solubility in organic solvents; particularly cyclic esters and in the neat monomers.<sup>[2,4,8]</sup> Most importantly, it is used industrially because of the high activity and high molecular weight PLLA produced (up to  $10^5$  or  $10^6$   $g\ mol^{-1}$ ).<sup>[4,40]</sup> However, elevated temperatures ( $>120$  °C) and neat conditions are required to reach these high molecular weights and there are concerns and debates in literature about the toxicity of  $Sn(Oct)_2$ .<sup>[2,4,8,41,42]</sup> While it is FDA (Food and Drug Administration) approved in the U.S. and used as a food additive, there are concerns with using the PLA produced from Sn(II) initiators for biomedical applications.<sup>[4,8]</sup>



Sn(II) hydroxides are harmful and irritants and there is potential for toxic Sn(IV) hydrolysis products to form.<sup>[2,29]</sup> The main issue associated with these toxicity concerns is that trace Sn residues are challenging to remove and only polymer with less than 1% by weight residue is allowed, with thorough purification or low initiator loading required to achieve this.<sup>[2,4,8,29,42]</sup> Ultimately, Sn is therefore not suitable in the long-term future, as it limits the applications of the produced PLA, and there is a desire to find a less toxic and environmentally benign alternative initiator system. Another major disadvantage to Sn(Oct)<sub>2</sub> is that there is no stereocontrol when *rac*-LA is used. The stereocontrol and tacticity of the PLA is crucial otherwise the thermal properties are diminished and biodegradability impacted negatively.<sup>[1,2,8,10,12,28]</sup> Control of the tacticity enables the control of both the polymers' microstructure and bulk physical properties, such as biodegradability, durability, flexibility, strength, thermal properties and crystallinity, and therefore crucially the potential applications of the material.<sup>[8,12,28,43]</sup>

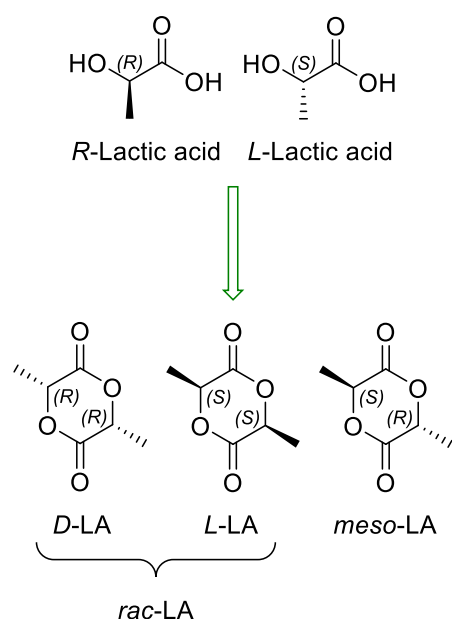


Figure 32. The possible stereoisomers for lactic acid and, the cyclic dimer, LA.<sup>[7,9,28]</sup>

The stereochemistry of PLA is derived from the chirality of lactic acid, where there are two optical enantiomers: *D*-lactic acid and *L*-lactic acid (Figure 32).<sup>[7,9,10]</sup> This results in three possible stereoisomers for LA, due to the cyclisation of two lactic acid units, and two stereocentres: as (*R,R*-) *D*-LA, (*S,S*-) *L*-LA and (*S,R*-) *D,L* / *meso*-LA (Figure 32). *D*-LA and *L*-LA are enantiomers and when mixed in a 50:50, racemic

composition, produce *rac*-LA. The latter diastereomer, *meso*-LA, contains an internal mirror plane and is therefore achiral.<sup>[7–9,28]</sup> Both *rac*-LA and *L*-LA are available commercially.<sup>[2]</sup> In the absence of racemisation or epimerisation, stereoregular PLA can be produced by controlling the order of insertion of the incoming monomer LA units and consequently the tacticity of the PLA. There are a range of tacticities and microstructures accessible using the different stereoisomers of LA (*Figure 33*).<sup>[1,2,4,8,12,28]</sup>

This control can result in the increased degree of crystallinity (long-range order) and regularity, strengthens the intermolecular forces between the polymer chains and improve how well the polymer packs. This has implications, particularly on the thermal properties, such as the melting temperature ( $T_m$ ) and glass transition temperature ( $T_g$ ). The  $T_g$  being the temperature where the polymer changes from a brittle and hard material to being more flexible. Isotactic semi-crystalline homopolymers, PDLA and PLLA, display high, well-defined melting temperatures of 180 °C and a  $T_g$  of 50–65 °C.<sup>[9,12,28,34,44]</sup> Combining these isotactic polymer chains, either separately as a stereocomplex (most effectively as a 50:50 mixture of PDLA and PLLA) or as block copolymers, improves and increases the  $T_m$  up to 230 °C depending on the factors aforementioned and the molecular weight.<sup>[9,12,44,45]</sup> This is because the structures are more stable and crystalline together than being separate chains of enantiopure homopolymer. While the  $T_m$  increases, the  $T_g$  is maintained at around 60 °C.<sup>[12]</sup> Heterotactic and syndiotactic PLA; where syndiotactic is semi-crystalline and heterotactic is amorphous (no long-range order), display lower melting and glass transition temperatures compared to isotactic PLA.<sup>[9,12,28]</sup> Amorphous atactic PLA, where there is no control over the order of insertion and stereoselectivity, displays an undefined melting temperature.<sup>[28,44]</sup> Due to the superior thermal properties, isotactic PLA is the most desired industrially<sup>[7,8]</sup> with heterotactic PLA not finding as widespread use and syndiotactic PLA having not been investigated thoroughly as yet.<sup>[8]</sup>

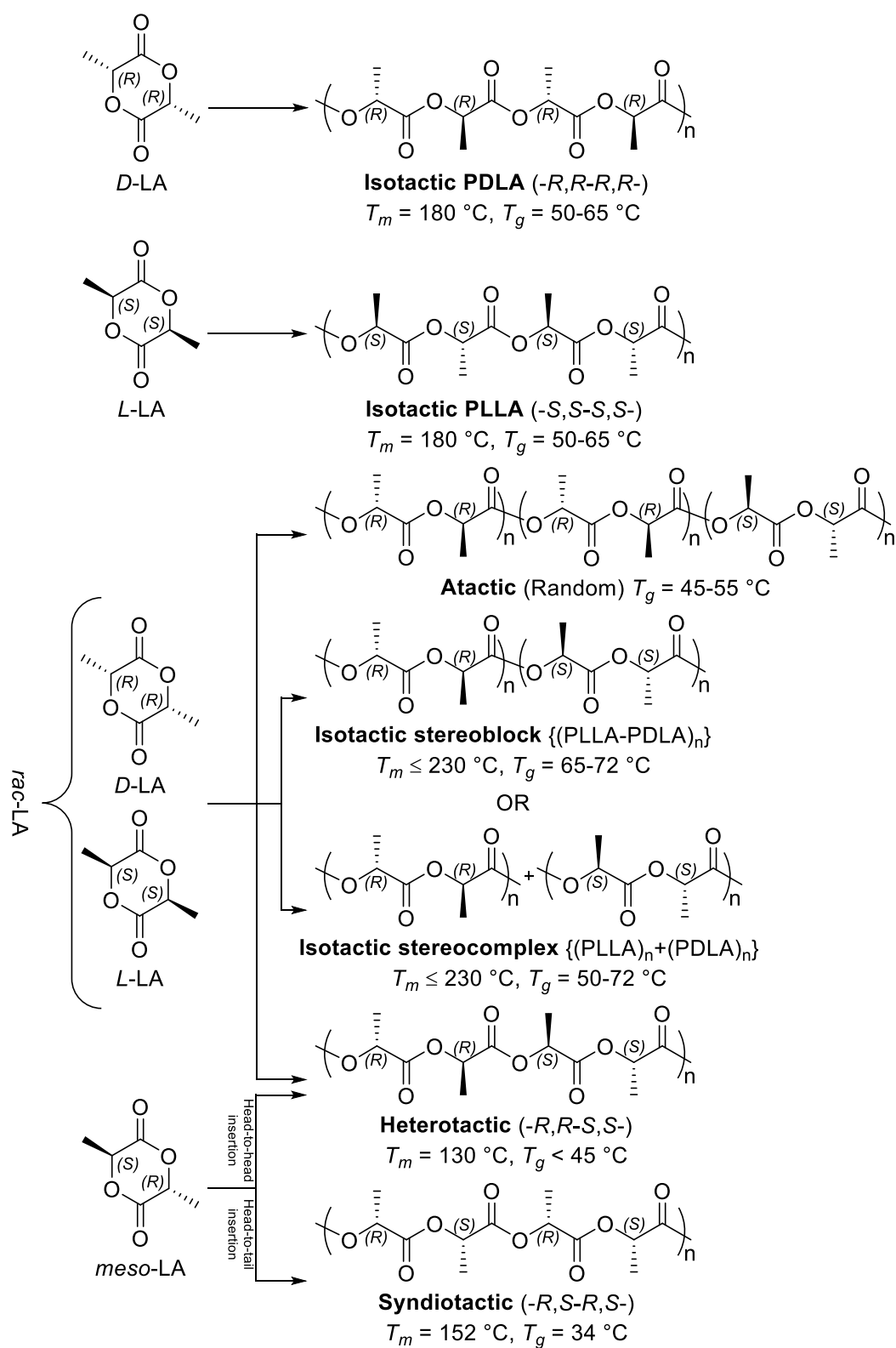
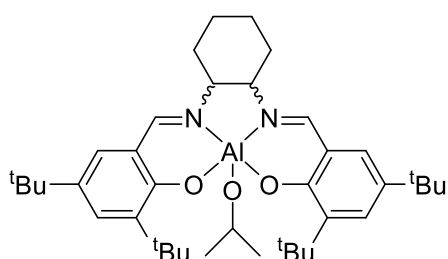


Figure 33. The tacticities and microstructures possible in the stereoselective ROP of LA.<sup>[1,4,8,9,12,16,28,34,44,46]</sup>

There are two mechanisms responsible for the stereoselective ROP of *rac*-LA: chain-end-control (CEM) and enantiomorph-site-control (SCM).<sup>[1,8]</sup> Chain-end-control

depends on the chirality of the terminal LA unit of the propagating polymer chain end bound to the initiator (the last LA unit inserted into the polymer chain) controlling the chirality of the next incoming monomer inserted.<sup>[1,8]</sup> Generally, this mechanism is associated using a hindered, achiral initiator. The initiator does not need to be chiral because of the stereogenicity of LA, the polymer chain and chain end. Although it is important to stress that chiral complexes are still able to operate under CEM. For example, it was shown by Chrisholm *et al.*, that the well-known Al(III)–alkoxide complexes (*Figure 34*) reported by Feijen and co-workers were operating under CEM despite the chirality of the (*R,R*)–Jacobsen ligand.<sup>[47–49]</sup>



*Figure 34.* Feijen's Al(III)–*rac*– and (*R,R*)–cyclohexylsalen–isopropoxide complexes.<sup>[48,49]</sup>

Enantiomeric-site-control occurs when the chirality of the initiator controls the chirality of the next incoming LA monomer inserted, and not the chain end of the propagating polymer chain.<sup>[1,8]</sup> Generally, this mechanism occurs using inherently chiral initiators with asymmetric ancillary ligands, but the chirality can be adopted during the reaction even if achiral ligands are used. This latter point can be exemplified well by work done from Jones and Byers.<sup>[50,51]</sup> Jones and co-workers showed that the achiral Zr(IV)–*meso*–2,2'–bipyrrrolidine salen complex was more selective than the analogous chiral (*R,R*) and (*S,S*) complexes (*Figure 35*) for the ROP of *rac*–LA because it was able to isomerise, after misinsertions of the LA units, in solution, to adopt and convert chiral configurations ( $\Lambda$  and  $\Delta$ ).<sup>[50]</sup> As will be discussed later (**Section 3.3**), Byers and co-workers achieved stereocontrol, *via* a SCM mechanism, using an achiral Fe–*bis*(imino)pyridine complex and the addition of achiral silanols to generate an *in-situ* chiral Fe centre. This was achieved by 'desymmetrisation' and a change in the coordination framework of the complex upon silanol addition.<sup>[51]</sup> It is also possible that the stereoselectivity is controlled by both mechanisms, cooperatively or uncooperatively.<sup>[8,52,53]</sup> Therefore, it is not

possible to predict the stereoselective mechanism simply by observing the structure of the initiator, and kinetic analysis, using *rac*-LA, *L*-LA and *D*-LA, is required to help deduce this information.

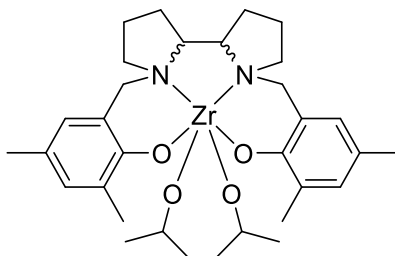


Figure 35. Jones' Zr(IV)-*meso*-, (*R,R*)- and (*S,S*)-2,2'-bipyrrolidine salan-bis(isopropoxide) complexes.<sup>[50]</sup>

Therefore, the overall aim in this area, of the ROP of LA, is exploring and developing alternative initiator systems to the industrially used Sn(Oct)<sub>2</sub>. Systems that are more selective, can provide stereocontrol and access PLA with superior properties and open new application opportunities. While also being less toxic and environmentally benign, to allow the PLA's use in applications such as biomedical and nullify concerns; currently hindering the application of PLA. Systems that are more active or maintain the high activity achieved using Sn(Oct)<sub>2</sub> are also desired.<sup>[2,8,29]</sup>

### 3.3 Fe-mediated ring opening polymerisation and project aims

Despite the numerous benefits associated with iron (Fe); such as the high abundance, low toxicity, low cost (both at industrial and commercial scales) and the potential for air-stability, there are limited examples of Fe-mediated ring opening polymerisation (ROP) in literature.<sup>[54-58]</sup> This is particularly the case using Fe(III) systems for cyclic esters such as lactide (LA). Indeed, in the production of PLA, the low toxicity and environmentally benign nature of Fe is attractive and makes it an ideal candidate for future and more extensive applications to food packaging and biomedical uses. As discussed in **Section 3.2**, these applications are currently limited using Sn(Oct)<sub>2</sub> industrially due to toxicity concerns and hence finding an alternative Fe based benign system may potentially negate these concerns.<sup>[4,8]</sup>

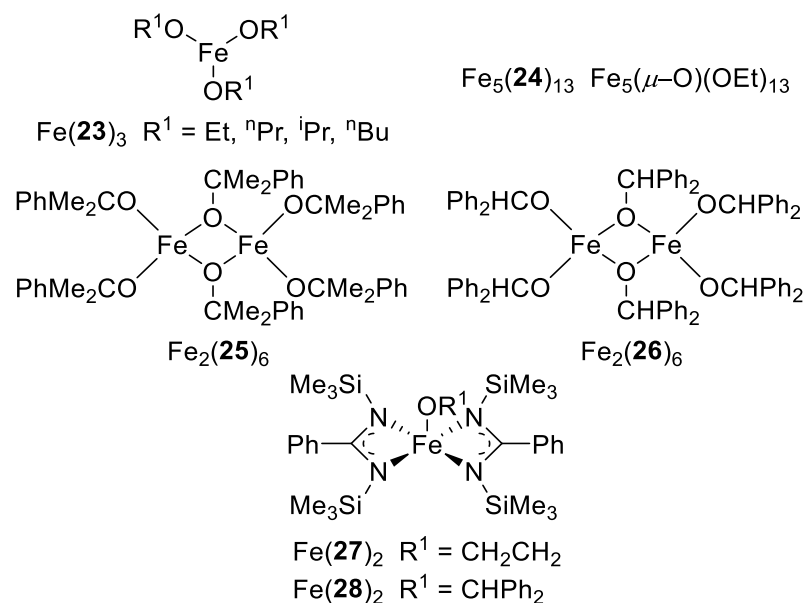


Figure 36. Simple ferric alkoxide and derivatives reported by Liao and Tolman.<sup>[59–61]</sup>

Early studies reported simple ferric alkoxides,  $\text{Fe}(\text{OR})_3$ , and derivatives were active for the ROP of *rac*-LA; a racemic mixture of LA monomers (Figure 36).<sup>[59–61]</sup> Liao and co-workers applied  $\text{Fe}(\text{OR})_3$  initiators  $\{\text{Fe}(\mathbf{23})_3\}$  under solvent-free conditions for melt polymerisation ( $>130^\circ\text{C}$ ). High conversions (90–96%) were observed after 48 hours with the highest molecular weight polymer achieved at a lactide-to-Fe initiator ratio of 1000:1  $\{\text{Fe}(\text{OEt})_3, M_n = 61400 \text{ g mol}^{-1}, \text{Đ} = 1.61\}$ . Increasing temperature and the steric bulk, moving away from using  $\text{Fe}(\text{OEt})_3$  initiator, decreased the molecular weight and broadened the observed dispersity. Despite stereoselective isotactic control being achieved ( $P_m = 0.54\text{--}0.72$ ), MALDI-ToF (Matrix-assisted laser desorption / ionisation–Time of Flight) analysis indicated undesired intermolecular transesterification side-reactions were taking place during the melt polymerisation, with the alkoxide groups bound on the initiator being converted to growing PLA chains.<sup>[59]</sup> It was proposed that a coordination–insertion mechanism was in operation.

Tolman and co-workers reported ferric alkoxide cluster initiators, derived from ethoxide and benzyl alkoxide, for the solution polymerisation of *rac*-LA using toluene. High conversions and activity with good control of the molecular weight and narrow dispersity was achieved at  $70^\circ\text{C}$  after 21 minutes for  $\text{Fe}_5(\mathbf{24})_{13}$  {97% conversion,  $\text{Đ} = 1.17$ } and 35 minutes for  $\text{Fe}_2(\mathbf{25})_6$  {98% conversion,  $M_n = 34000$

$\text{gmol}^{-1}$ ,  $\bar{D} = 1.60$ ) (Figure 36). This was at a lactide-to-Fe initiator ratio of 450:1 with no racemisation being observed.<sup>[60]</sup> The observation of ethoxy end groups in the  $^1\text{H}$  NMR spectroscopy suggested the mechanism was coordination-insertion. No racemisation was observed as only one methine peak in the decoupled  $^1\text{H}$  NMR spectroscopy was detected when using *L*-LA.<sup>[60]</sup> Building on this work, Tolman synthesised two mononuclear ferric amidinate-alkoxide complexes {Fe(**27**)<sub>2</sub> and Fe(**28**)<sub>2</sub>} and another dinuclear ferric alkoxide complex {Fe<sub>2</sub>(**26**)<sub>6</sub>} with the same alkoxide group for direct comparison (Figure 36). Fe<sub>2</sub>(**26**)<sub>6</sub> and Fe(**28**)<sub>2</sub> were applied to the polymerisation of *meso*-LA; the mononuclear amidinate-alkoxide complex {Fe(**28**)<sub>2</sub>} displayed reduced activity and control in toluene at 70 °C compared to the dinuclear alkoxide complex {[LA]:[initiator] = 1000:1; Fe<sub>2</sub>(**26**)<sub>6</sub>, conversion = 96% after 52 minutes,  $M_n = 61200 \text{ gmol}^{-1}$ ,  $\bar{D} = 1.34$  vs. Fe(**28**)<sub>2</sub>, conversion = 88% after 77 minutes,  $M_n = 39500 \text{ gmol}^{-1}$ ,  $\bar{D} = 1.88$ }. No stereocontrol was observed from either initiators and both were less effective than the Fe<sub>5</sub>(**24**)<sub>13</sub>.<sup>[61]</sup>

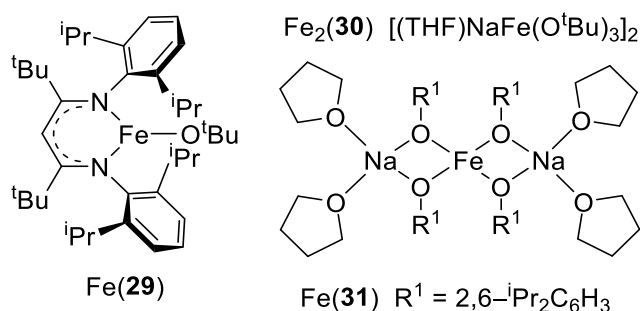
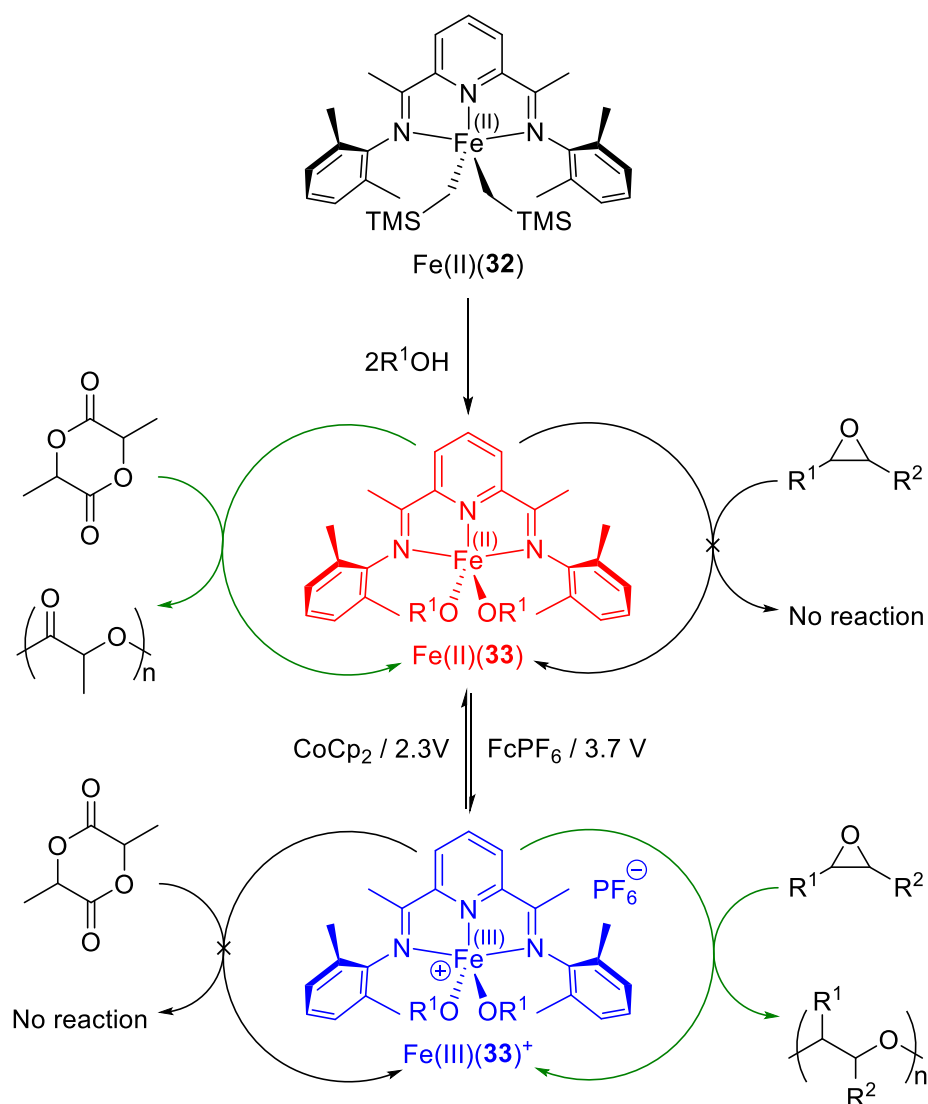


Figure 37. Gibson's Fe(II)- $\beta$ -diketiminato complex and hetero-dinuclear Fe(II)-alkoxide complexes.<sup>[62,63]</sup>

Gibson *et al.* reported, soon after, the preparation and application of a mononuclear Fe(II)-*tert*-butoxide complex {Fe(**29**)} stabilised by a *tert*-butyl substituted, two coordinate  $\beta$ -diketiminato ligand (Figure 37).<sup>[62]</sup> This was inspired by Holland who applied the first Fe(II) initiator to the ROP of LA.<sup>[64]</sup> Rapid and controlled polymerisation using Fe(**29**) was observed at room temperature in toluene, comparable to that of Zn(II)(**29**), with high conversion after 20 minutes, high molecular weight and narrow distribution achieved ([*rac*-LA]:[Fe] = 100:1, 94% conversion,  $M_n = 37500 \text{ gmol}^{-1}$ ,  $\bar{D} = 1.12$ ). However, transesterification side-reactions were present and atactic PLA was obtained.<sup>[62]</sup> Gibson and co-workers also reported

two hetero–dinuclear Fe(II)–alkoxide complexes {Fe<sub>2</sub>(**30**)/Fe(**31**)}, with the anionic Fe alcoholate / alkoxide species stabilised by sodium metal counteranions, for the ROP of *rac*-LA in dichloromethane at room temperature (Figure 37).<sup>[63]</sup>

Byers and co-workers have explored a Fe–*bis*(imino)pyridine–*bis*(alkoxide) complex {Fe(II)(**33**) / Fe(III)(**33**)<sup>+</sup>}, in significant detail, as a switchable catalyst for polymerisation *via* orthogonal redox control with the reversible sequential addition of exogenous chemical oxidising / reducing agents or by electrochemical means using electrodes; this concept is depicted in Scheme 18.<sup>[65–67]</sup> Depending on the oxidation state of the Fe metal centre, the complex can selectively initiate either the ROP of LA or epoxide.



Scheme 18. Byers' redox-switchable Fe(II/III)–*bis*(imino)pyridine–*bis*(alkoxide) initiator by the use of chemical agents or electrochemistry.<sup>[65–67]</sup>



The discrete neutral complex with an Fe(II) centre {Fe(II)(**33**)} or generated *in-situ*, by the addition of the appropriate alcohol to the Fe(II)-*bis*(imino)pyridine-*bis*(alkyl) precursor complex {Fe(II)(**32**)}, was an active initiator for the ROP of *rac*-LA to atactic PLA (*Scheme 18*). At a lactide-to-Fe initiator ratio of 50:1, at room temperature in dichloromethane for three hours, both the isolated and *in-situ* generated complex; using two equivalents of 4-methoxyphenol ([LA]:[Fe]:[alcohol] = 50:1:2), displayed similar results with 93% and 88% conversion respectively. Moderate molecular weights were obtained with narrow dispersities {Fe(II)(**33**),  $M_n = 6800 \text{ gmol}^{-1}$ ,  $\mathcal{D} = 1.16$  and *in-situ* Fe(II)(**33**),  $M_n = 6200 \text{ gmol}^{-1}$ ,  $\mathcal{D} = 1.18$ }. The activity was sensitive to the electronics of the added alcohol with electron-rich phenols and aliphatic donating alcohols more effective than electron-deficient.<sup>[65]</sup> The displayed living polymerisation behaviour and the stability of the catalytic system, shown by the ability to generate the species *in-situ*, enabled the ROP of *rac*-LA to be 'switched' off by the addition of the one electron oxidising agent ferrocenium hexafluorophosphate. This generated the dormant cationic Fe(III)(**33**)<sup>+</sup>, with the Fe(III) centre completely inactive with negligible reactivity to LA (*Scheme 18*). The reduction of the Fe(III) species *via* the *in-situ* addition of the reducing agent cobaltocene restored the Fe(II) oxidation state.

It was found that the opposite trend of reactivity was present when epoxides were applied instead of *rac*-LA (*Scheme 18*). The cationic Fe(III)(**33**)<sup>+</sup> species was active for epoxide polymerisation, using cyclohexene oxide (CHO), and the reduced Fe(II)(**33**) was inactive / dormant towards CHO. This switch was postulated to be due to the increased electrophilic activation with the electron-deficient Fe(III) centre resulting in CHO polymerisation and the nucleophilic activation of the alkoxide auxiliary ligands with the electron-rich Fe(II) centre resulting in lactide polymerisation. This chemoselectivity and complementary reactivity enabled the production of a redox-switchable diblock copolymer with ester and ether linkages. Recently, Byers' reported the first example of using electrochemistry to control the 'switch' of any catalyst by using Fe(II)(**33**) (*Scheme 18*).<sup>[67]</sup> Thus, the use of stoichiometric amounts of chemical oxidising / reducing agents could be circumvented. Using a sacrificial lithium reverse electrode and carbon working electrode, the chemoselectivity could

be controlled using an applied potential *in-situ*; a potential of 2.3 V triggered lactide polymerisation and a potential of 3.7 V triggered epoxide polymerisation. Using these means, the sequential polymerisation of the monomers, in a non-equimolar mixture of epoxide and *rac*-LA ([LA]:[CHO] = 1:5), in dichloromethane and <sup>n</sup>Bu<sub>4</sub>NPF<sub>6</sub> electrolyte (0.1 M), allowed the formation of block copolymers at room temperature.<sup>[67]</sup>

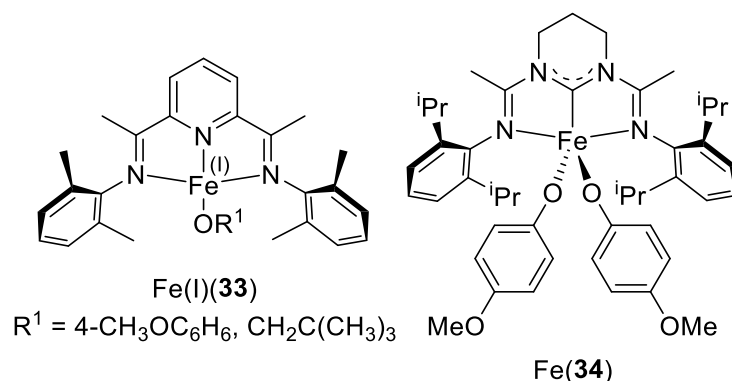


Figure 38. Byers' Fe(I)-*bis*(imino)pyridine-alkoxide and Fe-carbenodiamidine-*bis*(alkoxide).<sup>[57,68]</sup>

Aside from the switchable catalysis work (*Scheme 18*), Byers' explored other systems. From the observation that the activity of Fe(II)(**33**) increased when electron donating alcohols / alkoxide groups (R<sup>1</sup>) were used, Byers' prepared and applied a Fe-*bis*(amidinato)-*N*-heterocyclic carbene-*bis*(alkoxide) complex {Fe(**34**)} to the ROP of *rac*-LA (*Figure 38*).<sup>[68]</sup> This ancillary ligand, also known as carbenodiamidine (CDA), is strongly  $\sigma$ -donating in comparison to *bis*(imino)pyridine. The complex facilitated controlled solution polymerisation in 1,2-dimethoxyethane solvent at room temperature, and while the reaction rate was similar, the molecular weight was approximately four times higher than the analogous Fe(II)(**33**) with 4-methoxyphenol alkoxide auxiliary ligands. Indeed, kinetic investigation revealed the complex was seven times more active {Fe(**34**), [LA]:[Fe] = 50:1,  $M_n = 39500 \text{ gmol}^{-1}$ }. This difference in activity was rationalised to be resulting from slow initiation rates with an induction period followed by fast propagation rates. Increasing the lactide concentration shortened this induction period resulting in higher conversion, activity and molecular weights {[LA]:[Fe] = 5000:1, 85% conversion, 8 hours,  $M_n > 350000 \text{ gmol}^{-1}$ ,  $\mathcal{D} = 1.20$ }.<sup>[68]</sup> Intrigued by how the oxidation state had such a dramatic effect on reactivity for Fe(II)(**33**) and the observation that electron-rich Fe species were superior for LA

polymerisation, Byers' prepared complexes Fe(I)(**33**) ( $R^1 = 4\text{-CH}_3\text{OC}_6\text{H}_6, \text{CH}_2\text{C}(\text{CH}_3)_3$ ) with an Fe(I) centre for the polymerisation of a variety of cyclic esters and carbonates (Figure 38).<sup>[57]</sup> Unexpectedly, while the complexes were active with high molecular weight and narrow chain length distribution, both were less active than the analogous Fe(II)–*bis*(imino)pyridine–*bis*(alkoxide) complexes in the solution polymerisation of *rac*-LA at room temperature {[LA]:[Fe] = 500:1; Fe(I)(**33**),  $R^1 = 4\text{-CH}_3\text{OC}_6\text{H}_6$ , 90 minutes, 88% conversion,  $M_n = 74100 \text{ gmol}^{-1}$ ,  $\bar{D} = 1.13$  vs. analogous Fe(II)(**33**),  $R^1 = 4\text{-CH}_3\text{OC}_6\text{H}_6$ , 10 minutes, 94% conversion,  $M_n = 94800 \text{ gmol}^{-1}$ ,  $\bar{D} = 1.37$ }.<sup>[57]</sup> It was concluded the difference in reactivity, between Fe(I)(**33**) and Fe(II)(**33**), was due to the change in electron donating ability of the neutral vs. singly reduced *bis*(imino)pyridine ancillary ligand and not the change in oxidation state of the Fe centre as was observed for Fe(II)(**33**) vs. Fe(III)(**33**)<sup>+</sup>. Although the charge of the overall complex in Fe(**33**) may also have had an impact.<sup>[57]</sup>

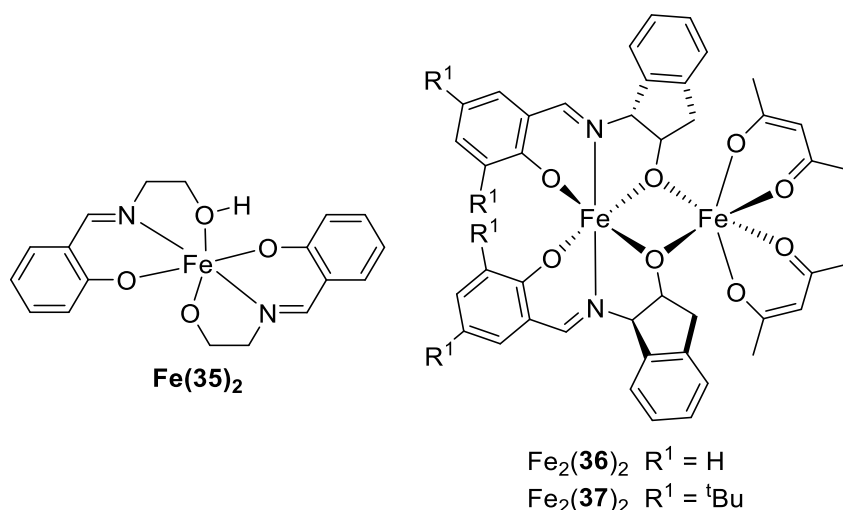


Figure 39. Mononuclear and dinuclear Fe(III)–phenoxy–imine complexes.<sup>[58,69]</sup>

Both mononuclear and dinuclear Fe(III) complexes bearing phenoxy–imine / Schiff base [ONO], bidentate ‘half–salen’, ligands have also been synthesised, reported and applied to the ROP of *L*-LA (Figure 39).<sup>[58,69]</sup> Silvino *et al.* applied the mononuclear Fe(**35**)<sub>2</sub> complex under solvent–free conditions for the melt polymerisation of *L*-LA at >120 °C.<sup>[58]</sup> However, this complex was a less effective initiator compared to other Fe examples. Kang *et al.* applied the commercially available, metal precursor Fe(acac)<sub>3</sub> and two dinuclear Fe(III)–chiral phenoxy–imine– $\beta$ -diketonate complexes derived from Fe(acac)<sub>3</sub> {Fe<sub>2</sub>(**36/37**)<sub>2</sub>(acac)<sub>2</sub>}.<sup>[69]</sup> Fe(acac)<sub>3</sub> was used as a means of

comparison for the two complexes. High activity was observed with the complexes using *L*-LA with no alcohol initiator at a lactide-to-Fe initiator ratio of 100:1. Despite the structural similarities, Fe<sub>2</sub>(**37**)<sub>2</sub>(acac)<sub>2</sub> was, in particular, highly active with Fe<sub>2</sub>(**36**)<sub>2</sub>(acac)<sub>2</sub> displaying inferior behaviour to that of Fe(acac)<sub>3</sub>. Under solvent-free melt conditions (130 °C) for Fe<sub>2</sub>(**37**)<sub>2</sub>(acac)<sub>2</sub>, 97% conversion was achieved in one hour with high molecular weights and narrow dispersities observed {*M*<sub>n</sub> = 12500 gmol<sup>-1</sup>, Đ = 1.40}. Kinetic investigations concluded a living polymerisation was in effect and the difference in the observed molecular weights and theoretical molecular weights in all cases were down to transesterification side-reactions {Fe<sub>2</sub>(**37**)<sub>2</sub>(acac)<sub>2</sub>, *M*<sub>n</sub> = 12500 gmol<sup>-1</sup> vs. *M*<sub>n,theoretical</sub> = 14000 gmol<sup>-1</sup>}. Lower activity was observed when applied to the melt polymerisation of *rac*-LA {Fe<sub>2</sub>(**37**)<sub>2</sub>(acac)<sub>2</sub>, 78% conversion, 30 minutes, *M*<sub>n</sub> = 7700 gmol<sup>-1</sup>, Đ = 1.19} and the solution polymerisation of *L*-LA in toluene at 130 °C {Fe<sub>2</sub>(**37**)<sub>2</sub>(acac)<sub>2</sub>, 92% conversion, two hours, *M*<sub>n</sub> = 8800 gmol<sup>-1</sup>, Đ = 1.27}; no stereocontrol was achieved using *rac*-LA. The mechanism was not discussed, although, due to the structure of the dinuclear complexes, many catalytic species were proposed using ESI-MS that could result in initiation; complicating any mechanistic study.<sup>[69]</sup>

For the Fe examples discussed thus far, although they have been active as initiators for polymerisation, minimal or no stereocontrol has been achieved with inferior atactic PLA being produced. As discussed in **Section 3.2**, the stereocontrol and tacticity of the PLA is crucial otherwise the polymers' microstructure and bulk physical properties are diminished and impacted negatively.<sup>[1,2,10,12,28]</sup>

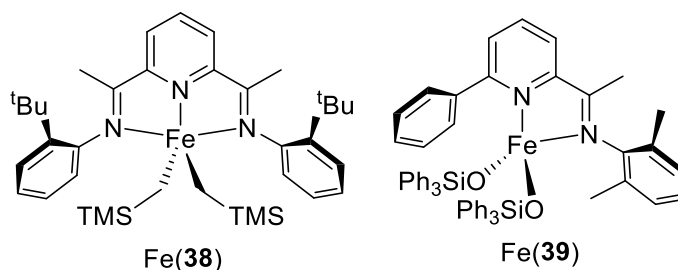
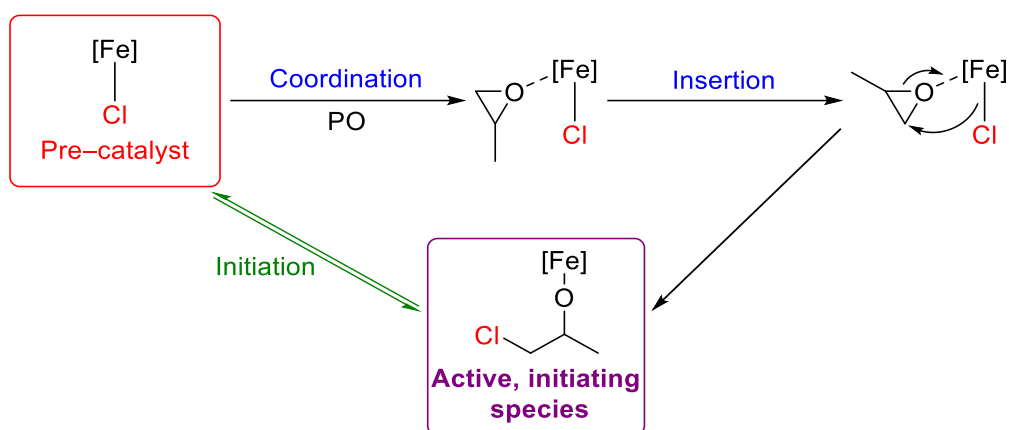


Figure 40. Byers' Fe(II)-*tert*-butyl substituted *bis*(imino)pyridine-*bis*(alkyl) and Fe(II)-mono(imino)pyridine-*bis*(siloxide) complexes.<sup>[51]</sup>

Byers' sought to improve the stereoselectivity by the *in-situ* generation of chiral Fe(II)-*bis*(imino)pyridine-*bis*(siloxide) complexes through the addition of silanols to

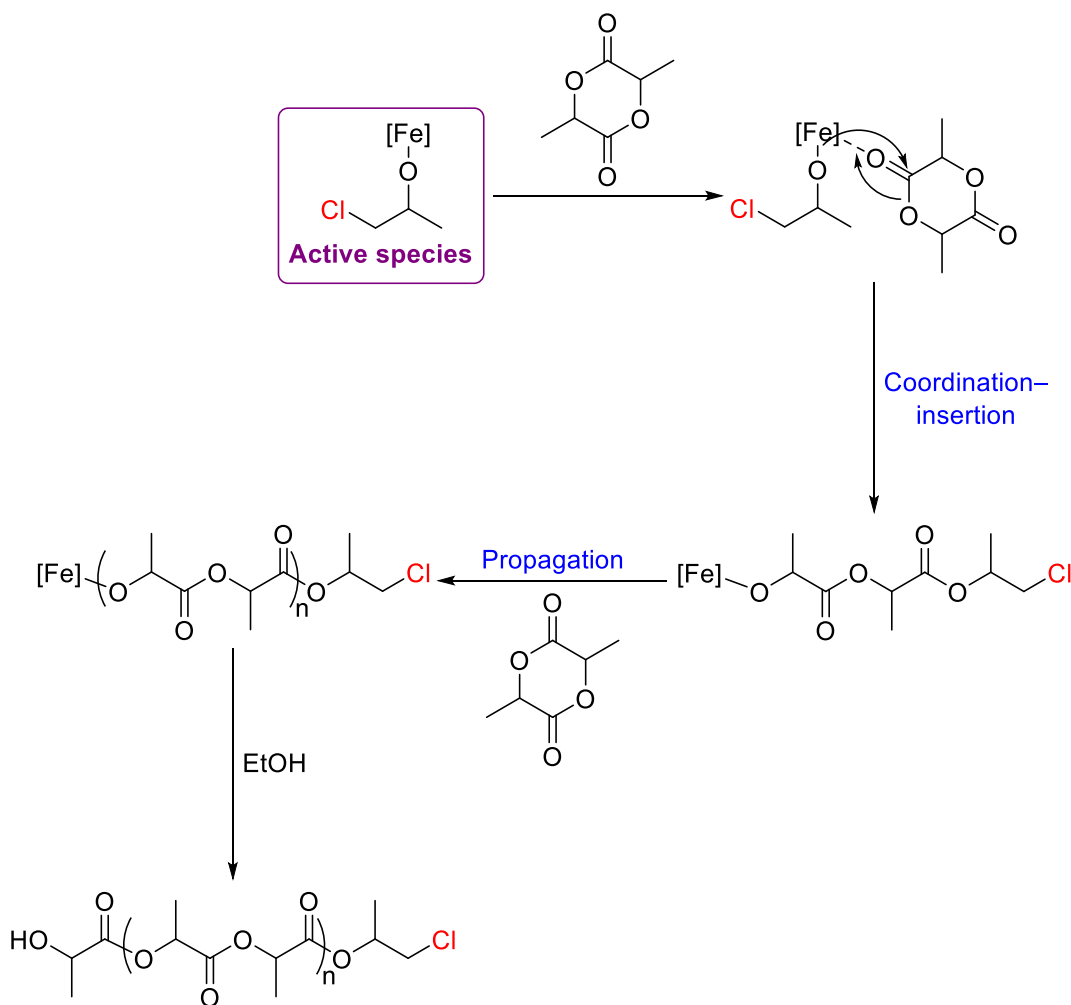
the achiral Fe(II)(**32**) complex (*Scheme 18*) and derived *tert*-butyl substituted Fe(II)(**38**) complex (*Figure 40*).<sup>[51]</sup> Heterotacticity was observed in the ROP of *rac*-LA following this rationale ( $P_m = 0.25$ – $0.50$ ), using a range of sterically varied silanols, coupled with a slight reduction in the control of molecular weight. The most selective combinations for the solution polymerisation, in tetrahydrofuran at room temperature for nine hours with a lactide-to-Fe initiator-to-alcohol ratio of 50:1:2, were Fe(**38**) with two equivalents of MePh<sub>2</sub>SiOH ( $P_m = 0.25$ ) and Fe(**39**) with two equivalents of Ph<sub>3</sub>SiOH ( $P_m = 0.27$ ). The stereoselective mechanism was proposed to be *via* enantiomorphic-site-control and not chain-end-control. ‘Desymmetrisation’ and a change in the coordination number, with dissociation of one of the imine arms of the ancillary ligand, upon addition of the silanol, resulted in a C<sub>1</sub>-symmetric chiral Fe(II) environment and the heterotactic stereoselectivity. This originated from a C<sub>s</sub>-symmetric achiral Fe(II) environment with both imine arms bound.<sup>[51]</sup>

Recently, as was discussed in **Section 2.1**, Duan *et al.* prepared a range of air-stable Fe(III)-salen-chloride complexes and applied them to the solution ROP of *rac*-LA.<sup>[54]</sup> There are particularly few examples of Fe(III)-chloride complexes in literature due to the required need for initiation to an active species to catalyse ROP.<sup>[54,70]</sup> Generally, a moderate isotactic bias was observed ( $P_m = 0.53$ – $0.78$ ) for complexes Fe(**A**-**C**/**E**-**H**)Cl (**Section 2.1**, *Scheme 1*) and at the time the highest level of stereocontrol reported for an Fe initiator. Slight heteroselectivity could be favoured by modification of the ligand backbone at specific reaction conditions {Fe(**D**)Cl,  $P_m = 0.44$ ; Fe(**G**)Cl,  $P_m = 0.37$ ; Fe(**H**)Cl,  $P_m = 0.47$  at 100 °C for 17.4, 5.1 and 2 hours respectively}. The highest isotacticity was observed using Fe(**A**)Cl { $P_m = 0.78$ } at a lactide-to-Fe initiator ratio of 100:1 and, although not as active as previous Fe examples applied at room temperatures, was conducted at a relatively mild 60 °C for 24 hours. Overall, the dispersity was broader for these complexes however ( $\bar{M}_w/\bar{M}_n = 1.38$ – $2.36$ ).<sup>[54]</sup>



Scheme 19. Postulated mechanism of initiation to the active Fe(III)-salen-alkoxide species.<sup>[54]</sup>

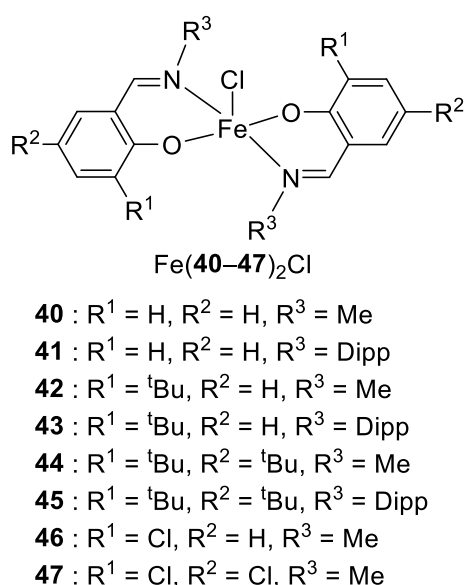
Propylene oxide (PO) was used as both the solvent and co-initiator for the polymerisations by Duan.<sup>[54]</sup> After the opening of the PO epoxide and insertion of the Fe(III)-chloride bond of the pre-catalyst, *via*  $\sigma$ -bond metathesis, the *in-situ* generated Fe(III)-salen-alkoxide was determined to be the active species (Scheme 19). Evidence for this was observed from MALDI-ToF analysis with the alkoxide end group present on the PLA. Kinetic analysis deduced a chain end stereoselective mechanism (CEM) was in operation for the Fe(III)-salen-alkoxide active species, and not enantiomeric-site-control, by using chiral complexes Fe(**A/B**)Cl with *rac*-cyclohexyl and (*R,R*)-cyclohexyl backbones respectively. Identical rates of polymerisation were displayed for both complexes when applied to *rac*-LA and when Fe(**B**)Cl was applied to *L*-LA and *D*-LA; these observations would not be observed if an enantiomeric-site-control mechanism was occurring.



*Scheme 20.* Duan's lactide polymerisation mechanism *via* coordination–insertion using the initiated active Fe(III)–alkoxide species.<sup>[54]</sup>

Using MALDI–ToF analysis, the lactide polymerisation mechanism was concluded to be a coordination–insertion mechanism (*Scheme 20*). After generation of the active Fe(III)–salen–alkoxide species using PO (*Scheme 19*), LA monomers propagate *via* continuously coordinating to the metal species and inserting into the Fe(III)–alkoxide bond to form the PLA (*Scheme 20*). The series of peaks with a repeating unit of  $144 \text{ gmol}^{-1}$ , for LA, and  $94.5 \text{ gmol}^{-1}$  residual mass, for the chloropropanol end group, suggested only the LA was ring–opened and not the PO solvent after initiation. As the PO epoxide is asymmetric, there are two possible sites of attack by the Fe(III)–chloride bond for regioselective opening and insertion. Using a range of NMR spectroscopic techniques it was determined the end group was  $\text{ClCH}_2\text{CH}(\text{CH}_3)\text{O-}$  with the less sterically hindered carbon atom being attacked (*Scheme 19*).<sup>[54]</sup> Duan highlighted the importance of the PO concentration in the polymerisations and, in

addition to neat PO, various ratios of a mixture of PO:toluene were applied to Fe(A) with the polymerisation rate and conversion studied. Increasing the concentration of [PO], favoured initiation with the equilibrium pushing the reaction forward, resulting in the increased rate of polymerisation up to a threshold concentration (*Scheme 19*). This value was determined to be about 50% [PO]:[toluene] and the activity was constant above this value due to sufficient PO being present for all the Fe(III)–chloride bonds of the metal complex to react.<sup>[54]</sup>



*Figure 41.* Shaver and Garden's Fe(III)–bis(phenoxy–imine)–chloride complexes.<sup>[56]</sup>

A decrease in the concentration of PO was attempted by Shaver, Garden and co-workers using eight Fe(III)–bis(phenoxy–imine)–chloride, 'half–salen' complexes {Fe(40–47)<sub>2</sub>Cl} as a mixture in toluene (*Figure 41*).<sup>[56]</sup> This was due to toxicity and carcinogenic concerns raised with using the PO epoxide; decreasing the biocompatibility, and at such excess in the solution polymerisations reducing the atom efficiency; compromising the benefits of using Fe.<sup>[56]</sup> The complexes were active for the solution ROP of *rac*–LA, at a higher temperature of 120 °C for 24 hours resulting in conversions >95% with broad chain length distributions and uncontrolled molecular weights observed ( $\bar{M}_w/\bar{M}_n = 1.4–4.0$ ). This was proposed to be due to undesired intramolecular and intermolecular transesterification side–reactions. A mixture of toluene and a lower amount PO was used, in comparison to Duan,<sup>[54]</sup> with a lactide–to–Fe initiator–to–PO ratio of 100:1:50. Initial work concluded high conversions were



obtainable with PO amounts as low as 50 equivalents. Blank control reactions concluded both Fe initiator and PO were required for ROP. Decreasing the reaction time to two hours resulted in varied conversions, irreproducibility, high amounts of transesterification and uncontrolled polymerisation. This implied a rate determining induction period was occurring to activate the Fe(III)–*bis*(phenoxy–imine)–chloride pre-catalyst to the active *in-situ* Fe(III)–alkoxide species. The length of this period, suggested to be possibly dependant on the strength of the Fe(III)–Cl bond and the Lewis acidity of the Fe(III) centre.<sup>[56]</sup> The increase in conversion from 1% to 90%, when a Fe(III)–Cl complex was stirred in excess PO for 16 hours to ensure activation and complete initiation before LA addition, provides evidence for this induction period. Therefore, this reinforced Duan’s observation that excess PO is essential for the equilibrium to favour controlled initiation and polymerisation. However, no stereocontrol was achieved using these complexes.<sup>[56]</sup>

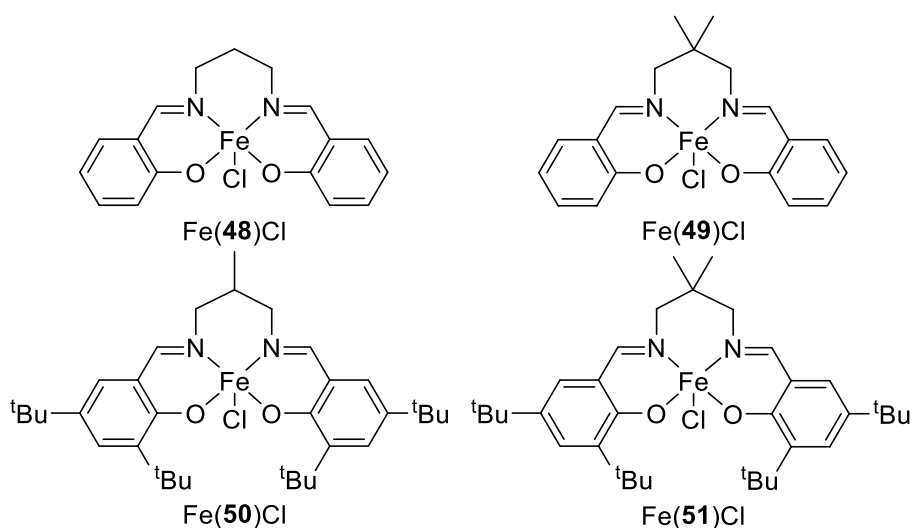


Figure 42. Duan’s more recent reported Fe(III)–salen–chloride complexes.<sup>[71]</sup>

Duan and co-workers reported four further Fe(III)–salen–chloride complexes to explore how modifications on the ligand backbone effected the activity and stereoselectivity of the ROP of *rac*-LA (Figure 42).<sup>[71]</sup> The solution polymerisations were carried out using PO as both the solvent and co-initiator at 25 °C and a lactide-to-Fe initiator ratio of 100:1. These complexes appear more active than Fe(A–H)Cl with similar broad dispersity, achieving conversions of 99% and 98% for Fe(48/49)Cl, in ten and eight hours respectively {Fe(48)Cl;  $M_n = 16126 \text{ gmol}^{-1}$ ,  $\mathcal{D} = 1.33$  and Fe(49)Cl;  $M_n = 15686 \text{ gmol}^{-1}$ ,  $\mathcal{D} = 1.87$ }. Complexes Fe(50/51)Cl were slightly less

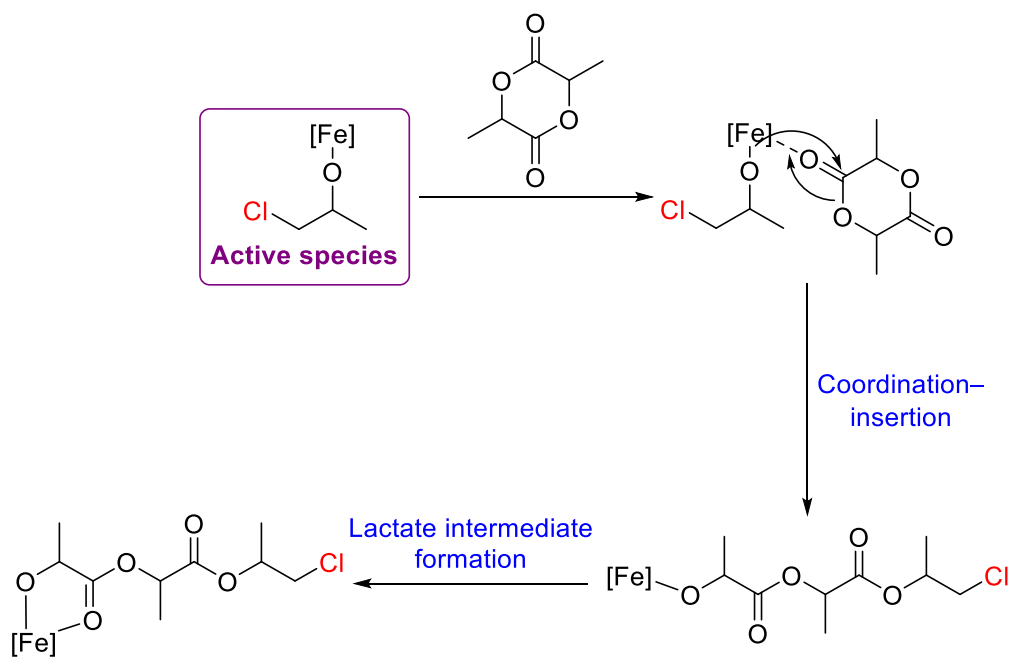
active with conversions of 56% and 54% in 12 hours {Fe(**50**)Cl;  $M_n = 7555 \text{ gmol}^{-1}$ ,  $\bar{D} = 1.45$  and Fe(**51**)Cl;  $M_n = 7969 \text{ gmol}^{-1}$ ,  $\bar{D} = 1.06$ }.<sup>[71]</sup> All complexes displayed moderate isotactic stereocontrol ( $P_m = 0.68\text{--}0.77$ ).<sup>[71]</sup>

These ligand backbones used by Duan, for Fe(**C/D/E/48/51**)Cl, are identical to the wide range of well-known Al–salen complexes studied by Nomura *et al.*<sup>[72,73]</sup> It is hard to directly compare between the iron and aluminium complexes due to differences in the polymerisation conditions, such as temperature and the auxiliary ligand (Cl vs. Et / OBn). Generally, Nomura's complexes were significantly slower, as expected and inherent with aluminium complexes, but superior in isotacticity and more controlled {Fe(**51**)Cl; [LA]:[Fe] = 100:1 in PO, 12 hours, 54% conversion at room temperature,  $M_n = 7969 \text{ gmol}^{-1}$ ,  $\bar{D} = 1.06$ ,  $P_m = 0.72$  vs. Al(**51**)Et; [LA]:[Fe]:[BnOH] = 100:1:1 in toluene, six hours, 93% conversion at 70 °C,  $M_n = 20200 \text{ gmol}^{-1}$ ,  $\bar{D} = 1.06$ ,  $P_m = 0.93$  vs. Al(**39**)OBn, [LA]:[Fe] = 100:1:1 in toluene, five hours, 94% conversion at 70 °C,  $M_n = 21200 \text{ gmol}^{-1}$ ,  $\bar{D} = 1.08$ ,  $P_m = 0.92$ }.<sup>[71,73]</sup>

As mentioned in **Section 2.1**, Lamberti and co-workers reported the preparation of the first Fe(III)–salalen complex {Fe(**I**)Cl}, together with Fe(III)–salan {Fe(**J**)Cl} and –salen {Fe(**K/L**)} complexes (**Section 2.1, Figure 5**), soon after the synthesised Fe(III)–salalen complexes {Fe(**1–7**)Cl} had been applied to the ROP of *rac*-LA described in this chapter.<sup>[55]</sup> Lamberti's complexes were applied to the ROP of cyclic esters such as *L*-LA and  $\epsilon$ -caprolactone.<sup>[55]</sup> The discussion over the use of PO as a solvent / co-initiator and an induction period was corroborated in this work. Three of the complexes were unsuccessfully applied to the solution polymerisation of *L*-LA at a lactide-to-Fe initiator ratio of 100:1 in PO solvent (2.0 mL) for four hours at 60 °C. Fe(**I/J**)Cl were completely inactive and Fe(**K**)Cl obtained a low conversion of 33%. Adding one equivalent of *bis*(triphenylphosphoranylidene) ammonium chloride (PPNCl) co-initiator to Fe(**K**)Cl, promoting the opening of the PO epoxide and initiation to the active Fe(III)–alkoxide, increased conversion to 63% in the four hours. Still, no activity was observed when PPNCl was added to Fe(**I/J**)Cl to the surprise of the authors. Lamberti's explanation for no activity being observed for Fe(**I/J**)Cl, despite being active for the ROP of  $\epsilon$ -caprolactone, was the formation of stable five-membered chelate ring, lactate intermediates with the Lewis acidic Fe(III) centre

after insertion of the LA (*Scheme 21*).<sup>[55]</sup> These would form adjacent to the growing polymer chain with the Fe binding to the alkoxide and ester functionalities. These stable species would discourage further LA monomers to insert and suppress the activity.<sup>[55]</sup>

However, as was discussed by Duan<sup>[54]</sup> and Shaver<sup>[56]</sup> previously (together with findings made herein under **Sections 3.4** and **3.5**), it was more likely four hours at 60 °C was an insufficient induction period for efficient initiation with the equilibrium remaining towards the Fe(III)–chloride species and not the active Fe(III)–alkoxide species. The complexes were not trialled with *rac*-LA and, therefore, the early work described in this chapter consists of the application of the Fe(III)–salalen complexes {Fe(**1–7**)Cl} to the ROP of *rac*-LA.



*Scheme 21.* Lambert's proposed bidentate lactate intermediate formation.<sup>[55]</sup>

Following on from the work presented herein this Chapter, further relevant Fe examples have since been reported and worthy of mention. Herres–Pawlis and co-workers reported the application of three robust Fe(II)–guanidine complexes {Fe(**52–54**)Cl<sub>2</sub>} (*Figure 43*) to the controlled melt polymerisation of unpurified technical-grade *rac*-LA and recrystallised *L*-LA at 150 °C.<sup>[74]</sup> The two Lewis acidic complexes, bearing anthranilic acid methyl ester (asme) guanidine ligand frameworks {Fe(**53/54**)Cl<sub>2</sub>}, displayed remarkable activity and were tested at a range of lactide–

to–initiator ratios from 500:1 to catalyst concentrations as low as 5000:1 (*L*–LA;  $M_n = 32300$ – $147000 \text{ gmol}^{-1}$ ,  $\bar{D} = 1.3$ – $1.6$  and *rac*–LA;  $M_n = 35500$ – $77300 \text{ gmol}^{-1}$ ,  $\bar{D} = 1.5$ ).<sup>[74]</sup> Indeed, these complexes were superior to the previously known fastest, robust Fe initiator for LA polymerisation reported by the same group {[technical *rac*–LA]:[Fe] = 500:1, 150 °C; Fe(**53**)Cl<sub>2</sub>,  $k_{app} = 5.46 \times 10^{-4} \text{ s}^{-1}$  and Fe(**54**)Cl<sub>2</sub>,  $k_{app} = 43.5 \times 10^{-4} \text{ s}^{-1}$  vs.  $k_{app} = 0.13 \times 10^{-4} \text{ s}^{-1}$ }.<sup>[74,75]</sup> With a focus on finding a more realistic, sustainable, biocompatible catalyst for industrial LA polymerisation, Fe(**53/54**)Cl<sub>2</sub> were compared to Sn(Oct)<sub>2</sub> using recrystallised *L*–LA. Measuring the  $k_p$  values, it was found the Fe initiators surpassed the current industrial standard {[*L*–LA]:[Fe] = 1000:1, 150 °C; Fe(**53**)Cl<sub>2</sub>,  $k_p = 0.092 \pm 0.01 \text{ Lmol}^{-1}\text{s}^{-1}$  and Fe(**54**)Cl<sub>2</sub>,  $k_p = 0.554 \pm 0.02 \text{ Lmol}^{-1}\text{s}^{-1}$  vs. Sn(Oct)<sub>2</sub>,  $k_p = 0.084 \pm 0.02 \text{ Lmol}^{-1}\text{s}^{-1}$ }.<sup>[74]</sup>

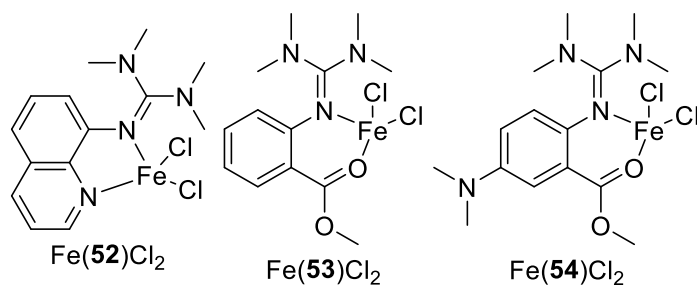
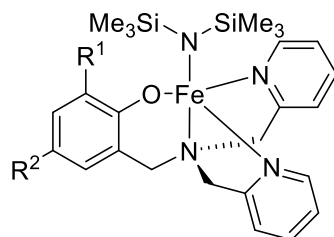


Figure 43. Herres–Pawlis’ reported robust Fe(II)–guanidine complexes.<sup>[74]</sup>

Soon after, Marin *et al.* reported the synthesis of a range of six Fe(II) complexes using tripodal amino–phenolate ligand frameworks (Figure 44). These complexes displayed remarkable activity when applied as initiators for *rac*–LA polymerisation at room temperature with the addition of isopropanol co–initiator for more effective initiation (48–93% yield after 0.5–120 minutes).<sup>[76]</sup> High molecular weights and isotacticity was afforded ( $M_n = 16700$ – $79900 \text{ gmol}^{-1}$ ,  $P_m = 0.68$ – $0.84$ ) and the stereoselectivity was increased further by decreasing the temperature (Fe(**55**); 0 °C,  $P_m = 0.91$  and -10 °C  $P_m = 0.92$ ). Thermal gravimetric analysis (TGA) revealed decomposition temperatures of up to 350 °C for selected PLA samples and a strong correlation between molecular weight and degradation temperature; with the degree of stereoselectivity having no impact on this temperature. These findings were stressed as higher degradation temperatures increase the processing temperature window (difference between the melting and degradation temperatures), as currently PLA’s narrow range is one major drawback industrially.

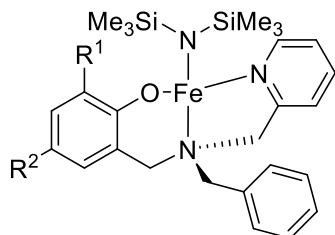


Fe(55)  $R^1 = \text{CPh}_3$ ,  $R^2 = \text{Me}$

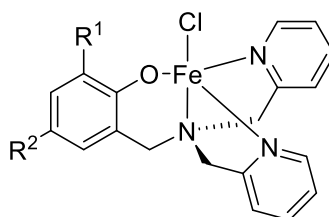
Fe(56)  $R^1 = \text{OCH}_3$ ,  $R^2 = \text{Me}$

Fe(57)  $R^1 = \text{CH}(\text{CH}_3)_2$ ,  $R^2 = \text{H}$

Fe(58)  $R^1 = \text{CH}(\text{CH}_3)(\text{CH}_2\text{CH}_3)$ ,  $R^2 = \text{H}$



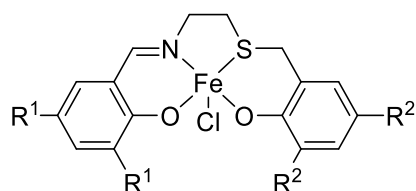
Fe(59)  $R^1 = \text{CPh}_3$ ,  $R^2 = \text{Me}$



Fe(60)  $R^1 = \text{CPh}_3$ ,  $R^2 = \text{Me}$

Figure 44. Marin's reported Fe(II)-tripodal complexes.<sup>[76]</sup>

Building on the work discussed using Fe(III)-salalen complexes, described in this chapter, a research group colleague, Stewart, reported the synthesis and application of Fe(III)-imine-thio-bis(phenolate) / 'thiolen' {ONSO} complexes (Figure 45) to the ROP of *rac*-LA.<sup>[77]</sup> It was shown the presence of the sulfur atom increased the activity and isotacticity of the Fe(III) initiators (76–96% conversion, reaction time = 0.5–96 hours,  $M_n = 5750\text{--}16500 \text{ gmol}^{-1}$ ,  $P_m = 0.57\text{--}0.89$ ); indeed as far as we are aware these represent the most isoselective Fe(III) initiators reported to date.<sup>[77]</sup> This enhancement was proposed to result from the softer, more hemilabile sulfur donor atom allowing more space around the Fe(III) centre for reactivity.



Fe(61–65)Cl

61 :  $R^1 = \text{H}$ ,  $R^2 = \text{tBu}$

62 :  $R^1 = \text{tBu}$ ,  $R^2 = \text{tBu}$

63 :  $R^1 = \text{Cl}$ ,  $R^2 = \text{tBu}$

64 :  $R^1 = \text{Br}$ ,  $R^2 = \text{tBu}$

65 :  $R^1 = \text{tBu}$ ,  $R^2 = \text{Br}$

Figure 45. Stewart's reported Fe(III)-thiolen complexes.<sup>[77]</sup>

Recently, Neffe and co-workers reported a study, that bears relevance with the Fe(III)–acetate work discussed in this Chapter.<sup>[78]</sup> With the objective of finding an alternative to toxic Sn(Oct)<sub>2</sub> initiator, the ROP of *L*-LA was achieved using simple, commercially available Fe(OAc)<sub>2</sub> as the initiator with simple amide co-initiators as non-polymerisable catalytic adjuncts (NPCAs). The reaction temperature could be reduced from 165 °C to as low as 105 °C under solvent-free melt conditions (105 °C, four hours reaction time, 50–97% conversion,  $M_n = 8200\text{--}15500 \text{ gmol}^{-1}$ ,  $\mathcal{D} = 1.06\text{--}1.12$ ). These NPCAs were applied to form active Fe(II) species *in-situ*, increase the solubility of the reaction mixture and activity.<sup>[78]</sup>

### 3.4 Ring opening polymerisation of *rac*-lactide using Fe(3)Cl

Building on the work done by Duan, the solution polymerisation of *rac*-LA was attempted using Fe(3)Cl synthesised in **Section 2.3** (*Scheme 5*).<sup>[54]</sup> This was carried out in PO, purified by vacuum distillation before use, to act as both the solvent and co-initiator at a range of reaction conditions (*Table 10*).<sup>[54–56,71]</sup> The *rac*-LA was singly recrystallised using toluene before being used. In the majority of entries, a lactide-to-Fe initiator ratio of 100:1 was applied unless stated otherwise. On the whole, for all solution polymerisations under the reaction conditions applied, predictable molecular weights, narrow dispersities ( $\mathcal{D} = 1.07\text{--}1.18$ ), moderate-to-high conversions and a moderate isotactic bias was observed. All PLA obtained from Fe(3)Cl, indeed from all Fe(III)–salalen–chloride complexes, using PO were generally bimodal as measured by GPC analysis (**Section 7.3**). This will be discussed further in **Section 3.7**; both chain length distributions were treated together for the number average molecular weight ( $M_n$ ) values.

Initially, two control reactions were attempted. The precursor ferric chloride (FeCl<sub>3</sub>), used in the synthesis for the Fe(III)–salalen–chloride complexes, was applied (*Table 10*, entry 2). The polymerisation displayed the highest activity and conversion observed in this study (96% conversion, 24 hours, 60 °C). However, no stereoselectivity was observed and the polymerisation was uncontrolled with a broad dispersity. To confirm whether the PO would partake in copolymerisation, with the propagating LA monomers, and was a suitable reaction solvent, *rac*-LA was not

included for one reaction (Table 10, entry 3).  $^1\text{H}$  NMR spectroscopy confirmed no reaction had taken place and poly(propylene glycol) was not observed.

Table 10. Solution polymerisation of *rac*-LA using Fe(3)Cl.

Entry	Initiator	Temp (°C)	Time (days)	Conv. <sup>a</sup> (%)	$P_m$ <sup>b</sup>	$M_{n,theoretical}$ <sup>c</sup> ( $\text{gmol}^{-1}$ )	$M_n$ <sup>d</sup> ( $\text{gmol}^{-1}$ )	$\bar{D}$ <sup>d</sup>
1	Fe(3)Cl	40	7	80	0.80	11600	11900	1.11
2	FeCl <sub>3</sub>	60	1	96	0.50	13950	6400	2.26
3 <sup>e</sup>	Fe(3)Cl	60	1	0	–	–	–	–
4 <sup>f</sup>	Fe(3)Cl	60	2	62	0.78	4550	4550	1.12
5 <sup>g</sup>	Fe(3)Cl	60	3	0	–	–	–	–
6 <sup>h</sup>	Fe(3)Cl	60	3	34	–	–	–	–
7	Fe(3)Cl	60	3	76	0.77	11050	10800	1.18
8 <sup>i</sup>	Fe(3)Cl	80	1	63	0.75	4650	6300	1.07
9	Fe(3)Cl	80	1	72	0.79	10450	9400	1.11
10 <sup>j</sup>	Fe(3)Cl	80	1	78	0.67	11350 <sup>k</sup>	11250	1.02
11 <sup>l</sup>	Fe(3)Cl	80	1	60	0.68	8750	3750	1.12

Conditions: *rac*-LA (0.4 g), PO (2.0 mL), [LA]:[Fe] = 100:1 under inert conditions. <sup>a</sup> Determined by  $^1\text{H}$  NMR spectroscopy. <sup>b</sup> Determined by  $^1\text{H}$  { $^1\text{H}$ } NMR spectroscopy;  $P_m$  = probability of isotactic enchainment. <sup>c</sup>  $M_{n,theoretical}$  = [(Conversion/100 x [LA]/[Initiator] x  $M_{r,LA}$ ) + chloropropanol end group MW] = [(Conversion/100 x [LA]/[Initiator] x 144.1260) + 93.5300]. <sup>d</sup> Determined *via* GPC (triple detection analysis) in THF solvent. <sup>e</sup> [LA]:[Fe] = 0:1. <sup>f</sup> [LA]:[Fe] = 50:1. <sup>g</sup> [LA]:[I]:[PO] = 100:1:1 in toluene. <sup>h</sup> CHO (2.0 mL) instead of PO (2.0 mL). <sup>i</sup> [LA]:[Fe]:[BnOH] = 100:1:1. <sup>j</sup> [LA]:[Fe]:[Et<sub>3</sub>N]:[BnOH] = 100:1:1:1 in toluene (5.0 mL) without the presence of PO. <sup>k</sup>  $M_{n,theoretical}$  = [(Conversion/100 x [LA]/[BnOH] x  $M_{r,LA}$ ) + benzyl alcohol end group MW] = [(Conversion/100 x [LA]/[BnOH] x 144.1260) + 107.1320]. <sup>l</sup> Polymerisation was carried out under air.

Using Fe(3)Cl, a moderate isotactic bias ( $P_m = 0.77$ ) and high conversion was achieved at 60 °C for three days (Table 10, entry 7). This was in good agreement with Lamberti's work, as previously mentioned, with the same complex observing no

conversion after four hours for the ROP of *L*-LA.<sup>[55]</sup> The isotacticity could be increased at 40 °C accompanied with a prolonged reaction time of seven days ( $P_m = 0.80$ ). A chain end controlled stereoselective mechanism (CEM) was more likely occurring in this study owing to the similarity to Duan's Fe(III)–salen–chloride complexes and because of the lack of inherent chirality in all Fe(III)–salalen–chloride complexes synthesised.<sup>[54]</sup> Examples of decoupled  $^1\text{H}$   $\{^1\text{H}\}$  NMR spectra, focussed on the methine region, used to determine the  $P_m$  values can be found in **Section 7.2** (Figures 103 and 104).

This stereoselectivity was maintained ( $P_m = 0.79$ ) despite increasing the temperature to 80 °C with a reduced reaction time of one day required for high conversion. Indeed, Fe(**3**)Cl was more stereoselective and active than the analogous Al(III)–salalen–methyl complex at this temperature {Al(**3**)Me; 73% conversion, 80 °C, three days,  $P_m = 0.61$ }.<sup>[79]</sup> This is potentially due to the increased Lewis acidity or increased bond lengths resulting in a more accessible metal centre for Fe(III) compared to Al(III). Compared with Duan's analogous Fe(III)–salen–chloride complex, at 60 °C, Fe(**3**)Cl was less active but achieved a higher isotacticity and controlled polymerisation {Fe(**E**)Cl; 96% conversion, 18.3 hours,  $\bar{D} = 1.61$ ,  $P_m = 0.53$  vs. Fe(**3**)Cl; 76% conversion, three days,  $\bar{D} = 1.18$ ,  $P_m = 0.77$ }. Activity and stereoselectivity was reduced but still present when carrying out the polymerisation under air. There was a significant reduction, however, in the molecular weight with a narrow dispersity being maintained (Table 10, entry 11).

The isotactic polymers derived from Fe(**3**)Cl at 40, 60 and 80 °C were analysed using MALDI–ToF mass spectrometry (Table 10, entries 1, 7 and 9). The role of the PO acting as a co–initiator was confirmed by the identification of chloropropanol as the end group, in all cases, and evidence that a coordination–insertion mechanism was in operation, as was expected from Duan's findings.<sup>[54]</sup> At 40 °C, an asymmetric series centred on 9914  $\text{g mol}^{-1}$  and tailing off towards a lower molecular weight was observed (Figure 46). This molecular weight was similar to that observed *via* GPC analysis indicating minimal undesired side–reactions occurred ( $M_{p,\text{MALDI-ToF}} = 9914 \text{ g mol}^{-1}$  vs.  $M_{n,\text{GPC}} = 11900 \text{ g mol}^{-1}$  vs.  $M_{n,\text{theoretical}} = 11600 \text{ g mol}^{-1}$ ). The repeating LA chain was present with the peak separation of 144  $\text{g mol}^{-1}$ . Another minor asymmetric



series of lower intensity tailing at low molecular weights was observed, with a peak separation of  $72 \text{ gmol}^{-1}$ , for a small amount of transesterification side-reactions. At  $60 \text{ }^\circ\text{C}$ , the MALDI-ToF spectrum was similar with the molecular weight value close to that observed from GPC analysis ( $M_{p,\text{MALDI-ToF}} = 8331 \text{ gmol}^{-1}$  vs.  $M_{n,\text{GPC}} = 10800 \text{ gmol}^{-1}$  vs.  $M_{n,\text{theoretical}} = 11050 \text{ gmol}^{-1}$ ) (Section 7.4, Figure 111). Transesterification was reduced when raised to  $80 \text{ }^\circ\text{C}$ , although at lower molecular weight there were cyclic oligomer side-product peaks (Section 7.4, Figure 112).

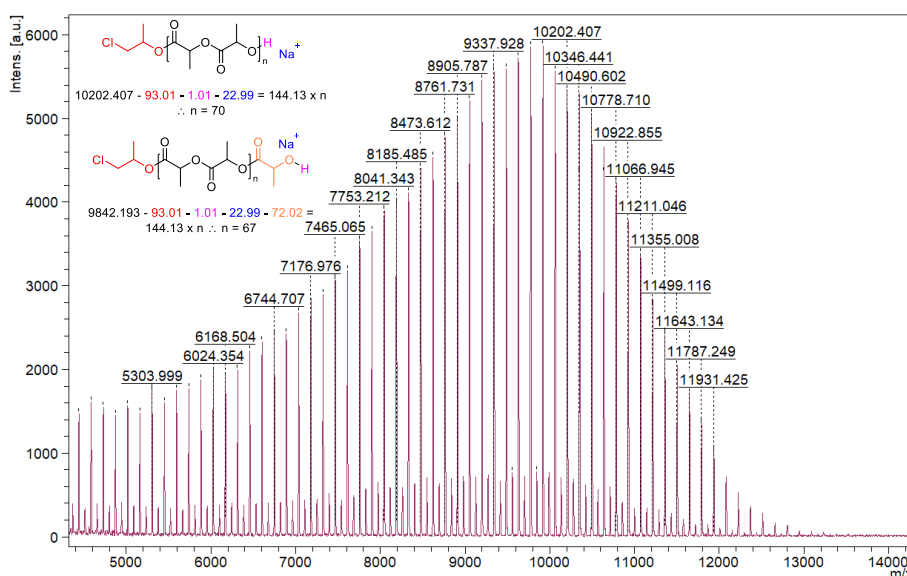


Figure 46. MALDI-ToF spectrum of the PLA attained using Fe(3)Cl at  $40 \text{ }^\circ\text{C}$  for seven days (Table 10, entry 1) ( $M_{p,\text{MALDI-ToF}} = 9914 \text{ gmol}^{-1}$ ,  $M_{n,\text{GPC}} = 11900 \text{ gmol}^{-1}$ ,  $M_{n,\text{theoretical}} = 11600 \text{ gmol}^{-1}$ ).

Further reactions were studied alongside the general solution polymerisations. Doubling the amount of Fe(3)Cl at  $60 \text{ }^\circ\text{C}$ , halved the molecular weight of the polymer and demonstrated the dependence on the [Fe] concentration and suggested each Fe centre initiates a polymer chain {[LA]:[Fe] = 100:1; 76% conversion,  $M_n = 10800 \text{ gmol}^{-1}$  vs. [LA]:[Fe] = 50:1; 62% conversion,  $M_n = 4550 \text{ gmol}^{-1}$ }. This reduced molecular weight outcome was also achieved at  $80 \text{ }^\circ\text{C}$  with the addition of one equivalent of benzyl alcohol {[LA]:[Fe]:[BnOH] = 100:1:1; 63% conversion,  $M_n = 6300 \text{ gmol}^{-1}$  vs. [LA]:[Fe] = 100:1; 72% conversion,  $M_n = 9400 \text{ gmol}^{-1}$ }. This demonstrated that after initiation, alkoxide exchange occurs with the Fe(III)-alkoxide species resulting in a greater number of growing polymer chains and a reduced average molecular weight. The MALDI-ToF spectrum of the polymer, resulted in two overlapping symmetrical series (Figure 47). The major series consists of the expected

BnO- / -H end groups and the second minor series with the PO initiated, chloropropanol end group. There was a small amount of transesterification side-reactions for the major series. The two series were centred on 4309  $\text{gmol}^{-1}$ ; reasonably close to the theoretical and experimental molecular weight, determined from GPC analysis ( $M_{p,\text{MALDI-ToF}} = 4309 \text{ gmol}^{-1}$  vs.  $M_{n,\text{GPC}} = 6300 \text{ gmol}^{-1}$  vs.  $M_{n,\text{theoretical}} = 4650 \text{ gmol}^{-1}$ ).

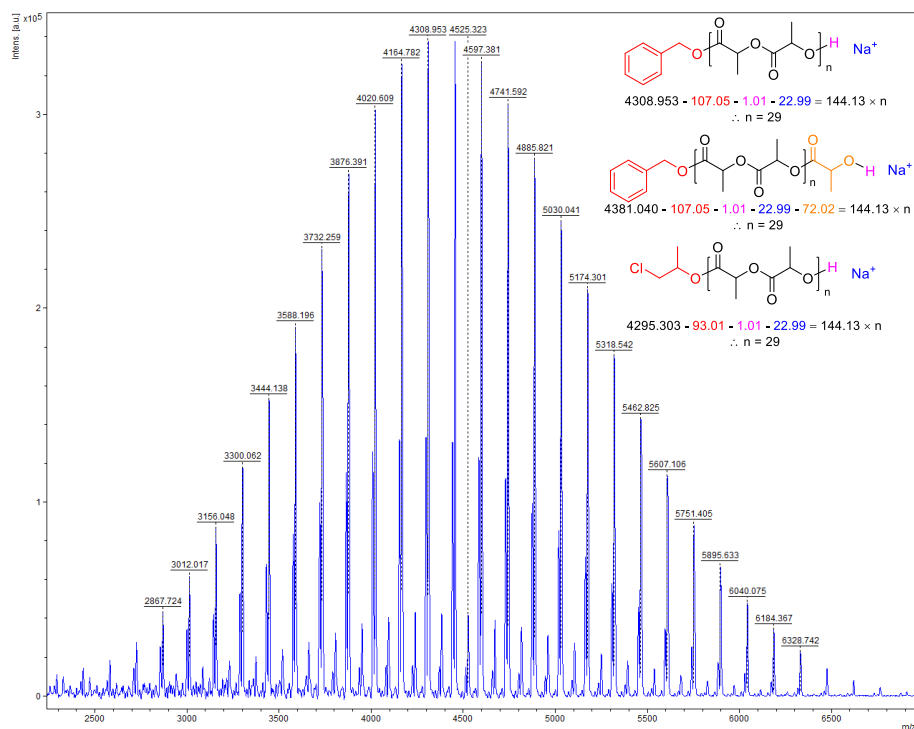
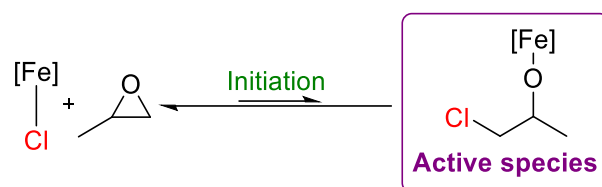


Figure 47. MALDI-ToF spectrum of the PLA attained using Fe(3)Cl at 80 °C for 24 hours with one equivalent of benzyl alcohol in PO (Table 10, entry 8) ( $M_{p,\text{MALDI-ToF}} = 4309 \text{ gmol}^{-1}$ ,  $M_{n,\text{GPC}} = 6300 \text{ gmol}^{-1}$ ,  $M_{n,\text{theoretical}} = 4650 \text{ gmol}^{-1}$ ).

There were attempts to reduce, and move away from, the use of PO epoxide.<sup>[56]</sup> No activity was observed when attempting to use catalytic amounts of PO for initiation, in toluene (Table 10, entry 5), instead of using an excess amount of epoxide. As discussed earlier in Section 3.3, this is believed to be due to the low concentration of PO failing to push the equilibrium and initiation forward and, hence, the polymerisation not occurring (Scheme 22).<sup>[54,56]</sup> Attempting to use the more sterically hindered and symmetrical cyclohexene oxide (CHO) resulted in poor activity (Table 10, entry 6).



Scheme 22. Determined equilibrium for initiation and failed attempt at using one equivalent of PO.

The removal of PO, as was desired by Shaver,<sup>[56]</sup> was achieved by carrying out the solution polymerisation in toluene (5.0 mL) using Fe(3)Cl at 80 °C for 24 hours (Table 10, entry 10). Catalytic amounts (one equivalent) of benzyl alcohol and triethylamine were added to remove the auxiliary chloride group and generate the proposed Fe(III)–salalen–benzyl alkoxide species. As triethylamine is a weak nucleophile it is assumed its role was to act strictly as a base and scavenge produced hydrochloric acid in the polymerisation mixture, after initiation to the Fe(III)–benzyl alkoxide species. This alternative method of initiation is reported for other trivalent metal halide complexes such as indium.<sup>[80–82]</sup> To avoid possible error with the addition of the benzyl alcohol using the Eppendorf pipette, in this particular instance, the reaction was scaled up (1.00 g of *rac*-LA) while maintaining a lactide-to-Fe initiator-to-benzyl alcohol-to-triethylamine ratio of 100:1:1:1. The polymerisation was comparable to that conducted with PO; with a slight increase of conversion but a reduction in isotacticity {[LA]:[Fe] = 100:1 in PO; 72% conversion,  $M_n = 9400 \text{ gmol}^{-1}$ ,  $P_m = 0.79$ ,  $\bar{D} = 1.11$  vs. [LA]:[Fe]:[Et<sub>3</sub>N]:[BnOH] = 100:1:1:1 in toluene; 78% conversion,  $M_n = 11250 \text{ gmol}^{-1}$ ,  $P_m = 0.67$ ,  $\bar{D} = 1.02$ }. This reduction in stereoselectivity may be due to the change of solvent and polarity, from PO to toluene, and not related to the co-initiators. Additionally, there was an increase in molecular weight, as expected with the increased conversion, and the dispersity was narrowed. A crucial observation, from the GPC chromatogram (Section 7.3, Figure 106), was that monomodality and one polymer species was present in this instance unlike the bimodality acquired when using PO solvent for Fe(3)Cl; this is further discussed in Section 3.7. The MALDI-ToF spectrum consisted of a symmetrical series, centred on  $6903 \text{ gmol}^{-1}$ , with no observed transesterification side-reactions (Figure 48). The molecular weight was lower than that observed from GPC analysis and the

theoretical; which the latter were in close agreement. The residual mass was determined to be BnO– / –H end groups.

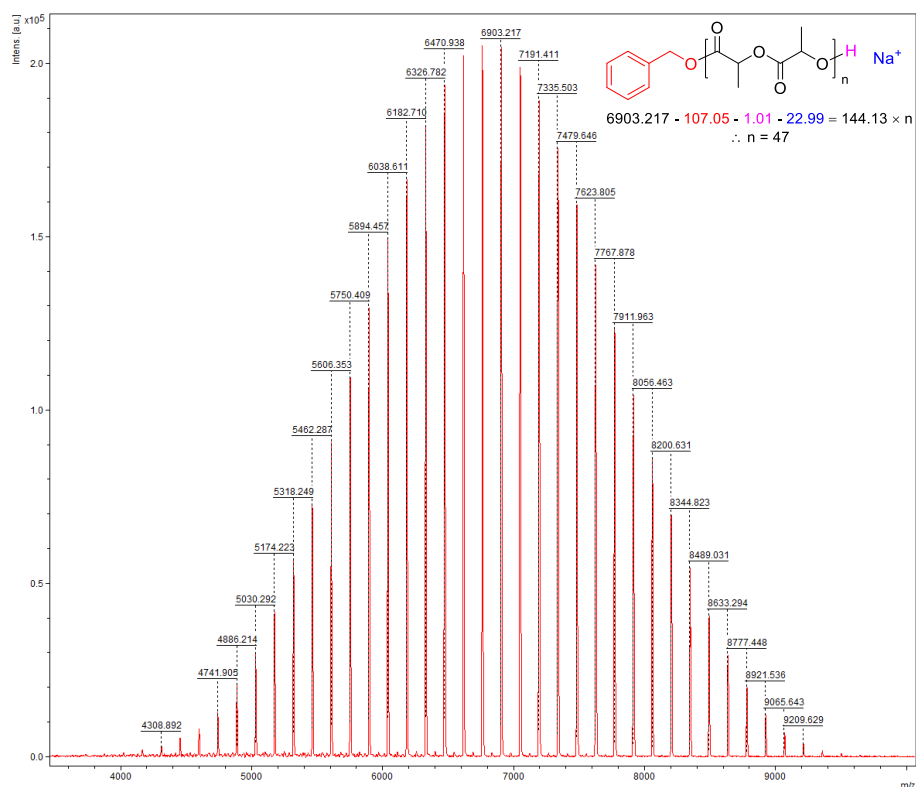


Figure 48. MALDI–ToF spectrum of the PLA attained using Fe(3)Cl at 80 °C for 24 hours with one equivalent of benzyl alcohol and triethylamine in toluene (Table 10, entry 10) ( $M_{p,MALDI-ToF} = 6903 \text{ gmol}^{-1}$ ,  $M_{n,GPC} = 11250 \text{ gmol}^{-1}$ ,  $M_{n,theoretical} = 11350 \text{ gmol}^{-1}$ ).

### 3.5 Batch kinetic investigation using Fe(3)Cl

To explore this proposed equilibrium for initiation using PO solvent, for the solution polymerisation of *rac*–LA, as was discussed in Section 3.3, batch kinetics was conducted. This was achieved using Fe(3)Cl at 80 °C for a lactide–to–Fe initiator ratio of [100]:[1] and analysing the conversion from each separate polymerisation at varying reaction times using <sup>1</sup>H NMR spectroscopy. Undertaking one polymerisation and taking small crude aliquots of the reaction mixture under a flow of argon, to measure the conversion, was not possible due to the PO’s low boiling point of 34 °C. Within the first six hours, there was an induction period for the *in-situ* generation of the Fe(3)–alkoxide species with the PO acting as a co–initiator, where no activity occurred and no LA was consumed (Figure 49).

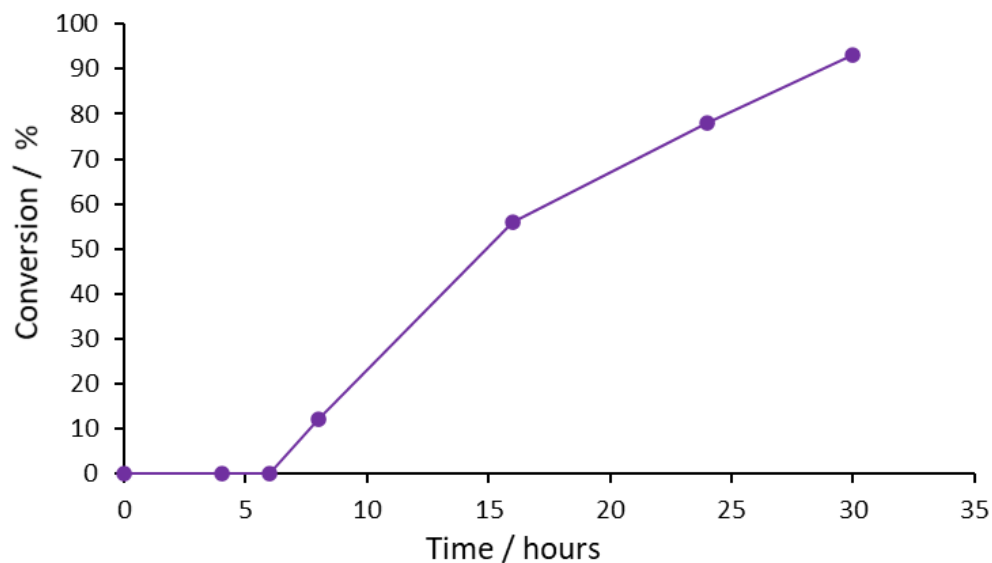


Figure 49. Kinetic plot of *rac*-LA conversion vs. reaction time for Fe(3)Cl at 80 °C ([LA]<sub>0</sub> = 1.39 M).

This provides evidence for Lamberti observing no conversion with this complex for the solution polymerisation of *L*-LA, at the same lactide-to-Fe initiator ratio of 100:1 in PO solvent (2.0 mL), for four hours at a reduced temperature of 60 °C (**Section 3.3**).<sup>[55]</sup> This time period was insufficient for efficient induction and polymerisation, with the initiation equilibrium remaining towards the Fe(III)-chloride species and not the active Fe(III)-alkoxide species (**Section 3.4, Scheme 22**). After this 6 hour induction period, the *rac*-LA was consumed using Fe(3)Cl with a first order dependence ( $k_{app} = 0.105 \pm 0.01 \text{ h}^{-1}$ ,  $R^2 = 0.97$ , [LA]<sub>0</sub> = 1.39 M) as displayed from the semi-logarithmic plot (*Figure 50*).

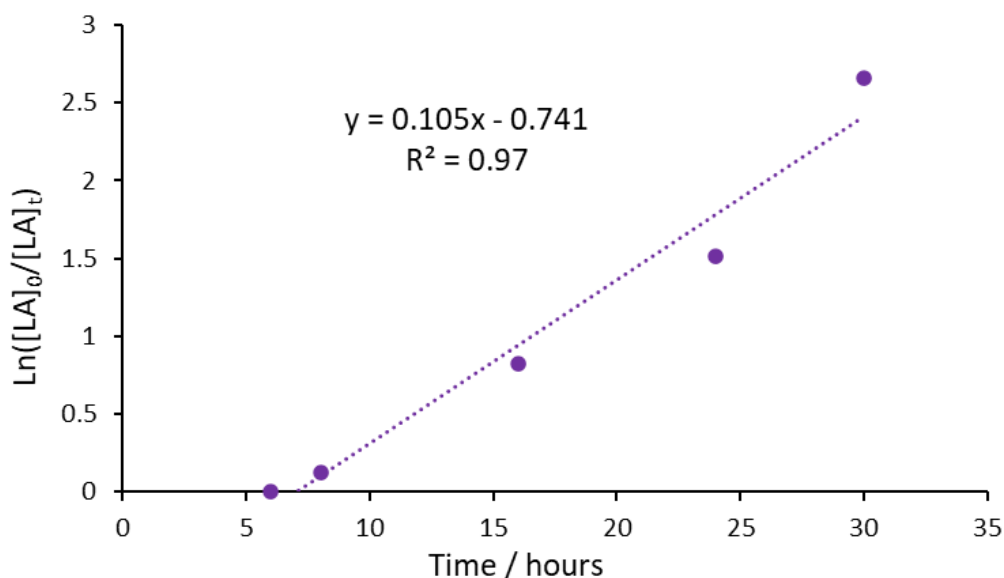


Figure 50. Semi-logarithmic plot of the ROP of *rac*-LA using Fe(3)Cl at 80 °C ([LA]<sub>0</sub> = 1.39 M).

### 3.6 Ring opening polymerisation of *rac*-lactide using other Fe(III)-chloride complexes

The other Fe(III)-salalen-chloride complexes were applied and compared to Fe(3)Cl for the ROP of *rac*-LA in PO solvent (Table 11). Maintaining the ethylene ligand backbone, the aryl substituents were modified. Decreasing the steric bulk or introducing chloro-functionality; and increasing the Lewis acidity of the Fe(III) centre, increased the observed activity. After six and four hours at 60 and 80 °C respectively for Fe(1/4)Cl {R<sup>1</sup> = H / Cl}, high conversion was achieved. This change in ligand also resulted in the reduction of stereocontrol ( $P_m = 0.54-0.61$ ). Compared to Fe(1/4)Cl, the analogous Al(III)-salalen-methyl complexes reported, in toluene with one equivalent of benzyl alcohol, were less active and the stereoselectivity observed was reversed and heterotactic {80 °C; Al(1)Me, three days, 86% conversion,  $P_m = 0.26$  and Al(4)Me, one day, 96% conversion,  $P_m = 0.37$ }.<sup>[79]</sup>

Table 11. Solution polymerisation of *rac*-LA using Fe(1/2/4-7)Cl.

Entry	Initiator	Temp (°C)	Time (days/ hours)	Conv. <sup>a</sup> (%)	$P_m$ <sup>b</sup>	$M_{n,theoretical}$ <sup>c</sup> (gmol <sup>-1</sup> )	$M_n$ <sup>d</sup> (gmol <sup>-1</sup> )	$\bar{D}$ <sup>d</sup>
1	Fe(1)Cl	60	0.25 / 6	76	0.61	11050	10300	1.30
2	Fe(1)Cl	80	0.17 / 4	42	0.61	6150	6400	1.09
3	Fe(2)Cl	60	2 / 48	94	0.59	13650	10700 <sup>e</sup>	1.27 <sup>e</sup>
4	Fe(2)Cl	80	1 / 24	93	0.61	13500	11850 <sup>e</sup>	1.35 <sup>e</sup>
5	Fe(4)Cl	60	0.25 / 6	80	0.56	11600	7650	1.11
6	Fe(4)Cl	80	0.17 / 4	93	0.54	13500	11150	1.14
7	Fe(5)Cl	80	0.125 / 3	59	0.69	8600	5250	1.13
8	Fe(5)Cl	80	4 / 96	92	0.62	13350	8750	1.22
9	Fe(6)Cl	60	4 / 96	85	0.64	12350	11600	1.13
10	Fe(6)Cl	80	2 / 96	92	0.56	13350	12700	1.19
11	Fe(7)Cl	60	1 / 24	60	0.54	8750	10400	1.03
12	Fe(7)Cl	80	0.67 / 16	95	0.56	13800	12150	1.09

Conditions: *rac*-LA (0.4 g), PO (2.0 mL), [LA]:[Fe] = 100:1 under inert conditions. <sup>a</sup> Determined by <sup>1</sup>H NMR spectroscopy. <sup>b</sup> Determined by <sup>1</sup>H {<sup>1</sup>H} NMR spectroscopy;  $P_m$  = probability of isotactic enchainment. <sup>c</sup>  $M_{n,theoretical}$  = [(Conversion/100 x [LA]/[Fe] x  $M_{r,LA}$ ) + chloropropanol end group MW] = [(Conversion/100 x [LA]/[Fe] x 144.1260) + 93.5300]. <sup>d</sup> Determined *via* GPC (triple detection analysis) in THF solvent. <sup>e</sup> Determined *via* GPC (refractive index analysis only due to anomalous light scattering signals) in THF solvent referenced against polystyrene standards with a correction factor of 0.58.

Although temperature was increased, a lower conversion was realised for Fe(**1**)Cl at 80 °C with respect to 60 °C {80 °C, four hours, 42% conversion vs. 60 °C, six hours, 76% conversion}. Possibly this could be due to an induction period, as observed by batch kinetics for Fe(**3**)Cl (**Section 3.5**), or the formation of a less active dinuclear species. The latter may also explain why the dispersity narrowed when the temperature was increased {60 °C,  $\bar{D}$  = 1.30 vs. 80 °C,  $\bar{D}$  = 1.09}. Duan postulated this rationale for the counterintuitive lower activity for less sterically bulky ligands.<sup>[54]</sup> Indeed, as was discussed and debated in **Section 2.3**, single-crystal X-ray diffraction did unambiguously determine the  $\mu$ -oxo-bridged Fe(III) dimer, [Fe(**1**)<sub>2</sub>O] that would provide evidence for this proposition. Elemental analysis was consistent, however, that the Fe(III)-salalen-chloride had indeed been formed in the bulk of the sample. MALDI-ToF analysis of the polymer produced from Fe(**1/4**)Cl will be described in **Section 3.7**.

The methyl aryl substituted Fe(**2**)Cl {R<sup>1</sup> = Me} complex behaved as an intermediate between the unsubstituted or chloro-functionalised Fe(**1/4**)Cl complexes {R<sup>1</sup> = H / Cl} and the *tert*-butyl substituted Fe(**3**)Cl complex {R<sup>1</sup> = <sup>t</sup>Bu}. Stereoselectivity was reduced and activity was increased compared to Fe(**3**)Cl {80 °C, one day; Fe(**2**)Cl, 93% conversion,  $P_m$  = 0.61 vs. Fe(**3**)Cl, 72% conversion,  $P_m$  = 0.79} and the opposite trend when compared with Fe(**1/4**)Cl; although the isotacticity of Fe(**2**)Cl was maintained in relation to Fe(**1**)Cl despite the lower activity displayed {80 °C, four hours; Fe(**1**)Cl, 42% conversion,  $P_m$  = 0.61 and Fe(**4**)Cl, 93% conversion,  $P_m$  = 0.54}. A reasonable degree of molecular control was achieved using Fe(**1/2/4**) and the observed experimental values were close to the theoretically calculated values based on conversion.

Both stereoselectivity and activity were hindered when modifying the ethylene ligand backbone of Fe(**3**)Cl. While maintaining the aryl substituents, installing the rigid six-membered aminopiperidine ring and reducing the flexibility of the ligand backbone {Fe(**5**)Cl} demonstrated moderate isotacticity ( $P_m$  = 0.62–0.69) but inhibited reactivity at 60 °C and only minimal activity at 80 °C; the latter temperature requiring three days for a moderate 59% conversion and four days for a high 92% conversion. The molecular weight was lower than expected for a polymerisation at



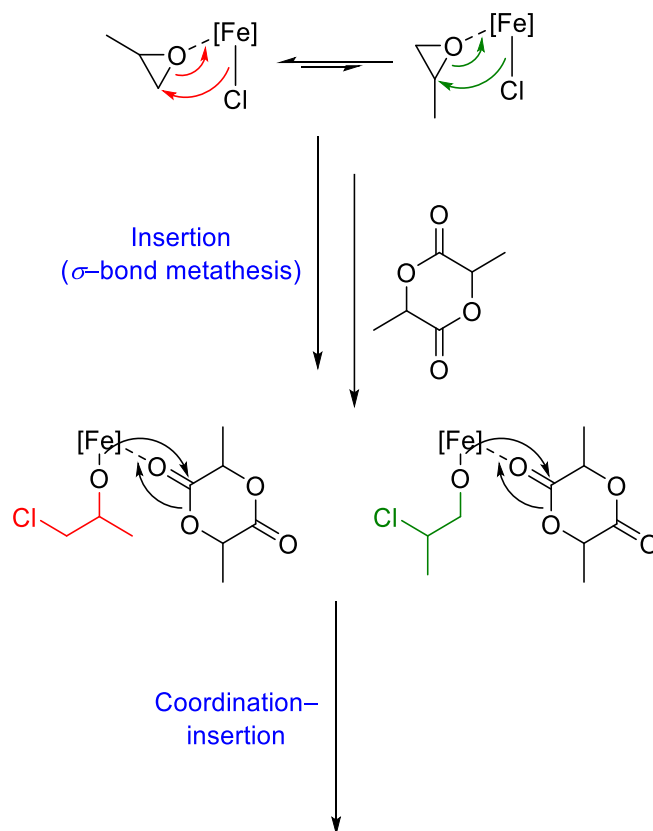
80 °C (*Table 11*, entries 7 and 8). Similar stereoselectivity was observed for the analogous Al(III)–salalen–methyl complex, however, activity was dramatically slower compared to Fe(5)Cl {Al(5)Me; 80 °C in toluene with one equivalent of benzyl alcohol, 10 days, 88% conversion,  $P_m = 0.63$ }.<sup>[83]</sup> Preserving the aryl substituents and introducing a planar phenyl ring into the ethylene backbone {Fe(6)Cl}, also hindered activity, requiring double the reaction time to achieve a high conversion compared to Fe(3)Cl {60 °C, four days, 85% conversion and 80 °C, two days, 92% conversion}. Only a slight degree of isotacticity was attained ( $P_m = 0.56$ – $0.64$ ) and, despite the prolonged reaction time, reasonable molecular weights were obtained. The complex had similar stereoselectivity to the analogous Al(III)–salalen–methyl complex with a higher activity in comparison {Al(6)Me; 80 °C in toluene with one equivalent of benzyl alcohol, four days, 73% conversion,  $P_m = 0.61$ }.<sup>[84]</sup> The unsubstituted Fe(7)Cl complex { $R^1 = H$ } with a diaminocyclohexane ligand backbone, in comparison with the unsubstituted Fe(1)Cl, displayed reduced activity and high conversion was reached at 60 and 80 °C after one day and 16 hours respectively. This reduced activity was potentially due to the decreased flexibility of the ligand backbone and steric crowding around the Fe(III) centre. Minimal stereoselectivity was achieved but there was good molecular weight control with narrow distributions ( $\mathcal{D} = 1.03$ – $1.09$ ). Fe(7)Cl was dramatically more active than the analogous Al(III)–salalen–benzyl complex {Al(7)OBn; 80 °C in toluene, four days, 83% conversion,  $P_m = 0.57$ }.<sup>[85]</sup> Overall, all complexes (*Tables 10* and *11*) achieved a moderate or slight isotactic bias; with Fe(3)Cl remaining the most stereoselective, and the molecular weight was generally well controlled, with the main exception being Fe(5)Cl with molecular weights lower than expected after a prolonged reaction time. Compared with Duan’s Fe(III)–salen–chloride complexes ( $\mathcal{D} = 1.38$ – $2.36$ ), all the chain length distributions were narrow but, with respect to the Fe(III)–salalen–chloride complexes in this study, slightly broader for Fe(2/5)Cl.<sup>[54]</sup>

### 3.7 End group analysis and bimodality discussion

Generally, for all the solution polymerisations in PO using Fe(1–7)Cl, bimodality was observed in the GPC chromatograms indicating two separate polymer species. In most cases, this consisted of two distinct peaks and in instances a smaller second

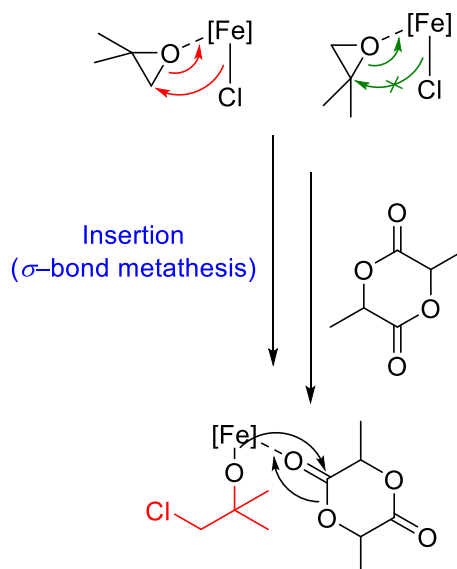
'shoulder' peak (**Section 7.3**). No GPC evidence was provided by Duan for the application of Fe(III)–salen–chloride complexes in PO; presumably monomodality was observed although broad chain length distributions were present ( $\bar{M}_w = 1.38\text{--}2.36$ ).<sup>[54]</sup> Furthermore, as discussed earlier (**Section 3.4**), monomodality was observed when carrying out the reaction in toluene with no PO present and using catalytic amounts of benzyl alcohol and triethylamine to generate the proposed active Fe(3)OBn species (**Section 3.4**, *Table 10*, entry 10). This indicated that bimodality was only observed when PO was used and was not inherent with the Fe(III) complex.

Two initial hypotheses were thought to cause this observed bimodality. The first was concerned with the unsymmetrical nature of PO. The two possible sites of attack on the PO by the Fe(III)–Cl bond and regioselective opening of the epoxide ring *via*  $\sigma$ –bond metathesis, resulting in two active Fe(III)–alkoxide initiating species being generated (*Scheme 23*). One species being more active and propagating the monomer faster or one species being formed more favourably and in a greater concentration; attack of the sterically unhindered carbon (**red reaction path**) would logically be significantly faster and more likely. Both possibilities would result in one higher molecular weight polymer and two separate polymer species.



*Scheme 23.* The regioselective opening and two possible sites of attack resulting in two active Fe(III)–alkoxide initiating species.

There were attempts to investigate this hypothesis such as with the use of the symmetrical CHO epoxide instead of PO (**Section 3.4**, *Table 10*, entry 6). Only one active Fe(III)–alkoxide initiating species would be generated and potentially the GPC chromatogram would be monomodal. Unfortunately, the epoxide was too sterically hindered and initiation unfavourable so that no polymer was recovered due to low activity. The solution polymerisation was attempted in multiple cases using distilled 1,2-epoxy-2-methylpropane solvent instead of PO. The rationale was that attack of the sterically unhindered carbon was encouraged by making the substituted carbon more sterically crowded, thus forming only one active Fe(III)–alkoxide species and monomodal PLA (*Scheme 24*). Unfortunately, again activity was minimal with this solvent and no polymer was recovered.



Scheme 24. Attempted use of 1,2-epoxy-2-methylpropane as the solvent of polymerisation.

As discussed in **Section 2.9**, unsuccessful attempts were made to synthesise the Fe(III)–salalen–ethoxide complex. Applying this alkoxide complex to ROP would be intriguing and bypass the need for initiation of the Fe(III) complex. This also could have been used to further confirm the bimodality was not inherent with the Fe(III) complex and for comparison with generating the Fe(III)–salalen–benzyl alkoxide species *in-situ* by conducting the polymerisation in toluene, with catalytic amounts of benzyl alcohol and triethylamine (**Section 3.4**, Table 10, entry 10).

The second hypothesis was propane-1,2-diol (PD) was present in the PO solvent, as a small quantity of impurity formed from the hydrolysis of the epoxide. This diol could initiate a distinct second growing polymer species and the observed bimodality in the GPC chromatogram. This theory was originally dismissed as no evidence was present from using MALDI–ToF analysis on the PLA produced using Fe(3)Cl and because the PO was distilled before use. It was thought that the large difference in boiling point between PD (187 °C) and PO (34 °C) was sufficient to prevent enough diol to pass over the distillation and cause the second peak in the GPC chromatogram when using the PO solvent for polymerisation.

However, MALDI–ToF analysis of the PLA derived using Fe(1/2/4–7)Cl confirmed the presence of PD capped end groups and this hypothesis; therefore the second series or peak in the GPC chromatogram was due to diol impurity in the distilled PO solvent

initiating a second polymer species. Most likely this evidence from MALDI–ToF analysis was absent from the PLA produced using Fe(3)Cl because of the intensity and size of the higher average molecular weight polymer produced from the initiating PD species. For example, for the polymerisation using Fe(3)Cl at 80 °C, GPC analysis indicated the second peak or the higher molecular weight series to have an average molecular weight ( $M_n$ ) of 19250  $\text{g mol}^{-1}$  (Section 7.3, Figure 105). This would likely not be ionised ('fly') and detected in the MALDI–ToF analysis due to the magnitude of the molecular weight. The monomodality observed in the GPC chromatogram for the toluene polymerisation without the use of PO also supports this diol hypothesis (Section 7.3, Figure 106).

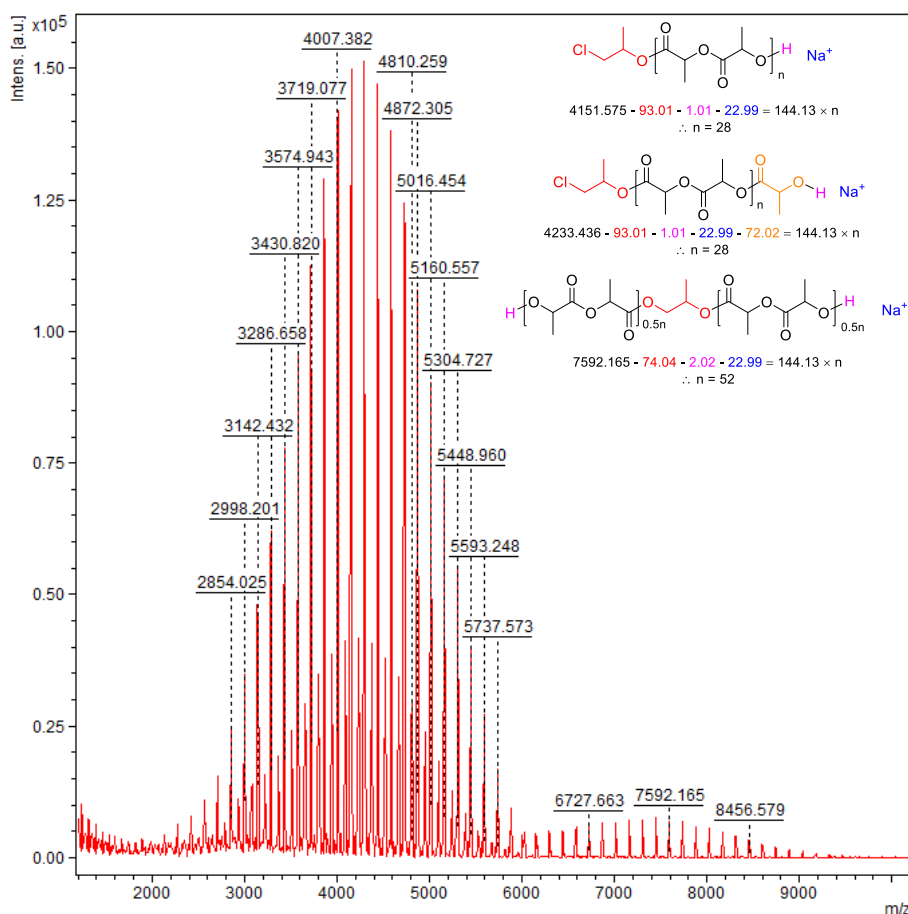


Figure 51. MALDI–ToF spectrum of the PLA attained using Fe(1)Cl at 80 °C for four hours (Table 11, entry 2) ( $M_{p, \text{MALDI-ToF}} = 4439 \text{ g mol}^{-1}$  (chloropropanol end groups) and  $7592 \text{ g mol}^{-1}$  (PD end groups),  $M_{n, \text{GPC}} = 6400 \text{ g mol}^{-1}$ ,  $M_{n, \text{theoretical}} = 6150 \text{ g mol}^{-1}$ ).

For the PLA derived from Fe(1)Cl, in the MALDI–ToF analysis, there were two symmetrical series (Figure 51). The intensity of the higher molecular weight series

( $M_p = 7592$ ) was much reduced, the peak spacing was  $144 \text{ gmol}^{-1}$  for the repeating LA units and there was no indication of undesired side-reactions. The residual mass was determined to be PD capped end groups caused from PD impurity in the PO solvent. Chloropropanol was accounted as the end group for the lower symmetrical series ( $M_p = 4439$ ) and a small degree of undesired transesterification was present.

MALDI-ToF analysis, of the PLA derived from Fe(4/7)Cl, displayed three overlapping series. For Fe(4)Cl, transesterification side-reactions were prevalent for each series and in decreasing molecular weight, the residual mass was assigned PD, chloropropanol and cyclic oligomeric (no end group) (Section 7.4, Figure 113). All three series were centred around  $5505 \text{ gmol}^{-1}$  for Fe(7)Cl. The major series has a chloropropanol end group and the minor series a PD end group. Cyclic oligomer was determined the residual mass for the low molecular weight tail (Section 7.4, Figure 117). Both Fe(5/6)Cl complexes displayed two distinct series for the PLA produced at  $80 \text{ }^\circ\text{C}$ , the high molecular weight series with PD capped end groups and the lower molecular weight series with chloropropanol end groups for the PLA (Section 7.4, Figures 114 and 115). There was a small amount of peaks due to transesterification in both cases. The series were more overlapped for the PLA produced at  $60 \text{ }^\circ\text{C}$  using Fe(6)Cl and cyclic oligomers were present at low molecular weight (Section 7.4, Figure 116).

### 3.8 Investigation of initiators and conditions for the ring opening polymerisation of *rac*-lactide using an Fe(III)-acetate complex

Encouraged by the circumvention of PO in the solution polymerisation for Fe(3)Cl (Section 3.4, Table 10, entry 10), by using catalytic amounts of benzyl alcohol and triethylamine in toluene, it was decided to explore this method of initiation for the Fe(III)-acetate complexes. Despite the slight reduction in stereocontrol using this initiation method for Fe(3)Cl, the GPC chromatogram was monomodal; steering clear of any PD impurity impact, and the MALDI-ToF spectrum was perfectly symmetrical and showed no indication of transesterification side-reactions. Activity and molecular weight was increased together with a greater control of polymerisation with the distribution narrowed. For these reasons, the polymerisation conditions and

effect of the co-initiators, in a 24 hour reaction time period, was initially investigated using the first Fe(III)–acetate complex that was synthesised, Fe(**9**<sub>meso</sub>)OAc (Table 12).

Table 12. Solution and melt polymerisation of *rac*-LA using Fe(**9**<sub>meso</sub>)OAc with different equivalents of benzyl alcohol and triethylamine co-initiators.

Entry	Temp (°C)	BnOH eq.	Et <sub>3</sub> N eq.	Conv. <sup>c</sup> (%)	$P_m^d$	$M_{n,theoretical}^e$ (g mol <sup>-1</sup> )	$M_n^f$ (g mol <sup>-1</sup> )	$\bar{D}^f$
1 <sup>a</sup>	130	0	0	0	–	–	–	–
2 <sup>a</sup>	130	1	0	0	–	–	–	–
3 <sup>a</sup>	130	1	1	83	0.48	36000	43500	1.80
4 <sup>b</sup>	80	0	0	0	–	–	–	–
5 <sup>b</sup>	80	1	0	0	–	–	–	–
6 <sup>b</sup>	80	1	1	0	–	–	–	–
7 <sup>b</sup>	100	1	1	51	0.49	7450	6600	1.09
8 <sup>b</sup>	100	1	2	44	0.49	6450	7550	1.12

<sup>a</sup> Conditions: *rac*-LA (1.0 g), solvent-free, [LA]:[Fe(**9**<sub>meso</sub>)OAc] = 300:1, 24 hours under inert conditions.

<sup>b</sup> Conditions: *rac*-LA (0.4 g), toluene (4.0 mL), [LA]:[Fe(**9**<sub>meso</sub>)OAc] = 100:1, 24 hours under inert conditions. <sup>c</sup> Determined by <sup>1</sup>H NMR spectroscopy. <sup>d</sup> Determined by <sup>1</sup>H {<sup>1</sup>H} NMR spectroscopy;  $P_m$  = probability of isotactic enchainment. <sup>e</sup>  $M_{n,theoretical} = [(Conversion/100 \times [LA]/[BnOH] \times M_{r,LA}) + \text{benzyl alcohol end group MW}] = [(Conversion/100 \times [LA]/[BnOH] \times 144.1260) + 107.1320]$ . <sup>f</sup> Determined *via* GPC (refractive index analysis) in THF solvent referenced against polystyrene standards with no correction factor.

At 130 °C, it was observed that both benzyl alcohol and triethylamine co-initiators were required, to remove the auxiliary acetate group and generate the proposed Fe(III)–salalen–benzyl alkoxide species, for active and efficient polymerisation. As triethylamine is sterically hindered and a weak nucleophile it is assumed its role was to act strictly as a base, likely by scavenging produced acetic acid in the polymerisation mixture. This facilitates the attack of the Fe centre by the more nucleophilic benzyl alcohol co-initiator and initiation to the generated Fe(III)–benzyl

alkoxide species, with polymerisation occurring *via* a coordination–insertion mechanism as no reactivity was observed without the triethylamine. Alternatively, it is thought unlikely that triethylamine ( $pK_a = 11$ ) could be promoting deprotonation of the benzyl alcohol ( $pK_a = 15$ ), notably increasing polymerisation activity and encouraging an additional activated monomer mechanism, operating alongside, due to the unfavourable difference in  $pK_a$  ( $K_c \approx -10^4$ ). Hence, the observation that no reactivity occurs without triethylamine indicates the reaction mechanism is solely dependent on this coordination–insertion mechanism, as without at least one equivalent of each co–initiator no reactivity was observed.

These observations slightly differ with that reported by Stewart when applying Fe(III)–thiolen–chloride complexes using the same polymerisation protocol, with one equivalent of both benzyl alcohol and triethylamine co–initiators.<sup>[77]</sup> At low temperature (40 °C), there was evidence that a competing activated monomer mechanism was operating alongside the expected coordination–insertion mechanism. The low temperature was insufficient for complete displacement of the chloride auxiliary ligand, for initiation to the active Fe(III)–thiolen–alkoxide initiating species.<sup>[77]</sup> Furthermore, reactivity was still achieved without triethylamine at 80 °C ([LA]:[Fe]:[BnOH]=100:1:1). After conducting NMR spectroscopic studies, using an Al(III)–thiolen–chloride complex, it was hypothesised triethylamine was required for the formation of the alkoxide initiating species and resulting classical coordination–insertion mechanism operating and without triethylamine an activated monomer mechanism would operate. Despite the theoretically unfavourable differences in  $pK_a$  between triethylamine and benzyl alcohol, this report also highlights deprotonation of the benzyl alcohol is possible.<sup>[77]</sup>

As would be expected, the activity and molecular weight was greater for the melt polymerisation conducted at 130 °C compared to the solution polymerisation in toluene at 100 °C (*Table 12*, entry 3 vs. entry 7). However, this was accompanied by a less controlled polymerisation, a large difference in between the experimental and theoretical molecular weights and a much broader distribution (130 °C, 83% conversion,  $M_n = 43500 \text{ gmol}^{-1}$ ,  $M_{n,\text{theoretical}} = 36000 \text{ gmol}^{-1}$ ,  $\mathcal{D} = 1.80$  vs. 100 °C, 51% conversion,  $M_n = 6600 \text{ gmol}^{-1}$ ,  $M_{n,\text{theoretical}} = 7450 \text{ gmol}^{-1}$ ,  $\mathcal{D} = 1.09$ ). There was no



reactivity observed at 80 °C (Table 12, entries 4, 5 and 6) even when using one equivalent of each co-initiator (Table 12, entry 6). Doubling the amount of triethylamine to two equivalents, at 100 °C, assuring all acetic acid would be quenched, reduced the conversion slightly but increased the molecular weight. The chain length distribution was maintained with a larger difference between the experimental and theoretical molecular weight values observed (Table 12, entry 7 vs. entry 8). There was no stereoselectivity observed in all cases ( $P_m = 0.48\text{--}0.49$ ).

### 3.9 Ring opening polymerisation of *rac*-lactide using Fe(III)-acetate complexes

Using the findings from Section 3.8, all synthesised Fe(III)-acetate complexes (Section 2.5, Scheme 8) were trialled for the ROP of *rac*-LA using catalytic amounts of benzyl alcohol and triethylamine with a lactide-to-Fe initiator-to-benzyl alcohol-to-triethylamine ratio of 100:1:1:1 in toluene at 100 °C for 24 hours (Table 13).

Initially, a control reaction using the Fe(OAc)<sub>2</sub> precursor was applied as the Fe initiator. Low reactivity was observed accompanied with a broad chain length distribution and no stereoselectivity (38% conversion,  $\bar{D} = 1.70$ ,  $P_m = 0.50$ ). Generally, low conversion and no stereoselectivity was observed with the salalen complexes and the polymerisations were less predictable (examples of homonuclear decoupled spectra used to calculate the  $P_m$  values for Fe(III)-acetate complexes can be found in Section 7.5). Retaining the ethylene ligand backbone, the aryl substituents were modified. Compared with the *tert*-butyl substituted Fe(3)OAc { $R^1 = \text{}^t\text{Bu}$ ,  $R^2 = \text{Me}$ ,  $R^3 = \text{}^t\text{Bu}$ , 57% conversion}, decreasing the steric bulk {Fe(1)OAc;  $R^1 = \text{H}$ , 26% conversion}, unexpectedly decreased the activity despite the presumed increase in Lewis acidity on the Fe(III) centre. Although, both decreasing this steric bulk on the imine-phenolate moiety ( $R^1$ ) and introducing bromo-functionality on the amine-phenolate moiety ( $R^3$ ) did improve the activity {Fe(11)OAc;  $R^1 = \text{H}$ ,  $R^3 = \text{Br}$ , 91% conversion}. Alternatively, increasing the Lewis acidity, by installing an electron withdrawing phenyl group on the amine donor atom and replacing an electron donating Me group {Fe(10)OAc;  $R^1 = \text{}^t\text{Bu}$ ,  $R^2 = \text{Ph}$ ,  $R^3 = \text{}^t\text{Bu}$ , 60% conversion}, resulted in a minimal difference on activity.

Table 13. Solution polymerisation of *rac*-LA using Fe(1/3/5/6/8-17)OAc with benzyl alcohol and triethylamine co-initiators.

Class of complex	Entry	Initiator	Conv. <sup>a</sup> (%)	$P_m$ <sup>b</sup>	$M_{n,theoretical}$ <sup>c</sup> (g mol <sup>-1</sup> )	$M_n$ <sup>d</sup> (g mol <sup>-1</sup> )	$\bar{D}$ <sup>d</sup>
Salalen	1	Fe(OAc) <sub>2</sub>	38	0.50	5600	6700	1.70
	2	Fe(1)OAc	26	–	3850	2000	1.17
	3	Fe(3)OAc	57	0.53	8300	6550	1.13
	4	Fe(5)OAc	5	–	850	–	–
	5	Fe(6)OAc	40	0.46	5850	5700	1.08
	6	Fe(10)OAc	60	0.45	8750	7300	1.26
	7	Fe(11)OAc	91	0.50	13200	16200	1.20
	8	Fe(12)OAc	43	0.50	6300	6700	1.10
Salan	9	Fe(8 <sub>meso</sub> )OAc	92	0.58	13350	19900	1.30
	10	Fe(8 <sub>RR</sub> )OAc	21	–	3150	1850	1.27
	11	Fe(8 <sub>SS</sub> )OAc	32	–	4700	2050	1.20
	12	Fe(9 <sub>meso</sub> )OAc	51	0.49	7450	6600	1.09
	13	Fe(13)OAc	93	0.67	13500	8700	1.09
Salen	14	Fe(14)OAc	95	0.56	13800	7500	1.49
	15	Fe(15)OAc	67	0.71	9750	7750	1.16
	16	Fe(16)OAc	94	0.61	13650	8500	1.65
	17	Fe(17)OAc	89	0.71	12950	11700	1.46

Conditions: *rac*-LA (0.4 g), 100 °C, [LA]:[Fe]:[Et<sub>3</sub>N]:[BnOH] = 100:1:1:1 in toluene (4.0 mL), 24 hours under inert conditions. <sup>a</sup> Determined by <sup>1</sup>H NMR spectroscopy. <sup>b</sup> Determined by <sup>1</sup>H {<sup>1</sup>H} NMR spectroscopy;  $P_m$  = probability of isotactic enchainment. <sup>c</sup>  $M_{n,theoretical} = [(Conversion/100 \times [LA])/[BnOH] \times M_{r,LA}) + \text{benzyl alcohol end group MW}] = [(Conversion/100 \times [LA])/[BnOH] \times 144.1260] + 107.1320$ . <sup>d</sup> Determined *via* GPC (refractive index analysis) in THF solvent referenced against polystyrene standards with no correction factor.

Installing the rigid six-membered aminopiperidine ring or a planar phenyl ring into the ethylene ligand backbone, reduced the flexibility of the ligand and decreased the activity (*Table 13*, entries 4 and 5). Indeed, the aminopiperidine backbone rendered the complex inactive. Changing the ethylene ligand backbone to a more flexible propylene ligand backbone also resulted in a reduction in conversion (*Table 13*, entry 8).<sup>[55]</sup> In nearly all salalen cases, the observed experimental molecular weights were lower than the theoretical molecular weights calculated using the conversion. However, chain length distributions were narrow ( $\bar{D} = 1.10\text{--}1.26$ ) and monomodal on the GPC chromatograms (**Section 7.6**, *Figures 123–133*).

MALDI–ToF analysis on the PLA produced using Fe(**3/10**)OAc (*Figure 52* and **Section 7.7**, *Figure 135*), consisted of a major symmetrical series with, as expected, the residual mass determined to be BnO– / –H end groups, and a minor series with ethoxide end groups. In the unit cells of the solid–state structures for these complexes, confirmed using single–crystal X–ray diffraction, molecules of the solvent of recrystallisation, ethanol, were present. In addition to this, an OH stretch was observed in the IR spectrum for Fe(**10**)OAc. These ethanol molecules would act as additional initiating groups and account for the difference between the lower observed molecular weights and that expected theoretically. There was a negligible degree of undesired transesterification side–reactions observed from the MALDI–ToF analysis. In comparison to the Fe(III)–salalen–chloride complexes (**Sections 3.4** and **3.6**), the Fe(III)–salalen–acetate complexes were significantly less stereoselective, required a higher temperature to achieve a moderate conversion and were less active.

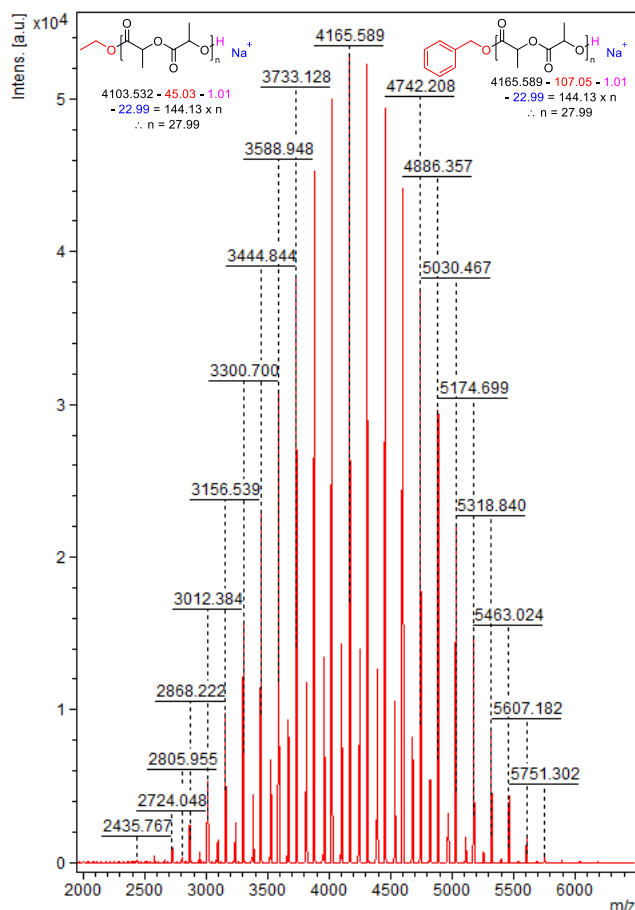


Figure 52. MALDI–ToF spectrum of the PLA attained using Fe(**3**)OAc at 100 °C for 24 hours (Table 13, entry 3) ( $M_{p,\text{MALDI-ToF}} = 4166 \text{ gmol}^{-1}$  (BnOH end groups) and  $4104 \text{ gmol}^{-1}$  (EtOH end groups),  $M_{n,\text{GPC}} = 6550 \text{ gmol}^{-1}$ ,  $M_{n,\text{theoretical}} = 8300 \text{ gmol}^{-1}$ ).

Higher conversions were achieved using the Fe(III)–salan and –salen–acetate complexes, with respect to the salalen complexes, under these reaction conditions. Decreasing the steric bulk of the aryl substituents, increased the observed activity as would be expected {Fe(**8***meso*)OAc;  $R^1 = \text{Me}$ , 92% conversion vs. Fe(**9***meso*)OAc;  $R^1 = \text{tBu}$ , 51% conversion}. Exploring the chirality of the bipyrrrolidine salan backbone and the stereoisomers Fe(**8***RR*/**8***SS*)OAc were significantly less active compared to Fe(**8***meso*)OAc. As was discussed in Section 2.8, this may be due to a change in the solid–state and complex structure to a Fe(**8***RR*/**8***SS*)Y<sub>2</sub> species.

Reducing the salalen ligand backbone **5**; used in the complexation to form Fe(**5**)OAc, via the use of sodium borohydride (Section 2.2, Scheme 4) to produce **13** and, after subsequent complexation, Fe(**13**)OAc, vastly improved activity while a narrow dispersity was maintained {Fe(**5**)OAc; 5% conversion vs. Fe(**13**)OAc; 93% conversion,

$\bar{D} = 1.09$ }. Additionally, there was a small degree of stereocontrol observed ( $P_m = 0.67$ ). Two symmetrical series centred on around  $5300 \text{ gmol}^{-1}$  were observed, in the MALDI–ToF analysis (**Section 7.7, Figure 136**), with  $\text{BnO-} / \text{-H}$  end groups for the major series and ethoxide end groups, from initiation by the ethanol molecules present in the solid–state unit cell, for the minor series. There was no undesired transesterification side–reactions observed, emphasising the control achieved with this more active complex compared with the other Fe(III)–acetate complexes.

For the Fe(III)–salen–acetate complexes, installing planarity and a phenyl ring into the backbone resulted in a minimal–to–moderate effect on the polymerisation activity {Fe(**14**)OAc; 95% conversion vs. Fe(**16**)OAc; 94% conversion and Fe(**15**)OAc; 67% conversion vs. Fe(**17**)OAc; 89% conversion}. As expected, decreasing the steric bulk of the aryl substituents, increased the observed activity, but to a smaller degree for the phenyl backbone {Fe(**16**)OAc vs. Fe(**17**)OAc} with high conversion being achieved in both unsubstituted cases. There was stereocontrol for all Fe(III)–salen–acetate complexes ( $P_m = 0.56\text{--}0.71$ ), with both Fe(**15/17**) displaying the highest isotacticity observed for the Fe(III)–acetate complexes in this study. Fe(**15**)OAc was also more isotactic than the analogous Fe(**15**)Cl but less active.<sup>[54]</sup> Although, compared with the active Fe(**13**)OAc salen complex, the polymerisations were less controlled with broader dispersities observed ( $\bar{D} = 1.16\text{--}1.65$ ). This was further demonstrated in the MALDI–ToF analysis for Fe(**15**)OAc (**Section 7.7, Figure 137**) where a minor series for transesterification side–reactions was in operation, with peak separations of  $72 \text{ gmol}^{-1}$ , together with only a major series for the  $\text{BnO-} / \text{-H}$  end groups.

The more active Fe(**8<sub>meso</sub>/13/16/17**)OA complexes were tested further at a lower temperature of  $80 \text{ }^\circ\text{C}$  (*Table 14*) in an attempt to increase the isotactic control. While, this made no difference on the isotacticity, high conversions were still achieved and narrower chain length distributions observed for all complexes. Again, the experimental molecular weights were lower than that expected theoretically potentially due to ethanol molecules in the solid–state structures from the recrystallisation process. MALDI–ToF analysis on the PLA produced from Fe(**8<sub>meso</sub>**)OAc at  $80 \text{ }^\circ\text{C}$  indicated no transesterification side–reactions and consisted of

only a symmetric series centred on 4887 gmol<sup>-1</sup> with BnO– / –H end groups determined from the residual mass (Section 7.7, Figure 134).

Table 14. Solution polymerisation of *rac*-LA using Fe(**8**<sub>meso</sub>/**13**/**16**/**17**)OAc with benzyl alcohol and triethylamine co-initiators at 80 °C.

Entry	Initiator	Time (days)	Conv. <sup>a</sup> (%)	$P_m^b$	$M_{n,theoretical}$ (gmol <sup>-1</sup> ) <sup>c</sup>	$M_n$ (gmol <sup>-1</sup> ) <sup>d</sup>	$\mathcal{D}^d$
1	Fe( <b>8</b> <sub>meso</sub> )OAc	1	96	0.58	13950	8100	1.09
2	Fe( <b>13</b> )OAc	1	94	0.66	13650	9900	1.07
3	Fe( <b>16</b> )OAc	1	95	0.61	13800	10750	1.49
4	Fe( <b>17</b> )OAc	1	82	0.71	11950	11050	1.37

Conditions: *rac*-LA (0.4 g), 80 °C, [LA]:[Fe]:[Et<sub>3</sub>N]:[BnOH] = 100:1:1:1 in toluene (4.0 mL), 24 hours under inert conditions. <sup>a</sup> Determined by <sup>1</sup>H NMR spectroscopy. <sup>b</sup> Determined by <sup>1</sup>H {<sup>1</sup>H} NMR spectroscopy;  $P_m$  = probability of isotactic enchainment. <sup>c</sup>  $M_{n,theoretical} = [(Conversion/100 \times [LA])/[BnOH] \times M_{r,LA}] + \text{benzyl alcohol end group MW} = [(Conversion/100 \times [LA])/[BnOH] \times 144.1260] + 107.1320$ . <sup>d</sup> Determined *via* GPC (refractive index analysis) in THF solvent referenced against polystyrene standards with no correction factor.

### 3.10 Conclusion and future work

All synthesised Fe(III)–salalen–chloride complexes were applied to the ROP of *rac*-LA using PO as both the solvent and co-initiator. All complexes were active and reactivity trends were studied and related to variations in the ligand framework. In particular, Fe(**3**)Cl was an effective initiator with predictable molecular weights, narrow dispersities ( $\mathcal{D} = 1.07\text{--}1.18$ ), moderate-to-high conversions and a moderate isotactic bias ( $P_m = 0.75\text{--}0.80$ ) observed under the reaction conditions applied. This complex was further investigated and batch kinetics revealed a six hour induction period for the *in-situ* generation of the active Fe(**3**)–alkoxide initiating species with the PO acting as a co-initiator. In this period, no LA was consumed and this agrees with the work conducted by Lamberti.<sup>[55]</sup>

The observed bimodality in the GPC chromatograms, for the PLA obtained using the Fe(III)–salalen–chloride initiators, was scrutinised and, after MALDI–ToF analysis studies, was deemed to be as a result of trace impurities of propane–1,2–diol (PD) being present in the PO solvent despite purification *via* distillation prior to its use. This postulation was supported by the monomodal GPC chromatogram observed after discovering an alternative polymerisation protocol, circumventing the need for PO, by carrying out the solution polymerisation in toluene and using catalytic amounts of benzyl alcohol and triethylamine as co–initiators.

This alternative method of initiation was explored further for the synthesised Fe(III)–acetate complexes. Both benzyl alcohol and triethylamine were required for initiation and all complexes were trialled at 100 °C. The two complexes, Fe(**13**)OAc and Fe(**17**)OAc, were the most effective initiators observing slight isotactic bias ( $P_m = 0.67$  and  $P_m = 0.71$  respectively).

While the Fe(III)–salalen–chloride and Fe(III)–acetate complexes were applied to ROP, other Fe complexes synthesised in **Chapter 2**, such as Fe(III)–*bis*(phenoxy–imine) complexes, have of yet not been applied to polymerisation and this would be of interest. Further kinetic studies, including the use of *L*– and *D*–LA, would also be required to further elucidate the stereoselective mechanism operating in this study. This could be achieved using the alternative polymerisation protocol and taking aliquots from the toluene mixture. This is more ideal than having to carry out a larger number of batch reactions using PO, with the solvent’s boiling point being lower than the reaction conditions.

### 3.11 References

- [1] M. J. Stanford, A. P. Dove, *Chem. Soc. Rev.* **2010**, *39*, 486–494.
- [2] J. Payne, P. McKeown, M. D. Jones, *Polym. Degrad. Stab.* **2019**, *165*, 170–181.
- [3] M. Rabnawaz, I. Wyman, R. Auras, S. Cheng, *Green Chem.* **2017**, *19*, 4737–4753.
- [4] O. Dechy-Cabaret, B. Martin-Vaca, D. Bourissou, *Chem. Rev.* **2004**, *104*, 6147–6176.
- [5] P. McKeown, M. D. Jones, *Sustain. Chem.* **2020**, *1*, 1–22.

- [6] Y. Tokiwa, B. P. Calabia, *Appl. Microbiol. Biotechnol.* **2006**, *72*, 244–251.
- [7] E. T. H. Vink, K. R. Rábago, D. A. Glassner, B. Springs, R. P. O’Connor, J. Kolstad, P. R. Gruber, *Macromol. Biosci.* **2004**, *4*, 551–564.
- [8] J. A. Byers, A. B. Biernesser, K. R. Delle Chiaie, A. Kaur, J. A. Kehl, *Advances in Polymer Science 279: Synthesis, Structure and Properties of Poly(Lactic Acid)*, Springer International Publishing, **2018**, pp. 67–118.
- [9] M. Stolt, A. Södergård, *Prog. Polym. Sci.* **2002**, *27*, 1123–1163.
- [10] P. VanWouwe, M. Dusselier, E. Vanleeuw, B. Sels, *ChemSusChem* **2016**, *9*, 907–921.
- [11] A. C. Albertsson, I. K. Varma, *Biomacromolecules* **2003**, *4*, 1466–1486.
- [12] H. Tsuji, *Macromol. Biosci.* **2005**, *5*, 569–597.
- [13] R. P. Pawar, S. U. Tekale, S. U. Shisodia, J. T. Totre, A. J. Domb, *Recent Patents on Regenerative Medicine* **2014**, *4*, 40–51.
- [14] A. Gregor, E. Filová, M. Novák, J. Kronek, H. Chlup, M. Buzgo, V. Blahnová, V. Lukášová, M. Bartoš, A. Nečas, J. Hošek, *J. Biol. Eng.* **2017**, *11*, 1–21.
- [15] A. J. R. Lasprilla, G. A. R. Martinez, B. H. Lunelli, A. L. Jardini, R. M. Filho, *Biotechnol. Adv.* **2012**, *30*, 321–328.
- [16] K. M. Nampoothiri, N. R. Nair, R. P. John, *Bioresour. Technol.* **2010**, *101*, 8493–8501.
- [17] R. Auras, B. Harte, S. Selke, *Macromol. Biosci.* **2004**, *4*, 835–864.
- [18] X. Zhang, M. Fevre, G. O. Jones, R. M. Waymouth, *Chem. Rev.* **2018**, *118*, 839–885.
- [19] D. Bourguignon, *EPRS* **2017**, *Plastics in a circular economy*, PE 603.940.
- [20] M. D. Jones, J. Payne, *ChemSusChem* **2021**, *14*, 4041–4070.
- [21] V. Piemonte, S. Sabatini, F. Gironi, *J. Polym. Environ.* **2013**, *21*, 640–647.
- [22] L. A. Román-Ramírez, P. McKeown, M. D. Jones, J. Wood, *ACS Catal.* **2019**, *9*, 409–416.
- [23] P. McKeown, L. A. Román-Ramírez, S. Bates, J. Wood, M. D. Jones, *ChemSusChem* **2019**, *12*, 5233–5238.
- [24] J. Payne, P. McKeown, M. F. Mahon, E. A. C. Emanuelsson, M. D. Jones, *Polym. Chem.* **2020**, *11*, 2381–2389.
- [25] L. A. Román-Ramírez, P. McKeown, C. Shah, J. Abraham, M. D. Jones, J. Wood, *Ind. Eng. Chem. Res.* **2020**, *59*, 11149–11156.
- [26] K. Ishihara, S. Ohara, H. Yamamoto, *Science* **2000**, *290*, 1140–1142.
- [27] Y. Zhao, Z. Wang, J. Wang, H. Mai, B. Yan, F. Yang, *J. Appl. Polym. Sci.* **2004**, *91*, 2143–2150.



- [28] C. M. Thomas, *Chem. Soc. Rev.* **2010**, *39*, 165–173.
- [29] R. H. Platel, L. M. Hodgson, C. K. Williams, *Polym. Rev.* **2008**, *48*, 11–63.
- [30] A. Duda, S. Penezek, *Macromolecules* **1990**, *23*, 1636–1639.
- [31] M. Dusselier, P. Van Wouwe, A. Dewaele, P. A. Jacobs, B. F. Sels, *Science* **2015**, *349*, 78–80.
- [32] Y. Zhu, C. Romain, C. K. Williams, *Nature* **2016**, *540*, 354–362.
- [33] R. Datta, M. Henry, *J. Chem. Technol. Biotechnol.* **2006**, *81*, 1119–1129.
- [34] D. Garlotta, *J. Polym. Environ.* **2001**, *9*, 63–84.
- [35] E. T. H. Vink, K. R. Rábago, D. A. Glassner, P. R. Gruber, *Polym. Degrad. Stab.* **2003**, *80*, 403–419.
- [36] E. T. H. Vink, S. Davies, *Ind. Biotechnol.* **2015**, *11*, 167–180.
- [37] S. C. Roşca, D. A. Roşca, V. Dorcet, C. M. Kozak, F. M. Kerton, J. F. Carpentier, Y. Sarazin, *Dalton Trans.* **2013**, *42*, 9361–9375.
- [38] A. Chuma, H. W. Horn, W. C. Swope, R. C. Pratt, L. Zhang, B. G. G. Lohmeijer, C. G. Wade, R. M. Waymouth, J. L. Hedrick, J. E. Rice, *J. Am. Chem. Soc.* **2008**, *130*, 6749–6754.
- [39] J. C. Buffet, J. Okuda, *Polym. Chem.* **2011**, *2*, 2758–2763.
- [40] P. Degée, P. Dubois, R. Jérôme, S. Jacobsen, H. G. Fritz, *Macromol. Symp.* **1999**, *144*, 289–302.
- [41] C. R. Álvarez-Chávez, S. Edwards, R. Moure-Eraso, K. Geiser, *J. Clean. Prod.* **2012**, *23*, 47–56.
- [42] H. R. Kricheldorf, I. Kreiser-Saunders, A. Stricker, *Macromolecules* **2000**, *33*, 702–709.
- [43] C. K. Williams, M. A. Hillmyer, *Polym. Rev.* **2008**, *48*, 1–10.
- [44] S. Brochu, R. E. Prud'homme, I. Barakat, R. Jérôme, *Macromolecules* **1995**, *28*, 5230–5239.
- [45] H. Tsuji, T. Tajima, *Polym. Int.* **2015**, *64*, 54–65.
- [46] B. M. Chamberlain, M. Cheng, D. R. Moore, T. M. Ovitt, E. B. Lobkovsky, G. W. Coates, *J. Am. Chem. Soc.* **2001**, *123*, 3229–3238.
- [47] M. H. Chisholm, J. C. Gallucci, K. T. Quisenberry, Z. Zhou, *Inorg. Chem.* **2008**, *47*, 2613–2624.
- [48] Z. Zhong, P. J. Dijkstra, J. Feijen, *Angew. Chem. Int. Ed.* **2002**, *41*, 4510–4513.
- [49] Z. Zhong, P. J. Dijkstra, J. Feijen, *J. Am. Chem. Soc.* **2003**, *125*, 11291–11298.
- [50] M. D. Jones, S. L. Hancock, P. McKeown, P. M. Schäfer, A. Buchard, L. H. Thomas, M. F. Mahon, J. P. Lowe, *Chem. Commun.* **2014**, *50*, 15967–15970.

- [51] C. M. Manna, A. Kaur, L. M. Yablon, F. Haeffner, B. Li, J. A. Byers, *J. Am. Chem. Soc.* **2015**, *137*, 14232–14235.
- [52] A. Pilone, K. Press, I. Goldberg, M. Kol, M. Mazzeo, M. Lamberti, *J. Am. Chem. Soc.* **2014**, *136*, 2940–2943.
- [53] M. H. Chisholm, N. J. Patmore, Z. Zhou, *Chem. Commun.* **2005**, 127–129.
- [54] R. Duan, C. Hu, X. Li, X. Pang, Z. Sun, X. Chen, X. Wang, *Macromolecules* **2017**, *50*, 9188–9195.
- [55] M. Cozzolino, V. Leo, C. Tedesco, M. Mazzeo, M. Lamberti, *Dalton Trans.* **2018**, *47*, 13229–13238.
- [56] E. Fazekas, G. S. Nichol, J. A. Garden, M. P. Shaver, *ACS Omega* **2018**, *3*, 16945–16953.
- [57] K. R. Delle Chiaie, A. B. Biernesser, M. A. Ortuño, B. Dereli, D. A. Iovan, M. J. T. Wilding, B. Li, C. J. Cramer, J. A. Byers, *Dalton Trans.* **2017**, *46*, 12971–12980.
- [58] A. C. Silvino, A. L. C. Rodrigues, J. A. L. C. Resende, *Inorg. Chem. Commun.* **2015**, *55*, 39–42.
- [59] X. Wang, K. Liao, D. Quan, Q. Wu, *Macromolecules* **2005**, *38*, 4611–4617.
- [60] B. J. O’Keefe, S. M. Monnier, M. A. Hillmyer, W. B. Tolman, *J. Am. Chem. Soc.* **2001**, *123*, 339–340.
- [61] B. J. O’Keefe, L. E. Breyfogle, M. A. Hillmyer, W. B. Tolman, *J. Am. Chem. Soc.* **2002**, *124*, 4384–4393.
- [62] V. C. Gibson, E. L. Marshall, D. Navarro-Llobet, A. J. P. White, D. J. Williams, *J. Chem. Soc. Dalton. Trans.* **2002**, 4321–4322.
- [63] D. S. McGuinness, E. L. Marshall, V. C. Gibson, J. W. Steed, *J. Polym. Sci. A Polym. Chem.* **2003**, *41*, 3798–3803.
- [64] J. M. Smith, R. J. Lachicotte, P. L. Holland, *Chem. Commun.* **2001**, *1*, 1542–1543.
- [65] A. B. Biernesser, B. Li, J. A. Byers, *J. Am. Chem. Soc.* **2013**, *135*, 16553–16560.
- [66] A. B. Biernesser, K. R. Delle Chiaie, J. B. Curley, J. A. Byers, *Angew. Chem. Int. Ed.* **2016**, *55*, 5251–5254.
- [67] M. Qi, Q. Dong, D. Wang, J. A. Byers, *J. Am. Chem. Soc.* **2018**, *140*, 8–12.
- [68] C. M. Manna, H. Z. Kaplan, B. Li, J. A. Byers, *Polyhedron* **2014**, *84*, 160–167.
- [69] Y. Y. Kang, H. R. Park, M. H. Lee, J. An, Y. Kim, J. Lee, *Polyhedron* **2015**, *95*, 24–29.
- [70] S. Doherty, R. J. Errington, N. Housley, W. Clegg, *Organometallics* **2004**, *23*, 2382–2388.
- [71] Y. Liang, R. Duan, C. Hu, L. Li, X. Pang, W. Zhang, X. Chen, *Chinese J. Polym. Sci.* **2018**, *36*, 185–189.

- [72] N. Nomura, R. Ishii, M. Akakura, K. Aoi, *J. Am. Chem. Soc.* **2002**, *124*, 5938–5939.
- [73] N. Nomura, R. Ishii, Y. Yamamoto, T. Kondo, *Chem. - A Eur. J.* **2007**, *13*, 4433–4451.
- [74] R. D. Rittinghaus, P. M. Schäfer, P. Albrecht, C. Conrads, A. Hoffmann, A. N. Ksiazkiewicz, O. Bienemann, A. Pich, S. Herres-Pawlis, *ChemSusChem* **2019**, *12*, 2161–2165.
- [75] U. Herber, K. Hegner, D. Wolters, R. Siris, K. Wrobel, A. Hoffmann, C. Lochenie, B. Weber, D. Kuckling, S. Herres-Pawlis, *Eur. J. Inorg. Chem.* **2017**, *2017*, 1341–1354.
- [76] P. Marin, M. J.-L. Tschan, F. Isnard, C. Robert, P. Haquette, X. Trivelli, L.-M. Chamoreau, V. Guérineau, I. del Rosal, L. Maron, V. Venditto, C. M. Thomas, *Angew. Chem. Int. Ed* **2019**, *58*, 12585–12589.
- [77] J. A. Stewart, P. McKeown, O. J. Driscoll, M. F. Mahon, B. D. Ward, M. D. Jones, *Macromolecules* **2019**, *52*, 5977–5984.
- [78] T. Naolou, A. Lendlein, A. T. Neffe, *Front. Chem.* **2019**, *7*, 1–12.
- [79] E. L. Whitelaw, G. Loraine, M. F. Mahon, M. D. Jones, *Dalton Trans.* **2011**, *40*, 11469–11469.
- [80] J. Beament, M. F. Mahon, A. Buchard, M. D. Jones, *New J. Chem.* **2017**, *41*, 2198–2203.
- [81] A. Pietrangelo, M. A. Hillmyer, W. B. Tolman, *Chem. Commun.* **2009**, 2736–2737.
- [82] A. Pietrangelo, S. C. Knight, A. K. Gupta, L. J. Yao, M. A. Hillmyer, W. B. Tolman, *J. Am. Chem. Soc.* **2010**, *132*, 11649–11657.
- [83] P. McKeown, M. G. Davidson, J. P. Lowe, M. F. Mahon, L. H. Thomas, T. J. Woodman, M. D. Jones, *Dalton Trans.* **2016**, *45*, 5374–5387.
- [84] S. M. Kirk, G. Kociok-Köhn, M. D. Jones, *Organometallics* **2016**, *35*, 3837–3843.
- [85] S. L. Hancock, M. F. Mahon, M. D. Jones, *Dalton Trans.* **2013**, *42*, 9279–9285.

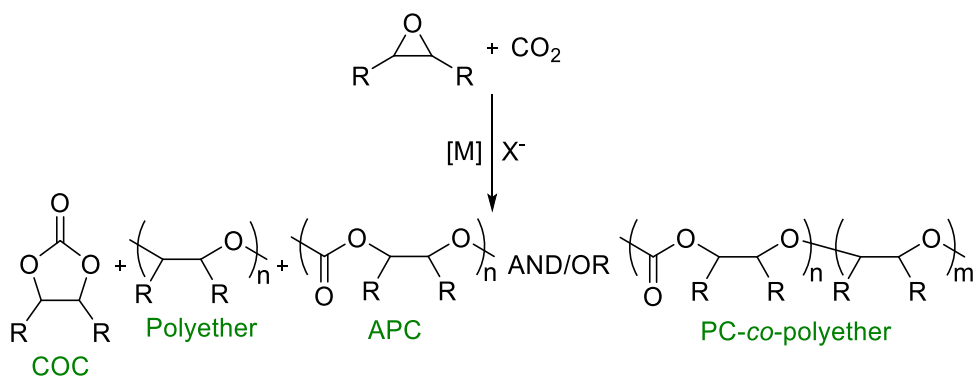
## **Chapter 4.**

### **Catalytic CO<sub>2</sub> / epoxide coupling and cyclic carbonate formation**

## 4. Catalytic CO<sub>2</sub> / epoxide coupling and cyclic carbonate formation

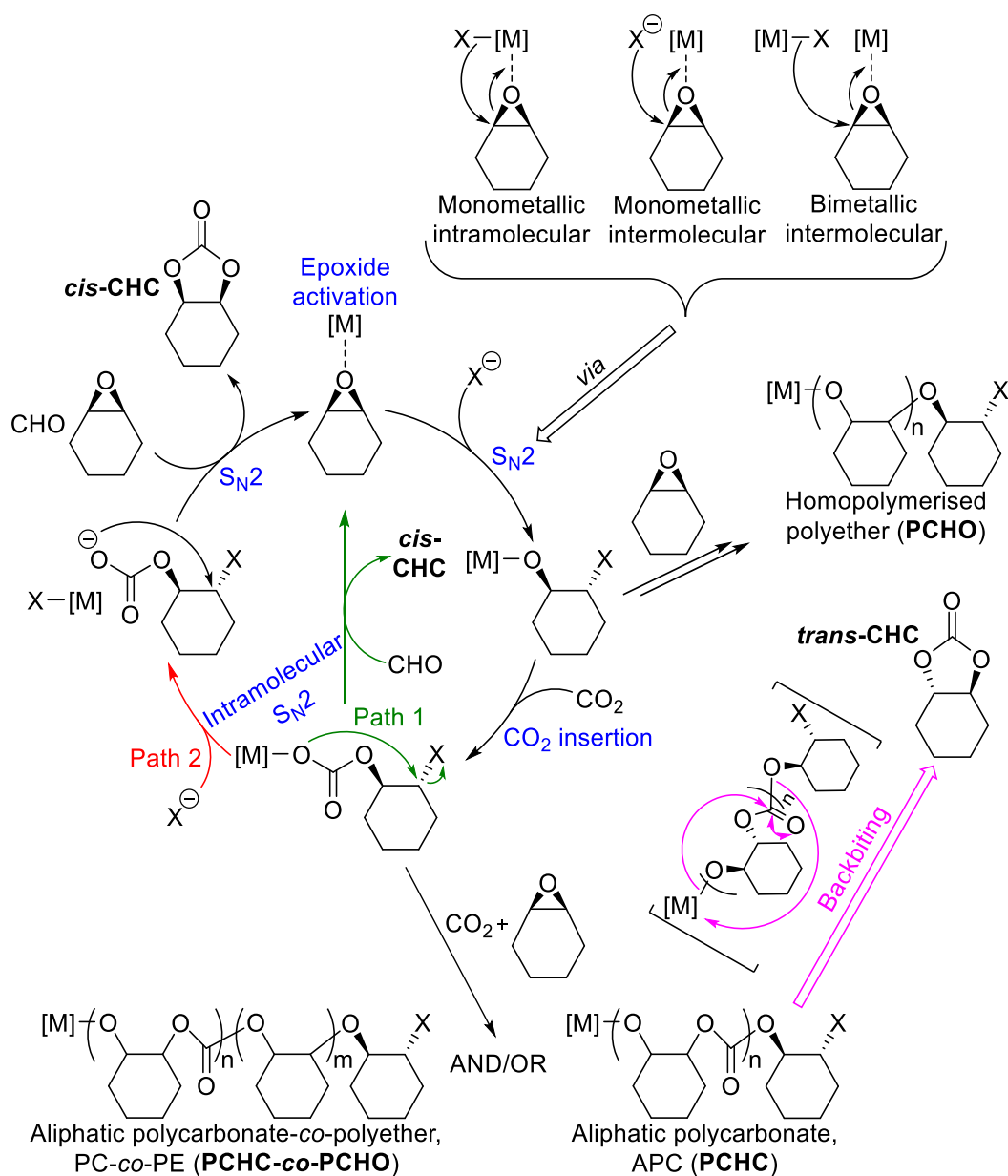
### 4.1 Introduction to catalytic CO<sub>2</sub> / epoxide coupling

The catalytic coupling of thermodynamically stable, kinetically inert CO<sub>2</sub> and reactive, highly energetic epoxide enables the formation of either aliphatic polycarbonates (APCs) and / or cyclic organic carbonates (COCs); both of which are useful, in demand products and hold a range of applications across multiple industries.<sup>[1–9]</sup> This atom efficient reaction is commonly and efficiently achieved, with a homogeneous binary system, using a Lewis acid catalyst and anionic, nucleophilic co-catalyst, to selectively target one of these products; as illustrated by *Scheme 25*. It is also a more sustainable alternative to the traditionally used, toxic phosgene method, of synthesis.<sup>[2,4–7,10–14]</sup> Which product that is formed, how selectively this is achieved with less / no side-products {polyether and polycarbonate-co-polyether polymer (PC-co-polyether)} and the activity depends on the catalyst / co-catalyst system, reaction conditions and nature of the epoxide reagent.<sup>[1,4,9,15]</sup> There are few effective examples of Fe-mediated catalysts that are switchable, depending on the reaction conditions, and can produce both products selectively; these will be discussed in **Sections 4.2** and **4.3**.<sup>[1,3,7,11,16,17]</sup> COCs are used as lithium-ion battery electrolytes, high boiling aprotic polar solvents, plasticisers, fuel additives, anti-foam additives due to their poor flammability and non-toxicity, monomers for polymerisation or copolymerisation with cyclic esters and intermediates in industry and organic, synthetic research.<sup>[1–9]</sup> APCs are used as sealants, coatings, adhesives, binders, electrical insulators and flame retardants in electronics, and primarily in the production of polyurethanes by being used as a CO<sub>2</sub>-derived hydroxy-terminated polymer; 'polyol' and replacing conventional, petrochemically derived polyether polyols.<sup>[3,18]</sup> This is due to their favourable properties such as durability, low weight or lightness, transparent nature, resistance to high-impact or strength and processability.<sup>[1,4]</sup>



*Scheme 25.* General reaction sequence to form either COCs or APCs using a homogeneous, binary catalytic system.

The generally accepted catalytic cycle for CO<sub>2</sub> / epoxide coupling is shown in *Scheme 26*, using cyclohexene oxide (CHO) as the epoxide in this case.<sup>[3,4,9,14,16,19,20]</sup> CHO is a bicyclic, internal epoxide and, compared to alternatives such as propylene oxide (PO), a more challenging substrate due to the high steric hindrance and regioselectivity issues arising from the ability to form four different products.<sup>[16]</sup> Initiation begins with the Lewis acid catalyst interacting and coordinating with the oxygen heteroatom of the epoxide ring. There is subsequent ring opening of the now activated epoxide *via* S<sub>N</sub>2 nucleophilic attack (X<sup>-</sup>). This can occur through three possible mechanisms where the nucleophile originates from either the auxiliary ligand of the Lewis acid metal catalyst centre bound to the epoxide (monometallic intramolecular), the auxiliary ligand of an unbound metal catalyst centre (bimetallic intermolecular) or from external nucleophilic co-catalyst added to the reaction mixture (monometallic intermolecular). The generated metal-alkoxide can undergo either further, repeated epoxide coordination and insertions to form the undesired polyether side-product, in this case poly(cyclohexene oxide) (PCHO), or CO<sub>2</sub> is activated and inserted into the metal-oxygen bond to form a metal-carbonate intermediate species. This metal-carbonate will either proceed with further alternate epoxide / CO<sub>2</sub> insertions and propagation to form the APC product, in this example poly(cyclohexene carbonate) (PCHC), or an intramolecular S<sub>N</sub>2, ‘backbiting’, cyclisation reaction, to close the ring and form the five-membered COC product with elimination of the halide.<sup>[3,4,14,19,20]</sup>

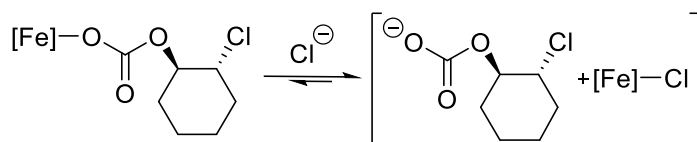


Scheme 26. The generally accepted mechanism for metal-mediated CO<sub>2</sub>/epoxide coupling.

(Adapted from references).<sup>[3,4,9,14,16,19-21]</sup>

Using CHO as the epoxide, after intramolecular backbiting of the metal-carbonate intermediate, the *cis*-CHC product is selectively formed due to the two S<sub>N</sub>2 attacks and overall double-inversion of the CHO stereochemistry around the cycle. Lamberti and co-workers proposed, after conducting NMR spectroscopic, mechanistic studies using an Al(III)-salalen-chloride complex with tetrabutylammonium chloride (TBAC) co-catalyst, this intramolecular S<sub>N</sub>2 reaction can occur *via* two pathways.<sup>[20]</sup> Using one equivalent of externally added co-catalyst, the oxygen atom of the metal-carbonate attacks and the reaction proceeds through 'Path 1'. If excess equivalents

of co-catalyst is added to the reaction mixture, exchange and displacement of a carbonate anion is promoted and the metal-chloride complex regenerated. The formation of this carbonate anion agrees with that postulated by Buchard *et al.* using their switchable dinuclear Fe(III) catalyst.<sup>[3]</sup> Whereby, it is suggested exchange reactions occur between the Fe-carbonate species and chloride anions, facilitated by the *bis*(triphenylphosphoranylidene)iminium chloride (PPNCl) co-catalyst (*Scheme 27*).<sup>[3,14]</sup> As the free carbonate anion would be expected to be more nucleophilic than the metal-carbonate intermediate, the reaction would occur *via* 'Path 2' (*Scheme 26*). This rationale agrees with the general observation, in literature, that as the equivalents of co-catalyst is increased, the selectivity for the *cis*-CHC product is improved. The formation of the more nucleophilic, free carbonate anion and ring closing is promoted and competitive further binding and insertion of epoxide molecules for copolymerisation; side-reactions in this case if the CHC product is desired, is discouraged.<sup>[3,14,20,22,23]</sup> It is also important to highlight that, if the APC product is desired and the catalyst is able to form this product, it is therefore important to use less or even no equivalents of co-catalyst to discourage ring closing and promote epoxide / CO<sub>2</sub> propagation.<sup>[3,22]</sup>



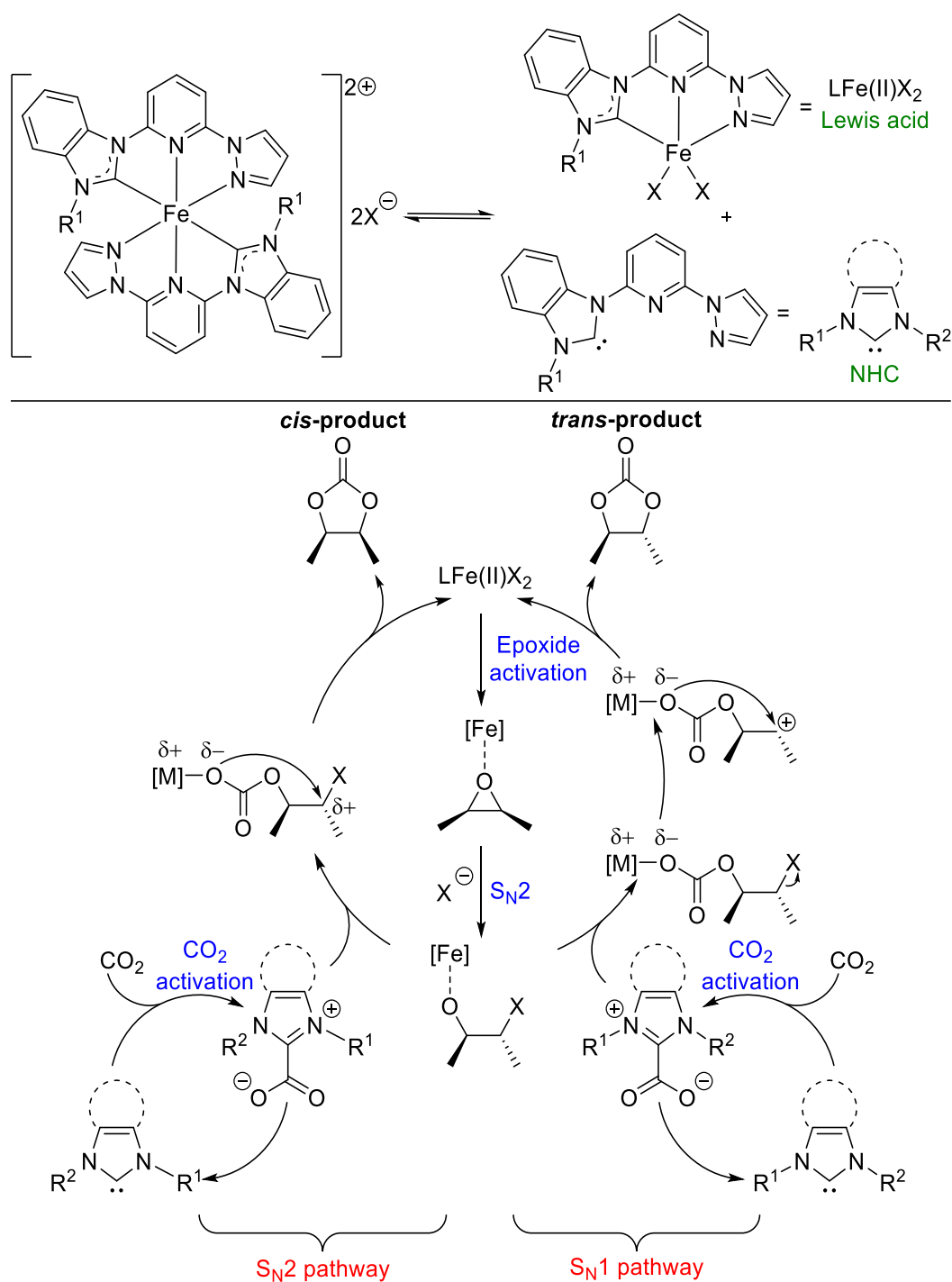
*Scheme 27.* Proposed exchange reactions upon addition of co-catalyst, such as PPNCl, to favour the formation of the carbonate anion.<sup>[3,14]</sup>

For the PCHC product to form, the rate of CO<sub>2</sub> activation must be faster than epoxide insertion and homopolymerisation to form PCHO. In addition to this rate, the catalyst must be selective and reaction conditions tuned so accidental, consecutive epoxide insertions do not occur before CO<sub>2</sub> insertion to achieve a high percentage of carbonate linkages. Otherwise, the number of ether linkages will increase in the APC, forming a PC-co-polyether copolymer product (in this example PCHC-co-PCHO). When using CHO as the epoxide, another side-product that can form is the thermodynamic *trans*-CHC product formed from backbiting side-reactions of the APC polymer chain.<sup>[9,21,24]</sup> This side-reaction can be reduced by a selective catalytic



system and altering the reaction conditions.<sup>[3,4,14,19,20]</sup> Predominantly, in the majority of cases, the formation of the *cis*-CHC product is rarer in literature, and harder to form than PCHC, due to the bicyclic ring strain.<sup>[3,4,9,21,25]</sup> Therefore, *trans*-CHC is more commonly preferred over *cis*-CHC (if COC products are observed in the reaction) *via* backbiting of the APC product (*Scheme 26*).<sup>[9,21,24]</sup>

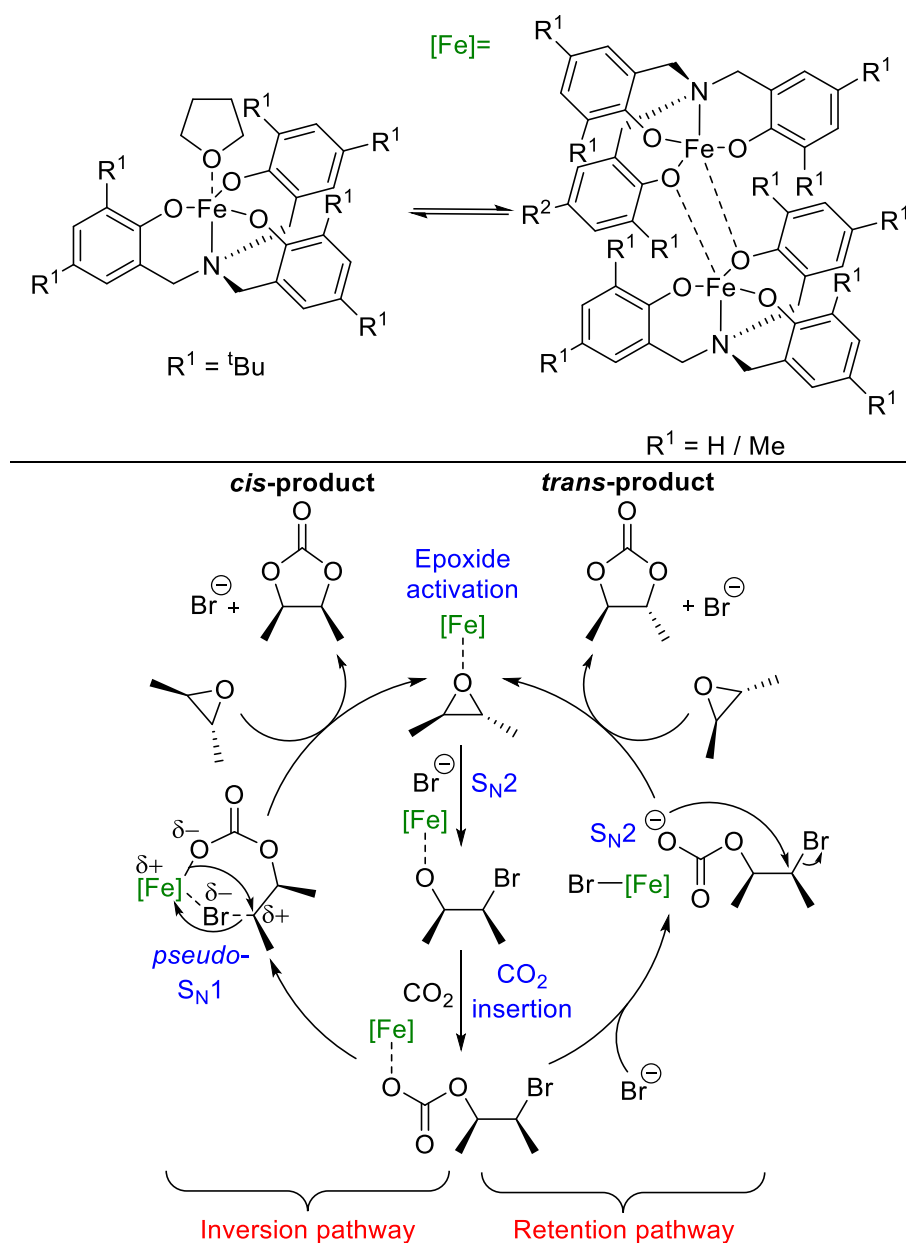
Although it is important to note, carbonate products with stereochemistry inverted compared to that of the starting epoxide can form *via* other mechanistic means for other internal epoxides and catalytic systems.<sup>[9]</sup> For example, for *trans*- or *cis*-2-butene oxide (*trans*- / *cis*-2-BO), Dai and Kleij report that an overall inversion of the stereochemistry can be achieved *via* S<sub>N</sub>1 type mechanisms for their Fe systems.<sup>[1,4,9,14,23,26–28]</sup> Dai and co-workers report, for their *bis*(pincer)-pyridine bridged-Fe(II) complex with *cis*-2-BO, the *trans*-product is formed *via* an S<sub>N</sub>1 reaction pathway with the halide leaving the metal carbonate species and a carbenium cation formed (*Scheme 28*). The ring closes on the *sp*<sup>2</sup>-hybridised carbon atom and there is no retention of the original stereochemistry of the epoxide. The *cis*-product is formed *via* the same S<sub>N</sub>2 attack by the metal carbonate species (*Scheme 28* and [Path 1, Scheme 26](#)). The subtle difference with this system is that no, externally added co-catalyst is required, to open the epoxide ring. Using HR-MS, it was suggested that the octahedral *bis*(pincer)-Fe(II) complex dissociates and ‘falls apart’ to produce another Lewis acidic Fe(II)X<sub>2</sub> species and a free N-heterocyclic carbene (NHC) (*Scheme 28*). Both these Lewis acidic, catalytically active species are in equilibrium and activate the epoxide; while there is synergic activation of the CO<sub>2</sub> by the free carbene. This results in the epoxide ring being opened by either halide weakly coordinating anions or the halide auxiliary ligands bound in the metal complex. Therefore, there are no exchange reactions taking place, as was discussed earlier by Buchard *et al.* (*Scheme 27*), the metal remains bound to the carbonate and the free carbonate anion species does not form; discouraging the intramolecular S<sub>N</sub>2 reaction.<sup>[3]</sup> The result of this mechanism is that there is a higher chance of a mixture of *cis*-to *trans*-carbonate products and the ratio depends on the leaving group ability of the halide on the S<sub>N</sub>1 pathway (*Scheme 28*).



Scheme 28. Dai's proposed mechanism for forming both the *cis*- and *trans*-products using *cis*-2-BO and *bis*(pincer)-pyridine bridged-Fe(II) complex / suggested dissociation species.<sup>[26]</sup>

In 2013, both the *trans*- and *cis*- carbonate products are produced and the stereochemistry controlled when using Kleij and co-workers', mononuclear and dinuclear, Fe(III)-amino-triphenolate complexes and either *trans*- or *cis*-2-BO substrate (Scheme 29).<sup>[14,23]</sup> The catalysis of these complexes will be discussed further

in Section 4.2 (Figure 54), but the mechanistic considerations will be focused on here.



Scheme 29. Kleij and co-worker's proposed ring closing mechanism to get both retention in stereochemistry to form the *trans*-product and inversion in stereochemistry to form the *cis*-product using *trans*-2-BO and mononuclear / dinuclear, amino-triphenolate-Fe(III) complexes. (Adapted from references).<sup>[1,4,23,27,28]</sup>

The product that was formed was dependent on the amount of external co-catalyst added. If a large excess of co-catalyst is employed, such as tetrabutylammonium bromide (TBAB), there is retention of the stereochemistry from the starting epoxide in the reaction. When the amount is reduced, there is divergence in the

stereochemistry and a mixture of the *cis*- and *trans*- carbonate products or complete inversion over the course of the reaction. For example, when the dinuclear Fe(III)-methyl substituted-amino-triphenolate catalyst (*Scheme 29*) was applied using *cis*-2-BO as the substrate, >99% and 95% of the *cis*-product was achieved using 16 and ten equivalents of TBAB (4.0 and 2.5 mol%) respectively. Decreasing to five equivalents (1.25 mol%) of TBAB, resulted in a mixture of 21% for the *trans*-product and 69% for the *cis*-product. Below and at 2.5 equivalents, the selectivity switches and inversion becomes dominant, with 26%:74% at 2.5 equivalents and 11%:89% at 0.5 equivalents for the *cis*-:*trans*-products.

After exploring both *trans*- or *cis*-2-BO, the mechanism was proposed to be that shown in *Scheme 29* via two different ring closing pathways accounting for the difference in selectivity.<sup>[9,14,23]</sup> The mechanism is very similar to that generally accepted and discussed earlier (*Scheme 26*); the Fe catalyst coordinates to the epoxide and the ring is opened by S<sub>N</sub>2 attack by a bromide anion from the external co-catalyst. This results in inversion of the stereochemistry and the Fe-carbonate species is formed after CO<sub>2</sub> insertion. To form the *trans*-product, when *trans*-2-BO was used as the substrate, there is excess co-catalyst and halide anions resulting in competition between the linear carbonate and excess bromide anions for the vacant Fe coordination site. This results in exchange reactions, in agreement with that suggested and discussed earlier by Buchard (*Scheme 27*), and dissociation of the Fe-carbonate species to the more nucleophilic, free carbonate anion.<sup>[3]</sup> This results in backbiting and an outer sphere, S<sub>N</sub>2 ring closing pathway to the *trans*-product and the second inversion (overall retention in the stereochemistry over the course of the whole reaction). This postulation was supported by the observation that polar solvents favour this selectivity as the carbonate anion species is stabilised more effectively.<sup>[4,14,23]</sup> The *cis*-product is formed, when low amounts of halide co-catalyst is added. This discourages formation of the free linear carbonate anion, remains bound to the metal centre, and the inner sphere, ring closing pathway is mediated by the Fe catalyst. Due to the available, vacant *cis*-coordination site on the Fe complex, the bound bromide (originating from the first S<sub>N</sub>2 attack to open the epoxide) interacts and dissociates from the linear carbonate to the metal centre.<sup>[23]</sup>

The resulting  $sp^2$ -hybridised carbon centre undergoes a *pseudo*- $S_N1$  ring closing reaction and the *cis*-product (overall inversion in the stereochemistry over the course of the whole reaction).

## 4.2 Fe-mediated $CO_2$ / epoxide coupling: phenoxy-amine and phenoxy-imine frameworks

There has been extensive research in the area of  $CO_2$  / epoxide coupling, to form either COCs and APCs, with the focus being on using metal complexes based on chromium, cobalt, magnesium, aluminium and zinc; these have been well reviewed.<sup>[2,11,14,15,29–33]</sup> However, despite the recent resurgence of iron in contemporary catalysis, examples for active and selective Fe-mediated  $CO_2$  / epoxide coupling remain less prevalent and explored despite the benefits of this element already discussed in **Section 3.3**. A range of different classes of ligand frameworks have been applied for both mononuclear- and dinuclear-Fe examples; these have recently been well reviewed by Della Monica and Kerton.<sup>[1,4]</sup> Two broad classes that have been successfully and widely applied include phenoxy-amine and phenoxy-imine ligands; more specifically such as salen, bidentate phenoxy-imine (half-salen), amino-triphenolate, amino-*bis*(phenolate), reduced Robson, and more recently salan and salalen ligands.

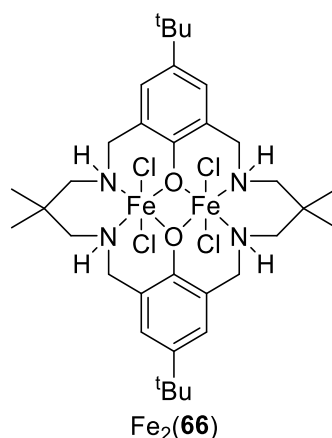


Figure 53. Buchard and Williams' dinuclear  $Fe(III)_2(\mathbf{66})$  complex.<sup>[3]</sup>

Buchard *et al.* reported a significant breakthrough in this area in 2011 with the synthesis and application of an air-stable dinuclear  $Fe_2(\mathbf{66})$  complex using a macrocyclic phenoxy-amine, 'reduced Robson' ligand framework (Figure 53).<sup>[1,3]</sup> The

complex was able to selectively form both *cis*-CHC or PCHC, using the more challenging CHO epoxide, depending on the reaction conditions and the amount of PPnCl co-catalyst; one of the few examples for a 'switchable' Fe catalyst in CO<sub>2</sub> / epoxide coupling.<sup>[3,16,17,22]</sup> In neat conditions and the absence of PPnCl; to discourage ring closing and COC product formation (**Section 4.1**), copolymerisation to form PCHC was achieved at a low catalyst loading of 0.1 mol% at 80 °C and mild CO<sub>2</sub> pressure ( $\leq 10$  atm).<sup>[3]</sup> At 10 atm of CO<sub>2</sub> there was high product selectivity for perfectly alternating PCHC (99% PCHC with 99% carbonate linkages) with only traces of *trans*-CHC observed (*via* backbiting side reactions of the PCHC), good activity (TOF = 47 h<sup>-1</sup> after five hours and 29 h<sup>-1</sup> after 24 hours) and reasonable molecular weights with narrow dispersity  $\{M_n = 3100 \text{ gmol}^{-1}, \text{Đ} = 1.18$  after five hours and  $M_n = 11700 \text{ gmol}^{-1}, \text{Đ} = 1.13$  after 24 hours}.<sup>[3]</sup> The activity was dramatically increased to a TOF value of 107 h<sup>-1</sup>, by lowering the metal loading to 0.01 mol% for 24 hours while the exclusive selectivity was maintained. This was accompanied by a bimodal distribution using GPC analysis  $\{M_n = 17200 \text{ gmol}^{-1}, \text{Đ} = 1.03$  and  $M_n = 8100 \text{ gmol}^{-1}, \text{Đ} = 1.06\}$ . The pressure of the polymerisation can be reduced to a remarkably low CO<sub>2</sub> pressure of one atmosphere and remain active (29% conversion, TOF = 6 h<sup>-1</sup> after 48 hours), although the selectivity was hindered to 93% PCHC containing only 66% carbonate linkages and 7% of *trans*-CHC side-product.<sup>[3]</sup>

When PPnCl co-catalyst was added to the reaction, generation of the anionic carbonate species and ring closing was favoured, the selectivity was switched and the *cis*-CHC product was formed. The explanation proposed by the authors for this mechanistic switch was discussed earlier in **Section 4.1**.<sup>[3]</sup> Under mild conditions, at one atm of CO<sub>2</sub> and 80 °C for 48 hours, with a low metal catalyst loading of 0.1 mol% and PPnCl co-catalyst loading of 0.4 mol%, the *cis*-CHC was exclusively formed (99%) with a TOF value of 9 h<sup>-1</sup> (41% conversion after 48 hours). The importance of excess co-catalyst and chloride anions for effective ring closing was demonstrated when reducing the PPnCl amounts: the activity was dramatically reduced when lowering to 0.2 mol% (33% conversion after 120 hours, TOF = 3 h<sup>-1</sup>) accompanied with 3% *trans*-CHC side-product and lowering to 0.1 mol% resulted in some competing copolymerisation. Both CHC and PCHC products were formed (89% and 11%

respectively) while the reactivity increased despite the lower amounts (20% conversion after 24 hours, TOF = 8 h<sup>-1</sup>). Alternatively, increasing the pressure of CO<sub>2</sub> to 10 atm, also resulted in a less selective and controlled reaction with both CHC (76%) and PCHC (24%) produced. However, only trace amounts of *trans*-CHC were detected (96% of the CHC was *cis*-CHC) and all the linkages in the PCHC were carbonate (99%). The conversion was dramatically increased to 90% by increasing the metal catalyst loading to 1 mol% and co-catalyst loading to 2 mol% while the selectivity was maintained; this was accompanied by a reduced TOF value of 4 h<sup>-1</sup>.<sup>[3]</sup>

To expand the epoxide scope and test the functional tolerance, Fe<sub>2</sub>(**66**) was applied to both PO and SO terminal epoxides. Copolymerisation with only the Fe catalyst did not occur despite attempting at a higher temperature {PO; 40 °C and SO; 80 °C} and 10 atm of CO<sub>2</sub>. However, the combination of Fe<sub>2</sub>(**66**) catalyst and PPNCI co-catalyst {[Fe]:[PPNCI] = 1:2} was extremely effective at converting PO and SO to propylene carbonate (PC) and styrene carbonate (SC) at such mild conditions (1 atm of CO<sub>2</sub>). Even at a low temperature of 25 °C for 24 hours there was conversion to the COC product {PO; 18% conversion, TOF = 8 h<sup>-1</sup>, [Fe]:[PPNCI] = 0.1 mol%:0.2 mol% and SO; 17% conversion, TOF = 1 h<sup>-1</sup>, [Fe]:[PPNCI] = 0.5 mol%:1 mol%}. The activity was improved by increasing temperature and adjusting the catalyst / co catalyst loadings for SO {PO; 34 °C, TOF = 21 h<sup>-1</sup>, [Fe]:[PPNCI] = 0.1 mol%:0.2 mol% and SO; 80 °C, TOF = 35 h<sup>-1</sup>, [Fe]:[PPNCI] = 0.1 mol%:0.2 mol%}.<sup>[3]</sup>

Recently, Kleij and co-workers reported another phenoxy-amine Fe system based upon amino-triphenolate ligands to form both mononuclear and dinuclear variants (*Figure 54*) and, since then, have been heavily explored.<sup>[27,28]</sup> Initially, the dinuclear Fe<sub>2</sub>(**74**)<sub>2</sub> complex was reported with dimethyl substitution at positions R<sup>1</sup> and R<sup>2</sup>.<sup>[28]</sup> However, it was found, using MALDI-ToF analysis, single-crystal X-ray diffraction and UV-visible (UV-Vis) spectroscopy titration studies, this dinuclear structure was prone to dissociation to the more reactive, and the proposed catalytically active, mononuclear Fe(**69**) complex.<sup>[28]</sup> This structure was stabilised and coordinated to donor molecules, such as DMSO, pyridine or PO, to saturate the Fe(III) centre.<sup>[28]</sup>

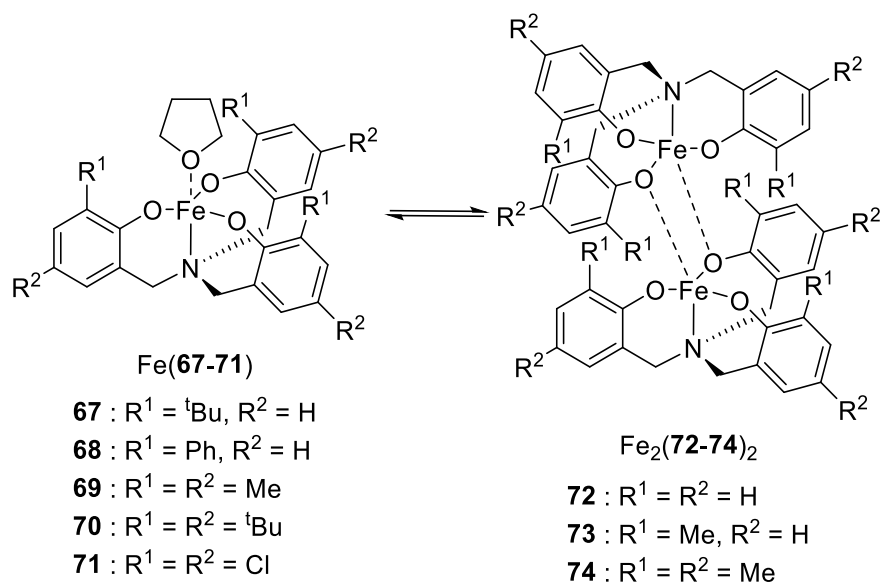


Figure 54. Kleij and co-workers', mononuclear and dinuclear, Fe(III)-amino-triphenolate complexes.<sup>[16,23,27,28]</sup>


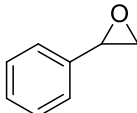

Using Fe<sub>2</sub>(**74**)<sub>2</sub> with tetrabutylammonium iodide (TBAI) or bromide (TBAB) co-catalyst in methyl ethyl ketone (MEK) solvent, the corresponding COCs were selectively formed (>99%) from a large range of terminal epoxides; neither catalyst or co-catalyst were active alone.<sup>[28]</sup> High yields were observed (TBAB co-catalyst; 56–96%) under mild conditions at two bar of CO<sub>2</sub>, 25 °C for 18 hours with catalyst and excess co-catalyst loadings of 0.5 mol% and 5 mol% respectively. Although, the activities were low at such mild conditions (PO epoxide, TBAB co-catalyst, TOF = 7 h<sup>-1</sup>). More challenging, non-terminal epoxides and oxetanes were accessed by increasing the temperature to 85 °C with generally modest yields and high selectivity (85–96%) to one of the COC products in the reaction mixtures (*cis*- vs. *trans*-). In the case of using the sterically hindered CHO, a modest conversion of 51% was achieved (TBAB co-catalyst) with a TOF value of 6 h<sup>-1</sup> and a mixture of *cis*-CHC and PCHC was observed; although the polymeric species contained both carbonate and ether linkages. This result was important as revealed a glimpse at the potential for a switchable catalytic system.<sup>[28]</sup>

The complexes were studied further to ascertain the structure of the active Fe species and whether the mononuclear or dinuclear variants were existing.<sup>[27]</sup> This was achieved by varying the *ortho*-position on the phenolate rings (R<sup>1</sup>) and



maintaining the substitution on the para position ( $R^2 = H$ ) to synthesise Fe(**67/68**) and Fe<sub>2</sub>(**72/73**)<sub>2</sub> (Figure 54). It was revealed, using a combination of <sup>1</sup>H NMR spectroscopy, single-crystal X-ray diffraction, solution magnetic susceptibility (the dinuclear complexes displayed lower high-spin  $\mu_{\text{eff}}$  values compared to the mononuclear complexes due to antiferromagnetic coupling),<sup>[8]</sup> cyclic voltammetry, elemental and MALDI analysis, that the *ortho*-position was crucial to the dinuclear vs. mononuclear formation. Hydrogen and methyl substitution favoured the dinuclear species {Fe<sub>2</sub>(**72/73**)<sub>2</sub>} and the bulkier *tert*-butyl and phenyl groups favoured the mononuclear species {Fe(**67/68**)}. However, the less sterically bulky dinuclear structures dissociated to the mononuclear variant upon addition of a Lewis base such as pyridine or epoxide; as was the case before with Fe(**69**) and Fe<sub>2</sub>(**74**)<sub>2</sub>.<sup>[28]</sup>

Table 15. CO<sub>2</sub> coupling with PO, SO and *trans*-2-BO catalysed by Fe(**67/68**) or Fe<sub>2</sub>(**72/73**)<sub>2</sub> and TBAB to the corresponding COC products. [Adapted from reference]<sup>[27]</sup>

Substrate	Solvent	Spectroscopic yields <sup>a</sup> (%)				
		Fe( <b>67</b> )	Fe( <b>68</b> )	Fe <sub>2</sub> ( <b>72</b> ) <sub>2</sub>	Fe <sub>2</sub> ( <b>73</b> ) <sub>2</sub>	
	PO	DCM	82	78	16	13
		MEK	85	88	56	72
	SO	DCM	90	67	12	10
	<i>trans</i> -2-BO	DCM <sup>b</sup>	12	52	15	13
		MEK <sup>b</sup>	50	82	83	75

Conditions: Fe(**67**) and Fe(**68**) (0.02 mmol) or Fe<sub>2</sub>(**72**)<sub>2</sub> and Fe<sub>2</sub>(**73**)<sub>2</sub> (0.01 mmol), TBAB (0.1 mmol), solvent (5 mL), epoxide (2.0 mmol), 10 bar CO<sub>2</sub>, 25 °C, 18 h. <sup>a</sup> Determined *via* <sup>1</sup>H NMR spectroscopy using mesitylene (2.0 mmol) as an internal standard. <sup>b</sup> 85 °C.

The complexes were applied to the CO<sub>2</sub> / epoxide coupling of three epoxides (PO, SO and *trans*-2-BO) with TBAB co-catalyst at 10 bar of CO<sub>2</sub> in DCM and methyl ethyl ketone (MEK) solvent to study the dimer–monomer equilibrium (Table 15). The mononuclear complexes were more active in nearly all cases with modest–to–high yields observed. Using MEK enhanced the activities of the dinuclear species to yields nearly comparable to the more sterically hindered mononuclear complexes for PO and *trans*-2-BO substrates; indeed, the sterically hindered dinuclear Fe(**68**) complex

was considerably less active in comparison for *trans*-2-BO in MEK.<sup>[27]</sup> MEK is considered a coordinating solvent and hence, was proposed to cause the dissociation of the dinuclear structures {Fe<sub>2</sub>(**72/73**)<sub>2</sub>} to the more catalytically active mononuclear-MEK adduct species, with a more accessible Fe(III) centre, and the higher observed yields. In addition, the higher temperature of 85 °C, required for the *trans*-2-BO substrate, was also attributed to contributing to this dissociation to the mononuclear species.<sup>[27]</sup>

As mentioned earlier, using Fe<sub>2</sub>(**74**)<sub>2</sub> for the coupling of CO<sub>2</sub> with more challenging, non-terminal epoxides and oxetanes resulted in generally modest yields to the COC products, with both the *cis*- and *trans*-geometrical isomers observed; generally one isomer was heavily favoured over the other.<sup>[28]</sup> As was discussed in **Section 4.1**, this was explored further in 2013, where the stereochemistry could be controlled using Fe(**70**) and Fe<sub>2</sub>(**72/74**)<sub>2</sub> to form both the *trans*- and *cis*- carbonate products from either *trans*- or *cis*-2-BO (*Scheme 29*). The mechanistic considerations involved in CO<sub>2</sub> / epoxide coupling using these complexes was studied and a catalytic cycle was proposed (*Scheme 29*).<sup>[14,23]</sup>

As commented earlier, building on the observation that a mixture of *cis*-CHC and PCHC was obtained after the coupling of CO<sub>2</sub> with CHO using Fe<sub>2</sub>(**74**)<sub>2</sub>, Pescarmona and Kleij further investigated the potential for switching between selectively forming *cis*-CHC and PCHC.<sup>[16]</sup> Under solvent-free, supercritical CO<sub>2</sub> conditions (scCO<sub>2</sub>, 80 bar CO<sub>2</sub>), using Fe(**69/70/71**) at 85 °C for three hours, the selectivity could be fully tuned by the nature and the relative amount of co-catalyst added to favour either the backbiting, ring closing pathway to form *cis*-CHC or further epoxide insertion and propagation to form PCHC (as discussed mechanistically in **Section 4.1**) from the crucial metal-carbonate intermediate species. The ring closing pathway being dramatically favoured if the nucleophile was a good leaving group (X<sup>-</sup>) or displaced the metal-carbonate species to form the metal-halide complex and generate the more nucleophilic anionic carbonate species in an exchange reaction. A range of co-catalysts such as: TBAF, TBAC, TBAB, TBAI and PPNCl, were screened at varying equivalents with a Fe(**69**) loading of 0.5 mol% and it was observed that at higher ratios of co-catalyst-to-[Fe] (10:1), the *cis*-CHC was favoured, in agreement with

that reported by Buchard discussed previously.<sup>[3]</sup> However, despite the *cis*-CHC never being exclusively formed (>99%), both high selectivity and high conversion were achieved using TBAC, TBAB and PPNCI (92–96% *cis*-CHC and 83–94% conversion). The selectivity was switched when using a lower one equivalent of co-catalyst; the PCHC being formed exclusively with only carbonate linkages, using TBAC and PPNCI, with high conversions (78 and 98% conversion respectively). Taking into account the higher pressure of 80 bar CO<sub>2</sub> being used at 85 °C, the metal loading of 5 mol% is high in comparison with other systems in literature.

Despite the formation of PCHC, the molecular weights were low and oligomeric using GPC analysis ( $M_n < 2500 \text{ gmol}^{-1}$ ). Therefore, the catalyst and co-catalyst loadings were both lowered to 0.1 mol% and 0.1 mol%: 0.025 mol% respectively in an attempt to increase the growing polymer chain. All three Fe(**69/70/71**) complexes were applied to compare structure–activity–relationships (SARs) and most success was observed using TBAC and PPNCI for PCHC selectivity. It was found the *tert*-butyl- and methyl-substituted complexes {Fe(**69/70**)} displayed similar activity (*Table 16*), suggesting that sterics had minimal influence on the reaction. While the complex with chloro-functionality {Fe(**71**)}, regardless of the increase in Lewis acidity on the Fe(III) centre, observed diminished reactivity due to a proposed decrease in solubility in the scCO<sub>2</sub> and reaction mixture. Despite the lower loadings, the molecular weights remained low with broad bimodal distributions {for example: *Table 16*, entry 2;  $M_n = 1509$  and  $6022 \text{ gmol}^{-1}$ ,  $\mathcal{D} = 1.25$  and  $1.05$  analysing each peak separately}. The bimodality observed was proposed to occur due to residual water impurities in the reaction mixtures carried out in pressurised, parallel batch reactor vessels; supported by the indication of hydroxyl end groups *via* <sup>1</sup>H NMR spectroscopy and MALDI–ToF mass spectrometry. The water acted as a chain transfer agent, preventing polymer chain growth and resulted in the low molecular weights. Indeed, carrying out the reaction in a Schlenk vessel under anhydrous conditions dramatically improved the polymerisation {Fe(**69**); anhydrous conditions, 3 bar of CO<sub>2</sub>, 53% PCHC yield,  $M_n = 6490 \text{ gmol}^{-1}$  and  $18814 \text{ gmol}^{-1}$ ,  $\mathcal{D} = 1.28$  and  $1.04$  vs. standard conditions, 10 bar of CO<sub>2</sub>, 59% PCHC yield,  $M_n = 3257 \text{ gmol}^{-1}$ ,  $\mathcal{D} = 1.28$ }. However, it was also noted that for these ‘anhydrous conditions’, the CHO was dried using calcium hydride and

vacuum distilled and, as far as it is made aware, implies specifically the CHO was used as received commercially for the standard reactions. Therefore, despite not being mentioned by the authors, it is important to consider the 1,2-cyclohexanediol, formed *via* hydrolysis of the epoxide, as another possible chain transfer agent present in these reactions; although this was not presumably observed in the MALDI-ToF spectra. Nonetheless, these results do demonstrate the need for purification of the epoxide and anhydrous conditions if aiming to produce APCs and not oligomers.

Table 16. CO<sub>2</sub> / CHO coupling reaction catalysed by Fe(**69/70/71**) and TBAC or PPNCI co-catalyst. [Selected from reference]<sup>[16]</sup>

Entry	Catalyst	Co-catalyst	Conv. <sup>c</sup> (%)	Product selectivity (%)		
				<i>cis</i> -CHC <sup>d</sup>	PCHC <sup>d,e</sup>	PCHO <sup>c</sup>
1 <sup>a</sup>	Fe( <b>69</b> )	TBAC	25	0	>99	0
2 <sup>a</sup>	Fe( <b>69</b> )	PPNCI	56	0	>99	0
3 <sup>a</sup>	Fe( <b>70</b> )	TBAC	27	0	>99	0
4 <sup>a</sup>	Fe( <b>70</b> )	PPNCI	55	0	>99	0
5 <sup>a</sup>	Fe( <b>71</b> )	TBAC	3	0	>99	0
6 <sup>a</sup>	Fe( <b>71</b> )	PPNCI	17	10	90	0
7 <sup>b</sup>	Fe( <b>69</b> )	TBAC	14	8	92	0
8 <sup>b</sup>	Fe( <b>69</b> )	PPNCI	40	0	>99	0
9 <sup>b</sup>	Fe( <b>70</b> )	TBAC	30	0	>99	0
10 <sup>b</sup>	Fe( <b>70</b> )	PPNCI	25	0	>99	0
11 <sup>b</sup>	Fe( <b>71</b> )	TBAC	5	0	0	>99
12 <sup>b</sup>	Fe( <b>71</b> )	PPNCI	6	0	0	>99

Conditions: <sup>a</sup> [Fe] catalyst (0.1 mol%, 1 eq.), co-catalyst (0.1 mol%, 1 eq.), CHO (6.0 mmol), 80 bar CO<sub>2</sub>, 85 °C, 3 h. <sup>b</sup> [Fe] catalyst (0.1 mol%, 4 eq.), co-catalyst (0.025 mol%, 1 eq.), CHO (6.0 mmol), 80 bar CO<sub>2</sub>, 85 °C, 3 h. <sup>c</sup> Determined *via* <sup>1</sup>H NMR spectroscopy. <sup>d</sup> Determined *via* <sup>1</sup>H NMR spectroscopy and IR analysis. <sup>e</sup> >99% carbonate linkages in all cases.

In 2015, following on from this work, Pescarmona extensively investigated further, using Fe(III)-pyridylamino-*bis*(phenolate) complexes {Fe(**75/76**)} (Figure 55). This was under solvent-free, supercritical CO<sub>2</sub> conditions (scCO<sub>2</sub>, 80 bar CO<sub>2</sub>) at 60 / 85 °C with various co-catalysts (TBAC, TBAB, TBAI, TBAAc and PPNCI) and epoxides; focussing mainly on CHO and 4-vinylcyclohexene oxide (VCHO).<sup>[17]</sup> As was the case

before, the selectivity could be fully tuned, using CHO as the substrate, by the relative amount of co-catalyst added; the *cis*-CHC being formed with high selectivity with excess co-catalyst. Using TBAB co-catalyst observed the highest activity and exclusive product selectivity {Fe(**75**), 60 °C, 18 hours, [Fe]:[co-catalyst] = 0.5 mol%:5mol%, COC selectivity: TBAC = 83%, TBAB = >99%, TBAI = 91%, TBAAc = 85%, PPNCl = 95%}.<sup>[17]</sup>

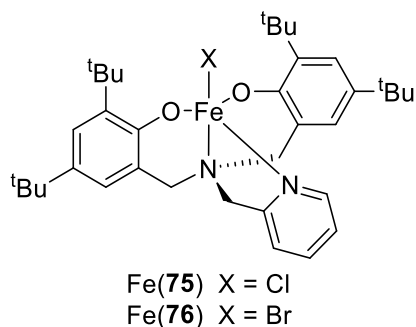


Figure 55. Pescarmona's Fe(III)-pyridylamino-*bis*(phenolate) complexes.<sup>[17]</sup>

The Fe(III)-pyridylamino-*bis*(phenolate) complexes differ slightly to the amino-triphenolates with the apical auxiliary ligand now being occupied by a labile, nucleophilic halide anion. For this reason, the catalysts displayed bifunctionality and, in the complete absence of co-catalyst, were able to copolymerise CHO to PCHC with 88% selectivity for Fe(**75**) at a 5 mol% catalyst loading; the highest displayed in the study. When the auxiliary ligand halide was modified to a bromide {Fe(**76**)}, selectivity dropped, and conversion increased. Despite not being noted in these particular entries, when PCHC had been produced in other cases, there were high amounts of carbonate linkages (94->99%). Although the activities were low {Fe(**75**), TOF = 0.9 h<sup>-1</sup> and Fe(**76**), TOF = 1.2 h<sup>-1</sup>}, they could be drastically increased when one equivalent of co-catalyst was added but the selectivity would then be hindered.

Unlike for the *cis*-CHC formation, using TBAAc as a co-catalyst displayed the highest selectivity for the PCHC product (86%) in comparison to the other nucleophilic co-catalysts; the larger, sterically hindered anion favouring further propagation. In comparison, the TBAB co-catalyst displayed the joint lowest PCHC selectivity (60%), due to the better bromide leaving group favouring ring closing to the cyclised product, and the highest activity.

The PCHC polymer products obtained were of low molecular weight and oligomeric in nature with narrow dispersities  $\{M_n = 704\text{--}1612 \text{ gmol}^{-1}, \text{Đ} = 1.0\text{--}1.2\}$ . This was proposed to be due to the competition between polymer propagation and *cis*-CHC formation, and, as was the case with the amino-triphenolates, traces of water impurity acting as a chain transfer agent; causing termination and the low molecular weights. Although, as remarked by the authors, the use of unpurified, commercially received substrates, with traces of water impurity in the reaction mixtures, demonstrate the robustness of the Fe(**75/76**) catalysts. If potential higher molecular weights are desired, purification and distillation will evidently need to be required.<sup>[17]</sup>

The tolerance and robustness was also demonstrated by applying Fe(**75**) to a large range of epoxides (COC formation was favoured for all terminal epoxides), and, in particular, VCHO as the substrate.<sup>[17]</sup> Upon shifting from CHO to VCHO, under optimised conditions with one equivalent of co-catalyst, the selectivity to poly(vinylcyclohexene carbonate) (PVCHC) increased to up to 99% but the conversion and activity remained low  $\{\text{Fe}(\mathbf{75}), 60 \text{ }^\circ\text{C}, 18 \text{ hours}, [\text{Fe}]:[\text{co-catalyst}] = 0.5 \text{ mol}\%: 5 \text{ mol}\%, \text{PVCHC selectivity}; \text{TBAC} = 98\%, \text{TBAB} = 78\%, \text{TBAAc} = 99\%, \text{PPNCl} = 95\%\}$ . The microstructure of these polycarbonates was explored and  $^{13}\text{C}\{^1\text{H}\}$  NMR spectroscopy observed atactic polymers for both CHO and VCHO. As the pendant vinyl groups for PVCHC allowed the potential for post-modification to enhance the chemical and mechanical properties, a free-radical cross-linking, thiol-ene reaction was achieved using 1,3-propanedithiol and 2,2'-azobis(2-methylpropionitrile) (AIBN) radical initiator. This cross-linking resulted in an increase in the glass transition temperature ( $T_g$ ) by 55 °C for the thermosetting polymer, compared to the original native PVCHC polymer, as observed using differential scanning calorimetry (DSC) analysis. It also displayed enhanced chemical resistance and insolubility for a range of organic solvents.

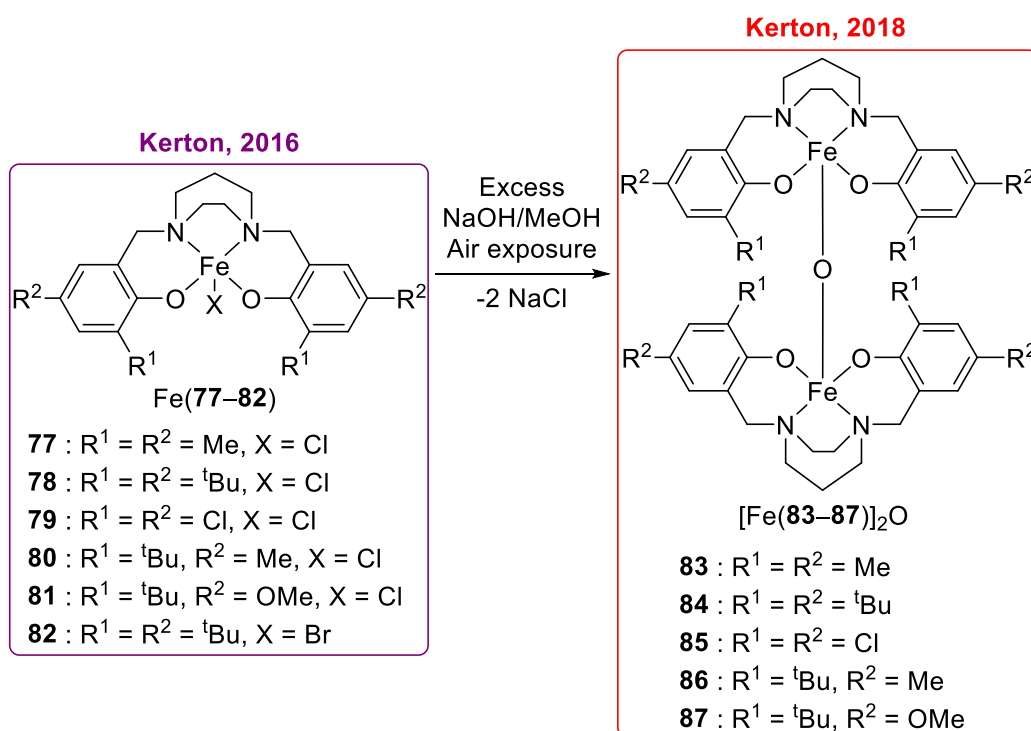


Figure 56. Kerton's Fe(III)–amino–bis(phenolate) complexes containing a homopiperazinylligand backbone.<sup>[8,34]</sup>

Since 2016, Kerton and co-workers have also comprehensively explored Fe(III)–amino–bis(phenolate) complexes. The sterics and electronics on the donor atoms and geometry of the Fe(III) centre were varied and the complexes applied to CO<sub>2</sub> / epoxide coupling to ascertain SARs and crucial factors contributing to selective product control.<sup>[8,22,34]</sup> Initially, a range of these complexes containing the homopiperazinylligand backbone were studied (Figure 56). Firstly, Fe(**77–82**) with auxiliary halide groups were screened with the terminal epoxide PO, at 20 bar of CO<sub>2</sub> at 100 °C for 22 hours with a low metal catalyst loading of 0.025 mol% and TBAB co-catalyst loading of 0.1 mol% ([Fe]:[TBAB]:[PO] = 1:4:4000), in solvent-free conditions to form propylene carbonate (PC).<sup>[34]</sup> Early studies showed TBAB and PPNCI co-catalysts were more effective for ring opening compared to PPNN<sub>3</sub> and 4-(dimethylamino)pyridine (DMAP) and hence TBAB was chosen.<sup>[34]</sup> As expected, from the control reactions, Fe(**78**) by itself with no co-catalyst resulted in no reactivity and a low conversion of 33% was observed with only TBAB co-catalyst. There are no stereoselectivity challenges here for the COC product due to the use of a terminal epoxide unlike that for CHO. The benchmark, *tert*-butyl substituted Fe(**78**), observed

high activity under the selected reaction conditions (74% conversion, TOF = 135 h<sup>-1</sup>) and this value increased with a raised pressure (40 bar of CO<sub>2</sub>, TOF = 153 h<sup>-1</sup>), and conversion decreased with shorter reaction times or smaller propylene oxide amounts as would be expected (six hours, 25% conversion or [Fe]:[TBAB]:[PO] = 1:4:1000, 58% conversion).<sup>[34]</sup> Upon installing chloro-functionality and electron-withdrawing groups (EWGs), the activity increased further to 173 h<sup>-1</sup> {Fe(**79**)} due to increased Lewis acidity. The introduction of methoxy or methyl electron-donating groups (EDGs) was detrimental and decreased activity {Fe(**80**), TOF = 55 h<sup>-1</sup> and Fe(**81**), TOF = 62 h<sup>-1</sup>}. Replacing the chloride axial, auxiliary ligand with a bromide also resulted in a decreased activity {Fe(**82**), TOF = 62 h<sup>-1</sup>} with the postulation that the larger radius of the bromide hindered incoming epoxide substrate to the Fe(III) centre *via* steric repulsion, as it would have been assumed hypothetically that the bromide was a better leaving group and encouraged ring closing and hence increased activity; this postulation was in agreement with Pescarmona.<sup>[17,34]</sup>

The epoxide scope was expanded using Fe(**78**), to convert a range of sterically and electronically varied substrates to their COC products, at the same reaction conditions.<sup>[34]</sup> High functional tolerance was displayed, particularly by the use of allylglycidyl ether (AGE) and glycidol (GLY); epoxides with terminal allyl and hydroxy groups respectively, which both afforded high activities (GLY, 78% conversion, TOF = 142 h<sup>-1</sup> and AGE, 52% conversion, TOF = 95 h<sup>-1</sup>).<sup>[34]</sup> However, low conversions were observed using more sterically hindered epoxides such as styrene oxide (SO) and CHO, and no evidence for polymer formation was observed (31% and 9% conversion respectively).<sup>[34]</sup>

During the CO<sub>2</sub> / epoxide coupling reactions, using Fe(**77–82**), it was observed that the colour of the reaction mixtures changed from dark purple to dark red / brown.<sup>[8]</sup> It was postulated that this was due to the *in-situ* formation of the  $\mu$ -oxo-bridged Fe(III) dimer species causing this colour change. In 2018, for this reason, the analogous [Fe(**83–87**)]<sub>2</sub>O,  $\mu$ -oxo-bridged complexes, were synthesised to compare directly with the mononuclear Fe(**77–82**) complexes in their catalysis for CO<sub>2</sub> / epoxide coupling (*Figure 56*).<sup>[8]</sup> [Fe(**83–87**)]<sub>2</sub>O and Fe(**77–82**) were screened using identical reaction conditions as before but with PPNCl co-catalyst. It was found that

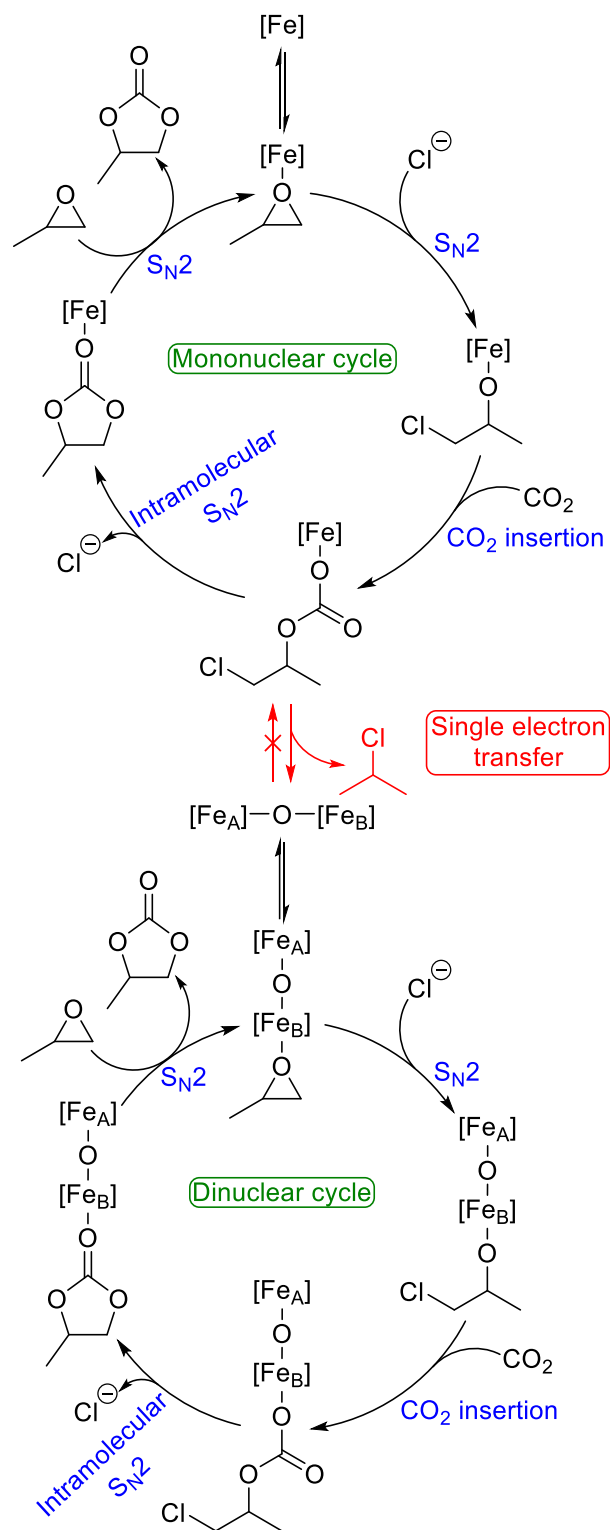


the  $\mu$ -oxo-bridged Fe(III) complexes were all less active than their mononuclear structural counterpart {for example: Fe(**78**); 40% conversion, TOF = 31 h<sup>-1</sup> vs. [Fe(**84**)]<sub>2</sub>O, 29% conversion, TOF = 11 h<sup>-1</sup>}.<sup>[8]</sup> Only the propylene carbonate (PC) product and no polycarbonate and polyether side-products were observed using IR and <sup>1</sup>H NMR spectroscopy. Various parameters, such as temperature, pressure, time, metal loading and nature of co-catalyst, were explored using [Fe(**84**)]<sub>2</sub>O.<sup>[8]</sup> Likewise to previous examples, co-catalyst was required for reactivity and, especially here, because the  $\mu$ -oxo-bridged species lacked a nucleophilic auxiliary ligand for ring opening and displayed low conversion by itself. Unlike for Fe(**77–82**), conversion did not decrease for [Fe(**84**)]<sub>2</sub>O when reducing the equivalents of PPNCI from four to two (29% and 32% conversion respectively) and contrasted the optimum [Fe]:[co-catalyst] ratio of 1:4 observed for the analogues Fe(III)-chloride complexes.<sup>[8]</sup> Changing from PPNCI to either TBAB or TBAI co-catalyst resulted in a minimal decrease in activity, implying the size of the nucleophilic anion has minimal influence on the ring opening and backbiting and neither were the rate-determining step (RDS); in this case either PO coordination or CO<sub>2</sub> insertion was the RDS.<sup>[8]</sup>

While increasing temperature and not reducing the time expectedly afforded higher conversions, the CO<sub>2</sub> pressure displayed minimal influence on the activity. Indeed, surprisingly conversion was reduced when pressure was increased {pressure of CO<sub>2</sub>; 10 bar = 44% conversion, 20 bar = 29% conversion and 40 bar = 26% conversion}. This was postulated to be due to an anti-solvent / insolubility effect occurring and both the catalyst and co-catalyst precipitating out of solution. Another possibility was dilution of the concentration of epoxide substrate in the reaction mixture as the PO volume expanded due to greater CO<sub>2</sub> absorption.<sup>[8]</sup>

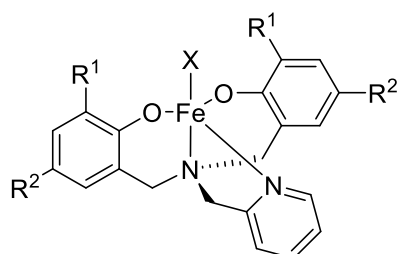
The observed colour change during the coupling reactions using Fe(**77–82**) was studied further and the *in-situ* formation of the  $\mu$ -oxo-bridged Fe(III) dimer species was postulated to be due to epoxide deoxygenation of the Fe(III)-chloride complex.<sup>[8]</sup> This species then also partakes in a 2<sup>nd</sup> less active catalytic cycle during the reaction (*Scheme 30*).<sup>[8]</sup> This hypothesis, and the formation of the  $\mu$ -oxo-bridged species, was supported using UV-Vis spectroscopy on the complexes and on aliquots of the reaction mixtures, and the identification of 2-chloropropane by-product *via* gas

chromatography–mass spectrometry (GC–MS).<sup>[8]</sup> This organochloride by–product was also observed in the stoichiometric reaction mixtures from <sup>1</sup>H NMR spectroscopy. This epoxide deoxygenation step was concluded to occur *via* a single electron transfer (SET) radical process of the  $\sigma^*$  orbital of the C–O bond from the Fe(III) centre as the reactivity is quenched and inhibited when performed with TEMPO (2,2,6,6–tetramethyl–1–piperidinyloxy); a commonly used radical scavenger.<sup>[8,35]</sup> After these findings and conducting kinetic studies the mechanism was deemed to be that shown in *Scheme 30*.<sup>[8]</sup> This discovery of epoxide deoxygenation is an important consideration, for CO<sub>2</sub> / epoxide coupling and copolymerisation, as it could be a potentially competing process and helps elucidate what actual active species may be present during these reactions upon possible transformation of the Fe(III) pre–catalyst.<sup>[4,8]</sup>

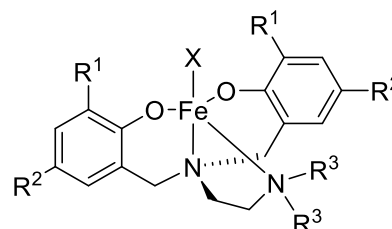


Scheme 30. Kerton and co-worker's proposed mechanism by mononuclear and dinuclear Fe(III)–amino–bis(phenolate) complexes. The dinuclear  $\mu$ -oxo-bridged Fe(III) species forming *via* a SET epoxide deoxygenation reaction of the Fe(III)–Cl complex. For the dinuclear cycle, for simplicity, the mechanism for only one Fe centre is shown. Both  $[\text{Fe}_\text{A}]$  and  $[\text{Fe}_\text{B}]$  are independent and could be active at the same time or separately. (Adapted from reference).<sup>[8]</sup>

In 2019, Kerton comprehensively built on this work to collect further SARs and, as well as using Fe(**78/79/81/82**) with diamino homopiperazinyl ligand backbones (Figure 56), synthesised and applied a further 12 Fe(III)–amino–bis(phenolate) complexes, with pendant amine donor groups, and a Fe(III)–salan–chloride complex to CO<sub>2</sub> / epoxide coupling (Figure 57).<sup>[22]</sup> This included re–synthesising and further applying Pescarmona’s Fe(III)–pyridylamino–bis(phenolate) complex {Fe(**75**) = Fe(**89**)} previously discussed.<sup>[17]</sup> The focus was to investigate the steric and electronic effect of the phenolate substituents, the arrangement and substituents on the pendant nitrogen donor atom and, not commonly discussed or explored in literature, the geometry of the Fe(III) centre {trigonal bipyramidal (tbp) vs. square based pyramidal (sbp)} on both the activity and product selectivity.<sup>[22]</sup>



Fe(**88**) R<sup>1</sup> = R<sup>2</sup> = Me, X = Cl  
 Fe(**89**) R<sup>1</sup> = R<sup>2</sup> = <sup>t</sup>Bu, X = Cl  
 Fe(**90**) R<sup>1</sup> = R<sup>2</sup> = Cl, X = Cl  
 Fe(**91**) R<sup>1</sup> = <sup>t</sup>Bu, R<sup>2</sup> = OMe, X = Cl  
 Fe(**92**) R<sup>1</sup> = <sup>t</sup>Bu, R<sup>2</sup> = OMe, X = Br



Fe(**93**) R<sup>1</sup> = R<sup>2</sup> = Me, R<sup>3</sup> = Me, X = Cl  
 Fe(**94**) R<sup>1</sup> = R<sup>2</sup> = Cl, R<sup>3</sup> = Me, X = Cl  
 Fe(**95**) R<sup>1</sup> = <sup>t</sup>Bu, R<sup>2</sup> = OMe, R<sup>3</sup> = Me, X = Cl  
 Fe(**96**) R<sup>1</sup> = <sup>t</sup>Bu, R<sup>2</sup> = OMe, R<sup>3</sup> = Et, X = Cl  
 Fe(**97**) R<sup>1</sup> = <sup>t</sup>Bu, R<sup>2</sup> = OMe, R<sup>3</sup> = <sup>i</sup>Pr, X = Cl  
 Fe(**98**) R<sup>1</sup> = <sup>t</sup>Bu, R<sup>2</sup> = OMe, R<sup>3</sup> = <sup>n</sup>Bu, X = Cl

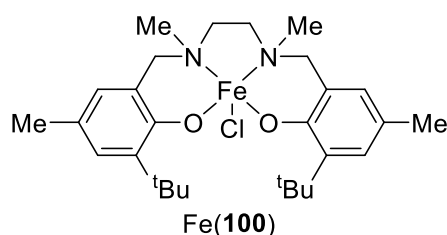
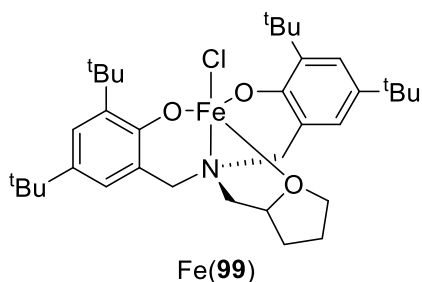


Figure 57. Kerton’s further comprehensive collection of Fe(III) complexes, focussing on an amino–bis(phenolate) framework, synthesised and applied to CO<sub>2</sub> / epoxide coupling.<sup>[22]</sup>

Firstly, all complexes {Fe(**88–100**)}, not previously reported, were screened with neat PO with PPNCl co–catalyst and the same conditions as before (20 bar of CO<sub>2</sub>, 100 °C, 22 hours, [Fe]:[PPNCl]:[PO] = 1:4:4000).<sup>[22]</sup> It was found that the tbp Fe(**88–99**) complexes were more active than the previously studied sbp Fe(**78/79/81/82**)

complexes.<sup>[8,22]</sup> This lower reactivity was attributed to epoxide deoxygenation occurring, forming the less active and corresponding  $\mu$ -oxo-bridged complexes  $\{[\text{Fe}(\mathbf{84}/\mathbf{85}/\mathbf{87})]_2\text{O}$ , *Scheme 30*). High conversions to the cyclic PC product were observed for all Fe(**88–100**) complexes and it was noted that, reactivity decreased when steric bulk was increased on the pendant nitrogen donor atoms  $\{\text{Fe}(\mathbf{95–98})\}$ . The chloro-substituted, Lewis acidic Fe(**90**) complex was the most active (99% conversion, TOF = 180 h<sup>-1</sup>) and was studied further.<sup>[22]</sup> Decreasing the temperature to 60 °C or pressure to 10 bar, reduced the reactivity (37% conversion and 76% conversion respectively) and no conversion was observed at room temperature. The TOF value could be increased to 1240 h<sup>-1</sup> by reducing the reaction time to two hours. The epoxide scope was also expanded to epichlorohydrin (ECH), AGE, phenylglycidyl ether (PGE) and SO using a reaction time of four hours, whereby high activities were observed (TOF = 993, 465, 627 and 422 h<sup>-1</sup> respectively).<sup>[22]</sup>

All complexes  $\{\text{Fe}(\mathbf{78}/\mathbf{79}/\mathbf{81}/\mathbf{82})$  and  $\text{Fe}(\mathbf{88–100})\}$  were applied to the more challenging internal CHO, at 60 °C, a high pressure of 60 bar of CO<sub>2</sub> for 22 hours  $\{[\text{Fe}]:[\text{PPNCl}]:[\text{CHO}] = 1:1:200, 0.5 \text{ mol\% of } [\text{Fe}]\}$ , with only one equivalent of co-catalyst, to probe the potential for ring opening copolymerisation (ROCOP) to the PCHC product.<sup>[22]</sup> Interestingly, all *tbp* complexes, except Fe(**96–98**) with sterically bulky pendant nitrogen donor atoms, exclusively formed the PCHC product with >99% carbonate linkages, low-to-modest molecular weights, narrow distributions ( $M_n = 3500\text{--}9200 \text{ g mol}^{-1}$ ,  $\text{Đ} = 1.02\text{--}1.14$ ) and no evidence for CHC formation.<sup>[22]</sup> Instead, Fe(**96–98**) achieved low conversions to the *cis*-CHC product (7–20%) with no PCHC observed. The *sbp* Fe(**78/79/81/82**) complexes were inactive and Fe(**100**) resulted in a low conversion of 34% to *cis*-CHC; the brick-red colour observed indicated epoxide deoxygenation was occurring. These results stressed the importance of the Fe(III) geometry on product selectivity and activity.<sup>[22]</sup>

The ROCOP was heavily influenced by the pendant nitrogen donor atom, phenolate substituents and halide auxiliary ligand.<sup>[22]</sup> The Fe(III)-Cl complex was more active than the corresponding Fe(III)-Br complex, and with *sp*<sup>2</sup>-hybridised pyridyl nitrogen pendant groups, electron donating aromatic substituents displayed higher conversions; sterics had minimal effect on reactivity. This trend was reversed when

modifying to  $sp^3$ -hybridised amine nitrogen groups, where electron withdrawing aromatic substituents increased activity. Therefore as well as the Fe(III) geometry, the combination of the pendant nitrogen group and electronics of the phenolate rings were essential for tuning the product activity and selectivity.<sup>[22]</sup>

The most active complex for ROCOP was found to be Fe(**91**) {99% conversion}, containing electron donating aromatic substituents and the pyridyl pendant nitrogen group, resulting in a modest molecular weight polymer and a narrow distribution ( $M_n = 9200 \text{ gmol}^{-1}$ ,  $\mathcal{D} = 1.14$ ).<sup>[22]</sup> Upon decreasing pressure, there remained modest reactivity at 7 bar  $\text{CO}_2$  but only 5% conversion was observed at 1 bar. Despite decreasing activity, good control was demonstrated with the molecular weights and dispersity remaining relatively constant {7 bar; 56% conversion,  $M_n = 5200 \text{ gmol}^{-1}$ ,  $\mathcal{D} = 1.09$ } and >99% carbonate linkages remained throughout.<sup>[22]</sup> Lastly, the catalyst was proven to be switchable when excess PPNCI co-catalyst was added (four equivalents) with the exclusive product shifting from perfectly alternating PCHC to *cis*-CHC (99% conversion); as was the case with the other rare switchable examples reported by Williams, Kleij and Pescarmona.<sup>[3,16,17,22]</sup>

There is a wide range of phenoxy-imine structures reported in literature, some recent examples are shown in *Figures 58* and *59*, and these have all been reviewed in detail by Della Monica.<sup>[1]</sup> This class of ligand framework has shown to achieve high activities to form the COC products. In 2013, Abu-Surrah and co-workers reported the use of Fe(II/III)-*bis*(phenoxy-imine)-chloride complexes for the selective coupling of  $\text{CO}_2$  with SO to form SC using one equivalent of TBAB (*Figure 58*) in solvent-free conditions.<sup>[36]</sup> It was demonstrated that the more electrophilic Fe(III) complexes {Fe(**101/102**) $_2\text{Cl}$ } were more active than the Fe(II) complexes {Fe(**103–105**) $\text{Cl}_2$ }, and the highest TOF value of  $209 \text{ h}^{-1}$  was observed using Fe(**101**) $_2\text{Cl}$ , bearing the naphthyl group on the donor imine atoms, at 5 bar of  $\text{CO}_2$ , 130 °C for seven hours. However, the thiophene Fe(II)(**103**) $\text{Cl}_2$  complex, bearing an aromatic sulfur donor atom, was more active than the other two Fe(II) complexes {Fe(**101**) $_2\text{Cl} = 74 \text{ h}^{-1}$ , Fe(**103**) $\text{Cl}_2 = 33 \text{ h}^{-1}$ , Fe(**104**) $\text{Cl}_2 = 12 \text{ h}^{-1}$ , Fe(**105**) $\text{Cl}_2 = 5 \text{ h}^{-1}$  at 130 °C, 5 bar of  $\text{CO}_2$ }.<sup>[36]</sup> In 2017, Abu-Surrah further built on this work by introducing a phenylene bridged backbone between the imine nitrogen donor atoms to form a range of Fe(III)-salen-chloride

(or alternatively Fe(III)–salophen–chloride) complexes bearing various EDGs or EWGs at the *ortho*-aromatic position (Figure 58).<sup>[37]</sup> These substituents all had beneficial effects on the activity, in relation to the unsubstituted complex {Fe(106)Cl}, for CO<sub>2</sub> / SO coupling to form the SC product at 6 bar of CO<sub>2</sub>, 130 °C for six hours with one equivalent of TBAB. In particular, Fe(109)Cl bearing diethylamine EWGs displayed the highest TOF and was twice as active in comparison to Fe(106)Cl {Fe(106)Cl = 136 h<sup>-1</sup> vs. Fe(109)Cl = 289 h<sup>-1</sup>}.<sup>[37]</sup>

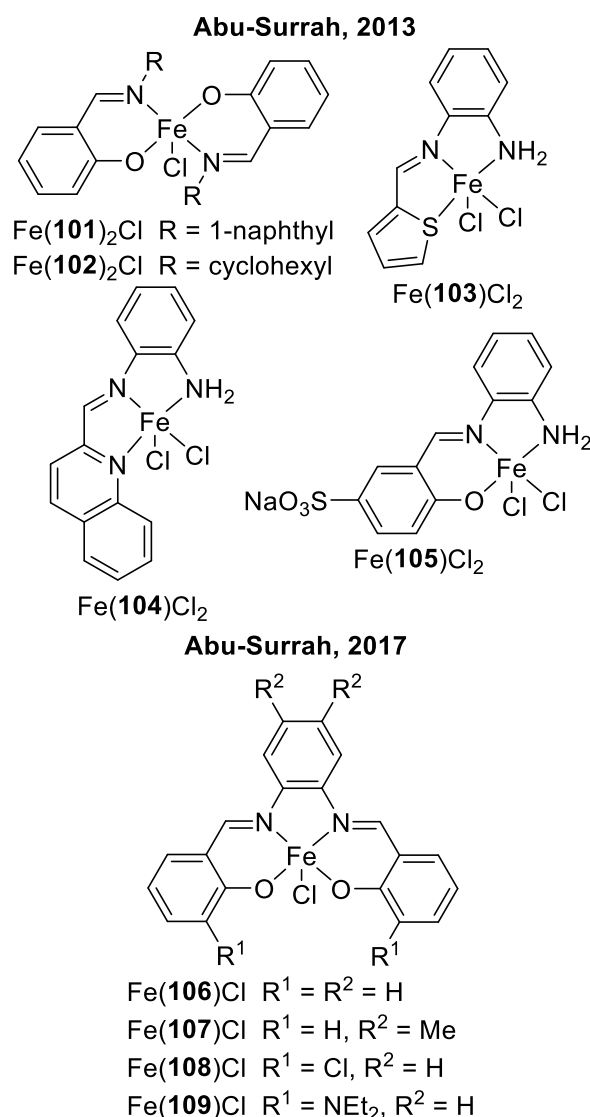


Figure 58. Abu-Surrah's Fe(II/III)–bis(phenoxy–imine)–chloride and Fe(III)–salen–chloride complexes.<sup>[36,37]</sup>

In 2018, Shaver, Garden and co-workers applied three similar, air-stable Fe(III)–bis(phenoxy–imine)–chloride complexes: Fe(40)<sub>2</sub>Cl, Fe(42)<sub>2</sub>Cl and Fe(46)<sub>2</sub>Cl containing unsubstitution, *tert*-butyl and chloro-groups at the *ortho*-aromatic

position to the exclusive formation of COC products; these were previously applied and discussed earlier in the ROP of *rac*-LA (**Section 3.3**, *Figure 41*).<sup>[25,38]</sup> The reaction conditions were explored using Fe(**42**)<sub>2</sub>Cl, where it was observed that both the [Fe] catalyst and TBAI co-catalyst were required for reactivity *via* a synergic effect; in agreement with that already discussed. It was determined that the optimum conditions were using distilled PO with 20 bar CO<sub>2</sub> at 120 °C for two hours using a low metal loading of 0.05 mol% and TBAB co-catalyst loading of 0.1 mol% ([PO]:[Fe]:[TBAX] = 2000:1:2).<sup>[25]</sup> Using these conditions, the complexes displayed remarkably high activities and the trend in reactivity was Fe(**42**)<sub>2</sub>Cl < Fe(**40**)<sub>2</sub>Cl < Fe(**46**)<sub>2</sub>Cl correlating with an increase in the electron withdrawing nature and subsequent increase in Lewis acidity for the Fe(III) centre {Fe(**40**)<sub>2</sub>Cl = 530 h<sup>-1</sup>, Fe(**42**)<sub>2</sub>Cl = 510 h<sup>-1</sup> and Fe(**46**)<sub>2</sub>Cl = 760 h<sup>-1</sup>}. Furthermore, the robustness of Fe(**46**)<sub>2</sub>Cl was demonstrated when high activities were still achieved when the reaction was conducted under air (TOF = 650 h<sup>-1</sup>) and 100 equivalents of water was added to the mixture (TOF = 430 h<sup>-1</sup>). The substrate scope was successfully expanded to five additional epoxides using this catalyst and the TOF value reached as high as 900 h<sup>-1</sup> for ECH. Interestingly, despite an extended reaction time of 24 hours, there was high activity observed for the sterically challenging, internal CHO (TOF = 80 h<sup>-1</sup>). The *cis*-CHC was exclusively formed, which as previously discussed (**Section 4.1**), is rare in literature due to the bicyclic ring strain. Of which, the majority of systems form the thermodynamic PCHC product or *trans*-CHC *via* backbiting or a mixture of products.<sup>[25]</sup>

Due to the vast range of reaction conditions possible for CO<sub>2</sub> / epoxide coupling, it is difficult to directly compare the activity of different Fe systems in literature, however as far as it is aware, the TOFs achieved using Fe(**46**)<sub>2</sub>Cl are among the highest reported for an Fe catalyst. It was proposed that the *tbp* metal geometry was critical for efficient catalysis; in agreement with literature, and the additional flexibility achieved using the phenoxy-imine ligand over more rigid frameworks, such as salen ligands, was advantageous in CO<sub>2</sub> / epoxide coupling.<sup>[14,22,39]</sup>

Examples of phenoxy-imine ligands with pendant, hemilabile nitrogen donor groups are also reported by Cuesta-Aluja and Repo (*Figure 59*).<sup>[40,41]</sup> Cuesta-Aluja *et al.*



studied two tridentate Fe(III)-*bis*(phenoxy-iminopyridinic) {NN'O} complexes {Fe(**110**/**111**)<sub>2</sub><sup>+</sup>}, differing by the chain length in the ligand backbone between the imine and pyridine donor groups, to the selective formation of SC.<sup>[40]</sup> Using metal loadings of 0.05 mol% and TBAB loadings of 0.25 mol% at 80 °C, 50 bar of CO<sub>2</sub> for one hour, TOF values of 401 h<sup>-1</sup> and 580 h<sup>-1</sup> were exhibited by Fe(**110**)<sub>2</sub><sup>+</sup> and Fe(**111**)<sub>2</sub><sup>+</sup> respectively. This difference in activity was postulated to occur due to differences in structural flexibility; the longer chain in Fe(**111**)<sub>2</sub><sup>+</sup> encourages dissociation of a hemilabile pyridine arm from the coordinatively saturated Fe centre for epoxide coordination, activation and hence catalysis. The authors offer no suggestion that the pendant pyridine groups are directly involved in the CO<sub>2</sub> / epoxide reaction but just in the wrapping of the Fe centre. The TOF value for Fe(**111**)<sub>2</sub><sup>+</sup> can be further increased to 900 h<sup>-1</sup> when decreasing the [Fe] and TBAB loadings to 0.025 mol% and 0.125 mol% respectively for 30 minutes. No reactivity was observed without the presence of co-catalyst. At this decreased [Fe] loading, Fe(**111**)<sub>2</sub><sup>+</sup> was also applied to eight further epoxides to their corresponding COC products, with the highest TOF value displayed using GLY (TOF = 3640 h<sup>-1</sup>). However, poor conversion, activity (TOF = 15 and 8 h<sup>-1</sup>) and selectivity was observed using CHO after 24 hours at an altered 0.2 mol% [Fe] loading; using both TBAB and PPNCI co-catalyst resulted in mixtures of PCHC (58% carbonate linkages) and CHC product.<sup>[40]</sup>

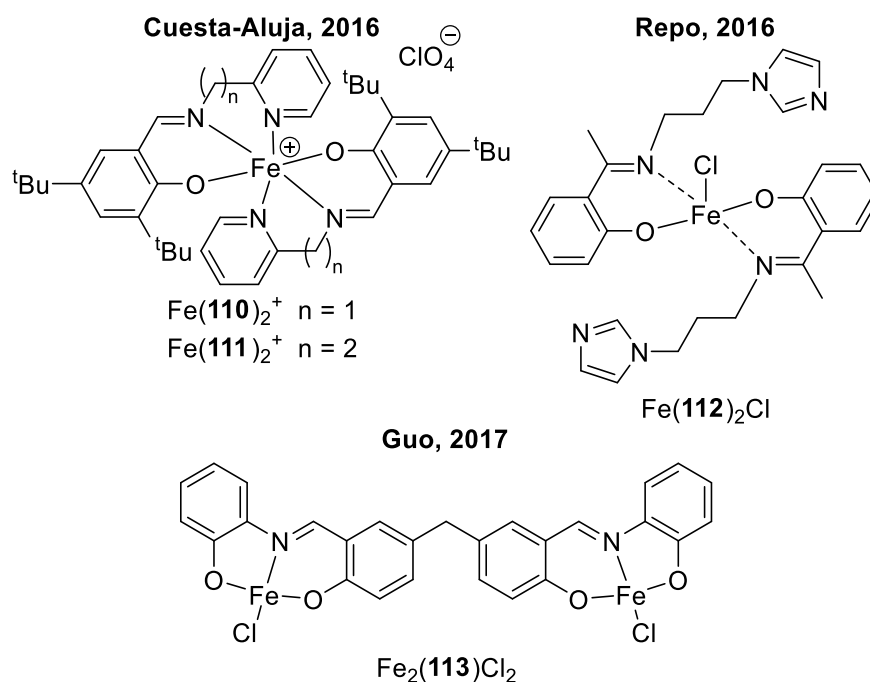


Figure 59. Cuesta–Aluja’s and Repo’s mononuclear Fe(III)–bis(phenoxy–imine) complexes and Guo’s dinuclear Fe(III)–bis(phenoxy–imine) complex.<sup>[40–42]</sup>

Repo and co-workers reported the synthesis and application of a bifunctional Fe(III)–bis(phenoxy–imino)–chloride complex with hemilabile, non-innocent imidazole pendant groups on the nitrogen donor atoms {Fe(**112**)<sub>2</sub>Cl} (Figure 59).<sup>[41]</sup> Unlike that for Cuesta–Aluja’s complexes, these Lewis basic groups are not coordinated to the Lewis acidic Fe(III) centre and therefore, this complex is able to act as a single component catalytic system, with no need for co-catalyst, for CO<sub>2</sub> / epoxide coupling. Using PO, the highest activity was observed at 100 °C, 10 bar of CO<sub>2</sub> for four hours using dichloromethane and a metal loading of 0.33 mol% (TOF = 56 h<sup>-1</sup>). Kinetic investigation, using *in-situ* FT–IR spectroscopy on the formation of PC, demonstrated the reaction proceeded with a first order dependence with respect to [Fe] to support an intramolecular mechanism and bifunctional catalyst. It was proposed the mechanism initiated with simultaneous coordination of the epoxide with the Lewis acidic Fe(III) centre and activation of a CO<sub>2</sub> molecule by a pendant imidazole group to form an intermediate anionic carbamate species. The activated epoxide is then opened by this anionic species and subsequent cyclisation or intramolecular ring closing regenerates Fe(**112**)<sub>2</sub>Cl and releases the COC product.<sup>[41]</sup> While Fe(**112**)<sub>2</sub>Cl effectively behaves as a single component catalytic system, the addition of TBAB co–

catalyst, to support ring opening of the epoxide, enhances activity (0.12 mol% of [Fe], 1 mol% of TBAB, three hours, TOF = 183 h<sup>-1</sup>). For this reason, these conditions were applied to four further epoxides: ECH, SO, 1-hexene oxide (HO) and CHO (TOF = 247 h<sup>-1</sup>, 96 h<sup>-1</sup>, 100 h<sup>-1</sup> and 8 h<sup>-1</sup> respectively).<sup>[41]</sup>

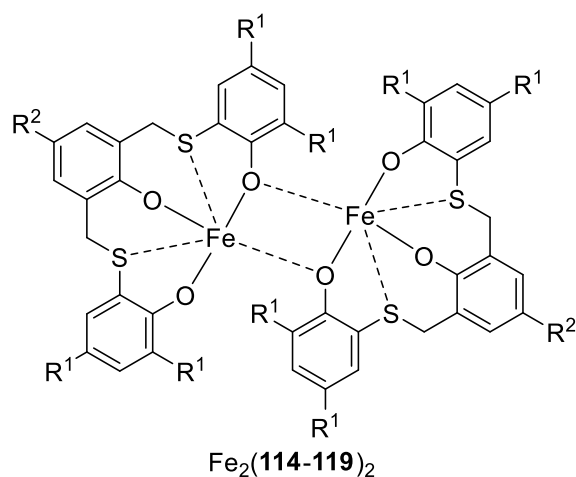
In 2017, Guo and co-workers reported a dinuclear, Fe(III)-bis(phenoxy-imino)-chloride complex {Fe<sub>2</sub>(**113**)Cl<sub>2</sub>} (*Figure 59*) to be the most active catalyst, for selective CO<sub>2</sub> / PO coupling to the PC product, for a series of complexes comprising of copper, zinc and iron.<sup>[42]</sup> This was achieved at 130 °C, 50 bar of CO<sub>2</sub> for three hours with 0.1 mol% of [Fe] and TBAB co-catalyst (selectivity = >99%, TOF = 323 h<sup>-1</sup>). However, as a result of the low yield obtained from the synthesis of Fe<sub>2</sub>(**113**)Cl<sub>2</sub>, the complex was not further applied to other epoxides.<sup>[42]</sup>

As previously discussed in **Sections 2.1** and **3.3**, Lamberti and co-workers reported the preparation of the first Fe(III)-salalen complex {Fe(**I**)Cl}, together with Fe(III)-salan {Fe(**J**)Cl} and -salen {Fe(**K/L**)Cl} complexes (**Section 2.1**, *Figure 5*).<sup>[43]</sup> These complexes were explored for their activity using PO at relatively mild conditions of 100 °C, 20 bar of CO<sub>2</sub> for 16 hours under solvent-free conditions with a metal loading of 0.025 mol% and varying equivalents of TBAB co-catalyst. Both catalyst and co-catalyst were required to observe reactivity.<sup>[43]</sup> Using two equivalents of TBAB (0.5 mol%) and varying the hybridisation of the nitrogen donor atoms, while maintaining the ethylene ligand backbone, aromatic substituents and chloride auxiliary ligand, the order of activity decreased from salan {Fe(**J**)Cl = 192 h<sup>-1</sup>} to salen {Fe(**K**)Cl = 160 h<sup>-1</sup>} to salalen {Fe(**I**)Cl = 110 h<sup>-1</sup>} in the selective formation of the PC product. Modifying the ethylene bridge on the Fe(**I**)Cl salalen complex, to a more flexible propylene backbone significantly increased reactivity {Fe(**L**)Cl = 193 h<sup>-1</sup>}; this observation agreed with that discussed by Garden.<sup>[25]</sup> As expected, increasing to four equivalents of TBAB, increased the observed activity {Fe(**J**)Cl = 213 h<sup>-1</sup>} and this higher loading was applied to the further screening of the complexes with SO and CHO.<sup>[43]</sup> The same reactivity trends observed for PO were present here, with the salan Fe(**J**)Cl and propyl bridged salalen Fe(**L**)Cl complexes displaying the highest activities {Fe(**J**)Cl and Fe(**L**)Cl; SO = 132 h<sup>-1</sup> and CHO = 35 h<sup>-1</sup>} with the *cis*-CHC, COC product exclusively formed using CHO.<sup>[43]</sup>

### 4.3 Fe-mediated CO<sub>2</sub> / epoxide coupling: thioether–phenolate frameworks

Another important class of ligand that has shown considerable success in CO<sub>2</sub> / epoxide coupling are thioether–phenolate frameworks.<sup>[6,7,19,44–46]</sup> Capacchione has heavily explored their use with Fe analogues and studied the role of softer, hemilabile sulfur donor atoms on catalysis. Their use has often been neglected in the past but recently progress has emerged and indeed this was well reviewed by Capacchione and co-workers recently.<sup>[15]</sup>

In 2015, the air-stable dinuclear Fe(III)–bis(thioether)–tri(phenolate) {OSOSO}, complex, Fe<sub>2</sub>(**114**)<sub>2</sub>, was synthesised and reported high activity for CO<sub>2</sub> / PO coupling to form PC exclusively (*Figure 60*).<sup>[6]</sup> It was determined the optimal solvent-free, reaction conditions for the system were at 100 °C, 20 bar of CO<sub>2</sub> for six hours using 0.025 mol% of [Fe] and 0.1 mol% of TBAB ([Fe]:[TBAB] = 1:2 molar ratio); resulting in an activity of 580 h<sup>-1</sup>.<sup>[6]</sup> The TBAB co-catalyst was more effective than other alternatives such as TBAI, PPNCl and DMAP. Using these conditions, the tolerance of the catalyst was demonstrated by its application to six further epoxides, resulting in high conversions and activities to their corresponding COC products. The two highest activities observed were that for ECH and GLY (TOF = 520 h<sup>-1</sup> and 633 h<sup>-1</sup> respectively).<sup>[6]</sup> As expected, the activity is reduced using CHO, with only 13% conversion observed, but remains an impressive 87 h<sup>-1</sup> to form the *cis*-CHC exclusively. Additionally, the stability of the complex was checked *via* the addition of excess pyridine and ECH (50 equivalents) where the dinuclear nature was preserved in solution with the magnetic moment and UV–vis spectrum unchanged.<sup>[6]</sup>



- 114** :  $\text{R}^1 = \text{R}^2 = \text{tBu}$   
**115** :  $\text{R}^1 = (\text{CH}_3)_2\text{Ph}$ ,  $\text{R}^2 = \text{tBu}$   
**116** :  $\text{R}^1 = \text{H}$ ,  $\text{R}^2 = \text{tBu}$   
**117** :  $\text{R}^1 = \text{Cl}$ ,  $\text{R}^2 = \text{tBu}$   
**118** :  $\text{R}^1 = \text{Me}$ ,  $\text{R}^2 = \text{Cl}$   
**119** :  $\text{R}^1 = \text{Me}$ ,  $\text{R}^2 = \text{tBu}$

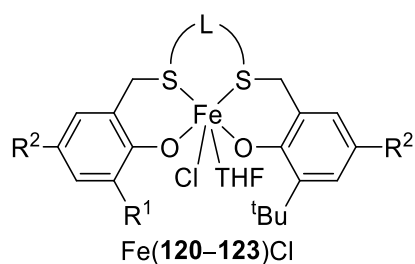
Figure 60. Capacchione's reported dinuclear Fe(III)–bis(thioether)–triphenolate {OSOSO} complexes.<sup>[6,44,45]</sup>

Five further variants were synthesised and the dinuclear Fe(III)–bis(thioether)–tri(phenolate) {OSOSO} family was expanded to probe SARs (Figure 60).<sup>[44,45]</sup>  $\text{Fe}_2(\mathbf{119})_2$ , consisting of methyl aromatic constituents at position  $\text{R}^1$ , was found to be the most active complex.<sup>[45]</sup> At relatively mild reaction conditions of 120 °C at 20 bar of  $\text{CO}_2$  with 0.01 mol% of catalyst and 0.1 mol% of TBAB ([PO]:[TBAB]:[Catalyst]=10000:10:1) for a short reaction period of one hour, 52% conversion and an activity of 5200  $\text{h}^{-1}$  was observed for  $\text{Fe}_2(\mathbf{119})_2$ . This enhanced catalytic system is further exemplified, when applied to a further epoxides, and particularly activities of 7000  $\text{h}^{-1}$ , 1300  $\text{h}^{-1}$  and 550  $\text{h}^{-1}$  for ECH, SO and CHO; indeed these activities are among the highest reported for Fe–mediated  $\text{CO}_2$  / epoxide coupling.<sup>[45]</sup> Introducing chloro–functionality at  $\text{R}^1$  or increasing the steric bulk decreased activity  $\{\text{Fe}_2(\mathbf{115}/\mathbf{117})_2$  and this was proposed to result from the decrease in Lewis acidity of the Fe(III) centre and the strengthening of the Fe–S bond, with sterics and solubility also playing a crucial role on the reaction rate.<sup>[45]</sup>

DFT calculations were performed to gain a deeper understanding into the reaction mechanism for these dinuclear catalysts.<sup>[45]</sup> It revealed, despite the presence of two

Fe(III) centres, only one centre was operating in the catalytic cycle and initial coordination of the epoxide to a Fe(III) centre was only possible *via* dissociation or detachment of a hemilabile sulfur atom to create the vacant coordination site required.<sup>[45]</sup> Overall, ring closing to form the COC product was found to be the rate determining step (RDS) for the monometallic reaction pathway and the lability of the sulfur donor atom is crucial to the system's activity.<sup>[15,45]</sup>

Later in 2018, attention shifted to mononuclear Fe(III)–*bis*(thioether)–*bis*(phenolate) {OSSO} complexes (*Figure 61*).<sup>[7]</sup> Upon activation with TBAB co-catalysts, these Fe systems were remarkably active at particularly mild neat conditions, of one bar of CO<sub>2</sub> and 35 °C, for COC formation from both internal and terminal epoxides. The most active catalyst was observed to be Fe(**123**)Cl with an activity of 290 h<sup>-1</sup> after one hour using 0.1 mol% metal loading, 0.5 mol% of TBAB co-catalyst and PO as the substrate ([PO]:[Fe]:[TBAB]=1000:1:5); although variations in the substituents on the ligand framework made only a minimal influence on the activity.<sup>[7]</sup>



- 120** : R<sup>1</sup> = CPh<sub>3</sub>, R<sup>2</sup> = Me, L = -CH<sub>2</sub>CH<sub>2</sub>-  
**121** : R<sup>1</sup> = R<sup>2</sup> = C(CH<sub>3</sub>)<sub>2</sub>Ph, L = -CH<sub>2</sub>CH<sub>2</sub>-  
**122** : R<sup>1</sup> = R<sup>2</sup> = Me, L = -CH<sub>2</sub>CH<sub>2</sub>-  
**123** : R<sup>1</sup> = R<sup>2</sup> = <sup>t</sup>Bu, L = -C<sub>6</sub>H<sub>10</sub>-

*Figure 61.* Capacchione's reported mononuclear Fe(III)–*bis*(thioether)–*bis*(phenolate) {OSSO} complexes.<sup>[7]</sup>

However, there was a deviation in the product formation when using CHO and the APC product, PCHC, was selectively afforded instead of *cis*-CHC with >99% carbonate linkages. The neat reaction conditions were modified to 10 bar of CO<sub>2</sub> at 80 °C with 0.1 mol% of both [Fe] and TBAC for a one hour reaction period.<sup>[7]</sup> Variations in the substituents on the ligand framework had more pronounced effects on the activity for PCHC formation; with Fe(**121**)Cl displaying the highest activity (TOF = 340 h<sup>-1</sup>) with reasonable molecular weights and narrow distribution (*M<sub>n</sub>* = 23200 gmol<sup>-1</sup> and 11000

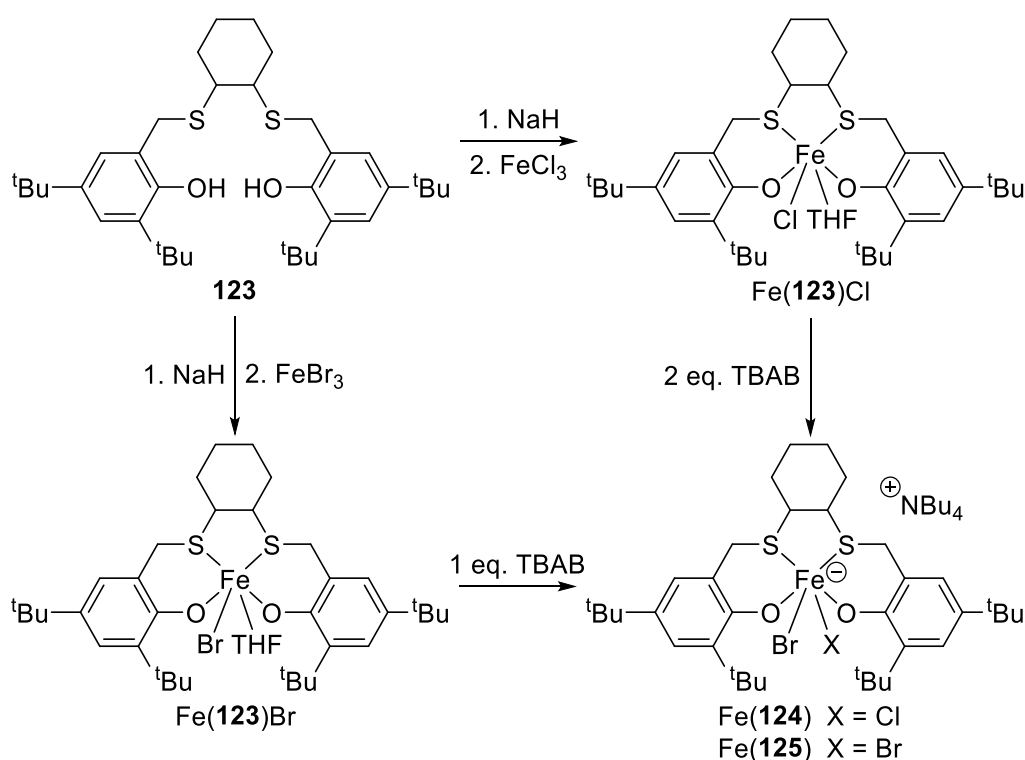
gmol<sup>-1</sup>, Đ = 1.01 and 1.03) by treating each peak separately for the bimodal polymer.<sup>[7]</sup> In the absence of co-catalyst, a low conversion of 16% (TOF = 27 h<sup>-1</sup>) with negligible carbonate linkages (7%) was observed after six hours. The activity was further increased to 400 h<sup>-1</sup> ( $M_n = 27800$  gmol<sup>-1</sup> and 12800 gmol<sup>-1</sup>, Đ = 1.01 and 1.06) using Fe(**121**)Cl with two equivalents of TBAC (0.2 mol%) and doubly distilled CHO over calcium hydride. As is commonly observed in literature, GPC analysis observed bimodality for the PCHC product and was attributed to traces of water impurity; hence, the CHO was distilled twice in this instance to minimise this impurity.<sup>[7]</sup>

A thorough kinetic study was investigated using FT-IR spectroscopy, and for PO / CO<sub>2</sub> coupling, there was second order and zero order dependence with respect to Fe(**121**)Cl and TBAB.<sup>[7]</sup> Crucially, however, this was conducted in the presence of excess TBAB and UV-Vis spectroscopy suggested the *in-situ* formation of a six-coordinate, anionic metallate ('ate'), ferrate catalytic species; this accounted for the behaviour that the second order dependence for Fe(**121**)Cl was only exclusively observed when two equivalents of TBAB was used.<sup>[7]</sup> This agreed with DFT calculations where the rate determining step was determined to be ring opening of the epoxide *via* two Fe centres. One [Fe] centre acting as a Lewis acid and coordinating / activating the epoxide and another [Fe] metallate centre providing the nucleophilic bromide for attack.

On the other hand, the reaction order was one with respect to Fe(**121**)Cl for CHO / CO<sub>2</sub> coupling. The epoxide ring opening was also proposed to be the rate determining step here *via* one Fe centre.<sup>[7]</sup> DFT calculations postulated the difference in product chemoselectivity between PO / CO<sub>2</sub> and CHO / CO<sub>2</sub> coupling was due to the crucial mononuclear Fe-carbonate intermediate species, from which either ring closing or further copolymerisation can occur. In the case of CHO, starting from this intermediate, the relative energy barrier for further chain propagation was lower and less energetically demanding than ring closure to form the COC product and the opposite trend was observed for PO.<sup>[7]</sup>

In 2019, the existence of these metallate, ferrate Fe(III) catalytic species was further confirmed when Fe(**124/125**) was isolated and characterised from both the chloro- and bromo-derivatives {Fe(**123**)Cl and Fe(**123**)Br} using two and one equivalents of

TBAB respectively (Scheme 31).<sup>[19]</sup> They were shown to potentially be the true catalytic species for CO<sub>2</sub> / epoxide coupling when it was demonstrated Fe(**124**) and Fe(**125**) complexes could be applied as single component catalytic systems for the formation of COC products from ten epoxide substrates. Under mild conditions of 35 °C, 1 bar of CO<sub>2</sub> and a [Fe] loading of 0.2 mol% with no co-catalyst for a six hour reaction period, low-to-moderate conversions and activities were observed (PO; 65% conversion, TOF = 54 h<sup>-1</sup>, SO; 26% conversion, TOF = 22 h<sup>-1</sup> and ECH; 42% conversion, TOF = 18 h<sup>-1</sup>).<sup>[19]</sup>



Scheme 31. Synthesis and isolation of anionic metallate Fe(III) species.<sup>[19]</sup>

Recently, with the aim of exploring the effect of the oxidation state on the Fe centre for CO<sub>2</sub> / epoxide coupling, Fe(II) and Fe(III) complexes {Fe(II)<sub>2</sub>(**126/127**)<sub>2</sub>, Fe(II)(**128**), Fe(III)<sub>2</sub>(**129/59b**)<sub>2</sub> and Fe(III)(**131**)} supported by *bis*(thioether)–phenolate {OSO} ligands were synthesised (Figure 62).<sup>[46]</sup> In solution, these complexes existed as either dinuclear or mononuclear species depending on the steric bulk of the aromatic substituents. The complexes were screened using 1–hexene oxide (HO) with 10 bar of CO<sub>2</sub>, in neat conditions at 90 °C for 24 hours using 0.1 mol% of [Fe] and 0.5 mol% of TBAB.<sup>[46]</sup> For the Fe(II) complexes, the activity depended on the aromatic groups



with the methyl substituted Fe(II)<sub>2</sub>(**126**)<sub>2</sub> the most active (TOF = 36 h<sup>-1</sup>) and the chloro- and diisopropyl-substituted complexes showing a similar, lower reactivity {TOF; Fe(II)<sub>2</sub>(**127**)<sub>2</sub> = 15 h<sup>-1</sup> and Fe(II)(**128**) = 17 h<sup>-1</sup>}. However, for the Fe(III) complexes, regardless of the ligand framework, all complexes displayed the same activity (TOF = 32 h<sup>-1</sup>).<sup>[46]</sup> After investigating thoroughly using UV-Vis spectroscopy, this was rationalised to be due to the Fe(III) complexes reacting with TBAB and forming the corresponding catalytic anionic metallate species, as previously discussed for the *bis*(thioether)-*bis*(phenolate) {OSSO} complexes, and that this was not occurring with the Fe(II) complexes. Fe(II)<sub>2</sub>(**126**)<sub>2</sub> and Fe(III)<sub>2</sub>(**129**)<sub>2</sub> were applied to further epoxides but were not as active in comparison with other reported systems for Capacchione.<sup>[15,46]</sup>

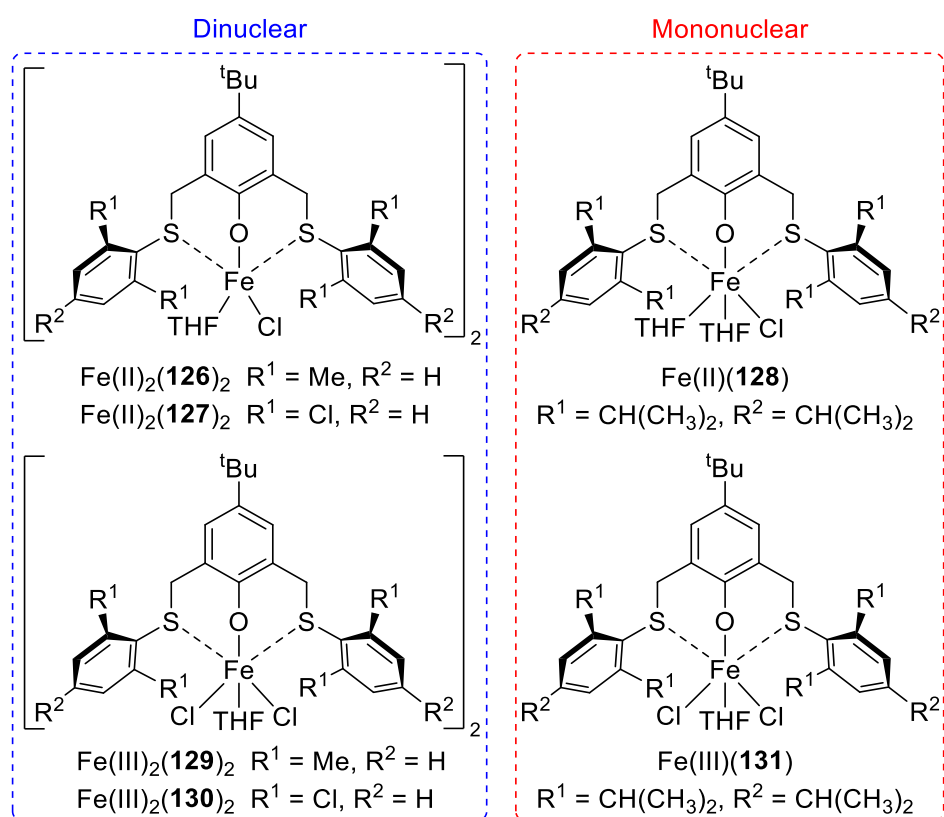


Figure 62. Capacchione's Fe(II) and Fe(III), mononuclear and dinuclear complexes bearing *bis*(thioether)-phenolate {OSO} ligand frameworks.<sup>[46]</sup>

## 4.4 Project aims

To our surprise, while Fe(III)–chloride complexes based on salalen, salan and salen ligand frameworks have been reported for CO<sub>2</sub> / epoxide coupling, to our knowledge, at the time, there were no examples of Fe(III)–acetate complexes being applied to CO<sub>2</sub> catalysis.<sup>[43]</sup> For this reason, it was decided to apply the large range of such complexes, synthesised and discussed in **Section 2.5** {Fe(1/3/5/6/8–17)OAc}, to study this catalytic process. Initially, screening of the complexes would be carried out to investigate SARs and from this, active and selective complexes would be explored further.

In 2019, building on from the work discussed using Fe(III)–salalen complexes for the ring opening polymerisation of *rac*-LA (**Sections 3.4–3.6**), a research group colleague, Stewart, reported the synthesis and application of Fe(III)–imine–thio–bis(phenolate) / ‘thiolen’–chloride complexes to the isoselective ROP of *rac*-LA {Fe(61–65)Cl, **Section 3.3**, *Figure 45*}.<sup>[47]</sup> There are scarce examples of thiolen frameworks in literature despite Kol and co-workers reporting their use when complexed with zirconium.<sup>[48,49]</sup> Despite the similarities shared with {OSSO} systems reported by Capacchione, discussed in **Section 4.3**, there was no example of thiolen–mediated CO<sub>2</sub> / epoxide coupling in literature. Interestingly, while attempting to recrystallise a Fe(III)–thiolen–chloride complex in air, the solid–state structure of a carbonato–bridged dinuclear, Fe species {[Fe(L)]<sub>2</sub>CO<sub>3</sub>}, *via* single–crystal X–ray diffraction, was reported.<sup>[47]</sup> As suggested by Muller and co-workers, this species could represent a potential intermediate for halide–free CO<sub>2</sub> / epoxide coupling.<sup>[50]</sup> It was proposed this occurred from oxygen incorporation from water and subsequent activation of atmospheric CO<sub>2</sub> *via* the sequence Fe(L)Cl → Fe(L)OH → [Fe(L)]<sub>2</sub>O → [Fe(L)]<sub>2</sub>CO<sub>3</sub>. This activation gave the suggestion that these Fe(III)–thiolen–chloride complexes would be able to efficiently catalysis CO<sub>2</sub> transformations. Due to this reason and the recent progress been reported with the use of softer, hemilabile sulfur donor atoms, it was decided to apply Stewart’s Fe(III)–thiolen–chloride {ONSO} complexes to CO<sub>2</sub> / epoxide coupling and compare these with the Fe(III)–salalen–chloride {ONNO} complexes {Fe(1–7)Cl} synthesised in **Section 2.3**, containing the

more commonly used, harder nitrogen donor atoms, to investigate the potential beneficial effect of having a sulfur atom.<sup>[15,47]</sup>

#### 4.5 CO<sub>2</sub> / cyclohexene oxide coupling using Fe(III)–acetate complexes and tetrabutylammonium chloride co–catalyst

All the Fe(III)–acetate complexes, discussed and synthesised earlier in **Section 2.5**, were tested for the catalytic coupling of CO<sub>2</sub> with distilled CHO. This would allow comparison between their structure frameworks and the activity and selectivity for this process. The reactions were performed under mild, solvent–free conditions with a 0.08 mol% catalyst loading and 0.64 mol% tetrabutylammonium chloride (TBAC) co–catalyst loading; commercially available and used as received, at 80 °C, 10 bar of CO<sub>2</sub> for 24 hours. The amounts of catalyst / co–catalyst to CHO were chosen following that employed by Lamberti, for their Al(III)–salalen complexes, and mainly due to the need for a sufficient volume of neat, reaction mixture to allow efficient stirring in the pressurised reactor chamber of the autoclave.<sup>[20]</sup> After the 24 hour time period, aliquots of the crude reaction mixture were taken for <sup>1</sup>H NMR spectroscopy to determine the product selectivity, conversion and activity of each reaction with each catalyst. This was achieved *via* integration of the observed characteristic methine proton resonance signals for *cis*–CHC, *trans*–CHC, PCHC and PCHO respectively compared with CHO (*Tables 17 and 18*). Under these conditions using these complexes, the *cis*–CHC was formed exclusively in the majority of cases. As mentioned earlier (**Section 4.1**), this product formation is rare in literature due to the bicyclic ring strain of CHC.<sup>[3,4,9,21,25]</sup> The use of excess co–catalyst, compared to the Fe catalyst, ensured ring closure and the double inversion, intramolecular S<sub>N</sub>2 pathway proceeded to form the *cis*–CHC product selectively (*Scheme 26*). The most common undesired side–product observed was the polyether, PCHO.

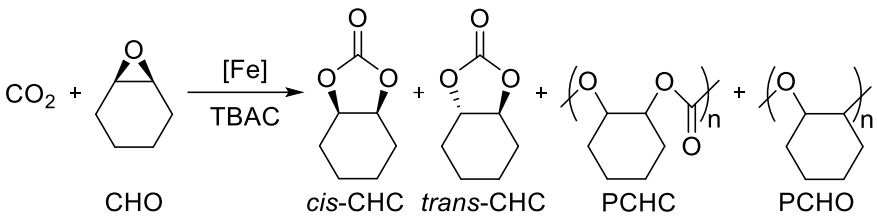
Alongside <sup>1</sup>H NMR spectroscopy, HR–MS and GPC analysis were applied to crude reaction mixtures to corroborate observations made. The presence of the cyclic CHC product was confirmed using ESI–MS, but this technique is unable to differentiate between the *cis*– and *trans*–CHC diastereomeric products. These can be distinguished using <sup>1</sup>H NMR spectroscopy, as would be expected theoretically, where

the methine proton resonance signal for *cis*-CHC is identified at  $\delta$  4.66 ppm and *trans*-CHC at  $\delta$  3.99 ppm, in agreement with that observed and reported in literature.<sup>[3]</sup> The methine proton resonance signal for the PCHC product is reported to appear close to that of the desired *cis*-CHC at  $\delta$  4.65 ppm.<sup>[3]</sup> Only one clear resonance signal was observed in this region in all cases and to ensure the identity of this signal was not that of the PCHC product, GPC analysis was used to confirm no evidence of polymer formation.

Initially, control reactions were conducted and the Fe(III)-salalen-acetate complexes applied to the coupling reaction. It was observed that no reaction took place with just solely the Fe catalyst with no nucleophilic TBAC co-catalyst to open the epoxide ring (*Table 17*, entry 6). Using TBAC, with Fe(OAc)<sub>2</sub> precursor or without any Fe catalyst displayed reactivity but with significantly decreased product selectivity for the *cis*-CHC (*Table 17*, entries 1 and 2, selectivity = 76% and 83% respectively). North and co-workers reported examples of salophen ligands (salen ligands with a 1,2-diaminophenyl bridge), that were able to carry out CO<sub>2</sub> / terminal epoxide coupling, without metal and halide co-catalyst, at 120 °C and 10 bar of CO<sub>2</sub>.<sup>[51]</sup> After conducting deuterium labelling studies with monodeuterated *trans*-decylene oxide, the reaction was postulated to occur *via* a H-bonding 'dual activation' mechanism; as will be discussed later.<sup>[51]</sup>

To check if salalen ligands held activity in this study, without the presence of metal, ligand **3** was applied to the coupling reaction with and without TBAC co-catalyst. The halide-free reaction displayed 0% conversion and activity was observed with the presence of co-catalyst but this was accompanied with poor selectivity (*Table 17*, entries 3 and 4). Overall, poor selectivity for the *cis*-CHC product was displayed for all the control reactions.

Table 17. CO<sub>2</sub> / CHO coupling reaction catalysed by Fe(1/3/5/6/10–12)OAc and TBAC.



Class of complex	Entry	Catalyst	Conv. <sup>a</sup> (%)	Selectivity	<i>cis</i> -CHC : <i>trans</i> -	TOF <sup>b</sup> (h <sup>-1</sup> )
				for <i>cis</i> -CHC <sup>a</sup> (%)	CHC : PCHC : PCHO ratio <sup>a</sup> (%)	
	1	Fe(OAc) <sub>2</sub>	48	76	76 : 1 : 0 : 23	25
	2	None	43	83	83 : 0 : 0 : 17	22
	3 <sup>c</sup>	Ligand <b>3</b>	0	–	–	0
	4	Ligand <b>3</b>	47	84	84 : 2 : 0 : 14	24
Salalen	5	Fe( <b>1</b> )OAc	40	>99	>99 : 0 : 0 : 0	21
	6 <sup>c</sup>	Fe( <b>3</b> )OAc	0	–	–	0
	7	Fe( <b>3</b> )OAc	45	>99	>99 : 0 : 0 : 0	23
	8 <sup>d</sup>	Fe( <b>3</b> )OAc	52	96	96 : 4 : 0 : 0	9
	9 <sup>e</sup>	Fe( <b>3</b> )OAc	47	>99	>99 : 0 : 0 : 0	24
	10	Fe( <b>5</b> )OAc	46	>99	>99 : 0 : 0 : 0	24
	11	Fe( <b>6</b> )OAc	44	>99	>99 : 0 : 0 : 0	23
	12	Fe( <b>10</b> )OAc	38	>99	>99 : 0 : 0 : 0	20
	13	Fe( <b>11</b> )OAc	46	>99	>99 : 0 : 0 : 0	24
	14	Fe( <b>12</b> )OAc	53	>99	>99 : 0 : 0 : 0	28

Conditions: [Fe] catalyst (0.08 mol%, 1 eq.), TBAC (0.64 mol%, 8 eq.), CHO (5.0 mL), 10 bar CO<sub>2</sub>, 80 °C, 24 h. <sup>a</sup> Determined *via* <sup>1</sup>H NMR spectroscopy using the methine resonances of *cis*-CHC (δ 4.66 ppm), *trans*-CHC (δ 3.99 ppm) and PCHO (δ 3.35 ppm). <sup>b</sup> TOF = [(Conv. (%) / 100) x (100 / 0.08 mol%)] / 24 h = [(Conv. / 100) x 1250] / 24. <sup>c</sup> No TBAC added. <sup>d</sup> Time = 72 h. <sup>e</sup> 20 bar of CO<sub>2</sub>.

After studying the Fe(III)–salalen–acetate complexes (Table 17), it was observed that, while retaining the ethylene ligand backbone, increasing the steric bulk at the aryl substituent position on the imine side of the backbone (R<sup>1</sup>), unexpectedly increased the conversion. This was despite the presumed decrease in Lewis acidity on the Fe(III) centre, due to the increasing electron donation of the bulkier aryl substituent *tert*-

butyl groups compared with hydrogen atoms, and the framework becoming more sterically hindered for catalysis and approaching substrate molecules; unfavourable electronic and steric effects not accounting for the increase in reactivity {Fe(**1**)OAc; R<sup>1</sup> = H, R<sup>2</sup> = Me, 40% conversion vs. Fe(**3**)OAc; R<sup>1</sup> = <sup>t</sup>Bu, R<sup>2</sup> = Me, 45% conversion}. Together with this increased conversion, selectivity was maintained at >99% for the *cis*-CHC product. Alternatively, increasing the Lewis acidity, by replacing the electron donating methyl group at R<sup>2</sup> and installing an electron withdrawing phenyl group on the amine donor atom also resulted in a decreased conversion {Fe(**10**)OAc; R<sup>1</sup> = <sup>t</sup>Bu, R<sup>2</sup> = Ph, 38% conversion}. Modifying Fe(**1**)OAc further, by varying the aryl substituents at R<sup>3</sup>, in the hope of making a more sterically unhindered, Lewis acidic complex; bromo-functionality was introduced. Varying these substituents, on the amine side of the backbone, increased the observed conversion {Fe(**11**)OAc; R<sup>1</sup> = H, R<sup>2</sup> = Me, R<sup>3</sup> = Br, 46% conversion} compared to Fe(**1**)OAc.

Focusing on Fe(**3**)OAc, further exploratory reactions revealed an increase in the pressure of CO<sub>2</sub> from 10 bar to 20 bar and reaction time from 24 hours to 72 hours resulted in a minor increase on conversion (*Table 17*, entry 7 vs. entries 8 and 9). The prolonged reaction time of 72 hours was accompanied by a slight decrease in product selectivity to 96%. Conversion and activity was marginally higher for this Fe(III)-salalen-acetate complex compared with the analogues Fe(III)-salalen-chloride complex but this will be discussed later in **Section 4.9** {Fe(**3**)OAc; 45% conversion vs. Fe(**3**)Cl; 41% conversion (**Section 4.9**, *Table 22*, entry 4)}.

While preserving the aryl substituents, modifying the ethylene ligand backbone of Fe(**3**)OAc by installing the rigid six-membered aminopiperidine ring or introducing a planar phenyl ring; both reducing the flexibility of the ligand backbone, resulted in minimal difference on reactivity {Fe(**5**)OAc; 46% conversion vs. Fe(**6**)OAc; 44% conversion}. Improving the flexibility of the ligand backbone by employing a propylene moiety, marginally increased conversion as was observed by Garden and Lamberti {Fe(**12**)OAc; 53% conversion}.<sup>[25,43]</sup>

Table 18. CO<sub>2</sub> / CHO coupling reaction catalysed by Fe(**8/13–17**)OAc and TBAC.

Class of complex	Entry	Catalyst	Conv. <sup>a</sup> (%)	Selectivity for <i>cis</i> -CHC <sup>a</sup> (%)	<i>cis</i> -CHC : <i>trans</i> -CHC : PCHC : PCHO ratio <sup>a</sup> (%)	TOF <sup>b</sup> (h <sup>-1</sup> )
Salan	1	Fe( <b>8<sub>meso</sub></b> )OAc	30	57	57 : 6 : 0 : 37	16
	2	Fe( <b>9<sub>meso</sub></b> )OAc	45	>99	>99 : 0 : 0 : 0	23
	3 <sup>c</sup>	Ligand <b>13</b>	0	–	–	0
	4	Ligand <b>13</b>	28	82	82 : 0 : 0 : 18	15
	5	Fe( <b>13</b> )OAc	66	>99	>99 : 0 : 0 : 0	34
Salen	6	Fe( <b>14</b> )OAc	28	>99	>99 : 0 : 0 : 0	15
	7	Fe( <b>15</b> )OAc	43	>99	>99 : 0 : 0 : 0	22
	8	Fe( <b>16</b> )OAc	52	>99	>99 : 0 : 0 : 0	27
	9	Fe( <b>17</b> )OAc	59	84	84 : 0 : 0 : 16	31

Conditions: [Fe] catalyst (0.08 mol%, 1 eq.), TBAC (0.64 mol%, 8 eq.), CHO (5.0 mL), 10 bar CO<sub>2</sub>, 80 °C, 24 h. <sup>a</sup> Determined *via* <sup>1</sup>H NMR spectroscopy using the methine resonances of *cis*-CHC (δ 4.66 ppm), *trans*-CHC (δ 3.99 ppm) and PCHO (δ 3.35 ppm). <sup>b</sup> TOF = [(Conv. (%) / 100) × (100 / 0.08 mol%)] / 24 h = [(Conv. / 100) × 1250] / 24. <sup>c</sup> No TBAC added.

Generally, compared to the salalen complexes, the Fe(III)–salan–acetate complexes were more effective (Table 18). Altering the ethylene backbone to a bipyrrolidine, and varying the hybridisation of the imine nitrogen donor atom to an amine donor atom (salalen to salan), preserved the product selectivity at >99% but offered no difference in the activity {Fe(**3**)OAc; R<sup>1</sup> = <sup>t</sup>Bu, 45% conversion vs. Fe(**9<sub>meso</sub>**)OAc; R<sup>1</sup> = <sup>t</sup>Bu, 45% conversion}. As was the case for the salalen complexes, decreasing the steric bulk of the aryl substituents, unexpectedly decreased the conversion despite the presumed increase in Lewis acidity on the Fe(III) centre {Fe(**8<sub>meso</sub>**)OAc; R<sup>1</sup> = Me, 30% conversion}. In addition to this decreased activity, the product selectivity was less controlled with 37% of PCHO and 6% of *trans*-CHC observed in the crude product

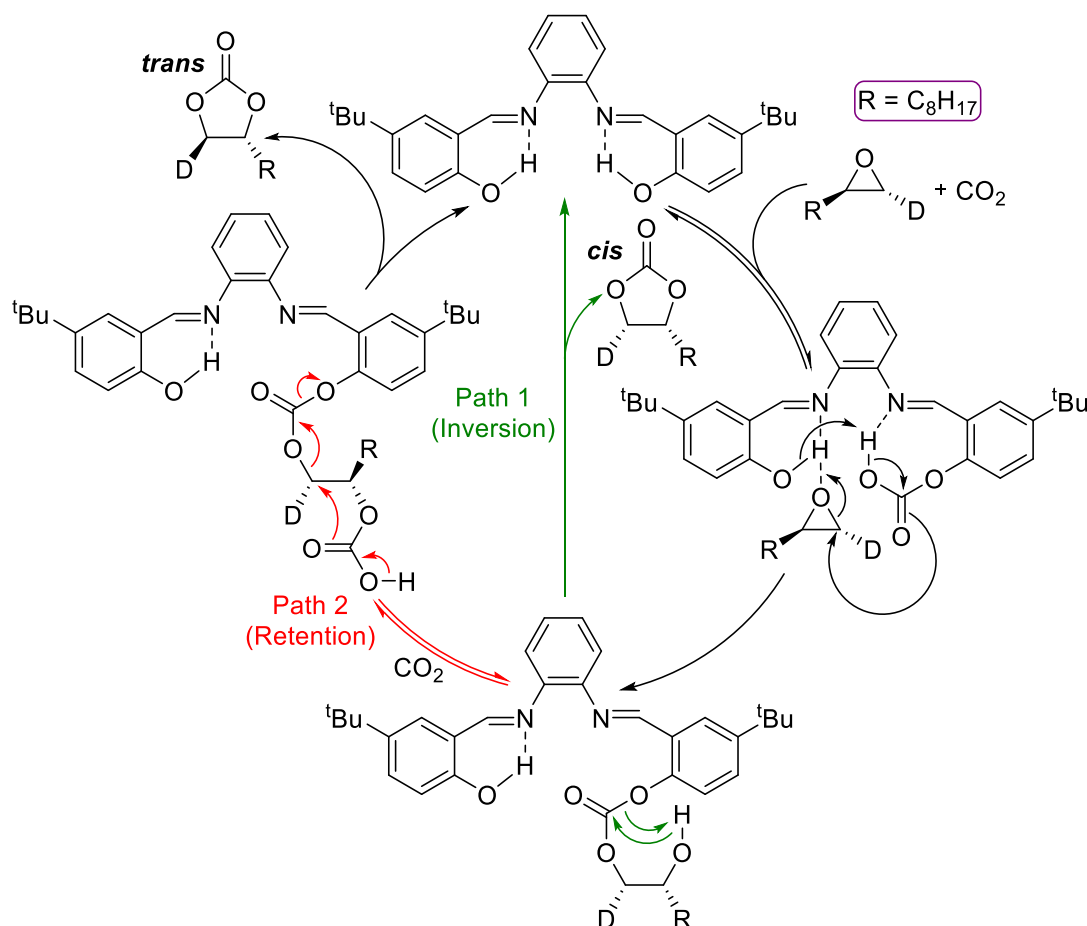
mixture {*cis*-CHC:*trans*-CHC:PCHC:PCHO ratio = 57:6:0:37}. This poor selectivity could be attributed to the poor elemental analysis afforded for Fe(**8**<sub>meso</sub>)OAc, where unreacted Fe(OAc)<sub>2</sub> precursor was attributed as the potential cause, and may explain and relate to this rare observation for low selectivity in this screening study. Overall, Fe(**13**)OAc, the reduced analogue of the Fe(III)–salalen–acetate complex Fe(**5**)OAc, containing an NH amine group and rigid aminopiperidine ring on the other nitrogen donor atom, was the most effective catalyst in this coupling study with a conversion of 66% and *cis*-CHC the exclusive product (*Table 18*, entry 5).

As was the case for the Fe(III)–salalen and –salan–acetate complexes, the reduction of steric bulk for the aryl substituents resulted in decreased conversion for the Fe(III)–salen–acetate complexes (*Table 18*, entries 6 vs. 7 and 8 vs. 9). Activity was increased using Fe(**17**)OAc, by introducing planarity and a phenyl ring into the ethylene backbone of Fe(**15**)OAc {Fe(**15**)OAc; 43% conversion vs. Fe(**17**)OAc; 59% conversion}, and this complex observed the second highest activity in this screening study. However, this higher reactivity was less controlled and was accompanied with a decreased product selectivity of 84% with the formation of the PCHO side-product {*cis*-CHC:*trans*-CHC:PCHC:PCHO ratio = 84:0:0:16}.

As was discussed earlier, North reported salophen ligands that carried out CO<sub>2</sub> / terminal epoxide coupling *via* a postulated ‘dual activation’ mechanism.<sup>[51]</sup> This cyclic carbonate synthesis mechanism relies on intramolecular H–bonding interactions, of the uncomplexed salophen, whereby the hydrogen atoms are shared between the imine and phenol groups on each side of the phenyl bridge. These hydrogen atoms can interact with incoming CO<sub>2</sub> and epoxide molecules and undergo organocatalysis. As illustrated by *Scheme 32*, the phenol groups on the salophen activate both the epoxide and CO<sub>2</sub> to produce a carbonic half–ester intermediate that initiates the intramolecular ring opening of the activated epoxide; the intramolecular H–bonding increasing the nucleophilicity of the weak nucleophilic phenol group, to give the inverted intermediate alcohol intermediate. There are two possible pathways from this intermediate to displace COC products. Immediate intramolecular cyclisation of the intermediate, with the alcohol group attacking the carbonyl of the carbonate, produces the *cis*-COC product with an overall inversion of the stereochemistry with



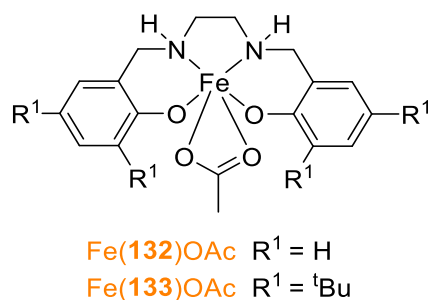
respect to the starting epoxide (**Path 1**). Another possibility, is that a second molecule of CO<sub>2</sub> is activated by the intermediate alcohol to produce a *bis*-carbonate intermediate which cyclises and collapses to eliminate the *trans*-COC product, with the second inversion step resulting in an overall retention of the stereochemistry with respect to the starting epoxide (**Path 2**), and returns to the salophen organocatalyst.<sup>[51]</sup>



*Scheme 32.* North's proposed mechanism for salophen-mediated CO<sub>2</sub>/epoxide coupling, to form both the *cis*- and *trans*-COC products, using monodeuterated *trans*-decylene oxide. (Modified from reference).<sup>[51]</sup>

The dramatic improvement in activity of the reduced Fe(**13**)OAc complex, compared to Fe(**5**)OAc {Fe(**13**)OAc; 66% vs. Fe(**5**)OAc; 46%} was attributed to the possible involvement of the NH group in H-bonding interactions, with the incoming CO<sub>2</sub> and epoxide molecules (ligand-substrate interactions), to complement metal mediation. Recently, Romain highlighted the importance of H-bonding, noncovalent interactions (NCIs) and hydrogen bond donors for catalytic reactions; in this example

for the ring opening polymerisation of *rac*-lactide using highly active Al–catam complexes.<sup>[52]</sup> To explore this concept further, the synthesis of two Fe(III)–salan–acetate complexes, Fe(**132**)OAc and Fe(**133**)OAc, with NH moieties was attempted (*Figure 63*). Both complexes contained ethylene backbones and were targeted to observe if activity increased with the number of NH groups. In comparison with the Fe(III)–salen–acetate complexes, Fe(**14**)OAc and Fe(**15**)OAc, with no NH groups and two imine functionalities, this rationale was observed {R<sup>1</sup> = H; Fe(**14**)OAc, 28% conversion vs. Fe(**132**)OAc, 36% conversion and R<sup>1</sup> = <sup>t</sup>Bu; Fe(**15**)OAc, 43% conversion vs. Fe(**133**)OAc, 58% conversion}. Product selectivity was maintained at >99% for Fe(**132**)OAc but the higher reactivity observed for Fe(**133**)OAc was accompanied with a decreased product selectivity of 92% {*cis*-CHC:*trans*-CHC:PCHC:PCHO ratio = 92:2:0:6}.



*Figure 63.* The targeted and attempted synthesis of Fe(III)–salan–acetate complexes, Fe(**132/133**)OAc, with NH moieties.

Characterisation for the complexes confirmed the coordination of the salan ligand to the Fe(III) metal centre *via* HR–MS and observed acetate bond and aromatic C=C stretches in the FT–IR spectra. However, due to the poor elemental analysis results observed for the bulk of the sample, and no solid–state structures, it cannot be confirmed with confidence that these complexes were synthesised. Nonetheless, the characterisation data acquired is included in **Section 6.10**.

Without the presence of metal, as was the case for ligand **3**, the salan ligand **13** was applied to the coupling reaction with and without TBAC co–catalyst to check for potential organocatalysis *via* H–bonding interactions. Despite the additional, hydrogen bond donor NH group, the halide–free reaction displayed 0% conversion and poor product selectivity with the TBAC co–catalyst (*Table 18*, entries 3 and 4).

Surprisingly, in the presence of TBAC, the activity was dramatically lower for ligand **13** compared to ligand **3** while the poor product selectivity was maintained {ligand **13**, 28% conversion vs. ligand **3**, 47% conversion}. As discussed by North, despite the presence of intramolecular H-bonding in salophen / salen ligands, analysis of the solid-state structures revealed the point group symmetry ( $C_1$  vs.  $C_2$  symmetry) and arrangement of the diiminobenzene plane in relation to the phenol rings may contribute to differences in organocatalytic activity and effectiveness. This hypothesis could potentially explain the inactivity of ligands **3** and **13** with the intramolecular H-bonding interactions incorrectly arranged and the diamine plane misaligned. However, as reminded by North, the solid-state structures may not reflect the active catalytic species in solution, as  $^1\text{H}$  NMR spectroscopy observed all compounds in the study to be the same  $C_2$ -symmetry regardless of their solid-state differences.

#### 4.6 Exploring $\text{CO}_2$ / cyclohexene oxide coupling with chiral complexes

As was discussed in **Section 2.8**, the chirality of the 2,2'-bipyrrolidine salan backbone of  $\text{Fe}(\mathbf{8}_{meso})\text{OAc}$  was explored and the synthesis of the two other possible stereoisomers  $\text{Fe}(\mathbf{8}_{RR})\text{OAc}$  and  $\text{Fe}(\mathbf{8}_{SS})\text{OAc}$  was attempted. The structure and coordination around the Fe centre could be altered *via* the chirality of the backbone to form potentially new species with increased activity when applied to different processes such as the asymmetric  $\text{CO}_2$  / epoxide coupling reaction.<sup>[53]</sup>

The enantiomeric complexes,  $\text{Fe}(\mathbf{8}_{RR})\text{OAc}$  and  $\text{Fe}(\mathbf{8}_{SS})\text{OAc}$ , were applied to the coupling of CHO with  $\text{CO}_2$  and compared with  $\text{Fe}(\mathbf{8}_{meso})\text{OAc}$  from the previous section (*Table 19*). Compared to the *meso* diastereomer, conversion increased moderately for the (*S,S*) stereoisomer and dramatically increased and doubled for the (*R,R*) stereoisomer. Additionally, the higher reactivity was more controlled and was accompanied with an increased product selectivity { $\text{Fe}(\mathbf{8}_{meso})\text{OAc}$ ; 30% conversion, 57% product selectivity vs.  $\text{Fe}(\mathbf{8}_{SS})\text{OAc}$ ; 47% conversion, >99% product selectivity vs.  $\text{Fe}(\mathbf{8}_{RR})\text{OAc}$ ; 60% conversion, >99% product selectivity}. HR-MS confirmed the coordination of the 2,2'-bipyrrolidine ligand to the Fe(III) metal centre and FT-IR was in agreement the Fe(III)-acetate complex was formed, however, single-crystal X-ray

diffraction confirmed the solid-state structure of Fe(**8<sub>RR</sub>**)OAc to be the six-coordinate, *pseudo*-octahedral Fe(**8<sub>RR</sub>**)Y<sub>2</sub> (Y = OEt, OAc, HOEt or HOAc) with two monodentate auxiliary groups instead of the expected single bidentate acetate auxiliary group. This may explain the stark increase in reactivity for the (*R,R*) enantiomer due to a change in the structure of this species in comparison to Fe(**8<sub>meso</sub>**)OAc. Unfortunately, the solid-state structure for Fe(**8<sub>SS</sub>**)OAc was not obtained therefore it is unknown whether the increased reactivity observed for this complex was due to a change in coordination around the metal centre {Fe(**8<sub>SS</sub>**)Y<sub>2</sub>} or solely the structure framework {Fe(**8<sub>SS</sub>**)OAc}.

Table 19. CO<sub>2</sub> / CHO coupling reaction catalysed by Fe(**8<sub>meso</sub>**/**8<sub>RR</sub>**/**8<sub>SS</sub>**)OAc and TBAC.

Class of complex	Entry	Catalyst	Conv. <sup>a</sup> (%)	Selectivity	<i>cis</i> -CHC : <i>trans</i> -	TOF <sup>b</sup> (h <sup>-1</sup> )
				for <i>cis</i> - CHC <sup>a</sup> (%)	CHC : PCHC : PCHO ratio <sup>a</sup> (%)	
<b>Salan</b>	1	Fe( <b>8<sub>meso</sub></b> )OAc	30	57	57 : 6 : 0 : 37	16
	2	Fe( <b>8<sub>RR</sub></b> )OAc	60	>99	>99 : 0 : 0 : 0	31
	3	Fe( <b>8<sub>SS</sub></b> )OAc	47	>99	>99 : 0 : 0 : 0	24

Conditions: [Fe] catalyst (0.08 mol%, 1 eq.), TBAC (0.64 mol%, 8 eq.), CHO (5.0 mL), 10 bar CO<sub>2</sub>, 80 °C, 24 h. <sup>a</sup> Determined *via* <sup>1</sup>H NMR spectroscopy using the methine resonances of *cis*-CHC (δ 4.66 ppm), *trans*-CHC (δ 3.99 ppm) and PCHO (δ 3.35 ppm). <sup>b</sup> TOF = [(Conv. (%) / 100) x (100 / 0.08 mol%)] / 24 h = [(Conv. / 100) x 1250] / 24.

#### 4.7 Applying various co-catalysts and conducting an epoxide scope using the Fe(III)-acetate complex, Fe(**13**)OAc

Using the most effective Fe(III)-acetate complex, Fe(**13**)OAc, other commercially available co-catalysts were trialled instead of TBAC (Table 20, entries 2, 3 and 4 vs. entry 1 or Table 18, entry 5). It was observed that all other alternatives had adverse effects on the activity of the catalysis. The exclusive product remained *cis*-CHC when

the co-catalyst was either tetrabutylammonium bromide (TBAB) or *bis*(triphenylphosphine)iminium chloride (PPNCI) but conversion was reduced. Using tetrabutylammonium acetate (TBAAC) as the co-catalyst, with the same acetate anion as the catalyst's auxiliary ligand, was both less selective and active. One potential and / or contributing reason for the observation of these results could be due to the solubility of the co-catalyst in the solvent-free conditions and in neat CHO. At room temperature, TBAC was the most soluble in the reaction mixture, before addition to the autoclave, and was observed to be the most active co-catalyst.

Table 20. CO<sub>2</sub> / CHO coupling reaction catalysed by Fe(**13**)OAc and various other co-catalysts.

Entry	Co-catalyst	Conv. <sup>a</sup> (%)	Selectivity for <i>cis</i> - CHC <sup>a</sup> (%)	<i>cis</i> -CHC : <i>trans</i> - CHC : PCHC : PCHO ratio <sup>a</sup> (%)	TOF <sup>b</sup> (h <sup>-1</sup> )
1	TBAC	66	>99	>99 : 0 : 0 : 0	34
2	TBAB	57	>99	>99 : 0 : 0 : 0	30
3	TBAAC	32	64	64 : 17 : 0 : 19	17
4	PPNCI	58	>99	>99 : 0 : 0 : 0	30

Conditions: [Fe] catalyst (0.08 mol%, 1 eq.), TBAC (0.64 mol%, 8 eq.), CHO (5.0 mL), 10 bar CO<sub>2</sub>, 80 °C, 24 h. <sup>a</sup> Determined *via* <sup>1</sup>H NMR spectroscopy using the methine resonances of *cis*-CHC (δ 4.66 ppm), *trans*-CHC (δ 3.99 ppm) and PCHO (δ 3.35 ppm). <sup>b</sup> TOF = [(Conv. (%) / 100) x (100 / 0.08 mol%)] / 24 h = [(Conv. / 100) x 1250] / 24.

Building on the results from Table 20, the Fe(**13**)OAc catalyst and TBAC co-catalyst combination was applied to a commercially available, terminal epoxide scope (Table 21). As was the case for the reactions using CHO as the epoxide, <sup>1</sup>H NMR spectroscopy, HR-MS and GPC analysis were all applied to the crude reaction mixtures after the reaction time period. <sup>1</sup>H NMR spectroscopy was used to identify the product and determine the COC yield, HR-MS corroborated the presence of the COC product and GPC analysis confirmed no polymer was formed. Robustness and

high functional group tolerance was observed and, while varying both the electronics and sterics of the distilled epoxide, moderate-to-high yields to the corresponding COC product was achieved.

Table 21. CO<sub>2</sub> coupling with a variety of epoxides catalysed by Fe(13)OAc and TBAC.

Entry	Epoxide	COC yield <sup>a</sup> (%)	TOF <sup>b</sup> (h <sup>-1</sup> )	
1		PO	79	41
2		SO	66	34
3		ECH	75	39
4		PGE	97	51
5 <sup>c</sup>		PGE	81	63
6		AGE	93	48

Conditions: [Fe] catalyst (0.08 mol%, 1 eq.), TBAC (0.64 mol%, 8 eq.), epoxide (5.0 mL), 10 bar CO<sub>2</sub>, 80 °C, 24 h. <sup>a</sup> Determined *via* <sup>1</sup>H NMR spectroscopy. <sup>b</sup> TOF = [(Conv. (%) / 100) x (100 / 0.08 mol%)] / 24 or 16 h = [(Conv. / 100) x 1250] / 24 or 16. <sup>c</sup> Reduced reaction time of 16 h.

As expected, propylene epoxide (PO) was more reactive and attained a higher observed yield (79% yield) compared to the internal, sterically bulky CHO due to its sterically unhindered structure (Table 18, entry 5, 66% conversion). There was similar reactivity, when installing a sterically bulky phenyl group on the terminal methyl, by applying styrene oxide (SO) with a modest 66% yield. This was presumed to be resulting from the similar steric profiles of SO and CHO and not electronics. The reactivity and ring opening of the epoxide was generally increased, as expected, by

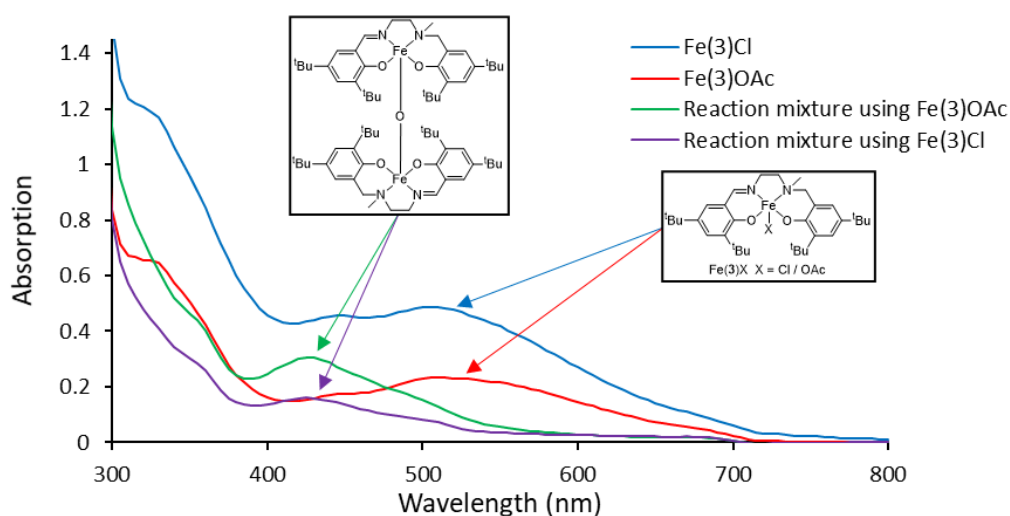
the addition of EWGs. A modest yield of 75% was produced with epichlorohydrin (ECH) bearing a chloro–EWG. High yields were realised using phenylglycidyl ether (PGE) and allylglycidyl ether (AGE) (97% and 93% yields respectively). When using PGE as the epoxide, towards the end of the 24 hour reaction period, there was solidification of the phenoxymethyl ethylene carbonate product, out of the crude reaction mixture, that inefficiently hindered the mechanical stirring of the autoclave reactor chamber. For this reason, the reaction was repeated at a reduced 16 hour reaction period and an increased TOF value of  $63 \text{ h}^{-1}$  was afforded (*Table 21*, entry 5).

#### 4.8 Examining colour change using ultraviolet–visible spectroscopy

During the  $\text{CO}_2$  / epoxide coupling reactions, and when applying CHO as the epoxide in particular, it was observed that the colour of the reaction mixtures changed from dark purple to dark red / brown. As noted and discussed in **Section 4.2**, this was also recently observed by Kerton and co–workers for their Fe(III)–amino–*bis*(phenolate)–chloride complexes.<sup>[8]</sup> It was postulated that this was due to epoxide deoxygenation of the Fe(III)–chloride complexes during the  $\text{CO}_2$  / epoxide coupling reaction to form a  $\mu$ –oxo–bridged Fe(III) dimer species. This species then also partakes in a 2<sup>nd</sup> less active catalytic cycle during the reaction. This hypothesis, and the formation of the  $\mu$ –oxo–bridged species, was supported using UV–Vis spectroscopy on the complexes and on aliquots of the reaction mixtures, and the identification of 2–chloropropane by–product *via* gas chromatography–mass spectrometry (GC–MS).<sup>[8,35]</sup> After these findings, conducting reactions using TEMPO and kinetic studies, the mechanism was deemed to be that shown in *Scheme 30* (**Section 4.2**).<sup>[8]</sup> Building on this work by Kerton, UV–Vis spectroscopy was explored to probe, the potential, that epoxide deoxygenation was occurring in this coupling study with the Fe(III)–acetate complexes to account for the change in colour of the reaction mixtures from dark purple to dark red / brown.<sup>[8]</sup>

In acetonitrile solvent and absorbance mode, as shown in *Figure 64*, UV–Vis spectroscopy was recorded between 300–800 nm for Fe(3)OAc, Fe(3)Cl and aliquots of the crude  $\text{CO}_2$  / CHO coupling reaction mixtures catalysed by these two catalysts

and TBAC (*Tables 17 and 22*). There were diagnostic absorption bands at 515 nm and a small peak at 450 nm for Fe(**3**)OAc and 505 nm and 445 nm for Fe(**3**)Cl. These were assigned as ligand-to-metal charge-transfer (LMCT) bands from the transitions between the phenolate moiety of the ligand and high-spin Fe(III) centre, as was accepted by Kerton and Lamberti,<sup>[8,34,43]</sup> and responsible for the visibly observed dark purple colour. As expected, with oxygen being a more electronegative heteroatom than chlorine, these transfer bands also indicatively show Fe(**3**)OAc is marginally more Lewis acidic than Fe(**3**)Cl. Most importantly, the absence of any observed absorption band around 430 nm suggested no  $\mu$ -oxo-bridged Fe(III) dimer species were present in the bulk of the samples before they were applied to CO<sub>2</sub> / epoxide coupling; in agreement with the elemental analysis results for the complexes discussed in **Chapter 2**. The absorption bands at and below 300 nm are not diagnostic, as they are present with or without Fe in literature,<sup>[43]</sup> and assigned as  $\pi$ - $\pi^*$  transitions between the phenolate rings of the ligand framework.

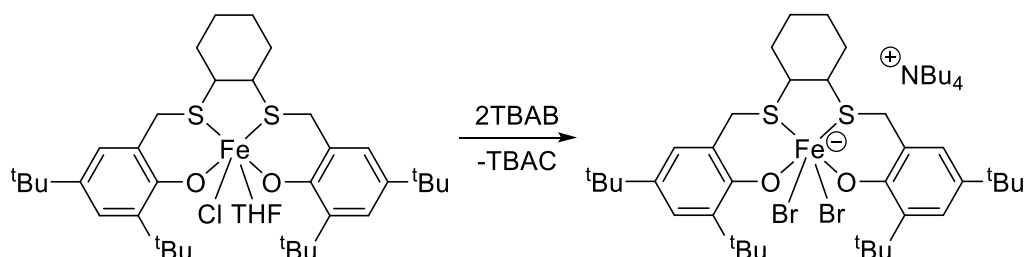


*Figure 64.* UV-Vis absorption spectra, recorded between 300–800 nm, for Fe(**3**)OAc, Fe(**3**)Cl and aliquots of the crude CO<sub>2</sub> / CHO coupling reaction mixtures catalysed using Fe(**3**)OAc and Fe(**3**)Cl.

After the CO<sub>2</sub> / CHO coupling reactions using Fe(**3**)OAc and Fe(**3**)Cl, by analysing aliquots of the crude reaction mixtures, show changes in the UV-Vis absorption spectra. There was a hypsochromic shift in the absorption bands toward 425 nm and 430 nm respectively due to the proposed formation of the  $\mu$ -oxo-bridged Fe(III) dimer species in the reaction mixture.<sup>[22]</sup> This formation is believed to be responsible for the change in colour of the reaction mixture to dark red / brown. Despite shifting



from a chloride to a more stable, bidentate auxiliary group, these UV–Vis spectroscopy observations agree with that reported by Kerton and implies that epoxide deoxygenation was occurring in this CO<sub>2</sub> / epoxide coupling study.<sup>[22]</sup>



Scheme 33. The formation of an anionic Fe(III) metallate species upon the addition of excess TBAB to Fe–bis(thioether)–bis(phenolate)–chloride complex.<sup>[7]</sup>

Recently, as discussed in **Section 4.3**, while applying mononuclear Fe–bis(thioether)–bis(phenolate) {OSSO}–chloride complexes to CO<sub>2</sub> / epoxide coupling and monitoring the reaction *via* UV–Vis spectroscopy, Capacchione and co-workers reported that upon the addition of excess TBAB to a Fe(III)–{OSSO}–Cl complex, the *in-situ* formation of six-coordinate, anionic Fe(III) metallate species was occurring (Schemes 31 and 33).<sup>[1,7]</sup> To confirm whether this species could be forming in this study and potentially contributing or causing the colour change, UV–Vis spectroscopy was conducted on a mixture of Fe(3)OAc combined with excess TBAC in acetonitrile (Figure 65). The solution remained purple, with no colour change observed, and the profile of the absorption spectrum was unchanged compared to that of just the Fe(3)OAc complex without TBAC (Figure 64). This suggested no anionic metallate species was forming in this study, causing the reaction mixture colour change.<sup>[7]</sup>

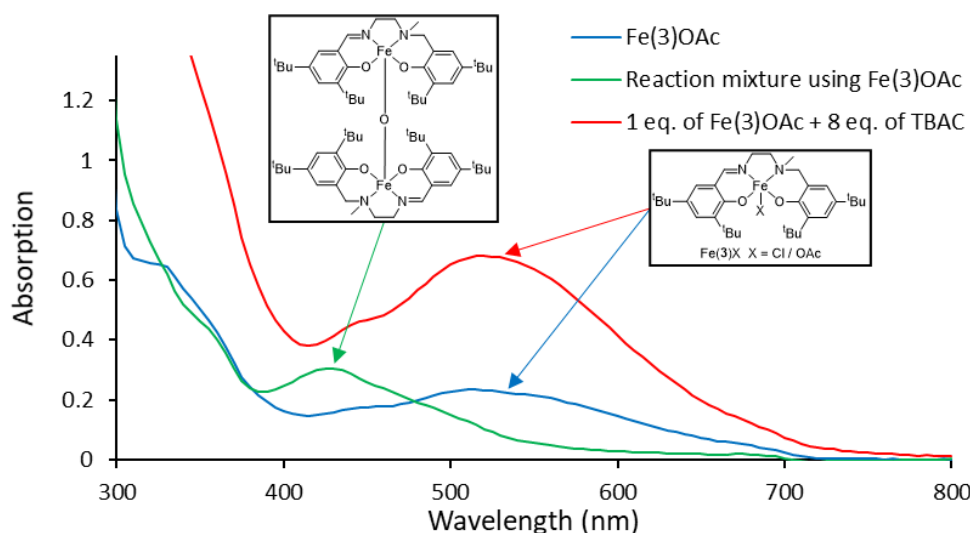


Figure 65. UV-Vis absorption spectra, recorded between 300–800 nm, for Fe(3)OAc, aliquots of the crude CO<sub>2</sub> / CHO coupling reaction mixture catalysed using Fe(3)OAc and a mixture of Fe(3)OAc with excess TBAC.

#### 4.9 CO<sub>2</sub> / cyclohexene oxide coupling using Fe(III)–salalen and –thiolen complexes and tetrabutylammonium chloride co-catalyst

As discussed in **Section 4.4**, despite the similarities shared with Capacchione’s {OSSO} systems, there was no example of thiolen-mediated CO<sub>2</sub> / epoxide coupling in literature. Due to the observation of a carbonato-bridged dinuclear Fe solid-state structure {[Fe(L)]<sub>2</sub>CO<sub>3</sub>}, suggesting the activation of atmospheric CO<sub>2</sub>, and the recent progress been reported with the use of softer, hemilabile sulfur donor atoms, it was decided to apply Stewart’s Fe(III)–thiolen {ONSO} complexes to CO<sub>2</sub> / epoxide coupling (Figure 66 and **Section 3.3**, Figure 45).<sup>[15,47]</sup> These were to be compared with the Fe(III)–salalen–chloride {ONNO} complexes {Fe(1–7)Cl}, synthesised in **Section 2.3**, to investigate the potential beneficial effect of having a softer, hemilabile donor sulfur atom (Figure 66).

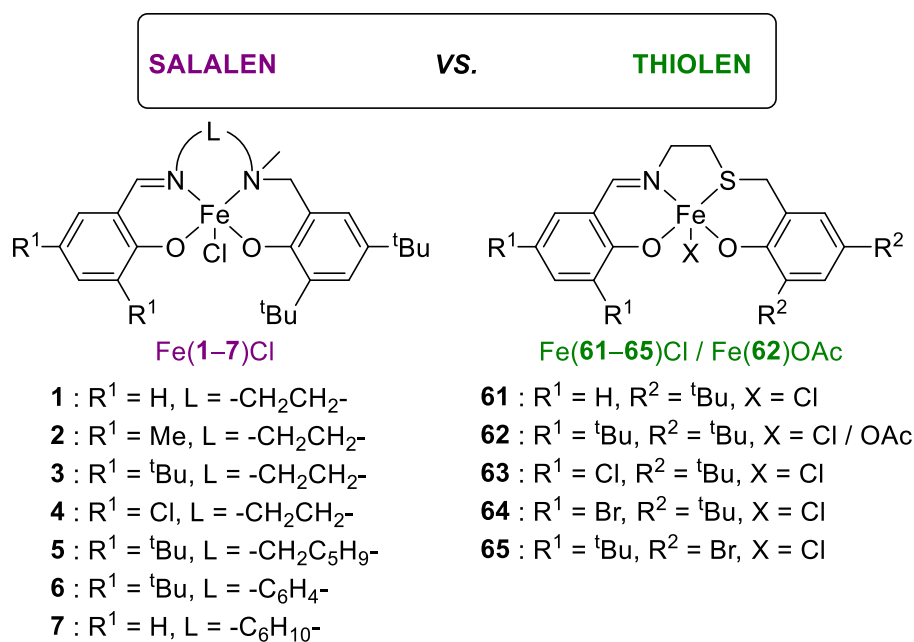


Figure 66. Stewart's Fe(III)–thiolen–chloride {ONSO} complexes compared with the synthesised Fe(III)–salalen–chloride {ONNO} complexes {Fe(1–7)Cl}.<sup>[47]</sup>

The Fe(III)–salalen and –thiolen–chloride complexes (Figure 66) were screened for the catalytic coupling of CO<sub>2</sub> with distilled CHO and TBAC co-catalyst (Table 22) using the same mild, solvent-free conditions and amounts used for the Fe(III)–acetate complexes (Section 4.5). As was the case earlier; the product selectivity, conversion and activity of each reaction was determined using <sup>1</sup>H NMR spectroscopy, by taking aliquots of the crude reaction mixture after the 24 hour reaction period. HR–MS and GPC analysis were applied alongside to corroborate observations made using <sup>1</sup>H NMR spectroscopy and ensure the *cis*–CHC product was indeed being formed and not PCHC. Overall, the strained *cis*–CHC product was exclusively formed at 80 °C, with the exception of Fe(64)Cl (Table 22). In all cases, the colour of the reaction mixtures changed during the reaction from dark purple to dark red / brown, as was observed for the Fe(III)–acetate complexes; this was attributed to the  $\mu$ -oxo-bridged Fe(III) dimer species forming in the reaction mixture *via* reported epoxide deoxygenation as discussed in Section 4.8.<sup>[8]</sup>

Table 22. CO<sub>2</sub> / CHO coupling reaction catalysed by Fe(1–7)Cl or Fe(61–65)Cl/ Fe(62)OAc and TBAC.

Class of complex	Entry	Catalyst	Conv. <sup>a</sup> (%)	Selectivity	<i>cis</i> -CHC : <i>trans</i> -	TOF <sup>b</sup> (h <sup>-1</sup> )
				for <i>cis</i> - CHC <sup>a</sup> (%)	CHC : PCHC : PCHO ratio <sup>a</sup> (%)	
	1	FeCl <sub>3</sub>	44	83	83 : 1 : 0 : 16	23
Salalen	2	Fe(1)Cl	53	>99	>99 : 0 : 0 : 0	28
	3	Fe(2)Cl	47	>99	>99 : 0 : 0 : 0	24
	4	Fe(3)Cl	41	>99	>99 : 0 : 0 : 0	21
	5	Fe(4)Cl	44	>99	>99 : 0 : 0 : 0	23
	6	Fe(5)Cl	48	>99	>99 : 0 : 0 : 0	25
	7	Fe(6)Cl	46	>99	>99 : 0 : 0 : 0	24
	8	Fe(7)Cl	51	>99	>99 : 0 : 0 : 0	27
Thiolen	9	Fe(61)Cl	47	>99	96 : 4 : 0 : 0	24
	10	Fe(62)Cl	43	>99	>99 : 0 : 0 : 0	22
	11	Fe(63)Cl	54	>99	>99 : 0 : 0 : 0	28
	12	Fe(64)Cl	51	90	90 : 1 : 0 : 9	27
	13	Fe(65)Cl	60	>99	>99 : 0 : 0 : 0	31
	14 <sup>c</sup>	Fe(65)Cl	75	94	94 : 1 : 0 : 5	156
	15	Fe(62)OAc	44	>99	>99 : 0 : 0 : 0	23

Conditions: [Fe] catalyst (0.08 mol%, 1 eq.), TBAC (0.64 mol%, 8 eq.), CHO (5.0 mL), 10 bar CO<sub>2</sub>, 80 °C, 24 h. <sup>a</sup> Determined *via* <sup>1</sup>H NMR spectroscopy using the methine resonances of *cis*-CHC (δ 4.66 ppm), *trans*-CHC (δ 3.99 ppm) and PCHO (δ 3.35 ppm). <sup>b</sup> TOF = [(Conv. (%) / 100) x (100 / 0.08 mol%)] / 24 h = [(Conv. / 100) x 1250] / 24. <sup>c</sup> 120 °C, 6 h.

Initially, the control reaction using FeCl<sub>3</sub> precursor with TBAC was carried out (Table 22, entry 1) and, although activity was present, *cis*-CHC was not the exclusive product with two additional undesired, minor side-products reducing the product selectivity: *trans*-CHC and PCHO identified in the reaction mixture. This result was

similar to the previously discussed TBAC control reaction without any metal catalyst, where PCHO alone hindered the selectivity (*Table 17*, entry 2). All control reactions stressed the need for an ancillary ligand framework around the Fe(III) centre to target that exclusivity in conjunction with the halide TBAC co-catalyst to aid epoxide ring opening and closing.

Unlike the Fe(III)-acetate complexes, for both the salalen and thioen complexes, decreasing the steric bulk at R<sup>1</sup> resulted in increasing Lewis acidity on the Fe(III) centre, reduced steric hindrance for incoming reagent molecules and an increased conversion {Fe(**1**)Cl; R<sup>1</sup> = H, 53% conversion vs. Fe(**2**)Cl; R<sup>1</sup> = Me, 47% conversion vs. Fe(**3**)Cl; R<sup>1</sup> = <sup>t</sup>Bu, 41% conversion and Fe(**61**)Cl; R<sup>1</sup> = H, 47% conversion vs. Fe(**62**)Cl; R<sup>1</sup> = <sup>t</sup>Bu, 44% conversion}. Despite the reduction in steric hindrance by the aryl substituents (R<sup>1</sup>) and increased reactivity, product selectivity was controlled and maintained at >99% for the *cis*-CHC product. Predominately, the salalen complexes were less active than their thioen counterparts in all cases except for the unsubstituted aryl structures; where in this one example the salalen complex was more active than the thioen analogue {Fe(**1**)Cl; R<sup>1</sup> = H, 53% conversion vs. Fe(**61**)Cl; R<sup>1</sup> = H, 47% conversion}. This enhanced thioen reactivity, as was the case for the ROP of *rac*-LA, was postulated to be due to the more labile, softer sulfur donor atom and the weaker metal-donor interaction / bond creating more space surrounding the Fe(III) centre for the binding of incoming reagent molecules, such as epoxide.<sup>[47]</sup> These structure-activity-relationships (SARs) observed, were similar to that for the complexes in the ROP of *rac*-LA.<sup>[47]</sup>

A very similar reactivity was achieved between the Fe(III)-thioen-chloride and-acetate complexes both bearing *tert*-butyl aryl substituents {R<sup>1</sup> = <sup>t</sup>Bu; Fe(**62**)Cl, X = Cl, 43% conversion vs. Fe(**62**)OAc; X = OAc, 44% conversion}. This trend deviates to the Fe-salalen-acetate and -chloride complexes bearing *tert*-butyl aryl substituents, as was previously discussed, with the acetate complex displaying minimally higher activity {Fe(**3**)OAc; 45% conversion vs. Fe(**3**)Cl; 41% conversion (**Section 4.5**, *Table 17*, entry 7)}. Indeed, for this *tert*-butyl aryl substitution with ethylene ligand backbones, this is the only example in this study where all four classes of Fe(III) complex {Fe(III)-salalen / thioen-acetate /chloride) can be compared directly. All the catalysts

resulted in similar conversions and exclusive selectivity (>99% for the *cis*-CHC) with the Fe-salalen-acetate complex only minimally the most active in this case. However, for the unsubstituted aryl ( $R^1 = H$ ), ethylene ligand backbones, whereby three classes of complex could be compared, the Fe(III)-salalen-chloride complex was moderately more active compared to the -acetate analogue and Fe(III)-thiolen-chloride ( $\{R^1 = H, L = CH_2CH_2; Fe(1)Cl, 53\%$  conversion vs.  $Fe(1)OAc, 40\%$  conversion vs.  $Fe(61)Cl, 47\%$  conversion}).

Focussing on the salalen and modifying the ethylene ligand backbone for  $Fe(3)Cl$ , by installing the rigid six-membered aminopiperidine ring or introducing a planar phenyl ring; both reducing the flexibility of the ligand backbone, resulted in increased activity ( $\{Fe(5)Cl; L = -CH_2C_5H_9-, 48\%$  conversion and  $Fe(6)Cl; L = -C_6H_4-, 46\%$  conversion}. Additionally, both these two modifications were minimally more active compared to their Fe(III)-acetate analogues ( $\{Fe(5)OAc; L = -CH_2C_5H_9-, 46\%$  conversion and  $Fe(6)OAc; L = -C_6H_4-, 44\%$  conversion} (*Table 17*, entries 10 and 11). There was a minimal decrease on reactivity upon moving from the ethylene ligand backbone of the unsubstituted  $Fe(1)Cl$  complex to a more inflexible and sterically hindered cyclohexane ring of the unsubstituted  $Fe(7)Cl$  complex ( $\{R^1 = H; Fe(1)Cl, L = -CH_2CH_2-, 53\%$  conversion vs.  $Fe(7)Cl, L = -C_6H_{10}-, 51\%$  conversion}).

Maintaining the ethylene ligand backbone for the salalen, the aryl substituents were modified by introducing chloro-functionality ( $R^1 = Cl$ ) to both the salalen and thiolen ligand frameworks. As expected, the increase in the Lewis acidity of the Fe(III) centre, increased the observed activity; the salalen complex was moderately less active than the thiolen ( $\{R^1 = Cl; Fe(4)Cl, 44\%$  conversion vs.  $Fe(63)Cl, 54\%$  conversion}. Using the Fe(III)-thiolen-chloride complexes, halide substitution was explored further by varying the chloro-functionality at the  $R^1$  position to the heavier bromide. This presumably decreased the Lewis acidity of the Fe(III) centre, due to the less electronegative halo-functionality, and resulted in the slight decrease in activity observed ( $\{Fe(63)Cl; R^1 = Cl, 54\%$  conversion vs.  $Fe(64)Cl; R^1 = Br, 51\%$  conversion}. In addition to this, the product selectivity was reduced to 90% and was the only Fe(III)-chloride complex in this study to not form the *cis*-CHC as the exclusive product at 80 °C. The activity was moderately increased further by shifting the bromo-

functionality from the imine–phenolate moiety ( $R^1$ ) to the thio–phenolate moiety ( $R^2$ ) {Fe(**65**)Cl;  $R^1 = \text{tBu}$ ,  $R^2 = \text{Br}$ , 60% conversion) with *cis*–CHC selectivity returning to >99%. This was the most active Fe(III)–chloride complex observed (TOF = 31 h<sup>-1</sup>) in this study and was similar to the Fe(III)–salen, –salan and –salalen–chloride complexes reported by Lamberti, using CHO at 20 bar CO<sub>2</sub>, 100 °C for 22 hours (TOF = 24–35 h<sup>-1</sup>).<sup>[43]</sup> Using a shorter reaction time period of six hours and increasing the temperature to 120 °C, the TOF value was increased to 156 h<sup>-1</sup> (Table 22, entry 14). However, this increased activity was accompanied with PCHO and *trans*–CHC formation decreasing the product selectivity to 94%.

#### 4.10 Investigating variant equivalents of co–catalyst and conducting an epoxide scope using the Fe(III)–thiolen–chloride complex, Fe(**65**)Cl

Building on the results from Table 22, using the most active Fe(**65**)Cl catalyst (synthesised by Stewart), the amount of equivalents of TBAC co–catalyst was varied to study the effect upon reactivity and selectivity (Table 23).<sup>[47]</sup> Without any TBAC and at zero equivalents, as was the case when applied to Fe(**3**)OAc earlier (Table 17, entry 6), there was no reactivity observed. The activity was improved when increasing the concentration of TBAC and the product selectivity was affected favourably; although a mixture of products was observed at two and four equivalents, the *cis*–CHC selectivity increased from 79% to 94% (Table 23, entries 2 and 3). Increasing the co–catalyst loading further to eight equivalents, as was done in all the screening reactions (Tables 17, 18 and 22), ensured the *cis*–CHC was the exclusive product formed (>99% product selectivity) and, in this case with the Fe(**65**)Cl catalyst, achieved the highest TOF value observed for the Fe(III)–chloride complexes at 80 °C (Table 22, entry 13 or Table 23, entry 4). These observations are in agreement with the findings reported by Lamberti’s Al(III)–salalen–chloride complexes.<sup>[20]</sup> As has been discussed in literature and in Section 4.1, these results highlight the importance of using a co–catalyst, and particularly at elevated amounts, to target COCs for this reaction, specifically *cis*–CHC in this case. This encourages the generation of carbonate anions, promotes the intramolecular ring closing reaction and discourages further binding and insertion of epoxide molecules to form PCHC.<sup>[3,20]</sup> Although, again just to note, despite using no or low amounts of TBAC and

favouring further binding and discouraging the ring closing path, there was no reactivity and the PCHC product was not observed; this demonstrated the Fe(III) catalyst was not 'switchable' at these reaction conditions.

Table 23. CO<sub>2</sub> / CHO coupling reaction catalysed by Fe(65)Cl and various equivalents of TBAC co-catalyst.

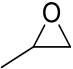
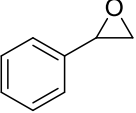
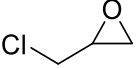
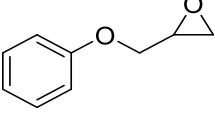
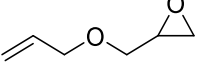
Entry	Equivalents of co-catalyst	Conv. <sup>a</sup> (%)	Selectivity for <i>cis</i> - CHC <sup>a</sup> (%)	<i>cis</i> -CHC : <i>trans</i> - CHC : PCHC : PCHO ratio <sup>a</sup> (%)	TOF <sup>b</sup> (h <sup>-1</sup> )
1	0	8	0	0 : 0 : 0 : >99	4
2	2	8	79	79 : 8 : 0 : 13	4
3	4	42	94	94 : 4 : 0 : 2	22
4	8	60	>99	>99 : 0 : 0 : 0	31

Conditions: [Fe] catalyst (0.08 mol%, 1 eq.), TBAC, CHO (5.0 mL), 10 bar CO<sub>2</sub>, 80 °C, 24 h. <sup>a</sup> Determined via <sup>1</sup>H NMR spectroscopy using the methine resonances of *cis*-CHC (δ 4.66 ppm), *trans*-CHC (δ 3.99 ppm) and PCHO (δ 3.35 ppm). <sup>b</sup> TOF = [(Conv. (%) / 100) x (100 / 0.08 mol%)] / 24 h = [(Conv. / 100) x 1250] / 24.

As was the case for Fe(13)OAc, a substrate scope using a range of commercially available, terminal epoxides was conducted using Fe(65)Cl; the most active Fe(III)-Cl catalyst, and TBAC co-catalyst (Table 24). <sup>1</sup>H NMR spectroscopy, HR-MS and GPC analysis were all applied to the crude reaction mixtures after the reaction time period for the COC product identification and COC yield determination. Moderate-to-high yields to the corresponding cyclic organic carbonate (COC) product was achieved and high functional group tolerance observed.



Table 24. CO<sub>2</sub> coupling with a variety of epoxides catalysed by Fe(65)Cl and TBAC.

Entry	Epoxide	COC yield <sup>a</sup> (%)	TOF <sup>b</sup> (h <sup>-1</sup> )
1		PO	81
2		SO	76
3		ECH	73
4 <sup>c</sup>		PGE	92
5		AGE	93

Conditions: [Fe] catalyst (0.08 mol%, 1 eq.), TBAC (0.64 mol%, 8 eq.), epoxide (5.0 mL), 10 bar CO<sub>2</sub>, 80 °C, 24 h. <sup>a</sup> Determined via <sup>1</sup>H NMR spectroscopy. <sup>b</sup> TOF = [(Conv. (%) / 100) x (100 / 0.08 mol%)] / 24 or 16 h = [(Conv. / 100) x 1250] / 24 or 16. <sup>c</sup> Reduced reaction time of 18 h.

The sterically unhindered PO was more reactive than CHO (*Table 24*, entry 1, 81% yield vs. *Table 22*, entry 13, 60% conversion). Activity was reduced by installing a sterically bulky phenyl group on the terminal methyl using SO (76% yield). With the exception of ECH (73% yield), the addition of EWGs resulted in increased reactivity and ring opening of the epoxide. The highest yield in a 24 hour reaction period was observed with AGE (93% yield). Due to the solidification of the phenoxyethyl carbonate product out of the crude reaction mixture, inefficiently hindering the mechanical stirring of the autoclave reactor chamber, the reaction time period for PGE was reduced to 18 hours and afforded the highest TOF value of 64 h<sup>-1</sup> (*Table 24*, entry 4).

Comparing the Fe(III)–thiolen–chloride complex {Fe(65)Cl} to the Fe(III)–salalen–acetate complex {Fe(13)OAc}, reveals that both complexes are almost identical in

activity for the terminal epoxides. The only exception is when using SO as the substrate; whereby Fe(**65**)Cl is modestly more active {Fe(**65**)Cl vs. Fe(**13**)OAc, Table 24 vs. Table 21: PO; 42 h<sup>-1</sup> vs. 41 h<sup>-1</sup>, SO; 40 h<sup>-1</sup> vs. 34 h<sup>-1</sup>, ECH; 38 h<sup>-1</sup> vs. 39 h<sup>-1</sup>, PGE; 64 h<sup>-1</sup> vs. 63 h<sup>-1</sup>, AGE; 48 h<sup>-1</sup> vs. 48 h<sup>-1</sup>}.

#### 4.11 Conclusion and future work

All synthesised Fe(III)–acetate complexes were applied to CO<sub>2</sub> / epoxide coupling; with the diverse range of ligand structural frameworks these were initially screened using distilled CHO at relatively mild, solvent–free conditions of 10 bar CO<sub>2</sub> at 80 °C for 24 hours to investigate the SARs. Interestingly, under the conditions, in the majority of cases the *cis*–CHC was formed exclusively (>99% product selectivity); this product formation is rare in literature due to the bicyclic ring strain of CHC. Control reactions demonstrated the need for both an ancillary ligand framework and Lewis acidic Fe(III) centre, to target a single product with moderate activity. This was in conjunction with the halide TBAC co–catalyst to aid epoxide ring opening and closing. Complex Fe(**13**)OAc, with a reduced aminopiperidine ligand backbone, was observed to be the most active catalyst for this reaction (TOF = 34 h<sup>-1</sup>) and demonstrated further high functional group tolerance when applied to a terminal epoxide substrate scope.

Using the 2,2'–bipyrrolidine salan backbone, the chirality of the ligand framework was explored {Fe(**8**<sub>meso</sub>/**8**<sub>RR</sub>/**8**<sub>SS</sub>)OAc} to see if a change in the structure and coordination around the Fe centre formed potentially new species with increased activity. The *R,R*–enantiomer exhibited a vast improvement in activity, in comparison to the *meso*–diastereomer, and this was attributed to the potential formation of an octahedral complex. The colour change observed during these coupling reactions, from typically dark purple to dark brown, was investigated using UV–Vis spectroscopy and was postulated to be due to the formation of  $\mu$ –oxo–bridged Fe(III) species as discussed by Kerton.<sup>[8]</sup>

To explore the potential beneficial effect of having a softer, hemilabile donor sulfur atom in the ligand framework for CO<sub>2</sub> / epoxide coupling, Stewart's synthesised Fe(III)–thiolen–chloride {ONSO} complexes were applied to CO<sub>2</sub> / CHO coupling and

compared with the Fe(III)–salalen–chloride {ONNO} complexes {Fe(1–7)Cl}, synthesised in **Section 2.3**; this work showed strong similarities to the progress made by Capacchione in this area.<sup>[15,47]</sup> Nearly all catalysts yielded the *cis*–CHC product exclusively with the thioen complexes tending to display higher activities than their salalen counterparts. Complex Fe(65)Cl, bearing bromo–functionality on the thio–phenolate moiety, was the most active catalyst with a TOF value of 31 h<sup>-1</sup> at 80 °C and could be increased further to 156 h<sup>-1</sup> when the temperature was increased to 120 °C. High functional group tolerance was demonstrated by this complex when applied to a terminal epoxide substrate scope. The importance of the number of equivalents of co–catalyst on product selectivity was also highlighted using TBAC.

While these Fe(III) catalysts are not as active in comparison to other examples in literature, kinetic investigations were not attempted but would provide mechanistic insight, such as the rate determining step. As highlighted by Della Monica and Kleij when reviewing the mechanistic guidelines for these coupling reactions, despite these mononuclear Fe(III) systems reported herein appearing relatively structurally simple, and most probably following the generally accepted mononuclear mechanism shown earlier (*Scheme 26*), complex mechanistic scenarios may arise.<sup>[9]</sup> There are peculiar examples of this in literature, such as Rieger’s mononuclear Fe(II)–tetraamine–dichloride catalysts displaying a dinuclear mechanistic pathway without the need for halide co–catalyst or Capacchione’s dinuclear Fe(III)–*bis*(thioether)–tri(phenolate) {OSOSO}, discussed in **Section 4.3**, following a mononuclear reaction pathway.<sup>[15,45,54]</sup> Therefore, further investigations would be useful to determine with more confidence the potential mechanism occurring in this study.

UV–Vis spectroscopy provided no evidence for the *in-situ* formation of a six–coordinate, anionic metallate catalytic species upon the addition of TBAC co–catalyst in this work. Kerton noted, for the Fe(III)–amino–*bis*(phenolate) complexes, that the order of addition of the reagents was important to their CO<sub>2</sub> / epoxide coupling reactions.<sup>[22]</sup> The PPnCl co–catalyst was poorly soluble in the epoxide neat reaction mixtures and to ensure solubility, their initial experimental protocol was the addition of Fe(III) catalyst to PPnCl in dichloromethane and subsequent removal of the solvent *in-vacuo*.<sup>[22]</sup> The remaining residue was soluble in epoxide and this was proposed to

result from the formation of anionic Fe(III) metallate species, with cationic PPN counterions; MALDI–ToF analysis provided evidence this was occurring.<sup>[22]</sup> It was observed in this study that none of the co–catalysts were completely, fully soluble in the neat, CHO reaction mixtures. However, it was observed that the TBAC co–catalyst afforded the higher conversions than alternatives, such as PPNCl and TBAB, and this was attributed to it being the most soluble. Therefore, to further confirm whether metallate species are forming in this study, Kerton’s experimental protocol, MALDI–ToF analysis and attempts at separately isolating these anionic species would need to be explored.<sup>[22]</sup>

Other interesting routes related to this work could be attempts at recycling the catalysts and using further chiral ligand frameworks. Dai and co–workers investigated the recyclability and stability of their *bis*(pincer)–pyridine bridged–Fe(II) complex.<sup>[26]</sup> It was demonstrated that the Fe(II) catalyst could be re–isolated from the COC product, after completion of the CO<sub>2</sub> / epoxide reaction, *via* precipitation using ethyl acetate and used further, without purification, for another six catalytic reactions or ‘cycles’ without deterioration in the product yield.<sup>[26]</sup> This could be attempted with the Fe(III) complexes in this study by exploring its solubility in various solvents.

While the Fe(III)–salalen, –thiolen and –acetate complexes were applied to CO<sub>2</sub> / epoxide coupling, other iron complexes synthesised in **Chapter 2**, such as Fe(III)–*bis*(phenoxy–imine) complexes, have of yet not been applied in depth and this would be of interest. As discussed in **Sections 2.10** and **2.11**, early work into synthesising chiral iron and aluminium complexes, using a salen ligand framework with the DPEN moiety, was conducted. It would be interesting to synthesise these and apply them to stereoselective CO<sub>2</sub> / epoxide reactions and attempt kinetic resolution experiments using terminal epoxides, such as *trans*– or *cis*–2–BO, to form enantiopure COC products.<sup>[1,9,23]</sup> There are few examples of catalysts that are able to do this process in literature.<sup>[9]</sup>

Also as discussed in **Section 2.11**, early work was also conducted into synthesising Mn(III)–salalen, –salan and –salen complexes. There is real potential in complexing the ligand frameworks, used for Fe(III)–salalen, –thiolen and –acetate complexes, to other Earth–abundant metals such as manganese, magnesium, and zinc and

exploring these for CO<sub>2</sub> / epoxide coupling; indeed Kerton and co-workers recently reported the synthesis and application of Mn(III)–amino–bis(phenolate) complexes.<sup>[55]</sup>

#### 4.12 References

- [1] F. Della Monica, A. Buonerba, C. Capacchione, *Adv. Synth. Catal.* **2019**, *361*, 265–282.
- [2] M. North, R. Pasquale, C. Young, *Green Chem.* **2010**, *12*, 1514–1539.
- [3] A. Buchard, M. R. Kember, K. G. Sandeman, C. K. Williams, *Chem. Commun.* **2011**, *47*, 212–214.
- [4] K. A. Andrea, F. M. Kerton, *Polym. J.* **2021**, *53*, 29–46.
- [5] B. Schäffner, F. Schäffner, S. P. Verevkin, A. Börner, *Chem. Rev.* **2010**, *110*, 4554–4581.
- [6] A. Buonerba, A. De Nisi, A. Grassi, S. Milione, C. Capacchione, B. Rieger, *Catal. Sci. Technol.* **2015**, *5*, 118–123.
- [7] F. Della Monica, B. Maity, T. Pehl, A. Buonerba, A. De Nisi, M. Monari, A. Grassi, B. Rieger, L. Cavallo, C. Capacchione, *ACS Catal.* **2018**, *8*, 6882–6893.
- [8] K. A. Andrea, T. R. Brown, J. N. Murphy, D. Jagota, D. McKearney, C. M. Kozak, F. M. Kerton, *Inorg. Chem.* **2018**, *57*, 13494–13504.
- [9] F. Della Monica, A. W. Kleij, *Catal. Sci. Technol.* **2020**, *10*, 3483–3501.
- [10] A.-A. G. Shaikh, S. Sivaram, *Chem. Rev.* **1996**, *96*, 951–976.
- [11] H. Büttner, L. Longwitz, J. Steinbauer, C. Wulf, T. Werner, *Top. Curr. Chem.* **2017**, *375*, 1–56.
- [12] L. Cuesta-Aluja, A. Campos-Carrasco, J. Castilla, M. Reguero, A. M. Masdeu-Bultó, A. Aghmiz, *J. CO<sub>2</sub> Util.* **2016**, *14*, 10–22.
- [13] G. Bresciani, M. Bortoluzzi, F. Marchetti, G. Pampaloni, *ChemSusChem* **2018**, *11*, 2737–2743.
- [14] C. Martín, G. Fiorani, A. W. Kleij, *ACS Catal.* **2015**, *5*, 1353–1370.
- [15] V. Paradiso, V. Capaccio, D. H. Lamparelli, C. Capacchione, *Catalysts* **2020**, *10*, 825.
- [16] M. Taherimehr, S. M. Al-Amsyar, C. J. Whiteoak, A. W. Kleij, P. P. Pescarmona, *Green Chem.* **2013**, *15*, 3083–3090.
- [17] M. Taherimehr, J. P. C. C. Sertã, A. W. Kleij, C. J. Whiteoak, P. P. Pescarmona, *ChemSusChem* **2015**, *8*, 1034–1042.
- [18] M. Cozzolino, K. Press, M. Mazzeo, M. Lamberti, *ChemCatChem* **2016**, *8*, 455–460.

- [19] F. Della Monica, A. Buonerba, V. Paradiso, S. Milione, A. Grassi, C. Capacchione, *Adv. Synth. Catal.* **2019**, *361*, 283–288.
- [20] M. Cozzolino, T. Rosen, I. Goldberg, M. Mazzeo, M. Lamberti, *ChemSusChem* **2017**, *10*, 1217–1223.
- [21] D. J. Darensbourg, J. C. Yarbrough, C. Ortiz, C. C. Fang, *J. Am. Chem. Soc.* **2003**, *125*, 7586–7591.
- [22] K. A. Andrea, E. D. Butler, T. R. Brown, T. S. Anderson, D. Jagota, C. Rose, E. M. Lee, S. D. Goulding, J. N. Murphy, F. M. Kerton, C. M. Kozak, *Inorg. Chem.* **2019**, *58*, 11231–11240.
- [23] C. J. Whiteoak, E. Martin, E. Escudero-Adán, A. W. Kleij, *Adv. Synth. Catal.* **2013**, *355*, 2233–2239.
- [24] Y. Liu, H. Zhou, J.-Z. Guo, W.-M. Ren, X.-B. Lu, *Angew. Chem. Int. Ed* **2017**, *56*, 4862–4866.
- [25] E. Fazekas, G. S. Nichol, M. P. Shaver, J. A. Garden, *Dalton Trans.* **2018**, *47*, 13106–13112.
- [26] F. Chen, N. Liu, B. Dai, *ACS Sustainable Chem. Eng.* **2017**, *5*, 9065–9075.
- [27] C. J. Whiteoak, B. Gjoka, E. Martin, M. M. Belmonte, E. C. Escudero-Adán, C. Zonta, G. Licini, A. W. Kleij, *Inorg. Chem.* **2012**, *51*, 10639–10649.
- [28] C. J. Whiteoak, E. Martin, M. M. Belmonte, J. Benet-Buchholz, A. W. Kleij, *Adv. Synth. Catal.* **2012**, *354*, 469–476.
- [29] J. W. Comerford, I. D. V Ingram, M. North, X. Wu, *Green Chem.* **2015**, *17*, 1966–1987.
- [30] T. Sakakura, K. Kohno, *Chem. Commun.* **2009**, 1312–1330.
- [31] G. Trott, P. K. Saini, C. K. Williams, *Phil. Trans. R. Soc. A* **2016**, *374*, 20150085.
- [32] A. Decortes, A. M. Castilla, A. W. Kleij, *Angew. Chem. Int. Ed* **2010**, *49*, 9822–9837.
- [33] C. M. Kozak, K. Ambrose, T. S. Anderson, *Coord. Chem. Rev.* **2018**, *376*, 565–587.
- [34] D. Alhashmialameer, J. Collins, K. Hattenhauer, F. M. Kerton, *Catal. Sci. Technol.* **2016**, *6*, 5364–5373.
- [35] D. J. Liptrot, M. S. Hill, M. F. Mahon, *Angew. Chem. Int. Ed.* **2014**, *53*, 6224–6227.
- [36] M. Sunjuk, A. S. Abu-Surrah, E. Al-Ramahi, A. K. Qaroush, A. Saleh, *Transit. Met. Chem.* **2013**, *38*, 253–257.
- [37] A. S. Abu-Surrah, H. M. Abdel-Halim, H. A. N. Abu-Shehab, E. Al-Ramahi, *Transit. Met. Chem.* **2017**, *42*, 117–122.
- [38] E. Fazekas, G. S. Nichol, J. A. Garden, M. P. Shaver, *ACS Omega* **2018**, *3*, 16945–

- 16953.
- [39] C. J. Whiteoak, N. Kielland, V. Laserna, E. C. Escudero-Adán, E. Martin, A. W. Kleij, *J. Am. Chem. Soc.* **2013**, *135*, 1228–1231.
- [40] L. Cuesta-Aluja, A. M. Masdeu-Bultó, *ChemistrySelect* **2016**, *1*, 2065–2070.
- [41] F. M. Al-Qaisi, M. Nieger, M. L. Kemell, T. J. Repo, *ChemistrySelect* **2016**, *1*, 545–548.
- [42] J. Peng, H.-J. Yang, Y. Geng, Z. Wei, L. Wang, C.-Y. Guo, *J. CO<sub>2</sub> Util.* **2017**, *17*, 243–255.
- [43] M. Cozzolino, V. Leo, C. Tedesco, M. Mazzeo, M. Lamberti, *Dalton Trans.* **2018**, *47*, 13229–13238.
- [44] A. Buonerba, F. Della Monica, A. De Nisi, E. Luciano, S. Milione, A. Grassi, C. Capacchione, B. Rieger, *Faraday Discuss.* **2015**, *183*, 83–95.
- [45] F. Della Monica, S. V. C. Vummaleti, A. Buonerba, A. De Nisi, M. Monari, S. Milione, A. Grassi, L. Cavallo, C. Capacchione, *Adv. Synth. Catal.* **2016**, *358*, 3231–3243.
- [46] F. Della Monica, M. Leone, A. Buonerba, A. Grassi, S. Milione, C. Capacchione, *Mol. Catal.* **2018**, *460*, 46–52.
- [47] J. A. Stewart, P. McKeown, O. J. Driscoll, M. F. Mahon, B. D. Ward, M. D. Jones, *Macromolecules* **2019**, *52*, 5977–5984.
- [48] A. Stopper, J. Okuda, M. Kol, *Macromolecules* **2012**, *45*, 698–704.
- [49] A. Stopper, K. Press, J. Okuda, I. Goldberg, M. Kol, *Inorg. Chem.* **2014**, *53*, 9140–9150.
- [50] J. A. Castro-Osma, M. North, W. K. Offermans, W. Leitner, T. E. Müller, *ChemSusChem* **2016**, *9*, 791–794.
- [51] X. Wu, C. Chen, Z. Guo, M. North, A. C. Whitwood, *ACS Catal.* **2019**, *9*, 1895–1906.
- [52] S. Gesslbauer, R. Savela, Y. Chen, A. J. P. White, C. Romain, *ACS Catal.* **2019**, *9*, 7912–7920.
- [53] M. D. Jones, S. L. Hancock, P. McKeown, P. M. Schäfer, A. Buchard, L. H. Thomas, M. F. Mahon, J. P. Lowe, *Chem. Commun.* **2014**, *50*, 15967–15970.
- [54] J. E. Dengler, M. W. Lehenmeier, S. Klaus, C. E. Anderson, E. Herdtweck, B. Rieger, *Eur. J. Inorg. Chem.* **2011**, 336–343.
- [55] A. I. Elkurtehi, F. M. Kerton, *Can. J. Chem.* **2021**, *99*, 202–208.

## **Chapter 5.**

**The further application of Fe(III) complexes: ring opening  
copolymerisation, terpolymerisation and degradation**



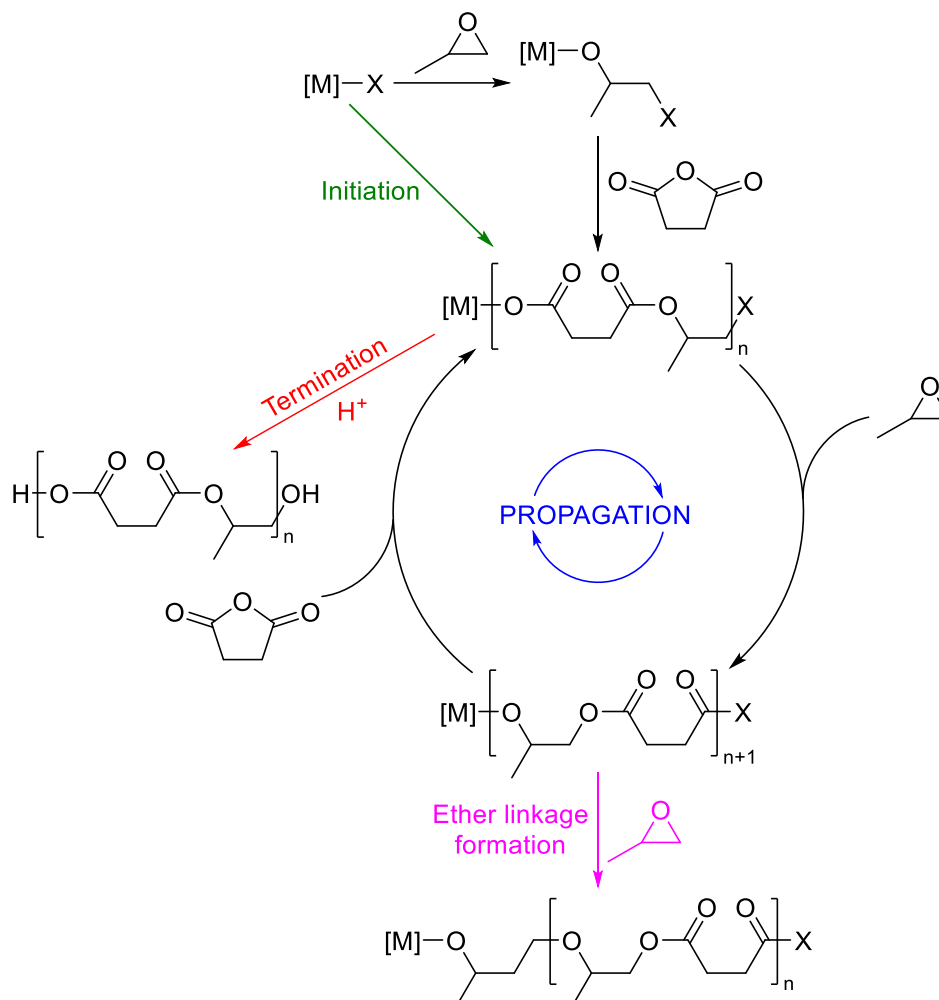
## 5. The further application of Fe(III) complexes: ring opening copolymerisation, terpolymerisation and degradation

### 5.1 Introduction, Fe-mediated ring opening copolymerisation and project aims

As discussed in **Section 3.1** (*Scheme 15*), PLA, and polyesters (PEs) in general, can be produced by step-growth polymerisation and ring opening polymerisation (ROP).<sup>[1-10]</sup> Using diols and diacids, the former has been the most commonly and industrially used synthetic route to access PEs. However, as previously mentioned, there are many drawbacks to this self-condensation reaction. Precise stoichiometry of the reagents and forcing conditions; using high temperatures or neat conditions, to remove the stoichiometric amount of water generated and overcome the high activation energy barrier, are needed to afford high molecular weight polymer.<sup>[2,4,8-11]</sup> Another crucial disadvantage is the lack of control in the overall polymerisation such as in molecular weight and molecular weight distribution.<sup>[10,12]</sup> The ROP of cyclic esters, such as lactide, to aliphatic PEs, is an industrially preferred route and, *via* the release of enthalpic ring strain, achieves superior control in the polymerisation.<sup>[2-4,9,13-18]</sup> However, there is a limited range of such polymerisable cyclic ester monomers available and, because only less rigid aliphatic, non-aromatic PEs can be generated, inferior and hence unsuitable thermal properties can be displayed.<sup>[10,12,19]</sup> For example, PLA has suffered from its low / modest glass transition temperature ( $T_g$ ) of 50–72 °C which has restricted its suitability to replace petrochemically derived polymers, such as polystyrene ( $T_g = 100$  °C), and its use in further applications.<sup>[3,7,10,14-16,18-25]</sup>

Another alternative, more versatile and promising method is ring opening copolymerisation (ROCOP) using epoxides and anhydride reagents with a catalytic / initiator system. This synthetic method is particularly attractive as it allows access to a broad range of PEs through the combination of a vast selection of commercially available epoxides and anhydrides.<sup>[12,19]</sup> Indeed, depending on the monomer, both reagents can be potentially sourced *via* renewable means.<sup>[10,12,26,27]</sup> PEs with superior and varying thermomechanical properties can be afforded owing to the inherent

amorphous, rigid semi-aromatic / aromatic backbones.<sup>[24]</sup> Hence, there is the potential capability to fine tune the epoxide / anhydride combination sets for any desired polymeric application.<sup>[10,26]</sup>



*Scheme 34.* The generally accepted mechanism for metal-mediated anhydride / epoxide ROCOP.  
(Adapted from reference).<sup>[19]</sup>

Both polyester (PE) and polycarbonate products can be formed using ROCOP and the generally accepted catalytic cycle for metal-mediated anhydride / epoxide ROCOP is shown in *Scheme 34*; the catalytic cycle for  $CO_2$  / epoxide ROCOP was shown in **Section 4.1** (*Scheme 26*).<sup>[10,19]</sup> Initiation begins with the metal pre-catalyst interacting and coordinating with the oxygen of the epoxide ring or anhydride. There is subsequent ring opening and insertion into the  $M-X$  bond to form either a metal-alkoxide or -carboxylate intermediate;  $X$  being a labile auxiliary ligand, such as alkoxide, halide, carboxylate or other initiating group. This process is then repeated

with the other monomer reagent to generate the first PE bond or ester linkage and the *in-situ* active initiating species.<sup>[10,19]</sup> Propagation then proceeds with successive and sequential epoxide / anhydride coordination and insertions of the growing alkoxide–carboxylate group. This is until the metal–oxygen bond is cleaved *via* termination, through post acid work–up of the polymer, to obtain the produced PE with the original auxiliary ligand and initiating group occupying one of the chain end groups of the polymer. An undesired side–reaction that can occur, and lower the perfectly alternating chemoselectivity, is sequential incorporation of only epoxide monomer (homopolymerisation) to form undesired polyether and ether linkages. Therefore, the catalytic system needs to selectively minimise this side–reaction and target the desired ester linkages.<sup>[10,19]</sup>

As was the case for the ROP of *rac*–LA and CO<sub>2</sub> / epoxide coupling (**Chapters 3 and 4**), despite the numerous benefits associated with iron (Fe) and recent resurgence of iron in contemporary catalysis, examples of Fe–mediated ROCOP are scarce in literature. Indeed, as far as we are aware, there were only six relevant examples of effective Fe catalytic systems for anhydride / epoxide ROCOP in literature.<sup>[26–31]</sup>

In 2014, building on work conducted for PO polymerisation and CO<sub>2</sub> / epoxide coupling, Nozaki and co–workers explored iron and manganese systems using a corrole, trianionic tetradentate porphyrin analogue, ligand framework with PPNX co–catalysts for epoxide homopolymerisation and anhydride / epoxide ROCOP; however the work was focussed on the manganese analogues.<sup>[28,32]</sup> All complexes were screened for ROCOP using glutaric anhydride (GA) and doubly distilled PO at 30 °C to form perfectly alternating PE, poly(propylene glutarate), in solvent–free, neat conditions ([GA]:[PO]:[Cat.]:[Co–cat.] = [100]:[2000]:[1]:[1]). Synthesised *bis*(triphenylphosphoranylidene)iminium pentafluorobenzoate ([PPN][OBzF<sub>5</sub>]) was used as the co–catalyst and the Fe complexes shown in *Figure 67* were applied for this study.<sup>[28]</sup> After 30 hours, Fe(**132**) observed no activity but Fe(**133/134**) were the most active complexes out of all the Fe and Mn complexes. High yields, reasonable molecular weights, narrow distributions and perfectly alternating PE were afforded {Fe(**133**); 99% yield,  $M_n = 8000 \text{ gmol}^{-1}$ ,  $\mathcal{D} = 1.2$  and Fe(**134**); 81% yield,  $M_n = 6900 \text{ gmol}^{-1}$ ,  $\mathcal{D} = 1.2$ }.<sup>[28]</sup> Surprisingly, despite the manganese complexes demonstrating

lower activity, the substrate scope was expanded using a manganese analogue and the Fe catalysts were taken no further.<sup>[28]</sup> Also, it is important to note that it appears no blank reaction using only [PPN][OBzF<sub>5</sub>] was applied, therefore it is unknown if the co-catalyst is enhancing activity or carrying out the copolymerisation solely and the Mn and Fe catalysts were cooperatively contributing to the observed reactivity.<sup>[28]</sup>

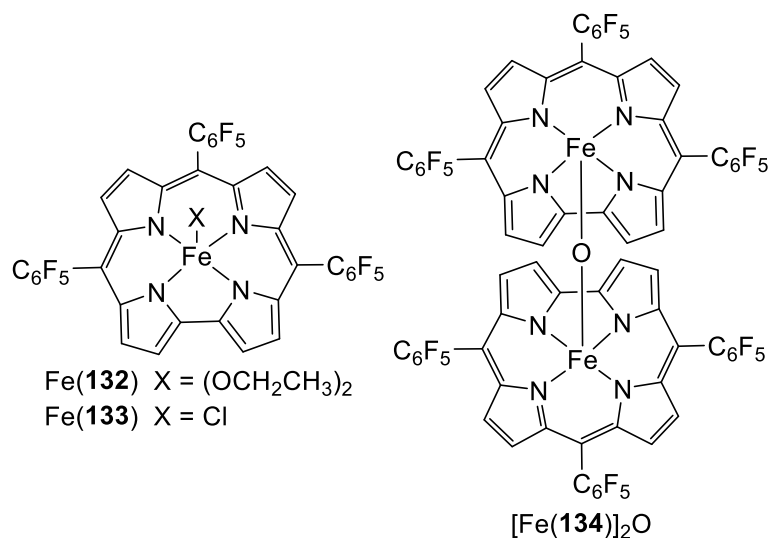


Figure 67. Nozaki's reported Fe-corrole complexes.<sup>[28]</sup>

Following on from the success achieved using Al, Co and Cr catalysts with structural frameworks such as salen ligands in literature,<sup>[10,33–38]</sup> Merna and co-workers reported the first application of Fe(III)-salen complexes (Figure 68) as catalysts for anhydride / epoxide ROCOP.<sup>[29]</sup> Phthalic anhydride (PA) and cyclohexene oxide (CHO) were specifically used as the monomers, with either DMAP or PPNCl as the co-catalyst, and at 110 °C in toluene ([PA]:[CHO]:[Cat.]:[Co-cat.] = [250]:[250]:[1]), perfectly alternating poly(1,2-cyclohexylene-1,2-phthalate) {poly(CHO-co-PA)} was formed.<sup>[29]</sup> After five hours, all Fe complexes {Fe(135–137)Cl} showed similar reactivity with low-to-moderate PA conversions, reasonable molecular weights, narrow dispersities and 100% ester linkages were observed (46–73% PA conversion,  $M_n = 6600\text{--}10300 \text{ gmol}^{-1}$ ,  $\mathcal{D} = 1.17\text{--}1.33$ ).<sup>[29]</sup> Significantly reduced reactivity and molecular weights were observed after one hour using PPNCl co-catalyst.<sup>[29]</sup>

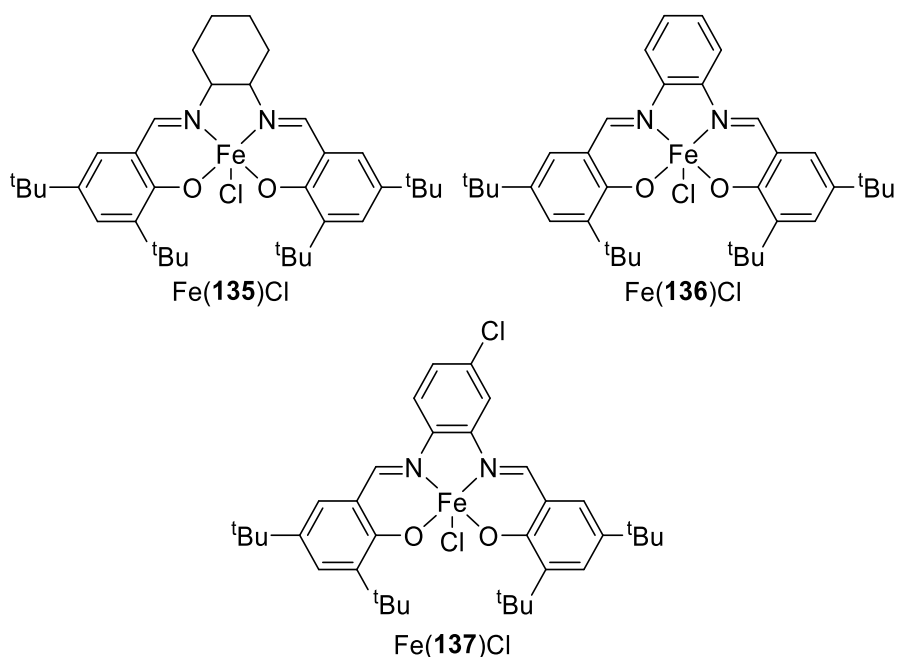
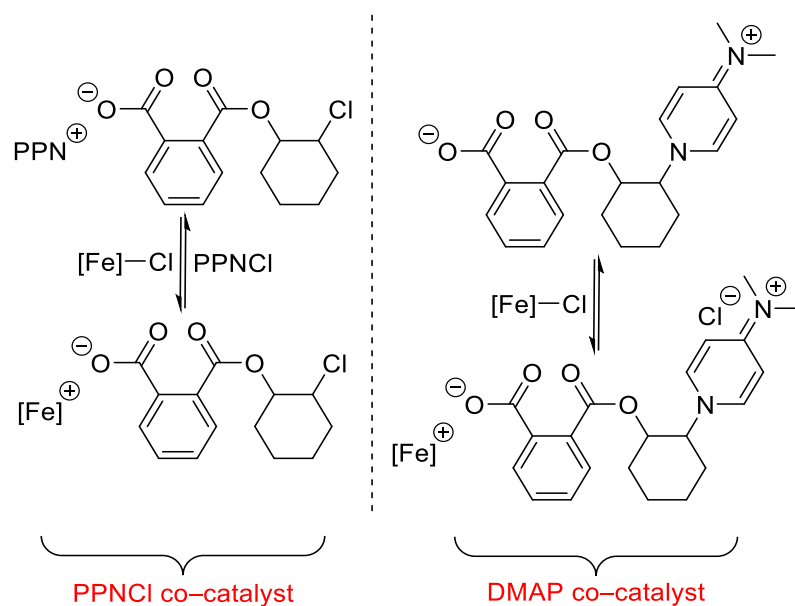


Figure 68. Merna's reported Fe(III)–salen–chloride complexes.<sup>[29]</sup>

However, despite these results, it was shown that the PPnCl and DMAP co-catalysts being used solely, were able to carry out the copolymerisation more effectively at the employed reaction conditions. Higher PA conversions and molecular weight poly(CHO-co-PA) was observed (five hours reaction time; PPnCl catalyst, 84% PA conversion,  $M_n = 14800 \text{ gmol}^{-1}$ ,  $\bar{D} = 1.31$  and DMAP catalyst, 43% PA conversion,  $M_n = 10600 \text{ gmol}^{-1}$ ,  $\bar{D} = 1.13$ ) with the 100% ester linkage chemoselectivity maintained.<sup>[29]</sup> This showed the Fe complexes as catalysts were uncooperative with the PPnCl co-catalyst and inhibited the overall reactivity.<sup>[29]</sup> For the PPnCl co-catalyst, this was proposed to result from a dynamic equilibrium existing for cation exchange, between  $[\text{Fe}]^+$  and  $\text{PPn}^+$ , to the growing anionic PE chain (*Scheme 35*). With the  $\text{PPn}^+$ -carboxylate polymer species being the major source of initiation, propagation and hence activity for the polymerisation and the  $[\text{Fe}]$  holding the  $[\text{Fe}]^+$ -carboxylate ionic pair more tightly causing propagation to slow. A similar proposition was thought to be occurring for the DMAP co-catalyst (*Scheme 35*), where the  $[\text{Fe}]-\text{Cl}$  complex disassociates, in a dynamic equilibrium, and forms a tight ionic pair with the zwitterionic DMAP-PE species and propagation becomes slower.<sup>[29]</sup>



Scheme 35. Merna's proposed equilibrium mechanism for the mutual interaction between the Fe(III)–salen–chloride complexes and propagating PE species.<sup>[29]</sup>

The observation that co-catalysts such as PPNCl can catalyse copolymerisation has been reported in other cases.<sup>[12,24,30,38–42]</sup> Alongside the Fe complexes, a Cr(III)–salen–chloride complex {Cr(**136**)Cl}; the chromium analogue of Fe(**136**)Cl, was applied as a benchmark catalyst for comparison. All Fe catalysts were considerably less effective than Cr(**136**)Cl under the same reaction conditions (PPNCl co-catalyst; one hour reaction time, 100% PA conversion,  $M_n = 12300 \text{ gmol}^{-1}$ ,  $\bar{D} = 1.26$  and DMAP co-catalyst; five hour reaction time, 100% PA conversion,  $M_n = 14300 \text{ gmol}^{-1}$ ,  $\bar{D} = 1.25$ ). Additionally, unlike the Fe complexes, the catalytic system showed an enhanced activity and cooperativity when the Cr catalyst was combined with a co-catalyst.<sup>[29]</sup>

Kleij and co-workers have made significant developments in this area using their amino-triphenolate complexes and, in particular, the Fe(III) analogue, Fe(**69**) (Section 4.2, Figure 54), was particularly effective as an initiator for ROCOP. Their goal was to vary both the anhydride and epoxide monomer sets (Figures 69 and 70), and use monomers sourced from renewable means, to access aliphatic or semi-aromatic PEs with exclusive chemoselectivity (100% ester linkages) and superior thermal properties.<sup>[26,27,31]</sup> In 2016, using Fe(**69**) or an Al(III)–salen–chloride complex {Al(**136**)Cl analogue, Figure 68} as the catalyst, with PPNCl co-catalyst, at mild reaction conditions (60 °C), perfectly alternating, aliphatic PEs were formed using six

partially or fully renewably, synthesized tricyclic anhydrides with either CHO or PO (Figure 69).<sup>[26]</sup> This was achieved using solvent-free, neat conditions for the PO monomer {5.5–8 hours reaction time, [anhydride]:[PO]:[Fe(69)]:[PPNCl] = 300:1500:1:0.9} and toluene for the CHO monomer {15–168 hours reaction time, [anhydride]:[CHO]:[Fe(69)]:[PPNCl] = 300:900:1:0.9}. Moderate-to-high molecular weight aliphatic polymer was produced using PO {Fe(69);  $M_n = 10400\text{--}17200\text{ gmol}^{-1}$ ,  $\bar{D} = 1.10\text{--}1.28$ } and low-to-moderate molecular weight using CHO ( $M_n = 4100\text{--}11600\text{ gmol}^{-1}$ ,  $\bar{D} = 1.23\text{--}1.58$ ). Crucially, using the Fe and Al catalysts, the fine-tuning of the  $T_g$  value for the PE, through variation of the monomer sets, was demonstrated across a remarkable 120 °C range from 66 to 184 °C. In fact, to the best of the authors' knowledge, these are the highest  $T_g$  values reported for fully alicyclic PEs to date.<sup>[26]</sup>

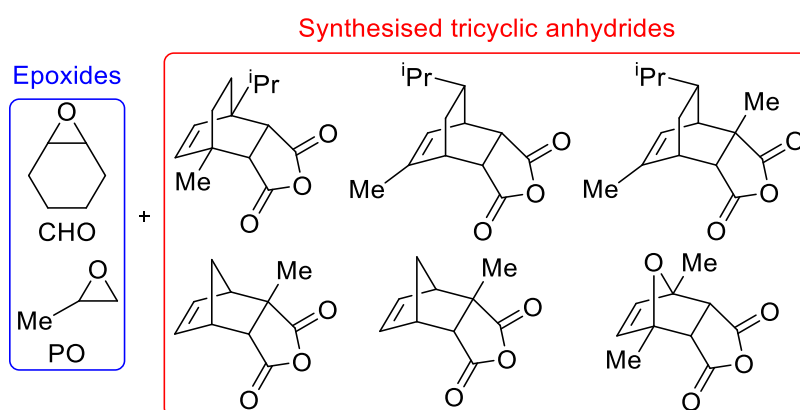


Figure 69. The six partially or fully renewably, synthesized tricyclic anhydrides coupled with either CHO or PO to form alternating PE by Kleij. (Adapted from reference).<sup>[26]</sup>

In 2017, attention then shifted to exploring more renewable epoxide monomer such as terpene oxides; including limonene oxide (LO), cyclohexadiene oxide (CHDO), carene oxide (CAO), menthene oxide (MEO) and limonene dioxide (LDO) (Figure 70).<sup>[27]</sup> These were coupled with rigid anhydrides; PA and naphthalic anhydride (NA), to afford fully alternating, semi-aromatic PEs. Generally, the reaction conditions remained mild (65 °C), using Fe(69) or the aluminium analogue as the catalyst and PPNCl co-catalyst, as part of a binary catalytic system. This was with a low metal catalyst loading (0.50 mol%) and either solvent (0.50 mL) or solvent-free conditions. Reaction times ranged between 24–100 hours depending on the monomer sets employed.<sup>[27]</sup> Focussing on the Fe catalyst, coupling the terpene-derived epoxides

with PA resulted in low-to-high molecular weight, perfectly alternating PE {Fe(**69**);  $M_n = 3200\text{--}24900 \text{ gmol}^{-1}$ ,  $\bar{D} = 1.20\text{--}2.41$ }. Coupling NA with CHO and LO resulted in low-to-moderate molecular weight, perfectly alternating PE {Fe(**69**), 72 hours reaction time; CHO,  $M_n = 2300\text{--}11400 \text{ gmol}^{-1}$ ,  $\bar{D} = 1.25\text{--}2.35$  and LO,  $M_n = 1600\text{--}2200 \text{ gmol}^{-1}$ ,  $\bar{D} = 1.36\text{--}1.52$ }.<sup>[27]</sup> Control reactions were conducted for the PA / LO ROCOP, where no activity was observed using Fe(**69**) by itself with no co-catalyst and PPnCl with no metal loading resulted in minimal reactivity; these results demonstrated a need for a binary catalytic system in this study.<sup>[27]</sup> Through variation of the monomer sets, the  $T_g$  value could be fine-tuned between a broad range of 59 to 243 °C.<sup>[27]</sup> The higher  $T_g$  values resulted from the PE comprising of more rigid, semi-aromatic backbones.<sup>[27]</sup>

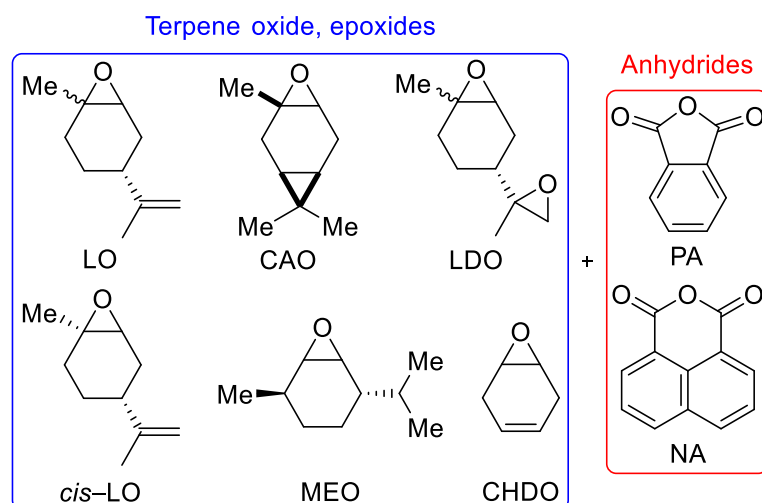


Figure 70. The terpene oxide, epoxides coupled with PA or NA to form alternating PE by Kleij.  
(Adapted from reference).<sup>[27]</sup>

Recently, this focus on the renewable terpene oxide, epoxide monomer was continued by exploring in depth those derived from the rigid, bio-sourced  $\beta$ -elemene (BE) terpene (Figure 71).<sup>[31]</sup> After precise and selective epoxidation of only one of the three double bonds,  $\beta$ -elemene monoxide (BEM) monomer was coupled with PA to form poly(BEM-*alt*-PA), alternating semi-aromatic PE with Fe(**69**) or Al(**69**) catalyst mediating the ROCOP (Figure 71).<sup>[31]</sup> PPnCl was used as the co-catalyst and, after optimisation, it was found more forcing conditions and higher temperatures were required, compared to previously studied sterically bulky monomer,<sup>[26,27]</sup> due to the particularly high steric demand of  $\beta$ -elemene oxides.<sup>[31]</sup> A



range of conditions were attempted (100 °C, 17–24 hours reaction time), in both toluene and neat, with a range of different ratios of reagents and catalyst, to afford the desired poly(BEM-*alt*-PA) with Fe(**69**) outperforming Al(**69**). Low-to-reasonable molecular weights and narrow distributions were observed {Fe(**69**);  $M_n = 4400\text{--}7800$   $\text{g mol}^{-1}$ ,  $\mathcal{D} = 1.19\text{--}1.28$ }. Despite the lower molecular weights displayed in this study, the results are impressive considering the bulky nature of the epoxide monomer. The measured  $T_g$  values were low (64–79 °C) and this was proposed to result from the lower  $M_n$  values, the observed bimodality and BEM regioisomers resulting in a more flexible polymer.<sup>[31]</sup>

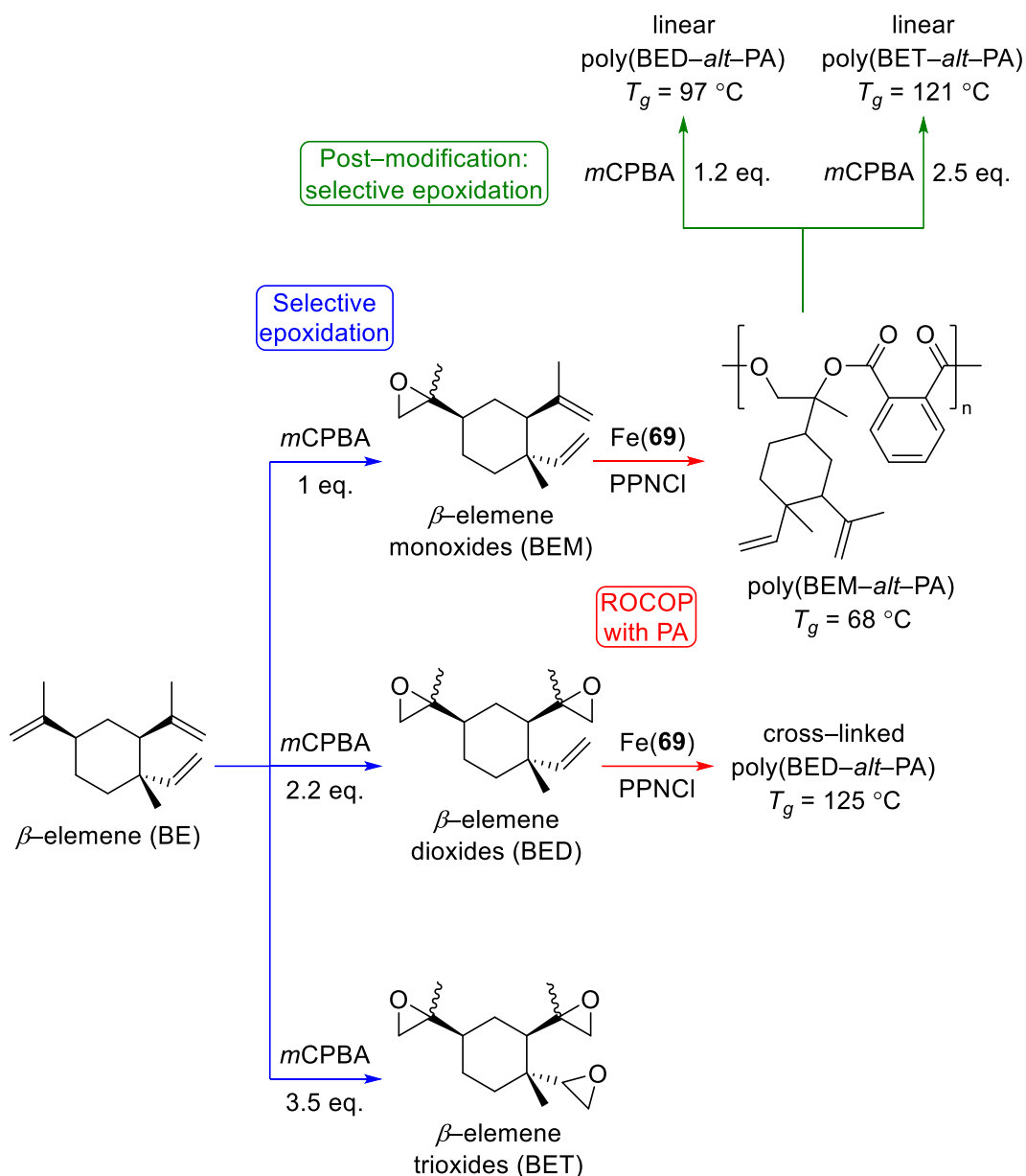


Figure 71. Overview on Kleij's explorations using terpene-based,  $\beta$ -elemene for epoxidation and ROCOP. (Adapted from reference).<sup>[31]</sup>

$\beta$ -Elemene dioxide (BED), resulting from selective double epoxidation of the BE, was then applied to ROCOP using Fe(69) catalyst and reactivity was improved by the presence of the two epoxide groups in the monomer (60–80 °C, 24–48 hours reaction time,  $M_n = 3500\text{--}8800\text{ gmol}^{-1}$ ) (Figure 71).<sup>[31]</sup> The viscosity of the copolymerisation mixtures were observed to increase and this was supported by a dramatic broadness in the molecular weight distribution ( $\mathcal{D} = 1.21\text{--}3.12$ ) and suggested cross-linking between the poly(BED-*alt*-PA) chains.<sup>[31]</sup>

A beneficial advantage of the BEM structure is that the two unreacted, orthogonal double bonds present in each monomer unit, allow for precise post-modification and manipulation of these functionalities on the polymer's backbone. In this study, for proof of concept, sequential epoxidations of poly(BEM-*alt*-PA) ( $T_g = 68\text{ }^\circ\text{C}$ ) were selectively carried out to form poly(BED-*alt*-PA) and poly( $\beta$ -elemene trioxide-*alt*-PA) {poly(BET-*alt*-PA)} (Figure 71).<sup>[31]</sup> This resulted in the fine-tuning of the  $T_g$  value from  $68\text{ }^\circ\text{C}$  to  $97\text{ }^\circ\text{C}$  to  $121\text{ }^\circ\text{C}$  respectively (Figure 71) and linear, uncured alternating PEs not accessible *via* ROCOP. This was unlike the cross-linked poly(BED-*alt*-PA) obtained using PA / BED ROCOP that displayed the highest  $T_g$  observed ( $T_g = 125\text{ }^\circ\text{C}$ ).<sup>[31]</sup>

Recently, the amino-triphenolate ligand framework was further examined and modified by Jiang and co-workers.<sup>[30]</sup> A range of dinuclear Fe(III)-amino-triphenolate complexes were synthesised {Fe<sub>2</sub>(**138-141**)}, along with the corresponding mononuclear analogue {Fe(**142**)}, *via* the introduction of a rigid phenylene bridge linking two amino-triphenolate ligand moieties (Figure 72).<sup>[30]</sup> All complexes were applied as catalysts, with PPNCl co-catalyst, to PA or CO<sub>2</sub> / CHO ROCOP to form PCHC, polycarbonate or poly(CHO-*co*-PA), PE products. Focusing on PA / CHO ROCOP, perfectly alternating poly(CHO-*co*-PA) (97-→99% ester linkages), with low degrees of ether linkages, were observed with remarkably high activity.<sup>[30]</sup> A range of reaction conditions, including both solution and neat polymerisations, were employed. Toluene was used for solution ROCOP at  $100\text{ }^\circ\text{C}$  for 1-to-3 hours reaction time ([PA]:[CHO]:[Fe]:[PPNCl]=[500]:[550]:[1]:[1]). Reasonable activity, molecular weights and narrow dispersities were observed for all Fe complexes (48-99% PA conversion, TOF =  $128\text{--}250\text{ h}^{-1}$ ,  $M_n = 8600\text{--}22500\text{ gmol}^{-1}$ ,  $\mathcal{D} = 1.19\text{--}1.33$ ).<sup>[30]</sup> The solvent-free, neat polymerisations at  $100\text{ }^\circ\text{C}$  were considerably more reactive (0.25-0.67 hours reaction time, 29-99% PA conversion, TOF =  $588\text{--}1180\text{ h}^{-1}$ , [PA]:[CHO]:[Fe]:[PPNCl]=[500]:[2500]:[1]:[1] or =[1000]:[5000]:[1]:[1]) but, while the molecular weight distributions remained narrow, lower molecular weight polymer was produced ( $M_n = 5400\text{--}16500\text{ gmol}^{-1}$ ,  $\mathcal{D} = 1.22\text{--}30$ ).<sup>[30]</sup>

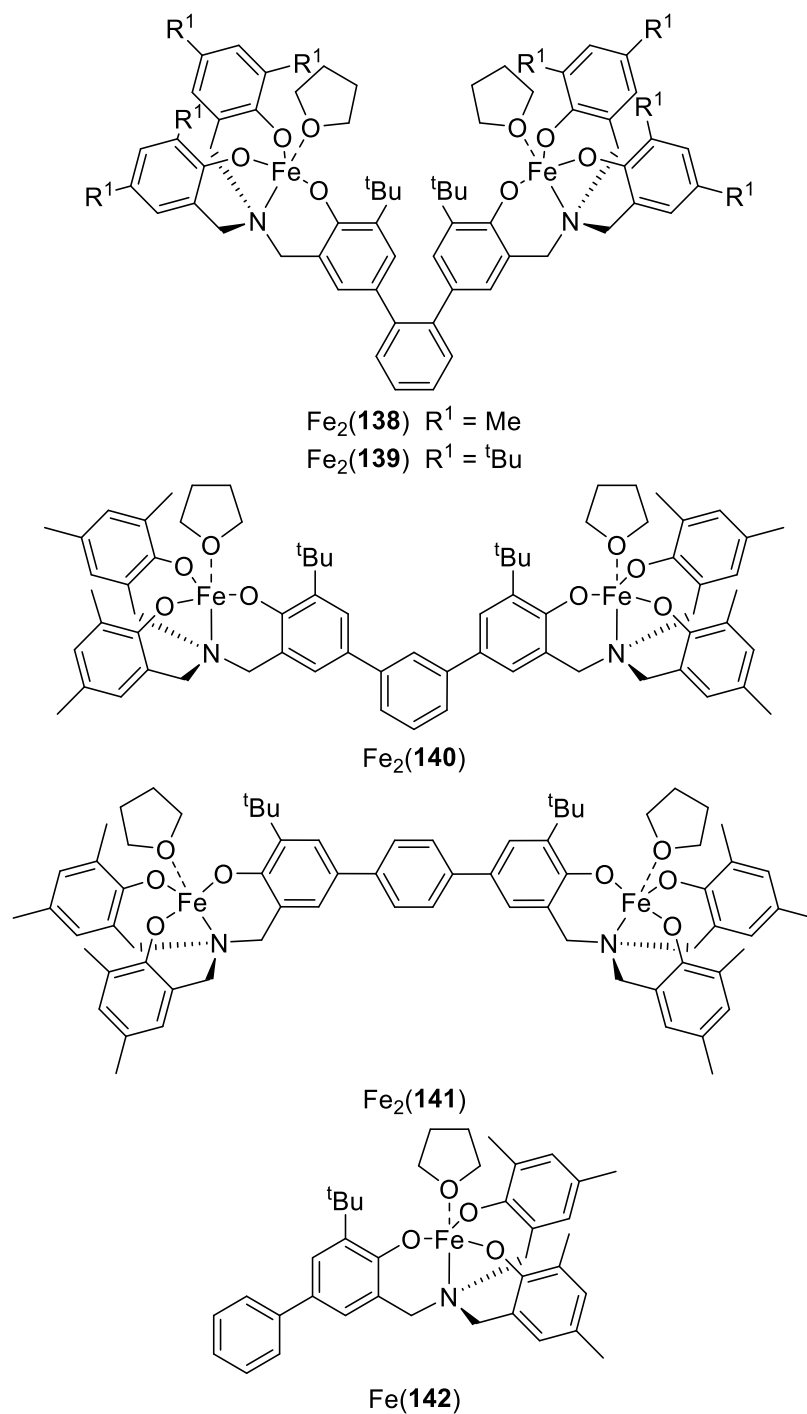


Figure 72. Jiang's reported dinuclear Fe(III)-amino-triphenolate complexes and mononuclear analogue.<sup>[30]</sup>

The highest activities were observed using the Fe(III) dinuclear complex containing the 1,2-phenylene linker backbone and methyl aromatic substituents and the mononuclear analogue {solution conditions;  $\text{Fe}_2(\mathbf{138}) = 240 \text{ h}^{-1}$  vs.  $\text{Fe}(\mathbf{142}) = 250 \text{ h}^{-1}$  and neat conditions;  $\text{Fe}_2(\mathbf{138}) = 1180 \text{ h}^{-1}$  vs.  $\text{Fe}(\mathbf{142}) = 1160 \text{ h}^{-1}$ } (Figure 72). The close similarity in reactivity for these two complexes suggested minimal synergistic,

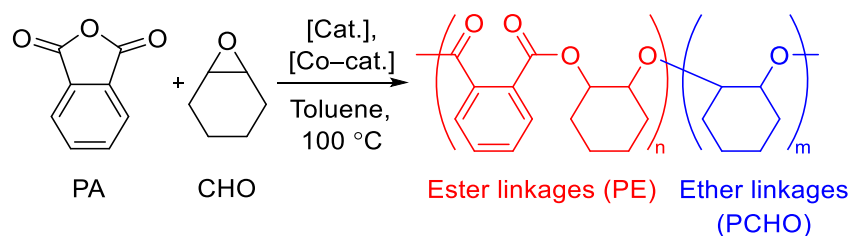
cooperative interactions were present between the two Fe(III) centres for Fe<sub>2</sub>(**138**). This was postulated to result from the significant steric hindrance of the growing polymer chain preventing such interactions.<sup>[30]</sup> On the other hand, there was cooperativity observed between the PPnCl co-catalyst used in this study with the Fe(III) complexes; the binary catalytic system being more active than the PPnCl being applied solely.<sup>[30]</sup> Unlike that for Merna and co-workers, discussed earlier, the PPnCl control reactions with no [Fe] present did not produce perfectly alternating poly(CHO-co-PA) (% ester linkages = 80–87%) and ether linkages were observed together with lower oligomeric molecular weights.<sup>[29,30]</sup>

Building on from the success found using the synthesised Fe(III) complexes (**Chapter 2**) for the ROP of *rac*-LA (**Chapter 3**) and CO<sub>2</sub> / epoxide coupling (**Chapter 4**), because of the emerging importance of ROCOP coupled with the benefits associated with iron, it was decided to explore this area. To start, the focus would be on using PA and CHO monomers as this coupling reaction is well characterised in literature and would provide a sound platform for initial investigations.<sup>[43]</sup> With the large range of Fe(III) catalysts available, it was hoped that a comprehensive study could be carried out to compare different structural frameworks and probe structure–activity–relationships (SARs) through screening reactions. As far as we are aware, this had not been attempted to such a scale before in this anhydride / epoxide ROCOP area and this goal was similar to, and was inspired by, that recently achieved by Kerton and co-workers for CO<sub>2</sub> / epoxide ROCOP and coupling to form APC and COC products.<sup>[44]</sup>

## 5.2 Initial investigations using Fe(**13**)OAc for ring opening copolymerisation in solution and hypothesis

Initial investigations probed the potential for a synthesised Fe(III) complex to mediate ROCOP. Fe(**13**)OAc was selected as the catalyst, with the highest overall activity displayed for CO<sub>2</sub> / epoxide coupling along with exclusive selectivity (**Chapter 4**), for the coupling of PA and CHO monomers (*Scheme 36*). PPnCl was used as the co-catalyst, as part of a binary catalytic system to selectively target the formation of the PE, poly(1,2-cyclohexylene-1,2-phthalate) {poly(CHO-co-PA)} and ester linkages. Reaction conditions were set at 100 °C in toluene

([PA]:[CHO]:[Fe]:[PPNCl]=[100]:[100]:[1]:[1]); as is employed in literature for solution ROCOP.<sup>[29,43]</sup> Despite, the high steric hindrance making CHO a more challenging substrate, compared to alternatives such as propylene oxide (PO), the sterically bulky and more rigid structural framework combined with aromatic PA allows access to semi-aromatic PEs with more favourable and higher  $T_g$  values. Due to this reason and because this monomer combination set is well explored and characterised in literature, they were chosen.<sup>[43]</sup> However, to note, both substrates are currently not sourced industrially *via* renewable means. Recently, it has been shown both can be obtained from biomass and synthesised from 1,4-cyclohexadiene or furans respectively; therefore, there is hope that future industrial, renewable routes can be developed.<sup>[10,19,26,45–49]</sup>



*Scheme 36.* Initial investigations into the ROCOP of PA and CHO using Fe(**13**)OAc catalyst and PPNCl co-catalyst in toluene.

The initial findings are shown in *Table 25*; while low-to-moderate PA conversions and high degrees of ester linkage (36–72 PA conversions, % ester linkages = 83–95%) were observed, after 1–3 hours reaction time at 100 °C, only low molecular weight, oligomeric poly(CHO-co-PA) was afforded ( $M_n = 1100\text{--}4150 \text{ gmol}^{-1}$ ,  $\mathcal{D} = 1.17\text{--}1.28$ ). The molecular weight increased as the reagents were further purified, such as further distilling the CHO (from singly distilled to triply distilled) and subliming or triply recrystallising the PA (*Table 25*, entries 1–4); these observations agree with that reported in literature.<sup>[12,40,50]</sup> Triply recrystallised PA, using hot toluene, was observed to be more successful than purification *via* hot filtration using chloroform and subsequent sublimation of the PA. Despite the low molecular weights, the polymerisation was well controlled. The PA conversion and  $M_n$  values were gradually raised by increasing the reaction time with the high % ester linkages and narrow dispersities maintained (*Table 25*, entries 4–6, % ester linkages = 92–95%,  $\mathcal{D} = 1.24\text{--}$

1.28). In agreement with literature, it was revealed that the PPNCI was active for the polymerisation with no [Fe] present (*Table 25*, entry 7).<sup>[29,30,39]</sup> This finding was significant as it implied the possibility that the [Fe] catalyst was not participating cooperatively with the PPNCI co-catalyst in the polymerisation; similar to that for Merna and unlike that for Jiang.<sup>[29,30]</sup>

*Table 25.* Initial investigations into the solution ROCOP of CHO / PA using Fe(**13**)OAc catalyst and PPNCI co-catalyst in toluene.

Entry	Anhydride	Epoxide	Time (h)	PA conv. <sup>a</sup> (%)	% ester linkages <sup>b</sup>	$M_n^c$ (gmol <sup>-1</sup> )	$\bar{D}^c$
1	Commercial PA	1 x dist. CHO	2	39	83	1100	1.17
2	Sublimed PA	1 x dist. CHO	1	40	91	1500	1.27
3	Sublimed PA	2 x dist. CHO	1	47	91	1250	1.22
4	3 x recry PA	3 x dist. CHO	1	36	92	2100	1.24
5	3 x recry PA	3 x dist. CHO	2.5	59	94	3600	1.24
6	3 x recry PA	3 x dist. CHO	3	72	95	4150	1.28
7 <sup>d</sup>	3 x recry PA	3 x dist. CHO	1	32	94	3250	1.20
8 <sup>e</sup>	3 x recry PA	3 x dist. CHO	48	23	65	–	–

Conditions: PA (0.3703 g, 2.5 mmol), CHO (0.253 mL, 2.5 mmol), catalyst (1 mol%, 0.025 mmol), co-catalyst (1 mol%, 0.025 mmol), [PA]:[CHO]:[Fe(**13**)OAc]:[PPNCI]=[100]:[100]:[1]:[1], toluene (1.0 mL), 100 °C. PA here was either purified *via* hot filtration using chloroform and sublimed or recrystallised (recry) using anhydrous toluene. <sup>a</sup> Determined by <sup>1</sup>H NMR spectroscopy (CDCl<sub>3</sub>) by integrating the resonances of PA ( $\delta$  7.88–8.07 ppm) and the aromatic phenylene resonances in the poly(CHO-*co*-PA) ( $\delta$  7.34–7.65 ppm). <sup>b</sup> Selectivity determined by <sup>1</sup>H NMR spectroscopy (CDCl<sub>3</sub>) by integrating the resonances of the ester linkages ( $\delta$  5.04–5.26 ppm) and the ether linkages ( $\delta$  3.57–3.66 ppm) of the rinsed (3 x 10 mL methanol) and dried, isolated poly(CHO-*co*-PA) polymer. <sup>c</sup> Determined *via* GPC (refractive index analysis) in THF solvent referenced against polystyrene standards with no correction factor. <sup>d</sup> No Fe(**13**)OAc added and only PPNCI as the catalyst. <sup>e</sup> No PPNCI co-catalyst added and only Fe(**13**)OAc.

It was rationalised that, whilst the PPNCI was more active as a catalyst than Fe(**13**)OAc, the higher reactivity was contributing to the undesired low molecular weight, oligomeric poly(CHO-*co*-PA) obtained. In literature, there are examples

where co-catalyst is not necessary and the catalyst; more specifically the auxiliary ligand on the catalyst, can sufficiently ring open the epoxide and anhydride without the aid of an added nucleophilic additive.<sup>[33,43]</sup> Fe(**13**)OAc, and all the synthesised Fe(III)–acetate complexes (**Section 2.5, Scheme 8**), bear resemblance to Williams and co-workers' zinc and magnesium dinuclear complexes, with the acetate auxiliary ligands present, and no co-catalyst was required in their study.<sup>[43]</sup>

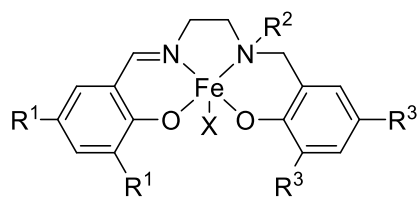
Thus, the hypothesis was that the Fe(III)–acetate complexes and the acetate auxiliary ligand present in each, must be able to initiate ring opening and the reaction without the presence of PPnCl co-catalyst. Although slower catalysis will be observed due to the use of a mononuclear catalyst and the element iron, in comparison with Williams, a higher molecular weight polymer may grow on the Fe(III) centre, compared with the earlier attempts using a binary system (*Table 25*), with the high degree of ester linkages maintained. Other benefits of this approach would be the avoidance of an extra additive and aiming to find simpler, alternative green catalytic systems based on benign and abundant iron. Additionally, this would allow the avoidance of phosphine based chemicals, with phosphorus becoming a potentially endangered element in the future due to the differences in global supply and demand.<sup>[51]</sup>

Indeed, attempting the PA / CHO ROCOP with only Fe(**13**)OAc catalyst (*Table 25*, entry 8), without any PPnCl co-catalyst, for an extended 48 hour reaction time, displayed reactivity; albeit a low PA conversion was observed, this result was crucial as demonstrated it was possible. Therefore, building on from this result, this developed polymerisation protocol and approach was found to be successful, as will be discussed next in **Section 5.3**, when conducted at 100 °C for three days to isolate higher molecular weight poly(CHO-co-PA).

### **5.3 Ring opening copolymerisation of phthalic anhydride and cyclohexene oxide using Fe(III) complexes in solution conditions**

A diverse range of fourteen Fe(L)X complexes, with structurally distinct frameworks, covering salalen, thioen, salan and salen (or salophen) classes of ligand, were screened as catalysts for PA / CHO ROCOP (overview shown in *Scheme 37*).



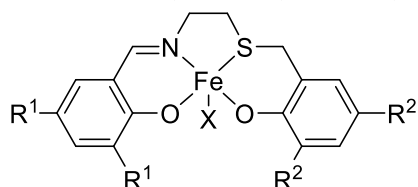


**Fe(1)OAc** : R<sup>1</sup> = H, R<sup>2</sup> = Me, R<sup>3</sup> = <sup>t</sup>Bu, X = OAc

**Fe(3)OAc** : R<sup>1</sup> = <sup>t</sup>Bu, R<sup>2</sup> = Me, R<sup>3</sup> = <sup>t</sup>Bu, X = OAc

**Fe(3)Cl** : R<sup>1</sup> = <sup>t</sup>Bu, R<sup>2</sup> = Me, R<sup>3</sup> = <sup>t</sup>Bu, X = Cl

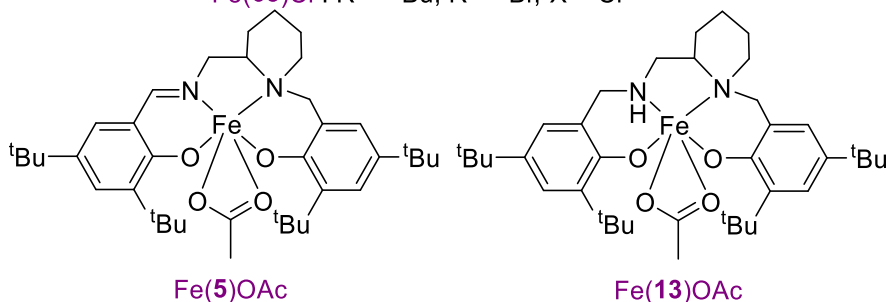
**Fe(10)OAc** : R<sup>1</sup> = <sup>t</sup>Bu, R<sup>2</sup> = Ph, R<sup>3</sup> = <sup>t</sup>Bu, X = OAc



**Fe(62)OAc** : R<sup>1</sup> = <sup>t</sup>Bu, R<sup>2</sup> = <sup>t</sup>Bu, X = OAc

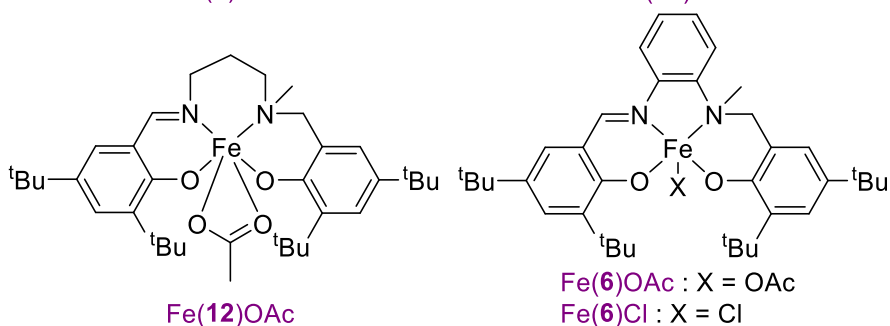
**Fe(62)Cl** : R<sup>1</sup> = <sup>t</sup>Bu, R<sup>2</sup> = <sup>t</sup>Bu, X = Cl

**Fe(65)Cl** : R<sup>1</sup> = <sup>t</sup>Bu, R<sup>2</sup> = Br, X = Cl



**Fe(5)OAc**

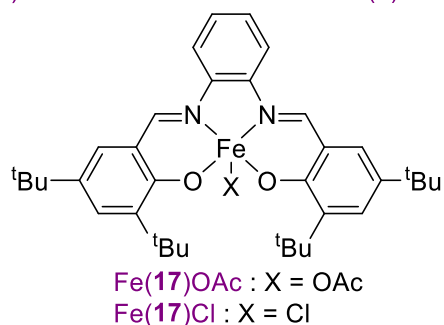
**Fe(13)OAc**



**Fe(12)OAc**

**Fe(6)OAc** : X = OAc

**Fe(6)Cl** : X = Cl



**Fe(17)OAc** : X = OAc

**Fe(17)Cl** : X = Cl

*Scheme 37.* Overview of the variety of Fe(III) initiators {Fe(L)X} applied in this study for the simple, alternating ROCOP of PA and CHO without any extra additives or co-catalyst. To note, when the ligands (L) were applied solely as organo-initiators, these were the corresponding diphenol compounds and not diphenolate; as is the case when complexed to the Fe(III) centre.

This screening was conducted at 100 °C for three days in toluene ([PA]:[CHO]:[Fe]=[100]:[100]:[1]), without the need for extra additives or co-catalyst, as part of a unary system (*Table 26*). This would allow comparison, between the Fe initiators, for their catalytic activity and chemoselectivity (% ester linkages) and the resulting molecular weights and dispersities of the isolated polymer. Despite these species being slower than the few alternate binary Fe catalytic systems in literature, on the whole, reasonable molecular weight polymer with high % ester linkages was afforded. Removing the co-catalyst allowed the Fe(III) centre to catalyse the reaction; indeed, there are scarce examples of metal systems in literature without such an additive and almost always, PPNCI is required in conjunction with a metal initiator (**Section 5.2**, *Scheme 36*).<sup>[10,26,27,29,30,33,34]</sup>

To determine the PA conversion, small aliquots of the crude reaction mixture were taken and <sup>1</sup>H NMR spectroscopy used to measure and compare the integrals of the observed aromatic resonance signals for unreacted PA and the poly(CHO-co-PA) (**Section 6.20**, *Figure 95*).<sup>[29,38,43,52]</sup> Isolation of a purified polymer; to ensure all residual, paramagnetic [Fe] catalyst and unreacted reagents were removed, was achieved by dissolving the crude product in dichloromethane and precipitating a white solid using acidified methanol (1 M). <sup>1</sup>H NMR spectroscopy was used on this purified polymer to determine the % ester linkages by comparing the integrals of the observed resonance signals for the ester linkages respectively to the ether linkages.<sup>[43,52]</sup> It was suggested by Williams that the use of deuterated dimethyl sulfoxide (DMSO-d<sub>6</sub>) minimised the overlap between the end groups for the poly(CHO-co-PA) and ether resonance signals.<sup>[43]</sup> Hence, this was attempted as a cross-check, but the chemoselectivity values observed were identical to that in CDCl<sub>3</sub>. In addition to this, it was found the poly(CHO-co-PA) was unexpectedly less soluble in the DMSO-d<sub>6</sub> and the residual water peak perturbed detection of the poly(CHO-co-PA) end group.<sup>[43]</sup>

Table 26. PA / CHO ROCOP in solution conditions using Fe(L)X and organic initiators.

Entry	Catalyst (Cat.)	PA conv. <sup>a</sup> (%)	Isolated yield (%)	% ester linkages <sup>b</sup>	$M_{n,theo}^c$ (gmol <sup>-1</sup> )	$M_n^d$ (gmol <sup>-1</sup> )	$\bar{D}^d$
1	None	5	–	46	–	–	–
2	Fe(OAc) <sub>2</sub>	42	51	39	10500	6100	1.24
3	FeCl <sub>3</sub>	– <sup>e</sup>	51	40	12700 <sup>e</sup>	6400	1.05
4	Fe( <b>1</b> )OAc	93	82	92	23100	11250	1.14
5	Ligand <b>3</b>	72	58	93	17750	15200	1.13
6	Fe( <b>3</b> )OAc	43	38	92	10750	10300	1.21
7	Fe( <b>3</b> )Cl	57	38	91	14150	8900	1.04
8	Ligand <b>5</b>	89	77	95	21950	16200	1.15
9	Fe( <b>5</b> )OAc	41	33	91	10250	8650	1.18
10	Ligand <b>6</b>	77	56	95	19000	19600	1.12
11	Fe( <b>6</b> )OAc	82	72	97	20350	15300	1.19
12 <sup>f</sup>	Fe( <b>6</b> )OAc	39	44	49	9750	7350	1.21
13	Fe( <b>6</b> )Cl	77	70	96	19100	13600	1.14
14	Fe( <b>10</b> )OAc	58	61	47	14450	9400	1.13
15	Fe( <b>12</b> )OAc	61	46	92	15200	10150	1.18
16	Ligand <b>13</b>	98	80	96	24150	14300	1.12
17	Fe( <b>13</b> )OAc	45	49	41	11250	6000	1.16
18	Ligand <b>17</b>	95	81	96	23450	29100	1.09
19	Fe( <b>17</b> )OAc	46	32	94	11500	11550	1.06
20	Fe( <b>17</b> )Cl	55	49	95	13700	12550	1.19
21	Fe( <b>62</b> )OAc	71	57	72	17650	8600	1.15
22	Fe( <b>62</b> )Cl	53	32	95	13200	13750	1.08
23	Fe( <b>65</b> )Cl	55	41	86	13700	10100	1.19

Conditions: 3 x recrystallised PA (0.3703 g, 2.5 mmol), 3 x distilled CHO (0.253 mL, 2.5 mmol), catalyst (1 mol%, 0.025 mmol), [PA]:[CHO]:[Cat.]=[100]:[100]:[1], toluene (1.0 mL), 100 °C, three days.

<sup>a</sup> Determined by <sup>1</sup>H NMR spectroscopy (CDCl<sub>3</sub>) by integrating the resonances of PA (δ 7.88–8.07 ppm) and the aromatic phenylene resonances in the poly(CHO-co-PA) (δ 7.34–7.65 ppm). <sup>b</sup> Selectivity determined by <sup>1</sup>H NMR spectroscopy (CDCl<sub>3</sub>) by integrating the resonances of the ester linkages (δ

5.04–5.26 ppm) and the ether linkages ( $\delta$  3.57–3.66 ppm) of the dried, isolated poly(CHO-co-PA) polymer. <sup>c</sup>  $M_{n,theoretical} = [(Conversion/100 \times [PA]/[Fe] \times M_r) + \text{end group MW from the corresponding auxiliary-cyclohexanol group of the complex (X) or methanol if ligand (L)}] = [(Conversion/100 \times [PA]/[Fe] \times 246.26 \text{ gmol}^{-1}) + \text{end group MW}]$ , assuming 100% ester linkages. <sup>d</sup> Determined *via* GPC (triple detection analysis) in THF solvent. <sup>e</sup>  $M_{n,theoretical}$  was calculated using isolated yield due to being unable to calculate PA conversion because of the highly paramagnetic FeCl<sub>3</sub> broadening the resonances of PA. <sup>f</sup> [PA]:[CHO]:[Cat.]=[100]:[600]:[1], two days.

To begin with, control reactions using the precursors, Fe(OAc)<sub>2</sub> and FeCl<sub>3</sub>, offered some reactivity but no chemocontrol for the polymers' linkages (*Table 26*, entries 2 and 3). This demonstrated the requirement for a structural ligand framework around the Fe(III) centre to ensure selective control. A blank reaction, with both substrates with no catalyst, showed no reactivity (*Table 26*, entry 1). Curiously, the aromatic phenolate moieties, on the ligand framework for the Fe(III)–salalen–acetate complexes, comprising of either *tert*-butyl substituents or unsubstitution resulted in no influence on the % ester linkages with both observing high degrees of chemocontrol {Fe(**1**)OAc vs. Fe(**3**)OAc, 92% ester linkages}. Although, as would be expected, the more sterically hindered Fe(**3**)OAc was less than half as active as the catalytically more accessible Fe(**1**)OAc, but both complexes did produce reasonable molecular weight polymer with narrow distributions {Fe(**1**)OAc; 93% PA conversion,  $M_n = 11250 \text{ gmol}^{-1}$ ,  $\mathcal{D} = 1.14$  and Fe(**3**)OAc; 43% PA conversion,  $M_n = 10300 \text{ gmol}^{-1}$ ,  $\mathcal{D} = 1.21$ }. Compared to Fe(**3**)OAc, the *tert*-butyl chloride analogue, Fe(**3**)Cl; the complex previously discussed to being a moderately isoselective initiator for the controlled ROP of *rac*-LA (**Section 3.4**,  $P_m = 0.75\text{--}0.80$ ), maintained the same chemoselectivity (91% ester linkages), was a more active initiator and resulted in a better distributed but lower molecular weight polymer {Fe(**3**)Cl; 57% PA conversion,  $M_n = 8900 \text{ gmol}^{-1}$ ,  $\mathcal{D} = 1.04$ }. A higher activity with a low degree of ester linkages {Fe(**10**)OAc, 61% PA conversion, 47% ester linkages) was observed when an electron withdrawing phenyl group was installed on the amine nitrogen donor atom ( $R^2 = \text{Ph}$ , *Scheme 37*).

Focussing on this amine donor atom, modifying this further to a softer, more hemilabile sulfur donor atom, and resulting thiolen class of ligand framework (**Section 3.3**, *Figure 45*), afforded enhanced activity and was accompanied with

moderate chemoselectivity for Fe(**62**)OAc. A polymer with a reduced molecular weight was produced but the polymerisation remained controlled {Fe(**3**)OAc vs. Fe(**62**)OAc, 71% PA conversion, % ester linkages = 72%,  $M_n = 8600 \text{ gmol}^{-1}$ ,  $\mathcal{D} = 1.15$ }. Unlike the salalen ligand framework, the opposite trend was observed when shifting from the acetate to the chloride analogue, Fe(**62**)Cl, with activity decreasing and a polymer containing higher % ester linkages, molecular weight and narrower dispersity isolated {Fe(**62**)Cl, 53% PA conversion, % ester linkages = 95%,  $M_n = 13750 \text{ gmol}^{-1}$ ,  $\mathcal{D} = 1.08$ }. In an attempt to increase both the Lewis acidity of the Fe(III) centre and activity, bromo–functionality was introduced into the Fe(III)–thiolen–chloride complex, using Fe(**65**)Cl. However, this was unsuccessful with both reactivity and chemoselectivity reduced (*Table 26*, entry 23).

Focussing back on the salalen ligand framework, the installation of a rigid, six-membered aminopiperidine ring and altering the ethylene backbone, drastically reduced the molecular weight and had minimal influence on both activity and selectivity {Fe(**3**)OAc vs. Fe(**5**)OAc, *Table 26*, entry 9}. Reducing the imine group, on the salalen framework, to an amine and corresponding Fe(**13**)OAc salan complex, increased the reactivity slightly but a polymer with poor % ester linkages and molecular weight was isolated {Fe(**13**)OAc, 45% PA conversion, % ester linkages = 41%,  $M_n = 6000 \text{ gmol}^{-1}$ ,  $\mathcal{D} = 1.16$ }. This result was unexpected, seeing that this complex was the most effective catalyst for CO<sub>2</sub> / CHO coupling (**Section 4.5**). It was postulated that the NH group was advantageous in this instance, by possibly providing additional H–bonding interactions with the CO<sub>2</sub> and CHO substrates and improving activity; however, it seems this negatively impacted this ROCOP reaction.<sup>[53]</sup> Alternatively, modifying the ligand backbone to a more flexible propylene moiety, considerably increased the activity compared to the ethylene bridge, whilst high % ester linkages, reasonable molecular weight and narrow distribution was maintained {{Fe(**3**)OAc vs. Fe(**12**)OAc, *Table 26*, entry 15}.

The most success was achieved when employing a phenyl ring in the backbone of the salalen ligand framework. These phenyl bridged, Fe(III)–salalen–acetate and chloride complexes observed the highest activities and chemoselectivities (77–82% PA conversion, >96% ester linkages) of the Fe systems studied {Fe(**6**)OAc and Fe(**6**)Cl,

*Table 26*, entries 11 and 13}. The highest molecular weight afforded for all the Fe(III) initiators, was using Fe(**6**)OAc with a narrow dispersity maintained ( $M_n = 15300 \text{ gmol}^{-1}$ ,  $\mathcal{D} = 1.19$ ). A reduction in the reaction time was attempted to two days by using an excess of CHO substrate ([PA]:[CHO]:[Cat.]=[100]:[600]:[1]), but significant, undesired ether linkages were formed and the chemocontrol of the polymerisation was lost (*Table 26*, entry 12). The corresponding phenyl bridged, Fe(III)–salen–acetate and chloride complexes {Fe(**17**)OAc and Fe(**17**)Cl} were not as active in comparison, but reasonably high molecular weights and high degree of ester linkages were realised (*Table 26*, entries 19 and 20).

Interestingly, as discussed earlier (**Section 5.1**), Fe(**17**)Cl is identical to Fe(**136**)Cl and, its use as a catalyst, in combination with PPnCl or DMAP co–catalyst was already reported by Merna and co–workers (110 °C in toluene, [PA]:[CHO]:[Cat.]:[Co–cat.]=[250]:[250]:[1]).<sup>[29]</sup> This was specifically intended to allow comparison between the single–component protocol developed here (*Table 26*, entry 20) with Merna’s binary catalytic system.<sup>[29]</sup> The traditional, more usual two–component method of ROCOP operated at dramatically smaller reaction times (one–five hours) but resulted in lower molecular weights ( $M_n = 3700\text{--}9700 \text{ gmol}^{-1}$ ) and slightly broader distribution ( $\mathcal{D} = 1.27\text{--}1.33$ ).<sup>[29]</sup> However, as highlighted earlier, it was proven that PPnCl and DMAP operated faster by themselves and, therefore, in the binary system the [Fe] was most likely not initiating or contributing to the ROCOP; rather it was inhibiting the reaction. Merna attempted control reactions with [Fe] present without co–catalyst, but for only 24 hours reaction time.<sup>[29]</sup> This duration is insufficiently short and hence no activity was observed for Fe(**136/137**)Cl (*Figure 68*). Although Fe(**135**)Cl, bearing a diaminocyclohexane backbone, demonstrated it was possible to observe moderate reactivity in 24 hours and a reasonable molecular weight was noted, albeit with a broad distribution (64% PA conversion,  $M_n = 9700 \text{ gmol}^{-1}$ ,  $\mathcal{D} = 1.52$ ).<sup>[29]</sup>

The most interesting finding of this study was that the ligand control reactions showed activity (*Table 26*, entries 5, 8, 10, 16 and 18), and it was realised that all frameworks were more effective as organocatalysts than the respective Fe(III) complex analogues. This bears strong resemblance to North and co–workers recent

application of salophen ligands, without metal and halide co-catalyst, to CO<sub>2</sub> / terminal epoxide coupling *via* a proposed intramolecular H-bonding, 'dual activation' mechanism; as was covered in **Section 4.5** (*Scheme 32*).<sup>[53]</sup> Although, activity was not observed for the salalen and salan ligand control reactions for CO<sub>2</sub> / CHO coupling (**Section 4.5**, *Tables 17 and 18*), it seems reactivity *via* H-bonding interactions and a possible 'dual activation' mechanism appears to be occurring for this ROCOP study.<sup>[53]</sup> This mechanism differs to that, of the more traditional, metal-mediated ROCOP mechanism (**Section 5.1**, *Scheme 34*), expected to be occurring when the Lewis acidic Fe(III) complexes {Fe(L)X} were applied as initiators; with the inherent labile, auxiliary chloride or acetate ligands (X) ring opening the monomer.<sup>[10,19]</sup>

Furthermore, as was the case for the Fe(III) complexes, the phenyl bridged 'ligands' were the most effective organo-initiators and these findings agree with the observations and propositions discussed by North; indeed **17** was one such salophen example applied by North for CO<sub>2</sub> / epoxide coupling.<sup>[53]</sup> The phenyl moiety appears crucial and, as discussed in **Section 4.5**, how the diiminobenzene plane specifically aligns itself, relative to the phenolate rings, and the overall point group symmetry contribute to the effectiveness of the H-bonding interactions and the catalytic activity. Differences in the observed activity may arise by a combination of these factors.<sup>[53]</sup>

All ligands / organocatalysts: **3**, **5**, **6**, **13** and **17** displayed high PA conversions (72–98% PA conversion), chemoselectivity (% ester linkages = 93–96%) and narrow dispersities ( $\bar{D} = 1.09–1.15$ ). Despite there being no Lewis acidic metal centre present for the growing PE, poly(CHO-*co*-PA) chains, reasonably high molecular weights were obtained ( $M_n = 14300–29100 \text{ gmol}^{-1}$ ). The ethylene bridged salalen framework was moderately less active than the rigid aminopiperidine backbone (**3** vs. **5**, *Table 26*, entries 5 and 8). In contrast to the trends observed for the respective Fe(III) complexes, the application of the reduced aminopiperidine, salan framework with an NH donor group (**13**) further improved activity (98% PA conversion), as would be anticipated with the potential for additional H-bonding interactions to occur with the PA and CHO substrates. This enhanced reactivity was accompanied with the high degree of ester linkages being maintained (% ester linkages = 96%). Identical to the

Fe(III) complexes, the salalen and salen structural frameworks bearing phenyl bridged backbones were the most effective organo–initiators with high activity, chemoselectivity and the highest molecular weights afforded. Remarkably, the application of phenyl salalen **6** and salophen **17** observed molecular weights of 19600 gmol<sup>-1</sup> and 29100 gmol<sup>-1</sup> respectively and a narrow distribution was maintained.

As far as we are aware, this is the first time these structurally simple, air–stable, classes of ligand: salalen, salan and salen / salophen, have been applied to anhydride / epoxide ROCOP. Even though the corresponding, analogous metal complexes, covering a wide variety of elements, have been heavily applied as initiators.<sup>[29,33–35,38,54,55]</sup> These findings seemed important as a simplistic, single–component, metal– and halide–free, organocatalytic approach was stumbled upon and investigated that formed highly alternating poly(CHO–co–PA) with reasonable molecular weight and dispersities. In the literature, there are scarce examples of organo–initiators and these tend to rely on two–component systems, such as Lewis pairs, with harsher, air–sensitive moieties based on organoboron and phosphazenes.<sup>[12,24,39–42,56–64]</sup> A drawback with this approach is the longer reaction times (three days), but this study does provide hope that other, simple, more reactive organic compounds may be effective one–component initiators for ROCOP, without the need for extra additives and the reaction time can be reduced. Additionally, as was highlighted by North, this work further reinforces the need for ligand control reactions throughout all catalysis and polymerisation studies.<sup>[53]</sup> This area of organocatalytic ROCOP is in its infancy but will no doubt emerge, and could potentially prove critical to future sustainable polymerisation research.<sup>[12,24,56]</sup> Recently, this area was well reviewed by Le Bideau and co–workers.<sup>[12]</sup>

Another consideration to discuss is the stability of the Fe(III) complexes, when used as initiators for ROCOP, at 100 °C for three days. If catalyst demetallation occurred in the reaction mixtures and free ligand was liberated; with these organocatalysts displaying enhanced activity in comparison to their respective Fe(III) complex analogues, it would be likely that the polymerisation was being initiated by these organic species and not the Fe(III) complex. However, it was proposed that this was not occurring in this study. The colour of the ROCOP reaction mixture was maintained



over the course of the whole three day duration. For example, if an Fe(III)–salalen–acetate complex was used, such as Fe(3)OAc, the dark purple colour would remain throughout. This observation differs to that for the CO<sub>2</sub> / CHO coupling discussed earlier (**Section 4.8**), where reaction mixtures typically changed from dark purple to dark red / brown. After conducting UV–Vis spectroscopy on these CO<sub>2</sub> / CHO coupling reaction mixtures and in agreement with literature, this colour change was proposed to result from the formation of the  $\mu$ -oxo-bridged Fe(III) dimer species.<sup>[65]</sup> Therefore, because the colour remained unchanged for ROCOP, this implied the Fe(III) initiator was stable, at these reaction conditions, and did not decompose or undergo epoxide deoxygenation to form the  $\mu$ -oxo-bridged Fe(III) dimer species. For further confirmation, two experiments were conducted: the solution ROCOP of PA / CHO using Fe(3)OAc was repeated (*Table 26*, entry 6) and Fe(3)OAc was simply stirred in toluene for three days at 100 °C. Both of these remained dark purple and aliquots of the crude mixtures were analysed using HR–MS. In both instances, the Fe(3)<sup>+</sup> ion was observed; indicative that the salalen ligand remained coordinated to the Fe(III) centre, and no free liberated ligand was observed. Therefore, it was proposed catalyst demetallation or decomposition was not occurring in this study.

The copolymers isolated were analysed, with DOSY (diffusion ordered spectroscopy) NMR spectroscopy confirming one polymeric species was present in the samples (*Figure 73*) and MALDI–ToF mass spectrometry providing evidence for the presence of both ester and ether linkages (**Section 7.10**, *Figures 167–172*). However, the MALDI–ToF spectra revealed complicated systems comprising of a range of potential end groups. It was determined and proposed these related to either the auxiliary ligands (X = OAc or Cl), hydrolysis and chloro–functionalisation; suggestive of chain transfer reactions occurring upon termination and when isolating the polymers with the acidified methanol / hydrochloric acid work-up (**Section 7.10**, *Figures 167–172*), or potentially cyclohexane / cyclohexene from potential Meerwein-Ponndorf-Verley reduction / Oppenauer oxidation (MPVO) side–reactions.<sup>[30,43,62,66]</sup> IR analysis was consistent with that reported in literature (**Section 6.21**, *Figures 98 and 99*).<sup>[29]</sup>

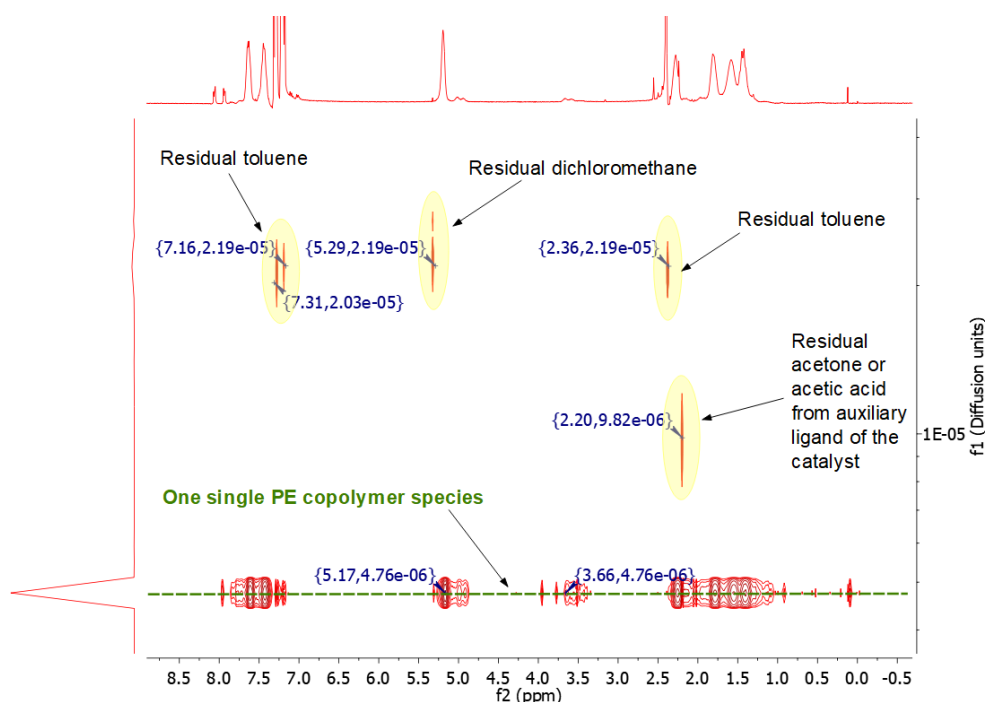


Figure 73. DOSY NMR spectrum of the poly(CHO-co-PA) obtained from the PA / CHO ROCOP in toluene using Fe(6)OAc (Table 26, entry 11) showing one polymeric species present. Crucially, the ester and ether linkage resonance signals belonged to this one polymeric species with a determined diffusion coefficient ( $D$ ) of  $4.8 \times 10^{-6} \text{ cm}^2 \text{ s}^{-1}$ .

#### 5.4 Ring opening copolymerisation of phthalic anhydride and cyclohexene oxide using Fe(III) complexes in neat conditions

Since the structural frameworks bearing phenyl bridged backbones were the most effective for solution ROCOP (Section 5.3, Table 26), in an effort to reduce the three day reaction time, these motifs were employed as initiators in solvent-free, neat reaction conditions. This was conducted using CHO in excess (800 eq.) to behave as both the substrate and solvent (Table 27); similar to that for the earlier  $\text{CO}_2$  / CHO coupling reactions (Section 4.5). In literature, it has been demonstrated that solvent-free, neat reaction conditions can significantly increase the rate of reaction, the activity of initiators and, in cases, improve the chemoselectivity to the ester linkages.<sup>[30,43]</sup>

To gauge the length of reaction time required for the neat ROCOP (Table 27), Fe(6)OAc was initially studied and it was realised that three days could be substantially reduced to 30 hours reaction time to achieve complete reactivity (100%

PA conversion, *Table 27*, entry 4). This enhanced reactivity may have been influenced by the higher solubility observed for the crystalline PA in the neat CHO reaction mixture.

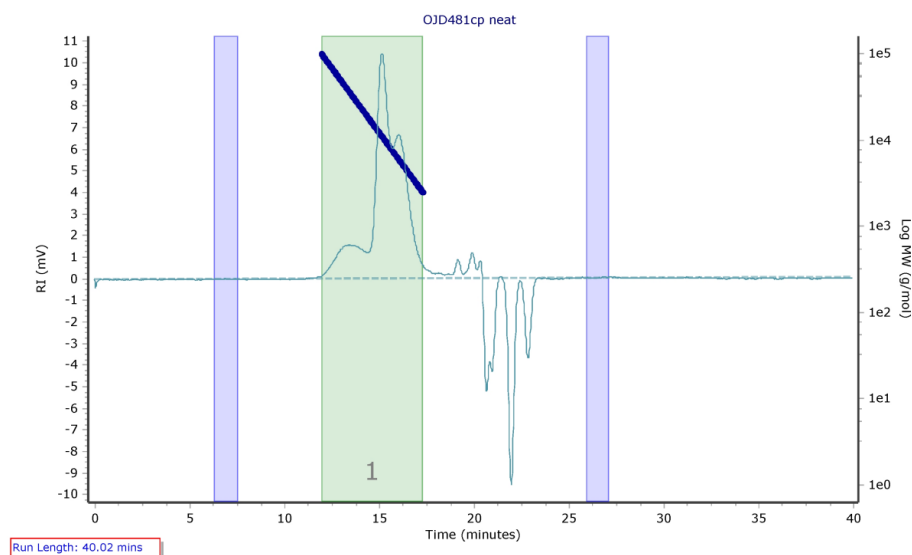
*Table 27.* PA / CHO ROCOP in neat conditions using Fe(L)X and organic initiators.

Entry	Catalyst (Cat.)	h <sup>a</sup>	PA conv. <sup>b</sup> (%)	Yield <sup>c</sup> (%)	% ester linkages <sup>d</sup>	$M_{n,theo}$ <sup>e</sup> (gmol <sup>-1</sup> )	$M_n$ <sup>f</sup> (gmol <sup>-1</sup> )	$\mathcal{D}$ <sup>f</sup>
1	<b>6</b>	30	100	97	69	25250	12500	1.17
2	Fe( <b>6</b> )OAc	24	34	51	24	8550	8100	1.67
3 <sup>g</sup>	Fe( <b>6</b> )OAc	72	30	44	20	7650	5750	2.46
4	Fe( <b>6</b> )OAc	30	100	95	69	24800	18900	1.20
5	Fe( <b>6</b> )Cl	30	74	86	45	18350	15750	1.17
6	<b>17</b>	30	32	24	49	8450	10400	1.10
7	Fe( <b>17</b> )OAc	30	66	71	50	16400	13250	1.28
8	Fe( <b>17</b> )Cl	30	66	74	49	16400	10100	1.35

Conditions: 3 x recrystallised PA (0.3703 g, 2.5 mmol), 1 x distilled CHO (2.0 mL, 20 mmol), catalyst (1 mol%, 0.025 mmol), [PA]:[CHO]:[Cat.]=[100]:[800]:[1], 100 °C. <sup>a</sup> h = Reaction time (hours). <sup>b</sup> Determined by <sup>1</sup>H NMR spectroscopy (CDCl<sub>3</sub>) by integrating the resonances of PA ( $\delta$  7.88–8.07 ppm) and the aromatic phenylene resonances in the poly(CHO–co–PA) ( $\delta$  7.34–7.65 ppm). <sup>c</sup> Yield = Isolated yield of the poly(CHO–co–PA) obtained after the CH<sub>2</sub>Cl<sub>2</sub> / acidified MeOH (1M) work-up. <sup>d</sup> Selectivity determined by <sup>1</sup>H NMR spectroscopy (CDCl<sub>3</sub>) by integrating the resonances of the ester linkages ( $\delta$  5.04–5.26 ppm) and the ether linkages ( $\delta$  3.26–3.67 ppm) of the dried isolated polymer. <sup>e</sup>  $M_{n,theoretical}$  = [(Conversion/100 x [PA])/[Fe] x  $M_r$ ] + end group MW, assuming 100% ester linkages. <sup>f</sup> Determined *via* GPC (triple detection analysis) in THF solvent. <sup>g</sup> Reaction temperature = 80 °C.

However, in contrast with the solution ROCOP reactions in toluene, this neat polymerisation was less controlled and was accompanied with broadening in the resonance signals in the ether linkage region and a decreased, low chemoselectivity (69% ester linkage) (**Section 6.20**, *Figure 96*).<sup>[52]</sup> The molecular weight of the polymer was higher, than that obtained in the solution ROCOP conditions, and a narrow distribution was still preserved ( $M_n$  = 18900 gmol<sup>-1</sup>,  $\mathcal{D}$  = 1.20 vs. *Table 26*, entry 11). A lower PA conversion was observed when reducing the reaction time to 24 hours (34% PA conversion) and this indicated, for this particular initiator, the optimum

reaction time was between this 24–30 hour period. This was in addition to significantly lower degrees of ester linkage and molecular weight. For this 24 hour reaction (*Table 27*, entry 2), the GPC chromatogram observed three peaks (*Figure 74*); alongside the usually observed bimodal peak, an unknown extra peak was present. The bimodal peak was observed in all cases for the solution ROCOP reactions (**Section 7.8**, *Figures 140–147*), using Fe(L)X and organic initiators, and is common in literature due to the presence of additional initiating species or chain transfer agents (CTAs) such as diol impurities in the CHO epoxide; as discussed in **Section 3.7** for the ROP of *rac*-LA using PO as the solvent, residual water or dicarboxylic acid impurities (phthalic acid) from hydrolysis of the PA.<sup>[18,29,30,40]</sup>



*Figure 74.* GPC chromatogram of the polymer attained using Fe(6)OAc at 100 °C for 24 hours (*Table 27*, entry 2) ( $M_{n,GPC} = 8100 \text{ gmol}^{-1}$ ,  $M_{n,theoretical} = 8550 \text{ gmol}^{-1}$ ,  $\bar{D} = 1.67$ ).

This was also observed for a reaction where a reduction in the temperature was attempted, to 80 °C for 3 days (30% PA conversion, *Table 27*, entry 3), to unsuccessfully improve the % ester linkages (**Section 7.8**, *Figure 149*). This additional peak was not attributed to being a separate PCHO, polyether species because analysis, on polymers isolated from both the solution and neat reaction conditions, using DOSY NMR spectroscopy, indicated the ester and ether linkage resonance signals were part of the same, single polymer entity (*Figures 73 and 75* and **Section 6.20**, *Figure 97*). Intriguingly, for the 30-hour reaction conducted at 100 °C (*Table 27*, entry 4), with a higher PA conversion (100% PA conversion), the extra peak

disappears and bimodality was only observed (Section 7.8, Figure 150). This suggested chain exchange reactions were occurring in the polymerisations; at least, before high conversions of PA were consumed. This is in agreement and consistent with the MALDI–ToF analysis where, as was the case and mentioned for the solution ROCOP reactions (Section 5.3), complicated systems comprising of multiple series of ether linkage repeating units and a range of potential end groups were observed (Section 7.10, Figures 173 and 174).

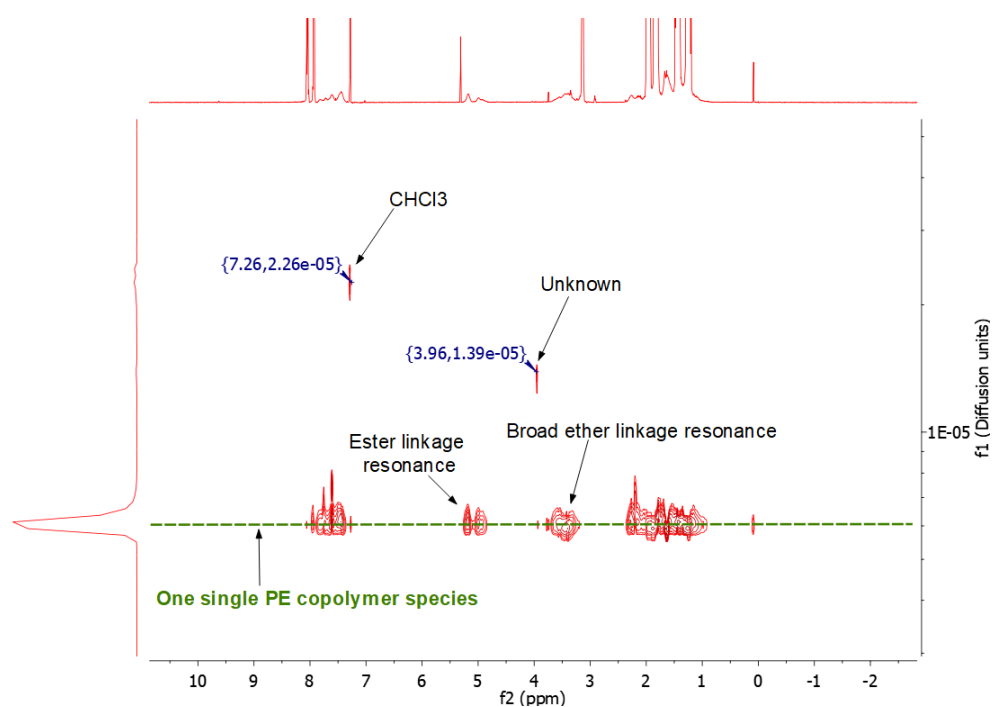


Figure 75. DOSY NMR spectrum of the polymer obtained from the PA / CHO ROCOP in neat conditions at 100 °C for 24 hours using Fe(6)OAc (Table 27, entry 2) showing one polymeric species present ( $D = 6.1 \times 10^{-6} \text{ cm}^2 \text{ s}^{-1}$ ). Despite the broad ether linkage resonance signal, it still belongs to this one polymeric species.

Therefore, using this 30–hour optimum reaction time probed by Fe(6)OAc, all the other phenyl bridged structural frameworks; both the Fe(III) complexes and respective ligands solely, were screened in the neat reaction conditions (Table 27, entries 1 and 5–8). Compared to Fe(6)OAc, the chloride analogue Fe(6)Cl was both less active and chemoselective {Fe(6)OAc vs. Fe(6)Cl; 74% PA conversion, % ester linkages = 45%} and, unlike that for the solution ROCOPs, the organo–initiator 6 observed identical reactivity and degrees of linkage, but resulted in a lower molecular weight polymer compared to both Fe(III) complexes (Table 27, entry 1 vs. entries 4

and 5). All the phenyl bridged salen structural frameworks {**17**, Fe(**17**)OAc and Fe(**17**)Cl} were not as effective as their corresponding salalen counterparts (*Table 27*, entries 6–8). The organo–initiator **17** was particularly disappointing in expectation, considering the success achieved from its use in the ROCOP conducted in toluene (**Section 5.3**, *Table 26*, entry 18), and was half as active compared to both Fe(**17**)OAc and Fe(**17**)Cl in the neat conditions. Furthermore, for Fe(**17**)OAc and Fe(**17**)Cl, three peaks were once again observed in the GPC analysis with a single polymer species observed *via* DOSY NMR spectroscopy. The reduction in the polymerisation control for the reactions in the neat, compared to that in solution, was evident in the MALDI–ToF analysis; where complicated systems comprising of multiple series were detected with a variety of potential end groups determined (**Section 7.10**, *Figures 175–177*). Ether linkage repeating units were most common for these series, consistent with <sup>1</sup>H NMR spectroscopy, but ester linkages were noted in cases. However, this observation may be associated to their propensity to ionize and not representative of the actual polymer sample. Overall, despite the chemoselectivity dropping significantly (% ester linkages = 45–69%), in comparison to the reactions in toluene, the neat ROCOPs are considerably faster (30 hours) and produce polymer with reasonable molecular weights and narrow dispersities ( $M_n = 10100\text{--}18900\text{ gmol}^{-1}$ ,  $\mathcal{D} = 1.10\text{--}1.35$ ).

## 5.5 Thermal analysis

A range of polymer samples, from the solution and neat ROCOP reactions, were selected for thermal analysis, *via* differential scanning calorimetry (DSC) (*Table 28*). As expected, the PEs were confirmed to be amorphous due to the absence of melting temperature ( $T_m$ ) and crystallisation temperature ( $T_c$ ) peaks. The  $T_g$  values, measured on the second heating cycle, were above the desired 100 °C target (**Section 5.1**) and reasonably ranged from 100–135 °C (**Section 7.9**); similar to other values reported in literature.<sup>[10,24,27,30,39,40,43,55,67,68]</sup> In this study, analysis of these  $T_g$  values proved challenging as not only were they generally dependant on the molecular weight and degrees of ester linkage; as discussion is commonly focused on in literature, but also on subtle changes in the molecular distribution of the polymer. Therefore, a balance of all three of these factors contributed to a higher  $T_g$  value. Indeed, concentrating

on the selection of polymers produced from solution ROCOP, the three highest  $T_g$  values recorded were 135 °C, 131 °C and 130 °C using Fe(**17**)OAc, Fe(**6**)Cl and **17** initiators respectively. These all comprised of the narrowest distributions observed ( $\mathcal{D} = 1.06$ – $1.14$ ). However, this reasoning fails to explain the particularly disappointing  $T_g$  value measured using initiator **6** ( $T_g = 106$  °C) with the corresponding polymer displaying the second highest molecular weight in this study, narrow distribution ( $\mathcal{D} = 1.12$ ) and high % ester linkages (95%). Overall, the 130 °C  $T_g$  value was promising considering the organic nature of the initiator and is competitive with other organocatalysts reported in literature.<sup>[24,39,40,57]</sup>

Table 28. Thermal properties of a selection of polymer samples obtained using DSC.

Entry	Polymer	Catalyst (Cat.)	% ester linkages <sup>c</sup>	$M_n$ (Da)	$\mathcal{D}$	$T_g^a$ (°C)	$T_d^b$ (°C)
1	Table 26, entry 6	Fe( <b>3</b> )OAc	92	10300	1.21	125	358
2	Table 26, entry 10	<b>6</b>	95	19600	1.12	106	355
3	Table 26, entry 11	Fe( <b>6</b> )OAc	97	15300	1.19	100	355
4	Table 26, entry 13	Fe( <b>6</b> )Cl	96	13600	1.14	131	356
5	Table 26, entry 18	<b>17</b>	96	29100	1.09	130	356
6	Table 26, entry 19	Fe( <b>17</b> )OAc	94	11550	1.06	135	351
7	Table 26, entry 20	Fe( <b>17</b> )Cl	95	12550	1.19	124	350
8	Table 27, entry 1	<b>6</b>	69	12500	1.17	110	354
9	Table 27, entry 4	Fe( <b>6</b> )OAc	69	18900	1.20	122	355
10	Table 27, entry 5	Fe( <b>6</b> )Cl	45	15750	1.17	114	354
11	Table 27, entry 7	Fe( <b>17</b> )OAc	50	13250	1.28	126	345
12	Table 27, entry 8	Fe( <b>17</b> )Cl	49	10100	1.35	120	341

<sup>a</sup> The  $T_g$  values were determined from the 2<sup>nd</sup> heating cycle. <sup>b</sup> The  $T_d$  values were measured at the end of the 2<sup>nd</sup> heating cycle.

The findings become more sophisticated and difficult to explain when shifting to the selection of polymers produced from neat ROCOP. Despite the broader dispersities and low % ester linkages, the  $T_g$  values ranged between 110–126 °C and were higher than expected. Complicated fragmentation patterns and significant ether linkages were observed using MALDI–ToF analysis. However, there must remain regions, in

the statistical polymer sample, of significant ester linkages to achieve these >100 °C values because pristine PCHO (100% ether linkages) is reported to have a dramatically reduced  $T_g$  value of around 67 °C.<sup>[69]</sup> It was determined by Darensbourg and co-workers using a binary Cr(III)–salen–chloride / PPNCI catalytic system, that small degrees of cross-linking can dramatically increase the  $T_g$  values of the resulting polymers.<sup>[38]</sup> As was discussed in **Section 5.1**, this was also observed by Kleij when exploring the  $T_g$  values for poly(BED-*alt*-PA).<sup>[31]</sup> This may account for the inconsistent trends occurring in this study if cross-linking was present and may explain why the polymer samples here, thermally outperformed Darensbourg's in this instance despite his higher molecular weights and chemoselectivity ( $T_g = 48$  °C,  $M_n = 18,000$  gmol<sup>-1</sup>,  $\bar{D} = 1.13$ , % ester linkages = >99%).<sup>[38]</sup> In addition to this, another consideration is the dichloromethane / acidified methanol purification protocol, as Williams and co-workers suggested their lower  $T_g$  values may have resulted from unoptimised purification of the isolated polymer.<sup>[43]</sup>

## 5.6 Attempted terpolymerisation using Fe(III) complexes

After successfully applying the Fe(III) complexes and organic initiators to PA / CHO ROCOP, it was decided to attempt the addition of a third monomer into the reaction mixture; and subsequent terpolymerisation.<sup>[10,43]</sup>

Recently, terpolymerisation has started to gain attention in literature with the goal of generating new materials *via* the production of block copolymers and improving upon the PEs and APCs accessed using a single ROCOP reaction.<sup>[43,70]</sup> With the use of a selective catalytic system, in cases 'switchable', the composition of the block copolymer can be controlled and is commonly achieved *via* sequential addition of the monomers or as a 'one-pot' reaction mixture. Hence, the properties can be tuned further to allow access to new applications.<sup>[10,43,61,71]</sup> Examples of such block copolymers include poly(ester-*b*-carbonate), poly(ester-*b*-ester) and poly(ester-*b*-ether).<sup>[10,19,70,71]</sup>

In literature, considerable focus has been devoted on using CO<sub>2</sub> and generating the poly(ester-*b*-carbonate).<sup>[10,43,72,73]</sup> This is because of the numerous benefits of using CO<sub>2</sub> as a reagent and because it allows simple and direct access to well defined blocks



with PEs, in one-pot reaction mixtures, due to the different ester and carbonate linkages present.<sup>[10,72–75]</sup> In addition to this, the added carbonate linkages and aliphatic repeating units can aid and improve properties such as biodegradability for the copolymer.<sup>[10,72]</sup> There are two methods to access them: the first includes the terpolymerisation of CO<sub>2</sub>, anhydride and epoxide monomer, and hence combines anhydride / epoxide ROCOP with CO<sub>2</sub> / epoxide ROCOP; two similar catalytic cycles.<sup>[10,19,43,71,72]</sup> The other, interesting method is combining CO<sub>2</sub> / epoxide ROCOP and lactone ROP; linking two distinct catalytic cycles.<sup>[10,19]</sup>

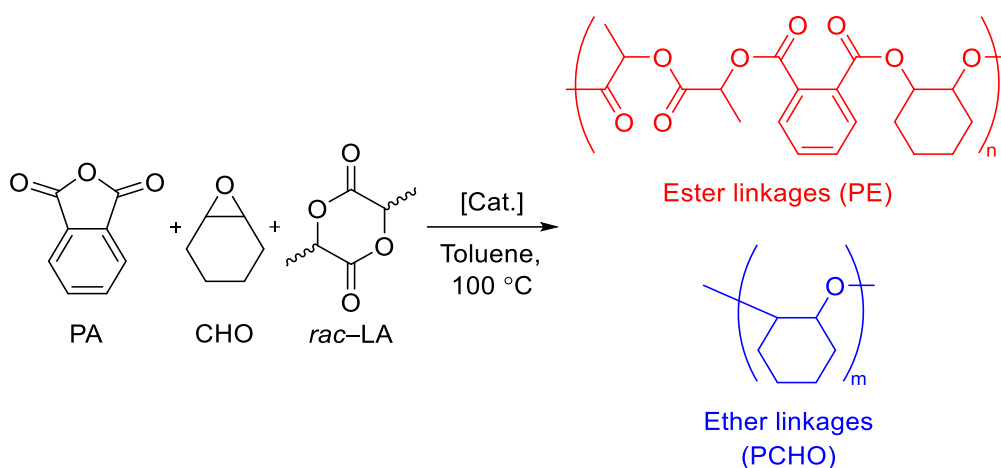
Therefore, building on the PA / CHO ROCOP studies from earlier (**Sections 5.3** and **5.4**) and combining with the findings from the CO<sub>2</sub> / epoxide coupling investigations (**Chapter 4**), it was hypothesised whether PA / CHO / CO<sub>2</sub> terpolymerisation could operate using the synthesised Fe(III) complexes (**Chapter 2**). The catalytic systems reported tend to favour the formation of the APC product and not the COC product when applied for CO<sub>2</sub> / epoxide coupling.<sup>[43,71,76,77]</sup> It is possible to obtain the APC product *via* COC reagents but this is a less common route.<sup>[78]</sup> As demonstrated in **Chapter 3**, the synthesised Fe(III) catalysts with TBAC co-catalyst exclusively formed the COC products and, without such co-catalyst, to encourage APC formation (discourage ring closure), the control reaction observed no reactivity after 24 hours (**Section 4.5**, *Table 17*, entry 6 and **Section 4.10**, *Table 23*, entry 1). As a check, this was further repeated using the most active catalyst Fe(**13**)OAc, at 10 bar of CO<sub>2</sub>, 100 °C for three days with CHO; identical conditions for ROCOP, using either no or one equivalent of TBAC co-catalyst. Unfortunately, there was no evidence for the formation of the PCHC product.

Alternatively, while the Fe(III) complexes did not favour APC formation, they have demonstrated to be active initiators for the ROP of *rac*-LA (**Chapter 3**). There are reports on the use of lactones in terpolymerisation to form either poly(ester-*b*-carbonate) and poly(ester-*b*-ester) copolymers.<sup>[10,18,19,70,71,77,79–81]</sup> However, there are limited examples on the use of LA in terpolymerisation, despite PLA being widely utilised in a range of commercial applications and the need to improve PLA's thermal properties.<sup>[61,73,75,78,82–86]</sup> Recently, promising developments have been made in this area: Williams and co-workers reported terpolymerisation using PA, PO and LA with

a Al(III)–salophen–chloride switchable catalyst, to yield poly(PLA–*b*–PPE) multiblock polyesters.<sup>[82]</sup> Soon after, using a dinuclear Zn catalyst, poly(PLA–*b*–PCHC) copolymer was synthesised.<sup>[83]</sup> This was using a new one–pot approach where the PLA repeating unit was obtained *via* the ROP of *O*–carboxyanhydride (LLA–OCA) with the release of CO<sub>2</sub> by–product. This CO<sub>2</sub> would be subsequently recaptured and recycled for the ROCOP with CHO to form the PCHC repeating unit.<sup>[83]</sup> This method resulted in near quantitative consumption of CO<sub>2</sub>, an atom economy of up to 91% and was promising from the point of view of CO<sub>2</sub> utilisation.<sup>[83]</sup> Li and co–workers recently demonstrated terpolymerisation with LA and a range of anhydrides and epoxides to produce sequence–controlled multiblock, polyester–polyol copolymers using a self–switchable, two–component organocatalytic system.<sup>[61]</sup> For these reasons, it was decided to attempt PA / CHO / *rac*–LA terpolymerisation.

To initially investigate the plausibility of the reaction, the PA / CHO ROCOP in toluene using Fe(6)OAc initiator (**Section 5.3**, *Table 26*, entry 11) was repeated and after the three day reaction period, *rac*–LA was sequentially added. This initiator was the most active Fe(III) initiator observed earlier and it was hypothesised that a Fe(III) centre would be required for the polymer chains of PLA to grow. However, no reactivity was observed after three further days upon LA addition at 100 °C.

This approach was revised and modified to include the *rac*–LA monomer at the start of the reaction, together with the other PA and CHO reagents, as a ‘one–pot’, crude reaction mixture (*Scheme 38*). This one–step protocol is identical to that applied by Li and co–workers.<sup>[61]</sup> Attempting this with Fe(6)OAc initiator, at 100 °C for three days; identical conditions to the ROCOP reaction, proved interesting and <sup>1</sup>H NMR spectroscopy, of an aliquot taken from the reaction mixture, observed low reactivity for *rac*–LA (8% conversion) and evidence for the formation of PLA as a small shoulder resonance signal corresponding to the methine proton environment; slightly overlapping the unreacted LA methine resonance signal. This was in addition to a low PA conversion (11% conversion) to poly(1,2–cyclohexylene–1,2–phthalate) and a moderate degree of ester linkages (% ester linkages = 87%).



*Scheme 38.* The attempted terpolymerisation of PA, CHO and *rac*-LA in toluene to produce block copolymers.

This believed PLA formation was clearer, with no resonance signals overlapping, when the ligand control reaction, using organo-initiator **6** was attempted (*Figure 76*). Both the PA and *rac*-LA conversions were higher for **6** (28% and 20% conversions respectively) and the methine resonance signal for the PLA was observed with a distinct quartet coupling pattern (*Figure 76*). This observation was postulated to be due to there being no stereocontrol for the PLA present in the polymerisation. As was demonstrated earlier, the organo-initiators were significantly more effective for solution ROCOP in comparison to the Fe(III) initiators (**Section 5.3**, *Table 26*). Therefore, another terpolymerisation was attempted with the addition of one equivalent of organo-initiator **6**, to encourage the PA / CHO reactivity, and one equivalent of Fe(**6**)OAc, with an Fe(III) centre to encourage PLA formation (*Table 29*, entry 3); a tandem catalytic approach.<sup>[19]</sup> This resulted in a minimal change in reactivity compared to that using **6** solely.

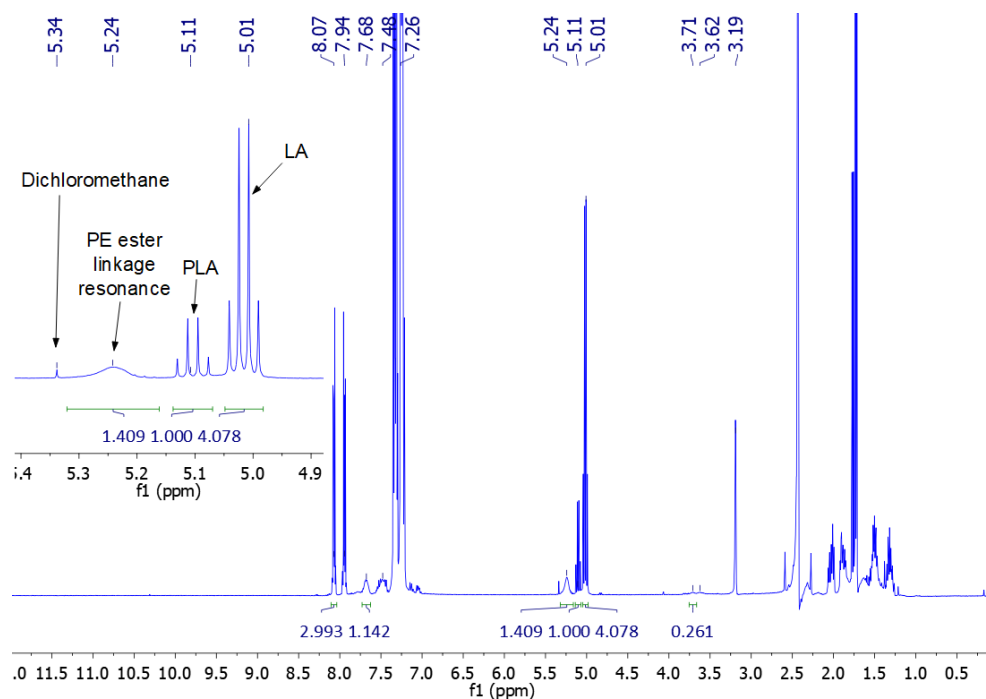


Figure 76. Crude <sup>1</sup>H NMR spectrum of the attempted PA / CHO / *rac*-LA terpolymerisation reaction mixture using organo-initiator **6** after three days (Table 29, entry 1).

In an effort, to observe higher reactivity, all three reactions were repeated with the reaction time increased to six days (Table 29, entries 4–6). For organo-initiator **6** (Section 6.23, Figure 100) and the combination of initiators **6** and Fe(**6**)OAc, the PA conversion increased moderately (59% and 44% PA conversion respectively) but there was minimal change for the *rac*-LA conversion (26% and 25% conversion respectively). There was no further reactivity using Fe(**6**)OAc for the additional three days (Table 29, entry 2 vs. entry 5). This result implied that Fe(**6**)OAc was not contributing as an initiator, instead hindering, when added in combination with **6**; the organo-initiator driving the polymerisation. A terpolymerisation was also attempted using *L*-LA instead of *rac*-LA (Table 29, entry 7). This was to check, whether the quartet resonance signal observed for PLA was originating from the reactivity of only one enantiomer of the *rac*-LA during the terpolymerisation. However, identical reactivity was displayed for *L*-LA which further clarified that no stereocontrol was being achieved in this polymerisation to afford this quartet coupling pattern observed. Overall, for all the terpolymerisations attempted, the chemoselectivity was reasonable (% ester linkages = 81–91%) and the formation of ether linkages and PCHO was low.

Table 29. Attempted PA / CHO / *rac*-LA terpolymerisation in solution conditions using Fe(6)OAc and organic initiator **6**.

Entry	Catalyst (Cat.)	Time (days)	PA conv. <sup>a</sup> (%)	<i>rac</i> -LA conv. <sup>a</sup>	% ester linkages <sup>b</sup>	$M_n^c$ (gmol <sup>-1</sup> )	$\bar{D}^c$
1	<b>6</b>	3	28	20	90	6150	1.11
2	Fe(6)OAc	3	11	8	87	7300	1.04
3 <sup>d</sup>	Fe(6)OAc + <b>6</b>	3	17	21	90	4800	1.07
4	<b>6</b>	6	59	26	91	9900	1.11
5	Fe(6)OAc	6	12	7	81	8950	1.10
6 <sup>d</sup>	Fe(6)OAc + <b>6</b>	6	44	25	89	6550	1.19
7 <sup>d,e</sup>	Fe(6)OAc + <b>6</b>	6	43	26	89	7050	1.13

Conditions: 3 x recrystallised PA (0.3703 g, 2.5 mmol), 3 x distilled CHO (0.253 mL, 2.5 mmol), 1 x recrystallised *rac*-LA (0.3603 g, 2.5 mmol), catalyst (1 mol%, 0.025 mmol), [PA]:[CHO]:[*rac*-LA]:[Cat.]=[100]:[100]:[100]:[1], toluene (2.0 mL), 100 °C, three days. <sup>a</sup> Determined by <sup>1</sup>H NMR spectroscopy (CDCl<sub>3</sub>). For PA conversion this was achieved by integrating the resonances of PA ( $\delta$  8.04–8.11 ppm) and the aromatic phenylene resonances in the PE ( $\delta$  7.63–7.73 ppm). For *rac*-LA this was achieved by integrating the methine resonance for PLA ( $\delta$  5.07–5.14 ppm) and comparing to the methine resonance for LA ( $\delta$  4.98–5.05 ppm). <sup>b</sup> Selectivity determined by <sup>1</sup>H NMR spectroscopy (CDCl<sub>3</sub>) by integrating the resonances of the ester linkages ( $\delta$  5.06–5.32 ppm) and the ether linkages ( $\delta$  3.66–3.76 ppm) from the crude reaction mixture. <sup>c</sup> Determined *via* GPC (triple detection analysis) in THF solvent. <sup>d</sup> [PA]:[CHO]:[*rac*-LA]:[Cat.]=[100]:[100]:[100]:[2]. <sup>e</sup> L-LA used instead of *rac*-LA.

After purification using dichloromethane / acidified methanol (1M) on the crude terpolymerisation reaction mixtures; as was employed for the ROCOP reactions (Section 5.3, Table 26 and Section 5.4, Table 27), the white polymer samples obtained were analysed *via* GPC and low-to-reasonable molecular weights were observed accompanied with narrow dispersities ( $M_n = 4800$ – $9900$  gmol<sup>-1</sup>,  $\bar{D} = 1.04$ – $1.19$ ). However, <sup>1</sup>H NMR spectroscopy, on the dried, purified polymer, unexpectedly observed the disappearance of the PLA resonance signal detected from the crude reaction mixture (Section 6.23, Figures 101 and 102). This was surprising as it was anticipated that if poly(1,2-cyclohexylene-1,2-phthalate) and PLA were formed, both would be incorporated into the same, single polymer species. As a check, DOSY NMR analysis was applied on an aliquot of crude reaction mixture which showed,

when focussed on the methine region, the PLA as a separate species to the PE copolymer {poly(CHO-co-PA)} species (Figure 77). The unreacted LA resonance signal was of equal diffusion coefficient to the PLA and hence implied the PLA must have been of oligomeric molecular weight. Therefore, unfortunately, it was rationalised that both PA / CHO ROCOP and the ROP of *rac*-LA were occurring simultaneously adjacent to one another, with two PE products forming instead of the expected one single polymer species. The PLA was then subsequently and unintentionally removed during to dichloromethane / acidified methanol (1M) purification work-up to isolate only the poly(1,2-cyclohexylene-1,2-phthalate) product.

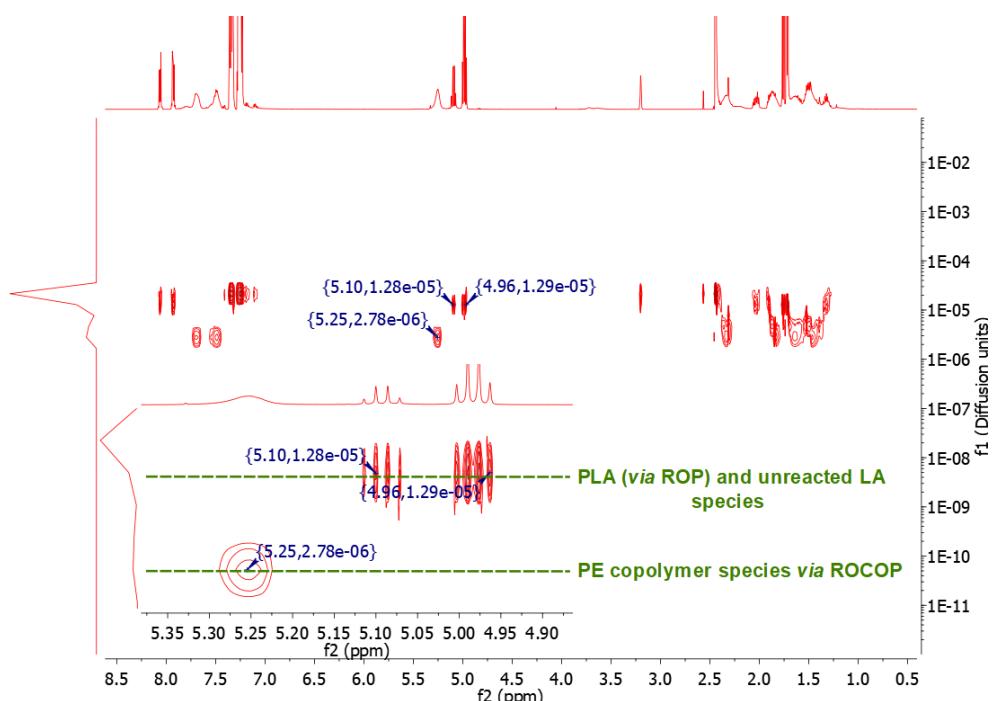


Figure 77. DOSY NMR spectrum of the attempted PA / CHO / *rac*-LA terpolymerisation crude reaction mixture using organo-initiator **6** (Table 29, entry 4). The methine region was focussed on, to show the PLA / LA ( $D = 1.3 \times 10^{-5} \text{ cm}^2 \text{ s}^{-1}$ ) and PE copolymer {poly(CHO-co-PA)} ( $D = 2.8 \times 10^{-6} \text{ cm}^2 \text{ s}^{-1}$ ) resonance signals as two separate species: not the same polymer.

## 5.7 Poly(lactic acid) degradation using Fe(III) complexes

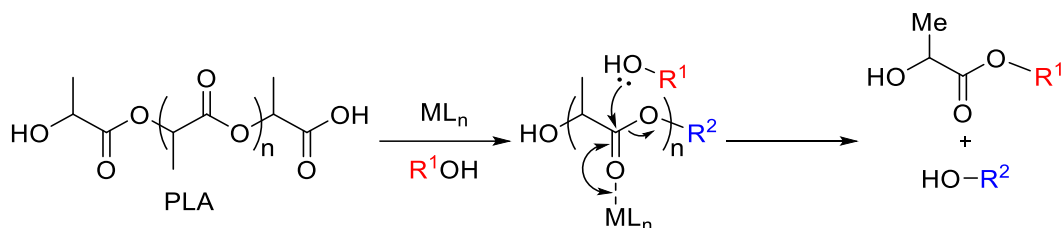
As was introduced and discussed in Section 3.1, one crucial advantage of PLA, and why it is such a promising biopolymer for the future, is because it holds potential integration into a circular economic model, rather than the currently unsustainable, linear model employed by the plastics economy.<sup>[1,2,13,87–90]</sup> This circular economy can

be accessed by PLA *via* efficient end-of-life (EOL) management such as chemical recycling. Recently, there has been increasing interest in this area for many plastics and for PLA, and entails two approaches: depolymerisation to recapture the lactide (LA) monomer (closed loop) or degradation to value added, useful chemicals (open loop).<sup>[1,2,89–91]</sup> Both routes are to platform chemicals that can retain or add material value and create a beneficial incentive for industry to adopt the circular economic model while reducing plastic waste.<sup>[1,2,89,92–95]</sup>

Focussing on PLA degradation, a variety of different chemical transformation methods have been developed but the direct transesterification of PLA with alcohols to produce lactate esters / alkyl lactates has recently gained increasing attention.<sup>[1,2,89,90,94]</sup> Most commonly this is performed using either methanol or ethanol to give methyl lactate (Me–LA) or ethyl lactate (Et–LA). Low molecular weight lactate esters can be used as additives and green solvents with their inherent low toxicity, biodegradability and low vapour pressure and hold potential applications in a range of industrial sectors such as agriculture, pharmaceuticals, foods, cosmetics, the polymer industry and paint formulation.<sup>[1,2,89,94,96,97]</sup> Identical to lactic acid, these lactate esters are also platform chemicals and can be transformed to a variety to other useful chemicals which includes LA and lactic acid; closing the loop for the PLA life cycle. Indeed, the current market value of Et–LA is higher than that of commodity PLA (Et–LA = £2.54–3.49 per kg and PLA = £1.69 per kg) and this could provide additional value to the PLA supply chain and incentivise recycling waste in industry.<sup>[89,96–99]</sup>

A wide variety of initiators have been reported to mediate the alcoholysis of PLA including simple organic acid catalysts such as H<sub>2</sub>SO<sub>4</sub>, ionic liquids (ILs), organocatalysts and simple metal-based salts.<sup>[1,2,89,94]</sup> In comparison, examples of Lewis acidic metal complexes are more limited in literature. Metal initiators, both simple metal salts and complexes, have focussed on elements such as: magnesium, calcium, sodium, zinc, iridium, ruthenium, aluminium, zirconium and hafnium.<sup>[1,2,89,94]</sup> The general mechanism for the metal-mediated degradation mechanism of PLA into lactate esters *via* transesterification with an alcohol is shown in *Scheme 39*. A particular noteworthy observation of this mechanism is that the

interaction between the Lewis acidic metal centre ( $ML_n$ ) and carbonyl oxygen is analogous to that in the coordination–insertion mechanism for the ROP of LA and production of PLA (**Section 3.2**, *Scheme 16*). Therefore, it has been hypothesised in this area that initiators active for PLA production could also be active for PLA degradation.<sup>[1]</sup>



*Scheme 39.* General metal–mediated degradation mechanism of PLA into lactate esters *via* transesterification with an alcohol where  $R^1$  and  $R^2$  denote the alcohol chain length and growth polymer chain respectively.<sup>[1,89,100]</sup>

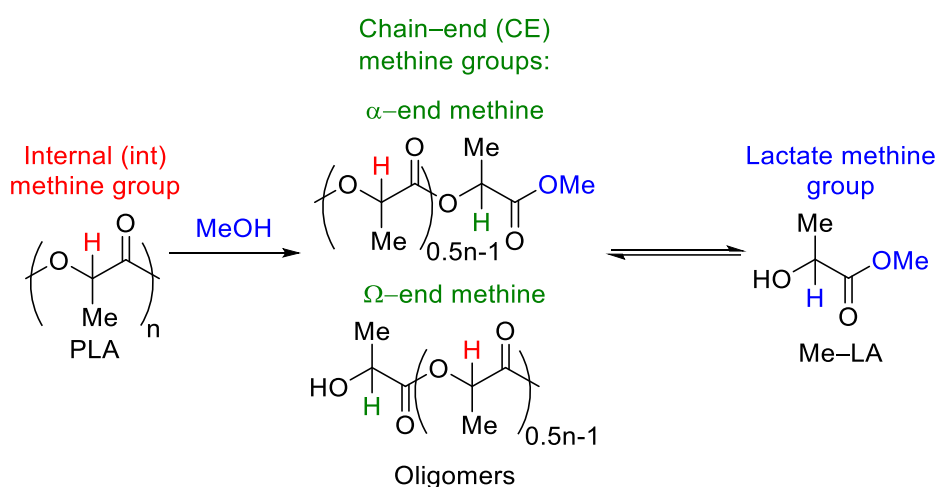
The use of Fe initiators for the degradation of PLA is scarce in literature. This is despite Liu *et al.* identifying the simple, commercially available metal salt,  $FeCl_3$  as a promising candidate in the methanolysis of PLA pellets ( $M_n = 102000 \text{ g mol}^{-1}$ ).<sup>[2,89,101]</sup> In the absence of solvent, optimised reaction conditions  $\{n(FeCl_3):n(PLA)=0.01:1$  or 1 mol%  $FeCl_3$ ,  $n(MeOH):n(PLA)=5:1\}$  afforded an 87% yield to Me–LA at 130 °C within four hours (PLA conversion = 96%). This activity was attributed to a relatively low activation energy barrier being observed for the system (110–135 °C,  $E_a = 32.4 \text{ kJ mol}^{-1}$ ). The particularly notable aspect of this study was the initiator could also be further reused six times, by recovering the Fe residue and removing the Me–LA product *via* distillation, without decrease in the observed activity. This is of interest to industry as initiator recovery for homogeneous catalysis is generally challenging and a short coming; however, in this work, a simple work–up was demonstrated.<sup>[89,101]</sup>

There is significant scope and opportunity in this area to further develop Fe initiators by using structural ligand frameworks to maintain or improve the activity, observed from  $FeCl_3$ , at milder reaction conditions.<sup>[1,99,102]</sup> Therefore, building on this work, it was decided to explore the synthesised Fe(III)–salalen–chloride complexes (**Section**



2.3, Scheme 5), previously shown to efficiently form PLA *via* the ROP of *rac*-LA (Sections 3.4 and 3.6), as initiators for PLA degradation.

Recently, the group has achieved high success in the methanolysis of PLA using metals such as zinc and magnesium.<sup>[92–95,100,103]</sup> Using the same amount and ratios of reagents and solvent used in these reports, initial experiments were conducted using Fe(3)Cl (Table 30), the most effective initiator for *rac*-LA ROP, to probe whether an Fe(III) complex could carry out the degradation of a commercially available PLA sample obtained from a Vegware™ plastic cup (PLLA,  $M_n = 45150 \text{ gmol}^{-1}$ ). Tetrahydrofuran was used as the solvent to dissolve the PLA and [Fe] initiator under an inert atmosphere, mild heating and stirring. Methanol was then added to the reaction solution and then stirred at the desired temperature and time duration. The ratio of tetrahydrofuran and methanol was maintained at 4:1, to ensure there corresponded seven equivalents of methanol per ester linkage with respect to the PLA. After the required time period, the reaction was accessed by taking an aliquot and  $^1\text{H}$  NMR spectroscopic analysis of the methine region ( $\delta$  4.2–5.2 ppm).<sup>[92,100,103]</sup>



Scheme 40. The two-step degradation process for PLA methanolysis, with the transformation of methine groups from internal reagent to chain-end intermediate to Me-LA product.<sup>[100]</sup>

It has previously been reported that the formation of Me-LA, from the methanolysis of PLA, proceeds *via* a two-step process (Scheme 40): firstly, the internal (int) methine groups ( $\delta$  5.09–5.21 ppm); assumed to be exclusively PLA due to the high molecular weight, undergo transesterification to become chain-end (CE) methine groups ( $\delta$  4.30–4.39 ppm and  $\delta$  5.09–5.21 ppm) in the formation of

oligomers.<sup>[92,100,103]</sup> Then in the second step, these are then converted to lactate methine groups ( $\delta$  4.23–4.29 ppm) upon formation of the Me–LA product as part of a reversible reaction.<sup>[92,103]</sup> Using this categorisation, the conversion of internal methine units or PLA ( $X_{\text{int/PLA}}$ ), Me–LA product selectivity ( $S_{\text{Me-LA}}$ ) and Me–LA yield ( $Y_{\text{Me-LA}}$ ) can be determined *via*  $^1\text{H}$  NMR spectroscopy (Figure 78).<sup>[92,100,103]</sup>

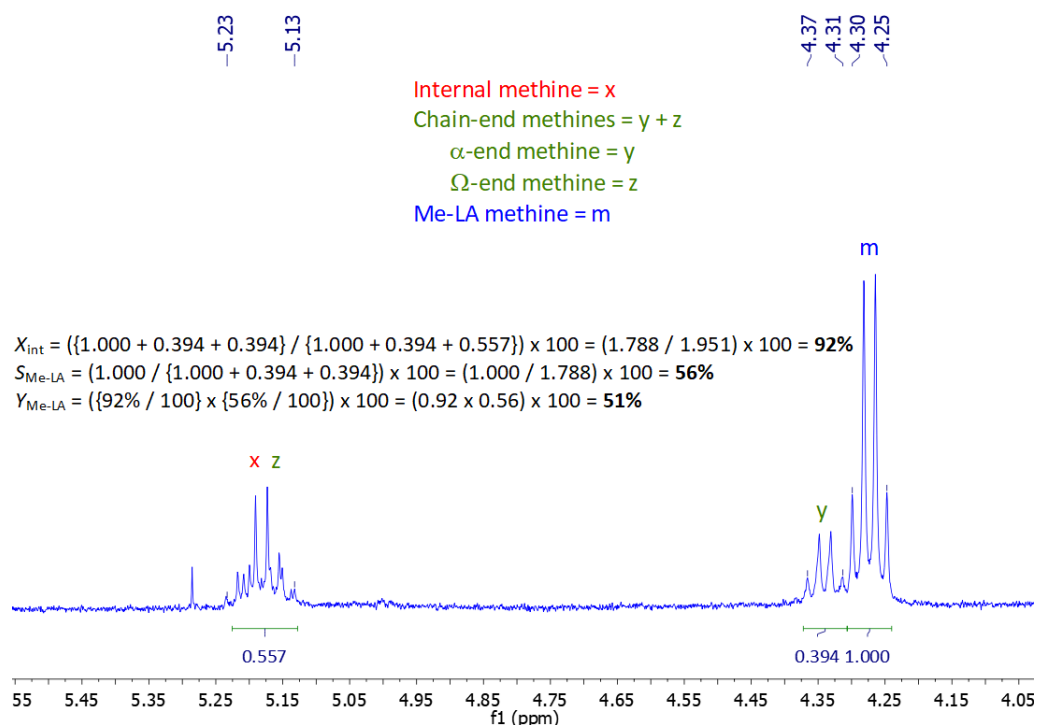


Figure 78. Crude  $^1\text{H}$  NMR spectrum focussed on the methine region for PLA methanolysis using Fe(3)Cl to form Me–LA (Table 30, entry 4). Methine resonance signals assigned to the degradation products and example calculations to determine  $X_{\text{int}}$ ,  $S_{\text{Me-LA}}$ , and  $Y_{\text{Me-LA}}$ .<sup>[92,100]</sup>

Initially, at a mild temperature of 80 °C; previously employed by Zn initiators,<sup>[94,103]</sup> with a moderate initiator loading of Fe(3)Cl (10 wt%, 1.2 mol%) for four days observed no reactivity (Table 30, entry 1). Harsher conditions were attempted at 130 °C with a higher initiator loading (20 wt%, 2.5 mol%) to confirm if reactivity was indeed possible. The reaction was monitored over three days (Table 30, entries 2–4). Moderate-to-high conversions were observed as time progressed ( $X_{\text{int/PLA}} = 57\text{--}92\%$ ) and both the Me–LA selectivity and yield increased more gradually ( $S_{\text{Me-LA}} = 31\text{--}56\%$ ,  $Y_{\text{Me-LA}} = 18\text{--}51\%$ ); indicative of the second, reversible reaction step being slower than the initial transesterification as would be expected (Scheme 40).

Table 30. Degradation of a Vegware™ PLA cup into Me-LA using Fe(III) initiators.

Entry	Initiator (Init.)	Weight% initiator loading	Temp (°C)	Time (hours)	$X_{\text{int/PLA}}$ (%)	$S_{\text{Me-LA}}$ (%)	$Y_{\text{Me-LA}}$ (%)
1 <sup>a</sup>	Fe(3)Cl	10	80	96	0	–	0
2 <sup>b</sup>	Fe(3)Cl	20	130	24	57	31	18
3 <sup>b</sup>	Fe(3)Cl	20	130	48	79	43	34
4 <sup>b</sup>	Fe(3)Cl	20	130	72	92	56	51
5 <sup>b</sup>	FeCl <sub>3</sub>	8	130	72	100	100	100
6 <sup>b</sup>	FeCl <sub>3</sub>	8	130	8	97	90	87
7 <sup>b</sup>	Fe(3)Cl	8	130	72	77	46	35
8 <sup>b</sup>	Fe(4)Cl	8	130	24	100	100	100
9 <sup>b</sup>	Fe(4)Cl	8	130	8	88	86	76
10 <sup>b</sup>	Fe(63)Cl	8	130	72	98	69	68

Conditions: <sup>a</sup> 0.25 g of PLA (Vegware™ PLLA cup),  $V_{\text{THF}} : V_{\text{MeOH}} = 4 \text{ mL} : 1 \text{ mL}$ ,  $n_{\text{MeOH}} : n_{\text{ester}} = 7 : 1$ . <sup>b</sup> 0.125 g of PLA (Vegware™ PLLA cup),  $V_{\text{THF}} : V_{\text{MeOH}} = 2 \text{ mL} : 0.5 \text{ mL}$ ,  $n_{\text{MeOH}} : n_{\text{ester}} = 7 : 1$ . <sup>c</sup> Internal methine group conversion, the PLA ( $X_{\text{int/PLA}}$ ), Me-LA selectivity ( $S_{\text{Me-LA}}$ ) and the Me-LA yield ( $Y_{\text{Me-LA}}$ ) was determined by <sup>1</sup>H NMR spectroscopy whereby  $Y_{\text{Me-LA}} = X_{\text{int/PLA}} \times S_{\text{Me-LA}}$ .

FeCl<sub>3</sub>, the initiator used by Liu and the precursor for the synthesis of Fe(3)Cl, was then applied as a comparison.<sup>[101]</sup> At a lower initiator loading of 8 wt%, FeCl<sub>3</sub> (3.6 mol%) was significantly more active and the reaction time could be dramatically reduced from three days to eight hours and still maintain a high yield of Me-LA (Table 30, entry 5 vs. 6). While at the same initiator loading of 8 wt%, Fe(3)Cl (0.97 mol%) observed a moderate PLA conversion but low Me-LA yield ( $X_{\text{int/PLA}} = 77\%$ ,  $Y_{\text{Me-LA}} = 35\%$ ) after three days.

These findings did provide interesting insight and revealed that, to be competitive with FeCl<sub>3</sub>, significant alteration of the ligand framework on the Fe(III) complex would be required to decrease the three day reaction time, enhance the Lewis acidity of the Fe(III) centre and activity. In addition to this, it seemed the presence or absence of a ligand framework made no difference on the product selectivity ( $S_{\text{Me-LA}}$ ). Introducing chloro-functionality and electron-withdrawing groups (EWGs) to the ligand framework; increasing the Lewis acidity of the Fe(III) centre, by the application of

Fe(4)Cl (Section 2.3, Scheme 5) as an initiator proved effective and the reaction was at completion when analysed after 24 hours and, as was the case for FeCl<sub>3</sub>, the reaction time could be dramatically reduced from three days to eight hours (Table 30, entries 8 and 9). In comparison, under the conditions employed, Fe(4)Cl was competitive with FeCl<sub>3</sub> {Fe(4)Cl;  $X_{\text{int/PLA}} = 88\%$ ,  $S_{\text{Me-LA}} = 86\%$ ,  $Y_{\text{Me-LA}} = 76\%$  vs. FeCl<sub>3</sub>;  $X_{\text{int/PLA}} = 97\%$ ,  $S_{\text{Me-LA}} = 90\%$ ,  $Y_{\text{Me-LA}} = 87\%$ } and demonstrates the strong influence the ligand framework can have on degradation upon structural modification. It also provides optimism that an Fe(III) complex can be found that displays superior activity at milder conditions than FeCl<sub>3</sub>.

Interestingly, despite the analogous chloro-functionalised Fe(III)-thiolen-chloride complex {Fe(63)Cl} (Section 3.3, Figure 45), synthesised by Stewart, being the more active initiator for the ROP of *rac*-LA, this was not the case for degradation and three days was still required for high reactivity (Table 30, entry 10).<sup>[104]</sup> This may result from the initiator having less propensity to degrade the PLA and wanting to repolymerise.

## 5.8 Conclusion and future work

Fourteen, air-stable Fe(III) complexes, comprising of salalen, thiolen, salan and salophen ligand structural frameworks, were applied as catalysts to PA / CHO ROCOP in toluene and compared to ascertain SARs. As part of a developed, single-component experimental protocol, with no extra additives or nucleophilic co-catalyst, alternating poly(CHO-co-PA) was produced with reasonable molecular weights, narrow dispersities and high degree of ester linkages. Fe(6)OAc, bearing a phenyl bridged salalen framework, was particularly encouraging as an initiator.

The most interesting finding of this study was discovered when the ligand control reactions were conducted, and it was realised that all ligand structural frameworks were more effective as organocatalysts than the respective Lewis acidic, Fe(III) complex analogues. As far as we are aware, this is the first time these structurally simple, air-stable, classes of ligand have been applied to anhydride / epoxide ROCOP and this bears strong resemblance to North's recent application of salophen ligands to CO<sub>2</sub> / terminal epoxide coupling.<sup>[53]</sup> This simplistic, single-component, metal- and halide-free, organocatalytic approach was investigated and alternating poly(CHO-

co-PA) with high PA conversions (72–98% PA conversion), high chemoselectivity (% ester linkages = 93–96%), reasonable molecular weight and dispersities was formed ( $M_n = 14300\text{--}29100 \text{ gmol}^{-1}$ ,  $\mathcal{D} = 1.09\text{--}1.15$ ). The application of the phenyl bridged, salalen **6** and salophen **17** observed the highest molecular weights with  $19600 \text{ gmol}^{-1}$  and  $29100 \text{ gmol}^{-1}$  respectively and a narrow distribution was maintained.

A drawback with this ROCOP approach, in toluene, were the longer reaction times required (three days) and in an effort to reduce this reaction time, the structural frameworks bearing phenyl bridged backbones were employed as initiators in solvent-free, neat reaction conditions using CHO in excess (800 eq.). This resulted in less controlled polymerisations and the chemoselectivity dropping significantly (% ester linkages = 45–69%), but considerably faster reactivity (30 hours), with reasonable molecular weights and narrow dispersities obtained ( $M_n = 10100\text{--}18900 \text{ gmol}^{-1}$ ,  $\mathcal{D} = 1.10\text{--}1.35$ ). The thermal properties of the copolymers were analysed *via* DSC and the PEs were confirmed to be amorphous and the  $T_g$  values were reasonably ranged from 100–135 °C. It was proposed, these values were not only generally dependant on higher molecular weight and degrees of ester linkages, but also on subtle changes in the molecular distribution of the polymer. It was perceived that small degrees of cross-linking may have been occurring that could have contributed to discrepancies in the trends.

There is potential to access higher molecular weights for anhydride / epoxide ROCOP *via* further purification of the monomers. Greiner and co-workers reported a purification method using sodium hydride and methyl iodide to further purify the epoxide reagent by removing any residual diol impurities and this could be attempted.<sup>[40,50]</sup> Now an experimental ROCOP protocol has been developed and effective initiators have been uncovered, the monomer set also needs to be altered away from PA and CHO to tune the PE's thermal properties and, similar to the work conducted by Kleij, use more renewably sourced reagents such as tricyclic anhydrides or terpene oxide epoxides such as limonene oxide (LO) or  $\beta$ -elemene oxides.<sup>[26,27,31]</sup> Also as discussed in **Section 2.10**, early work was also conducted into synthesising Mn(III)–salalen, –salan and –salen complexes. Recently, there was an example of the

application of a Mn(III)–amino–triphenolate complex to PA / ROCOP and, if such complexes were isolated it would be worthwhile applying them to this reaction.<sup>[67]</sup>

The terpolymerisation of PA, CHO and *rac*-LA monomer was attempted using Fe(6)OAc and **6** initiators as a ‘one-pot’, crude reaction mixture. However, despite the proposed formation of PLA, it was rationalised *via* <sup>1</sup>H NMR spectroscopy and DOSY NMR that, unfortunately, two separate polymer species were being formed unexpectedly and the PLA was unintentionally removed during the dichloromethane / acidified methanol purification work-up to isolate only the poly(CHO-*co*-PA), PA / CHO ROCOP product. The initiators were chosen due to their effectiveness for ROCOP, however further attempts could be tried using the most effective initiators for the ROP of *rac*-LA; this could include Fe(3)Cl or Stewart’s Fe(62/64/65)Cl (**Section 3.3, Figure 45**), to see if the PLA can incorporate into the poly(CHO-*co*-PA) to form one polymer species.<sup>[104]</sup> Although, the PCHC product has not been observed using the Fe(III) complexes in CO<sub>2</sub> / epoxide coupling (**Sections 4.5, 4.10 and 5.6**), terpolymerisation using PA, CHO and CO<sub>2</sub> may worth be attempting to see if the COC products ring open during the ROCOP to form carbonate linkages and poly(ester-*b*-carbonate).

The degradation of PLA to Me-LA was explored using Fe(III)–salalen–chloride initiators and compared to the precursor FeCl<sub>3</sub>. There is significant scope in this area to further develop Fe initiators by using structural ligand frameworks to maintain or improve the activity, observed from FeCl<sub>3</sub>, at milder reaction conditions.<sup>[1,99,102]</sup> It was revealed that, after significant alteration of the ligand framework and the introduction of chloro-functionality to increase the Lewis acidity of the Fe(III) centre, Fe(4)Cl was competitive with FeCl<sub>3</sub>; both requiring eight hours for high reactivity at 130 °C. Stewart’s Lewis acidic Fe(64/65)Cl complexes (**Section 3.3, Figure 45**), bearing bromo-functionality, are significantly faster for the ROP of *rac*-LA compared to Fe(4)Cl, and would be worth applying to PLA degradation to see if the reaction time can be further reduced.<sup>[104]</sup>

Lastly, other sustainable process could be explored using the synthesised Fe(III) complexes. Following the work conducted by Shaver and co-workers using their Fe(III)–bis(phenoxy–imine)–chloride complexes {Fe(40–47)<sub>2</sub>Cl, **Section 3.3, Figure**

41}, early investigations were made applying Fe(III)–salalen and –thiolen–chloride complexes as mediators to the atom transfer radical polymerisation (ATRP) of styrene using 2,2′–azobis(2–methylpropionitrile) (AIBN) radical initiator at 120 °C in toluene.<sup>[105]</sup> Polystyrene (PS) was produced but with a broad molecular weight distribution; the application of further Fe(III) complexes would be required to attempt to decrease this broad dispersity.

## 5.9 References

- [1] J. Payne, P. McKeown, M. D. Jones, *Polym. Degrad. Stab.* **2019**, *165*, 170–181.
- [2] P. McKeown, M. D. Jones, *Sustain. Chem.* **2020**, *1*, 1–22.
- [3] M. Stolt, A. Södergård, *Prog. Polym. Sci.* **2002**, *27*, 1123–1163.
- [4] P. VanWouwe, M. Dusselier, E. Vanleeuw, B. Sels, *ChemSusChem* **2016**, *9*, 907–921.
- [5] K. Ishihara, S. Ohara, H. Yamamoto, *Science* **2000**, *290*, 1140–1142.
- [6] Y. Zhao, Z. Wang, J. Wang, H. Mai, B. Yan, F. Yang, *J. Appl. Polym. Sci.* **2004**, *91*, 2143–2150.
- [7] C. M. Thomas, *Chem. Soc. Rev.* **2010**, *39*, 165–173.
- [8] R. H. Platel, L. M. Hodgson, C. K. Williams, *Polym. Rev.* **2008**, *48*, 11–63.
- [9] J. A. Byers, A. B. Biernesser, K. R. Delle Chiaie, A. Kaur, J. A. Kehl, *Advances in Polymer Science 279: Synthesis, Structure and Properties of Poly(Lactic Acid)*, Springer International Publishing, **2018**, pp. 67–118.
- [10] J. M. Longo, M. J. Sanford, G. W. Coates, *Chem. Rev.* **2016**, *116*, 15167–15197.
- [11] A. J. R. Lasprilla, G. A. R. Martinez, B. H. Lunelli, A. L. Jardini, R. M. Filho, *Biotechnol. Adv.* **2012**, *30*, 321–328.
- [12] D. Ryzhakov, G. Printz, B. Jacques, S. Messaoudi, F. Dumas, S. Dagorne, F. Le Bideau, *Polym. Chem.* **2021**, *12*, 2932–2946.
- [13] M. Rabnawaz, I. Wyman, R. Auras, S. Cheng, *Green Chem.* **2017**, *19*, 4737–4753.
- [14] O. Dechy-Cabaret, B. Martin-Vaca, D. Bourissou, *Chem. Rev.* **2004**, *104*, 6147–6176.
- [15] M. J. Stanford, A. P. Dove, *Chem. Soc. Rev.* **2010**, *39*, 486–494.
- [16] M. K. Nampoothiri, N. R. Nair, R. P. John, *Bioresour. Technol.* **2010**, *101*, 8493–8501.
- [17] E. T. H. Vink, K. R. Rábago, D. A. Glassner, B. Springs, R. P. O’Connor, J. Kolstad, P. R. Gruber, *Macromol. Biosci.* **2004**, *4*, 551–564.

- [18] G. L. Gregory, G. S. Sulley, L. P. Carrodegua, T. T. D. Chen, A. Santmarti, N. J. Terrill, K.-Y. Lee, C. K. Williams, *Chem. Sci.* **2020**, *11*, 6567–6581.
- [19] S. Paul, Y. Zhu, C. Romain, R. Brooks, P. K. Saini, C. K. Williams, *Chem. Commun.* **2015**, *51*, 6459–6479.
- [20] D. Garlotta, *J. Polym. Environ.* **2001**, *9*, 63–84.
- [21] S. Brochu, R. E. Prud'homme, I. Barakat, R. Jérôme, *Macromolecules* **1995**, *28*, 5230–5239.
- [22] J. Rieger, *J. Therm. Anal.* **1996**, *46*, 965–972.
- [23] A. Yoshioka, K. Tashiro, *Macromolecules* **2004**, *37*, 467–472.
- [24] A. Kummari, S. Pappuru, D. Chakraborty, *Polym. Chem.* **2018**, *9*, 4052–4062.
- [25] H. Tsuji, *Macromol. Biosci.* **2005**, *5*, 569–597.
- [26] M. J. Sanford, L. Peña Carrodegua, N. J. Van Zee, A. W. Kleij, *Macromolecules* **2016**, *49*, 6394–6400.
- [27] L. Peña Carrodegua, C. Martín, A. W. Kleij, *Macromolecules* **2017**, *50*, 5337–5345.
- [28] C. Robert, T. Ohkawara, K. Nozaki, *Chem. Eur. J.* **2014**, *20*, 4789–4795.
- [29] R. Mundil, Z. Hošťálek, I. Šeděnková, J. Merna, *Macromol. Res.* **2015**, *23*, 161–166.
- [30] Z. Shi, Q. Jiang, Z. Song, Z. Wang, C. Gao, *Polym. Chem.* **2018**, *9*, 4733–4743.
- [31] F. Della Monica, A. W. Kleij, *ACS Sustainable Chem. Eng.* **2021**, *9*, 2619–2625.
- [32] K. Nakano, K. Kobayashi, T. Ohkawara, H. Imoto, K. Nozaki, *J. Am. Chem. Soc.* **2013**, *135*, 8456–8459.
- [33] A. M. Diccio, G. W. Coates, *J. Am. Chem. Soc.* **2011**, *133*, 10724–10727.
- [34] E. H. Nejad, C. G. W. van Melis, T. J. Vermeer, C. E. Koning, R. Duchateau, *Macromolecules* **2012**, *45*, 1770–1776.
- [35] S. Huijser, E. HosseiniNejad, R. Sablong, C. De Jong, C. E. Koning, R. Duchateau, *Macromolecules* **2011**, *44*, 1132–1139.
- [36] E. Hosseini Nejad, A. Paoniasari, C. E. Koning, R. Duchateau, *Polym. Chem.* **2012**, *3*, 1308–1313.
- [37] E. H. Nejad, A. Paoniasari, C. G. W. Van Melis, C. E. Koning, R. Duchateau, *Macromolecules* **2013**, *46*, 631–637.
- [38] D. J. Darensbourg, R. R. Poland, C. Escobedo, *Macromolecules* **2012**, *45*, 2242–2248.
- [39] J. Zhang, L. Wang, S. Liu, Z. Li, *J. Polym. Sci.* **2020**, *58*, 803–810.
- [40] Z. Hošťálek, O. Trhlíková, Z. Walterová, T. Martinez, F. Peruch, H. Cramail, J.



- Merna, *Eur. Polym. J.* **2017**, *88*, 433–447.
- [41] B. Han, L. Zhang, B. Liu, X. Dong, I. Kim, Z. Duan, P. Theato, *Macromolecules* **2015**, *48*, 3431–3437.
- [42] H.-Y. Ji, X.-L. Chen, B. Wang, L. Pan, Y.-S. Li, *Green Chem.* **2018**, *20*, 3963–3973.
- [43] P. K. Saini, C. Romain, Y. Zhu, C. K. Williams, *Polym. Chem.* **2014**, *5*, 6068–6075.
- [44] K. A. Andrea, E. D. Butler, T. R. Brown, T. S. Anderson, D. Jagota, C. Rose, E. M. Lee, S. D. Goulding, J. N. Murphy, F. M. Kerton, C. M. Kozak, *Inorg. Chem.* **2019**, *58*, 11231–11240.
- [45] M. Winkler, C. Romain, M. A. R. Meier, C. K. Williams, *Green Chem.* **2015**, *17*, 300–306.
- [46] E. Mahmoud, D. A. Watson, R. F. Lobo, *Green Chem.* **2014**, *16*, 167–175.
- [47] C. Robert, F. De Montigny, C. M. Thomas, *ACS Catal.* **2014**, *4*, 3586–3589.
- [48] R. T. Mathers, M. J. Shreve, E. Meyler, K. Damodaran, D. F. Iwig, D. J. Kelley, *Macromol. Rapid Commun.* **2011**, *32*, 1338–1342.
- [49] W. Jia, Y. Sun, M. Zuo, Y. Feng, X. Tang, X. Zeng, L. Lin, *ChemSusChem* **2020**, *13*, 640–646.
- [50] O. Hauenstein, M. Reiter, S. Agarwal, B. Rieger, A. Greiner, *Green Chem.* **2016**, *18*, 760–770.
- [51] ACS Green Chemistry Institute, *The periodic table's endangered elements*, <https://www.acs.org/content/acs/en/greenchemistry/research-innovation/endangered-elements.html> (Accessed 16th July 2021).
- [52] M. Wang, J. Huang, Y. Xu, B. Han, Z. Duan, *Polym. Int.* **2019**, *68*, 1704–1709.
- [53] X. Wu, C. Chen, Z. Guo, M. North, A. C. Whitwood, *ACS Catal.* **2019**, *9*, 1895–1906.
- [54] J. Liu, Y.-Y. Bao, Y. Liu, W.-M. Ren, X.-B. Lu, *Polym. Chem.* **2013**, *4*, 1439–1444.
- [55] K. Bester, A. Bukowska, B. Myśliwiec, K. Hus, D. Tomczyk, P. Urbaniak, W. Bukowski, *Polym. Chem.* **2018**, *9*, 2147–2156.
- [56] S. Pappuru, D. Chakraborty, *Eur. Polym. J.* **2019**, *121*, 109276.
- [57] L. Lin, J. Liang, Y. Xu, S. Wang, M. Xiao, L. Sun, Y. Meng, *Green Chem.* **2019**, *21*, 2469–2477.
- [58] H. Li, J. Zhao, G. Zhang, *ACS Macro Lett.* **2017**, *6*, 1094–1098.
- [59] H. Li, H. Luo, J. Zhao, G. Zhang, *Macromolecules* **2018**, *51*, 2247–2257.
- [60] L.-F. Hu, D.-J. Chen, J.-L. Yang, X.-H. Zhang, *Molecules* **2020**, *25*, 253.
- [61] H.-Y. Ji, B. Wang, L. Pan, Y.-S. Li, *Angew. Chem. Int. Ed.* **2018**, *57*, 16888–16892.
- [62] X. Kou, Y. Li, Y. Shen, Z. Li, *Macromol. Chem. Phys.* **2019**, *220*, 1900416.

- [63] L. Hu, C. Zhang, H. Wu, J. Yang, B. Liu, H. Duan, X. Zhang, *Macromolecules* **2018**, *51*, 3126–3134.
- [64] A. Kummari, S. Pappuru, P. K. Gupta, D. Chakraborty, R. S. Verma, *Mater. Today Commun.* **2019**, *19*, 306–314.
- [65] K. A. Andrea, T. R. Brown, J. N. Murphy, D. Jagota, D. McKearney, C. M. Kozak, F. M. Kerton, *Inorg. Chem.* **2018**, *57*, 13494–13504.
- [66] W. J. van Meerendonk, R. Duchateau, C. E. Koning, G.-J. M. Gruter, *Macromolecules* **2005**, *38*, 7306–7313.
- [67] C. Martín, A. Pizzolante, E. C. Escudero-Adán, A. W. Kleij, *Eur. J. Inorg. Chem.* **2018**, *2018*, 1921–1927.
- [68] G. Si, L. Zhang, B. Han, Z. Duan, B. Li, J. Dong, X. Li, B. Liu, *Polym. Chem.* **2015**, *6*, 6372–6377.
- [69] I. G. J. Bayram, A. Oral, F. Kamil, *J. Chem.* **2013**, *2013*, 1–6.
- [70] T. Stößer, C. K. Williams, *Angew. Chem. Int. Ed.* **2018**, *57*, 6337–6341.
- [71] C. Romain, Y. Zhu, P. Dingwall, S. Paul, H. S. Rzepa, A. Buchard, C. K. Williams, *J. Am. Chem. Soc.* **2016**, *138*, 4120–4131.
- [72] S. Ye, W. Wang, J. Liang, S. Wang, M. Xiao, Y. Meng, *ACS Sustainable Chem. Eng.* **2020**, *8*, 17860–17867.
- [73] G. P. Wu, D. J. Darensbourg, X. B. Lu, *J. Am. Chem. Soc.* **2012**, *134*, 17739–17745.
- [74] M. Cozzolino, T. Rosen, I. Goldberg, M. Mazzeo, M. Lamberti, *ChemSusChem* **2017**, *10*, 1217–1223.
- [75] C. Hu, R. Duan, S. Yang, X. Pang, X. Chen, *Macromolecules* **2018**, *51*, 4699–4704.
- [76] C. Romain, J. A. Garden, G. Trott, A. Buchard, A. J. P. White, C. K. Williams, *Chem. Eur. J.* **2017**, *23*, 7367–7376.
- [77] L. P. Carrodegua, T. T. D. Chen, G. L. Gregory, G. S. Sulley, C. K. Williams, *Green Chem.* **2020**, *22*, 8298–8307.
- [78] A. K. Diallo, W. Guerin, M. Slawinski, J.-M. Brusson, J.-F. Carpentier, S. M. Guillaume, *Macromolecules* **2015**, *48*, 3247–3256.
- [79] T. Aida, K. Sanuki, S. Inoue, *Macromolecules* **1985**, *18*, 1049–1055.
- [80] S. Kernbichl, M. Reiter, F. Adams, S. Vagin, B. Rieger, *J. Am. Chem. Soc.* **2017**, *139*, 6787–6790.
- [81] C. Romain, C. K. Williams, *Angew. Chem. Int. Ed.* **2014**, *126*, 1633–1636.
- [82] T. Stößer, D. Mulryan, C. K. Williams, *Angew. Chem. Int. Ed.* **2018**, *57*, 16893–16897.

- [83] S. K. Raman, R. Raja, P. L. Arnold, M. G. Davidson, C. K. Williams, *Chem. Commun.* **2019**, 55, 7315–7318.
- [84] M. R. Kember, J. Copley, A. Buchard, C. K. Williams, *Polym. Chem.* **2012**, 3, 1196–1201.
- [85] D. J. Darensbourg, G. P. Wu, *Angew. Chem. Int. Ed.* **2013**, 52, 10602–10606.
- [86] L. Tang, W. Luo, M. Xiao, S. Wang, Y. Meng, *J. Polym. Sci. A Polym. Chem.* **2015**, 53, 1734–1741.
- [87] X. Zhang, M. Fevre, G. O. Jones, R. M. Waymouth, *Chem. Rev.* **2018**, 118, 839–885.
- [88] D. Bourguignon, *EPRS* **2017**, Plastics in a circular economy, PE 603.940.
- [89] M. D. Jones, J. Payne, *ChemSusChem* **2021**, 14, 4041–4070.
- [90] E. Feghali, L. Tauk, P. Ortiz, K. Vanbroekhoven, W. Eevers, *Polym. Degrad. Stab.* **2020**, 179, 109241.
- [91] V. Piemonte, S. Sabatini, F. Gironi, *J. Polym. Environ.* **2013**, 21, 640–647.
- [92] L. A. Román-Ramírez, P. McKeown, M. D. Jones, J. Wood, *ACS Catal.* **2019**, 9, 409–416.
- [93] P. McKeown, L. A. Román-Ramírez, S. Bates, J. Wood, M. D. Jones, *ChemSusChem* **2019**, 12, 5233–5238.
- [94] J. Payne, P. McKeown, M. F. Mahon, E. A. C. Emanuelsson, M. D. Jones, *Polym. Chem.* **2020**, 11, 2381–2389.
- [95] L. A. Román-Ramírez, P. McKeown, C. Shah, J. Abraham, M. D. Jones, J. Wood, *Ind. Eng. Chem. Res.* **2020**, 59, 11149–11156.
- [96] F. M. Lamberti, L. A. Román-Ramírez, P. McKeown, M. D. Jones, J. Wood, *Processes* **2020**, 8, 738.
- [97] C. S. M. Pereira, V. M. T. M. Silva, A. E. Rodrigues, *Green Chem.* **2011**, 13, 2658–2671.
- [98] F. M. Lamberti, L. A. Román-Ramírez, J. Wood, *J. Polym. Environ.* **2020**, 28, 2551–2571.
- [99] F. A. Leibfarth, N. Moreno, A. P. Hawker, J. D. Shand, *J. Polym. Sci. A Polym. Chem.* **2012**, 50, 4814–4822.
- [100] L. A. Román-Ramírez, P. McKeown, M. D. Jones, J. Wood, *ACS Omega* **2020**, 5, 5556–5564.
- [101] H. Liu, X. Song, F. Liu, S. Liu, S. Yu, *J. Polym. Res.* **2015**, 22, DOI: 10.1007/s10965-015-0783-6.
- [102] E. L. Whitelaw, M. G. Davidson, M. D. Jones, *Chem. Commun.* **2011**, 47, 10004–10006.

- [103] J. Payne, P. McKeown, O. Driscoll, G. Kociok-Köhn, E. A. C. Emanuelsson, M. D. Jones, *Polym. Chem.* **2021**, *12*, 1086–1096.
- [104] J. A. Stewart, P. McKeown, O. J. Driscoll, M. F. Mahon, B. D. Ward, M. D. Jones, *Macromolecules* **2019**, *52*, 5977–5984.
- [105] E. Fazekas, G. S. Nichol, J. A. Garden, M. P. Shaver, *ACS Omega* **2018**, *3*, 16945–16953.

**Chapter 6.**  
**Experimental**

## 6. Experimental section

### 6.1 General considerations

All the chemicals were commercially obtained from Merck and used as received unless stated otherwise. Cyclohexene oxide (CHO), propylene oxide (PO), styrene oxide (SO), epichlorohydrin (ECH), phenyl glycidyl ether (PGE) and allyl glycidyl ether (AGE) were stirred with magnesium sulfate ( $\text{MgSO}_4$ ) or calcium hydride ( $\text{CaH}_2$ ), cannula filtered and distilled before use. Cyclohexene oxide (CHO) was dried and distilled under argon using  $\text{MgSO}_4$  and a fractional distillation column with a thermometer to track the boiling point temperature of the CHO passing over. The first 10 mL of distilled CHO was discarded and final 10 mL of crude CHO was left in the distillation flask (in case of impurities). For  $\text{CO}_2$  / epoxide coupling and the neat ring opening copolymerisations (ROCOPs), the CHO was singly distilled. For the solution ROCOPs, the CHO was generally triply distilled unless mentioned otherwise. Benzyl alcohol (BnOH) and triethylamine ( $\text{NEt}_3$ ) were stirred with calcium hydride ( $\text{CaH}_2$ ) and distilled before use. Phthalic anhydride (PA) was triply recrystallised using dry toluene. *rac*-Lactide (*rac*-LA) was singly recrystallised using dry toluene.

For the synthesis of Fe(III) complexes under inert conditions and the preparation of reaction mixtures for polymerisation or  $\text{CO}_2$  / epoxide coupling, an MBraun LABmaster dp glovebox, standard Schlenk line techniques and oven-dried glassware were used. Dried and degassed, reaction solvents were collected from a Solvent Purification System (SPS). The Fe(III) complexes, together with all reagents used for polymerisation or  $\text{CO}_2$  / epoxide coupling, were stored in the MBraun LABmaster dp glovebox.

NMR spectroscopy was recorded on Bruker 400 II MHz or 500 MHz spectrometer instruments and referenced to residual solvent signals. Homonuclear decoupled NMR spectroscopy ( $^1\text{H}$   $\{^1\text{H}\}$  NMR) was recorded on a Bruker AV 400 MHz spectrometer to determine the probability of isotactic enchainment ( $P_m$ ).<sup>[1]</sup> Diffusion NMR spectroscopy (DOSY) was recorded on the Bruker 500 MHz spectrometer and used to observe how many species were present in the sample. This was acquired with help from Dr. T. Woodman. This was achieved using the standard Bruker pulse

sequence of ledbpgp2s, with a d1 value of five seconds, 16 scans per gradient level and 64k data points. Typically, the diffusion time (d20) was 0.05 seconds and the gradient pulse duration (p30) was 1500  $\mu$ s. Ten gradient strengths were used between 2 and 95%. The spectra were subsequently multiplied with a Fourier transformation (xf2) and phase corrected. The final DOSY NMR spectra and diffusion coefficients were obtained on MestReNova processing software.

Elemental analysis was performed by Mr. S. Boyer at London Metropolitan University and by Elemental Microanalysis Ltd. HR-MS / ESI-MS was conducted using a MicroToF electrospray quadrupole time-of-flight mass spectrometer, with the sample dissolved in acetonitrile at approximately 1  $\mu$ g mL<sup>-1</sup> concentration. Mass spectra were generally recorded in a positive loop injection mode set for a range of 50–1500 *m/z*. Ultraviolet-visible spectroscopy (UV-Vis) was performed using an Agilent Technologies Cary60 Spectrophotometer and Cary WinUV software. The samples were analysed in acetonitrile solvent and absorbance recorded between 300–800 nm. Fourier-transform infrared spectroscopy (FT-IR) were generally performed using a PerkinElmer Spectrum 100 FT-IR Spectrometer. The pressurised CO<sub>2</sub> / epoxide coupling reactions were performed using a Parr 5500 Series Compact Reactor with mechanical stirring and a Parr 4848 Reactor Controller for temperature control.

Evans' NMR spectroscopic method was conducted in deuterated chloroform (CDCl<sub>3</sub>) solvent using a capillary of pure CDCl<sub>3</sub>, Bruker 400 II MHz or 500 MHz Spectrometers generally at 298 K. Using this method, following the work reported by Piguet and Grant, the effective magnet moment ( $\mu_{\text{eff}}$ ) was calculated from the equation  $\mu_{\text{eff}} = \sqrt{8\chi_p T}$  where T is the temperature (K) and  $\chi_p$  the molar paramagnetic mass susceptibility ( $\mu\text{mol}^{-1}$ ) of the complex being measured.<sup>[2,3]</sup> The  $\chi_p$  is derived by taking into account the molar diamagnetic mass susceptibility, of CDCl<sub>3</sub> and of all the atoms ( $\chi_p = \chi_{\text{obs}} - \chi_d$ ), and calculating the observed mass susceptibility ( $\chi_{\text{obs}}$ ) from  $\chi_{\text{obs}} = -\frac{3\Delta f}{4\pi F m} \times \text{FW}$ .<sup>[2-4]</sup> The  $\Delta f$  is the observed shift and change in the frequency (Hz) of the CHCl<sub>3</sub> resonance of the CDCl<sub>3</sub> solvent in the presence of the paramagnetic complex from the reference value of the pure CDCl<sub>3</sub> in the capillary, F is the

spectrometer frequency (Hz),  $m$  is the mass of the measured complex ( $\text{gcm}^{-3}$ ) and  $3/4\pi$  is the shape factor of a cylindrical sample in a superconducting magnet. The formula weight (FW) is required to convert the units of  $\chi_{\text{obs}}$  from  $\mu\text{g}^{-1}$  to  $\mu\text{mol}^{-1}$ .<sup>[2-5]</sup>

GPC analysis was carried out on an Agilent 1260 Infinity series instrument at  $1 \text{ mL min}^{-1}$  at  $35 \text{ }^\circ\text{C}$  with a THF eluent using a PL gel  $5 \mu\text{m MIXED-D } 300 \times 7.5 \text{ mm}$  column packed with porous microbead particles. Detection was carried out using either refractive index (RI) exclusively or trianalysis methods with RI, light scattering (LS) and viscometer detectors.

The use of RI solely, is the most common method of detection that determines the amount or concentration of material eluting from the column as a function of retention time. The use of a conventional calibration curve, calculated by referencing to 11 polystyrene standards of narrow molecular weight ( $M_w$ ), ranging from 615–568000  $\text{gmol}^{-1}$ , allows the conversion to molecular weight as the material is eluting and therefore a molecular weight distribution.<sup>[6-9]</sup> However, there are limitations with RI as a detection method as polymers different to the standard are not absolute as they do not have the same chemistry and size in solution (hydrodynamic radius).<sup>[6-9]</sup> This is because the column is separating based on the size of the polymer in solvent and not molecular weight. This can ultimately result in inaccurate molecular weight values being calculated if the chemistries are significantly different between the polymer sample and polystyrene in THF solvent here.<sup>[6-9]</sup> Correction factors can be applied to aid the reduction in this error; for example  $\times 0.58$  for the molecular weights of PLA determined against PS standards.

Trianalysis or a triple detection method avoids this limitation, as it is not dependent on the chemistry of any standards / calibrants and determines the ‘absolute’ molecular weights.<sup>[6-9]</sup> Static LS involves irradiating the sample material eluting from the column with a monochromatic laser beam and measuring the intensity of the radiation that is scattered. Using the concentration and refractive index information; specifically the refractive index increment ( $dn/dc$ : the degree of which the refractive index of a solution varies as the concentration changes), obtained from the RI detector, this intensity is proportional to the molecular weight.<sup>[6-9]</sup> A low-angle light



scattering (LALS) detector was used here which measures the scattered light at an angle of  $7^\circ$  and is considered the most accurate molecular weight determination for large molecules such as polymers.<sup>[7]</sup> However, it can suffer from lower precision / sensitivity compare to other LS detectors.<sup>[7]</sup> The viscometer detector measures the solution viscosity (molecular size in solution) of the polymer eluting from the column. After the use of a standard to generate a universal calibration curve, that is not affected by the chemistry of the standard, and concentration information obtained from the RI detector, the intrinsic viscosity (IV) can be determined.<sup>[6,8,9]</sup> From the Mark–Houwink equation ( $[\eta] = KM^\alpha$ , where  $[\eta]$  is the IV, M is the molecular weight and K and  $\alpha$  are constants related to the polymer–solvent system) and calibration, the molecular weight can be determined for the polymer.<sup>[6,8,9]</sup> This can be combined and used to correct the molecular weight value obtained from the LS to determine a more accurate, absolute measurement of the molecular weight for the polymer in comparison to the use of RI alone.<sup>[6–9]</sup>

Therefore, triple analysis uses all three detectors in the determination of the absolute molecular weight, can display the overlays of the chromatograms from each detector and is suited for the characterisation of new synthesised polymers.<sup>[6–9]</sup> The other advantage of this method is it allows further insight into the polymer properties, that cannot be observed from only RI, such as polymer branching that can be investigated by analysis of the derived log Mark–Houwink plot ( $\log[\eta] = \log K + \alpha \log M$ ) from the viscometer or conformation plot ( $\log R_g = \log K + \nu \log M$ , where  $R_g$  is the radius of gyration and  $\nu$  and K are constants) from the LS detector.<sup>[6–9]</sup>

Matrix–assisted laser desorption / ionisation–Time of Flight (MALDI–ToF) analysis was carried out on a Bruker Autoflex speed instrument in linear positive reflector mode. The data was collected either by Dr. P. McKeown or myself with assistance from Dr. M. Levere. DCTB {*trans*-2-[3-(4-*tert*-butylphenyl)-2-methyl-2-propenyldiene]malononitrile} was used as the matrix and NaTFA (sodium trifluoroacetate) as the cationisation agent for ionisation. For the copolymers obtained from ROCOP, 2  $\mu\text{L}$  of a homogenised solution of DCTB (8  $\mu\text{L}$ , 40 mg / mL in THF), NaTFA (2  $\mu\text{L}$ . 0.1 M in THF) and polymer (8  $\mu\text{L}$ , 1 mg / mL in THF), in a ratio of matrix:salt:polymer = 4:1:4, was applied to a steel target, ionisation plate for analysis.

For the poly(lactic acid) obtained from ROP, 2  $\mu\text{L}$  of a homogenised solution of DCTB (10  $\mu\text{L}$ , 10 mg / mL in THF), NaTFA (2  $\mu\text{L}$ , 0.1 M in THF) and polymer (10  $\mu\text{L}$ , 5 mg / mL in THF), was applied to the steel target plate.

All single crystallographic data was collected on either a SuperNova or Excalibur, EOS detector diffractometer using Cu- $K_{\alpha}$  ( $\lambda = 1.54184 \text{ \AA}$ ) or Mo- $K_{\alpha}$  ( $\lambda = 0.71073 \text{ \AA}$ ) radiation and was recorded at 150(2) K. The data was collected and solved by Prof. M. Jones and Dr. P. McKeown with occasional assistance from Dr. M. Mahon. All structures were solved by direct methods and refined on all  $F^2$  data using the SHELXL-2014 suite of programs. All hydrogen atoms were included in idealised positions and refined using the riding model. Powder X-ray diffraction (pXRD) data was acquired by Dr. G. Kociok-Kohn and was collected on a STOE Stadi P, using Cu radiation (1.540598  $\text{\AA}$ ) and a Multi-MYTHEN detector, in transmission mode.

The Differential Scanning Calorimetry (DSC) analyses were recorded on a TA Instruments DSC Q20 for the polymer obtained from ROCOP. The sample was held at 40  $^{\circ}\text{C}$  for five minutes, cooled to -30  $^{\circ}\text{C}$  at 20  $^{\circ}\text{C}/\text{min}$ , held at this temperature for five minutes, heated to 150  $^{\circ}\text{C}$  at 20  $^{\circ}\text{C}/\text{min}$  (1<sup>st</sup> heating cycle), cooled to -30  $^{\circ}\text{C}$  at 20  $^{\circ}\text{C}/\text{min}$ , held at this temperature for five minutes, heated to 400  $^{\circ}\text{C}$  at 20  $^{\circ}\text{C}/\text{min}$  (2<sup>nd</sup> heating cycle) and cooled to -30  $^{\circ}\text{C}$  at 20  $^{\circ}\text{C}/\text{min}$ . Hence, the  $T_g$  values were determined from the 2<sup>nd</sup> heating cycle and the  $T_d$  values measured at the end of this cycle. Alongside the change in colour of the samples from white to dark brown, to check decomposition had occurred, in instances after heating to 400  $^{\circ}\text{C}$ , the sample was cooled to -30  $^{\circ}\text{C}$  at 20  $^{\circ}\text{C}/\text{min}$ , held at this temperature for 5 minutes and then again heated to 400  $^{\circ}\text{C}$  at 20  $^{\circ}\text{C}/\text{min}$ . Only a flat baseline was observed for this 3<sup>rd</sup> heating cycle and this was indicative that decomposition had occurred in the 2<sup>nd</sup> heating cycle.

Materials characterisation (GPC, HR-MS / ESI-MS, MALDI-ToF, DSC) facilities were provided through MC<sup>2</sup> at the University of Bath and particular help from Dr. M. Levere, Dr. R. Castaing and Dr. T. Woodman.

## 6.2 General procedure for salalen ligand preparation

Following the general *Scheme 2* described in **Section 2.1**, the appropriate diamine (10 mmol) was added dropwise to a solution of the salicylaldehyde (10 mmol) in methanol (50 mL). The yellow solution was stirred overnight and the solvent removed *in-vacuo* to afford the iminomonophenolate as a yellow / orange oil. Tetrahydrofuran (50 mL) was added and to the resulting yellow solution, the pre-prepared 3,5-di-*tert*-butyl-2-hydroxybenzylbromide (10 mmol, 2.99 g) (**Section 6.3**) was added as an off-white solid. Triethylamine (20 mmol, 2.79 mL) was added dropwise to the reaction mixture. The yellow suspension was refluxed for two hours. The ammonium salt by-product was removed *via* Büchner filtration and the solvent removed from the filtrate *in-vacuo* to afford an orange oil. The crude oil product was recrystallised using hot methanol to give the salalen ligand product. This procedure was conducted and characterised following previously reported literature.<sup>[10–14]</sup>

## 6.3 General procedure for 3,5-di-*tert*-butyl-2-hydroxybenzyl bromide precursor ( $R^3 = \text{tBu}$ ) preparation

Following the [blue reaction path](#) in *Scheme 2* described in **Section 2.1**, the 2,4-di-*tert*-butylphenol (60 g) was dissolved in methanol (80 mL) and added to a dropping funnel. Both lithium hydroxide monohydrate (1.00 g) and paraformaldehyde (9.00 g) were added to a round-bottom flask. Methanol (80 mL) was added to afford a white suspension. The 2,4-di-*tert*-butylphenol was added dropwise with stirring and, after addition, the yellow / brown mixture was refluxed for 6 hours to obtain an orange solution. The solvent was removed *in-vacuo* and hexane (40 mL) was added to the yellow / green solid. The mixture was filtered using Büchner apparatus to isolate the yellow / green solid and remove the green filtrate. This isolated solid was rinsed with further hexane (320 mL) until this yellow / green colour was no longer observable to obtain the purified substituted benzyl alcohol white solid. Further product crashed out of the green filtrate and was recovered.

The 3,5-di-*tert*-butyl-2-hydroxybenzyl alcohol was added to a round-bottom flask with chloroform (100 mL). Phosphorus tribromide (4.75 mL) was added dropwise

using a dropping funnel to the white suspension of benzyl alcohol and dropping funnel rinsed with further chloroform (50 mL). The resulting orange solution was stirred for 1.5 hours. Water (1000 mL) was added and the organic extraction was extracted and dried using magnesium sulfate. After filtration using Büchner apparatus, the solvent was removed *in-vacuo* to obtain an orange oil and placed in the freezer. A pale yellow solid product crashed out and was isolated. This procedure was conducted and characterised following previously reported literature.<sup>[15]</sup>

#### **6.4 General procedure for the synthesis of bipyrrolidine salan ligands**

Following the general *Scheme 3* described in **Section 2.1**, methanol (50 mL) was added to the paraformaldehyde (36.3 mmol, 5 eq.). As a liquid, *meso-* / *R,R-* / *S,S-* 2,2'-bipyrrolidine (7.25 mmol, 1 eq.) was added with a glass pipette and the substituted salicylaldehyde (14.5 mmol, 2 eq.) added *via* syringe to the white suspension. The mixture was refluxed for two hours and turned to a pale yellow / colourless solution upon heating. This solution was allowed to cool to room temperature with no stopper for slow evaporation. White solid crashed out of solution and was isolated *via* Büchner filtration and rinsed with further methanol. This procedure was conducted and characterised following previously reported literature.<sup>[16,17]</sup>

#### **6.5 General procedure for the synthesis of salan ligands *via* reduction**

Following the general *Scheme 4* described in **Section 2.1**, tetrahydrofuran (15 mL) and methanol (15 mL) was added to the salen or salalen ligand (6.22 mmol, 1 eq.). Sodium borohydride (62.2 mmol, 10 eq.) was added as a white solid in portions slowly to the yellow solution of ligand. The white suspension was stirred at room temperature overnight. Water (10 mL) was added, to quench the excess unreacted sodium borohydride, and the mixture was filtered *via* Büchner filtration. The white filtered solid was rinsed with further water and dried. This procedure was conducted and characterised following previously reported literature.<sup>[18–20]</sup>

## 6.6 General procedure for the synthesis of salen ligands

The appropriate salicylaldehyde (20 mmol, 2 eq.) and diamine (10 mmol, 1 eq.) were added *via* syringe to methanol (30 mL). The solution was stirred overnight at room temperature and the resulting suspension would be isolated *via* Büchner filtration and rinsed with further cold methanol. This procedure was conducted by adapting that employed for the synthesis of salalen ligands (Section 6.2) and by following previously reported literature.<sup>[21]</sup>

## 6.7 General complexation procedure carried out under air for Fe(III)–salalen–chloride complexes {Fe(1/3/5)Cl}

The salalen ligand (1.0 mmol) was placed in a flask and dissolved in tetrahydrofuran (30 mL). FeCl<sub>3</sub> (0.162 g, 1.0 mmol) was added as a black solid to the yellow solution and triethylamine (0.28 mL, 2.0 mmol) added dropwise. The reaction mixture was refluxed for 16 hours, filtered using Büchner apparatus and washed with further tetrahydrofuran. The solvent was removed *in-vacuo* to afford a crude solid that was rinsed with hexane (5 mL) and dried to give a dark purple product.

## 6.8 General complexation procedure carried out under argon for Fe(III)–salalen–chloride complexes {Fe(2/4/6/7)Cl}

The salalen ligand (1.0 mmol) was placed in a Schlenk flask, dried and transferred into the glovebox. Dry toluene (10 mL) was added and FeCl<sub>3</sub> (0.162 g, 1.0 mmol) added as a black solid to the yellow solution. Triethylamine (0.28 mL, 2.0 mmol) was added dropwise and the flask heated to 80 °C for two days. The reaction mixture was filtered *via* cannula, washed with further toluene and solvent removed *in-vacuo*. The crude solid was rinsed with hexane (5 mL) and dried to obtain a dark purple product.

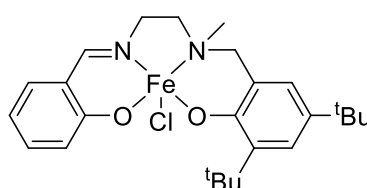
## 6.9 General complexation procedure carried out under air for Fe(III)–acetate complexes

Fe(OAc)<sub>2</sub> (0.174 g, 1.0 mmol) was placed in a round bottom flask in the glovebox. In air, ethanol (10 mL) was added to the Fe(OAc)<sub>2</sub> to form a brown suspension. The ligand (1.0 mmol) was added as a solid to this mixture and refluxed for 2.5 hours and

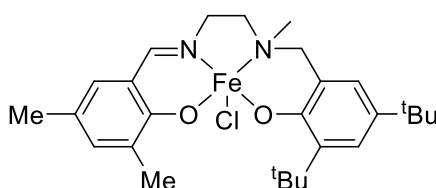
left to cool to room temperature for slow evaporation and recrystallisation in the reaction mixture. After Büchner filtration and rinsing with cold ethanol, the final product was isolated and dried.

## 6.10 Synthesis and characterisation of Fe(III) complexes

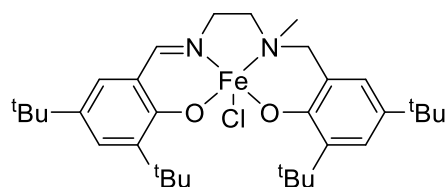
**Fe(1)Cl:** The complex was prepared following the general complexation procedure carried out under air. Yield: 0.149 g, 31%. ESI-MS (MeCN): Calcd  $m/z$   $[\text{C}_{25}\text{H}_{34}\text{FeN}_2\text{O}_2]^+$  = 450.1970, found  $m/z$  = 450.2044. Elemental analysis: Calcd for  $\text{C}_{25}\text{H}_{34}\text{ClFeN}_2\text{O}_2$  (found): C, 61.80 (61.87); H, 7.05 (7.16); N, 5.77 (5.63).



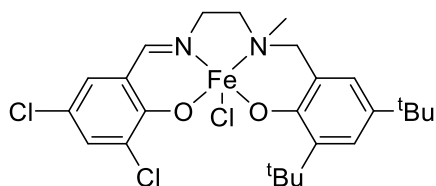
**Fe(2)Cl:** The complex was prepared following the general complexation procedure carried out under argon and recrystallised using diethylether to obtain crystals for single-crystal X-ray diffraction. Yield: 0.310 g, 60 %. ESI-MS (MeCN): Calcd  $m/z$   $[\text{C}_{27}\text{H}_{38}\text{FeN}_2\text{O}_2]^+$  = 478.2283, found  $m/z$  = 478.2284. Elemental analysis: Calcd for  $\text{C}_{27}\text{H}_{38}\text{ClFeN}_2\text{O}_2$  (found): C, 63.10 (58.67); H, 7.45 (8.30); N, 5.45 (4.27). MALDI-ToF MS: Calcd  $m/z$   $[\text{Fe(2)Cl}]^+$  (found) 513.197 (513.113).



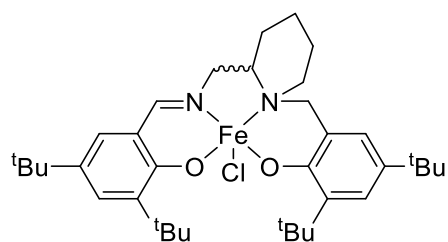
**Fe(3)Cl:** The complex was prepared following the general complexation procedure carried out under air and recrystallised using methanol / acetonitrile to obtain crystals for single-crystal X-ray diffraction. Yield: 0.220 g, 37%. ESI-MS (MeCN): Calcd  $m/z$   $[\text{C}_{33}\text{H}_{50}\text{FeN}_2\text{O}_2]^+$  = 562.3222, found  $m/z$  = 562.3257. Elemental analysis: Calcd for  $\text{C}_{33}\text{H}_{50}\text{ClFeN}_2\text{O}_2$  (found): C, 66.27 (66.13); H, 8.43 (8.49); N, 4.68 (4.57). MALDI-ToF MS: Calcd  $m/z$   $[\text{Fe(3)Cl}]^+$  (found) 597.291 (597.287) (See **Section 6.11**). Effective magnetic moment = 5.71  $\mu_B$  at 298 K in  $\text{CDCl}_3$ .



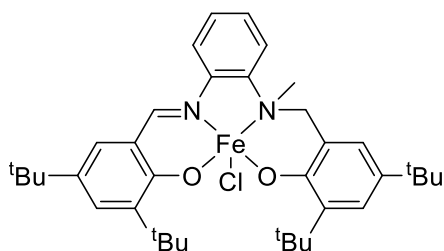
**Fe(4)Cl:** The complex was prepared following the general complexation procedure carried out under argon. Yield: 0.526 g, 95%. ESI-MS (MeCN): Calcd  $m/z$   $[\text{C}_{25}\text{H}_{32}\text{Cl}_2\text{FeN}_2\text{O}_2]^+ = 518.1190$ , found  $m/z = 518.1206$ . Elemental analysis: Calcd for  $\text{C}_{25}\text{H}_{32}\text{Cl}_3\text{FeN}_2\text{O}_2$  (found): C, 54.13 (54.39); H, 5.81 (6.10); N, 5.05 (5.25).



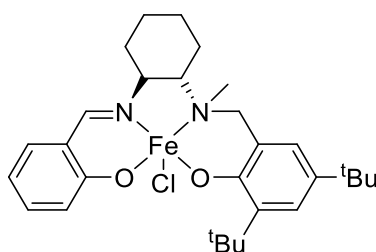
**Fe(5)Cl:** The complex was prepared following the general complexation procedure carried out under air and recrystallised using dichloromethane / hexane to obtain crystals for single-crystal X-ray diffraction. Yield: 0.291 g, 46%. ESI-MS (MeCN): Calcd  $m/z$   $[\text{C}_{36}\text{H}_{54}\text{FeN}_2\text{O}_2]^+ = 602.3535$ , found  $m/z = 602.3542$ . Elemental analysis: Calcd for  $\text{C}_{36}\text{H}_{54}\text{ClFeN}_2\text{O}_2$  (found): C, 67.76 (67.89); H, 8.53 (8.67); N, 4.39 (4.49). MALDI-ToF MS: Calcd  $m/z$   $[\text{Fe(6)Cl}]^+$  (found) 637.322 (637.470).



**Fe(6)Cl:** The complex was prepared following the general complexation procedure carried out under argon and recrystallised using dichloromethane / hexane to obtain crystals for single-crystal X-ray diffraction. Yield: 0.237 g, 37 %. ESI-MS (MeCN): Calcd  $m/z$   $[\text{C}_{37}\text{H}_{50}\text{FeN}_2\text{O}_2]^+ = 610.3222$ , found  $m/z = 610.3251$ . Elemental analysis: Calcd for  $\text{C}_{37}\text{H}_{50}\text{ClFeN}_2\text{O}_2$  (found): C, 68.78 (68.86); H, 7.80 (7.96); N, 4.34 (4.46).

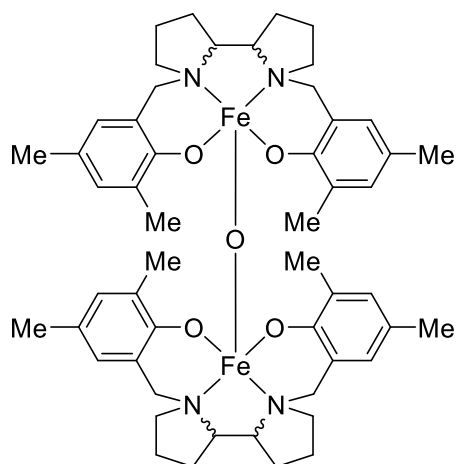


**Fe(7)Cl:** The complex was prepared following the general complexation procedure carried out under argon. Yield: 0.225 g, 42%. ESI–MS (MeCN): Calcd  $m/z$   $[\text{C}_{29}\text{H}_{40}\text{FeN}_2\text{O}_2]^+ = 504.2439$ , found  $m/z = 504.2417$ . Elemental analysis: Calcd for  $\text{C}_{29}\text{H}_{40}\text{ClFeN}_2\text{O}_2$  (found): C, 64.51 (64.73); H, 7.47 (7.59); N, 5.19 (5.32).

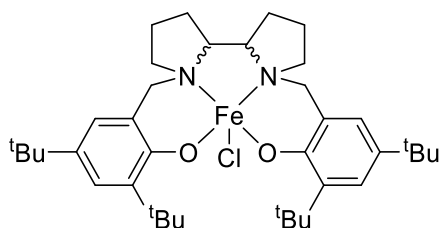


**[Fe(8<sub>meso</sub>)]<sub>2</sub>O:** Under air, the salen ligand (0.106 g, 0.259 mmol) was placed in a flask and dissolved in tetrahydrofuran (7 mL) to give a colourless solution. FeCl<sub>3</sub> (0.0421 g, 0.259 mmol) was added as a black solid and triethylamine (0.28 mL, 2.0 mmol) added dropwise to the dark purple solution. The reaction mixture was refluxed for 2.5 hours, filtered using Büchner apparatus and washed with further tetrahydrofuran. The solvent was removed *in-vacuo* to afford a crude dark purple / brown solid. All of this solid was recrystallised using hot acetonitrile (25 mL) and methanol (8 mL) and left to cool to room temperature for slow evaporation and recrystallisation. Small crystals were obtained; single–crystal X–ray diffraction confirmed the solid–state structure to be the  $\mu$ -oxo–bridged Fe(III)–salen complex. The crystals were isolated by Büchner apparatus and rinsed with cooled methanol to give a small yield of product. Yield: 0.0470 g, 19%. ESI–MS (MeCN): Calcd  $m/z$   $[\text{C}_{26}\text{H}_{34}\text{FeN}_2\text{O}_2]^+ = 462.1970$ , found  $m/z = 462.1963$ .

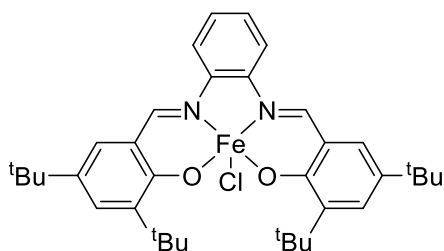




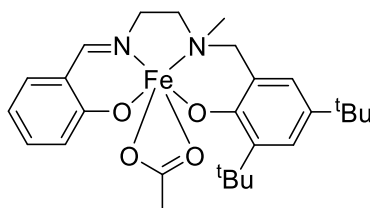
**Fe(9<sub>meso</sub>)Cl:** The salalen ligand (1.0 mmol) was placed in a Schlenk flask, dried and transferred into the glovebox. Toluene (10 mL) was added and FeCl<sub>3</sub> (0.162 g, 1.0 mmol) added as a black solid to the colourless solution. Triethylamine (0.28 mL, 2.0 mmol) was added dropwise and the flask heated to 60 °C for two days. The reaction mixture was filtered *via* cannula, washed with further toluene and solvent removed *in-vacuo*. The crude solid was rinsed with hexane (5 mL) and dried to obtain a dark purple product. Under air, a fraction of the sample was taken and recrystallised using hot diethylether / dichloromethane. This was left to cool to room temperature for slow evaporation to obtain crystals for single-crystal X-ray diffraction. Yield: 0.3164 g, 47%. ESI-MS (MeCN): Calcd  $m/z$  [C<sub>38</sub>H<sub>58</sub>FeN<sub>2</sub>O<sub>2</sub>]<sup>+</sup> = 630.3842, found  $m/z$  = 630.3963.



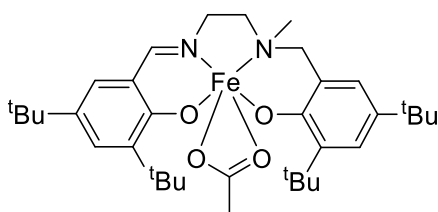
**Fe(17)Cl:** The synthesis and application of this complex was already reported by Mundil *et al.*<sup>[22]</sup> The complex was re-synthesised following the general complexation procedure carried out under argon. Yield = 0.330 g, 52%. ESI-MS (MeCN): Calcd  $m/z$  [C<sub>36</sub>H<sub>46</sub>FeN<sub>2</sub>O<sub>2</sub>]<sup>+</sup> = 594.2903, found  $m/z$  = 594.3000. In agreement with Mundil *et al.*<sup>[22]</sup> Effective magnetic moment = 5.59  $\mu_B$  at 298 K in CDCl<sub>3</sub>.



**Fe(1)OAc:** The complex was prepared following the general complexation procedure carried out under air for Fe(III)–acetate complexes. Yield: 0.292 g, 57%. ESI–MS (MeCN): Calcd  $m/z$   $[\text{C}_{25}\text{H}_{34}\text{FeN}_2\text{O}_2]^+ = 450.1970$ , found  $m/z = 450.2099$ . Elemental analysis: Calcd for  $\text{C}_{27}\text{H}_{37}\text{FeN}_2\text{O}_4 + \text{EtOH}$  (found): C, 62.70 (60.96), H, 7.80 (7.99), N, 5.04 (5.02). FT–IR:  $3673\text{ cm}^{-1}$  (O–H (alcohol), solvent),  $2988\text{ cm}^{-1}$ ,  $2962\text{ cm}^{-1}$ ,  $2905\text{ cm}^{-1}$  (C–H (alkyl)),  $1630\text{ cm}^{-1}$  (C=N),  $1598\text{ cm}^{-1}$ ,  $1551\text{ cm}^{-1}$ ,  $1472\text{ cm}^{-1}$ ,  $1447\text{ cm}^{-1}$ ,  $1408\text{ cm}^{-1}$ ,  $1394\text{ cm}^{-1}$  (C=C (Ar), C=O (acetate)). Effective magnetic moment =  $5.21\ \mu_B$  at 297 K in  $\text{CDCl}_3$ .

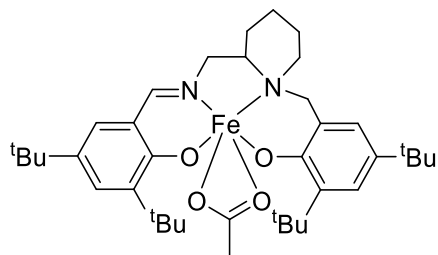


**Fe(3)OAc:** The complex was prepared following the general complexation procedure carried out under air for Fe(III)–acetate complexes. Yield: 0.238 g, 38%. ESI–MS (MeCN): Calcd  $m/z$   $[\text{C}_{33}\text{H}_{50}\text{FeN}_2\text{O}_2]^+ = 562.3222$ , found  $m/z = 562.3252$ . Elemental analysis: Calcd for  $\text{C}_{35}\text{H}_{53}\text{FeN}_2\text{O}_4 + \text{EtOH}$  (found): C, 66.56 (65.85), H, 8.91 (8.89), N, 4.20 (4.36). FT–IR:  $2954\text{ cm}^{-1}$ ,  $2901\text{ cm}^{-1}$ ,  $2866\text{ cm}^{-1}$  (C–H (alkyl)),  $1619\text{ cm}^{-1}$  (C=N),  $1536\text{ cm}^{-1}$ ,  $1459\text{ cm}^{-1}$ ,  $1441\text{ cm}^{-1}$ ,  $1412\text{ cm}^{-1}$  (C=C (Ar), C=O (acetate)). Effective magnetic moment =  $5.74\ \mu_B$  at 298 K in  $\text{CDCl}_3$ .

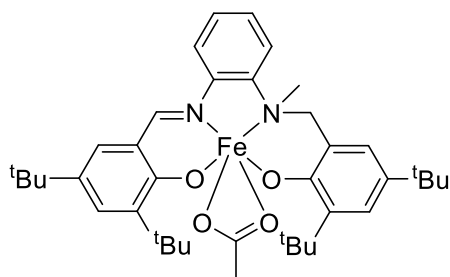


**Fe(5)OAc:** The complex was prepared following the general complexation procedure carried out under air for Fe(III)–acetate complexes. Yield: 0.359 g, 54%. ESI–MS

(MeCN): Calcd  $m/z$   $[\text{C}_{36}\text{H}_{54}\text{FeN}_2\text{O}_2]^+ = 602.3535$ , found  $m/z = 602.3549$ . Elemental analysis: Calcd for  $\text{C}_{38}\text{H}_{57}\text{FeN}_2\text{O}_4$  (found): C, 68.97 (69.21), H, 8.68 (8.86) N, 4.23 (4.36). FT-IR:  $2951\text{ cm}^{-1}$ ,  $2940\text{ cm}^{-1}$ ,  $2905\text{ cm}^{-1}$ ,  $2868\text{ cm}^{-1}$  (C-H (alkyl)),  $1621\text{ cm}^{-1}$  (C=N),  $1618\text{ cm}^{-1}$ ,  $1538\text{ cm}^{-1}$ ,  $1457\text{ cm}^{-1}$ ,  $1437\text{ cm}^{-1}$ ,  $1411\text{ cm}^{-1}$  (C=C (Ar), C=O (acetate)). Effective magnetic moment =  $5.46\ \mu_{\text{B}}$  at 297 K in  $\text{CDCl}_3$ .

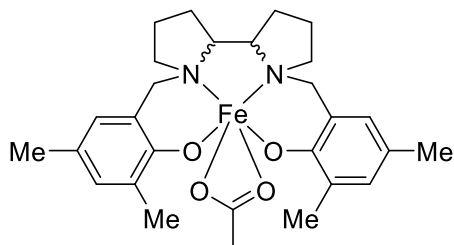


**Fe(6)OAc:** The complex was prepared following the general complexation procedure carried out under air for Fe(III)-acetate complexes. Yield: 0.513 g, 77%. ESI-MS (MeCN): Calcd  $m/z$   $[\text{C}_{37}\text{H}_{50}\text{FeN}_2\text{O}_2]^+ = 610.3216$ , found  $m/z = 610.3281$ . Elemental analysis: Calcd for  $\text{C}_{39}\text{H}_{53}\text{FeN}_2\text{O}_4$  (found): C, 69.95 (69.57), H, 7.98 (7.94) N, 4.18 (4.34). FT-IR:  $2951\text{ cm}^{-1}$ ,  $2902\text{ cm}^{-1}$ ,  $2866\text{ cm}^{-1}$  (C-H (alkyl)),  $1610\text{ cm}^{-1}$  (C=N),  $1598\text{ cm}^{-1}$ ,  $1580\text{ cm}^{-1}$ ,  $1529\text{ cm}^{-1}$ ,  $1456\text{ cm}^{-1}$ ,  $1416\text{ cm}^{-1}$  (C=C (Ar), C=O (acetate)). Effective magnetic moment =  $5.16\ \mu_{\text{B}}$  at 289 K in  $\text{CDCl}_3$ .

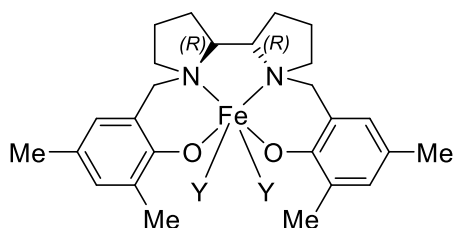


**Fe(8<sub>meso</sub>)OAc:** The complex was prepared following the general complexation procedure carried out under air for Fe(III)-acetate complexes. Yield: 0.278 g, 53%. ESI-MS (MeCN): Calcd  $m/z$   $[\text{C}_{26}\text{H}_{34}\text{FeN}_2\text{O}_2]^+ = 462.1970$ , found  $m/z = 462.2006$ . Elemental analysis: Calcd for  $\text{C}_{28}\text{H}_{37}\text{FeN}_2\text{O}_4 + \text{EtOH}$  (found): C, 63.49 (56.09), H, 7.64 (6.17), N, 4.94 (4.88). FT-IR:  $3752\text{ cm}^{-1}$  (O-H (alcohol), solvent),  $2982\text{ cm}^{-1}$ ,  $2905\text{ cm}^{-1}$  (C-H (alkyl)),  $1608\text{ cm}^{-1}$ ,  $1541\text{ cm}^{-1}$ ,  $1450\text{ cm}^{-1}$  (C=C (Ar), C=O (acetate)). Effective magnetic moment =  $5.18\ \mu_{\text{B}}$  at 298 K in  $\text{CDCl}_3$ . The elemental analysis observed for this complex was not optimal. This was presumably related to unreacted  $\text{Fe}(\text{OAc})_2$

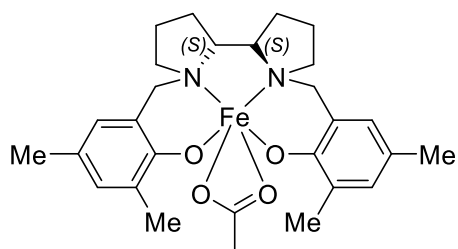
synthetic metal precursor. It is reported here, as the solid-state structure was determined using single-crystal X-ray diffraction with ESI-MS, FT-IR and the observed effective magnetic moment agreeing this species was present in the bulk of the sample.



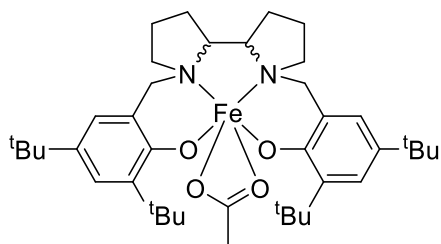
**Fe(8<sub>RR</sub>)Y<sub>2</sub> (Y = OEt, OAc, HOEt or HOAc) / 'Fe(8<sub>RR</sub>)OAc'**: The complex was prepared following the general complexation procedure carried out under air for Fe(III)-acetate complexes. Yield: 0.418 g, 80%. ESI-MS (MeCN): Calcd  $m/z$  [C<sub>26</sub>H<sub>34</sub>FeN<sub>2</sub>O<sub>2</sub>]<sup>+</sup> = 462.1970, found  $m/z$  = 462.2102. Elemental analysis: Calcd for C<sub>30</sub>H<sub>42.4</sub>FeN<sub>2</sub>O<sub>5.3</sub> (Based on solid-state structure) (found): C, 63.03 (62.96), H, 7.48 (7.38), N, 4.90 (4.99). FT-IR: 2964 cm<sup>-1</sup>, 2910 cm<sup>-1</sup> (C-H (alkyl)), 1718 cm<sup>-1</sup>, 1609 cm<sup>-1</sup>, 1540 cm<sup>-1</sup>, 1471 cm<sup>-1</sup>, 1445 cm<sup>-1</sup> (C=C (Ar), C=O (acetate)). Effective magnetic moment = 5.58 μ<sub>B</sub> at 298 K in CDCl<sub>3</sub> (Based on solid-state structure).



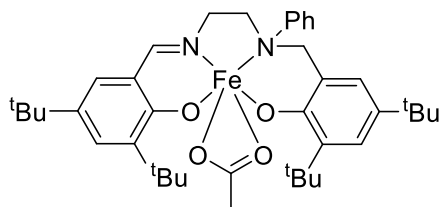
**Fe(8<sub>ss</sub>)OAc**: The complex was prepared following the general complexation procedure carried out under air for Fe(III)-acetate complexes. Yield: 0.423 g, 81%. ESI-MS (MeCN): Calcd  $m/z$  [C<sub>26</sub>H<sub>34</sub>FeN<sub>2</sub>O<sub>2</sub>]<sup>+</sup> = 462.1970, found  $m/z$  = 462.2123. Elemental analysis: Calcd for C<sub>28</sub>H<sub>37</sub>FeN<sub>2</sub>O<sub>4</sub> (found): C, 64.49 (63.65), H, 7.15 (7.32), N, 5.37 (5.29). FT-IR: 2964 cm<sup>-1</sup>, 2910 cm<sup>-1</sup> (C-H (alkyl)), 1721 cm<sup>-1</sup>, 1609 cm<sup>-1</sup>, 1543 cm<sup>-1</sup>, 1471 cm<sup>-1</sup>, 1445 cm<sup>-1</sup> (C=C (Ar), C=O (acetate)). Effective magnetic moment = 5.58 μ<sub>B</sub> at 291 K in CDCl<sub>3</sub>.



**Fe(9<sub>meso</sub>)OAc:** The complex was prepared following the general complexation procedure carried out under air for Fe(III)–acetate complexes. Yield: 0.510 g, 74%. ESI–MS (MeCN): Calcd  $m/z$   $[C_{38}H_{58}FeN_2O_2]^+$  = 630.3848, found  $m/z$  = 630.3863. Elemental analysis: Calcd for  $C_{40}H_{61}FeN_2O_4$  (found): C, 69.65 (69.33), H, 8.91 (8.92), N, 4.06 (4.15). FT–IR: 2948  $cm^{-1}$ , 2901  $cm^{-1}$ , 2865  $cm^{-1}$  (C–H (alkyl)), 1519  $cm^{-1}$ , 1390  $cm^{-1}$ , 1469  $cm^{-1}$ , 1440  $cm^{-1}$ , 1411  $cm^{-1}$  (C=C (Ar), C=O (acetate)). Effective magnetic moment = 5.58  $\mu_B$  at 298 K in  $CDCl_3$ .

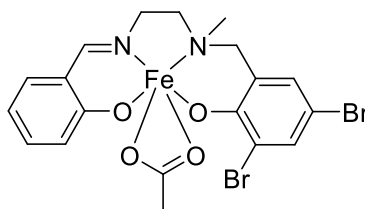


**Fe(10)OAc:** The complex was prepared following the general complexation procedure carried out under air for Fe(III)–acetate complexes. Yield: 0.419 g, 61%. ESI–MS (MeCN): Calcd  $m/z$   $[C_{38}H_{52}FeN_2O_2]^+$  = 624.3378, found  $m/z$  = 624.3488. Elemental analysis: Calcd for  $C_{40}H_{55}FeN_2O_4 + EtOH$  (found): C, 69.12 (67.56), H, 8.43 (8.20), N, 3.84 (3.90). FT–IR: 3415  $cm^{-1}$  (O–H (alcohol), solvent), 2961  $cm^{-1}$ , 2949  $cm^{-1}$ , 2901  $cm^{-1}$ , 2865  $cm^{-1}$  (C–H (alkyl)), 1620  $cm^{-1}$  (C=N), 1537  $cm^{-1}$  (C=C (Ar), C=O (acetate)). Effective magnetic moment = 5.25  $\mu_B$  at 298 K in  $CDCl_3$ .

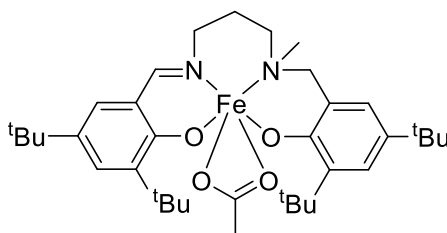


**Fe(11)OAc:** The complex was prepared following the general complexation procedure carried out under air for Fe(III)–acetate complexes. Yield: 0.339 g, 61%. ESI–MS (MeCN): Calcd  $m/z$   $[C_{17}H_{16}FeN_2O_2Br_2]^+$  = 493.8922, found  $m/z$  = 493.8944.

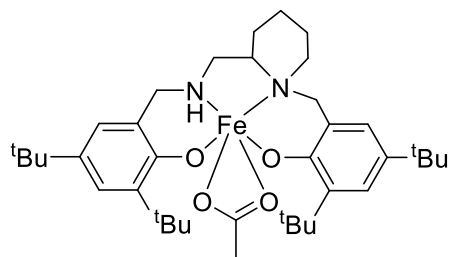
Elemental analysis: Calcd for  $C_{19}H_{19}FeN_2O_4Br_2$  (found): C, 41.12 (41.05), H, 3.45 (3.56), N, 5.05 (5.10). FT-IR:  $2919\text{ cm}^{-1}$ ,  $2853\text{ cm}^{-1}$  (C-H (alkyl)),  $1621\text{ cm}^{-1}$  (C=N),  $1597\text{ cm}^{-1}$ ,  $1541\text{ cm}^{-1}$ ,  $1540\text{ cm}^{-1}$ ,  $1468\text{ cm}^{-1}$ ,  $1441\text{ cm}^{-1}$ ,  $1414\text{ cm}^{-1}$  (C=C (Ar), C=O (acetate)). Effective magnetic moment =  $5.58\ \mu_B$  at 291 K in  $CDCl_3$ .



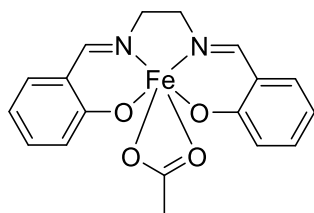
**Fe(12)OAc:** The complex was prepared following the general complexation procedure carried out under air for Fe(III)-acetate complexes. Yield: 0.319 g, 50%. ESI-MS (MeCN): Calcd  $m/z$   $[C_{34}H_{52}FeN_2O_2]^+$  = 576.3378, found  $m/z$  = 576.3464. Elemental analysis: Calcd for  $C_{36}H_{55}FeN_2O_4$  (found): C, 68.02 (64.75), H, 8.72 (8.45), N, 4.41 (4.31). FT-IR:  $3581\text{ cm}^{-1}$  (O-H (alcohol), solvent),  $2950\text{ cm}^{-1}$ ,  $2905\text{ cm}^{-1}$ ,  $2871\text{ cm}^{-1}$  (C-H (alkyl)),  $1611\text{ cm}^{-1}$  (C=N),  $1541\text{ cm}^{-1}$ ,  $1467\text{ cm}^{-1}$ ,  $1438\text{ cm}^{-1}$ ,  $1415\text{ cm}^{-1}$  (C=C (Ar), C=O (acetate)). Effective magnetic moment =  $4.57\ \mu_B$  at 298 K in  $CDCl_3$ .



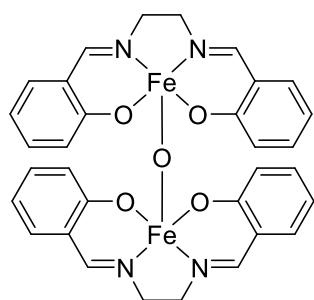
**Fe(13)OAc:** The complex was prepared following the general complexation procedure carried out under air for Fe(III)-acetate complexes. Yield: 0.445 g, 67%. ESI-MS (MeCN): Calcd  $m/z$   $[C_{36}H_{56}FeN_2O_2]^+$  = 604.3691, found  $m/z$  = 604.3683. Elemental analysis: Calcd for  $C_{38}H_{57}FeN_2O_4$  (found): C, 68.97 (67.99) H, 8.68 (9.10), N, 4.23 (4.29). FT-IR:  $2947\text{ cm}^{-1}$ ,  $2905\text{ cm}^{-1}$ ,  $2866\text{ cm}^{-1}$  (C-H (alkyl)),  $1551\text{ cm}^{-1}$ ,  $1459\text{ cm}^{-1}$ ,  $1438\text{ cm}^{-1}$ ,  $1415\text{ cm}^{-1}$  (C=C (Ar), C=O (acetate)). Effective magnetic moment =  $5.38\ \mu_B$  at 298 K in  $CDCl_3$ .



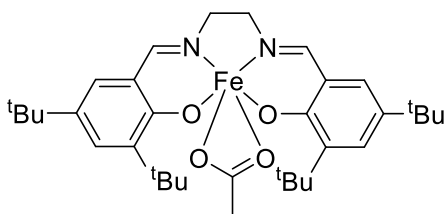
**Fe(14)OAc:** The complex was prepared following the general complexation procedure carried out under air for Fe(III)–acetate complexes. Yield: 0.091 g, 24%. ESI–MS (MeCN): Calcd  $m/z$   $[C_{16}H_{14}FeN_2O_2]^+$  = 322.0405, found  $m/z$  = 322.0424. Elemental analysis: Calcd for  $C_{18}H_{17}FeN_2O_4$  (found): C, 56.72 (57.43) H, 4.50 (4.51), N, 7.35 (7.62). FT–IR:  $3671\text{ cm}^{-1}$  (O–H (alcohol), solvent),  $2988\text{ cm}^{-1}$ ,  $2970\text{ cm}^{-1}$ ,  $2901\text{ cm}^{-1}$  (C–H (alkyl)),  $1626\text{ cm}^{-1}$  (C=N),  $1597\text{ cm}^{-1}$ ,  $1539\text{ cm}^{-1}$ ,  $1466\text{ cm}^{-1}$  (C=C (Ar), C=O (acetate)). Effective magnetic moment =  $5.26\ \mu_B$  at 291 K in  $CDCl_3$ .



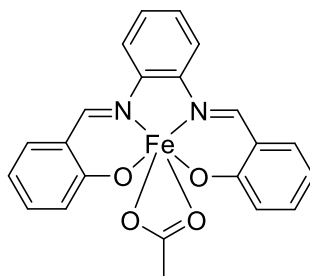
**[Fe(14)]<sub>2</sub>O:** The complex was prepared following the general complexation procedure carried out under air for Fe(III)–acetate complexes. The dark red crystals isolated were recrystallised using hot acetonitrile and slow evaporation at room temperature to obtain further red crystals. Single–crystal X–ray diffraction confirmed the unit cell of this acetonitrile recrystallised solid was consistent and matched with the data of the  $\mu$ -oxo–bridged Fe(III)–salen complex  $[Fe(\mathbf{14})]_2O$  reported in literature.<sup>[23]</sup> Elemental analysis: Calcd for  $C_{32}H_{28}Fe_2N_4O_5$  (found): C, 58.21 (57.00) H, 4.27 (4.33), N, 8.49 (7.92).



**Fe(15)OAc:** The complex was prepared following the general complexation procedure carried out under air for Fe(III)–acetate complexes. Yield: 0.091 g, 15%. ESI–MS (MeCN): Calcd  $m/z$   $[C_{32}H_{46}FeN_2O_2]^+$  = 546.2909, found  $m/z$  = 546.3028. Elemental analysis: Calcd for  $C_{34}H_{49}FeN_2O_4$  (found): C, 67.43 (64.46), H, 8.16 (7.89), N, 4.63 (4.64). FT–IR: 2954  $cm^{-1}$ , 2923  $cm^{-1}$ , 2903  $cm^{-1}$ , 2868  $cm^{-1}$  (C–H (alkyl)), 1621  $cm^{-1}$  (C=N), 1546  $cm^{-1}$ , 1535  $cm^{-1}$ , 1457  $cm^{-1}$ , 1437  $cm^{-1}$ , 1411  $cm^{-1}$  (C=C (Ar), C=O (acetate)). Effective magnetic moment = 4.61  $\mu_B$  at 298 K in  $CDCl_3$ . The elemental analysis was reasonably close, but not optimal compared to that expected. This was attributed to the possible formation of  $Fe(15)OAc \cdot H_2O$ ; potentially indicative of the complex displaying a hygroscopic nature, or the incorporation of a small amount of residual ethanol  $\{Fe(10)OAc \cdot EtOH\}$  or unreacted  $Fe(OAc)_2$  present in the sample.



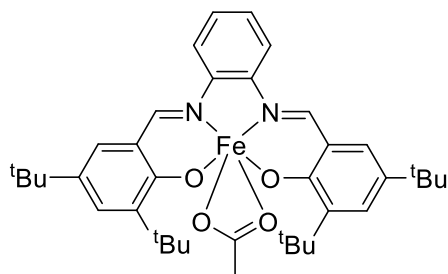
**Fe(16)OAc:** The complex was prepared following the general complexation procedure carried out under air for Fe(III)–acetate complexes. Yield = 0.308 g, 72%. ESI–MS (MeCN): Calcd  $m/z$   $[C_{20}H_{14}FeN_2O_2]^+$  = 370.0405, found  $m/z$  = 370.0550. Elemental analysis: Calcd for  $C_{38}H_{49}FeN_2O_4$  (found): C, 61.56 (61.08), H, 3.99 (3.98), N, 6.53 (6.62). FT–IR: 3661  $cm^{-1}$  (O–H (alcohol), solvent), 2971  $cm^{-1}$  (C–H (alkyl)), 1610  $cm^{-1}$  (C=N), 1578  $cm^{-1}$ , 1529  $cm^{-1}$ , 1463  $cm^{-1}$ , 1434  $cm^{-1}$  (C=C (Ar), C=O (acetate)). Effective magnetic moment = 4.66  $\mu_B$  at 290 K in  $CDCl_3$ .



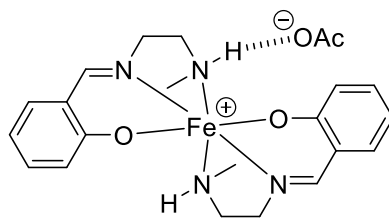
**Fe(17)OAc:** The complex was prepared following the general complexation procedure carried out under air for Fe(III)–acetate complexes. Yield = 0.313 g, 48%. ESI–MS (MeCN): Calcd  $m/z$   $[C_{36}H_{46}FeN_2O_2]^+$  = 594.2909, found  $m/z$  = 594.2919.



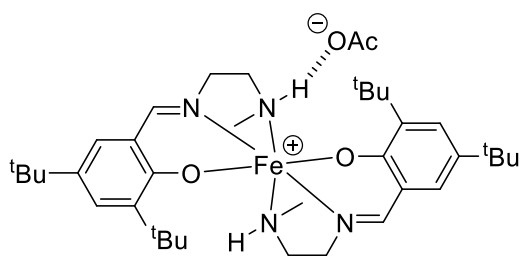
Elemental analysis: Calcd for  $C_{38}H_{49}FeN_2O_4$  (found): C, 69.82 (71.74), H, 7.56 (7.84), N, 4.29 (4.80). FT-IR:  $2952\text{ cm}^{-1}$ ,  $2905\text{ cm}^{-1}$ ,  $2869\text{ cm}^{-1}$  (C-H (alkyl)),  $1601\text{ cm}^{-1}$  (C=N),  $1580\text{ cm}^{-1}$ ,  $1551\text{ cm}^{-1}$ ,  $1527\text{ cm}^{-1}$ ,  $1457\text{ cm}^{-1}$ ,  $1425\text{ cm}^{-1}$ ,  $1412\text{ cm}^{-1}$  (C=C (Ar), C=O (acetate)). Effective magnetic moment =  $2.01\ \mu_B$  at 298 K in  $CDCl_3$ .



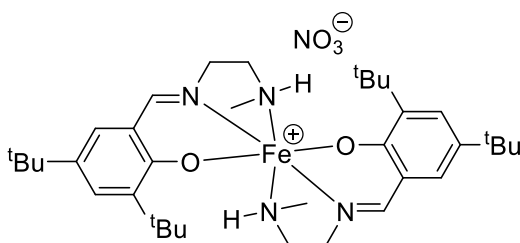
$Fe(\mathbf{18})_2^+AcO^-$ : Following *Scheme 11* described in **Section 2.9**, N-methylethylenediamine (2.0 mmol) was added dropwise to a solution of the salicylaldehyde (2.0 mmol) in methanol (10 mL). The yellow solution was stirred overnight and the solvent removed *in-vacuo* to afford the iminomonophenolate '*in-situ*' as a yellow oil.  $Fe(OAc)_2$  (1.0 mmol) was added as a solid to the yellow solution of iminomonophenolate in ethanol (2 mL) resulting in an intense dark purple mixture. Further ethanol was added to ensure all the  $Fe(OAc)_2$  was rinsed into the reaction mixture (4 x 2 mL). This was refluxed for 4.5 hours and left to cool to room temperature for slow evaporation. Solid failed to precipitate and the solvent was removed *in-vacuo* to afford an oily dark purple product. Cold hexane (2.0 mL) was added to precipitate a dark purple solid which was isolated *via* Büchner filtration, rinsed with further cold hexane (1 mL) and dried. Yield: 0.407 g, 87%. ESI-MS (MeCN): Calcd  $m/z$  [ $C_{20}H_{26}FeN_4O_2$ ] $^+$  = 410.1400, found  $m/z$  = 410.1530. Elemental analysis: Calcd for  $C_{22}H_{29}FeN_4O_4$  (found): C, 56.30 (54.57); H, 6.23 (6.13); N, 11.94 (9.88). FT-IR:  $3105\text{ cm}^{-1}$ ,  $2926\text{ cm}^{-1}$ ,  $2868\text{ cm}^{-1}$  (C-H (alkyl)),  $1626\text{ cm}^{-1}$  (C=N),  $1597\text{ cm}^{-1}$ ,  $1537\text{ cm}^{-1}$ ,  $1441\text{ cm}^{-1}$ ,  $1392\text{ cm}^{-1}$  (C=C (Ar), C=O (acetate)). Effective magnetic moment =  $4.31\ \mu_B$  at 298 K in  $CDCl_3$ . The elemental analysis was reasonably close, but not optimal compared to that expected. This was attributed to the possible formation of  $Fe(\mathbf{18})_2^+AcO^- \cdot H_2O$ ; potentially indicative of the complex displaying a hygroscopic nature, or the incorporation of a small amount of residual ethanol  $\{Fe(\mathbf{18})_2^+AcO^- \cdot EtOH\}$  or unreacted  $Fe(OAc)_2$  present in the sample.



Fe(**19**)<sub>2</sub><sup>+</sup>AcO<sup>-</sup>: Following *Scheme 11* described in **Section 2.9**, N-methylethylenediamine (2.0 mmol) was added dropwise to a solution of the 3,5-di-*tert*-butylsalicylaldehyde (2.0 mmol) in methanol (15 mL). The yellow solution was stirred for three days and the solvent removed *in-vacuo* to afford the iminomonophenolate '*in-situ*' as a yellow oil. Fe(OAc)<sub>2</sub> (1.0 mmol) was added as a solid to the yellow solution of iminomonophenolate in ethanol (2 mL) resulting in an intense dark purple mixture. Further ethanol was added to ensure all the Fe(OAc)<sub>2</sub> was rinsed into the reaction mixture (4 x 2 mL). This was refluxed for four hours and left to cool to room temperature for slow evaporation. Solid failed to precipitate and the solvent was removed *in-vacuo* to afford an oily dark purple product. Cold hexane (2.0 mL) was added to precipitate a dark purple solid which was isolated *via* Büchner filtration, rinsed with further cold hexane (1 mL) and dried. A fraction of the product (50 mg) was recrystallised using hot hexane and single-crystal X-ray diffraction confirmed the solid-state structure to be the Fe(**19**)<sub>2</sub><sup>+</sup>AcO<sup>-</sup> species. Yield: 0.521 g, 75%. ESI-MS (MeCN): Calcd *m/z* [C<sub>36</sub>H<sub>58</sub>FeN<sub>4</sub>O<sub>2</sub>]<sup>+</sup> = 634.3904, found *m/z* = 634.4051. Elemental analysis: Calcd for C<sub>38</sub>H<sub>61</sub>FeN<sub>4</sub>O<sub>4</sub> (found): C, 65.79 (62.61); H, 8.86 (8.71); N, 8.08 (7.37). FT-IR: 3159 cm<sup>-1</sup>, 2951 cm<sup>-1</sup>, 2866 cm<sup>-1</sup> (C-H (alkyl)), 1611 cm<sup>-1</sup> (C=N), 1534 cm<sup>-1</sup>, 1437 cm<sup>-1</sup>, 1413 cm<sup>-1</sup>, 1392 cm<sup>-1</sup> (C=C (Ar), C=O (acetate)). Effective magnetic moment = 4.61 μ<sub>B</sub> at 298 K in CDCl<sub>3</sub>. The elemental analysis was reasonably close, but not optimal compared to that expected. This was attributed to the possible formation of Fe(**19**)<sub>2</sub><sup>+</sup>AcO<sup>-</sup>·H<sub>2</sub>O; potentially indicative of the complex displaying a hygroscopic nature, or the incorporation of a small amount of residual ethanol {Fe(**19**)<sub>2</sub><sup>+</sup>AcO<sup>-</sup>·EtOH} or unreacted Fe(OAc)<sub>2</sub> present in the sample.

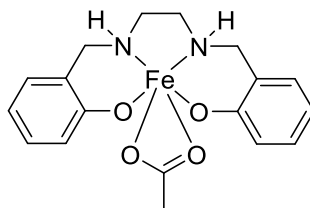


**Fe(19)<sub>2</sub><sup>+</sup>NO<sub>3</sub><sup>-</sup>**: Following *Scheme 12* described in **Section 2.9**, *N*-methylethylenediamine (2.0 mmol) was added dropwise to a solution of the 3,5-di-*tert*-butylsalicylaldehyde (2.0 mmol) in methanol (15 mL). The yellow solution was stirred for an hour to afford the iminomonophenolate '*in-situ*'. Fe(NO<sub>3</sub>)<sub>3</sub>·9H<sub>2</sub>O (1.0 mmol) was added as a solid to the yellow solution and the dark purple mixture was stirred overnight. Crystals were afforded from the mixture; single-crystal X-ray diffraction confirmed the solid-state structure to be the Fe(19)<sub>2</sub><sup>+</sup>NO<sub>3</sub><sup>-</sup> species. The crop of crystals was increased by placing the flask in the freezer overnight and then isolated *via* Büchner filtration. The product was rinsed with water (1 mL) and dried. Yield = 0.436 g, 63%. ESI-MS (MeCN): Calcd *m/z* [C<sub>36</sub>H<sub>58</sub>FeN<sub>4</sub>O<sub>2</sub>]<sup>+</sup> = 634.3904, found *m/z* = 634.4012. Elemental analysis: Calcd for C<sub>36</sub>H<sub>58</sub>FeN<sub>5</sub>O<sub>5</sub> (found): C, 62.06 (60.66); H, 8.39 (8.38); N, 10.05 (9.87). FT-IR: 3199 cm<sup>-1</sup> (C-H (alkenyl)), 2952 cm<sup>-1</sup>, 2867 cm<sup>-1</sup> (C-H (alkyl)), 1612 cm<sup>-1</sup> (C=N, N=O (nitrate)), 1536 cm<sup>-1</sup>, 1414 cm<sup>-1</sup>, 1384 cm<sup>-1</sup>, 1309 cm<sup>-1</sup>, 1248 cm<sup>-1</sup> (C=C (Ar), N=O (nitrate)). Effective magnetic moment = 5.49 μ<sub>B</sub> at 298 K in CDCl<sub>3</sub>. The elemental analysis was reasonably close, but not optimal compared to that expected. This was attributed to the possible formation of Fe(19)<sub>2</sub><sup>+</sup>NO<sub>3</sub><sup>-</sup>·H<sub>2</sub>O; potentially indicative of the complex displaying a hygroscopic nature, or the incorporation of a small amount of residual methanol {Fe(19)<sub>2</sub><sup>+</sup>NO<sub>3</sub><sup>-</sup>·MeOH} or unreacted Fe(OAc)<sub>2</sub> present in the sample.

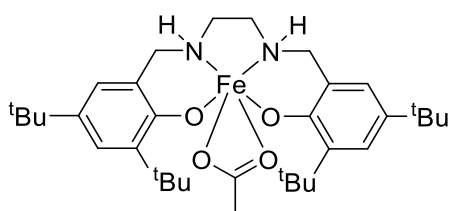


**Fe(132)OAc**: The attempted synthesis of this complex was prepared following the general complexation procedure carried out under air for Fe(III)-acetate complexes. Yield = 0.389 g, 50%. ESI-MS (MeCN): Calcd *m/z* [C<sub>16</sub>H<sub>18</sub>FeN<sub>2</sub>O<sub>2</sub>]<sup>+</sup> = 326.0712, found

$m/z = 326.0714$ . Elemental analysis: Calcd for  $C_{18}H_{21}FeN_2O_4$  (found): C, 56.12 (51.93), H, 5.50 (5.50), N, 7.27 (6.23). FT-IR: 3164 (C-H (aromatic)) 3062  $cm^{-1}$ , 3012  $cm^{-1}$ , 2921  $cm^{-1}$ , 2862  $cm^{-1}$  (C-H (alkyl)), 1707  $cm^{-1}$  (C=N), 1594  $cm^{-1}$ , 1547  $cm^{-1}$ , 1474  $cm^{-1}$ , 1449  $cm^{-1}$  (C=C (Ar), C=O (acetate)). Effective magnetic moment = 4.96  $\mu_B$  at 298 K in  $CDCl_3$ . The elemental analysis observed for this complex was not optimal. This was presumably related to unreacted  $Fe(OAc)_2$  synthetic metal precursor.



**Fe(133)OAc:** The attempted synthesis of this complex was prepared following the general complexation procedure carried out under air for Fe(III)-acetate complexes. Yield = 0.152 g, 12%. ESI-MS (MeCN): Calcd  $m/z$  [ $C_{32}H_{50}FeN_2O_2$ ] $^+$  = 550.3216, found  $m/z = 550.3211$ . Elemental analysis: Calcd for  $C_{34}H_{53}FeN_2O_4$  (found): C, 66.98 (34.86), H, 8.76 (5.03), N, 4.60 (1.53). FT-IR: 3182 (C-H (aromatic)) 2950  $cm^{-1}$ , 2906  $cm^{-1}$ , 2866  $cm^{-1}$  (C-H (alkyl)), 1714  $cm^{-1}$  (C=N), 1561  $cm^{-1}$ , 1532  $cm^{-1}$ , 1438  $cm^{-1}$ , 1412  $cm^{-1}$  (C=C (Ar), C=O (acetate)). Effective magnetic moment = 5.89  $\mu_B$  at 298 K in  $CDCl_3$ . The elemental analysis observed for this complex was poor and this was presumably related to unreacted  $Fe(OAc)_2$  synthetic metal precursor.



## 6.11 MALDI–ToF analysis of the Fe(3)Cl complex

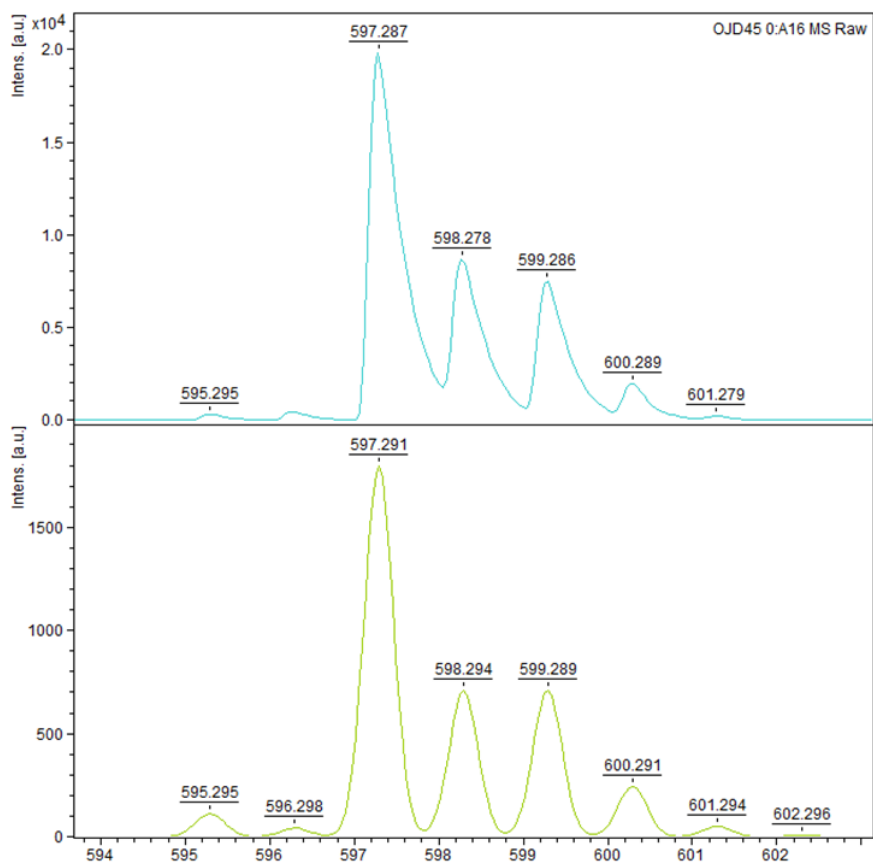


Figure 79. MALDI–ToF spectrum of Fe(3)Cl with a good match of the experimental isotopic distribution pattern with the theoretical.

## 6.12 Measured pXRD pattern of Fe(14)OAc complex

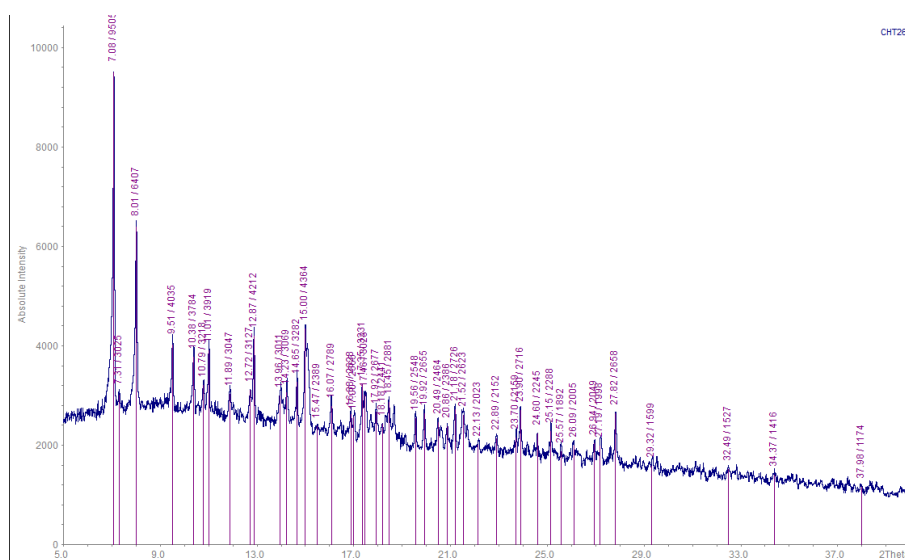


Figure 80. Measured pXRD pattern for Fe(14)OAc.

### 6.13 General solution ROP procedure using Fe(III)–salalen–chloride complexes in propylene oxide solvent

All polymerisations were carried out using Schlenk flasks with J Youngs taps under inert conditions, generally at a lactide–to–Fe initiator ratio of 100:1. The *rac*–lactide (0.4 g, 2.78 mmol) and Fe(1–7) (0.0278 mmol) were placed in the J Youngs tapped Schlenk flask. Distilled propylene oxide (2.0 mL) was added *via* syringe and the flask was placed in the preheated oil bath for the desired time duration. The flask was allowed to cool and an aliquot taken, diluted with deuterated chloroform and analysed *via*  $^1\text{H}$  NMR spectroscopy to determine the conversion of the PLA. Under air, the reaction mixture was transferred to a round bottom flask with dichloromethane and solvents removed *in-vacuo*. The purple solid was washed using methanol (3 x 10 mL) and decantation *via* syringe. The solid was dried using the Schlenk line and analysed *via* GPC, homonuclear decoupled ( $^1\text{H}$  { $^1\text{H}$ }) NMR spectroscopy and MALDI–ToF mass spectrometry.

Polymerisation conversion was determined, using  $^1\text{H}$  NMR spectroscopy in  $\text{CDCl}_3$ , from the relative integration of the methine region of the PLA ( $\delta$  5.12–5.20 ppm) against that of the LA ( $\delta$  4.94–5.01 ppm). The tacticity of the PLA ( $P_m$ ) was determined from its  $^1\text{H}$  { $^1\text{H}$ } NMR spectrum by decoupling the methine region. This removes the coupling between the methyl and methine environments and, results in the methine quartet resonance signal revealing a series of singlet resonance signals. These singlets relate to different stereochemical arrangements in the polymer chain for a series of four lactyl units or ‘tetrads’.<sup>[24]</sup> The relationship between adjacent stereocentres, in each lactyl unit, can be described either as ‘*iso*’ (*i*); *R,R* or *S,S*, linkages or ‘*syndio*’ (*s*); *R,S* or *S,R*, linkages.<sup>[24]</sup> In the absence of epimerisation or racemisation, for the polymerisation of *rac*–LA, there are five tetrads possible {*sis* (purely heterotactic), *sii*, *iis*, *iii* (purely isotactic), *isi* (purely heterotactic)}. Comparing the relative integration of these tetrads can determine the overall tacticity of the PLA, using Bernoullian statistics, and the probability of heterotactic enchainment,  $P_r$  ( $P_r = \sqrt{2 \times [sis]}$ ).<sup>[1,24,25]</sup> The  $P_m$  value can then be calculated using this  $P_r$  value ( $P_m = 1 - P_r$ ). Perfectly isotactic PLA has a  $P_m$  value of 1, perfectly heterotactic PLA a value

of 0 and atactic PLA a value of 0.5. Example  $^1\text{H}$   $\{^1\text{H}\}$  NMR spectra, with the relative integration of the  $[\textit{sis}]$  singlet, are shown in **Sections 7.2** and **7.5**.<sup>[24]</sup>

#### **6.14 General solution ROP procedure using Fe(III)–acetate complexes in toluene solvent and catalytic amounts of triethylamine and benzyl alcohol**

Polymerisations were carried out using Schlenk flasks with J Youngs taps under inert conditions at a lactide–to–Fe initiator–to–benzyl alcohol–to–triethylamine overall ratio of 100:1:1:1. The *rac*–lactide (0.4 g, 2.78 mmol) and Fe complex (0.0278 mmol) were placed in the J Youngs tapped Schlenk flask. Benzyl alcohol (0.0278 mmol) and triethylamine (0.0278 mmol) were added *via* an Eppendorf pipette. Dry toluene (4.0 mL) was added *via* syringe and the flask was placed in the preheated oil bath (80 °C / 100 °C) for the desired time duration. The flask was allowed to cool and an aliquot taken, diluted with deuterated chloroform and analysed *via*  $^1\text{H}$  NMR spectroscopy to determine the conversion of the PLA. Under air, the reaction mixture was transferred to a round bottom flask with dichloromethane and solvents removed *in-vacuo*. The purple solid was washed using methanol (3 x 10 mL) and decantation *via* syringe. The solid was dried using the Schlenk line and analysed *via* GPC,  $^1\text{H}$   $\{^1\text{H}\}$  NMR spectroscopy and MALDI–ToF mass spectrometry. The polymerisation conversion and tacticity of the PLA ( $P_m$ ) can be determined by that described in **Section 6.13**.

#### **6.15 Solution ROP procedure using Fe(3)Cl in toluene solvent and catalytic amounts of triethylamine and benzyl alcohol**

The same procedure and 100:1:1:1 ratio as that for **Section 6.14**, but using different amounts: *rac*–lactide (1.0 g, 6.94 mmol), Fe(3)Cl (0.0694 mmol), benzyl alcohol (0.0694 mmol), triethylamine (0.0694 mmol) and toluene (5.0 mL).

#### **6.16 General CO<sub>2</sub> / epoxide coupling reaction procedure**

All CO<sub>2</sub> / epoxide coupling reactions were carried out in a ratio of 1:8:1200 [catalyst (0.08 mol%)]:[co–catalyst (0.64 mol%)]:[epoxide]. Generally, tetrabutylammonium chloride (TBAC) was the co–catalyst and cyclohexene oxide (CHO) the epoxide.

The catalyst ( $4.21 \times 10^{-5}$  mol) and TBAC (0.094 g,  $3.37 \times 10^{-4}$  mol) were added as solids to a glass reactor vial in the glovebox. CHO (5 mL) was added to the vial *via* syringe to form a dark purple mixture. The vial was transferred out of the glovebox and placed in the autoclave under a flow of argon. The autoclave was cycled five times with CO<sub>2</sub> and finally left pressurised at 10 bar. The temperature was ramped to 80 °C and left for 24 hours with mechanical stirring. To note, extra care should always be taken when operating at elevated pressure; ensure the reactor is in good condition, the operator has undergone training and risk assessments have been prepared. After this time, the autoclave was cooled in an ice bath before bleeding to the air. An aliquot was taken of the crude dark red product mixture and analysed *via* <sup>1</sup>H NMR spectroscopy to determine conversion and selectivity. Electrospray ionisation-mass spectrometry (ESI–MS) was used to confirm the cyclic carbonate product was present in the mixture and GPC analysis to confirm no polymer was present.

### 6.17 Crude <sup>1</sup>H NMR spectra of CO<sub>2</sub> / epoxide coupling reaction mixtures

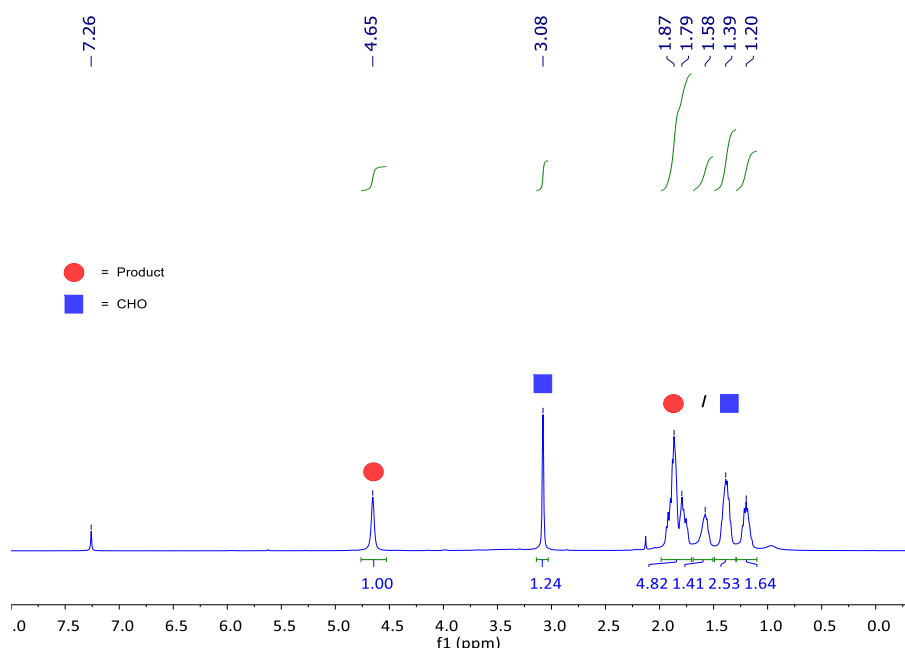


Figure 81. Crude <sup>1</sup>H NMR spectrum of the CO<sub>2</sub> / cyclohexene oxide (CHO) coupling reaction mixture using Fe(3)OAc (Section 4.5, Table 17, entry 7).

<sup>1</sup>H NMR spectroscopy consistent with literature.<sup>[26–29]</sup> ESI–MS (MeCN): Calcd  $m/z$  [C<sub>7</sub>H<sub>11</sub>O<sub>3</sub>]<sup>+</sup> = 143.0703, found  $m/z$  = 143.0729, calcd  $m/z$  [C<sub>7</sub>H<sub>10</sub>O<sub>3</sub>Na]<sup>+</sup> = 165.0522, found  $m/z$  = 165.0553.



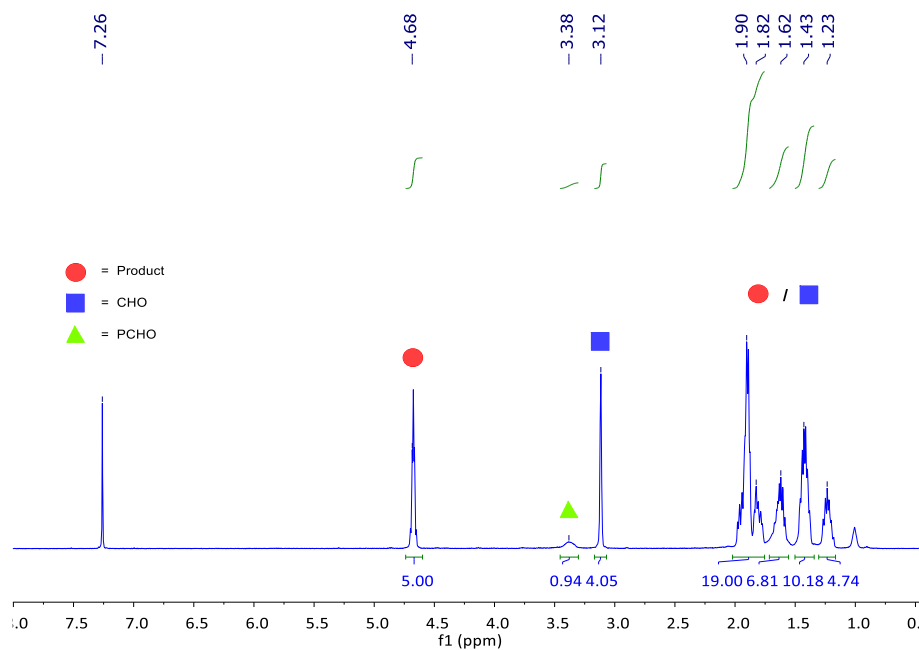


Figure 82. Crude  $^1\text{H}$  NMR spectrum of the  $\text{CO}_2$  / cyclohexene oxide (CHO) coupling reaction mixture using  $\text{Fe(17)OAc}$  (Section 4.5, Table 18, entry 9).

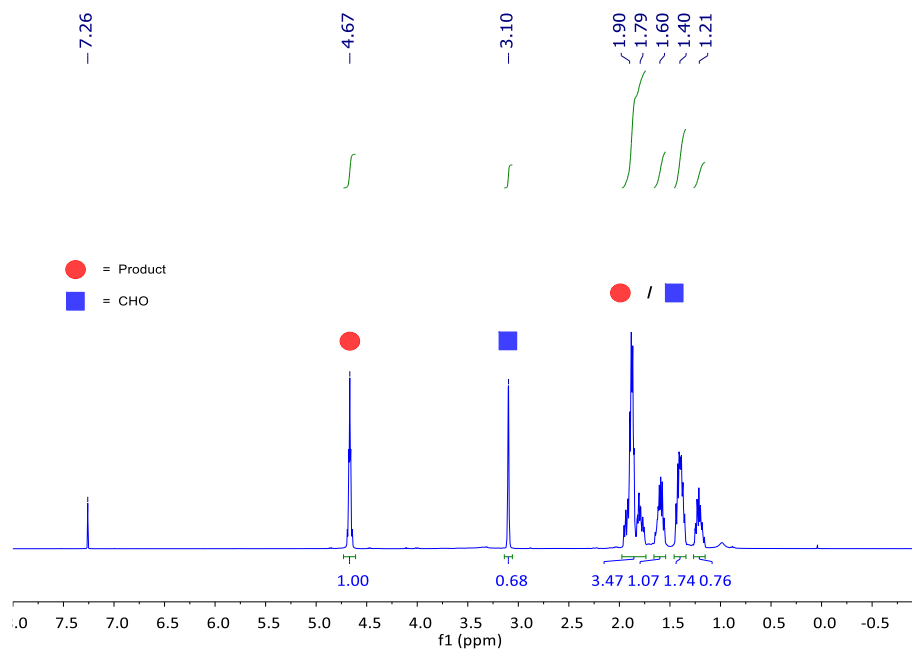


Figure 83. Crude  $^1\text{H}$  NMR spectrum of the  $\text{CO}_2$  / cyclohexene oxide (CHO) coupling reaction mixture using Stewart's  $\text{Fe(65)Cl}$  (Section 4.9, Table 22, entry 13).<sup>[30]</sup>

$^1\text{H}$  NMR spectroscopy consistent with literature.<sup>[26–28]</sup> ESI–MS (MeCN): Calcd  $m/z$   $[\text{C}_7\text{H}_{11}\text{O}_3]^+ = 143.0703$ , found  $m/z = 143.0741$ , calcd  $m/z$   $[\text{C}_7\text{H}_{10}\text{O}_3\text{Na}]^+ = 165.0522$ , found  $m/z = 165.0597$ .

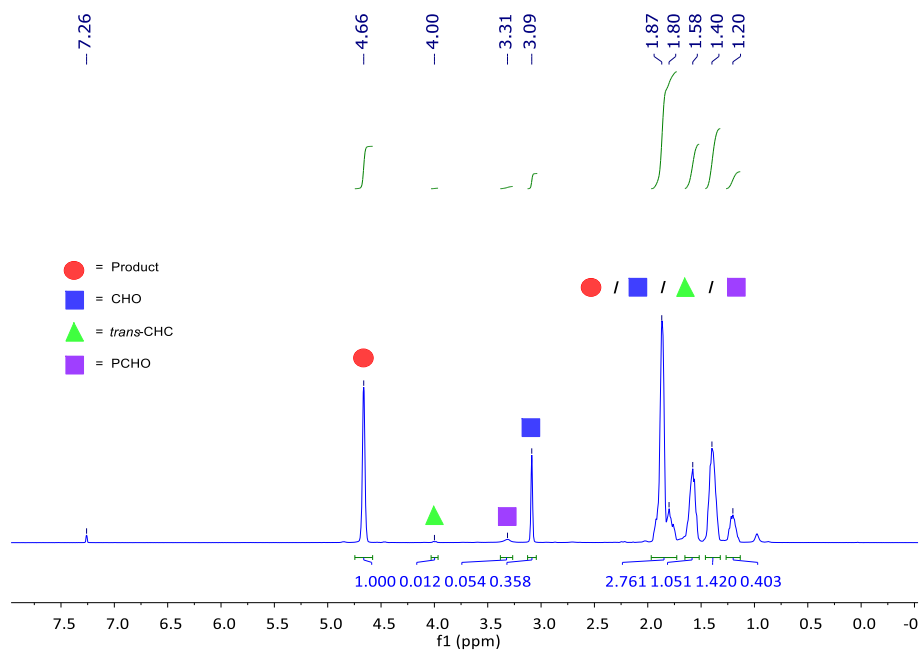


Figure 84. Crude  $^1\text{H}$  NMR spectrum of the  $\text{CO}_2$  / cyclohexene oxide (CHO) coupling reaction mixture using Stewart's  $\text{Fe}(\mathbf{65})\text{Cl}$  at  $120\text{ }^\circ\text{C}$  (Section 4.9, Table 22, entry 14).<sup>[30]</sup>

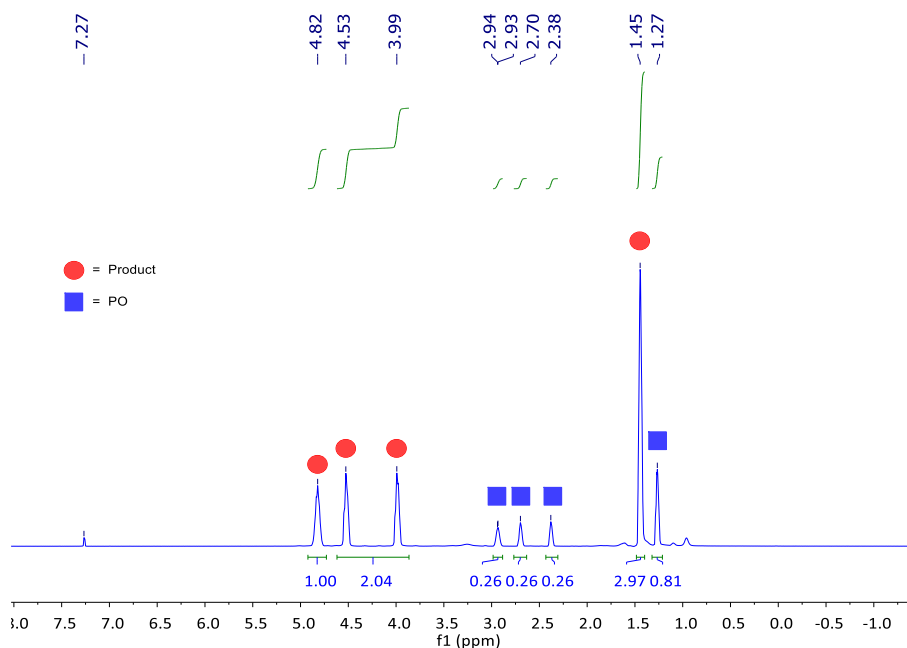


Figure 85. Crude  $^1\text{H}$  NMR spectrum of the  $\text{CO}_2$  / propylene oxide (PO) coupling reaction mixture using  $\text{Fe}(\mathbf{13})\text{OAc}$  (Section 4.7, Table 21, entry 1).

$^1\text{H}$  NMR spectroscopy consistent with literature.<sup>[26–28]</sup> ESI–MS (MeCN): Calcd  $m/z$   $[\text{C}_4\text{H}_7\text{O}_3]^+$  = 103.0390, found  $m/z$  = 103.0393, calcd  $m/z$   $[\text{C}_4\text{H}_6\text{O}_3\text{Na}]^+$  = 125.0209, found  $m/z$  = 125.0223.

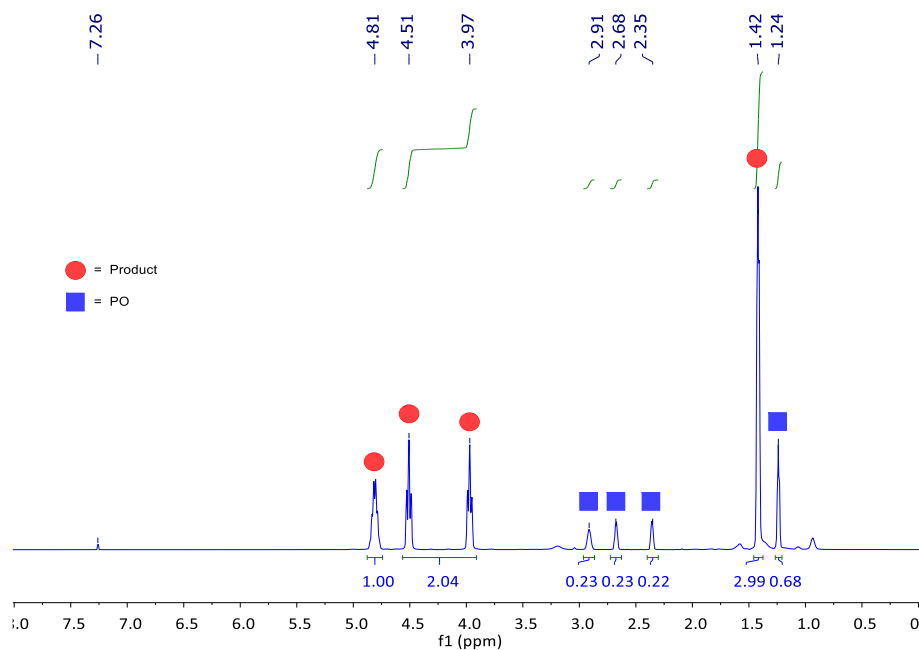


Figure 86. Crude  $^1\text{H}$  NMR spectrum of the  $\text{CO}_2$  / propylene oxide (PO) coupling reaction mixture using Stewart's  $\text{Fe}(65)\text{Cl}$  (Section 4.10, Table 24, entry 1).<sup>[30]</sup>

$^1\text{H}$  NMR spectroscopy consistent with literature.<sup>[26–28]</sup> ESI–MS (MeCN): Calcd  $m/z$   $[\text{C}_4\text{H}_6\text{O}_3\text{Na}]^+ = 125.0209$ , found  $m/z = 125.0226$ .

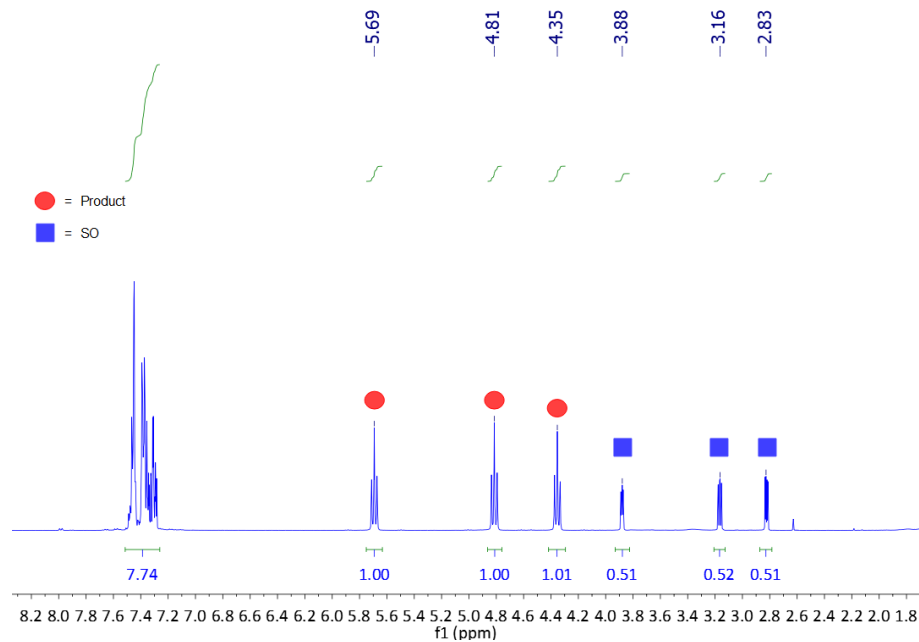


Figure 87. Crude  $^1\text{H}$  NMR spectrum of the  $\text{CO}_2$  / styrene oxide (SO) coupling reaction mixture using  $\text{Fe}(13)\text{OAc}$  (Section 4.7, Table 21, entry 2).

$^1\text{H}$  NMR spectroscopy consistent with literature.<sup>[26–28]</sup> ESI–MS (MeCN): Calcd  $m/z$   $[\text{C}_9\text{H}_9\text{O}_3]^+ = 165.0546$ , found  $m/z = 165.0588$ , calcd  $m/z$   $[\text{C}_9\text{H}_8\text{O}_3\text{Na}]^+ = 187.0366$ , found  $m/z = 187.0391$ .

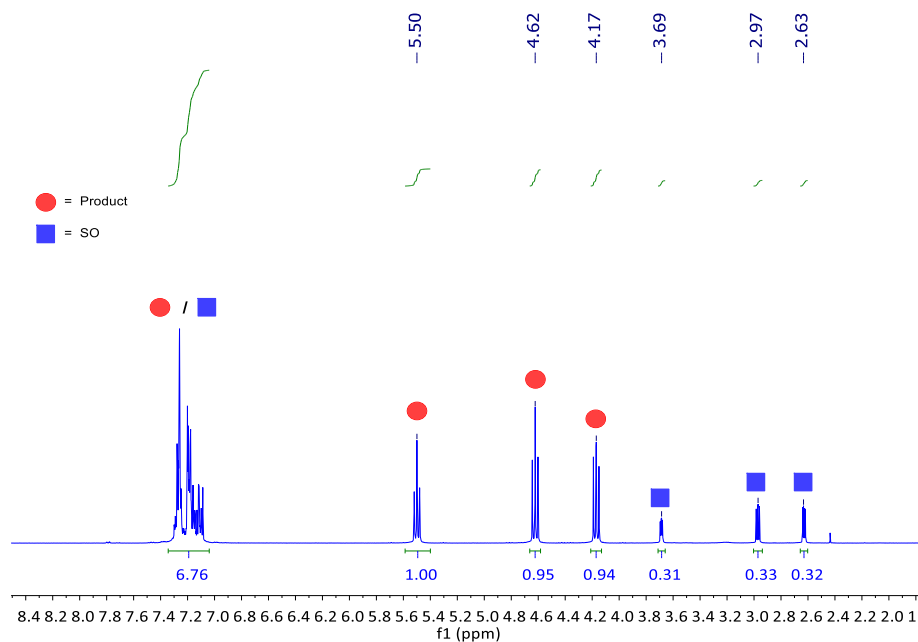


Figure 88. Crude  $^1\text{H}$  NMR spectrum of the  $\text{CO}_2$  / styrene oxide (SO) coupling reaction mixture using Stewart's  $\text{Fe}(\mathbf{65})\text{Cl}$  (Section 4.10, Table 24, entry 2).<sup>[30]</sup>

$^1\text{H}$  NMR spectroscopy consistent with literature.<sup>[26–28]</sup> ESI–MS (MeCN): Calcd  $m/z$   $[\text{C}_9\text{H}_8\text{O}_3\text{Na}]^+ = 187.0366$ , found  $m/z = 187.0377$ .

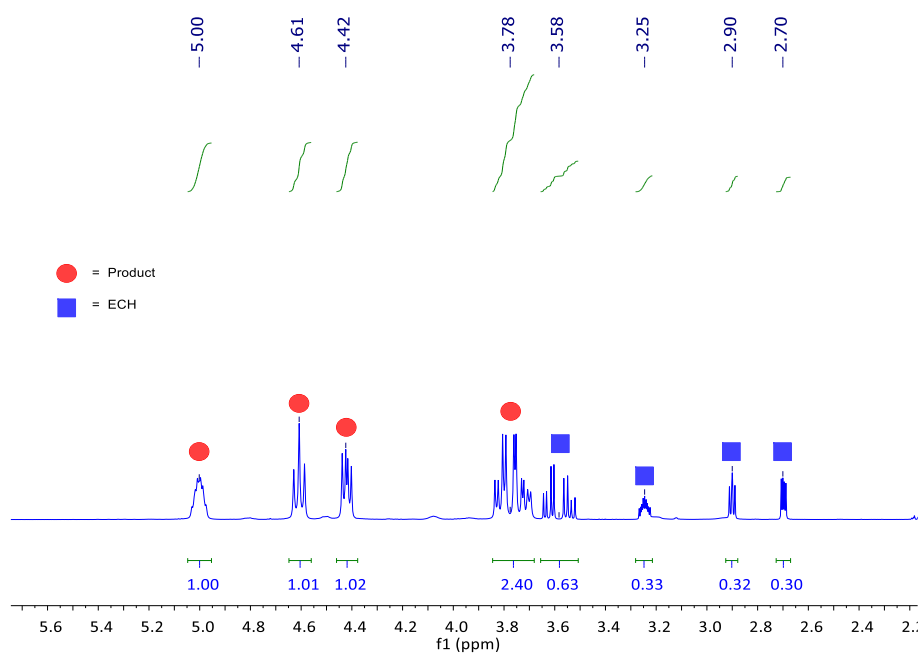


Figure 89. Crude  $^1\text{H}$  NMR spectrum of the  $\text{CO}_2$  / epichlorohydrin (ECH) coupling reaction mixture using  $\text{Fe}(\mathbf{13})\text{OAc}$  (Section 4.7, Table 21, entry 3).

$^1\text{H}$  NMR spectroscopy consistent with literature.<sup>[26–28]</sup>

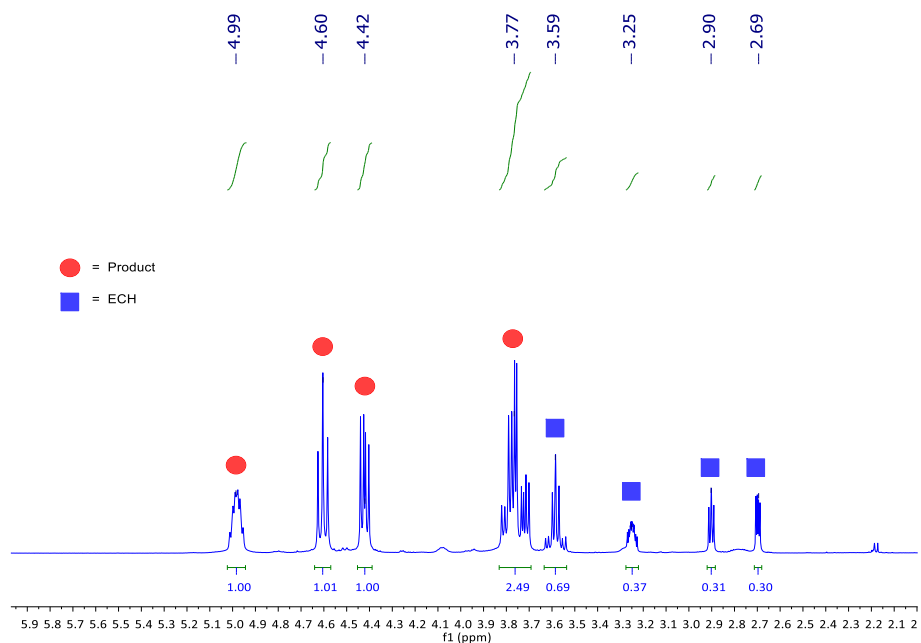


Figure 90. Crude  $^1\text{H}$  NMR spectrum of the  $\text{CO}_2$  / epichlorohydrin (ECH) coupling reaction mixture using Stewart's  $\text{Fe}(\mathbf{65})\text{Cl}$  (Section 4.10, Table 24, entry 3).<sup>[30]</sup>

$^1\text{H}$  NMR spectroscopy consistent with literature.<sup>[26–28]</sup> ESI-MS (MeCN): Calcd  $m/z$  [ $\text{C}_4\text{H}_5\text{ClO}_3\text{Na}$ ] $^+$  = 158.9819, found  $m/z$  = 158.9845.

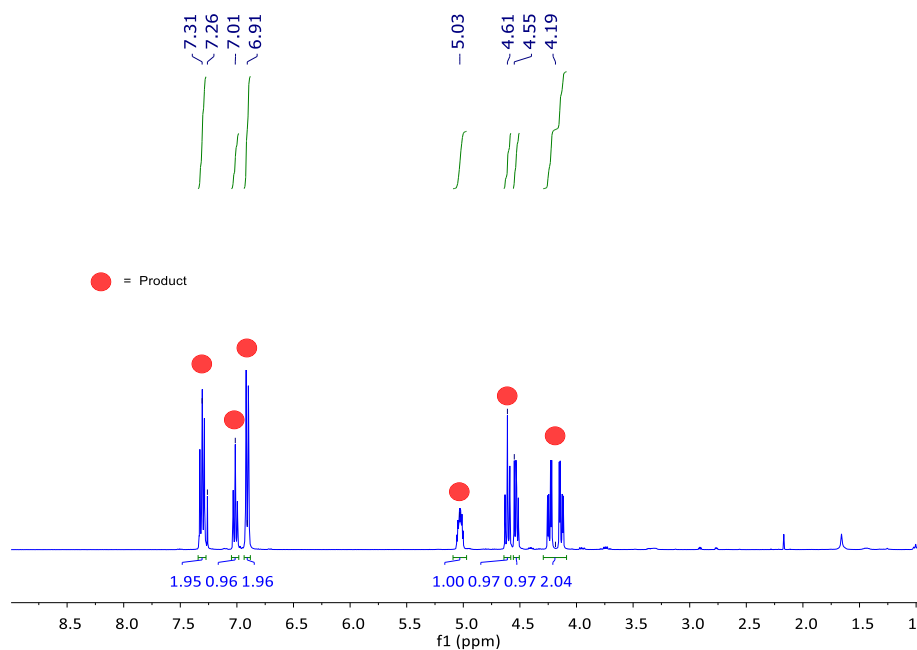


Figure 91. Crude  $^1\text{H}$  NMR spectrum of the  $\text{CO}_2$  / phenyl glycidyl ether (PGE) coupling reaction mixture using  $\text{Fe}(\mathbf{13})\text{OAc}$  (Section 4.7, Table 21, entry 4).

$^1\text{H}$  NMR spectroscopy consistent with literature.<sup>[26,27]</sup> ESI-MS (MeCN): Calcd  $m/z$   $[\text{C}_{10}\text{H}_{11}\text{O}_4]^+ = 195.0652$ , found  $m/z = 195.0596$ , calcd  $m/z$   $[\text{C}_{10}\text{H}_{10}\text{O}_4\text{Na}]^+ = 217.0471$ , found  $m/z = 217.0405$ .

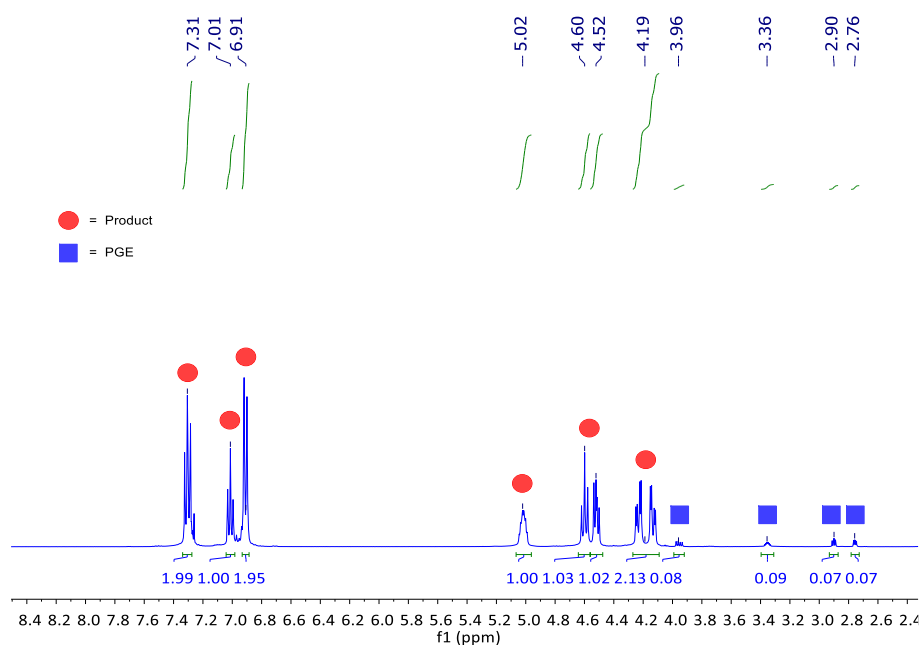


Figure 92. Crude  $^1\text{H}$  NMR spectrum of the  $\text{CO}_2$  / phenyl glycidyl ether (PGE) coupling reaction mixture using Stewart's  $\text{Fe}(\mathbf{65})\text{Cl}$  (Section 4.10, Table 24, entry 4).<sup>[30]</sup>

$^1\text{H}$  NMR spectroscopy consistent with literature.<sup>[26,27]</sup> ESI-MS (MeCN): Calcd  $m/z$   $[\text{C}_{10}\text{H}_{11}\text{O}_4]^+ = 195.0652$ , found  $m/z = 195.0659$ , calcd  $m/z$   $[\text{C}_{10}\text{H}_{10}\text{O}_4\text{Na}]^+ = 217.0471$ , found  $m/z = 217.0469$ .

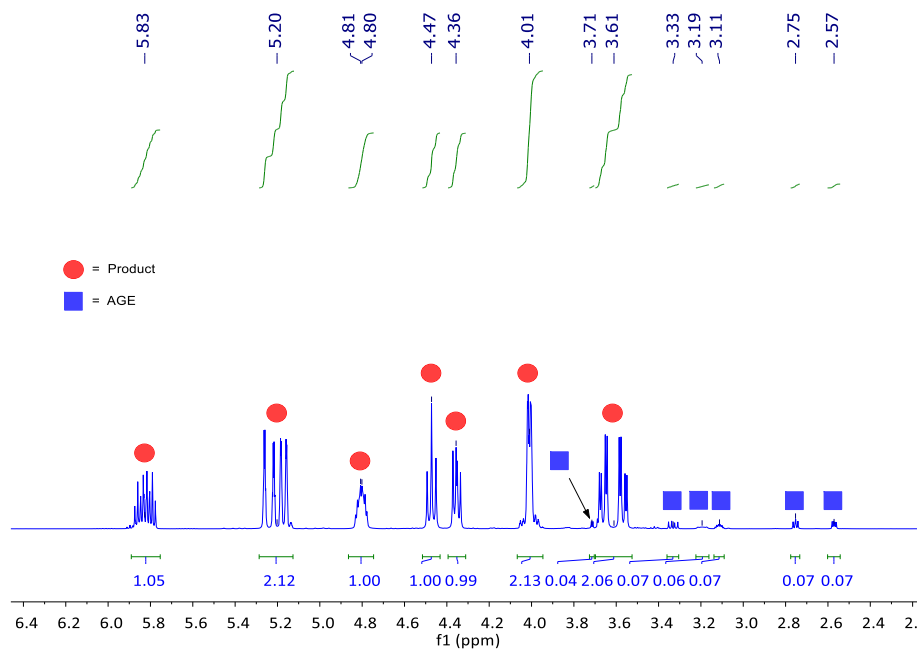


Figure 93. Crude  $^1\text{H}$  NMR spectrum of the  $\text{CO}_2$  / allyl glycidyl ether (AGE) coupling reaction mixture using Fe(**13**)OAc (Section 4.7, Table 21, entry 6).

$^1\text{H}$  NMR spectroscopy consistent with literature.<sup>[27,28]</sup> ESI-MS (MeCN): Calcd  $m/z$   $[\text{C}_7\text{H}_{11}\text{O}_4]^+ = 159.0652$ , found  $m/z = 159.0703$ , calcd  $m/z$   $[\text{C}_7\text{H}_{10}\text{O}_4\text{Na}]^+ = 181.0471$ , found  $m/z = 181.0491$ .

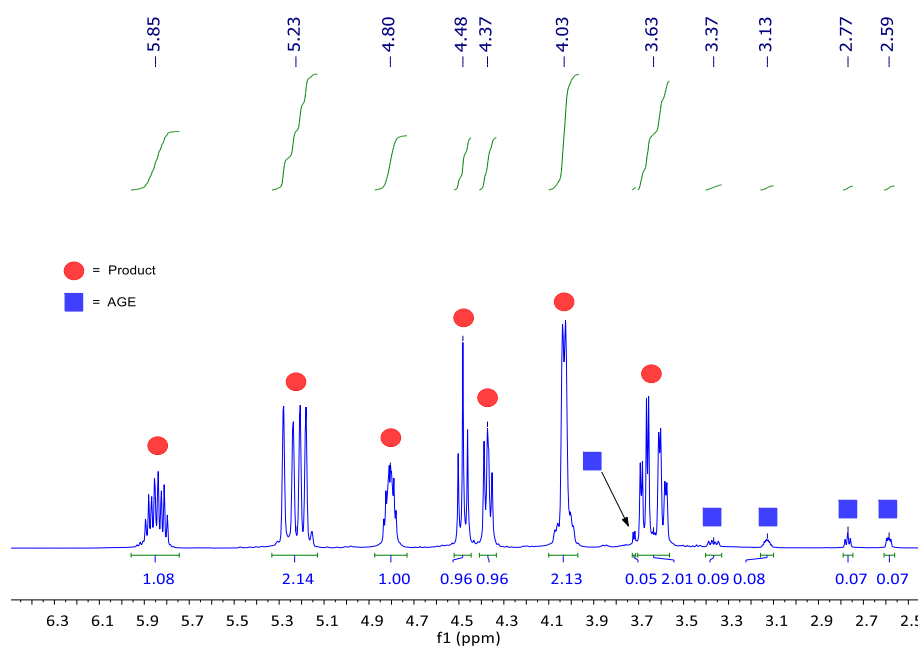


Figure 94. Crude  $^1\text{H}$  NMR spectrum of the  $\text{CO}_2$  / allyl glycidyl ether (AGE) coupling reaction mixture using Stewart's  $\text{Fe}(\mathbf{65})\text{Cl}$  (Section 4.10, Table 24, entry 5).<sup>[30]</sup>

$^1\text{H}$  NMR spectroscopy consistent with literature.<sup>[27,28]</sup> ESI-MS (MeCN): Calcd  $m/z$   $[\text{C}_7\text{H}_{11}\text{O}_4]^+$  = 159.0652, found  $m/z$  = 159.0661, calcd  $m/z$   $[\text{C}_7\text{H}_{10}\text{O}_4\text{Na}]^+$  = 181.0471, found  $m/z$  = 181.0481.

### 6.18 General procedure for the solution ROCOP of PA / CHO using $\text{Fe}(\text{III})$ -complexes or organic ligands in toluene solvent

The PA (2.5 mmol, 0.3703 g) and catalyst (0.025 mmol) were added as solids to a Schlenk flask in a glovebox. CHO (2.5 mmol, 0.253 mL) and dry toluene (1.0 mL) were added. The overall loading was 100:100:1 [PA]:[CHO]:[Cat.]. The flask was placed in a preheated oil bath (100 °C) for three days to stir. Before heating, the mixtures were typically dark purple if  $\text{Fe}(\text{L})\text{X}$  was used as the catalyst or yellow if only organic ligand (L) was used; undissolved white PA would be observed which would dissolve upon heating. After this reaction time, the flask was allowed to cool for a few minutes and an aliquot taken of the product mixture and analysed *via*  $^1\text{H}$  NMR spectroscopy to determine the conversion (and chemoselectivity). Dichloromethane was added to the flask to transfer all contents into a round bottom flask and solvents were removed *in-vacuo* and dried. To purify and isolate the copolymer (particularly to remove any iron residue and ensure the iron is cleaved off the polymer, together



with any unreacted PA), dichloromethane was added (~5 mL), to form a solution, followed by acidified methanol (1M, 70 mL) to precipitate a white copolymer solid. This was isolated *via* filtration, rinsed with methanol and dried in a vacuum oven at 30 °C overnight. This solid was then weighed to obtain an isolated yield and could be used for <sup>1</sup>H NMR spectroscopy; to determine the chemoselectivity, GPC, DSC, FT–IR and MALDI-ToF analysis.

### **6.19 General procedure for the neat ROCOP of PA / CHO using Fe(III)–complexes or organic ligands in toluene solvent**

The PA (2.5 mmol, 0.3703 g) and catalyst (0.025 mmol) were added as solids to a Schlenk flask in a glovebox. CHO (20 mmol, 2.0 mL) was added. The overall loading was 100:800:1 [PA]:[CHO]:[Cat.]. The flask was placed in a preheated oil bath (100 °C) for the desired time duration (30 hours typically). Before heating, the mixtures were typically dark purple / brown if Fe(L)X was used as the catalyst or yellow if only organic ligand (L) was used; undissolved white PA would be observed which would dissolve upon heat (from observation the PA appeared more soluble in these conditions than the ROCOP in toluene solvent). After this reaction time, the flask was allowed to cool for a few minutes and an aliquot taken of the product mixture and analysed *via* <sup>1</sup>H NMR spectroscopy to determine the conversion (and chemoselectivity). Dichloromethane was added to the flask to transfer all contents into a round bottom flask and solvents were removed *in-vacuo* and dried. To purify and isolate the copolymer (particularly to remove any iron residue and cleave off the polymer, together with unreacted PA), dichloromethane was added (~5 mL), to form a solution, followed by acidified methanol (1M, 70 mL) to precipitate a white copolymer solid. This was isolated *via* filtration, rinsed with methanol and dried in a vacuum oven at 30 °C overnight. This solid was then weighed to obtain an isolated yield and could be used for <sup>1</sup>H NMR spectroscopy, to determine the chemoselectivity, GPC, DSC, FT–IR and MALDI-ToF analysis. For the chemoselectivity determination, the whole broad resonance in the ether region was integrated regardless of end group consideration, as adjustment was not possible here for the neat reactions and the worst-case scenario would be the % ester linkages being calculated too low; this broadening of the ether linkages has been observed in literature.<sup>[31]</sup>

## 6.20 $^1\text{H}$ NMR and DOSY spectroscopic analysis on the polymers obtained from ROCOP

### Crude $^1\text{H}$ NMR spectra of a typical PA / CHO solution ROCOP reaction mixture

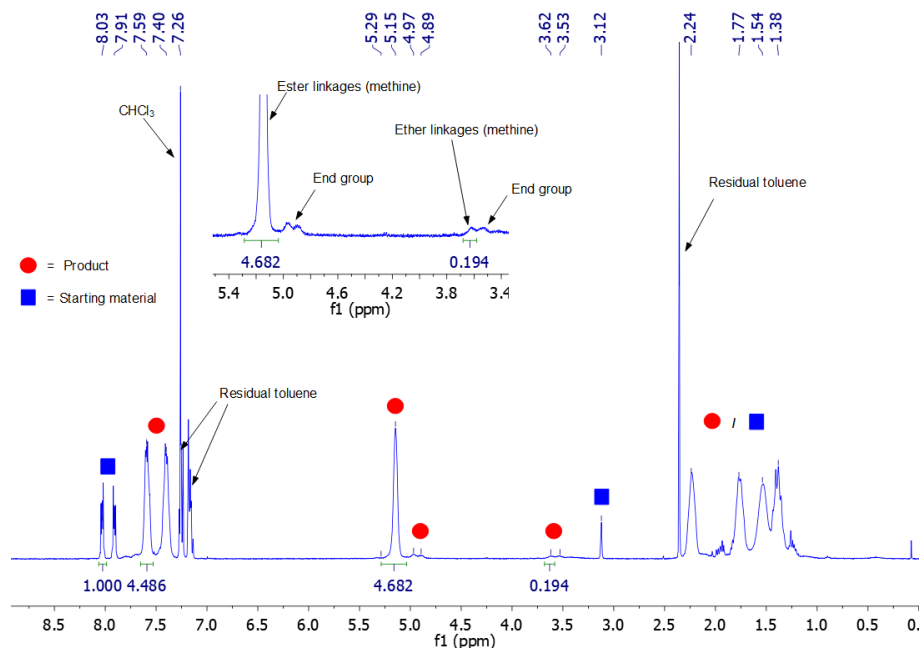


Figure 95. Crude  $^1\text{H}$  NMR spectrum of the solution PA / CHO ROCOP reaction mixture using Fe(6)OAc (Section 5.3, Table 26, entry 11).  $^1\text{H}$  NMR spectroscopy consistent with literature.<sup>[22,32]</sup>

## Crude $^1\text{H}$ NMR spectra of a typical PA / CHO neat ROCOP reaction mixture

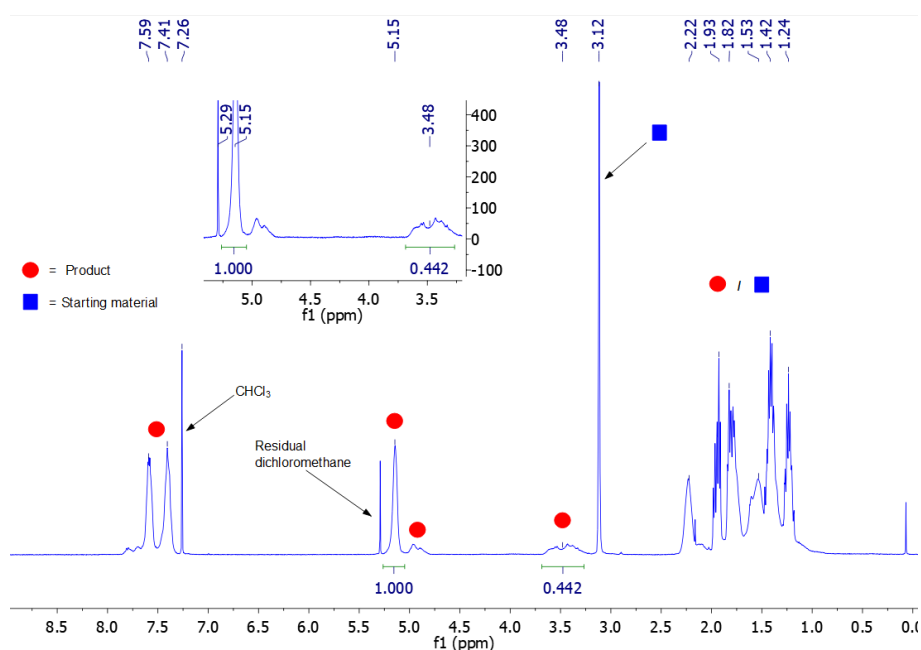


Figure 96. Crude  $^1\text{H}$  NMR spectrum of the neat PA / CHO ROCOP reaction mixture using  $\text{Fe}(\text{6})\text{OAc}$  (Section 5.4, Table 27, entry 4). The whole broad resonance in the ether region was integrated regardless of end group consideration, as adjustment was not possible here for the neat reactions and the worst-case scenario would be the % ester linkages being calculated too low; this broadening of the ether linkages is consistent with literature.<sup>[31]</sup>

## DOSY NMR spectra of isolated polyester obtained from PA / CHO ROCOP

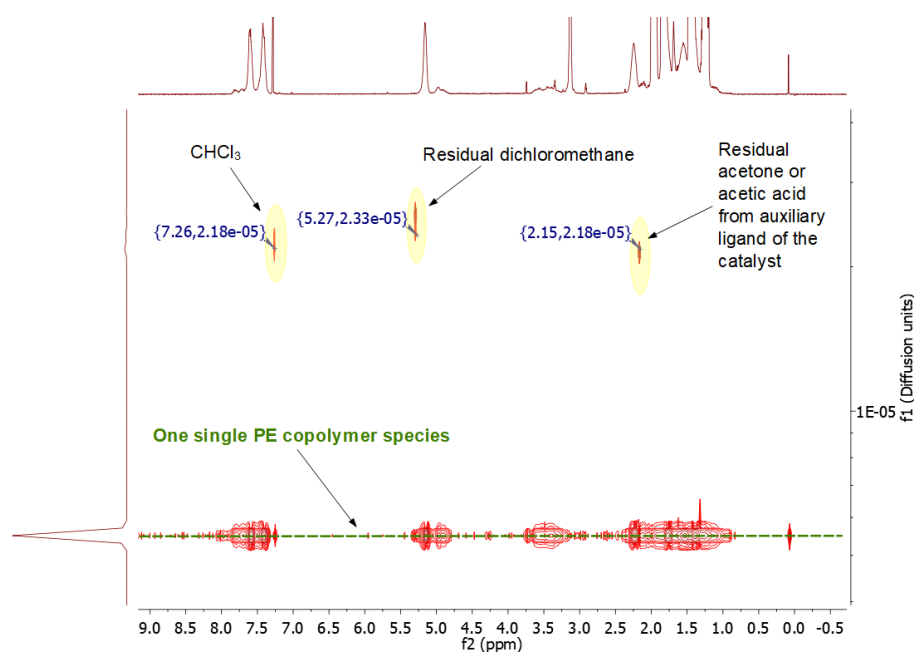


Figure 97. DOSY NMR spectrum of the isolated polymer obtained from the PA / CHO ROCOP in neat conditions at 100 °C for 30 hours using  $\text{Fe}(\text{6})\text{OAc}$  (Section 5.4, Table 27, entry 4) showing one

polymeric species present ( $D = 5.5 \times 10^{-6} \text{ cm}^2 \text{ s}^{-1}$ ). Despite the broad ether linkage resonance signal, it still belongs to this one polymeric species.

## 6.21 IR spectra of isolated polymer obtained from PA / CHO ROCOP

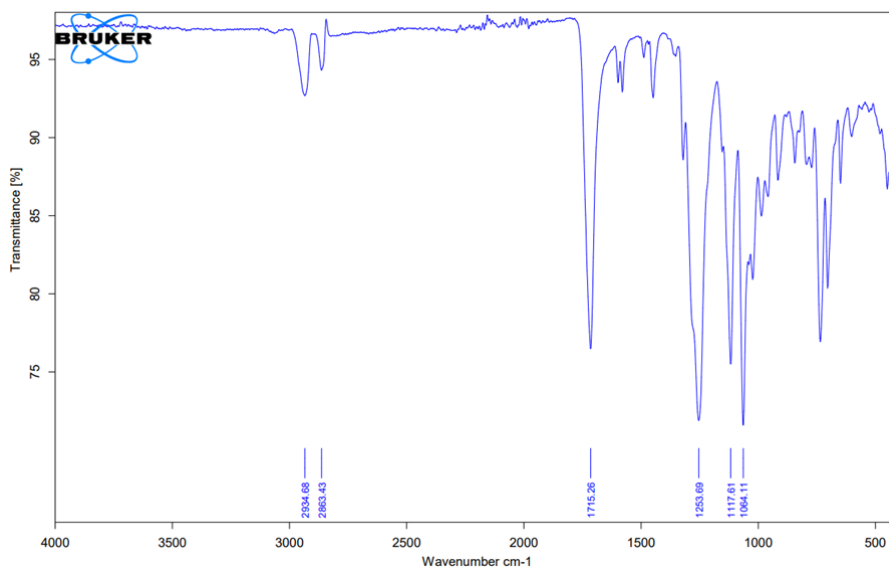


Figure 98. FT-IR spectrum of the isolated polymer obtained from the solution PA / CHO ROCOP using Fe(6)OAc (Section 5.3, Table 26, entry 11). Consistent with literature.<sup>[22]</sup>

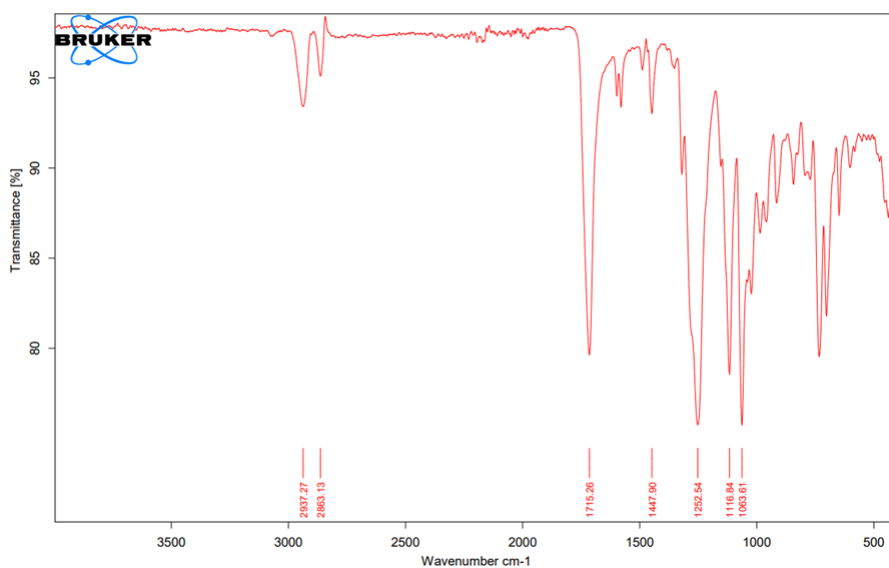


Figure 99. FT-IR spectrum of the isolated polymer obtained from the solution PA / CHO ROCOP using 17 (Section 5.3, Table 26, entry 18). Consistent with literature.<sup>[22]</sup>

## 6.22 General procedure for the attempted solution terpolymerisation of PA / CHO / *rac*-LA using Fe(III)-complexes or organic ligands in toluene solvent

The PA (2.5 mmol, 0.3703 g), *rac*-LA (2.5 mmol, 0.3603 g) and catalyst (0.025 mmol) were added as solids to a Schlenk flask in a glovebox. CHO (2.5 mmol, 0.253 mL) and dry toluene (2.0 mL) were added. The overall loading was 100:100:100:1 [PA]:[*rac*-LA]:[CHO]:[Cat.]. The flask was placed in a preheated oil bath (100 °C) for three or six days to stir. After this reaction time, the flask was allowed to cool for a few minutes. An aliquot was taken of the product mixture and analysed *via* <sup>1</sup>H NMR spectroscopy to determine the conversion, both of PA and *rac*-LA, and the chemoselectivity. Dichloromethane was added to the flask to transfer all contents into a round bottom flask and solvents were removed *in-vacuo* and dried. To purify and isolate the polymer (particularly to remove any iron residue and ensure the iron is cleaved off the polymer, together with any unreacted PA), dichloromethane was added (~5 mL), to form a solution, followed by acidified methanol (1M, 70 mL) to precipitate a white polymer solid. This was isolated *via* filtration, rinsed with methanol and dried in a vacuum oven at 30 °C overnight. This solid was then analysed further using <sup>1</sup>H NMR spectroscopy and GPC analysis. Unfortunately, it was found the PLA resonance signals had disappeared in the <sup>1</sup>H NMR spectra and only poly(1,2-cyclohexylene-1,2-phthalate) remained.

## 6.23 $^1\text{H}$ NMR spectra of crude reaction mixture and isolated polyester obtained from the attempted terpolymerisation of PA / CHO / *rac*-LA

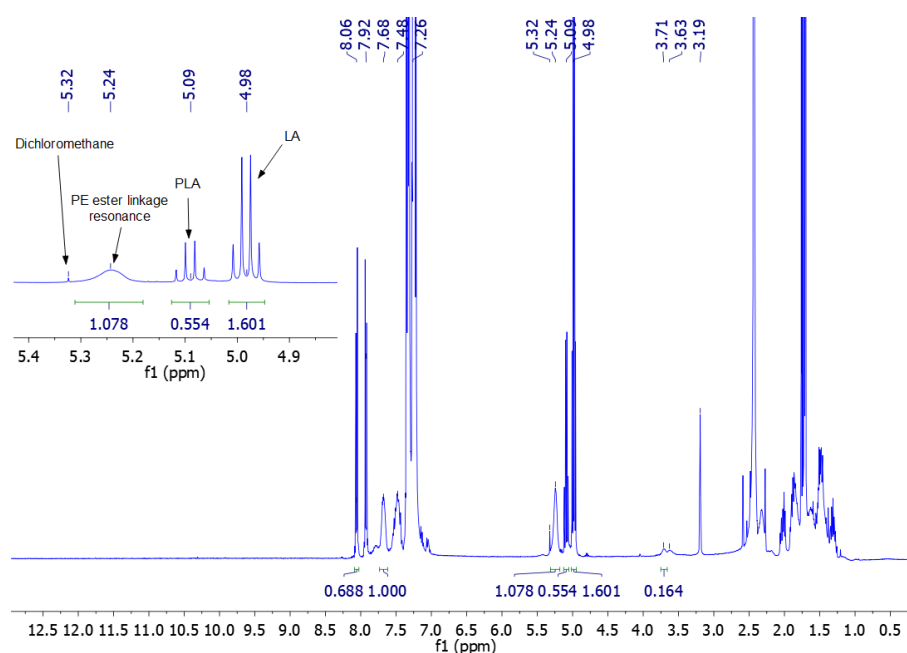


Figure 100. Crude  $^1\text{H}$  NMR spectrum of the attempted PA / CHO / *rac*-LA terpolymerisation reaction mixture using organo-initiator **6** after six days (Section 5.6, Table 29, entry 4).

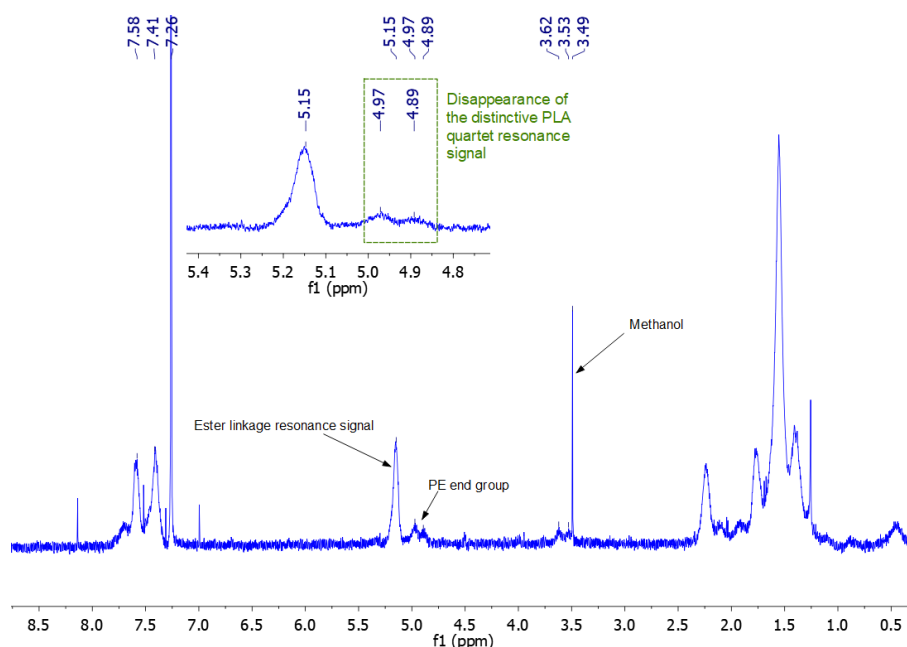


Figure 101.  $^1\text{H}$  NMR spectrum of the isolated polymer obtained from the attempted PA / CHO / *rac*-LA terpolymerisation after three days using organo-initiator  $\text{Fe}(\text{6})\text{OAc}$  (Section 5.6, Table 29, entry 2). The focussed methine region shows disappearance of the distinctive PLA quartet resonance signal observed in the crude reaction mixture.<sup>[32]</sup>

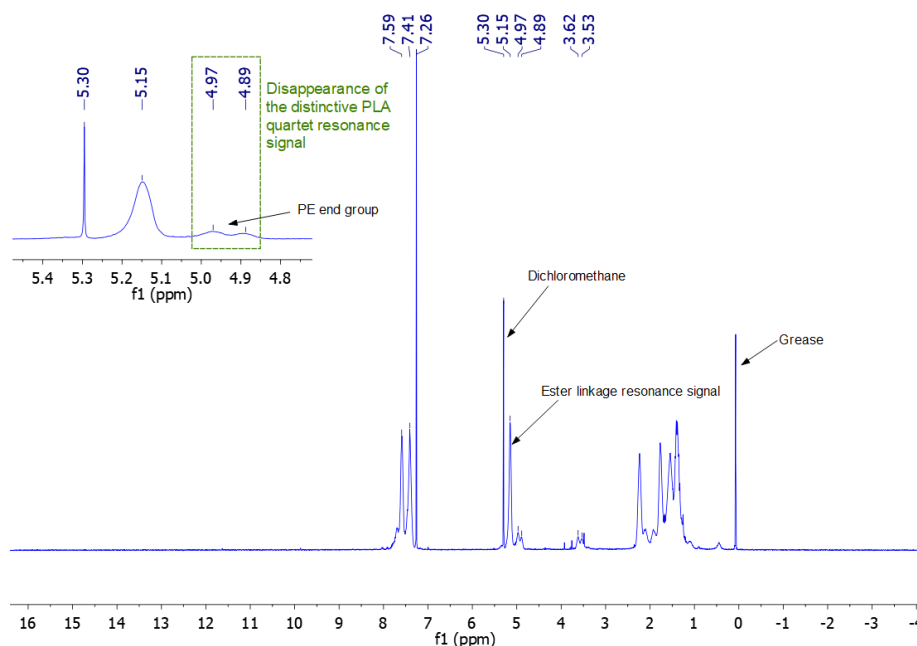


Figure 102.  $^1\text{H}$  NMR spectrum of the isolated polymer obtained from the attempted PA / CHO / *rac*-LA terpolymerisation after six days using organo-initiator **6** (Section 5.6, Table 29, entry 4). The focussed methine region shows disappearance of the distinctive PLA quartet resonance signal observed in the crude reaction mixture.<sup>[32]</sup>

## 6.24 General PLA degradation procedure using Fe(III)–salalen–chloride complexes and $\text{FeCl}_3$

All degradations were carried out using Schlenk flasks with J Youngs taps under inert conditions. The [Fe] initiator (8–20 wt%) was placed in the J Youngs tapped Schlenk flask in a glovebox. Under a flow of argon, PLA (0.125 g, Vegware™ PLLA cup,  $M_n = 45150 \text{ g mol}^{-1}$ ) was added to the flask. The PLA was dissolved in tetrahydrofuran (2.0 mL) with mild heating and stirring. Under a flow of argon, methanol (500  $\mu\text{L}$ ) was added ( $V_{\text{THF}} : V_{\text{MeOH}} = 2 \text{ mL} : 0.5 \text{ mL}$ ,  $n_{\text{MeOH}} : n_{\text{ester}} = 7 : 1$ ) and the flask was placed in a preheated oil bath (130 °C) for the desired time duration (8–72 hours). The flask was allowed to cool and an aliquot taken, diluted with deuterated chloroform and analysed *via*  $^1\text{H}$  NMR spectroscopy; focussing on the methine region ( $\delta$  4.2–5.2 ppm) to determine the conversion of internal methine units or PLA ( $X_{\text{int/PLA}}$ ), Me–LA product selectivity ( $S_{\text{Me-LA}}$ ) and Me–LA yield ( $Y_{\text{Me-LA}}$ ).

## 6.25 References

- [1] B. M. Chamberlain, M. Cheng, D. R. Moore, T. M. Ovitt, E. B. Lobkovsky, G. W. Coates, *J. Am. Chem. Soc.* **2001**, *123*, 3229–3238.
- [2] C. Piguet, *J. Chem. Educ.* **1997**, *74*, 815–816.
- [3] D. H. Grant, *J. Chem. Educ.* **1995**, *72*, 39–40.
- [4] G. A. Bain, J. F. Berry, *J. Chem. Educ.* **2008**, *85*, 532–536.
- [5] E. M. Schubert, *J. Chem. Educ.* **1992**, *69*, 62.
- [6] Agilent Technologies. Inc., *A guide to multi-detector gel permeation chromatography*, <https://www.agilent.com/cs/library/primers/Public/5990-7196EN.pdf>, **2012** (Accessed 5<sup>th</sup> December 2021).
- [7] Malvern Instruments Ltd., *Static Light Scattering technologies for GPC – SEC explained*, <https://www.chem.uci.edu/~dmitryf/manuals/Fundamentals/SLS%20Technologies%20GPC-SEC%20Explained.pdf>, **2015** (Accessed 5<sup>th</sup> December 2021).
- [8] Agilent Technologies. Inc., *Advanced GPC, The use of Advanced Detectors in GPC*, [https://www.agilent.com/cs/library/slidepresentation/public/3-The\\_use\\_of\\_Advanced\\_Detectors\\_in\\_GPC.pdf](https://www.agilent.com/cs/library/slidepresentation/public/3-The_use_of_Advanced_Detectors_in_GPC.pdf), **2012** (Accessed 5<sup>th</sup> December 2021).
- [9] Malvern Instruments Ltd., *Principles of Triple Detection GPC / SEC*, <https://www.chem.uci.edu/~dmitryf/manuals/Fundamentals/Principles%20of%20Triple%20Detection%20GPC.pdf>, **2015** (Accessed 5<sup>th</sup> December 2021).
- [10] E. L. Whitelaw, M. D. Jones, M. F. Mahon, *Inorg. Chem.* **2010**, *49*, 7176–7181.
- [11] E. L. Whitelaw, G. Loraine, M. F. Mahon, M. D. Jones, *Dalton Trans.* **2011**, *40*, 11469–11473.
- [12] S. M. Kirk, G. Kociok-Köhn, M. D. Jones, *Organometallics* **2016**, *35*, 3837–3843.
- [13] P. McKeown, M. G. Davidson, J. P. Lowe, M. F. Mahon, L. H. Thomas, T. J. Woodman, M. D. Jones, *Dalton Trans.* **2016**, *45*, 5374–5387.
- [14] S. L. Hancock, M. F. Mahon, M. D. Jones, *Dalton Trans.* **2013**, *42*, 9279–9285.
- [15] X. Wang, A. Thevenon, J. L. Brosmer, I. Yu, S. I. Khan, P. Mehrkhodavandi, P. L. Diaconescu, *J. Am. Chem. Soc.* **2014**, *136*, 11264–11267.
- [16] M. D. Jones, L. Brady, P. McKeown, A. Buchard, P. M. Schäfer, L. H. Thomas, M. F. Mahon, T. J. Woodman, J. P. Lowe, *Chem. Sci.* **2015**, *6*, 5034–5039.
- [17] M. D. Jones, S. L. Hancock, P. McKeown, P. M. Schäfer, A. Buchard, L. H. Thomas, M. F. Mahon, J. P. Lowe, *Chem. Commun.* **2014**, *50*, 15967–15970.
- [18] P. McKeown, M. G. Davidson, G. Kociok-Köhn, M. D. Jones, *Chem. Commun.* **2016**, *52*, 10431–10434.



- [19] S. M. Kirk, P. McKeown, M. F. Mahon, G. Kociok-Köhn, T. J. Woodman, M. D. Jones, *Eur. J. Inorg. Chem.* **2017**, 2017, 5417–5426.
- [20] P. McKeown, J. Brown-Humes, M. G. Davidson, M. F. Mahon, T. J. Woodman, M. D. Jones, *Dalton Trans.* **2017**, 46, 5048–5057.
- [21] S. L. Hancock, M. F. Mahon, M. D. Jones, *New J. Chem.* **2013**, 37, 1996–2001.
- [22] R. Mundil, Z. Hošťálek, I. Šeděnková, J. Merna, *Macromol. Res.* **2015**, 23, 161–166.
- [23] K. J. Gallagher, R. L. Webster, *Chem. Commun.* **2014**, 50, 12109–12111.
- [24] M. J. Stanford, A. P. Dove, *Chem. Soc. Rev.* **2010**, 39, 486–494.
- [25] M. Cheng, A. B. Attygalle, E. B. Lobkovsky, G. W. Coates, *J. Am. Chem. Soc.* **1999**, 121, 11583–11584.
- [26] E. Fazekas, G. S. Nichol, M. P. Shaver, J. A. Garden, *Dalton Trans.* **2018**, 47, 13106–13112.
- [27] D. Alhashmialameer, J. Collins, K. Hattenhauer, F. M. Kerton, *Catal. Sci. Technol.* **2016**, 6, 5364–5373.
- [28] M. Cozzolino, T. Rosen, I. Goldberg, M. Mazzeo, M. Lamberti, *ChemSusChem* **2017**, 10, 1217–1223.
- [29] A. Buchard, M. R. Kember, K. G. Sandeman, C. K. Williams, *Chem. Commun.* **2011**, 47, 212–214.
- [30] J. A. Stewart, P. McKeown, O. J. Driscoll, M. F. Mahon, B. D. Ward, M. D. Jones, *Macromolecules* **2019**, 52, 5977–5984.
- [31] M. Wang, J. Huang, Y. Xu, B. Han, Z. Duan, *Polym. Int.* **2019**, 68, 1704–1709.
- [32] P. K. Saini, C. Romain, Y. Zhu, C. K. Williams, *Polym. Chem.* **2014**, 5, 6068–6075.

## **Chapter 7.**

### **Appendix**

## 7. Appendix

### 7.1 Iron(III) complex single-crystal X-ray diffraction data

#### Fe(2)Cl

Empirical formula	C <sub>27</sub> H <sub>38</sub> ClFeN <sub>2</sub> O <sub>2</sub>	
Formula weight	513.89	
Temperature	150(2) K	
Wavelength	1.54184 Å	
Crystal system	Monoclinic	
Space group	<i>P</i> 2 <sub>1</sub> / <i>c</i>	
Unit cell dimensions	<i>a</i> = 14.6208(2) Å	$\alpha = 90^\circ$ .
	<i>b</i> = 9.64780(10) Å	$\beta = 91.9470(10)^\circ$ .
	<i>c</i> = 18.8682(2) Å	$\gamma = 90^\circ$ .
Volume	2659.98(5) Å <sup>3</sup>	
Z	4	
Density (calculated)	1.283 Mg/m <sup>3</sup>	
Absorption coefficient	5.661 mm <sup>-1</sup>	
F(000)	1092	
Theta range for data collection	3.024 to 72.557°.	
Index ranges	-18 ≤ <i>h</i> ≤ 13, -11 ≤ <i>k</i> ≤ 11, -19 ≤ <i>l</i> ≤ 23	
Reflections collected	22830	
Independent reflections	5167 [R(int) = 0.0294]	
Completeness to theta = 67.684°	100.0%	
Refinement method	Full-matrix least-squares on F <sup>2</sup>	
Data / restraints / parameters	5167 / 0 / 344	
Goodness-of-fit on F <sup>2</sup>	1.047	
Final R indices [I > 2σ(I)]	R <sub>1</sub> = 0.0401, wR <sub>2</sub> = 0.1267	
R indices (all data)	R <sub>1</sub> = 0.0471, wR <sub>2</sub> = 0.1331	
Extinction coefficient	n/a	
Largest diff. peak and hole	0.651 and -0.880 e.Å <sup>-3</sup>	

**Fe(3)Cl**

Empirical formula	C <sub>33</sub> H <sub>50</sub> ClFeN <sub>2</sub> O <sub>2</sub>	
Formula weight	598.05	
Temperature	150(2) K	
Wavelength	1.54184 Å	
Crystal system	Monoclinic	
Space group	<i>P</i> 2 <sub>1</sub> / <i>n</i>	
Unit cell dimensions	<i>a</i> = 17.1813(11) Å	$\alpha = 90^\circ$ .
	<i>b</i> = 9.6473(5) Å	$\beta = 94.446(5)^\circ$ .
	<i>c</i> = 19.3737(10) Å	$\gamma = 90^\circ$ .
Volume	3201.6(3) Å <sup>3</sup>	
Z	4	
Density (calculated)	1.241 Mg/m <sup>3</sup>	
Absorption coefficient	4.772 mm <sup>-1</sup>	
F(000)	1284	
Crystal size	0.2 x 0.2 x 0.05 mm <sup>3</sup>	
Theta range for data collection	3.313 to 68.248°.	
Index ranges	-20 ≤ <i>h</i> ≤ 20, -11 ≤ <i>k</i> ≤ 7, -23 ≤ <i>l</i> ≤ 22	
Reflections collected	20708	
Independent reflections	5855 [R(int) = 0.0531]	
Completeness to theta = 67.684°	100.0%	
Absorption correction	Semi-empirical from equivalents	
Max. and min. transmission	1.00000 and 0.84553	
Refinement method	Full-matrix least-squares on F <sup>2</sup>	
Data / restraints / parameters	5855 / 104 / 458	
Goodness-of-fit on F <sup>2</sup>	1.059	
Final R indices [I > 2σ(I)]	R <sub>1</sub> = 0.0400, wR <sub>2</sub> = 0.0979	
R indices (all data)	R <sub>1</sub> = 0.0533, wR <sub>2</sub> = 0.1036	
Extinction coefficient	n/a	
Largest diff. peak and hole	0.304 and -0.273 e.Å <sup>-3</sup>	

**[Fe(4)]<sub>2</sub>O**

Empirical formula	C <sub>54</sub> H <sub>74</sub> Cl <sub>4</sub> Fe <sub>2</sub> N <sub>4</sub> O <sub>6</sub>	
Formula weight	1128.67	
Temperature	150(2) K	
Wavelength	0.71073 Å	
Crystal system	Orthorhombic	
Space group	<i>Pbcn</i>	
Unit cell dimensions	<i>a</i> = 20.1226(2) Å	$\alpha = 90^\circ$ .
	<i>b</i> = 16.8897(2) Å	$\beta = 90^\circ$ .
	<i>c</i> = 17.1030(2) Å	$\gamma = 90^\circ$ .
Volume	5812.71(11) Å <sup>3</sup>	
Z	4	
Density (calculated)	1.290 Mg/m <sup>3</sup>	
Absorption coefficient	0.732 mm <sup>-1</sup>	
F(000)	2376	
Crystal size	0.400 x 0.300 x 0.200 mm <sup>3</sup>	
Theta range for data collection	3.367 to 29.901°.	
Index ranges	-27 ≤ <i>h</i> ≤ 26, -22 ≤ <i>k</i> ≤ 21, -22 ≤ <i>l</i> ≤ 22	
Reflections collected	86345	
Independent reflections	7695 [R(int) = 0.0346]	
Completeness to theta = 25.242°	99.7%	
Absorption correction	Semi-empirical from equivalents	
Max. and min. transmission	1.00000 and 0.88929	
Refinement method	Full-matrix least-squares on F <sup>2</sup>	
Data / restraints / parameters	7695 / 0 / 375	
Goodness-of-fit on F <sup>2</sup>	1.060	
Final R indices [I > 2σ(I)]	R <sub>1</sub> = 0.0409, wR <sub>2</sub> = 0.0922	
R indices (all data)	R <sub>1</sub> = 0.0609, wR <sub>2</sub> = 0.1041	
Extinction coefficient	n/a	
Largest diff. peak and hole	1.013 and -0.761 e.Å <sup>-3</sup>	

**Fe(5)Cl**

Empirical formula	C <sub>36</sub> H <sub>54</sub> ClFeN <sub>2</sub> O <sub>2</sub>	
Formula weight	638.11	
Temperature	150(2) K	
Wavelength	0.71073 Å	
Crystal system	Monoclinic	
Space group	<i>P</i> 2 <sub>1</sub> / <i>c</i>	
Unit cell dimensions	<i>a</i> = 11.4744(7) Å	$\alpha$ = 90°.
	<i>b</i> = 17.5040(10) Å	$\beta$ = 98.570(5)°.
	<i>c</i> = 17.6987(9) Å	$\gamma$ = 90°.
Volume	3515.1(3) Å <sup>3</sup>	
Z	4	
Density (calculated)	1.206 Mg/m <sup>3</sup>	
Absorption coefficient	0.537 mm <sup>-1</sup>	
F(000)	1372	
Crystal size	0.150 x 0.100 x 0.100 mm <sup>3</sup>	
Theta range for data collection	3.259 to 25.681°.	
Index ranges	-13 ≤ <i>h</i> ≤ 13, -21 ≤ <i>k</i> ≤ 21, -21 ≤ <i>l</i> ≤ 21	
Reflections collected	11866	
Independent reflections	11866 [R(int) = ?]	
Completeness to theta = 25.242°	99.8%	
Absorption correction	Semi-empirical from equivalents	
Max. and min. transmission	1.00000 and 0.82506	
Refinement method	Full-matrix least-squares on F <sup>2</sup>	
Data / restraints / parameters	11866 / 0 / 392	
Goodness-of-fit on F <sup>2</sup>	0.898	
Final R indices [I > 2σ(I)]	R <sub>1</sub> = 0.0340, wR <sub>2</sub> = 0.0731	
R indices (all data)	R <sub>1</sub> = 0.0555, wR <sub>2</sub> = 0.0763	
Extinction coefficient	n/a	
Largest diff. peak and hole	0.397 and -0.271 e.Å <sup>-3</sup>	

**Fe(6)Cl**

Empirical formula	C <sub>37</sub> H <sub>50</sub> ClFeN <sub>2</sub> O <sub>2</sub>	
Formula weight	646.09	
Temperature	150(2) K	
Wavelength	1.54184 Å	
Crystal system	Monoclinic	
Space group	<i>P</i> 2 <sub>1</sub> / <i>n</i>	
Unit cell dimensions	<i>a</i> = 17.077(4) Å	$\alpha = 90^\circ$ .
	<i>b</i> = 13.1990(15) Å	$\beta = 117.36(3)^\circ$ .
	<i>c</i> = 17.631(4) Å	$\gamma = 90^\circ$ .
Volume	3529.4(14) Å <sup>3</sup>	
Z	4	
Density (calculated)	1.216 Mg/m <sup>3</sup>	
Absorption coefficient	4.369 mm <sup>-1</sup>	
F(000)	1380	
Crystal size	0.050 x 0.050 x 0.020 mm <sup>3</sup>	
Theta range for data collection	4.381 to 66.599°.	
Index ranges	-20 ≤ <i>h</i> ≤ 19, -15 ≤ <i>k</i> ≤ 10, -20 ≤ <i>l</i> ≤ 20	
Reflections collected	21287	
Independent reflections	6237 [R(int) = 0.1224]	
Completeness to theta = 66.599°	100.0%	
Absorption correction	Semi-empirical from equivalents	
Max. and min. transmission	1.00000 and 0.30571	
Refinement method	Full-matrix least-squares on F <sup>2</sup>	
Data / restraints / parameters	6237 / 6 / 417	
Goodness-of-fit on F <sup>2</sup>	1.017	
Final R indices [I > 2σ(I)]	R <sub>1</sub> = 0.0767, wR <sub>2</sub> = 0.1537	
R indices (all data)	R <sub>1</sub> = 0.1459, wR <sub>2</sub> = 0.1854	
Extinction coefficient	<i>n/a</i>	
Largest diff. peak and hole	0.436 and -0.581 e.Å <sup>-3</sup>	

**[Fe(8<sub>meso</sub>)]<sub>2</sub>O**

Empirical formula	C <sub>56</sub> H <sub>74</sub> Fe <sub>2</sub> N <sub>6</sub> O <sub>5</sub>
Formula weight	1022.91
Temperature	150(2) K
Wavelength	1.54184 Å
Crystal system	Monoclinic
Space group	<i>I a</i>
Unit cell dimensions	a = 11.7857(4) Å      α = 90°. b = 16.4545(9) Å      β = 91.518(4)°. c = 27.0205(10) Å     γ = 90°.
Volume	5238.2(4) Å <sup>3</sup>
Z	4
Density (calculated)	1.297 Mg/m <sup>3</sup>
Absorption coefficient	4.860 mm <sup>-1</sup>
F(000)	2176
Crystal size	0.050 x 0.050 x 0.050 mm <sup>3</sup>
Theta range for data collection	3.145 to 72.104°.
Index ranges	-9 ≤ h ≤ 14, -16 ≤ k ≤ 20, -33 ≤ l ≤ 33
Reflections collected	17032
Independent reflections	7555 [R(int) = 0.0563]
Completeness to theta = 67.684°	100.0%
Refinement method	Full-matrix least-squares on F <sup>2</sup>
Data / restraints / parameters	7555 / 2 / 632
Goodness-of-fit on F <sup>2</sup>	1.014
Final R indices [I > 2σ(I)]	R <sub>1</sub> = 0.0529, wR <sub>2</sub> = 0.1282
R indices (all data)	R <sub>1</sub> = 0.0581, wR <sub>2</sub> = 0.1319
Absolute structure parameter	-0.003(5)
Extinction coefficient	n/a
Largest diff. peak and hole	0.790 and -0.464 e.Å <sup>-3</sup>



**Fe(9<sub>meso</sub>)Cl**

Empirical formula	C <sub>38</sub> H <sub>58</sub> ClFeN <sub>2</sub> O <sub>2</sub>	
Formula weight	666.16	
Temperature	150(2) K	
Wavelength	0.71073 Å	
Crystal system	Monoclinic	
Space group	<i>I</i> 2/ <i>a</i>	
Unit cell dimensions	$a = 22.9330(8) \text{ \AA}$	$\alpha = 90^\circ$ .
	$b = 12.8616(4) \text{ \AA}$	$\beta = 93.824(2)^\circ$ .
	$c = 25.5407(6) \text{ \AA}$	$\gamma = 90^\circ$ .
Volume	7516.6(4) Å <sup>3</sup>	
Z	8	
Density (calculated)	1.177 Mg/m <sup>3</sup>	
Absorption coefficient	0.505 mm <sup>-1</sup>	
F(000)	2872	
Theta range for data collection	3.296 to 25.680°.	
Index ranges	-27<= <i>h</i> <=27, -15<= <i>k</i> <=15, -31<= <i>l</i> <=31	
Reflections collected	69705	
Independent reflections	7117 [R(int) = 0.0665]	
Completeness to theta = 25.242°	99.8%	
Refinement method	Full-matrix least-squares on F <sup>2</sup>	
Data / restraints / parameters	7117 / 0 / 409	
Goodness-of-fit on F <sup>2</sup>	1.001	
Final R indices [I>2sigma(I)]	R <sub>1</sub> = 0.0457, wR <sub>2</sub> = 0.1097	
R indices (all data)	R <sub>1</sub> = 0.0639, wR <sub>2</sub> = 0.1194	
Extinction coefficient	n/a	
Largest diff. peak and hole	0.727 and -0.512 e.Å <sup>-3</sup>	

**Fe(3)OAc**

Empirical formula	C <sub>37</sub> H <sub>59</sub> FeN <sub>2</sub> O <sub>5</sub>	
Formula weight	667.71	
Temperature	150(2) K	
Wavelength	0.71073 Å	
Crystal system	Monoclinic	
Space group	<i>P</i> 2 <sub>1</sub> / <i>c</i>	
Unit cell dimensions	<i>a</i> = 11.3237(2) Å	$\alpha$ = 90°.
	<i>b</i> = 17.5348(3) Å	$\beta$ = 102.572(2)°.
	<i>c</i> = 19.3250(4) Å	$\gamma$ = 90°.
Volume	3745.15(12) Å <sup>3</sup>	
Z	4	
Density (calculated)	1.184 Mg/m <sup>3</sup>	
Absorption coefficient	0.444 mm <sup>-1</sup>	
F(000)	1444	
Crystal size	0.300 x 0.200 x 0.200 mm <sup>3</sup>	
Theta range for data collection	3.425 to 25.680°.	
Index ranges	-13 ≤ <i>h</i> ≤ 13, -20 ≤ <i>k</i> ≤ 21, -23 ≤ <i>l</i> ≤ 22	
Reflections collected	34954	
Independent reflections	7099 [R(int) = 0.0581]	
Completeness to theta = 25.242°	99.7%	
Refinement method	Full-matrix least-squares on F <sup>2</sup>	
Data / restraints / parameters	7099 / 3 / 447	
Goodness-of-fit on F <sup>2</sup>	1.014	
Final R indices [I > 2σ(I)]	R <sub>1</sub> = 0.0405, wR <sub>2</sub> = 0.1052	
R indices (all data)	R <sub>1</sub> = 0.0608, wR <sub>2</sub> = 0.1154	
Extinction coefficient	n/a	
Largest diff. peak and hole	0.579 and -0.362 e.Å <sup>-3</sup>	

**Fe(5)OAc**

Empirical formula	C <sub>38</sub> H <sub>57</sub> FeN <sub>2</sub> O <sub>4</sub>	
Formula weight	661.70	
Temperature	150(2) K	
Wavelength	1.54184 Å	
Crystal system	Monoclinic	
Space group	<i>P</i> 2 <sub>1</sub> / <i>n</i>	
Unit cell dimensions	<i>a</i> = 10.5080(2) Å	$\alpha = 90^\circ$ .
	<i>b</i> = 22.7778(3) Å	$\beta = 91.7990(10)^\circ$ .
	<i>c</i> = 15.3749(2) Å	$\gamma = 90^\circ$ .
Volume	3678.15(10) Å <sup>3</sup>	
Z	4	
Density (calculated)	1.195 Mg/m <sup>3</sup>	
Absorption coefficient	3.590 mm <sup>-1</sup>	
F(000)	1428	
Crystal size	0.100 x 0.050 x 0.050 mm <sup>3</sup>	
Theta range for data collection	3.469 to 70.076°.	
Index ranges	-8<= <i>h</i> <=12, -24<= <i>k</i> <=27, -18<= <i>l</i> <=18	
Reflections collected	28326	
Independent reflections	6997 [R(int) = 0.0396]	
Completeness to theta = 67.684°	100.0%	
Refinement method	Full-matrix least-squares on F <sup>2</sup>	
Data / restraints / parameters	6997 / 0 / 419	
Goodness-of-fit on F <sup>2</sup>	1.035	
Final R indices [I>2sigma(I)]	R <sub>1</sub> = 0.0379, wR <sub>2</sub> = 0.0962	
R indices (all data)	R <sub>1</sub> = 0.0494, wR <sub>2</sub> = 0.1010	
Extinction coefficient	n/a	
Largest diff. peak and hole	0.554 and -0.267 e.Å <sup>-3</sup>	

**Fe(6)OAc**

Empirical formula	C <sub>39</sub> H <sub>53</sub> FeN <sub>2</sub> O <sub>4</sub>	
Formula weight	669.68	
Temperature	150(2) K	
Wavelength	1.54184 Å	
Crystal system	Monoclinic	
Space group	<i>P</i> 2 <sub>1</sub> / <i>c</i>	
Unit cell dimensions	<i>a</i> = 18.011(4) Å	$\alpha = 90^\circ$ .
	<i>b</i> = 16.539(3) Å	$\beta = 105.64(3)^\circ$ .
	<i>c</i> = 12.734(4) Å	$\gamma = 90^\circ$ .
Volume	3652.6(15) Å <sup>3</sup>	
Z	4	
Density (calculated)	1.218 Mg/m <sup>3</sup>	
Absorption coefficient	3.625 mm <sup>-1</sup>	
F(000)	1436	
Theta range for data collection	2.548 to 66.578°.	
Index ranges	-21 ≤ <i>h</i> ≤ 14, -19 ≤ <i>k</i> ≤ 19, -12 ≤ <i>l</i> ≤ 15	
Reflections collected	19309	
Independent reflections	6439 [R(int) = 0.0853]	
Completeness to theta = 66.578°	100.0%	
Refinement method	Full-matrix least-squares on F <sup>2</sup>	
Data / restraints / parameters	6439 / 0 / 429	
Goodness-of-fit on F <sup>2</sup>	0.903	
Final R indices [I > 2σ(I)]	R <sub>1</sub> = 0.0539, wR <sub>2</sub> = 0.1001	
R indices (all data)	R <sub>1</sub> = 0.0996, wR <sub>2</sub> = 0.1136	
Extinction coefficient	n/a	
Largest diff. peak and hole	0.331 and -0.447 e.Å <sup>-3</sup>	

**Fe(8<sub>meso</sub>)OAc**

Empirical formula	C <sub>28</sub> H <sub>37</sub> FeN <sub>2</sub> O <sub>4</sub>
Formula weight	521.44
Temperature	150(2) K
Wavelength	1.54184 Å
Crystal system	Monoclinic
Space group	<i>P</i> 2 <sub>1</sub> / <i>n</i>
Unit cell dimensions	<i>a</i> = 17.5040(5) Å $\alpha = 90^\circ$ . <i>b</i> = 8.2528(2) Å $\beta = 96.933(3)^\circ$ . <i>c</i> = 17.7346(5) Å $\gamma = 90^\circ$ .
Volume	2543.16(12) Å <sup>3</sup>
Z	4
Density (calculated)	1.362 Mg/m <sup>3</sup>
Absorption coefficient	5.049 mm <sup>-1</sup>
F(000)	1108
Crystal size	0.050 x 0.020 x 0.020 mm <sup>3</sup>
Theta range for data collection	3.351 to 68.224°.
Index ranges	-21 ≤ <i>h</i> ≤ 20, -6 ≤ <i>k</i> ≤ 9, -21 ≤ <i>l</i> ≤ 21
Reflections collected	17559
Independent reflections	4645 [R(int) = 0.0393]
Completeness to theta = 67.684°	100.0%
Refinement method	Full-matrix least-squares on F <sup>2</sup>
Data / restraints / parameters	4645 / 0 / 321
Goodness-of-fit on F <sup>2</sup>	1.026
Final R indices [I > 2σ(I)]	R <sub>1</sub> = 0.0374, wR <sub>2</sub> = 0.0934
R indices (all data)	R <sub>1</sub> = 0.0451, wR <sub>2</sub> = 0.0979
Extinction coefficient	n/a
Largest diff. peak and hole	0.315 and -0.485 e.Å <sup>-3</sup>

**Fe(8<sub>RR</sub>)Y<sub>2</sub>**

Empirical formula	C <sub>117</sub> H <sub>160</sub> Fe <sub>4</sub> N <sub>8</sub> O <sub>21</sub>
Formula weight	2243.52
Temperature	150(2) K
Crystal system	Tetragonal
Space group	P4 <sub>1</sub> 2 <sub>1</sub> 2
Unit cell dimensions	a = 10.2477(1) Å      α = 90°. b = 10.2477(1) Å      β = 90°. c = 28.1421(5) Å      γ = 90°.
Volume	2955.35(8) Å <sup>3</sup>
Z, Density (calculated)	1, 1.261 Mg/m <sup>3</sup>
F(000), crystal size	1193.0, 0.157 × 0.079 × 0.029 mm
Radiation and μ	CuKα (λ = 1.54184) and 4.415 mm
Theta range for data collection	9.184 to 146.616°.
Index ranges	-12 ≤ h ≤ 12, -12 ≤ k ≤ 12, -34 ≤ l ≤ 34
Reflections collected	79340
Independent reflections	2968 [Rint = 0.0645, Rsigma = 0.0163]
Data/restraints/parameters	2968/99/217
Goodness-of-fit on F <sup>2</sup>	1.094
Final R indices [I > 2σ(I)]	R <sub>1</sub> = 0.0421, wR <sub>2</sub> = 0.1226
R indices [all data]	R <sub>1</sub> = 0.0458, wR <sub>2</sub> = 0.1266
Largest diff. peak and hole	0.46 and -0.37 e Å <sup>-3</sup>
Flack parameter	-0.005(3)

The asymmetric unit for **Fe(8<sub>RR</sub>)Y<sub>2</sub>** comprised half of one molecule. The remainder was generated *via* the 2-fold rotation axis on which the iron centre was located. (This axis also traveled through the midpoint between C3 and its symmetry equivalent). It became obvious quite early in the refinement process that the ligand based on O2 is disordered, and this had been modelled as 2 acetate components (with fractional occupancies of 30% and 35%) and one ethoxy substituent (with an occupancy of 35%). Some distance and ADP restraints were employed in the disordered region, to assist convergence.

**Fe(9<sub>meso</sub>)OAc**

Empirical formula	C <sub>40</sub> H <sub>61</sub> FeN <sub>2</sub> O <sub>4</sub>	
Formula weight	689.75	
Temperature	150(2) K	
Wavelength	1.54184 Å	
Crystal system	Triclinic	
Space group	<i>P</i> -1	
Unit cell dimensions	<i>a</i> = 10.9269(7) Å	$\alpha$ = 87.693(5)°.
	<i>b</i> = 13.1291(10) Å	$\beta$ = 81.168(4)°.
	<i>c</i> = 14.0182(7) Å	$\gamma$ = 80.394(6)°.
Volume	1959.1(2) Å <sup>3</sup>	
Z	2	
Density (calculated)	1.169 Mg/m <sup>3</sup>	
Absorption coefficient	3.389 mm <sup>-1</sup>	
F(000)	746	
Crystal size	0.050 x 0.050 x 0.040 mm <sup>3</sup>	
Theta range for data collection	3.191 to 66.599°.	
Index ranges	-12 ≤ <i>h</i> ≤ 12, -15 ≤ <i>k</i> ≤ 15, -16 ≤ <i>l</i> ≤ 13	
Reflections collected	12328	
Independent reflections	6890 [R(int) = 0.0523]	
Completeness to theta = 66.599°	99.8%	
Refinement method	Full-matrix least-squares on F <sup>2</sup>	
Data / restraints / parameters	6890 / 0 / 437	
Goodness-of-fit on F <sup>2</sup>	1.011	
Final R indices [I > 2σ(I)]	R <sub>1</sub> = 0.0515, wR <sub>2</sub> = 0.1124	
R indices (all data)	R <sub>1</sub> = 0.0747, wR <sub>2</sub> = 0.1210	
Extinction coefficient	n/a	
Largest diff. peak and hole	0.484 and -0.401 e.Å <sup>-3</sup>	

**Fe(10)OAc**

Empirical formula	C <sub>42</sub> H <sub>61</sub> FeN <sub>2</sub> O <sub>5</sub>	
Formula weight	729.77	
Temperature	150(2) K	
Wavelength	1.54184 Å	
Crystal system	Monoclinic	
Space group	<i>P</i> 2 <sub>1</sub> / <i>c</i>	
Unit cell dimensions	<i>a</i> = 14.7114(3) Å	$\alpha = 90^\circ$ .
	<i>b</i> = 24.5841(4) Å	$\beta = 101.320(2)^\circ$ .
	<i>c</i> = 11.2564(2) Å	$\gamma = 90^\circ$ .
Volume	3991.86(13) Å <sup>3</sup>	
Z	4	
Density (calculated)	1.214 Mg/m <sup>3</sup>	
Absorption coefficient	3.375 mm <sup>-1</sup>	
F(000)	1572	
Crystal size	0.050 x 0.050 x 0.050 mm <sup>3</sup>	
Theta range for data collection	3.063 to 72.675°.	
Index ranges	-17 ≤ <i>h</i> ≤ 16, -30 ≤ <i>k</i> ≤ 27, -9 ≤ <i>l</i> ≤ 13	
Reflections collected	29519	
Independent reflections	7842 [R(int) = 0.0642]	
Completeness to theta = 67.684°	100.0%	
Refinement method	Full-matrix least-squares on F <sup>2</sup>	
Data / restraints / parameters	7842 / 0 / 495	
Goodness-of-fit on F <sup>2</sup>	1.024	
Final R indices [I > 2σ(I)]	R <sub>1</sub> = 0.0521, wR <sub>2</sub> = 0.1225	
R indices (all data)	R <sub>1</sub> = 0.0754, wR <sub>2</sub> = 0.1343	
Extinction coefficient	n/a	
Largest diff. peak and hole	0.589 and -0.691 e.Å <sup>-3</sup>	



**Fe(11)OAc**

Empirical formula	C <sub>19</sub> H <sub>19</sub> Br <sub>2</sub> FeN <sub>2</sub> O <sub>4</sub>	
Formula weight	555.03	
Temperature	150(2) K	
Wavelength	1.54184 Å	
Crystal system	Monoclinic	
Space group	<i>P</i> 2 <sub>1</sub> / <i>n</i>	
Unit cell dimensions	<i>a</i> = 11.0677(4) Å	$\alpha = 90^\circ$ .
	<i>b</i> = 15.7116(7) Å	$\beta = 114.887(5)^\circ$ .
	<i>c</i> = 12.5007(5) Å	$\gamma = 90^\circ$ .
Volume	1971.91(16) Å <sup>3</sup>	
Z	4	
Density (calculated)	1.870 Mg/m <sup>3</sup>	
Absorption coefficient	11.133 mm <sup>-1</sup>	
F(000)	1100	
Crystal size	0.05 x 0.05 x 0.02 mm <sup>3</sup>	
Theta range for data collection	4.809 to 66.598°.	
Index ranges	-9 ≤ <i>h</i> ≤ 13, -18 ≤ <i>k</i> ≤ 18, -14 ≤ <i>l</i> ≤ 14	
Reflections collected	12215	
Independent reflections	3478 [R(int) = 0.0499]	
Completeness to theta = 66.598°	99.9%	
Refinement method	Full-matrix least-squares on F <sup>2</sup>	
Data / restraints / parameters	3478 / 0 / 255	
Goodness-of-fit on F <sup>2</sup>	1.060	
Final R indices [I > 2σ(I)]	R <sub>1</sub> = 0.0415, wR <sub>2</sub> = 0.0985	
R indices (all data)	R <sub>1</sub> = 0.0555, wR <sub>2</sub> = 0.1051	
Extinction coefficient	n/a	
Largest diff. peak and hole	0.983 and -0.556 e.Å <sup>-3</sup>	

**Fe(13)OAc**

Empirical formula	C <sub>38</sub> H <sub>59</sub> FeN <sub>2</sub> O <sub>4</sub>	
Formula weight	663.72	
Temperature	150(2) K	
Wavelength	0.71073 Å	
Crystal system	Triclinic	
Space group	<i>P</i> -1	
Unit cell dimensions	<i>a</i> = 15.4565(7) Å	$\alpha$ = 86.551(4)°.
	<i>b</i> = 16.0514(8) Å	$\beta$ = 86.834(4)°.
	<i>c</i> = 17.3452(8) Å	$\gamma$ = 76.058(4)°.
Volume	4165.3(3) Å <sup>3</sup>	
Z	4	
Density (calculated)	1.058 Mg/m <sup>3</sup>	
Absorption coefficient	0.397 mm <sup>-1</sup>	
F(000)	1436	
Crystal size	0.585 x 0.181 x 0.113 mm <sup>3</sup>	
Theta range for data collection	3.410 to 25.058°.	
Index ranges	-18<= <i>h</i> <=18, -19<= <i>k</i> <=18, -20<= <i>l</i> <=20	
Reflections collected	43424	
Independent reflections	14729 [R(int) = 0.0770]	
Completeness to theta = 25.058°	99.7%	
Absorption correction	Semi-empirical from equivalents	
Max. and min. transmission	1.00000 and 0.85376	
Refinement method	Full-matrix least-squares on F <sup>2</sup>	
Data / restraints / parameters	14729 / 2 / 845	
Goodness-of-fit on F <sup>2</sup>	0.944	
Final R indices [I>2sigma(I)]	R <sub>1</sub> = 0.0651, wR <sub>2</sub> = 0.1259	
R indices (all data)	R <sub>1</sub> = 0.1181, wR <sub>2</sub> = 0.1452	
Extinction coefficient	n/a	
Largest diff. peak and hole	0.627 and -0.484 e.Å <sup>-3</sup>	

**Fe(15)OAc**

Empirical formula	C <sub>34</sub> H <sub>49</sub> FeN <sub>2</sub> O <sub>4</sub>	
Formula weight	605.60	
Temperature	150(2) K	
Wavelength	0.71073 Å	
Crystal system	Orthorhombic	
Space group	<i>P b c a</i>	
Unit cell dimensions	<i>a</i> = 19.0502(18) Å	$\alpha = 90^\circ$ .
	<i>b</i> = 10.2223(6) Å	$\beta = 90^\circ$ .
	<i>c</i> = 34.8712(12) Å	$\gamma = 90^\circ$ .
Volume	6790.7(8) Å <sup>3</sup>	
Z	8	
Density (calculated)	1.185 Mg/m <sup>3</sup>	
Absorption coefficient	0.481 mm <sup>-1</sup>	
F(000)	2600	
Theta range for data collection	3.407 to 25.027°.	
Index ranges	-22 ≤ <i>h</i> ≤ 22, -11 ≤ <i>k</i> ≤ 12, -38 ≤ <i>l</i> ≤ 41	
Reflections collected	66723	
Independent reflections	5987 [R(int) = 0.0561]	
Completeness to theta = 25.027°	99.8%	
Refinement method	Full-matrix least-squares on F <sup>2</sup>	
Data / restraints / parameters	5987 / 0 / 383	
Goodness-of-fit on F <sup>2</sup>	1.097	
Final R indices [I > 2σ(I)]	R <sub>1</sub> = 0.0430, wR <sub>2</sub> = 0.0972	
R indices (all data)	R <sub>1</sub> = 0.0585, wR <sub>2</sub> = 0.1041	
Extinction coefficient	n/a	
Largest diff. peak and hole	0.298 and -0.375 e.Å <sup>-3</sup>	

**Fe(19)<sub>2</sub><sup>+</sup>AcO<sup>-</sup>**

Empirical formula	C <sub>40</sub> H <sub>68</sub> FeN <sub>4</sub> O <sub>5.50</sub>
Formula weight	748.83
Temperature	150(2) K
Wavelength	1.54184 Å
Crystal system	Monoclinic
Space group	<i>C</i> 2/ <i>c</i>
Unit cell dimensions	$a = 37.7306(9) \text{ \AA}$ $\alpha = 90^\circ$ . $b = 13.5244(4) \text{ \AA}$ $\beta = 97.066(3)^\circ$ . $c = 17.6514(6) \text{ \AA}$ $\gamma = 90^\circ$ .
Volume	8938.8(5) Å <sup>3</sup>
Z	8
Density (calculated)	1.113 Mg/m <sup>3</sup>
Absorption coefficient	3.043 mm <sup>-1</sup>
F(000)	3248
Crystal size	0.2 x 0.1 x 0.05 mm <sup>3</sup>
Theta range for data collection	3.475 to 66.596°.
Index ranges	-43 ≤ <i>h</i> ≤ 44, -9 ≤ <i>k</i> ≤ 16, -21 ≤ <i>l</i> ≤ 13
Reflections collected	14982
Independent reflections	7864 [R(int) = 0.0193]
Completeness to theta = 66.596°	99.6%
Refinement method	Full-matrix least-squares on F <sup>2</sup>
Data / restraints / parameters	7864 / 8 / 473
Goodness-of-fit on F <sup>2</sup>	1.037
Final R indices [I > 2σ(I)]	R <sub>1</sub> = 0.0566, wR <sub>2</sub> = 0.1628
R indices (all data)	R <sub>1</sub> = 0.0633, wR <sub>2</sub> = 0.1699
Extinction coefficient	<i>n/a</i>
Largest diff. peak and hole	0.645 and -0.486 e.Å <sup>-3</sup>

**Fe(19)<sub>2</sub><sup>+</sup>NO<sub>3</sub><sup>-</sup>**

Empirical formula	C <sub>37</sub> H <sub>59</sub> FeN <sub>5</sub> O <sub>6</sub>
Formula weight	725.74
Temperature	150(2) K
Wavelength	0.71073 Å
Crystal system	Monoclinic
Space group	<i>P</i> 2 <sub>1</sub> / <i>c</i>
Unit cell dimensions	<i>a</i> = 11.2646(7) Å $\alpha = 90^\circ$ . <i>b</i> = 20.2375(9) Å $\beta = 107.739(6)^\circ$ . <i>c</i> = 18.5120(12) Å $\gamma = 90^\circ$ .
Volume	4019.5(4) Å <sup>3</sup>
Z	4
Density (calculated)	1.199 Mg/m <sup>3</sup>
Absorption coefficient	0.422 mm <sup>-1</sup>
F(000)	1560
Theta range for data collection	3.409 to 25.027°.
Index ranges	-13 ≤ <i>h</i> ≤ 13, -24 ≤ <i>k</i> ≤ 23, -21 ≤ <i>l</i> ≤ 22
Reflections collected	30496
Independent reflections	7081 [R(int) = 0.1089]
Completeness to theta = 25.027°	99.8%
Refinement method	Full-matrix least-squares on F <sup>2</sup>
Data / restraints / parameters	7081 / 0 / 468
Goodness-of-fit on F <sup>2</sup>	1.049
Final R indices [I > 2σ(I)]	R <sub>1</sub> = 0.0921, wR <sub>2</sub> = 0.1802
R indices (all data)	R <sub>1</sub> = 0.1668, wR <sub>2</sub> = 0.2139
Extinction coefficient	n/a
Largest diff. peak and hole	0.530 and -0.513 e.Å <sup>-3</sup>

## 7.2 Homonuclear decoupled spectra of the PLA derived from Fe(3)Cl

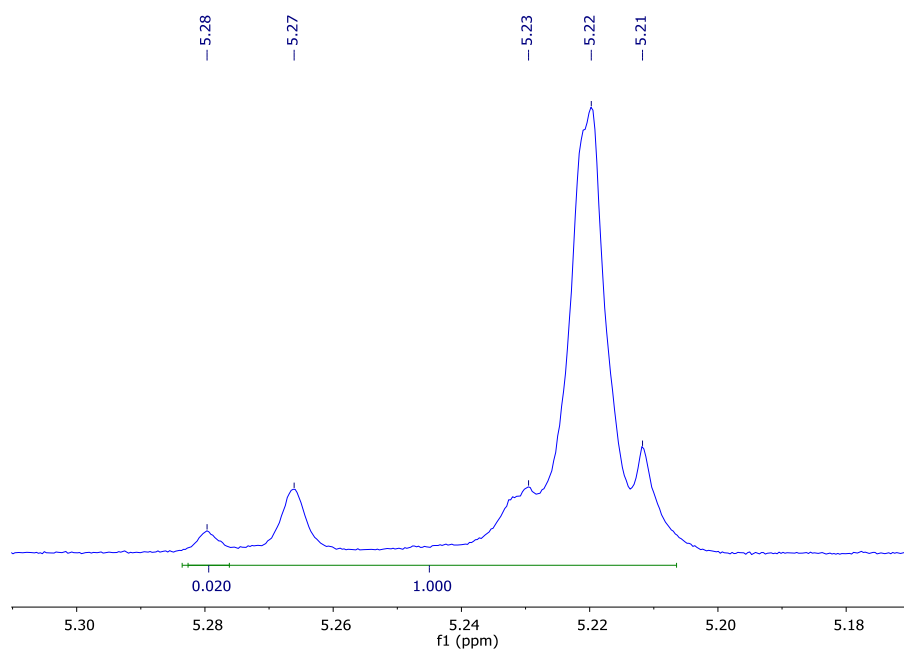


Figure 103.  $^1\text{H}$   $\{^1\text{H}\}$  NMR spectrum of the isotactic PLA attained using Fe(3)Cl at 40 °C for seven days (Section 3.4, Table 10, entry 1) ( $P_m = 0.80$ ).

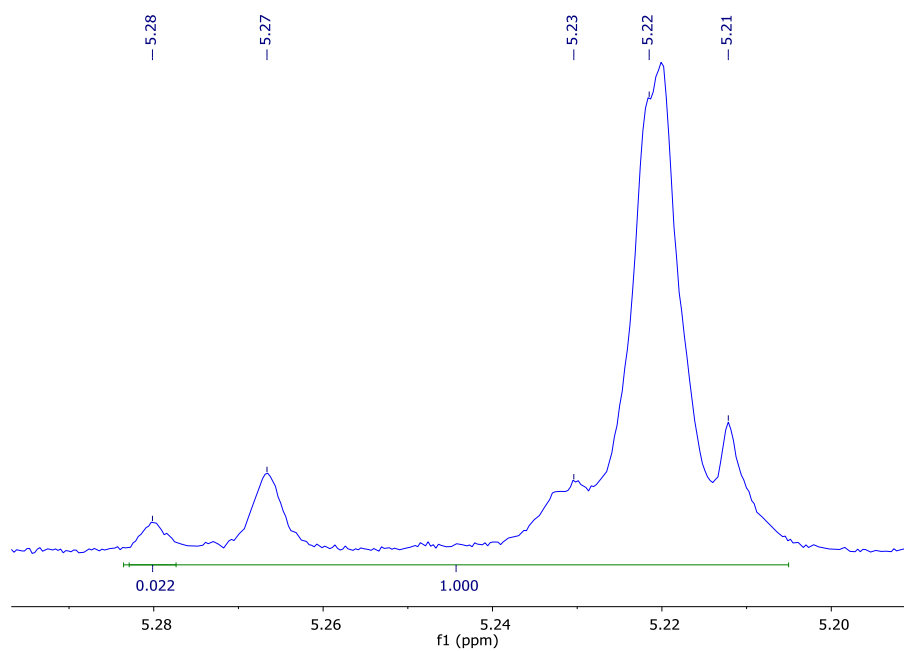


Figure 104.  $^1\text{H}$   $\{^1\text{H}\}$  NMR spectrum of the isotactic PLA attained using Fe(3)Cl at 80 °C for 24 hours (Section 3.4, Table 10, entry 9) ( $P_m = 0.79$ ).

### 7.3 GPC chromatograms of PLA derived from the Fe(III)–salen–chloride complexes

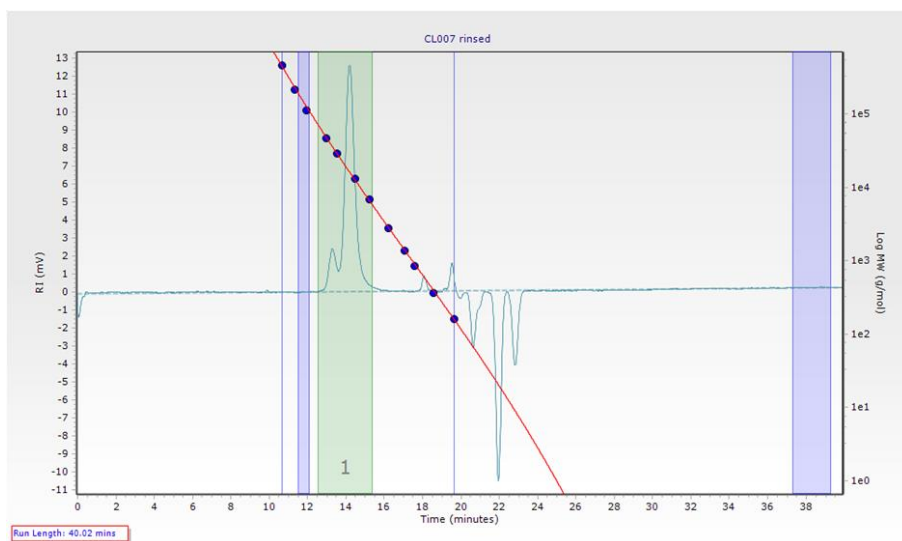


Figure 105. GPC chromatogram of the PLA attained using Fe(3)Cl at 80 °C for 24 hours (Section 3.4, Table 10, entry 9) ( $M_{n, \text{GPC}} = 9400 \text{ gmol}^{-1}$ ,  $M_{n, \text{theoretical}} = 10450 \text{ gmol}^{-1}$ ,  $\bar{D} = 1.11$ ). Peaks separately:  $M_{n, \text{GPC, peak 1}} = 19250 \text{ gmol}^{-1}$ ,  $\bar{D} = 1.11$ ,  $M_{n, \text{GPC, peak 2}} = 8650 \text{ gmol}^{-1}$ ,  $\bar{D} = 1.04$ ). Bimodality observed due to propane–1,2–diol impurity.

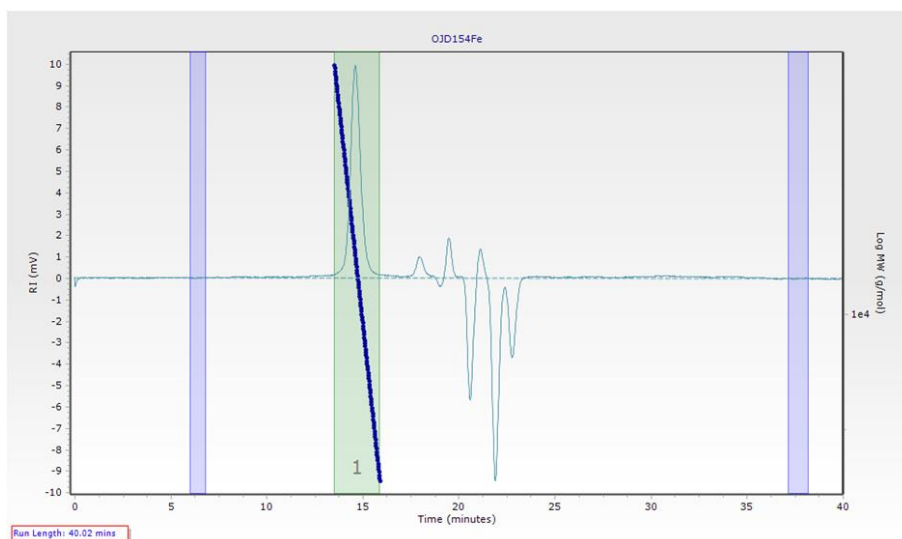


Figure 106. GPC chromatogram of the PLA attained using Fe(3)Cl at 80 °C for 24 hours with one equivalent of benzyl alcohol and triethylamine in toluene solvent (Section 3.4, Table 10, entry 10) ( $M_{n, \text{GPC}} = 11250 \text{ gmol}^{-1}$ ,  $M_{n, \text{theoretical}} = 11350 \text{ gmol}^{-1}$ ,  $\bar{D} = 1.02$ ).

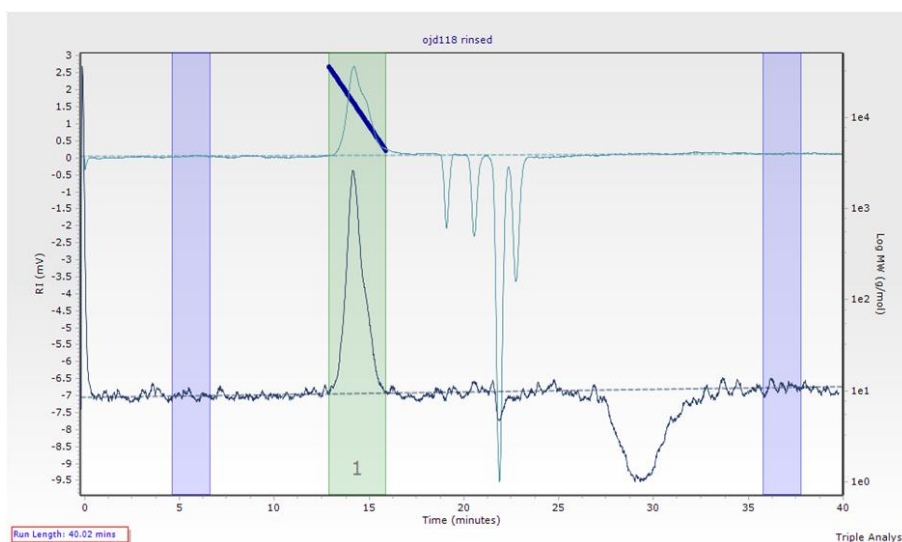


Figure 107. GPC chromatogram of the PLA attained using Fe(4)Cl at 80 °C for four hours (Section 3.6, Table 11, entry 6) ( $M_{n,GPC} = 11150 \text{ gmol}^{-1}$ ,  $M_{n,theoretical} = 13500 \text{ gmol}^{-1}$ ,  $\bar{D} = 1.14$ ).

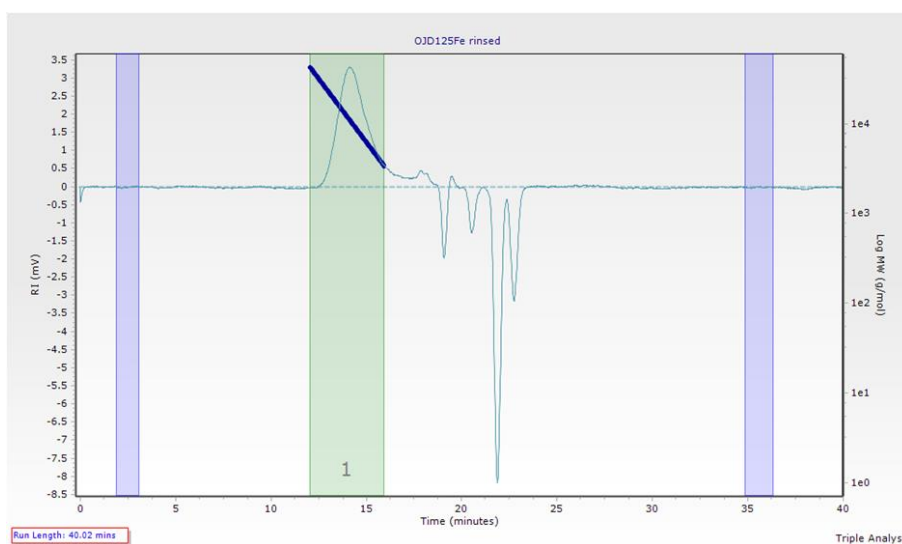


Figure 108. GPC chromatogram of the PLA attained using Fe(5)Cl at 80 °C for four days (Section 3.6, Table 11, entry 8) ( $M_{n,GPC} = 8750 \text{ gmol}^{-1}$ ,  $M_{n,theoretical} = 13350 \text{ gmol}^{-1}$ ,  $\bar{D} = 1.22$ ).



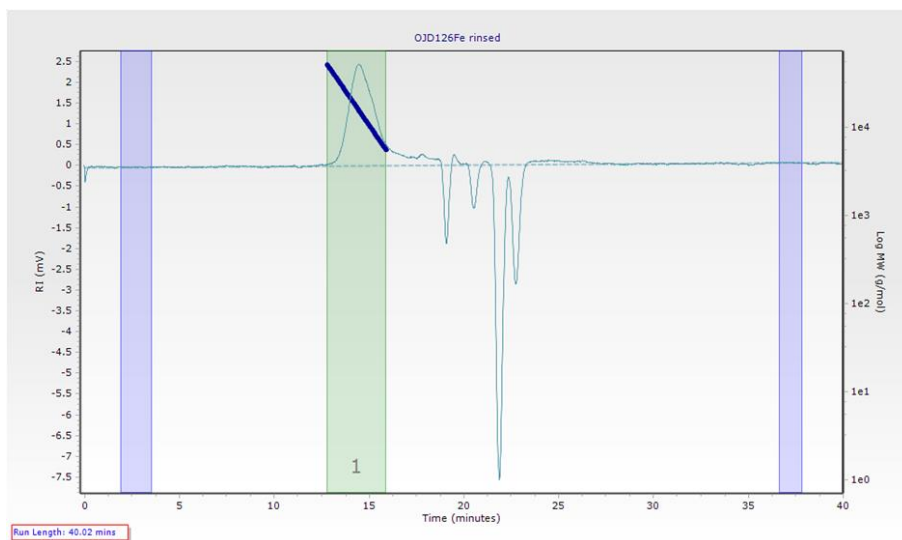


Figure 109. GPC chromatogram of the PLA attained using Fe(6)Cl at 80 °C for two days (Section 3.6, Table 11, entry 10) ( $M_{n,GPC} = 12700 \text{ gmol}^{-1}$ ,  $M_{n,theoretical} = 13350 \text{ gmol}^{-1}$ ,  $\mathcal{D} = 1.19$ ).

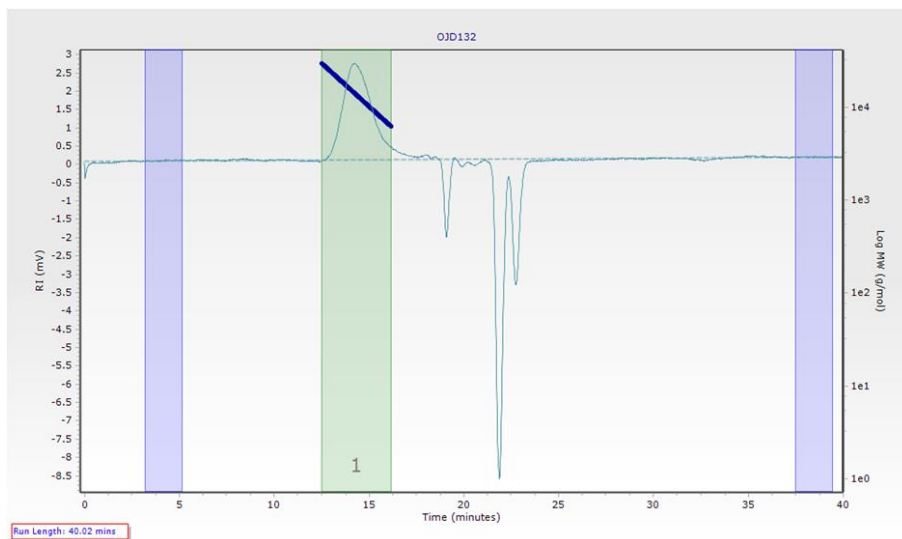


Figure 110. GPC chromatogram of the PLA attained using Fe(7)Cl at 80 °C for 16 hours (Section 3.6, Table 11, entry 12) ( $M_{n,GPC} = 12150 \text{ gmol}^{-1}$ ,  $M_{n,theoretical} = 13800 \text{ gmol}^{-1}$ ,  $\mathcal{D} = 1.09$ ).

## 7.4 MALDI-ToF analysis of the PLA derived from the Fe-salalen-chloride complexes

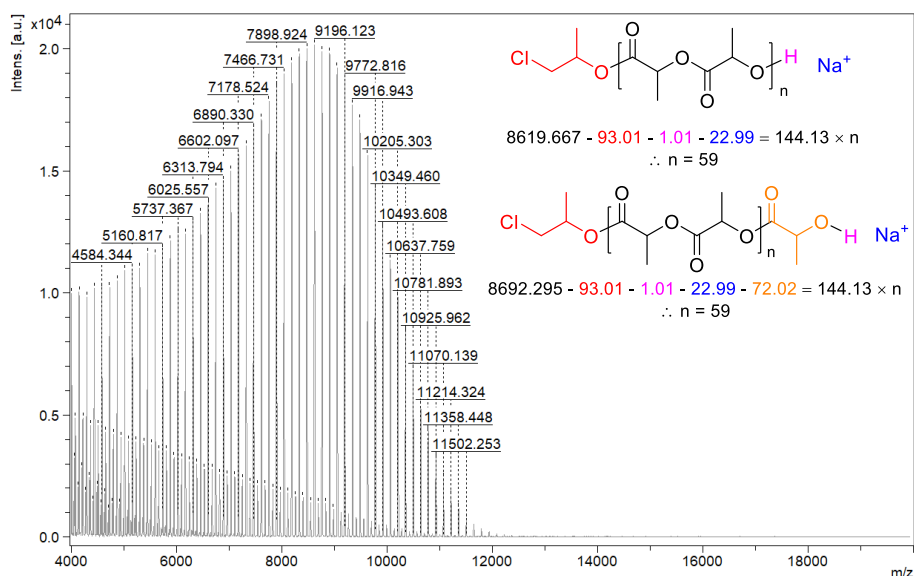


Figure 111. MALDI-ToF spectrum of the PLA attained using Fe(3)Cl at 60 °C for three days (Section 3.4, Table 10, entry 7) ( $M_{p,\text{MALDI-ToF}} = 8331 \text{ gmol}^{-1}$ ,  $M_{n,\text{GPC}} = 10800 \text{ gmol}^{-1}$ ,  $M_{n,\text{theoretical}} = 11050 \text{ gmol}^{-1}$ ).

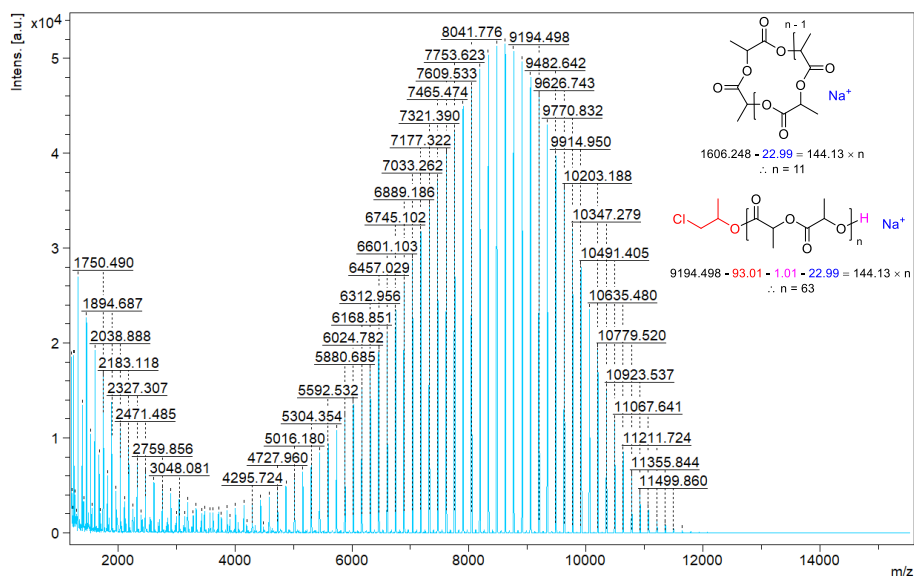


Figure 112. MALDI-ToF spectrum of the PLA attained using Fe(3)Cl at 80 °C for 24 hours (Section 3.4, Table 10, entry 9) ( $M_{n,\text{GPC}} = 9400 \text{ gmol}^{-1}$ ,  $M_{n,\text{theoretical}} = 10450 \text{ gmol}^{-1}$ ).

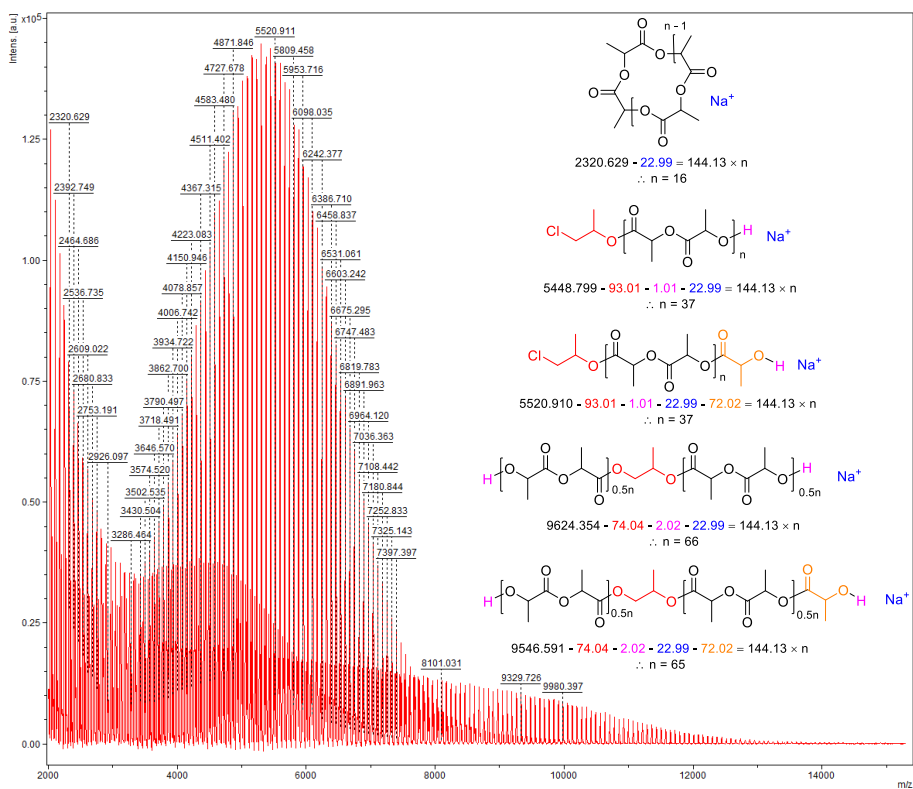


Figure 113. MALDI–ToF spectrum of the PLA attained using Fe(4)Cl at 80 °C for four hours (Section 3.6, Table 11, entry 6) ( $M_{n,GPC} = 11150 \text{ gmol}^{-1}$ ,  $M_{n,theoretical} = 13500 \text{ gmol}^{-1}$ ).

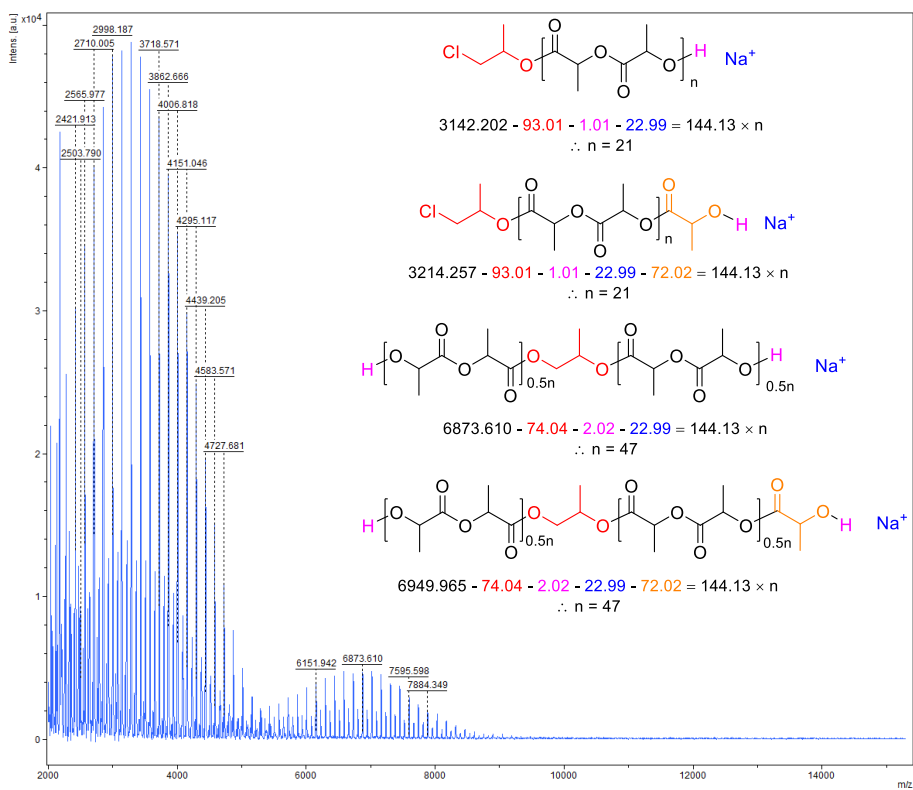


Figure 114. MALDI–ToF spectrum of the PLA attained using Fe(5)Cl at 80 °C for three days (Section 3.6, Table 11, entry 7) ( $M_{n,GPC} = 5250 \text{ gmol}^{-1}$ ,  $M_{n,theoretical} = 8600 \text{ gmol}^{-1}$ ).



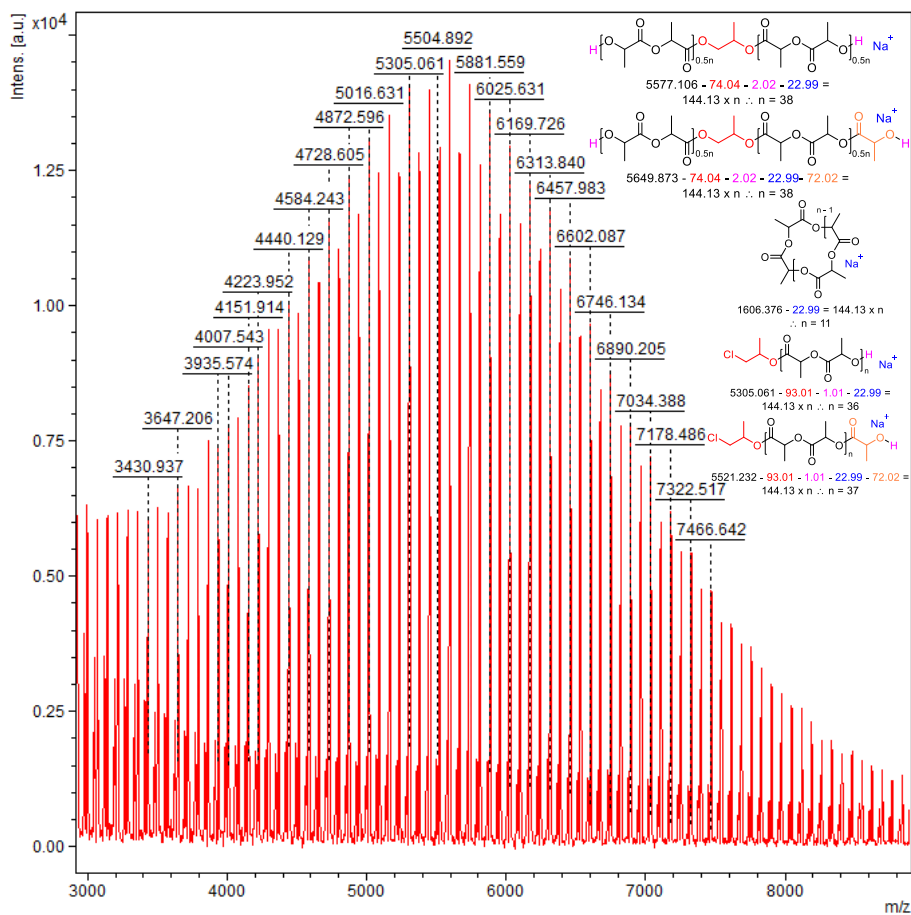


Figure 117. MALDI-ToF spectrum of the PLA attained using Fe(7)Cl at 80 °C for 16 hours (Section 3.6, Table 11, entry 12) ( $M_{p, \text{MALDI-ToF}} = 5505 \text{ g mol}^{-1}$ ,  $M_{n, \text{GPC}} = 12150 \text{ g mol}^{-1}$ ,  $M_{n, \text{theoretical}} = 13800 \text{ g mol}^{-1}$ ).

## 7.5 Homonuclear decoupled spectra of the PLA derived from the Fe(III)–acetate complexes

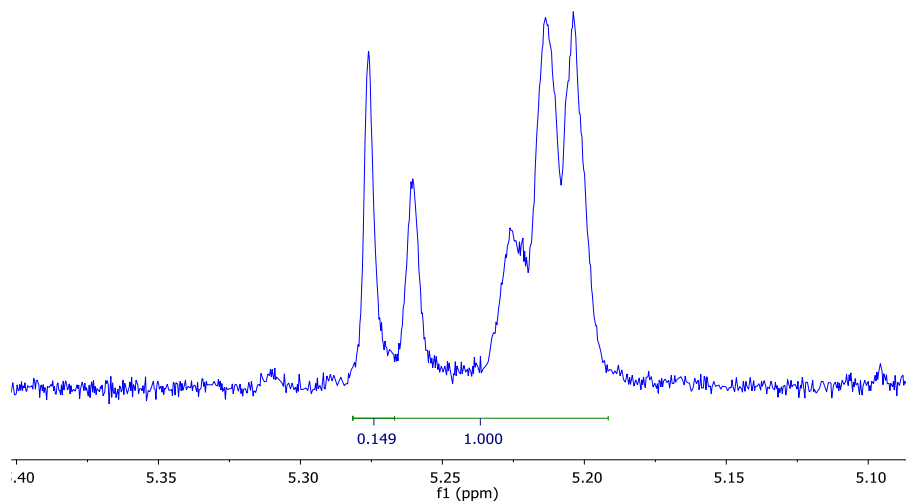


Figure 118.  $^1\text{H}$   $\{^1\text{H}\}$  NMR spectrum of the isotactic PLA attained using Fe(10)OAc at 100 °C for 24 hours (Section 3.9, Table 13, entry 6) ( $P_m = 0.45$ ).

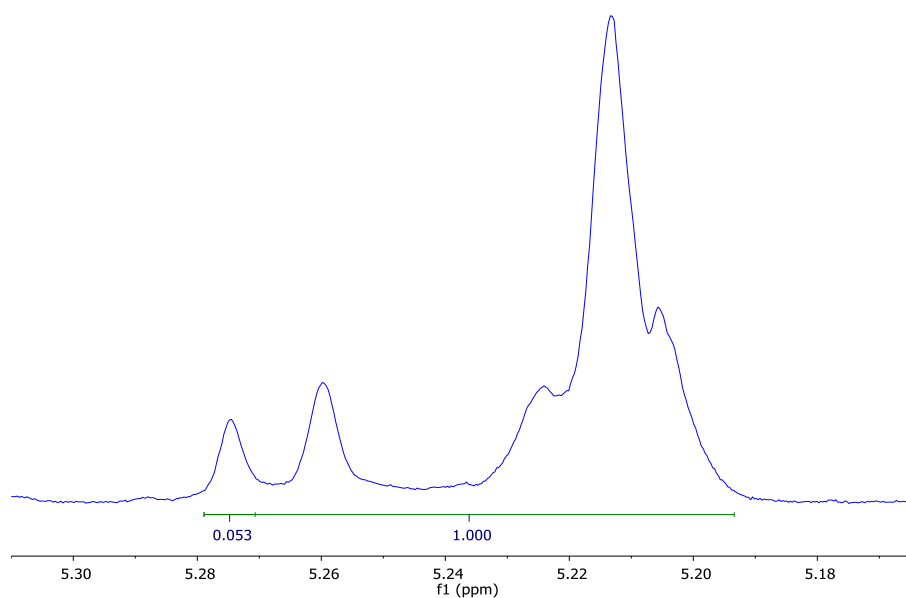


Figure 119.  $^1\text{H}$   $\{^1\text{H}\}$  NMR spectrum of the isotactic PLA attained using Fe(13)OAc at 100 °C for 24 hours (Section 3.9, Table 13, entry 13) ( $P_m = 0.67$ ).

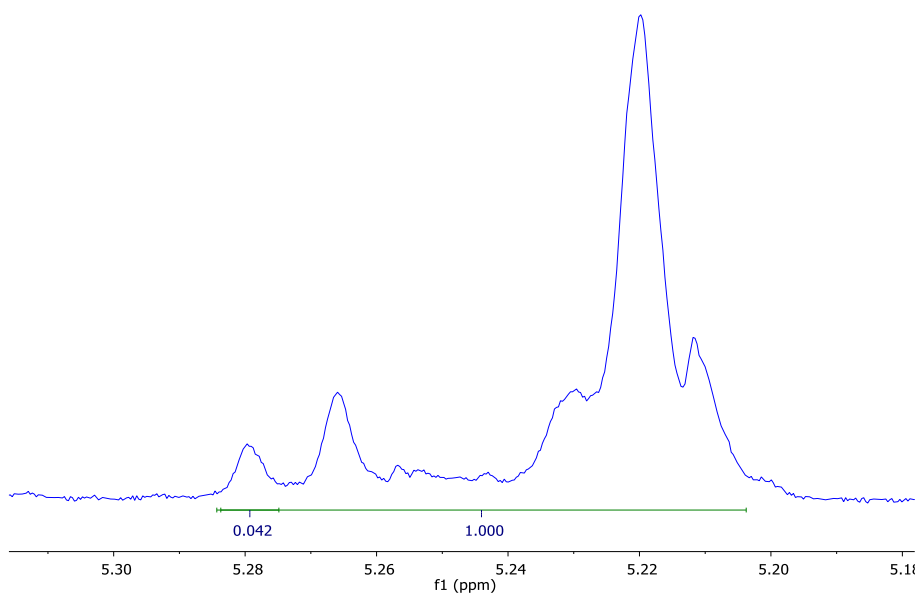


Figure 120.  $^1\text{H}$   $\{^1\text{H}\}$  NMR spectrum of the isotactic PLA attained using Fe(15)OAc at 100 °C for 24 hours (Section 3.9, Table 13, entry 15) ( $P_m = 0.71$ ).

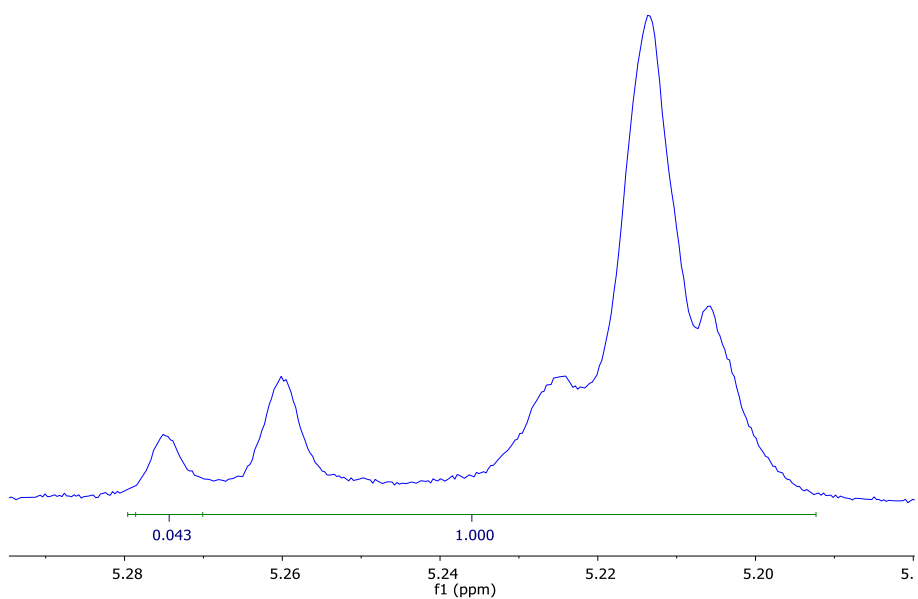


Figure 121.  $^1\text{H}$   $\{^1\text{H}\}$  NMR spectrum of the isotactic PLA attained using Fe(17)OAc at 100 °C for 24 hours (Section 3.9, Table 13, entry 17) ( $P_m = 0.71$ ).

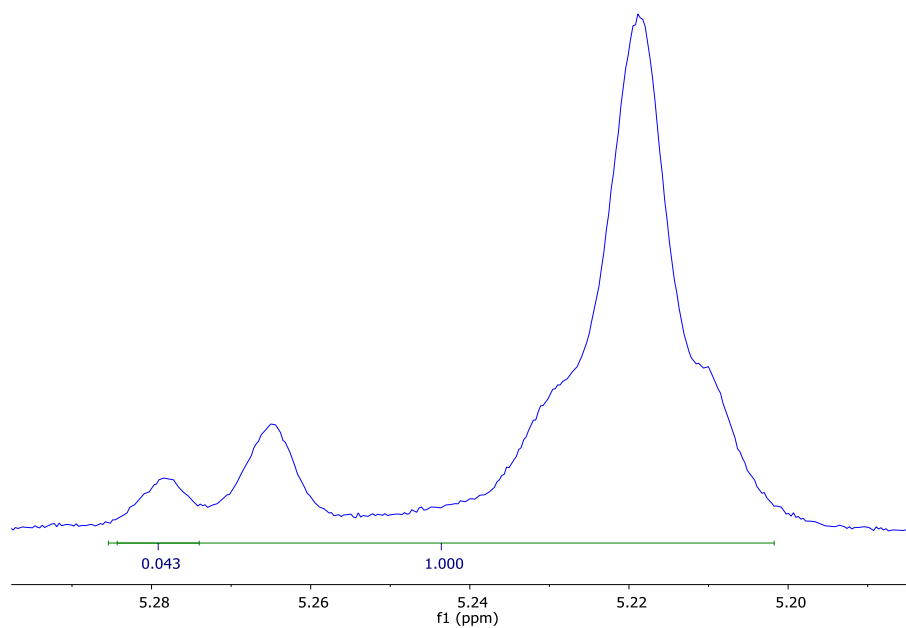


Figure 122.  $^1\text{H}$   $\{^1\text{H}\}$  NMR spectrum of the isotactic PLA attained using Fe(17)OAc at 80 °C for 24 hours (Section 3.9, Table 14, entry 4) ( $P_m = 0.71$ ).

## 7.6 GPC chromatograms of PLA derived from the Fe(III)–acetate complexes

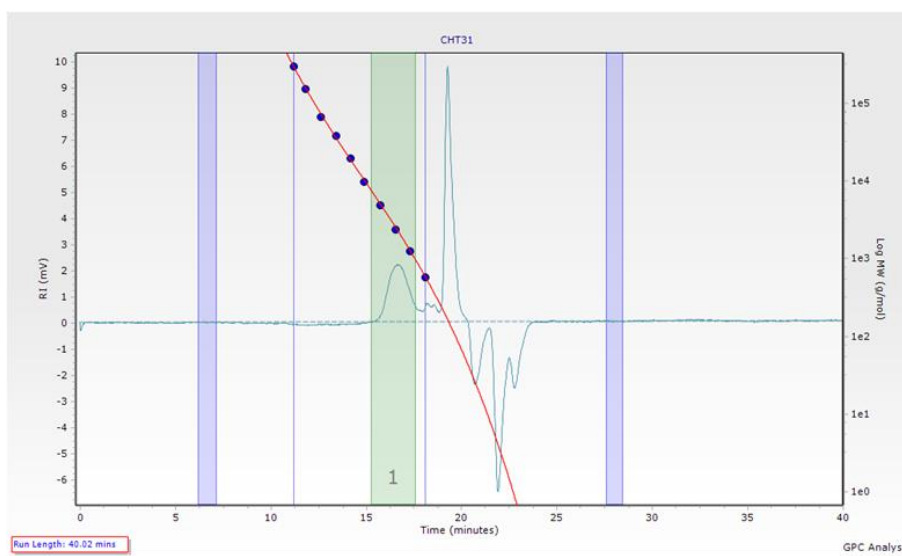


Figure 123. GPC chromatogram of the PLA attained using Fe(1)OAc at 100 °C for 24 hours (Section 3.9, Table 13, entry 2) ( $M_{n,\text{GPC}} = 2000 \text{ gmol}^{-1}$ ,  $M_{n,\text{theoretical}} = 3850 \text{ gmol}^{-1}$ ,  $\bar{D} = 1.17$ ).



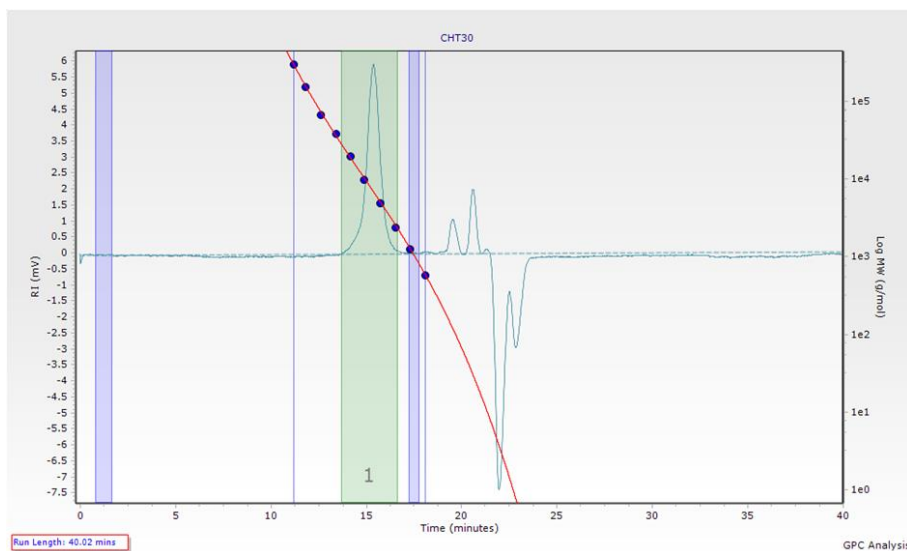


Figure 124. GPC chromatogram of the PLA attained using Fe(3)OAc at 100 °C for 24 hours (Section 3.9, Table 13, entry 3) ( $M_{n,GPC} = 6550 \text{ gmol}^{-1}$ ,  $M_{n,theoretical} = 8300 \text{ gmol}^{-1}$ ,  $\bar{D} = 1.13$ ).

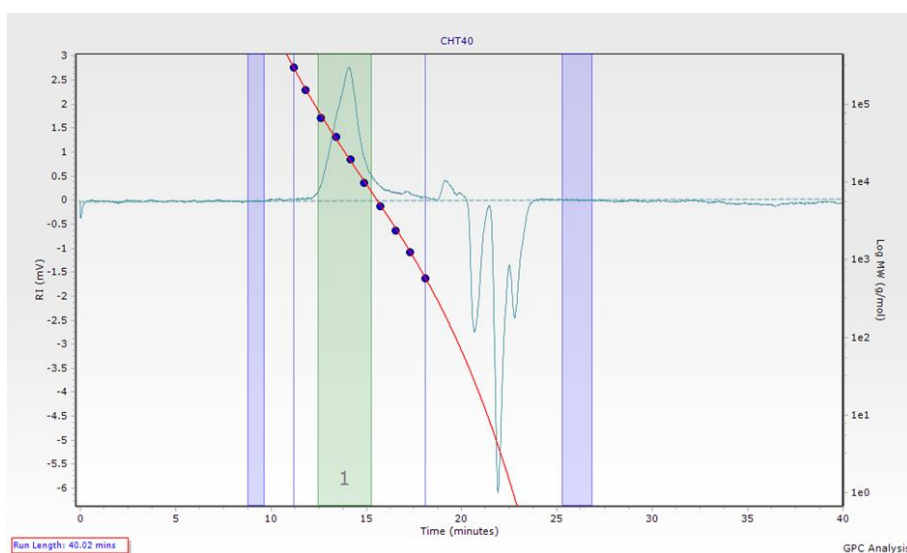


Figure 125. GPC chromatogram of the PLA attained using Fe(8<sub>meso</sub>)OAc at 100 °C for 24 hours (Section 3.9, Table 13, entry 9) ( $M_{n,GPC} = 19900 \text{ gmol}^{-1}$ ,  $M_{n,theoretical} = 13400 \text{ gmol}^{-1}$ ,  $\bar{D} = 1.30$ ).

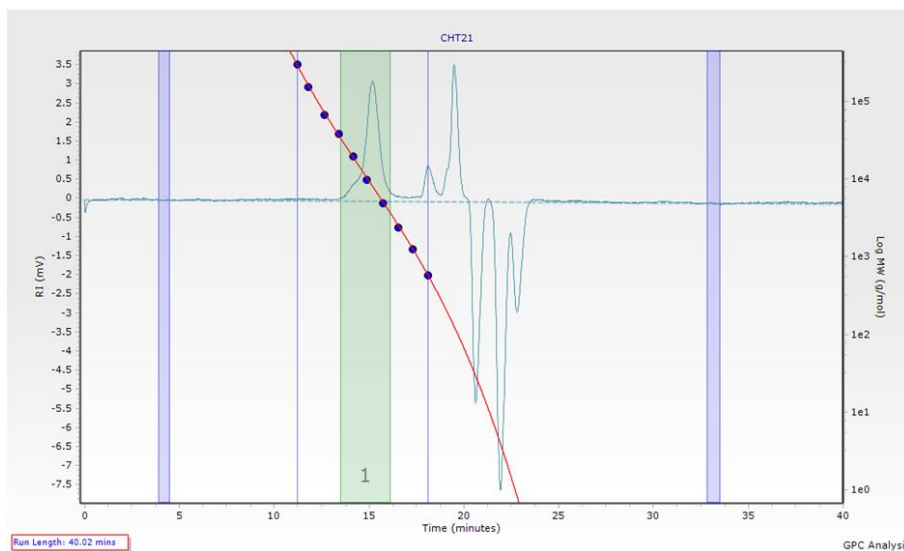


Figure 126. GPC chromatogram of the PLA attained using Fe(**9***meso*)OAc at 100 °C for 24 hours (Section 3.9, Table 13, entry 12) ( $M_{n,GPC} = 6600 \text{ gmol}^{-1}$ ,  $M_{n,theoretical} = 7450 \text{ gmol}^{-1}$ ,  $\bar{D} = 1.09$ ).

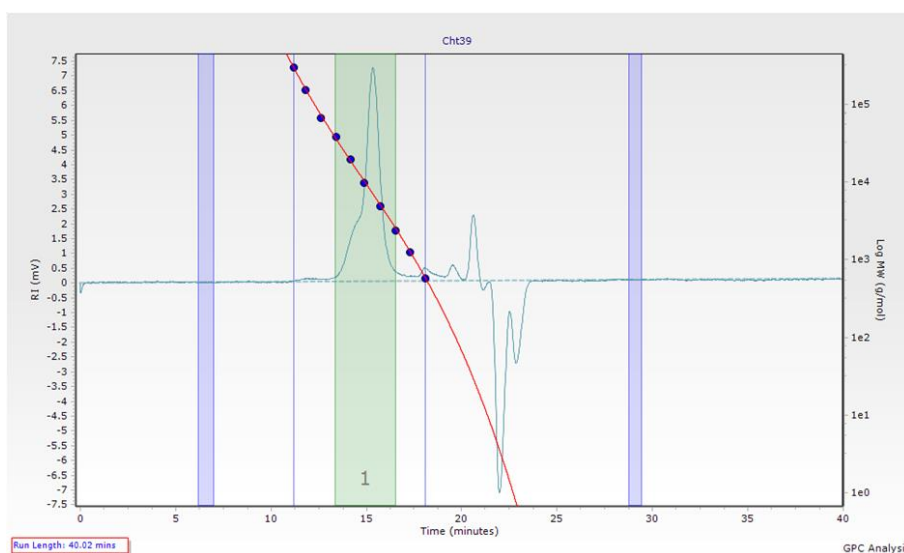


Figure 127. GPC chromatogram of the PLA attained using Fe(**10**)OAc at 100 °C for 24 hours (Section 3.9, Table 13, entry 6) ( $M_{n,GPC} = 7300 \text{ gmol}^{-1}$ ,  $M_{n,theoretical} = 8750 \text{ gmol}^{-1}$ ,  $\bar{D} = 1.26$ ).

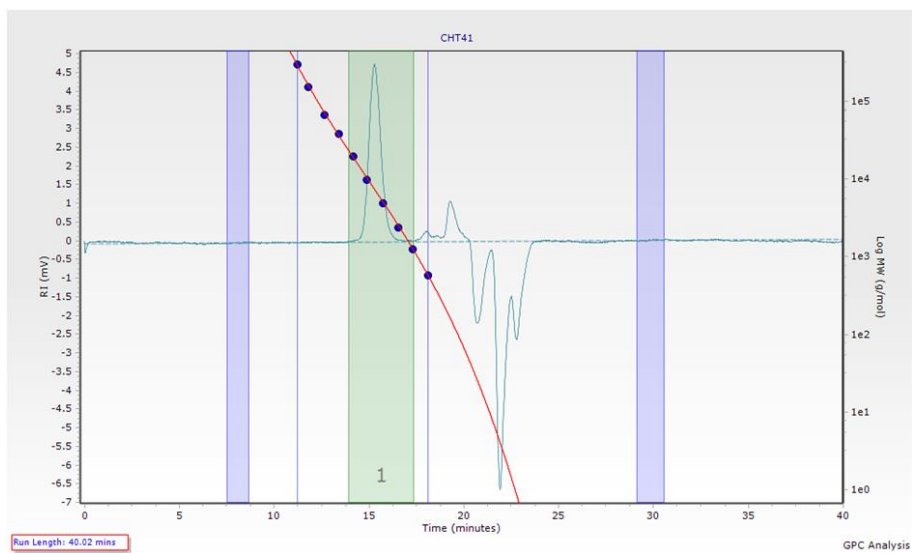


Figure 128. GPC chromatogram of the PLA attained using Fe(12)OAc at 100 °C for 24 hours (Section 3.9, Table 13, entry 8) ( $M_{n,GPC} = 6700 \text{ gmol}^{-1}$ ,  $M_{n,theoretical} = 6300 \text{ gmol}^{-1}$ ,  $\bar{D} = 1.10$ ).

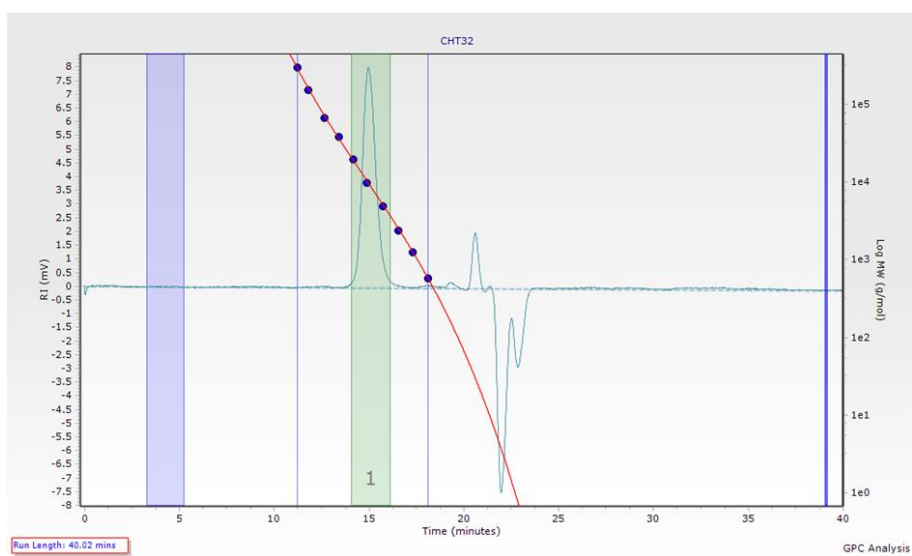


Figure 129. GPC chromatogram of the PLA attained using Fe(13)OAc at 100 °C for 24 hours (Section 3.9, Table 13, entry 13) ( $M_{n,GPC} = 8700 \text{ gmol}^{-1}$ ,  $M_{n,theoretical} = 13500 \text{ gmol}^{-1}$ ,  $\bar{D} = 1.09$ ).

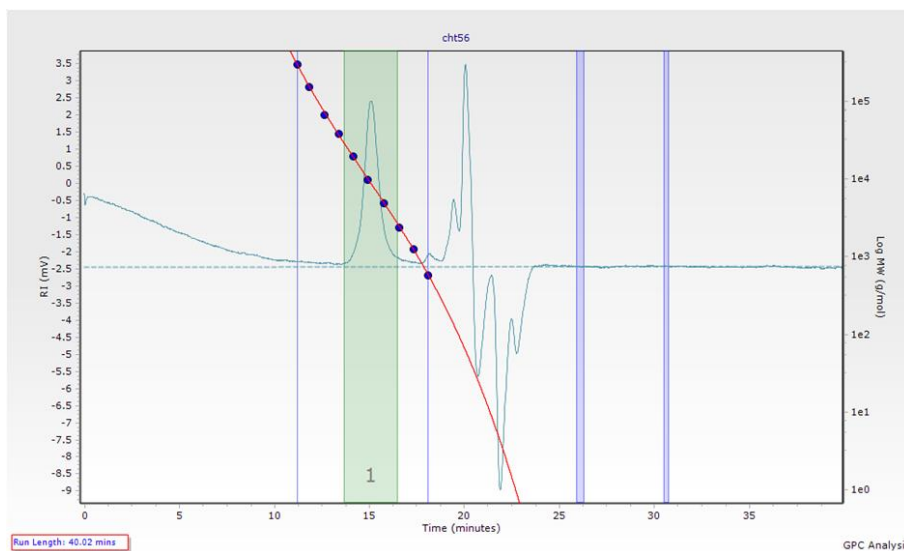


Figure 130. GPC chromatogram of the PLA attained using Fe(15)OAc at 100 °C for 24 hours (Section 3.9, Table 13, entry 15) ( $M_{n,GPC} = 7750 \text{ gmol}^{-1}$ ,  $M_{n,theoretical} = 9800 \text{ gmol}^{-1}$ ,  $\bar{D} = 1.16$ ).

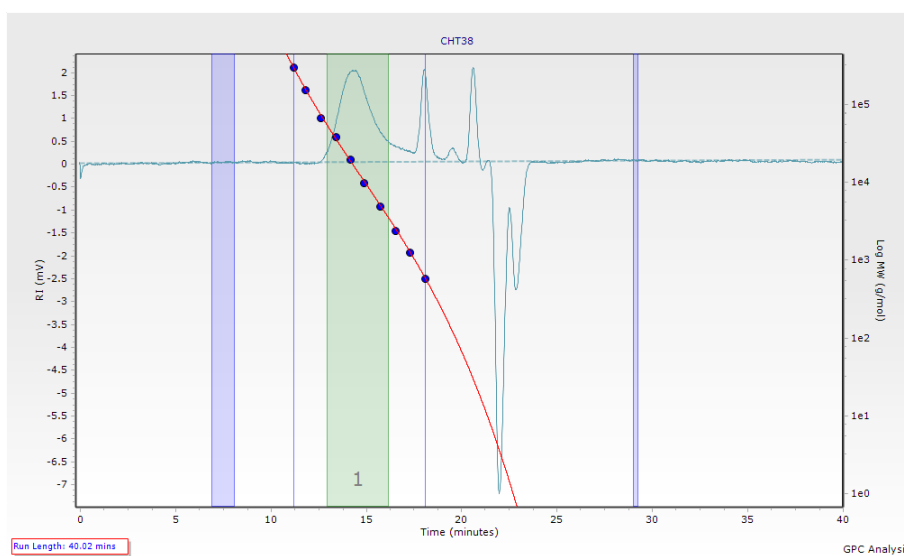


Figure 131. GPC chromatogram of the PLA attained using Fe(17)OAc at 100 °C for 24 hours (Section 3.9, Table 13, entry 17) ( $M_{n,GPC} = 11700 \text{ gmol}^{-1}$ ,  $M_{n,theoretical} = 12900 \text{ gmol}^{-1}$ ,  $\bar{D} = 1.46$ ).

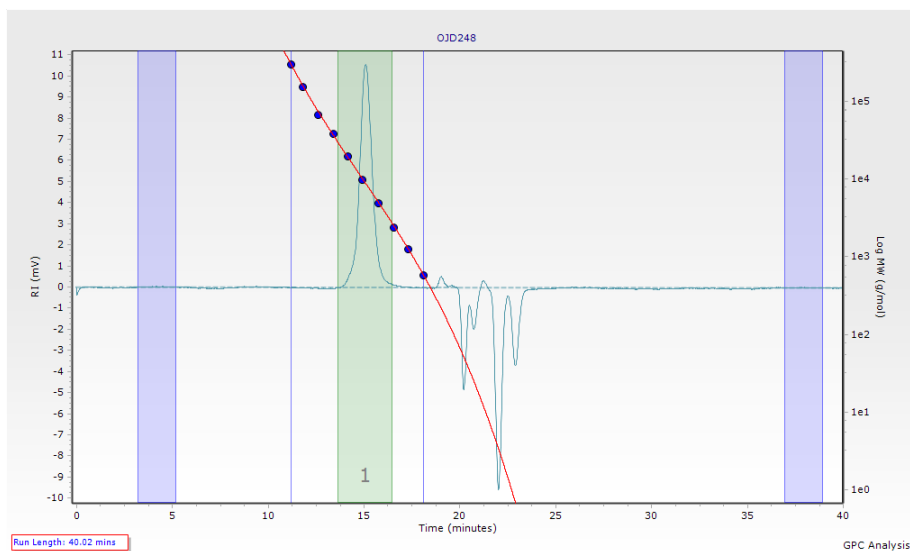


Figure 132. GPC chromatogram of the PLA attained using Fe(**8<sub>meso</sub>**)OAc at 80 °C for 24 hours (Section 3.9, Table 14, entry 1) ( $M_{n,GPC} = 8100 \text{ gmol}^{-1}$ ,  $M_{n,theoretical} = 13950 \text{ gmol}^{-1}$ ,  $\bar{D} = 1.09$ ).

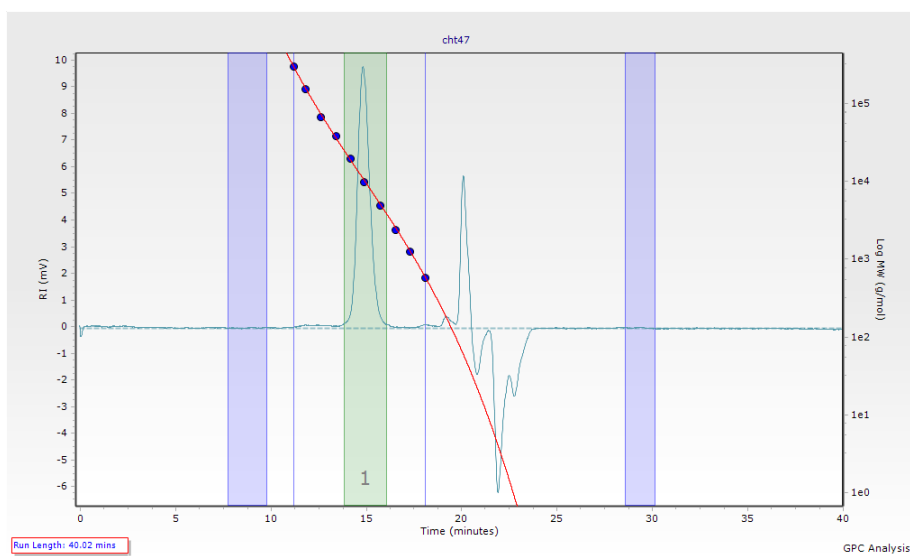


Figure 133. GPC chromatogram of the PLA attained using Fe(**13**)OAc at 80 °C for 24 hours (Section 3.9, Table 14, entry 2) ( $M_{n,GPC} = 9900 \text{ gmol}^{-1}$ ,  $M_{n,theoretical} = 13650 \text{ gmol}^{-1}$ ,  $\bar{D} = 1.07$ ).

## 7.7 MALDI-ToF analysis of the PLA derived from the Fe(III)-acetate complexes

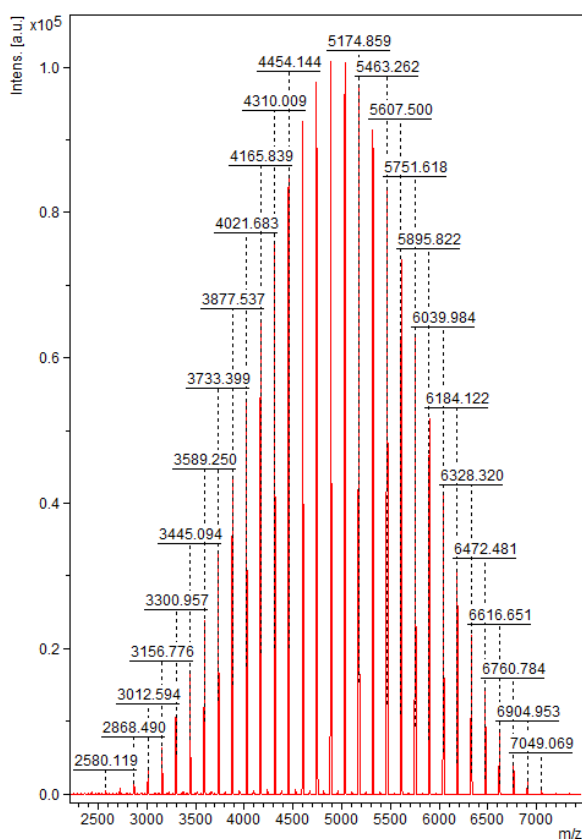


Figure 134. MALDI-ToF spectrum of the PLA attained using Fe(**8***meso*)OAc at 80 °C for 24 hours (Section 3.9, Table 14, entry 1) ( $M_{p,\text{MALDI-ToF}} = 4887 \text{ gmol}^{-1}$  (BnOH end groups),  $M_{n,\text{GPC}} = 8100 \text{ gmol}^{-1}$ ,  $M_{n,\text{theoretical}} = 13950 \text{ gmol}^{-1}$ ).

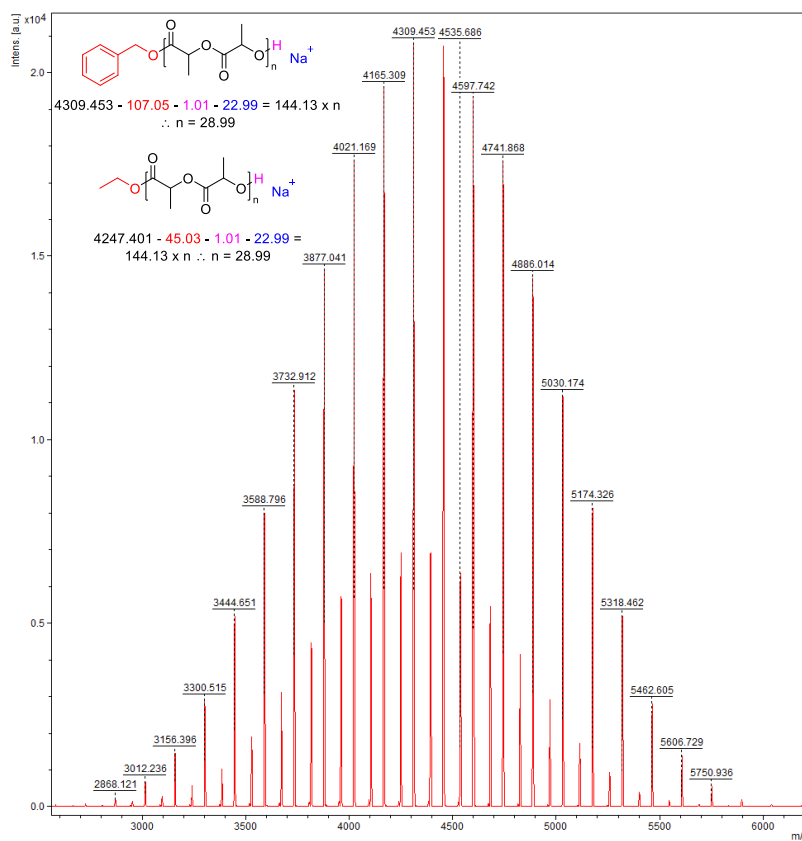


Figure 135. MALDI–ToF spectrum of the PLA attained using Fe(10)OAc at 100 °C for 24 hours (Section 3.9, Table 13, entry 6) ( $M_{p,\text{MALDI-ToF}} = 4309 \text{ gmol}^{-1}$  and  $4247 \text{ gmol}^{-1}$ ,  $M_{n,\text{GPC}} = 7300 \text{ gmol}^{-1}$ ,  $M_{n,\text{theoretical}} = 8750 \text{ gmol}^{-1}$ ).

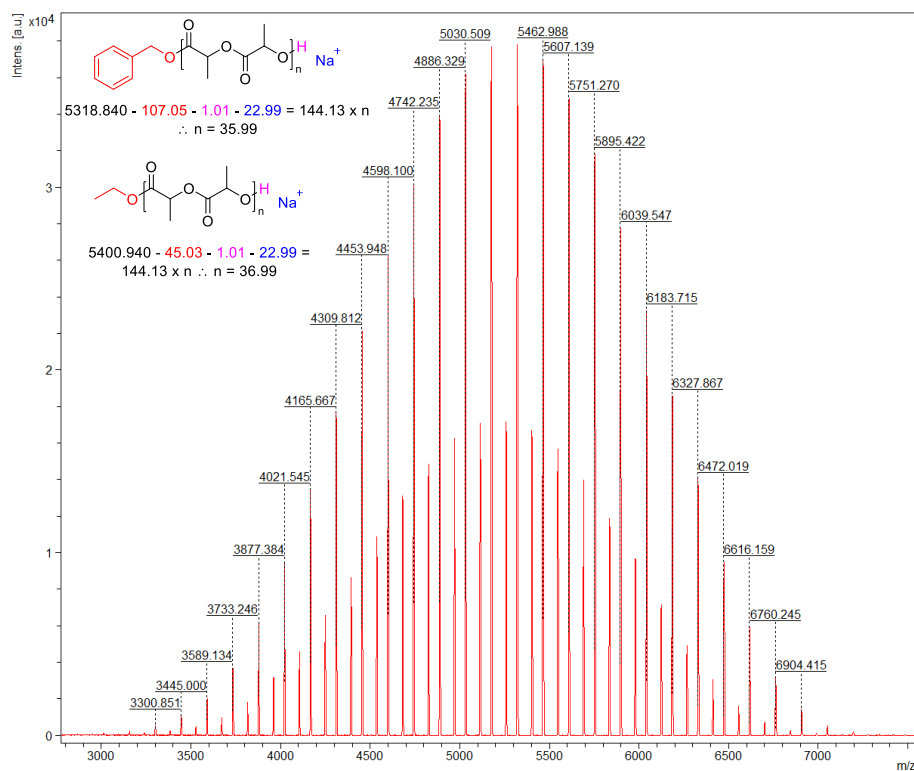


Figure 136. MALDI–ToF spectrum of the PLA attained using Fe(13)OAc at 100 °C for 24 hours (Section 3.9, Table 13, entry 13) ( $M_{p,MALDI-ToF} = 5319 \text{ g mol}^{-1}$  (BnOH end groups) and  $5401 \text{ g mol}^{-1}$  (EtOH end groups),  $M_{n,GPC} = 8700 \text{ g mol}^{-1}$ ,  $M_{n,theoretical} = 13500 \text{ g mol}^{-1}$ ).

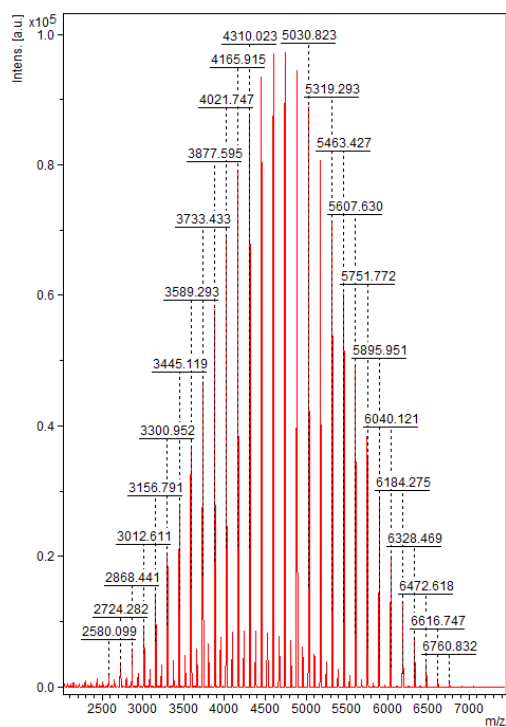


Figure 137. MALDI–ToF spectrum of the PLA attained using Fe(15)OAc at 100 °C for 24 hours (Section 3.9, Table 13, entry 15) ( $M_{p,MALDI-ToF} = 4742 \text{ g mol}^{-1}$  (BnOH end groups) and  $4815 \text{ g mol}^{-1}$  (BnOH end groups and transesterification),  $M_{n,GPC} = 7750 \text{ g mol}^{-1}$ ,  $M_{n,theoretical} = 9750 \text{ g mol}^{-1}$ ).



## 7.8 GPC chromatograms of the polymer derived from the ROCOP of PA and CHO

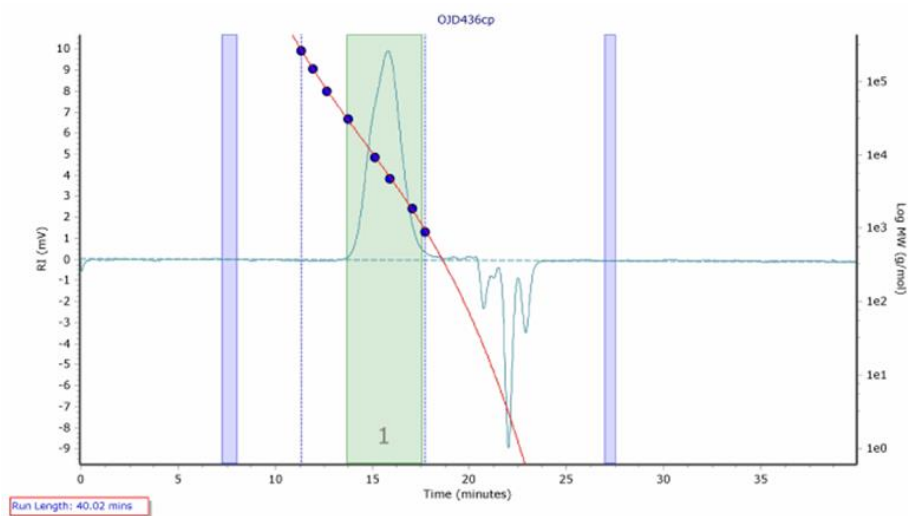


Figure 138. GPC chromatogram of the polymer attained from PA / CHO solution ROCOP using  $\text{Fe}(\text{OAc})_2$  at  $100^\circ\text{C}$  for three days (Section 5.3, Table 26, entry 2) ( $M_{n,\text{GPC}} = 6100 \text{ gmol}^{-1}$ ,  $M_{n,\text{theoretical}} = 10500 \text{ gmol}^{-1}$ ,  $\bar{D} = 1.24$ ).

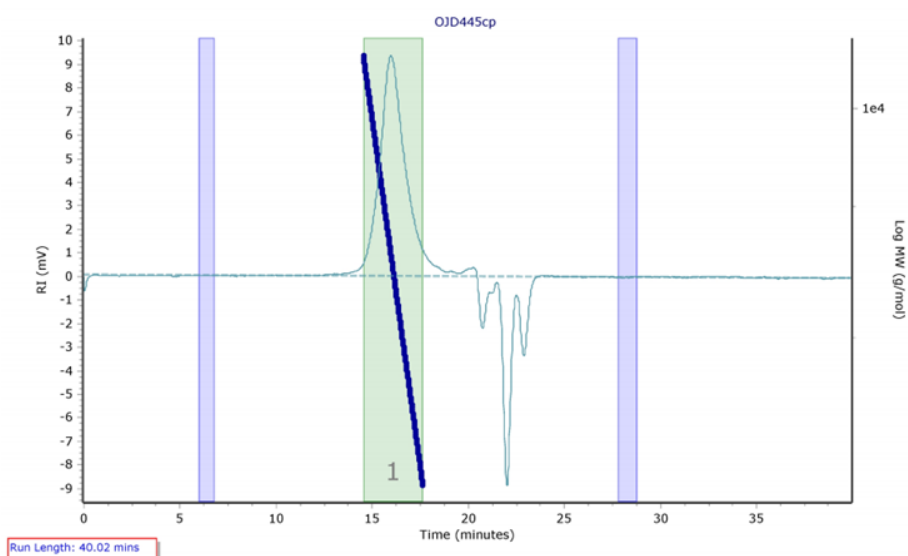


Figure 139. GPC chromatogram of the polymer attained from PA / CHO solution ROCOP using  $\text{FeCl}_3$  at  $100^\circ\text{C}$  for three days (Section 5.3, Table 26, entry 3) ( $M_{n,\text{GPC}} = 6400 \text{ gmol}^{-1}$ ,  $M_{n,\text{theoretical}} = 12700 \text{ gmol}^{-1}$ ,  $\bar{D} = 1.05$ ).

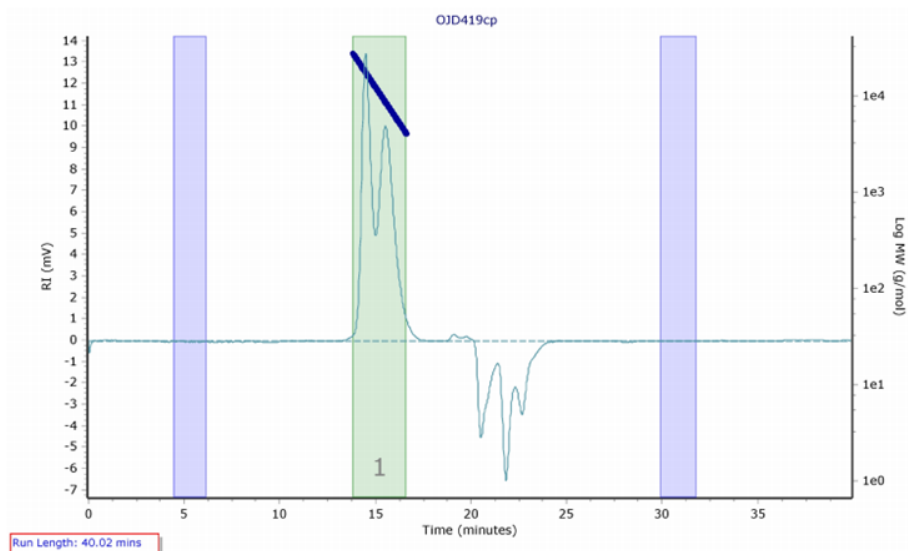


Figure 140. GPC chromatogram of the polymer attained from PA / CHO solution ROCOP using Fe(3)OAc at 100 °C for three days (Section 5.3, Table 26, entry 6) ( $M_{n,GPC} = 10300 \text{ gmol}^{-1}$ ,  $M_{n,theoretical} = 10750 \text{ gmol}^{-1}$ ,  $\bar{D} = 1.21$ ).

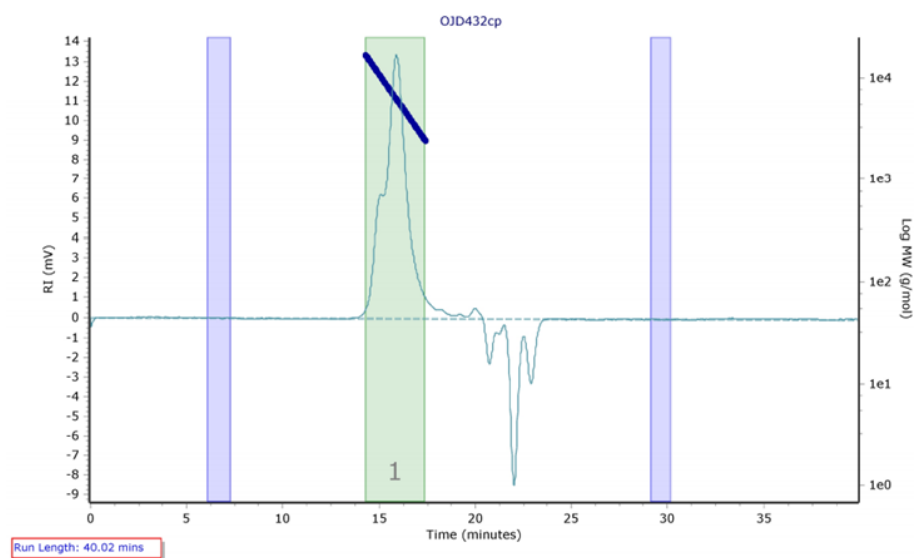


Figure 141. GPC chromatogram of the polymer attained from PA / CHO solution ROCOP using Fe(13)OAc at 100 °C for three days (Section 5.3, Table 26, entry 17) ( $M_{n,GPC} = 6000 \text{ gmol}^{-1}$ ,  $M_{n,theoretical} = 11250 \text{ gmol}^{-1}$ ,  $\bar{D} = 1.16$ ).

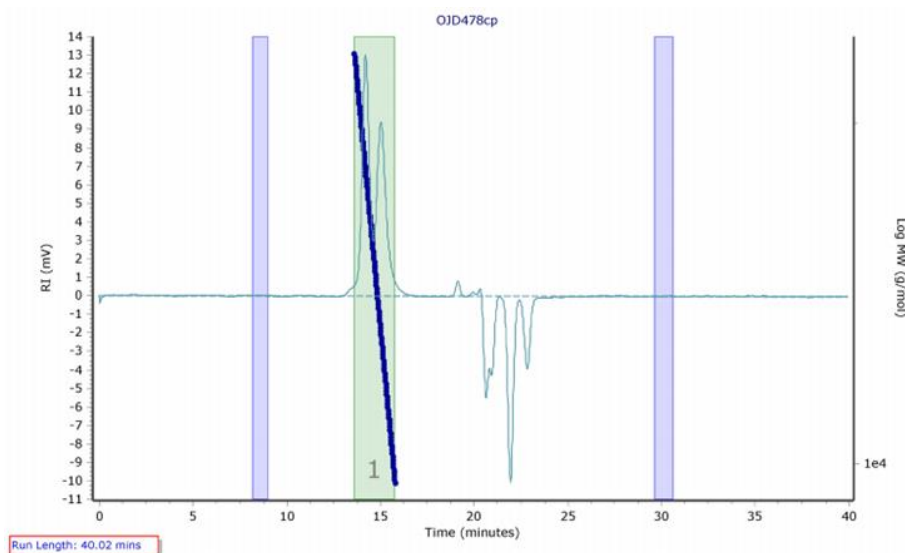


Figure 142. GPC chromatogram of the polymer attained from PA / CHO solution ROCOP using ligand **6** at 100 °C for three days (Section 5.3, Table 26, entry 10) ( $M_{n,GPC} = 19600 \text{ gmol}^{-1}$ ,  $M_{n,theoretical} = 19000 \text{ gmol}^{-1}$ ,  $\mathcal{D} = 1.12$ ).

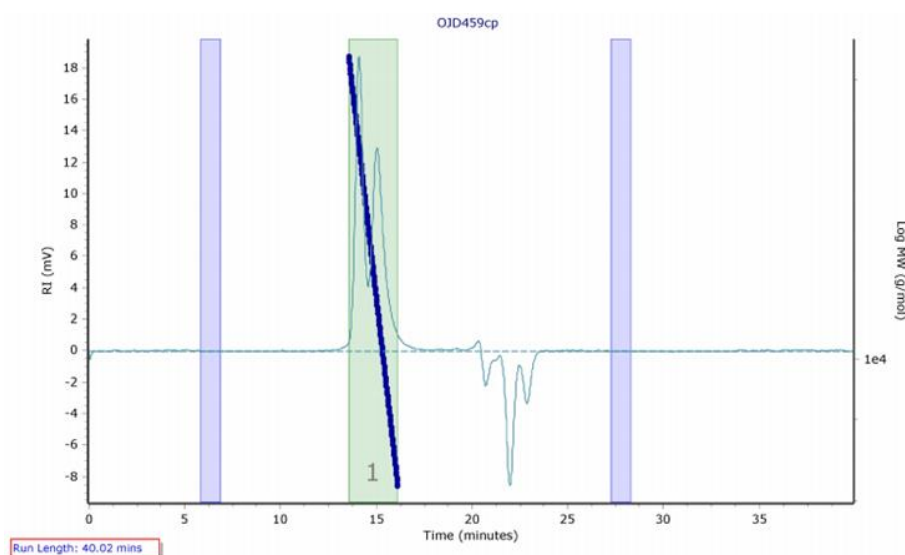


Figure 143. GPC chromatogram of the polymer attained from PA / CHO solution ROCOP using **Fe(6)OAc** at 100 °C for three days (Section 5.3, Table 26, entry 11) ( $M_{n,GPC} = 15300 \text{ gmol}^{-1}$ ,  $M_{n,theoretical} = 20350 \text{ gmol}^{-1}$ ,  $\mathcal{D} = 1.19$ ).

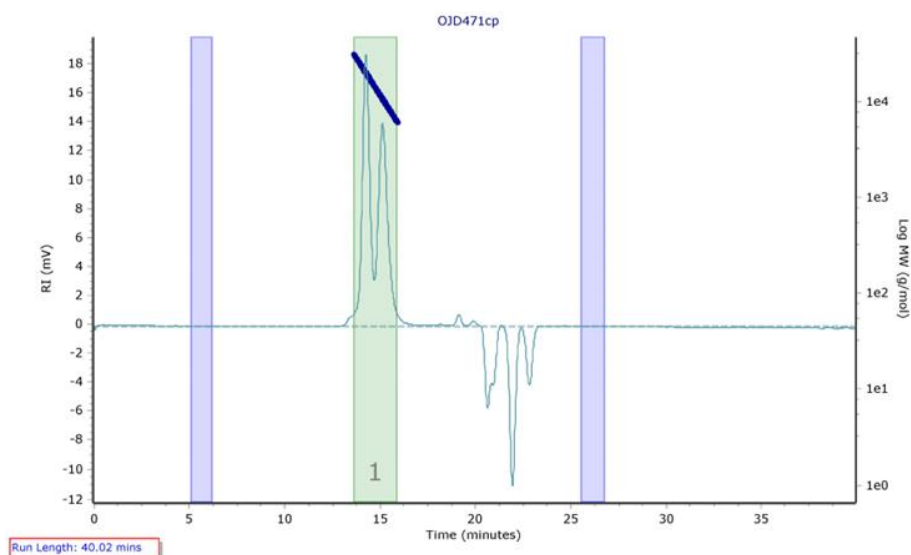


Figure 144. GPC chromatogram of the polymer attained from PA / CHO solution ROCOP using Fe(6)Cl at 100 °C for three days (Section 5.3, Table 26, entry 13) ( $M_{n,GPC} = 13600 \text{ gmol}^{-1}$ ,  $M_{n,theoretical} = 19100 \text{ gmol}^{-1}$ ,  $\bar{D} = 1.14$ ).

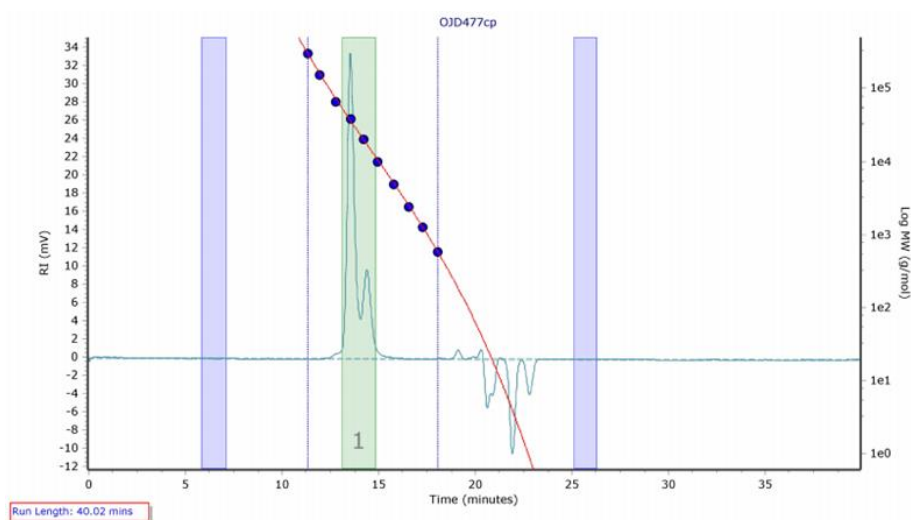


Figure 145. GPC chromatogram of the polymer attained from PA / CHO solution ROCOP using ligand 17 at 100 °C for three days (Section 5.3, Table 26, entry 18) ( $M_{n,GPC} = 29100 \text{ gmol}^{-1}$ ,  $M_{n,theoretical} = 23450 \text{ gmol}^{-1}$ ,  $\bar{D} = 1.09$ ).

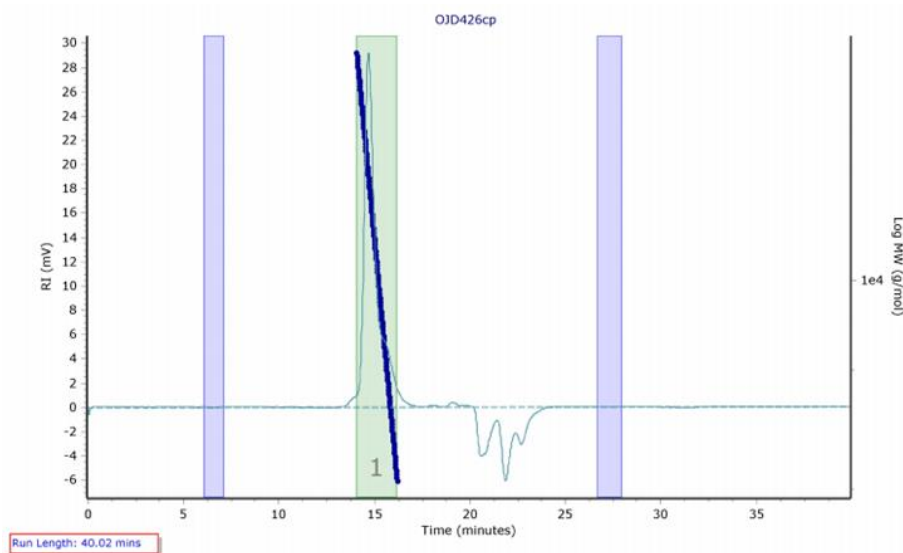


Figure 146. GPC chromatogram of the polymer attained from PA / CHO solution ROCOP using Fe(17)OAc at 100 °C for three days (Section 5.3, Table 26, entry 19) ( $M_{n,GPC} = 11550 \text{ g mol}^{-1}$ ,  $M_{n,theoretical} = 11500 \text{ g mol}^{-1}$ ,  $\bar{D} = 1.06$ ).

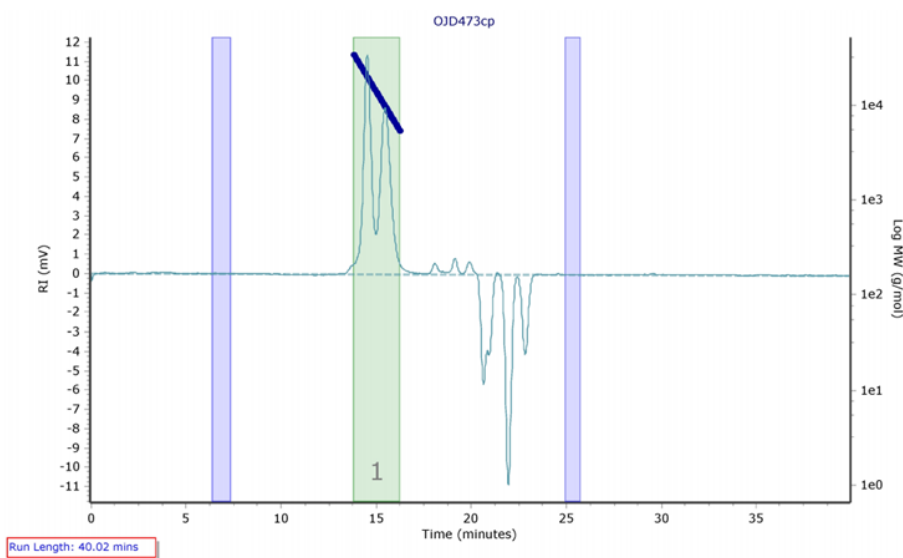


Figure 147. GPC chromatogram of the polymer attained from PA / CHO solution ROCOP using Fe(17)Cl at 100 °C for three days (Section 5.3, Table 26, entry 20) ( $M_{n,GPC} = 12550 \text{ g mol}^{-1}$ ,  $M_{n,theoretical} = 13700 \text{ g mol}^{-1}$ ,  $\bar{D} = 1.19$ ).

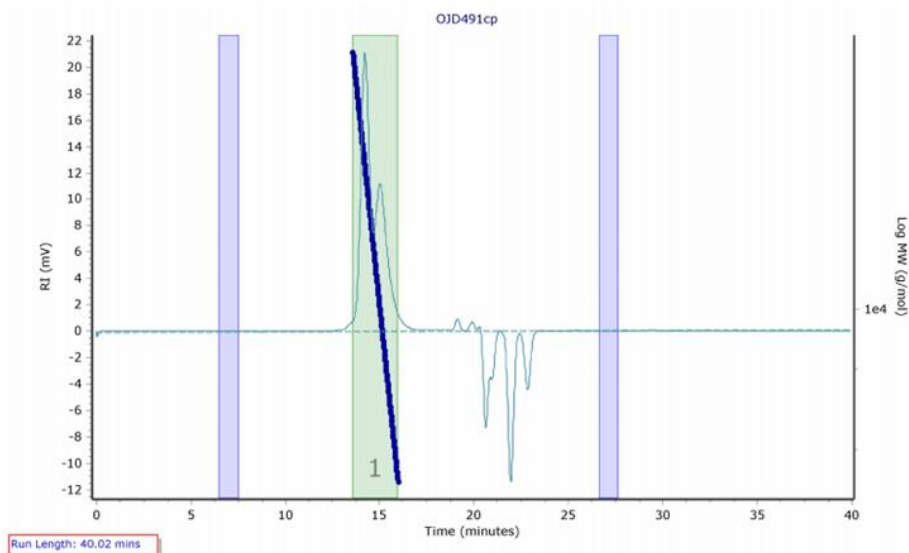


Figure 148. GPC chromatogram of the polymer attained from PA / CHO neat ROCOP using ligand **6** at 100 °C for 30 hours (Section 5.4, Table 27, entry 1) ( $M_{n, \text{GPC}} = 12500 \text{ gmol}^{-1}$ ,  $M_{n, \text{theoretical}} = 25250 \text{ gmol}^{-1}$ ,  $\bar{D} = 1.17$ ).

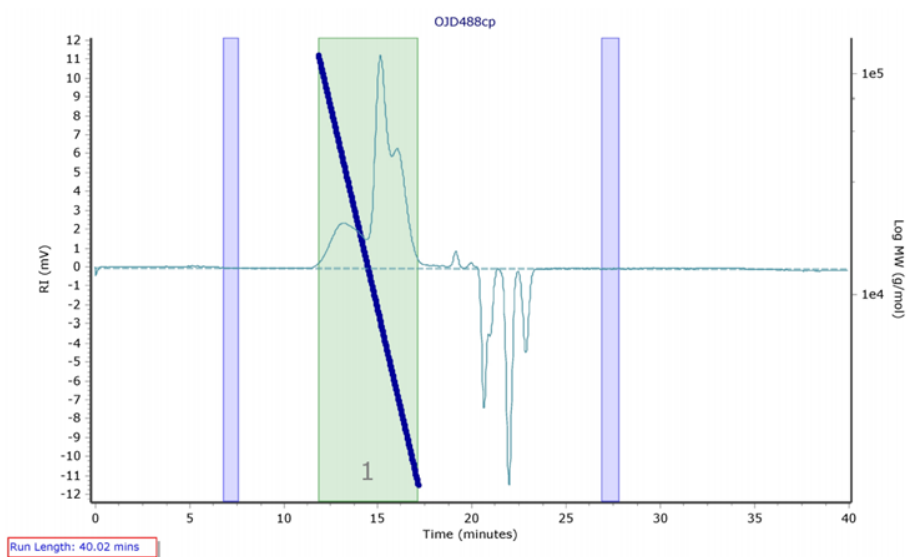


Figure 149. GPC chromatogram of the polymer attained from PA / CHO neat ROCOP using Fe(**6**)OAc at 80 °C for 72 hours (Section 5.4, Table 27, entry 3) ( $M_{n, \text{GPC}} = 5750 \text{ gmol}^{-1}$ ,  $M_{n, \text{theoretical}} = 7650 \text{ gmol}^{-1}$ ,  $\bar{D} = 2.46$ ).

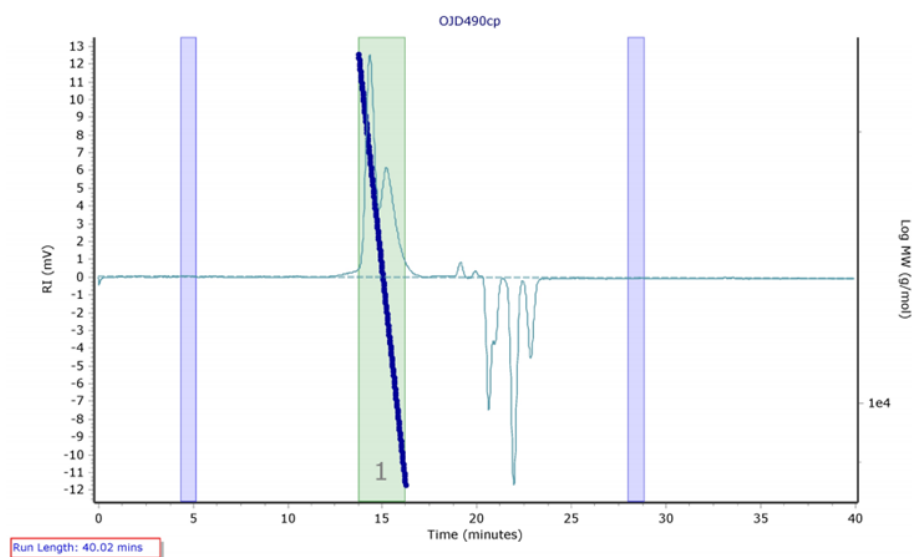


Figure 150. GPC chromatogram of the polymer attained from PA / CHO neat ROCOP using Fe(6)OAc at 100 °C for 30 hours (Section 5.4, Table 27, entry 4) ( $M_{n,GPC} = 18900 \text{ gmol}^{-1}$ ,  $M_{n,theoretical} = 24800 \text{ gmol}^{-1}$ ,  $\bar{D} = 1.20$ ).

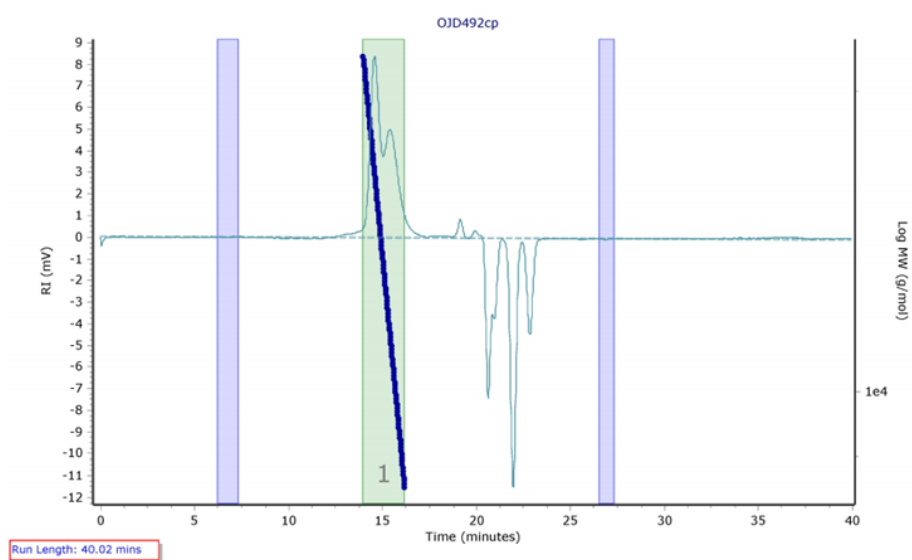


Figure 151. GPC chromatogram of the polymer attained from PA / CHO neat ROCOP using Fe(6)Cl at 100 °C for 30 hours (Section 5.4, Table 27, entry 5) ( $M_{n,GPC} = 15750 \text{ gmol}^{-1}$ ,  $M_{n,theoretical} = 18350 \text{ gmol}^{-1}$ ,  $\bar{D} = 1.17$ ).

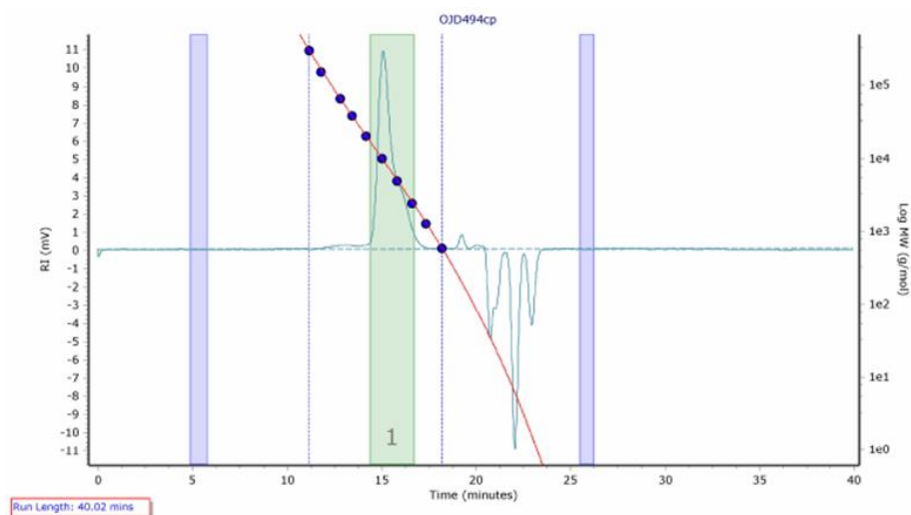


Figure 152. GPC chromatogram of the polymer attained from PA / CHO neat ROCOP using ligand **17** at 100 °C for 30 hours (Section 5.4, Table 27, entry 6) ( $M_{n,GPC} = 10400 \text{ gmol}^{-1}$ ,  $M_{n,theoretical} = 8450 \text{ gmol}^{-1}$ ,  $\bar{D} = 1.10$ ).

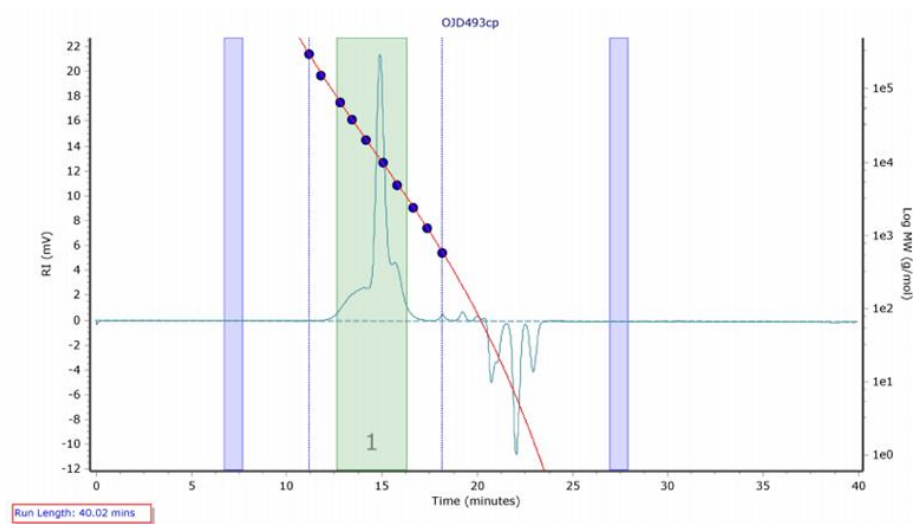


Figure 153. GPC chromatogram of the polymer attained from PA / CHO neat ROCOP using Fe(**17**)OAc at 100 °C for 30 hours (Section 5.4, Table 27, entry 7) ( $M_{n,GPC} = 13250 \text{ gmol}^{-1}$ ,  $M_{n,theoretical} = 16400 \text{ gmol}^{-1}$ ,  $\bar{D} = 1.28$ ).



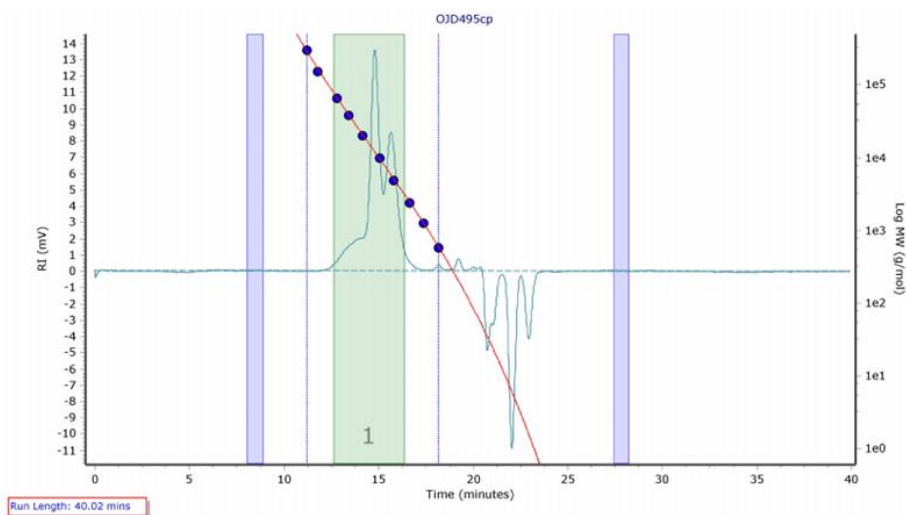


Figure 154. GPC chromatogram of the polymer attained from PA / CHO neat ROCOP using Fe(17)Cl at 100 °C for 30 hours (Section 5.4, Table 27, entry 8) ( $M_{n,GPC} = 10100 \text{ gmol}^{-1}$ ,  $M_{n,theoretical} = 16400 \text{ gmol}^{-1}$ ,  $\bar{D} = 1.35$ ).

## 7.9 DSC curves of the polymer derived from the ROCOP of PA and CHO

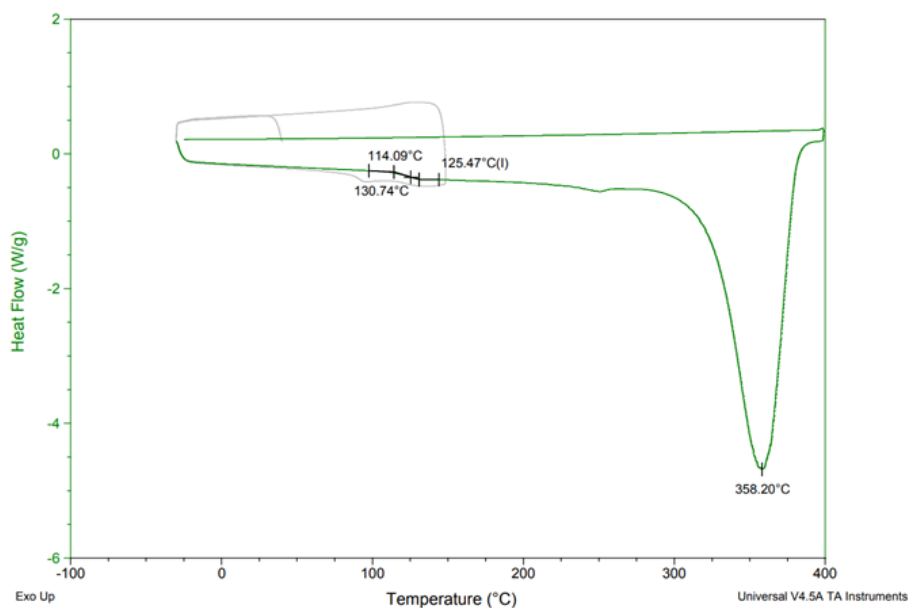


Figure 155. DSC curve of the polymer attained from PA / CHO solution ROCOP using Fe(3)OAc (Section 5.5, Table 28, entry 1).

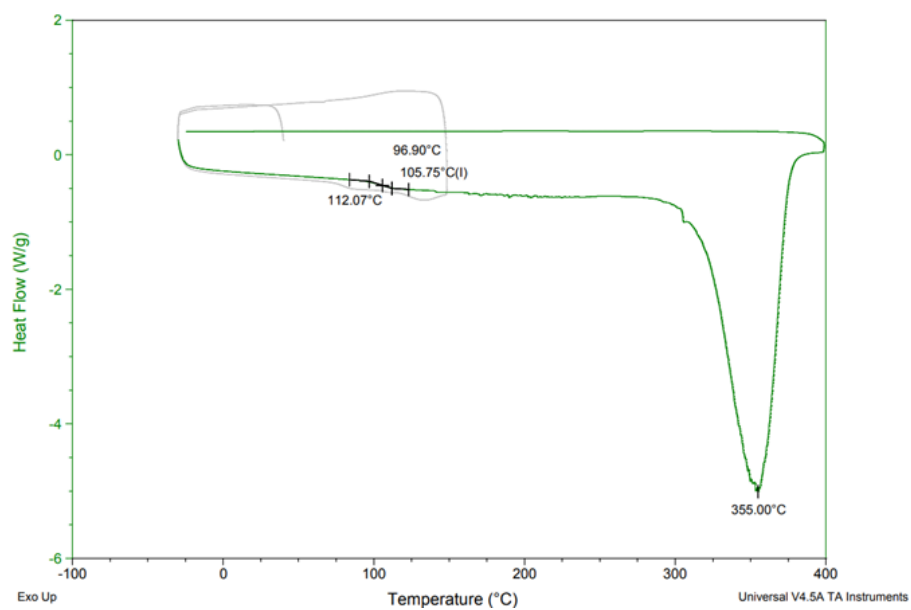


Figure 156. DSC curve of the polymer attained from PA / CHO solution ROCOP using ligand **6** (Section 5.5, Table 28, entry 2).

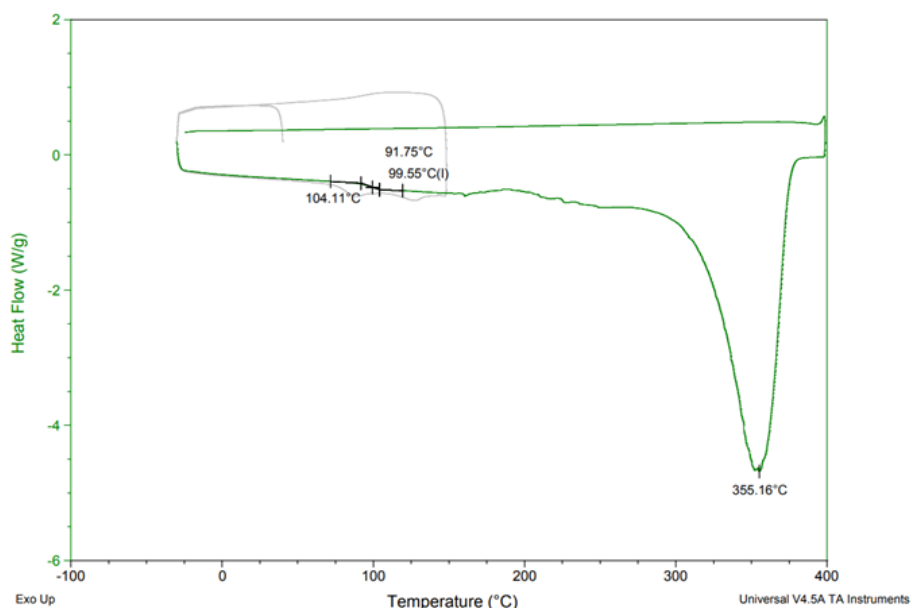


Figure 157. DSC curve of the polymer attained from PA / CHO solution ROCOP using Fe(6)OAc (Section 5.5, Table 28, entry 3).

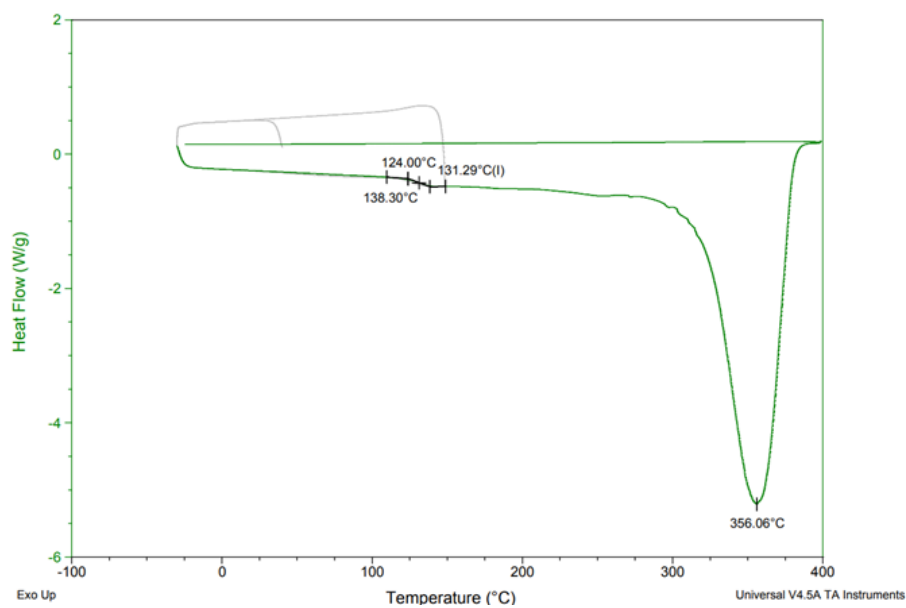


Figure 158. DSC curve of the polymer attained from PA / CHO solution ROCOP using Fe(6)Cl (Section 5.5, Table 28, entry 4).

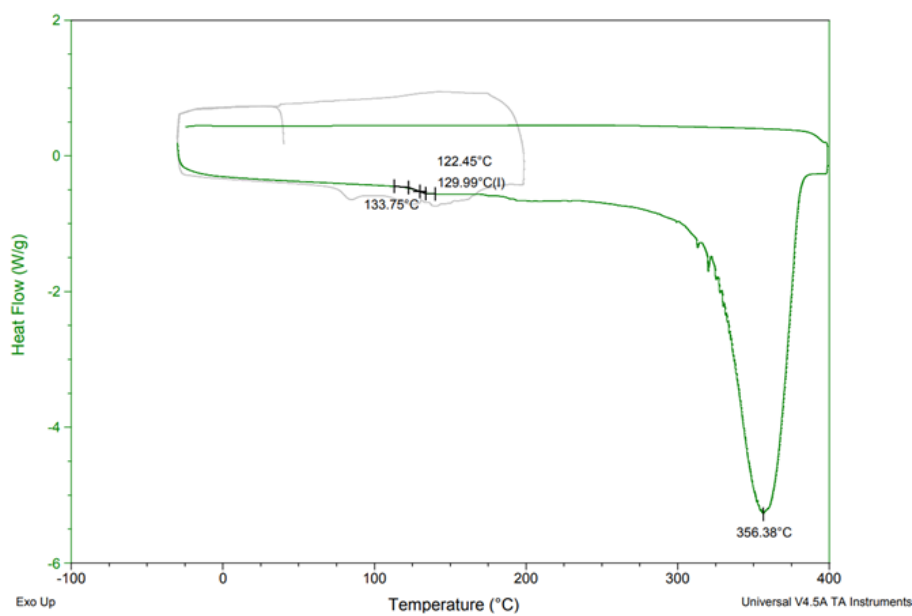


Figure 159. DSC curve of the polymer attained from PA / CHO solution ROCOP using ligand 17 (Section 5.5, Table 28, entry 5).

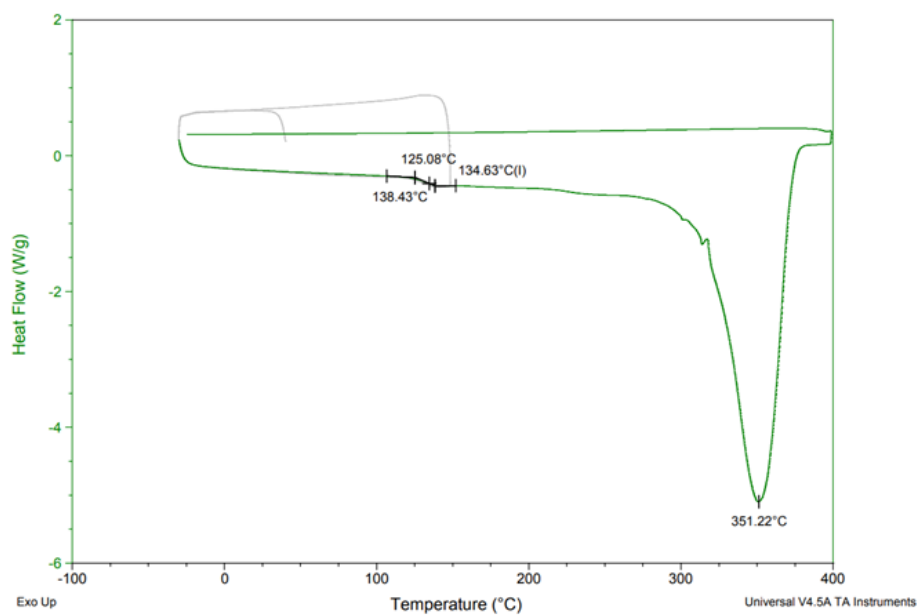


Figure 160. DSC curve of the polymer attained from PA / CHO solution ROCOP using Fe(17)OAc (Section 5.5, Table 28, entry 6).

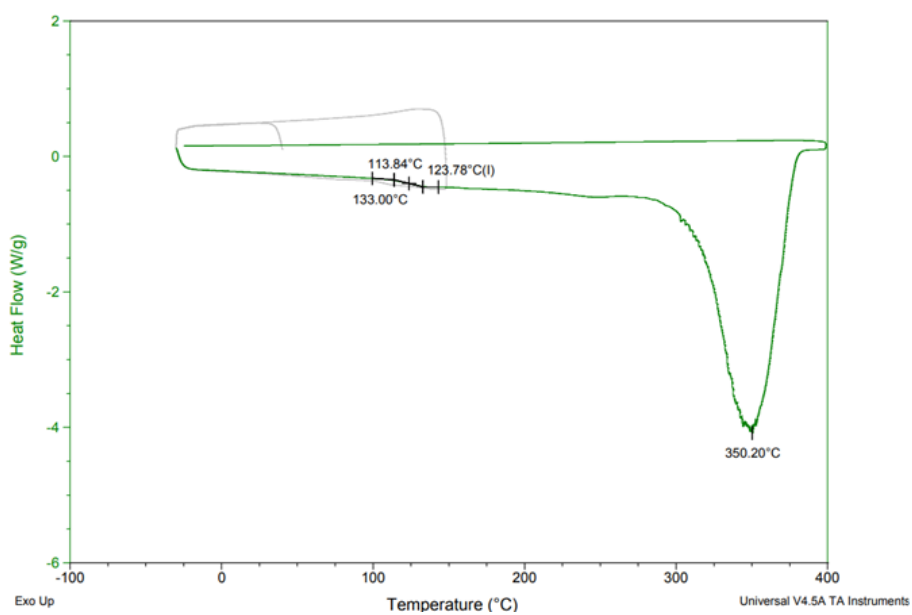


Figure 161. DSC curve of the polymer attained from PA / CHO solution ROCOP using Fe(17)Cl (Section 5.5, Table 28, entry 7).

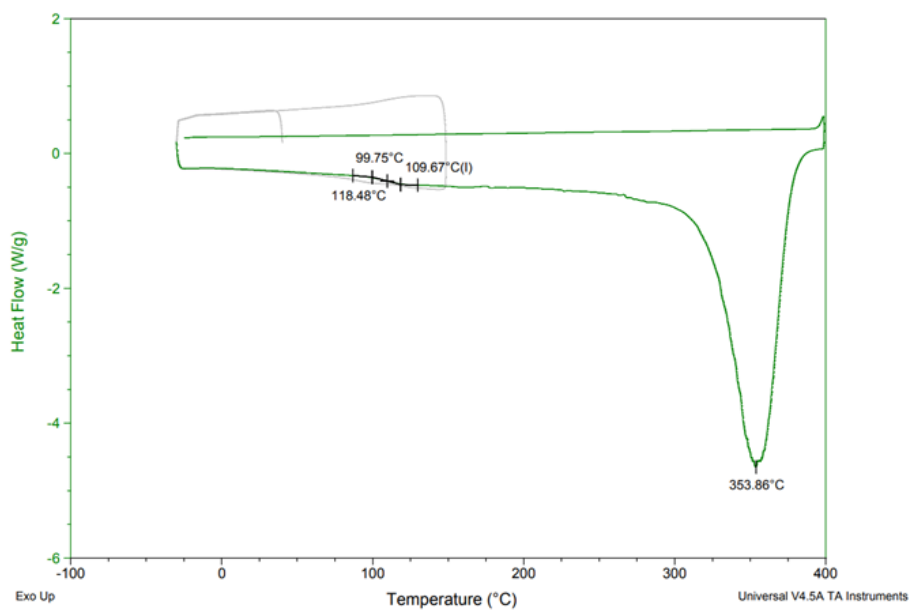


Figure 162. DSC curve of the polymer attained from PA / CHO neat ROCOP using ligand **6** (Section 5.5, Table 28, entry 8).

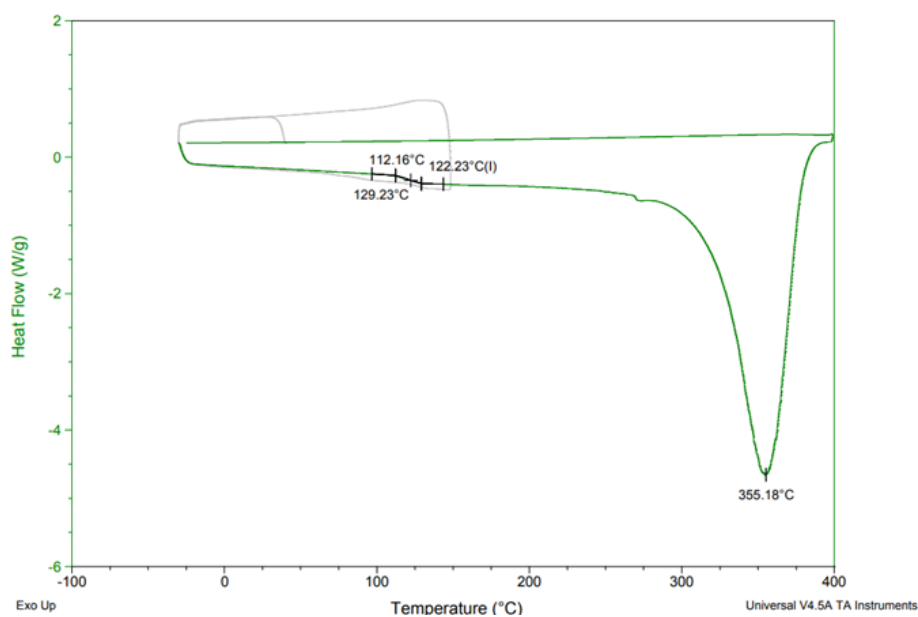


Figure 163. DSC curve of the polymer attained from PA / CHO neat ROCOP using Fe(**6**)OAc (Section 5.5, Table 28, entry 9).

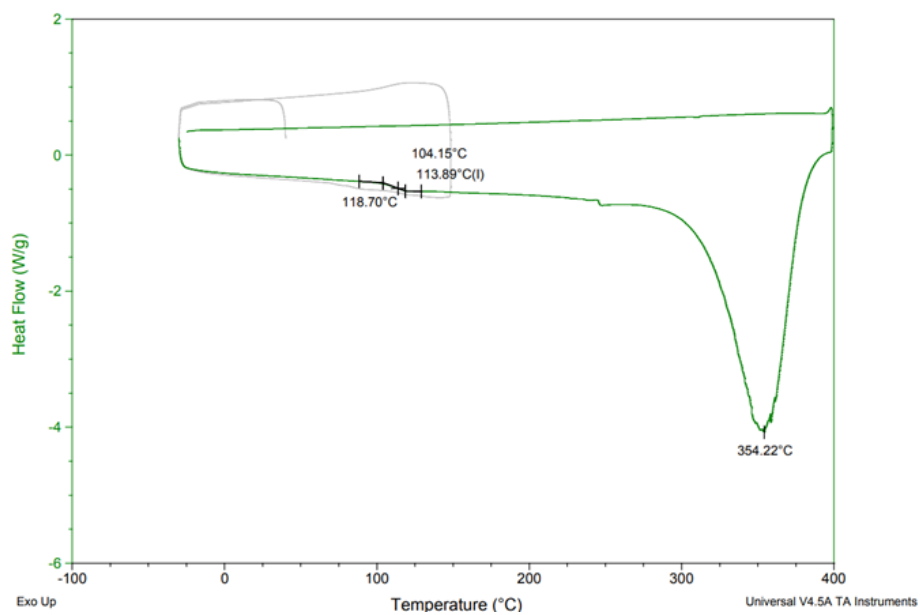


Figure 164. DSC curve of the polymer attained from PA / CHO neat ROCOP using Fe(6)Cl (Section 5.5, Table 28, entry 10).

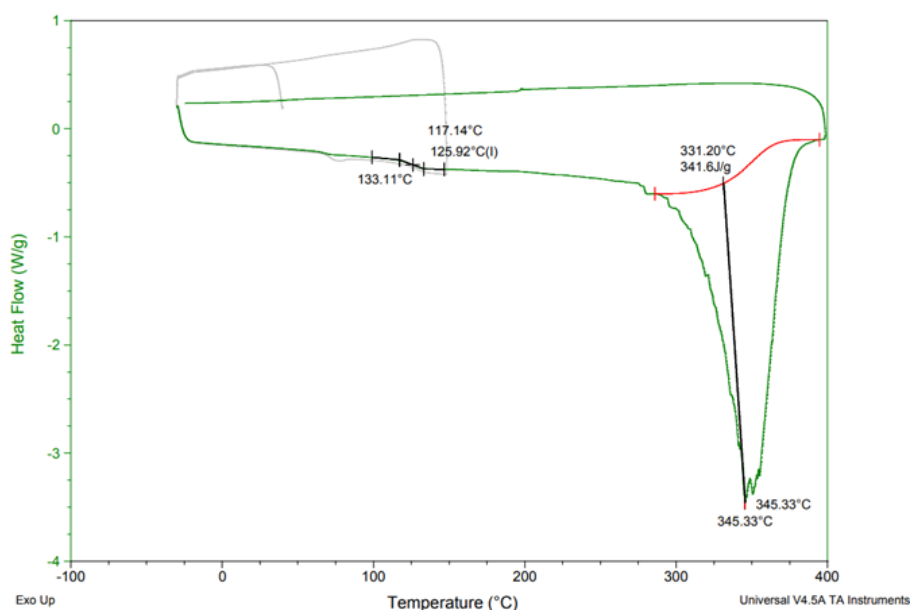


Figure 165. DSC curve of the polymer attained from PA / CHO neat ROCOP using Fe(17)OAc (Section 5.5, Table 28, entry 11).

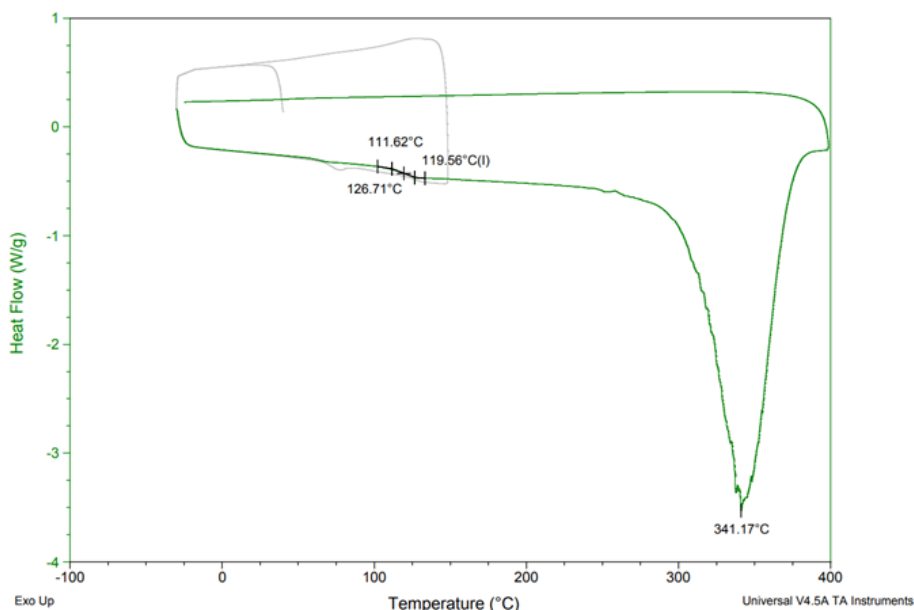


Figure 166. DSC curve of the polymer attained from PA / CHO neat ROCOP using Fe(17)Cl (Section 5.5, Table 28, entry 12).

## 7.10 MALDI–ToF analysis of the polymer derived from the ROCOP of PA and CHO

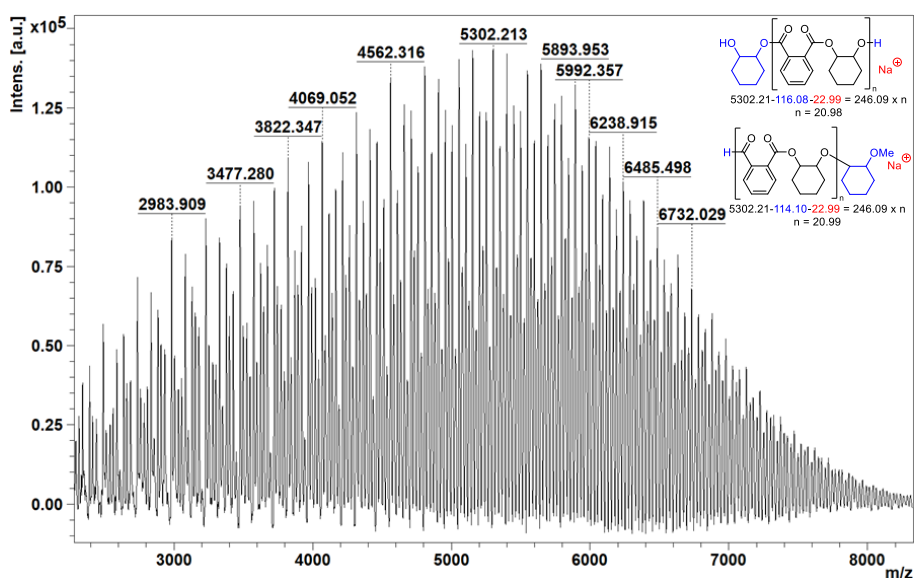


Figure 167A. MALDI–ToF spectrum of the polymer attained from PA / CHO solution ROCOP using Fe(3)OAc at 100 °C for three days (Section 5.3, Table 26, entry 6) ( $M_{p,MALDI-ToF} = 5302 \text{ gmol}^{-1}$ ,  $M_{n,GPC} = 10300 \text{ gmol}^{-1}$ ).

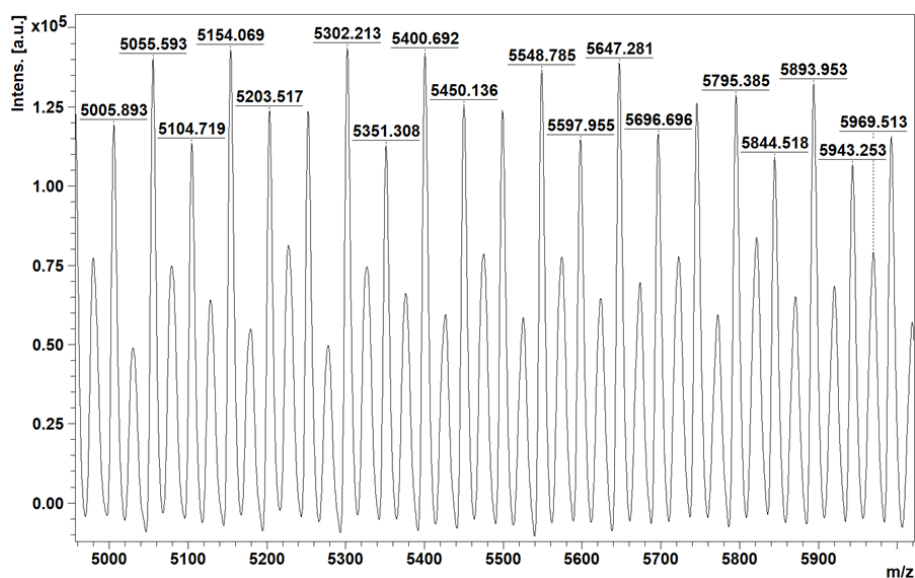


Figure 167B. Zoomed in MALDI–ToF spectrum of the polymer attained from PA / CHO solution ROCOP using Fe(3)OAc at 100 °C for three days (Section 5.3, Table 26, entry 6).

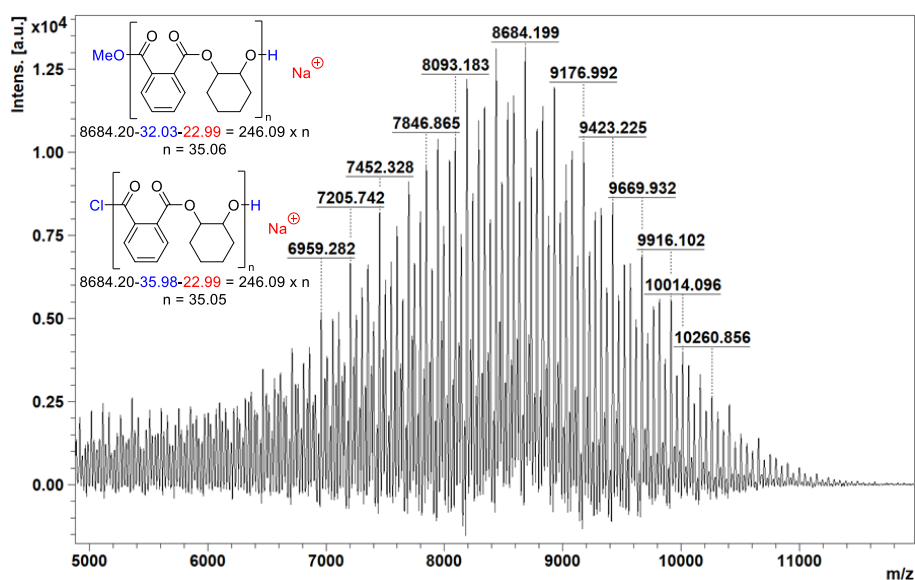


Figure 168A. MALDI–ToF spectrum of the polymer attained from PA / CHO solution ROCOP using ligand **6** at 100 °C for three days (Section 5.3, Table 26, entry 10) ( $M_{p,\text{MALDI-ToF}} = 8684 \text{ gmol}^{-1}$ ,  $M_{n,\text{GPC}} = 19600 \text{ gmol}^{-1}$ ).



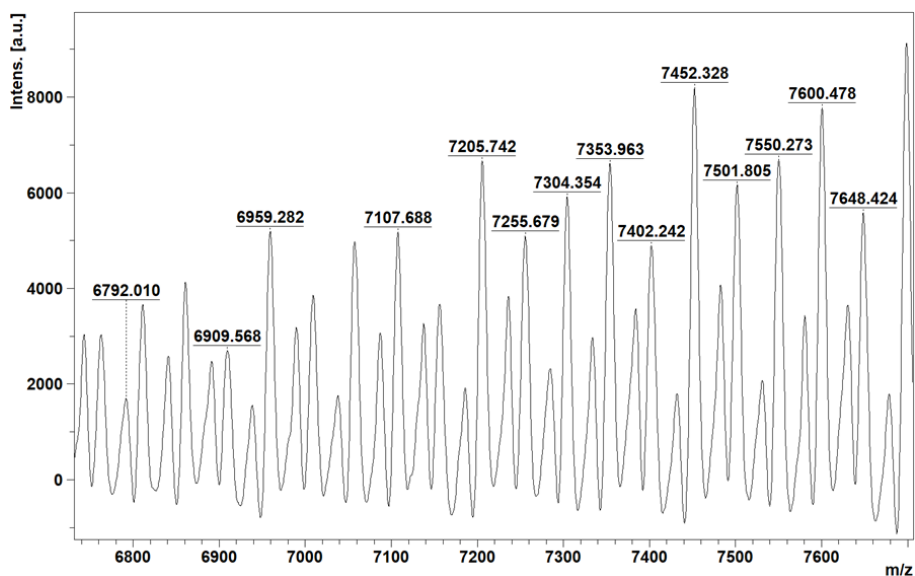


Figure 168B. Zoomed in MALDI-ToF spectrum of the polymer attained from PA / CHO solution ROCOP using ligand **6** at 100 °C for three days (Section 5.3, Table 26, entry 10).

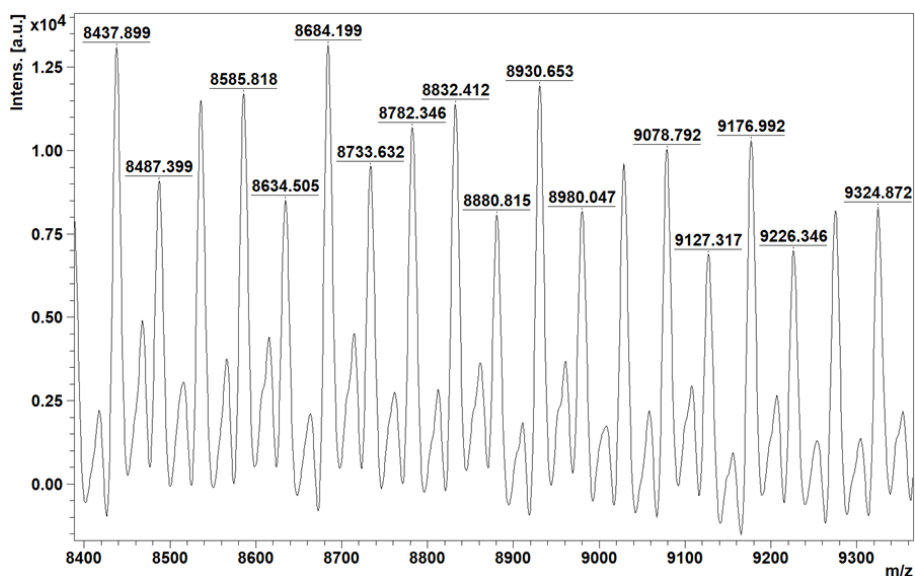


Figure 168C. Zoomed in MALDI-ToF spectrum of the polymer attained from PA / CHO solution ROCOP using ligand **6** at 100 °C for three days (Section 5.3, Table 26, entry 10).

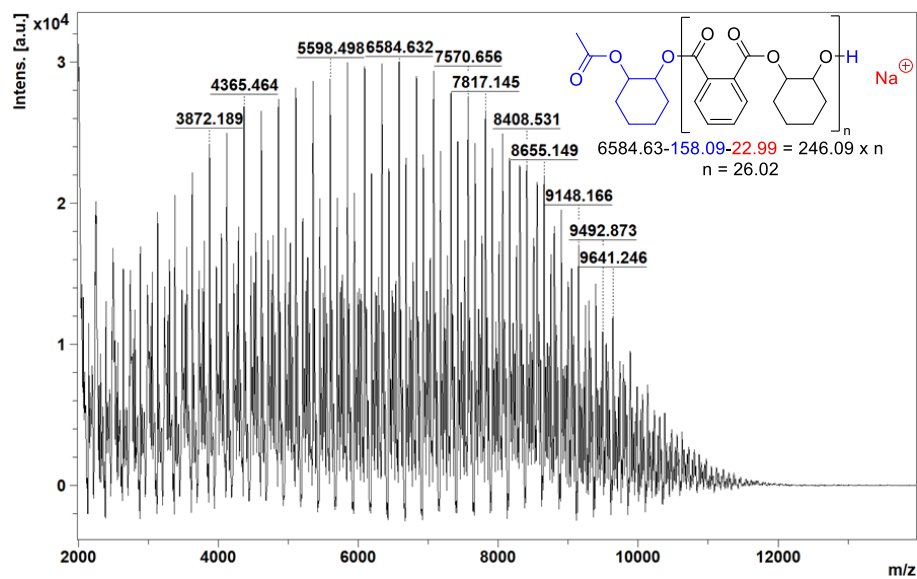


Figure 169A. MALDI–ToF spectrum of the polymer attained from PA / CHO solution ROCOP using Fe(6)OAc at 100 °C for three days (Section 5.3, Table 26, entry 11) ( $M_{p, \text{MALDI-ToF}} = 6585 \text{ gmol}^{-1}$ ,  $M_{n, \text{GPC}} = 15300 \text{ gmol}^{-1}$ ).

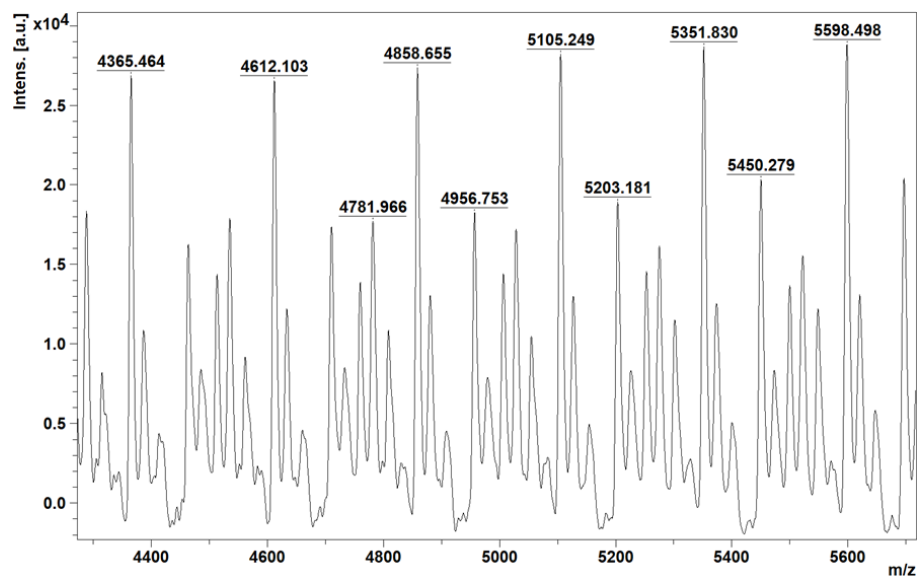


Figure 169B. Zoomed in MALDI–ToF spectrum of the polymer attained from PA / CHO solution ROCOP using Fe(6)OAc at 100 °C for three days (Section 5.3, Table 26, entry 11).

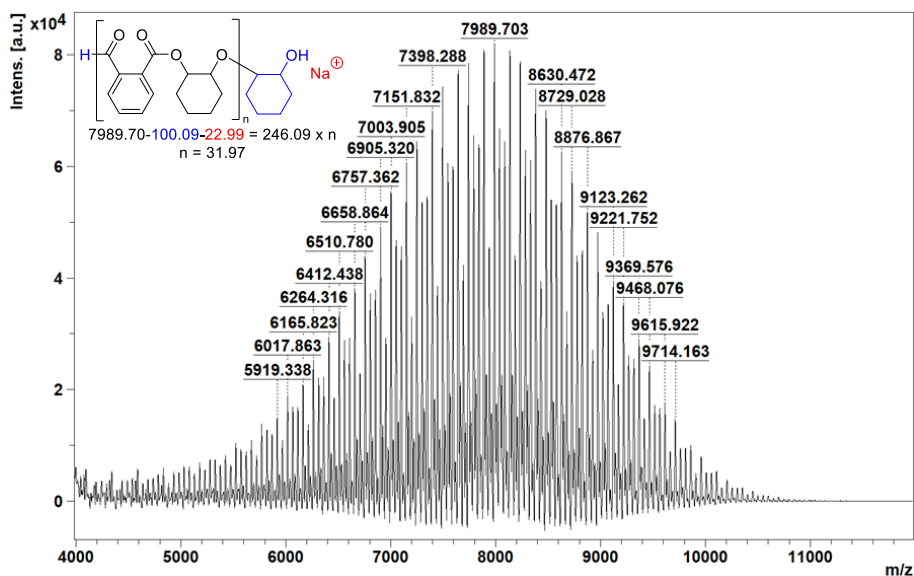


Figure 170A. MALDI–ToF spectrum of the polymer attained from PA / CHO solution ROCOP using Fe(6)Cl at 100 °C for three days (Section 5.3, Table 26, entry 13) ( $M_{p, \text{MALDI-ToF}} = 7990 \text{ gmol}^{-1}$ ,  $M_{n, \text{GPC}} = 13600 \text{ gmol}^{-1}$ ).

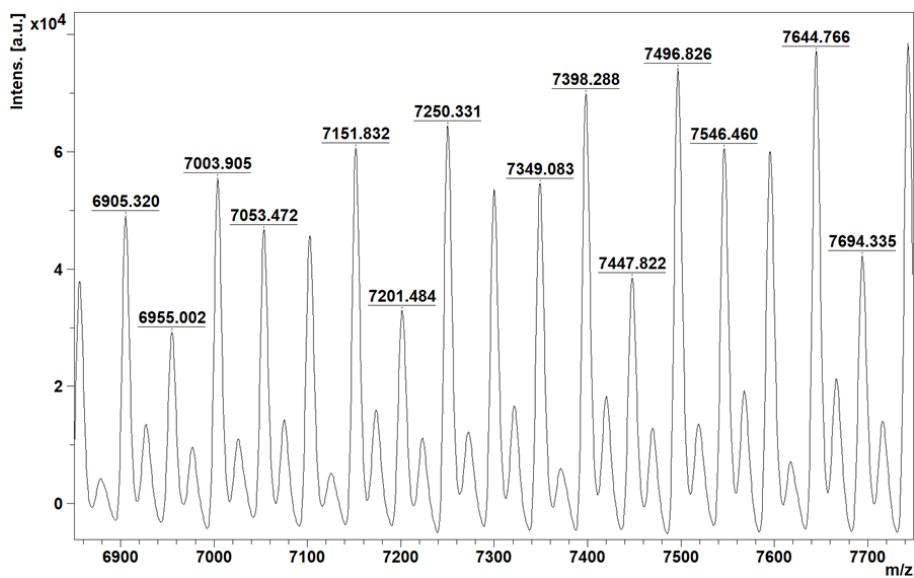


Figure 170B. Zoomed in MALDI–ToF spectrum of the polymer attained from PA / CHO solution ROCOP using Fe(6)Cl at 100 °C for three days (Section 5.3, Table 26, entry 13).

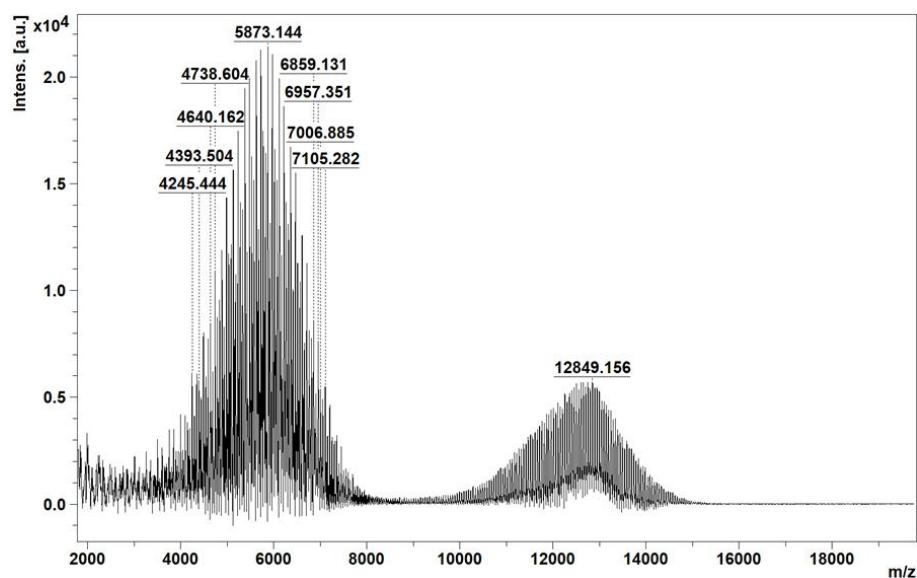


Figure 171A. MALDI–ToF spectrum of the polymer attained from PA / CHO solution ROCOP using Fe(17)OAc at 100 °C for three days (Section 5.3, Table 26, entry 19) ( $M_{p,\text{MALDI-ToF}} = 5873 \text{ gmol}^{-1}$  and  $12849 \text{ gmol}^{-1}$ ,  $M_{n,\text{GPC}} = 11550 \text{ gmol}^{-1}$ ).

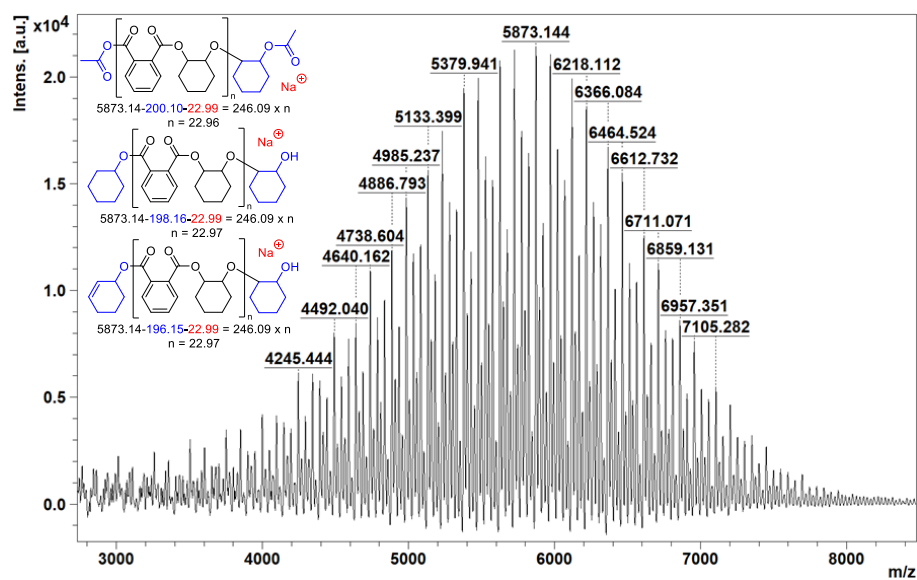


Figure 171B. Lower series MALDI–ToF spectrum of the polymer attained from PA / CHO solution ROCOP using Fe(17)OAc at 100 °C for three days (Section 5.3, Table 26, entry 19) ( $M_{p,\text{MALDI-ToF}} = 5873 \text{ gmol}^{-1}$ ,  $M_{n,\text{GPC}} = 11550 \text{ gmol}^{-1}$ ).

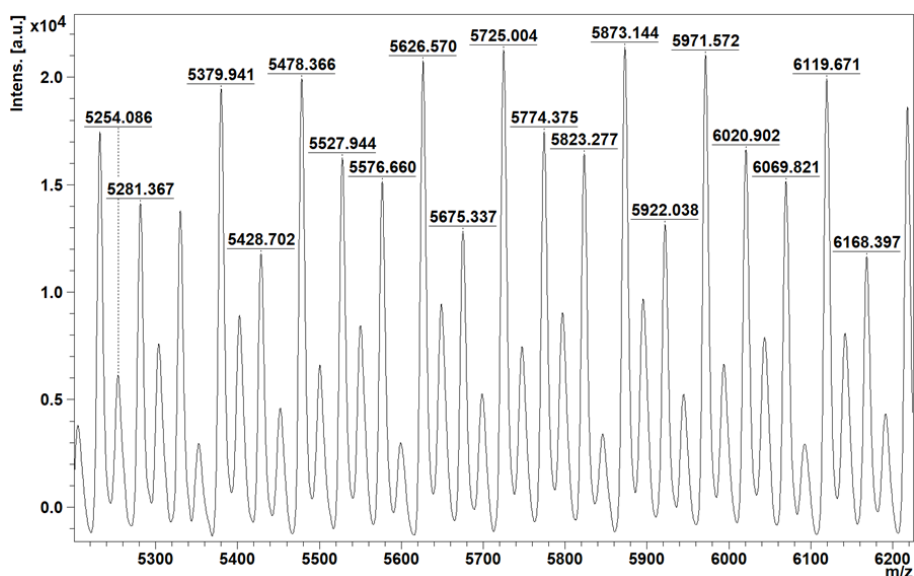


Figure 171C. Zoomed in lower series MALDI–ToF spectrum of the polymer attained from PA / CHO solution ROCOP using Fe(17)OAc at 100 °C for three days (Section 5.3, Table 26, entry 19).

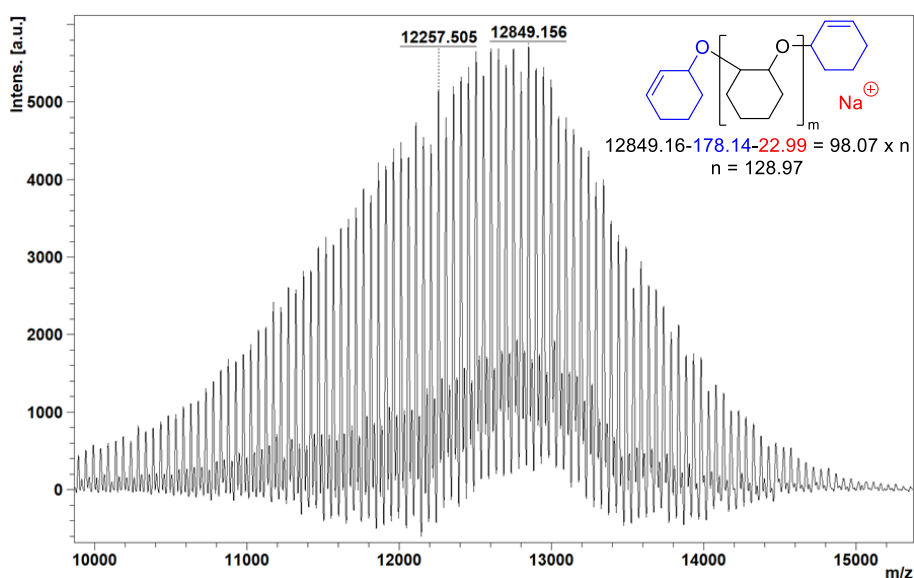


Figure 171D. Higher series MALDI–ToF spectrum of the polymer attained from PA / CHO solution ROCOP using Fe(17)OAc at 100 °C for three days (Section 5.3, Table 26, entry 19) ( $M_{p, \text{MALDI-ToF}} = 12849 \text{ g mol}^{-1}$ ,  $M_{n, \text{GPC}} = 11550 \text{ g mol}^{-1}$ ).

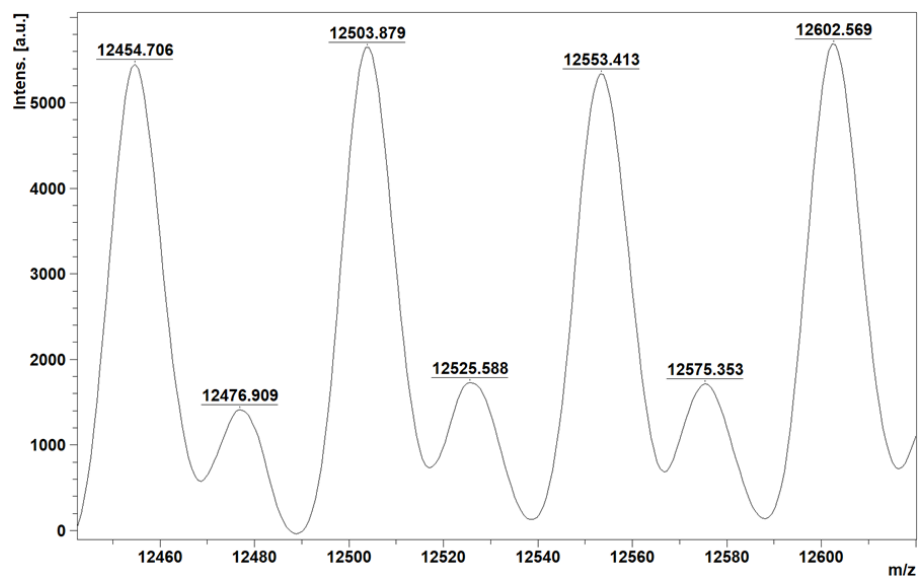


Figure 171E. Zoomed in higher series MALDI–ToF spectrum of the polymer attained from PA / CHO solution ROCOP using Fe(17)OAc at 100 °C for three days (Section 5.3, Table 26, entry 19).

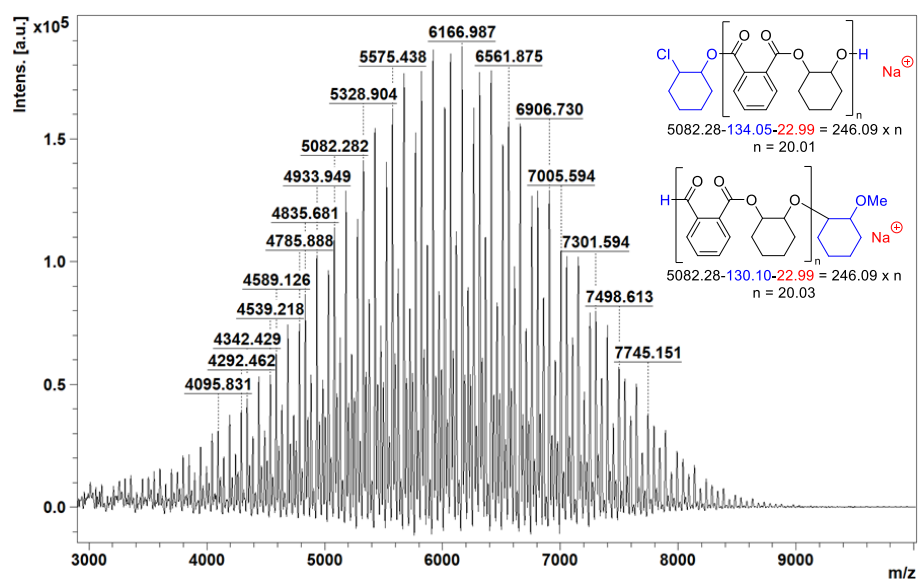


Figure 172A. MALDI–ToF spectrum of the polymer attained from PA / CHO solution ROCOP using Fe(17)Cl at 100 °C for three days (Section 5.3, Table 26, entry 20) ( $M_{p,\text{MALDI-ToF}} = 6167 \text{ gmol}^{-1}$ ,  $M_{n,\text{GPC}} = 12550 \text{ gmol}^{-1}$ ).

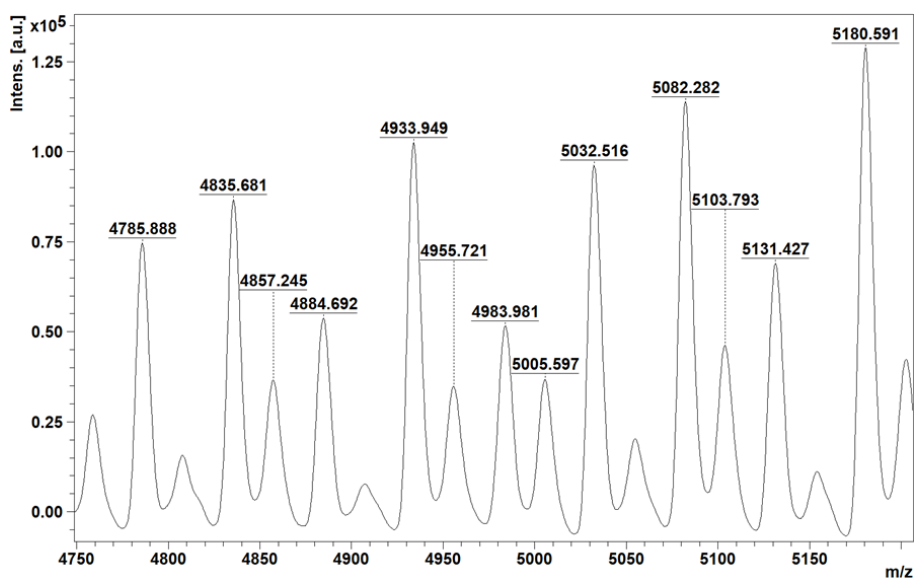


Figure 172B. Zoomed in MALDI–ToF spectrum of the polymer attained from PA / CHO solution ROCOP using Fe(17)Cl at 100 °C for three days (Section 5.3, Table 26, entry 20).

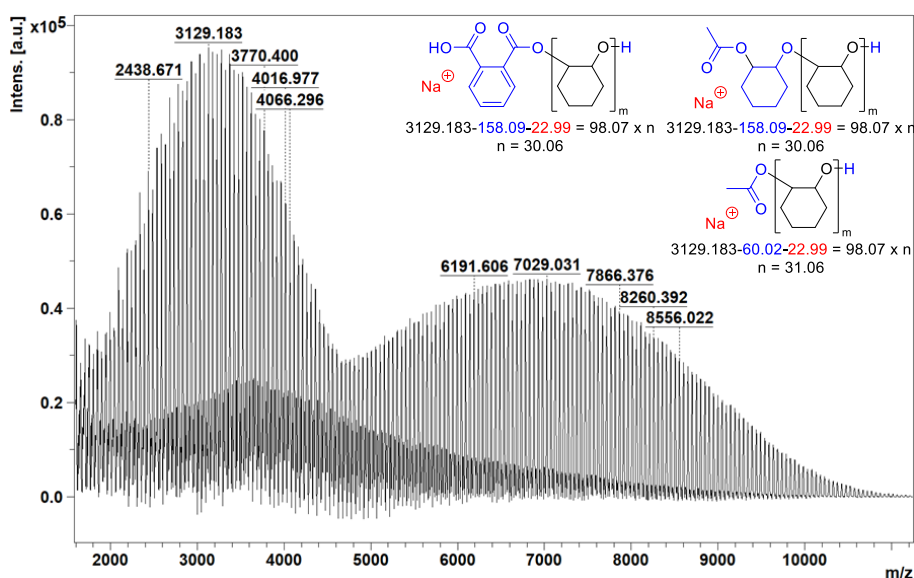


Figure 173A. MALDI–ToF spectrum of the polymer attained from PA / CHO neat ROCOP using Fe(6)OAc at 100 °C for 24 hours (Section 5.4, Table 27, entry 2) ( $M_{p, \text{MALDI-ToF}} = 3129 \text{ gmol}^{-1}$  and  $7029 \text{ gmol}^{-1}$ ,  $M_{n, \text{GPC}} = 8100 \text{ gmol}^{-1}$ ).

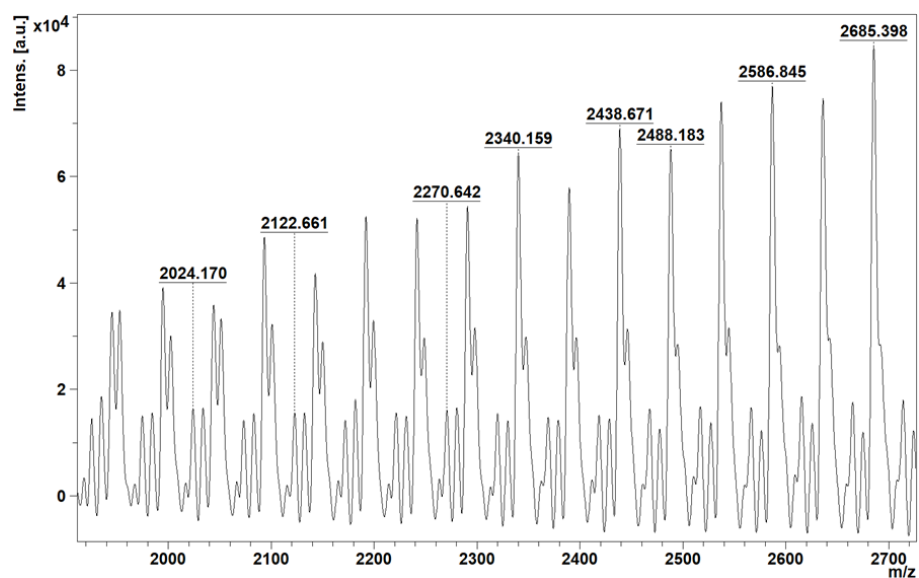


Figure 173B. Lower series, zoomed in MALDI–ToF spectrum of the polymer attained from PA / CHO neat ROCOP using Fe(6)OAc at 100 °C for 24 hours (Section 5.4, Table 27, entry 2).

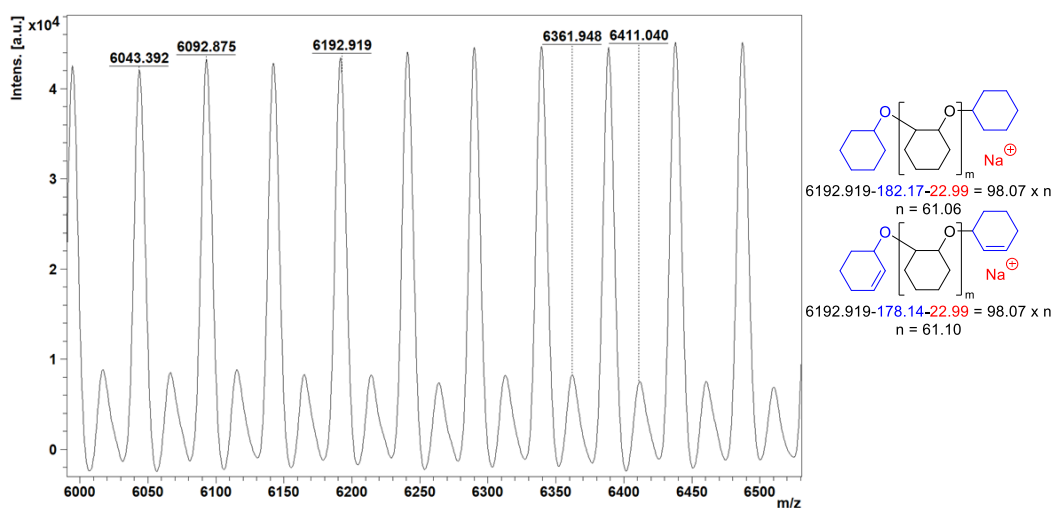


Figure 173C. Higher series, zoomed in MALDI–ToF spectrum of the polymer attained from PA / CHO neat ROCOP using Fe(6)OAc at 100 °C for 24 hours (Section 5.4, Table 27, entry 2).



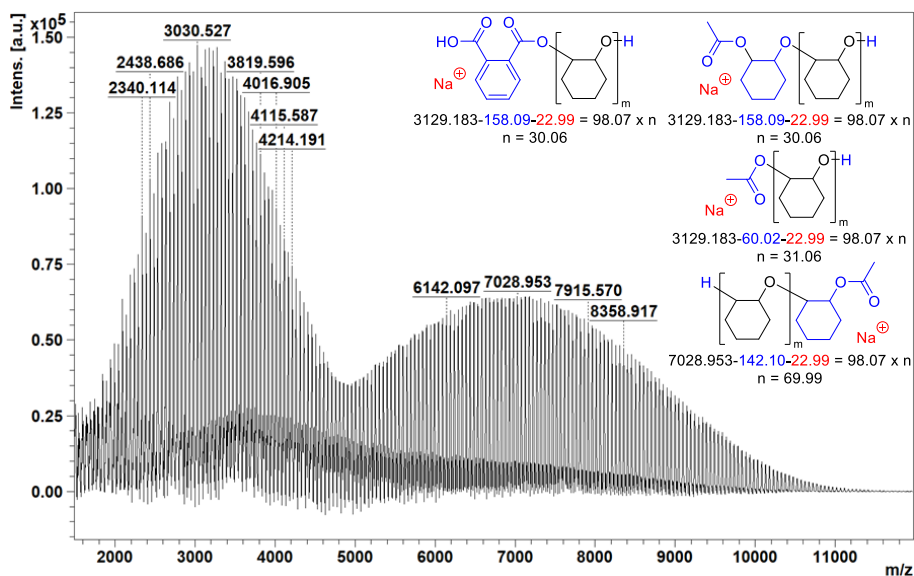


Figure 174A. MALDI-ToF spectrum of the polymer attained from PA / CHO neat ROCOP using Fe(6)OAc at 80 °C for 72 hours (Section 5.4, Table 27, entry 3) ( $M_{p,\text{MALDI-ToF}} = 3031 \text{ gmol}^{-1}$  and  $7029 \text{ gmol}^{-1}$ ,  $M_{n,\text{GPC}} = 5750 \text{ gmol}^{-1}$ ).

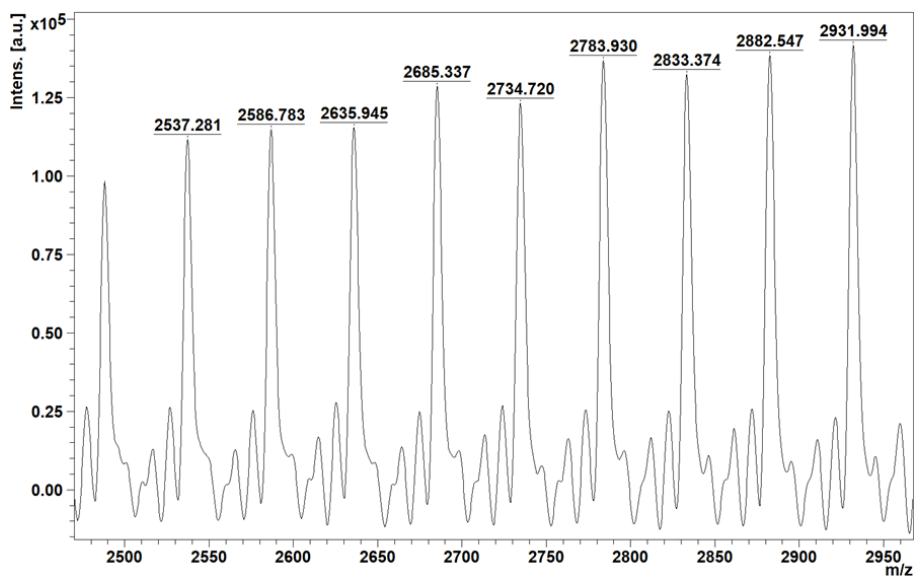


Figure 174B. Lower series, zoomed in MALDI-ToF spectrum of the polymer attained from PA / CHO neat ROCOP using Fe(6)OAc at 80 °C for 72 hours (Section 5.4, Table 27, entry 3).

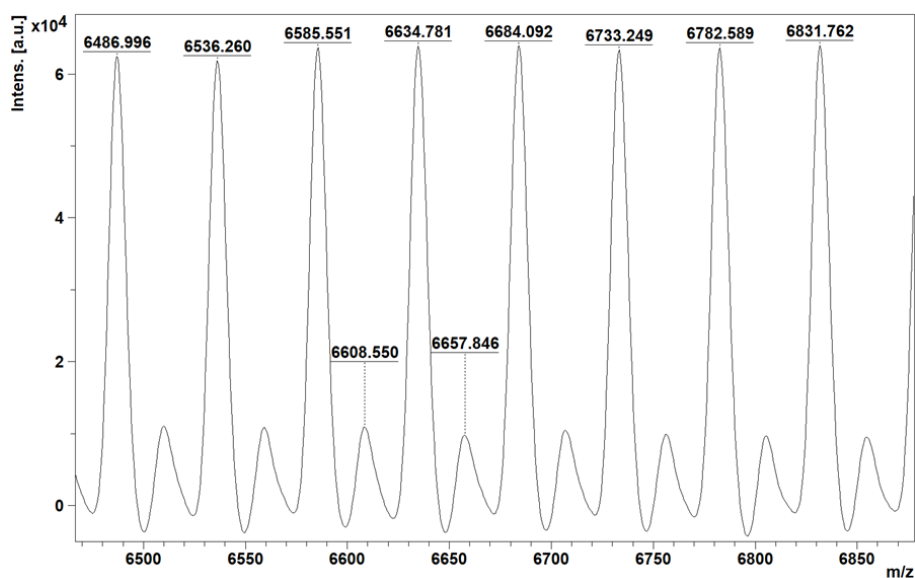


Figure 174C. Higher series, zoomed in MALDI-ToF spectrum of the polymer attained from PA / CHO neat ROCOP using Fe(6)OAc at 80 °C for 72 hours (Section 5.4, Table 27, entry 3).

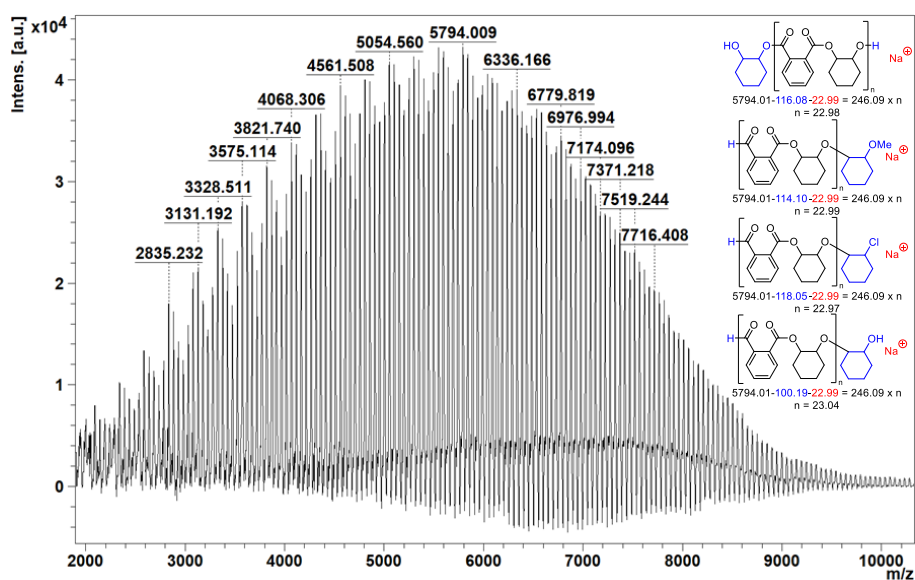


Figure 175A. MALDI-ToF spectrum of the polymer attained from PA / CHO neat ROCOP using Fe(6)OAc at 100 °C for 30 hours (Section 5.4, Table 27, entry 4) ( $M_{p,MALDI-ToF} = 5794 \text{ gmol}^{-1}$ ,  $M_{n,GPC} = 18900 \text{ gmol}^{-1}$ ).

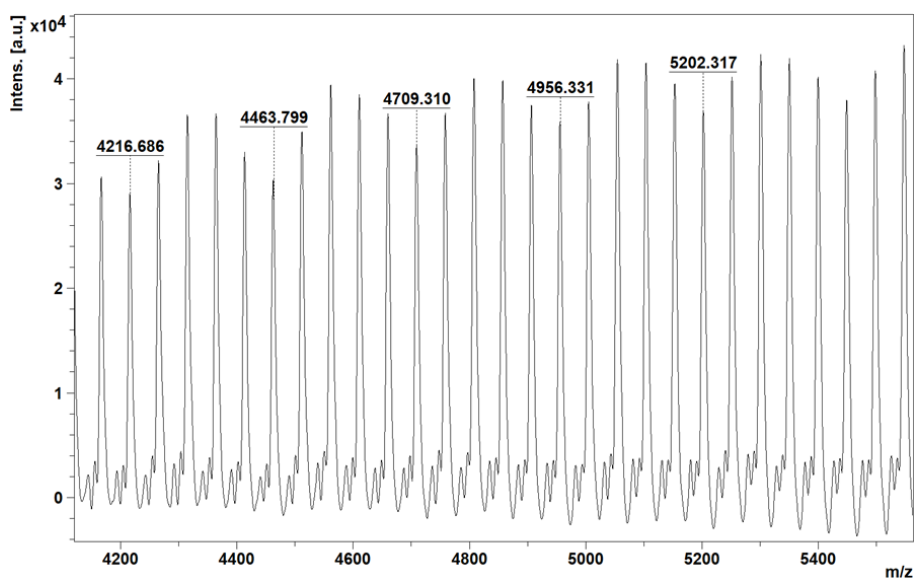


Figure 175B. Zoomed in MALDI–ToF spectrum of the polymer attained from PA / CHO neat ROCOP using Fe(6)OAc at 100 °C for 30 hours (Section 5.4, Table 27, entry 4).

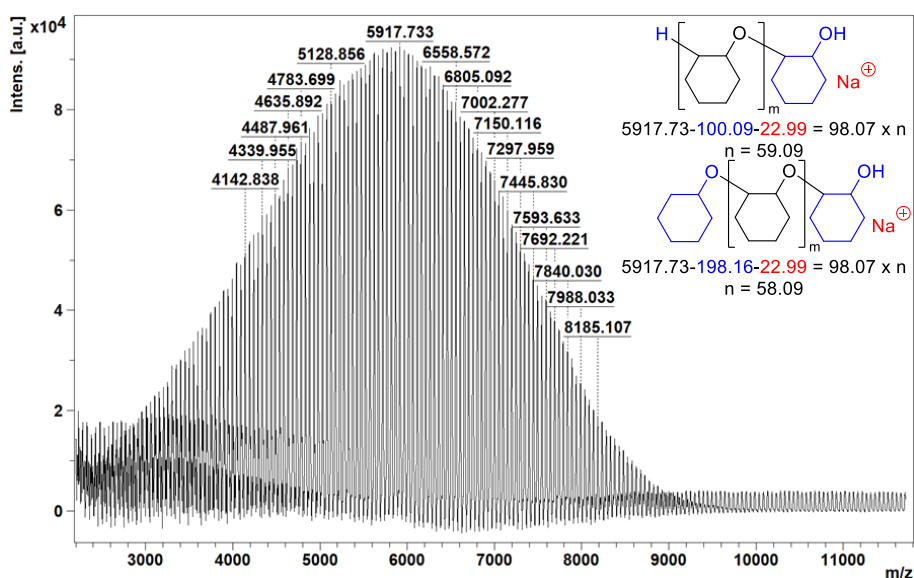


Figure 176A. MALDI–ToF spectrum of the polymer attained from PA / CHO neat ROCOP using Fe(6)Cl at 100 °C for 30 hours (Section 5.4, Table 27, entry 5) ( $M_{p,MALDI-ToF} = 5918 \text{ gmol}^{-1}$ ,  $M_{n,GPC} = 15750 \text{ gmol}^{-1}$ ).

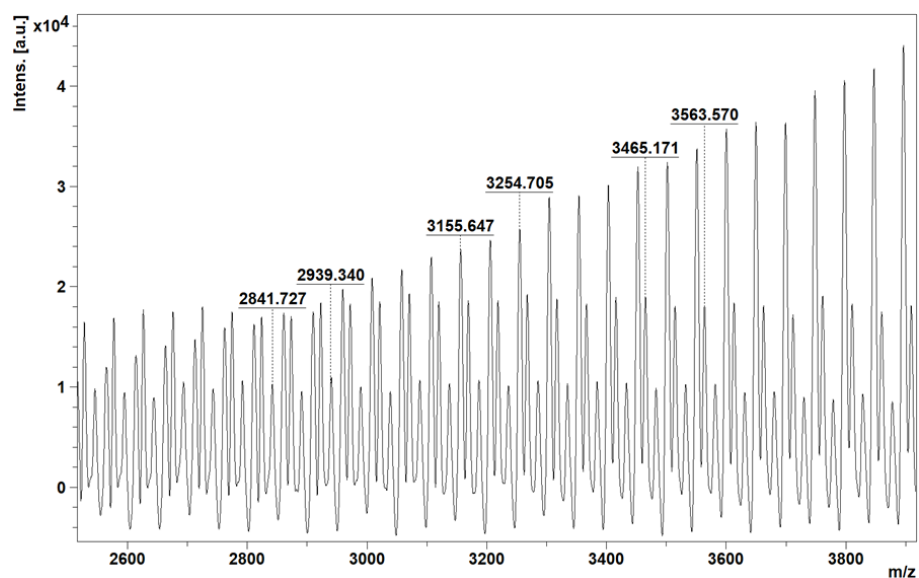


Figure 176B. Lower molecular weight, zoomed in MALDI-ToF spectrum of the polymer attained from PA / CHO neat ROCOP using Fe(6)Cl at 100 °C for 30 hours (Section 5.4, Table 27, entry 5).

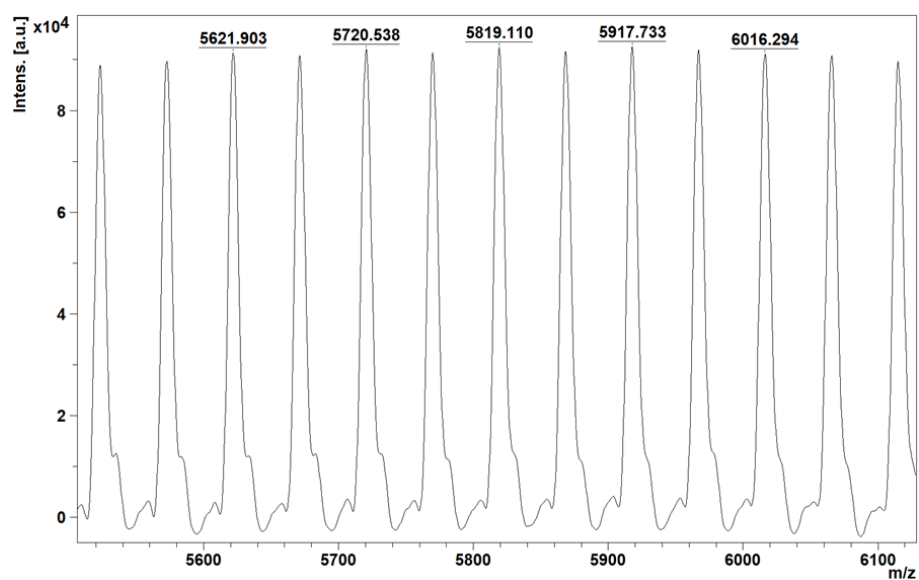


Figure 176C. Middle molecular weight, zoomed in MALDI-ToF spectrum of the polymer attained from PA / CHO neat ROCOP using Fe(6)Cl at 100 °C for 30 hours (Section 5.4, Table 27, entry 5).

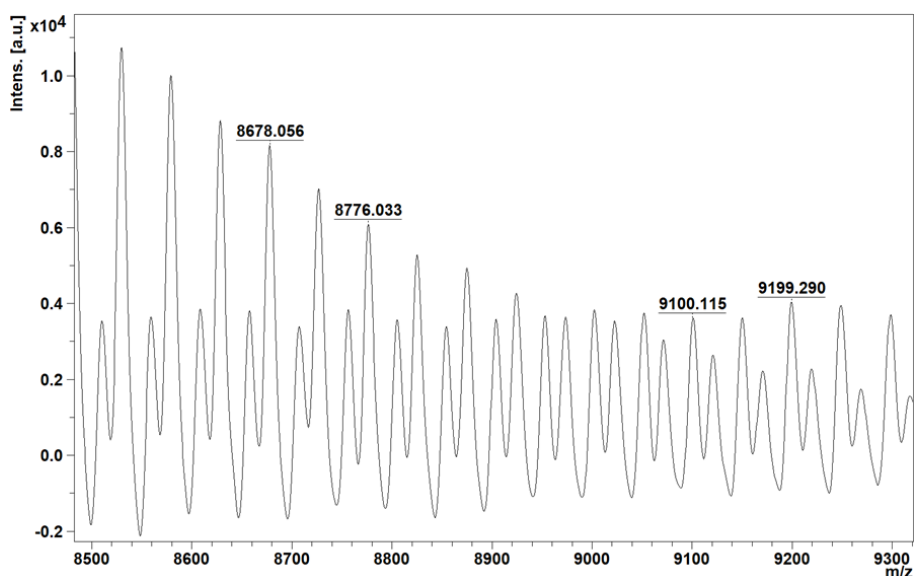


Figure 176D. Higher molecular weight, zoomed in MALDI–ToF spectrum of the polymer attained from PA / CHO neat ROCOP using Fe(6)Cl at 100 °C for 30 hours (Section 5.4, Table 27, entry 5).

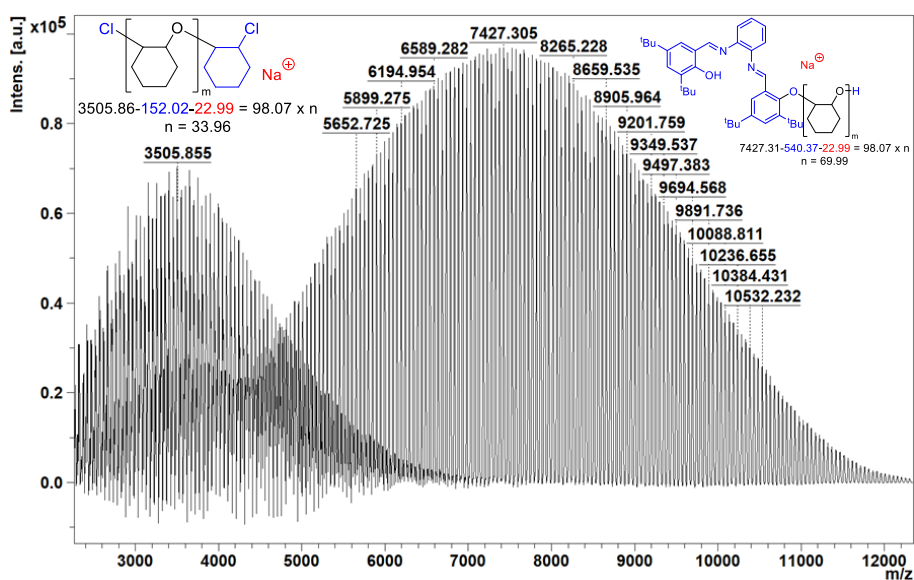


Figure 177A. MALDI–ToF spectrum of the polymer attained from PA / CHO neat ROCOP using ligand **17** at 100 °C for 30 hours (Section 5.4, Table 27, entry 6) ( $M_{p, \text{MALDI-ToF}} = 3506 \text{ gmol}^{-1}$  and  $7427 \text{ gmol}^{-1}$ ,  $M_{n, \text{GPC}} = 10400 \text{ gmol}^{-1}$ ).

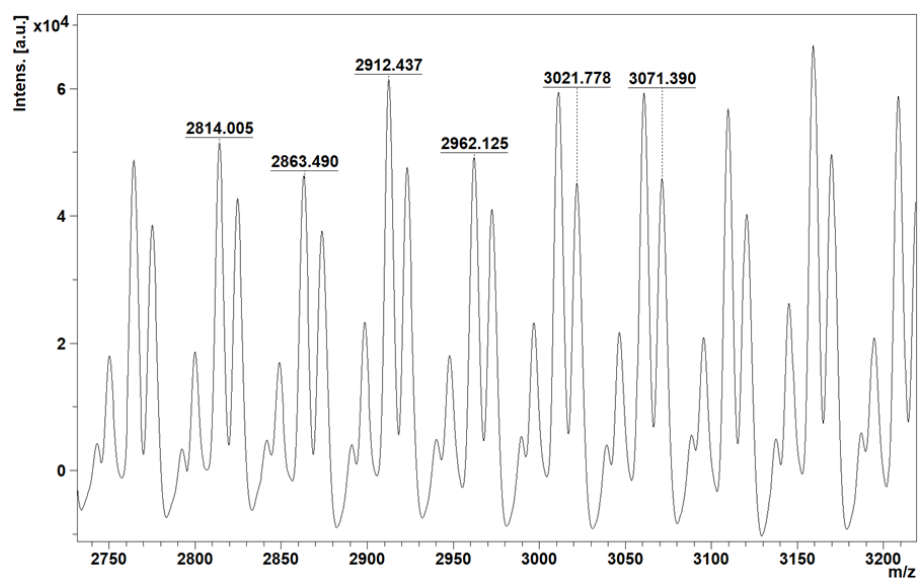


Figure 177B. Lower series, zoomed in MALDI–ToF spectrum of the polymer attained from PA / CHO neat ROCOP using ligand **17** at 100 °C for 30 hours (Section 5.4, Table 27, entry 6).

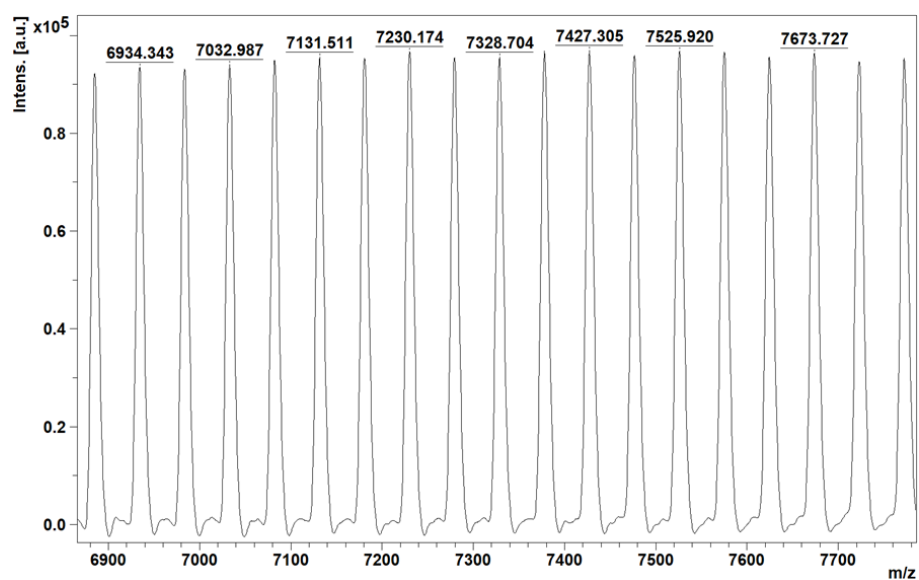


Figure 177C. Higher series, zoomed in MALDI–ToF spectrum of the polymer attained from PA / CHO neat ROCOP using ligand **17** at 100 °C for 30 hours (Section 5.4, Table 27, entry 6).